Investigations of LIMD1 in miRNA-mediated gene silencing and cancers

Yigen Li, MSc, BSc (Hons)

Thesis submitted to Queen Mary University of London for the degree of

Doctor of Philosophy

May 2018

Required statement of originality for inclusion in research degree theses

I, YIGEN LI, confirm that the research included within this thesis is my own work or that where it has been carried out in collaboration with, or supported by others, that this is duly acknowledged below and my contribution indicated. Previously published material is also acknowledged below.

I attest that I have exercised reasonable care to ensure that the work is original, and does not to the best of my knowledge break any UK law, infringe any third party's copyright or other Intellectual Property Right, or contain any confidential material.

I accept that the College has the right to use plagiarism detection software to check the electronic version of the thesis.

I confirm that this thesis has not been previously submitted for the award of a degree by this or any other university.

Signature: 

Date: 01.05.2018

To myself I am only a child playing on the beach, while vast oceans of truth lie undiscovered before me

Sir Isaac Newton

Abstract

In recent years, LIM domains-containing protein 1 (LIMD1) has been identified as a critical component in microRNA (miRNA)-induced silencing complex (miRISC) to regulate miRNA-mediated gene silencing. Human Argonaute (AGO) 2 with its family members (AGO1-4) are critical for the biogenesis of miRNA and thus miRNA-mediated gene silencing. In this study, we have investigated the direct interaction interfaces between LIMD1 and AGO2. A distinct interface within LIMD1, amino acid (a.a) 140-166, is identified to be responsible for the binding to AGO2 and other members of AGO family. Furthermore, the Linker-2 (L2) domain within AGO2 is identified to be responsible for LIMD1 binding and its dependency on the phosphorylation at serine 387 (S387) residue within the L2 domain of AGO2. The phospho-mimic mutant (S387E) enhances the binding of AGO2 to LIMD1, whereas the phospho-deficient mutant (S387A) attenuates AGO2-LIMD1 interaction. In addition, the association of LIMD1 with other AGOs is also dependent on the phosphorylation at the equivalent conserved serine residue within the L2 domain on other AGOs.

In addition to the above aspects, LIMD1 is a tumour suppressor gene frequently down-regulated in more than 75% human lung tumours. Because of their loss of expressions or functions, it is of the inherent difficulty in targeting tumour suppressor genes to treat cancers. In this study, the concept of synthetic lethality was used to identify possible protein kinases, the ablation of which are synthetically lethal to LIMD1 negative cancer cell lines. As a result, drugs that target these kinases may represent novel targeted therapies for LIMD1 negative lung tumours. ACVR2B and STK39 are validated to be synthetically lethal with LIMD1 loss. Additionally, the complete loss of LIMD1 expression causes a dramatic increase of STK39 expression due to miRNA-mediated gene silencing pathway. The inverse relationship between LIMD1 and STK39 may represent a conserved and fundamental signalling response and may be a predictive marker for STK39-targeted therapy.

Keyword: LIMD1, Argonaute, miRNA silencing, miRISC, synthetic lethality, STK39, p38

Publications:

Argonaute Utilization for miRNA Silencing Is Determined by Phosphorylation-Dependent Recruitment of LIM-Domain-Containing Proteins

Katherine S. Bridge[†], Kunal M. Shah[†], **Yigen Li**[†], Daniel E. Foxler, Duncan C. Miller, Sybil C.K. Wong, Kathryn M. Davidson, John G. Foster, Ruth Rose, Michael R. Hodgkinson, Paulo S. Ribeiro, A. Aziz Aboobaker, Kenta Yashiro, Xiaozhong Wang, Paul R. Graves, Michael J. Plevin, Dimitris Lagos & Tyson V. Sharp
Cell reports. 2017 Jul 5; 20(1):173-187

Acknowledgements

I would like to express my immeasurable gratitude to Dr Tyson V. Sharp for giving me the opportunity to learn and work at his lab, and for his stimulating suggestions, guidance and support from the very first day when I started the MSc project to the very last day of my PhD study. His inspiration and especially his encouragement are greatly appreciated when I faced crisis situations. Also, his patience and humour always helped to deal with the pressure of my PhD.

I would also like to show my gratitude to Dr Sybil C.K. Wong, Dr Daniel E. Foxler, and John G. Foster for teaching me their techniques at the very beginning of my PhD. I would also like to sincerely thank Dr Daniel E. Foxler, Dr Katherine S. Bridge, Kunal M. Shah for being my toughest critics. My sincere thanks also go to especially Dr Katherine S. Bridge, Kunal M. Shah and other co-authors who contribute to our Cell Reports publication; to Ian Spendlove for providing IHC techniques with regards to my research; to Michael J. Plevin for providing the mass spectrometric analysis; to Miss Kathryn M. Davidson for kind help and discussion during the PhD study; to everyone in the same office of mine for sharing such small spaces for four years; to Barts Cancer Institute, Queen Mary University of London, especially to Dr Vipul Bhaka and Dr Ashley Browne for providing technical supports; and to all colleagues and friends who are not listed above for helping me.

I would also like to thank The Great Britain-China Educational Trust (GBCET) for generously funding my stipend.

Lastly, my deepest thanks to my beloved parents who funded this research and most of my stipend. Without their loving considerations and supports all through these years, I would not be here. Although we are miles away, I am always thinking of you. I would never forget the tears in your eyes every time you see me off at the airport. Love you.

Abbreviations

A (Ala)	alanine (for amino acid)
A	adenine (for nucleotide)
a.a	amino acids
ABD	argonaute-binding domain
AB-motif	AGO-binding motif
ACVR2B	activin A receptor type IIB
AGO	argonaute
AP-1	activator protein 1
APS	ammonium persulphate
bp	base pair
BPI	bioactive peptide induced
BRAF	B-Raf Proto-Oncogene, Serine/Threonine Kinase
BSA	bovine serum albumin
C	cytosine (for nucleotide)
CAT1	cationic 1
C.elegans	Caenorhabditis elegans
C3CER1	chromosome 3 common eliminated region 1
cab39	calcium-binding protein 39
Cam	Ca++/calmodulin
cAMP	cyclic adenosine monophosphate
Cas9	CRISPR-associated protein 9
CCR4-NOT4	carbon catabolite repression 4-negative on TATA-less
CCT	conserved C-terminal
CDS	coding DNA sequence
CEP1	C.elegans p53-like protein 1
cGAS	cGMP-AMP synthase
ChREBP	carbohydrate responsive element binding protein
CMV	cytomegalovirus
CNOT	CCR4-NOT Transcription Complex Subunit
co-IP	co-immunoprecipitation
CREB	cAMP response element-binding protein
CRKL	CRK Like Proto-Oncogene, Adaptor Protein
CRISPR	Clustered Regularly Interspaced Short Palindromic Repeats
CSL	CEP1 synthetic lethal protein
D (Asp)	aspartic acid (for amino acid)
DCP	decapping protein
DCPS	Scavenger mRNA-decapping enzyme
DDX6	DEAD box protein 6
DGCR8	DiGeorge Syndrome Critical Region 8
Dis3L	Dis3-like exonuclease
DMEM	Dulbecco's Modified Eagle's Medium
DNA	deoxyribonucleic acid
DSP	dual-specificity phosphatase
dsRBD	double-stranded RNA-binding domain
dsRNA	double-stranded RNA
E (Glu)	glutamic acid (for amino acid)
E.coli	Escherichia coli

ECL	enhanced chemi-luminescence Reagent
EDC4	enhancer of decapping 4
EDTA	ethylenediaminetetraacetic acid
EGFP	enhanced green fluorescent protein
eIF	eukaryotic translation initiation factor
EJC	exon-exon junction complex
endo-siRNA	endogenous siRNA
eRF	Eukaryotic release factor
ERK	extracellular signal-regulated kinase
exo-siRNA	exogenous siRNA
EYFP	enhanced yellow fluorescent protein
F (Phe)	phenylalanine (for amino acid)
FBS	fetal bovine serum
FGF9	fibroblast growth factor 9
FHIT	fragile Histidine Triad
FITC	fluorescein isothiocyanate
FL	full length
FPKM	fragments per kilobases million
Fra-1	Fos-related antigen 1
G	guanine (for nucleotide)
G (Gly)	glycine (for amino acid)
GAGH	GW182/AIN-1/Gawky homolog
GCK	germinal centre kinase
GPCR	G protein-coupled receptor
GST	glutathione S-transferase
GW182	glycine-tryptophan repeats containing protein of 182 kDa
GW-repeats	glycine-tryptophan repeats
HBEC	human bronchi epithelial cell
HIF	hypoxia-inducible factor
His	histidine
HRE	hypoxia response element
HRP	horseradish peroxidase
HRV 3C	human rhinovirus 3C
Hsc70	heat chock cognate 70
Hsp90	heat shock protein 90
HSV TK promoter	Herpes simplex virus thymidine kinase promoter
IFA	immunofluorescence assay
IFN	interferon
IL-6	interleukin-6
IPTG	Isopropyl β-D-1-thiogalactopyranoside
IRES	internal ribosomal entry site
ITAF	IRES trans-acting factors
JIP	JNK interacting protein
JNK	the c-Jun NH2-terminal kinase
KCC	K-Cl cotransporter
kDa	kilo Daltons
KEGG	Kyoto Encyclopedia of Genes and Genomes
KLD	kinase-ligase-DpnI
KSR	kinase suppressor of Ras
L1	Linker 1

LAW	LIMD1, AJUBA and WTIP
LB	Luria Bertani
LDC	ligation-dependent cloning
LIC	ligation-independent cloning
LIMD1	LIM domains-containing protein 1
LOH	loss of heterozygosity
m^7GTP	7-Methylguanosine-5'-triphosphate
MAP2K	MAP kinase kinase
MAP3K	MAP kinase kinase kinase
MAP4K	MAP kinase kinase kinase kinase
MAPK	mitogen-activated protein kinase
MAPKAPK2	MAPK-activated protein kinase 2
MBP	maltose binding protein
MDA5	melanoma differentiation associated factor 5
MEC-3	Mechanosensory protein 3
messenger RNA	mRNA
Met-tRNA	methionine-tRNA
MID	middle
miRISC	miRNA-induced silencing complex
miRNA	microRNA
MKP	MAPK phosphatase
MLK	mixed lineage kinase
mTan	mTangerine
MTR3	mRNA transport regulator 3
MUSCLE	Multiple Sequence Comparison by Log-Expectation
N	asparagine (for nucleotide)
NCC	N-Cl cotransporter
NGD	no-go mRNA decay
NKCC	Na-K-Cl cotransporter
NLS	nuclear localisation signal
NMD	nonsense-mediated decay
NSCLC	non-small cell lung cancer
NSD	nonstop mRNA decay
nt	nucleotide
O/N	overnight
ODDD	oxygen dependent degradation domain
oligo(U)	oligouridines
ORF	open reading frame
P	proline (for nucleotide)
PABP	poly(A)-binding protein
PABC	poly(A)-binding protein c-terminal domain
PACT	protein activator of PKR
PAK	p21-activated kinase
PAM2	PABP interacting motif 2
PAN	poly(A)-nuclease
PARN	poly(A)-specific ribonuclease
PAZ	PIWI Argonaute Zwille
P-bodies	processing bodies
PBS	phosphate buffered saline
PCR	polymerase chain reaction

PFA	paraformaldehyde
PHD	prolyl hydroxylase
PI	propidium iodide
piRNA	PIWI-interacting RNA
PIWI	P-element induced wimpy testis
PKC	protein kinase C
PKR	protein kinase R
PLB	passive lysis buffer
PLK1	polo-like kinase 1
poly(A)	polyadenine, polyadenylation
post-TCs	post-termination ribosomal complexes
pRB	retinoblastoma protein
pri-miRNA	primary miRNA
PTB-1	polypyrimidine tract-binding protein 1
PTC	premature termination codon
PVDF	polyvinylidene difluoride
Q	glutamine (for nucleotide)
qRT-PCR	quantitative real time polymerase chain reaction
RANK	receptor activator of NF-κB
RANK-L	RANK ligand
RASSF1	Ras association domain family member 1
RBP	RNA-binding protein
RdRp	RNA-dependent RNA polymerase
RELT	Receptor expressed in lymphoid tissues
RG4	RNA G-quadruplex
RIG-I	retinoic acid-inducible gene I
RIPA	radio-immunoprecipitation assay
RISC	RNA-induced silencing complex
RLR	RIG-1 like receptor
RNA	ribonucleic acid
RNAi	RNA interference
ROMK	renal outer medullary potassium channel
RRM	RNA recognition motif
S (Ser)	serine (for amino acid)
SAEC	small airway epithelial cells
SBE	SMAD binding element
SCLC	small cell lung cancer
SD	silencing domain
SDS	sodium dodecyl sulphate
SDS-PAGE	SDS-polyacrylamide gel electrophoresis
SG	stress granule
siRNA	small interfering RNA
Ski	superkiller family
SLBP	stem-loop-binding protein
SLC12	sodium chloride cotransporter 12
SPAK	STE20/SPS1-related proline-alanine-rich protein kinase (allase for STK39 gene)
ssRNA	single-stranded RNA
STK39	serine/threonine kinase 39
SV40	simian virus 40

T	thymine (for nucleotide)
T (The)	threonine (for amino acid)
TBE	Tris-borate-EDTA
TEMED	N,N,N’,N’-tetramethylethylenediamine
TEV	tobacco etch virus
TGF-β	transforming growth factor beta
TGS	tumour suppressor gene
TLR	Toll-like receptor
TNF-α	tumour necrosis factor-α
TNRC6	trinucleotide repeat containing 6 (human orthologue of GW-182)
TRAF6	TNF receptor-associated factor 6
TRBP	HIV TAR RNA-binding protein
tRNA	transfer RNA
TSS	transcription start site
TTP	tristetraprolin
U	uracil (for nucleotide)
UBA	ubiquitin-association
uORF	upstream ORF
UPF	up-frameshift suppressor
UTR	untranslated region
VEGF	vascular endothelial growth factor
VHL	von Hippel-Lindau
VO	vector only
W	tryptophan (for amino acid)
WNK	with-no-lysine kinase
WT	wild-type
WTIP	Wilms' tumour one interacting protein
Xpr	Xpress
XRN1	exonuclease 1
Y-box binding protein 1	YBOX1
Y (Tyr)	tyrosine (for amino acid)
ZAP	zinc-finger antiviral protein
ZRE	ZAP response element
2’-5’ OAS	2’-5’-oligoadenylate synthetases

Contents

List of figures

List of tables

Chapter 1

Introduction

1 Introduction

1.1 Thesis overview

This thesis focuses on the biological functions of the tumour suppressor protein LIM domains-containing 1 (LIMD1) involved in miRNA-mediated gene silencing. LIMD1 interacts with Argonaute (AGO) 2, the key component of miRNA-induced silencing complex (miRISC), to control the gene expression on the post-transcriptional level [1]. However, the precise interaction/association with AGO2 is unclear. In addition, little is known about how LIMD1 and its family members (AJUBA and WTIP) associated with human AGO proteins (AGOs) with regards to the high homology within the phosphorylation-dependent L2 domain of AGOs. The present studies will help to improve our knowledge of LIMD1 characteristics in miRISC assembly and put forward a more detailed mechanism of miRNA-mediated silencing.

The loss of LIMD1 has been correlated with a variety of cancers, but it is difficult to treat these LIMD1 negative cancer by simply targeting LIMD1. To address these questions, each result chapter presents experimental findings that address the precise interfaces responsible for AGO2-LIMD1 interaction, potential LAW-AGOs interaction and the mechanisms, and how LIMD1 regulates a novel oncogene, STK39, which shows synthetic lethality with LIMD1 loss.

The first two results chapters focus on AGO2-LIMD1 interaction/association with respect to miRISC assembly. The first results chapter investigated and characterised the precise interfaces both within AGO2 and LIMD1 for their physical interaction (**Chapter 3**). The second results chapter broadened the AGO2-LIMD1 interaction to their family members, four human AGOs (AGO1-4) and LAW family members (AJUBA and WTIP) with respect to the mechanism found between AGO2 and LIMD1 (**Chapter 4**). In the final results chapter, the concept of synthetic lethality was employed to identify the synthetic lethal genes with LIMD1. The mechanism for such gene(s) and the potential approach for cancer treatment were discussed (**Chapter 7**). Because this thesis contains two separate studies, the results will be presented separately following after each introduction chapter and discussed individually for each study (**Chapter 5** and **Chapter 8**).

The degradation of messenger RNA (mRNA) is not only achieved by the decay pathway but also mediated by non-coding RNAs. Therefore, to be relevant to this project, mRNA degradation pathways will be reviewed. The discovery and the machinery of RNA interference (RNAi) will then be introduced. The main focus will be miRNA-mediated gene silencing including the biogenesis of miRNA and the assembly. The degradation of mRNA competes with translation initiation, depending on which group of proteins bound to the mRNA. In addition, the miRNA-mediated gene silencing involves translational repression. As a result, the eukaryotic translation will be outlined to provide the background of translation initiation and a better understanding of the miRNA-mediated translational repression. Past and current models of the mechanism of miRNA-mediated gene silencing, as well as the function of LIMD1 involved in miRNA-mediated gene silencing, will be discussed, followed by the first two results chapters. The known properties of STK39 biology will then also be presented separately after the first study.

1.2 Messenger RNA degradation pathways

The degradation of mRNA is an essential step in gene expression to regulate the abundance of mRNAs. This includes the detection and rapid degradation of any RNA molecules with defects in synthesis, processing, or folding. In addition, mRNA degradation can also be dictated by non-coding RNAs with RNA-binding proteins at the post-transcriptional level. The degradation of mRNA is ubiquitous in all cells and the rate various to control the mRNA abundance to meet the various needs for the individual protein within cells. Therefore, the degradation of mRNA is accurately controlled at differential rates by various machinery [2].

1.2.1 Deadenylation-dependent mRNA decay

In eukaryotic cells, the 5’ cap structure and the 3’ polyadenylation (poly(A)) tail of mRNA are required for translational efficiency and protecting the mRNA from the non-specific degradation in the cytoplasm. The poly(A) tail is an important structure in regulating the mRNA decay; deadenylation of mRNAs is the initial step in mRNA decay, followed by the degradation of mRNAs in a 3’ – 5’ direction by the exosome complex (**Figure 1.1**).

Alternatively, following the deadenylation, decapping and degradation in a 5' – 3' direction dictated by decapping proteins (DCPs) and the exonuclease 1 (XRN1).

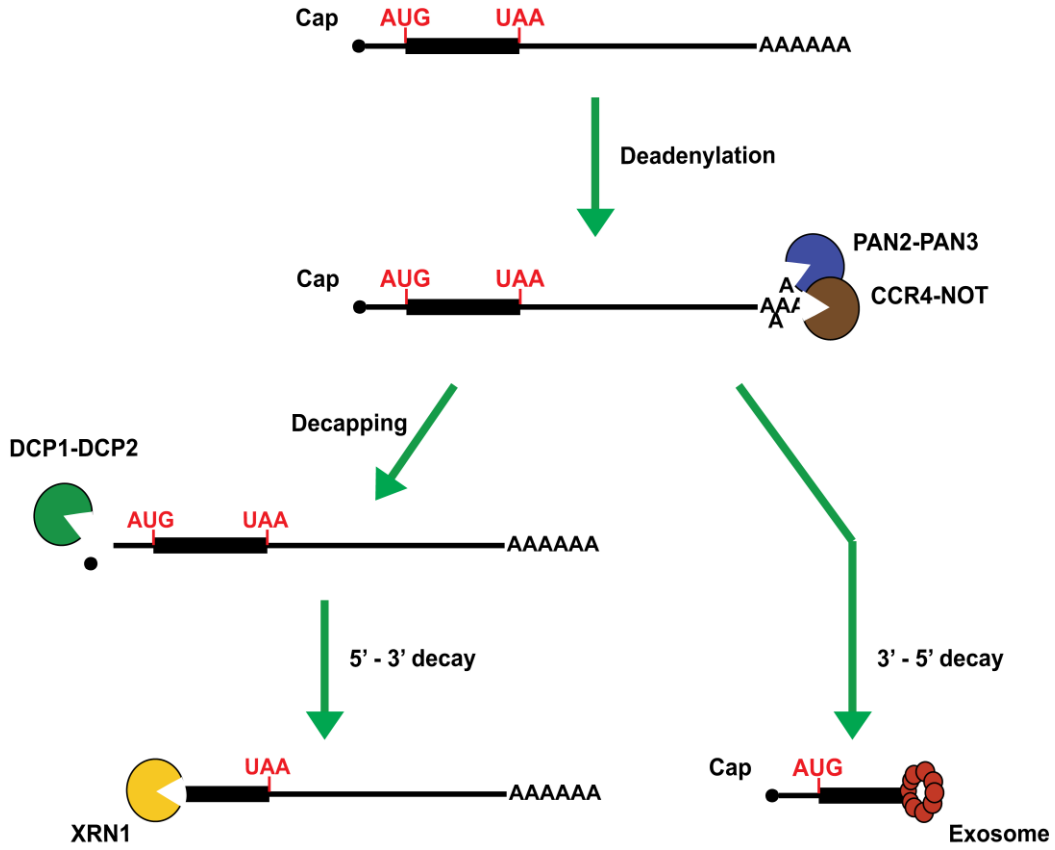

Figure 1.1 The deadenylation-dependent degradation of mRNA
The deadenylation-dependent mRNA degradation initiates when two main deadenylases complexes, PAN2-PAN3 and CCR4-NOT, remove the poly(A) tail. Following the deadenylation, mRNA is degraded by the exosome in a 3' – 5' direction. The residual cap structure is then hydrolysed by the scavenger decapping enzyme (DCPS). Alternatively, mRNA is decapped by DCP1-DCP2, followed by the degradation by XRN1 in a 5' – 3' direction.

Mammalian deadenylation contains two consecutive steps which involve two major deadenylases complexes, poly(A)-nuclease 2 (PAN2)-PAN3 and carbon catabolite repression 4-negative on TATA-less (CCR4-NOT) (**Figure 1.1**) [3, 4]. PAN2 is responsible for digest the distal adenines (As) and CCR4 then digests the approximately As. Therefore, deletion of PAN2 results in a long poly(A) tail, whereas deletion of CCR4 leaves the final approximately As. The promoted decay was observed when either PAN2 or CCR4 was overexpressed [4, 5]. The PAN2-PAN3 complex, as the poly(A)-specific

nucleases, binds to the poly(A) tail by the interaction between (poly(A)-binding protein c-terminal domain) PABC and poly(A)-binding protein (PABP)-interacting motif 2 (PAM2) within the N-terminus of PAN3 [6]. The enzymatic activity of PAN2-PAN3 relies on the PAN2 and mainly depends on the interaction with PABC. It was also demonstrated that PAN3 could directly bind to poly(A) tail and supply PAN2 with poly(A) RNA as the substrate [7]. The PAN2-PAN3 complex initiates to trim the distal poly(A) until the final 25 As due to the dissociation of PABC with poly(A) tail [4, 8]. Subsequently, the CCR4-NOT multi-deadenylase complex, which is the major deadenylases complex in eukaryotes, removes the remaining As to complete the deadenylation step [5, 9, 10]. The PAN2-PAN3 and CCR4-NOT are recruited by eukaryotic release factor 1 (eRF1) and eRF3 [11]. CCR4-NOT can also be recruited by the interaction with RNA binding proteins (RBPs) such as PUF, POP2 and tristetraprolin [12, 13].

After deadenylation, mRNA body is degraded in the 3’ – 5’ direction by the cytoplasmic exosome, which is a multi-protein complex. It consists of nine core subunits and one enzymatically active ribonuclease [14]. According to the crystal structure, human Ribosomal RNA-processing protein 41 (RRP41), RRP45, RRP46, RRP43, mRNA transport regulator 3 (MTR3) and RRP42 form the RNase PH domain ring, and C.elegans p53-like protein 1 (CEP1) synthetic lethal protein (CSL) 4, RRP4 and RRP40 form the cap [15]. Human cytoplasmic Dis3 (also known as RRP44 mainly expressed in the nucleus)-like exonuclease (Dis3L) associated with the exosome ring performs the enzymatic activity. The human superkiller family (Ski) complex (consisting of Ski2, Ski3 and Ski8) serves as the cofactor to be associated with and regulate the activity of the exosome [16]. After mRNA body is degraded by the exosome, the residual cap structure is hydrolysed by the scavenger decapping enzyme (DCPS) and Fragile Histidine Triad (FHIT) [17, 18].

In addition to the 3’ – 5’ decay, mRNA degradation can also occur in a 5’ – 3’ direction after deadenylation. This step is initiated by the binding of the holoenzyme DCP1-DCP2 to the 5’ m^7G cap structure. DCP2 catalyses the cap structure and generates 5’ monophosphorylated mRNA body. The catalytic activity of DCP2 requires its binding to the 5’ end of mRNA, but the cap structure is normally protected by the eukaryotic initiation factor 4F (eIF4F) complex. Therefore, RCK/p54 represses the mRNA translation

to release the eIF4F complex from mRNA so that DCP2 is accessible to the 5' cap structure [19]. Besides, LSM1-7 complex associated with Pat1 binds to the deadenylated mRNA which in turn inhibiting the translation and activates the decapping process [19, 20]. The decapped mRNA is then destructed by 5' – 3' exonuclease XRN1 (**Figure 1.1**).

1.2.2 Deadenylation-independent mRNA decay

Nonstop mRNA decay (NSD) degrades mRNAs without the stop codon for translation to control the mRNA quality [21]. The degradation is not required deadenylation. Nonstop mRNAs result from the abortion of transcription, premature polyadenylation or point mutations which disrupt the in-frame stop codon. Therefore, during the first round of translation, the ribosome reaches the very 3' end of mRNA (poly(A) tail) and remains stalled onto the mRNA [21] (**Figure 1.2**). The C-terminal domain of Ski7 recognises this stalled ribosome and in turn recruiting the Ski complex (consisting of Ski2, Ski3 and Ski8). The exosome complex is then recruited to the 3' end and start degrading mRNA in a 3' – 5' direction. The C-terminal domain of Ski7 mimics the GTPase domain of eRF3 [22, 23]. As a result, in addition to mediating NSD, Ski7 can dissociate the stalled ribosome from the 3' end of mRNA and recycle it for translation of the normal mRNA. By contrast, Ski7 was found in the yeast, and it is not conserved in mammals. Therefore, mammalian cells utilise HBS1, which is homologous to Ski7, to interacting with Ski complex and conduct the NSD degraded by exosome [24].

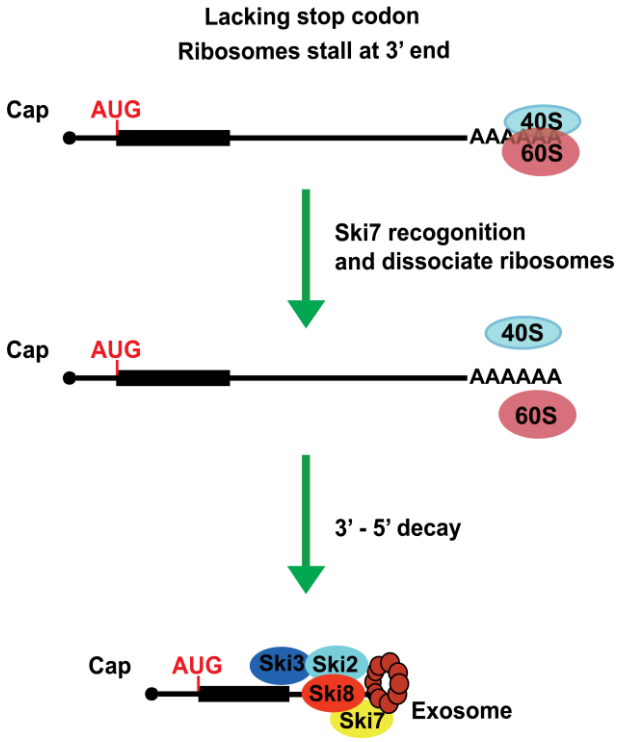

Figure 1.2 Nonstop mRNA decay (NSD) pathway
NSD pathway does not require deadenylation as an initial step for mRNA degradation. The defective mRNA is lacking the stop codon. As a result, the ribosome is unable to dissociate from mRNA and remains stalled at the very 3' end. Ski7 (HBS1 in mammalian cells) recognises the stalled ribosome and release ribosomes from mRNA. Ski7/HBS1 recruits Ski2-Ski3-Ski8 complex and exosome, leading to the major mRNA degradation pathway in a 3' – 5' direction.

In addition to the exonucleolytic decay, Global analysis of the mammalian RNA degradome revealed that endonucleolytic decay is also a deadenylation-independent pathway for mRNA degradation [25]. The two fragments of the endonucleolytic cleavage are digested by both decapping followed by the degradation in the 5' – 3' direction by XRN1, and the deadenylation pathway followed by the degradation in the 3' – 5' direction by exosome (**Figure 1.3**). The endonucleolytic cleavage can be triggered by numerous endonuclease [26]. For instance, The Zc3h12a protein has the endonucleolytic activity due to the PilT N-terminus (PIN)-like domain on its N-terminus [27, 28]. It modulates the immune response by targeting interleukin-6 (IL-6); *Zc3h12a*-deficient cells exhibited the overexpressed IL-6. The *Zc3h12a*-deficient mice grew slowly

and suffered from immune disorders [27]. In addition, the RNAi process also depends on the endonucleolytic activities by RISC, which will be described in **Chapter 1.3.5**.

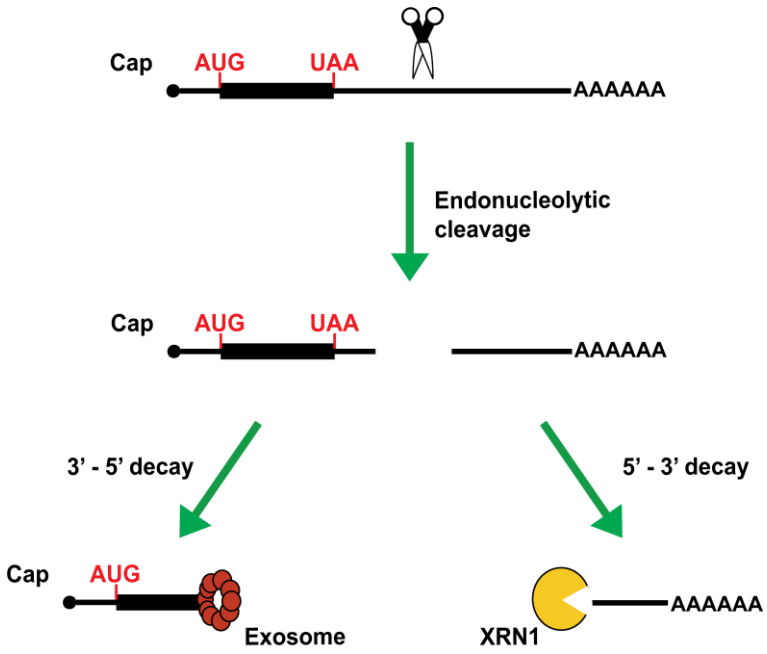

Figure 1.3 Endonucleolytic cleavage conducts the deadenylation-independent degradation of mRNA
For the deadenylation-independent mRNA degradation pathway, endonuclease (for example Zc3h12a or AGO2) cleaves the mRNA into two fragments, followed by the degradation in a 3' – 5' decay and a 5' – 3' decay.

Endonucleolytic activities are also involved in mRNA surveillance pathways to control the quality of mRNA in the cytoplasm. In addition to NSD, two more surveillance pathways have the role to eliminate mRNA with specific errors to prevent producing potentially defective proteins: **1**) nonsense-mediated decay (NMD) eliminates mRNAs containing a premature termination codon (PTC) to minimize the truncated protein products [29], and **2**) no-go mRNA decay (NGD) removes mRNAs containing the stalled ribosomes due to the secondary structure of mRNA or the collision of ribosomes during translation [30, 31]. PTC (nonsense codon) is a result of mutations in genes, errors in transcription and splicing which retains introns. The exon-exon junction complex (EJC) assembles approximately 20-24 nucleotides (nts) upstream of an exon-exon junction during mRNA splicing and remains deposited onto the mRNA. The function of EJC is to

provide a position-specific memory of the splicing event to determine whether the mRNA is defective or not. For the normal mRNA, the EJC displaces when the ribosome encounters the EJC site during the pioneer round of translation (**Figure 1.4**). However, if the ribosome reaches a PTC which locates approximately >50-55 nts upstream of EJC, the ribosome then recruits Up-Frameshift Suppressor (UPF) 1 and SMG1 by the interaction with eRF1-eRF3. SMG1 phosphorylates UPF1 after binding to UPF2-UPF3 within the downstream EJC on the mRNA [32]. The phosphorylated UPF1 subsequently phosphorylates and activates SMG6 for the endonucleolytic cleavage (**Figure 1.4**) [33, 34]. SMG6 is vital for the NMD pathway, the deletion of which was revealed to be unable to degrade the faulty mRNAs [34, 35]. Following the endonucleolytic cleavage, the mRNA undergo the 5' – 3' and 3' – 5' decay (**Figure 1.4**).

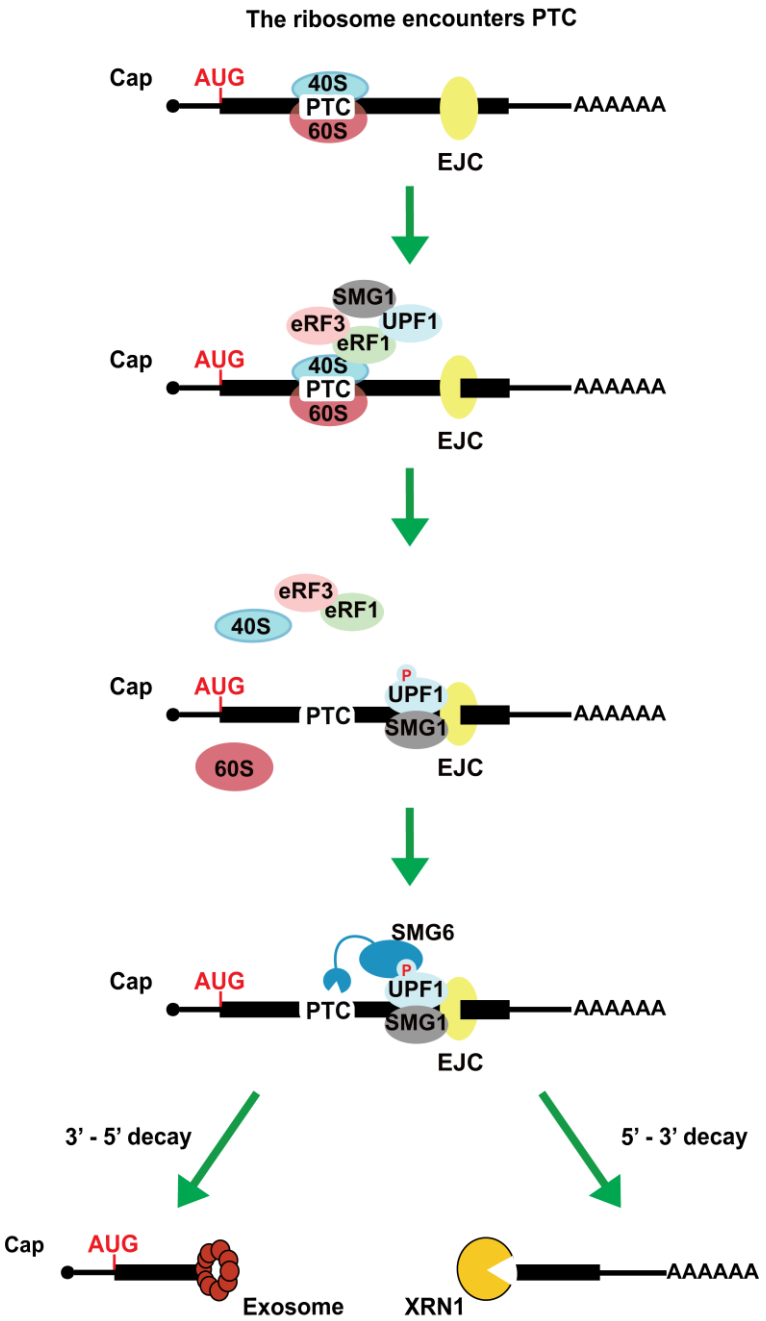

Figure 1.4 Nonsense mRNA decay (NMD) pathway
The NMD pathway eliminates the mRNA containing PTCs. When the ribosome encounters the EJC site during the pioneer round of translation; if PTC locates approximately >50-55 nts upstream of EJC, the ribosome then recruits UPF1 and SMG1 by the interaction with eRF1-eRF3. SMG1 phosphorylates UPF1 after binding to UPF2-UPF3 within the downstream EJC on the mRNA. The phosphorylated UPF1 then phosphorylates SMG6 to activate the endonucleolytic cleavage. After the cleavage, two fragments undergo the degradation in a 3' – 5' decay and a 5' – 3' decay.

NGD is initiated as the result of the stalled elongation during mRNA translation when the ribosome reaches the stem-loop structure in the mRNA or rare codons [36, 37]. The recent study showed that the ribosome collision is a crucial trigger for NGD and the cleavage of mRNA is required for multiple stalled ribosomes [30]. However, if the defective mRNA with the stalled ribosome near the initiation codon, it is not subject to NGD as the result that multiple ribosomes do not accommodate [30]. The ribosomes accommodate at the stall site causing the collision which subsequently recruits HBS1. HBS1, exhibiting the structural similarities to eRF3, dissociates the stalled ribosome from mRNA. With the assistance of its binding partner Dom34, HBS1-Dom34 complex induces the endonucleolytic cleavage at the stall site. 3' – 5' decay by exosome and 5' – 3' decay by XRN1 consequently start to degrade the two fragments (**Figure 1.5**) [2].

The deadenylation-independent mRNA degradation also takes place in the regulation of the histone mRNA. The degradation of histone mRNA helps to keep the balance between the histone protein and DNA replication to avoid the toxic to cell proliferation [38]. Histone mRNA contains a stem-loop structure instead of a poly(A) tail close to the stop codon. Its rapid degradation occurs at the end of S phase or when DNA replication is inhibited and is initiated by the addition of short oligouridines (oligo(U)) to the 3' end of the histone mRNA [39]. The oligo(U) serves as the substrate for the LSM1-7 complex, which subsequently recruits the decapping complex and the decay machinery factors to degrade the histone mRNA in a 5' – 3' direction [40]. Simultaneously, the exosome complex is recruited by the LSM1-7 complex and degrade the histone mRNA in a 3' – 5' direction [39] (**Figure 1.6**).

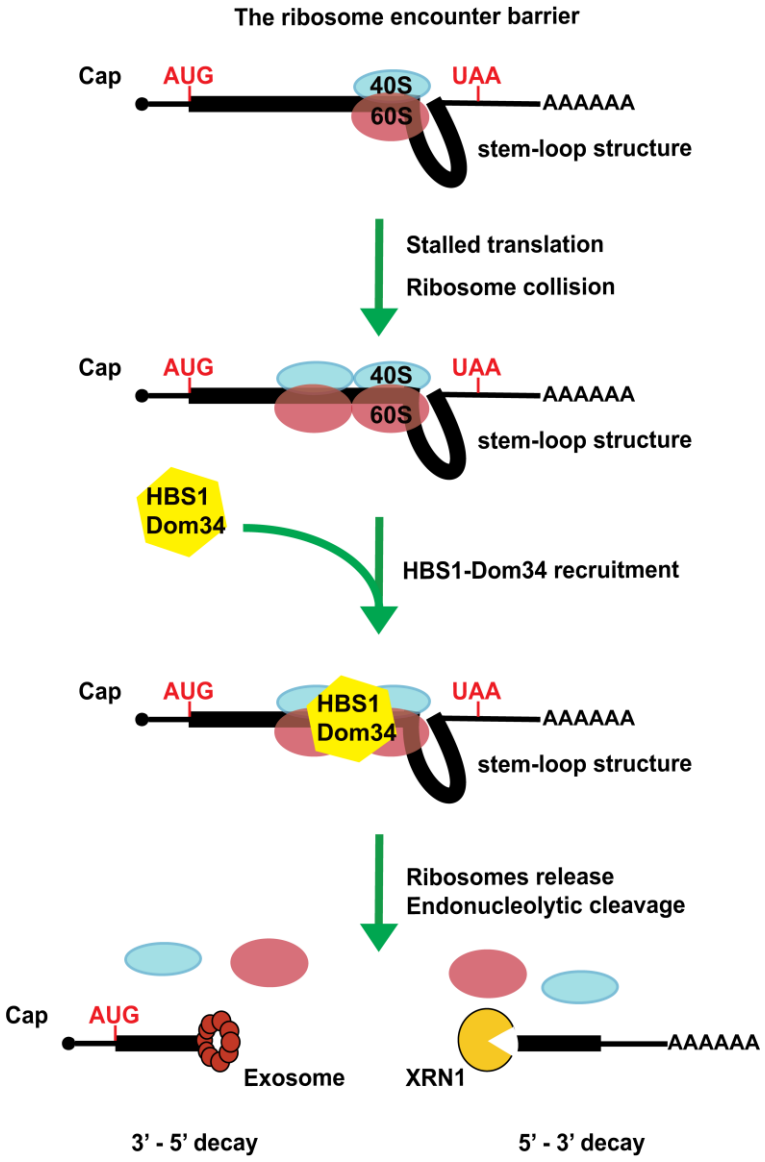

Figure 1.5 No-go mRNA decay (NGD) pathway
The NGD pathway eliminates the mRNA containing the stem-loop structure or the rare codon, which result in the collision of multiple ribosomes during the translation. The collision of ribosomes recruits the HBS1-Dom34 complex. The HBS1-Dom34 complex dissociates the stalled ribosomes from mRNA and induces the endonucleolytic cleavage at the stall site. After the cleavage, two fragments undergo the degradation in a 3' – 5' decay and a 5' – 3' decay.

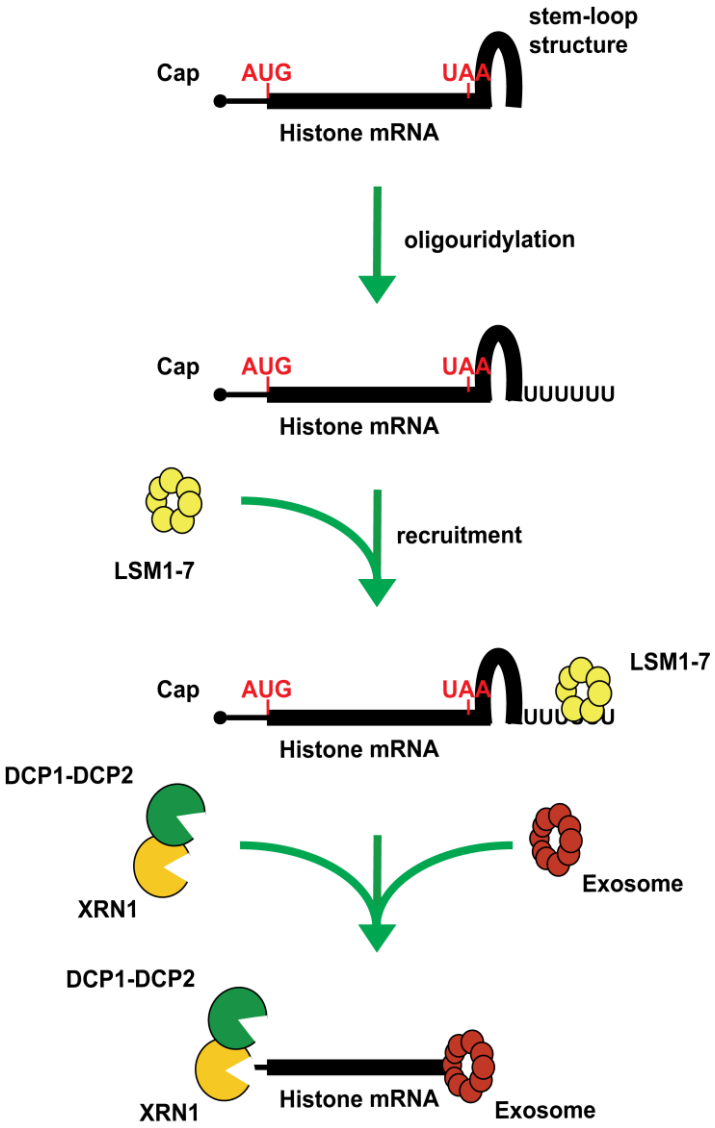

Figure 1.6 Degradation of the histone mRNA
The degradation of histone mRNA occurs at the end of S phase or when DNA replication is inhibited. Given that the histone mRNA lacks the poly(A) tail, the degradation is not deadenylation-dependent. It is initiated by the oligouridylation of the stem-loop sequence at the 3' end. The poly(U) tail permits the binding of the LSM1-7 complex, which subsequently recruit the decapping and decay machinery factors (DCPs, XRN1 and Exosome) to degrade the histone mRNA in both 5' – 3' and 3' – 5' direction.

1.2.3 Anti-viral response of the mRNA degradation

Viruses induce double-stranded RNAs (dsRNAs) during their replication. Depletion of NMD factors resulted in the increased replication of the alphaviruses Semliki Forest virus [41]. Therefore, in addition to the elimination of defective mRNAs, the mRNA degradation pathway is also playing a crucial role in anti-viral response as an innate immunity to destruct the viral RNAs (**Figure 1.7**). Interferon (IFN)-based anti-viral innate immunity is one of two anti-viral defence mechanism and is well characterised [42-44]. IFN-activated mRNA degradation pathway is one part of IFN-based innate immunity. 2'-5'-oligoadenylate synthetases (2'-5'OAS) are activated by the binding of long viral dsRNAs. This results in the binding of the cellular endonuclease RNase L and facilitates the dimerisation of RNase L. Consequently, the dimerised RNase L non-specifically degrades RNAs including both viral and host RNAs [45]. Moreover, viral RNA contains a zinc-finger anti-viral protein (ZAP) response element (ZRE). Once recognising and binding to ZRE, ZAP recruits the cellular RNA decay machinery, including DCP1-DCP2, poly(A)-specific ribonuclease (PARN) and exosome [46]. In addition to the above-mentioned viral RNA degradation pathways, IFN-based innate immunity also contains other pathways. For instance, the pattern recognition receptors, including Toll-like receptors (TLRs), retinoic acid-inducible gene I (RIG-I)-like receptors (RLRs), melanoma differentiation associated factor 5 (MDA5) and cGMP-AMP synthase (cGAS), detect the viral DNA/RNA and mediate downstream transcription factors which consequently eliminate the infected cells by programmed cell death [42-44].

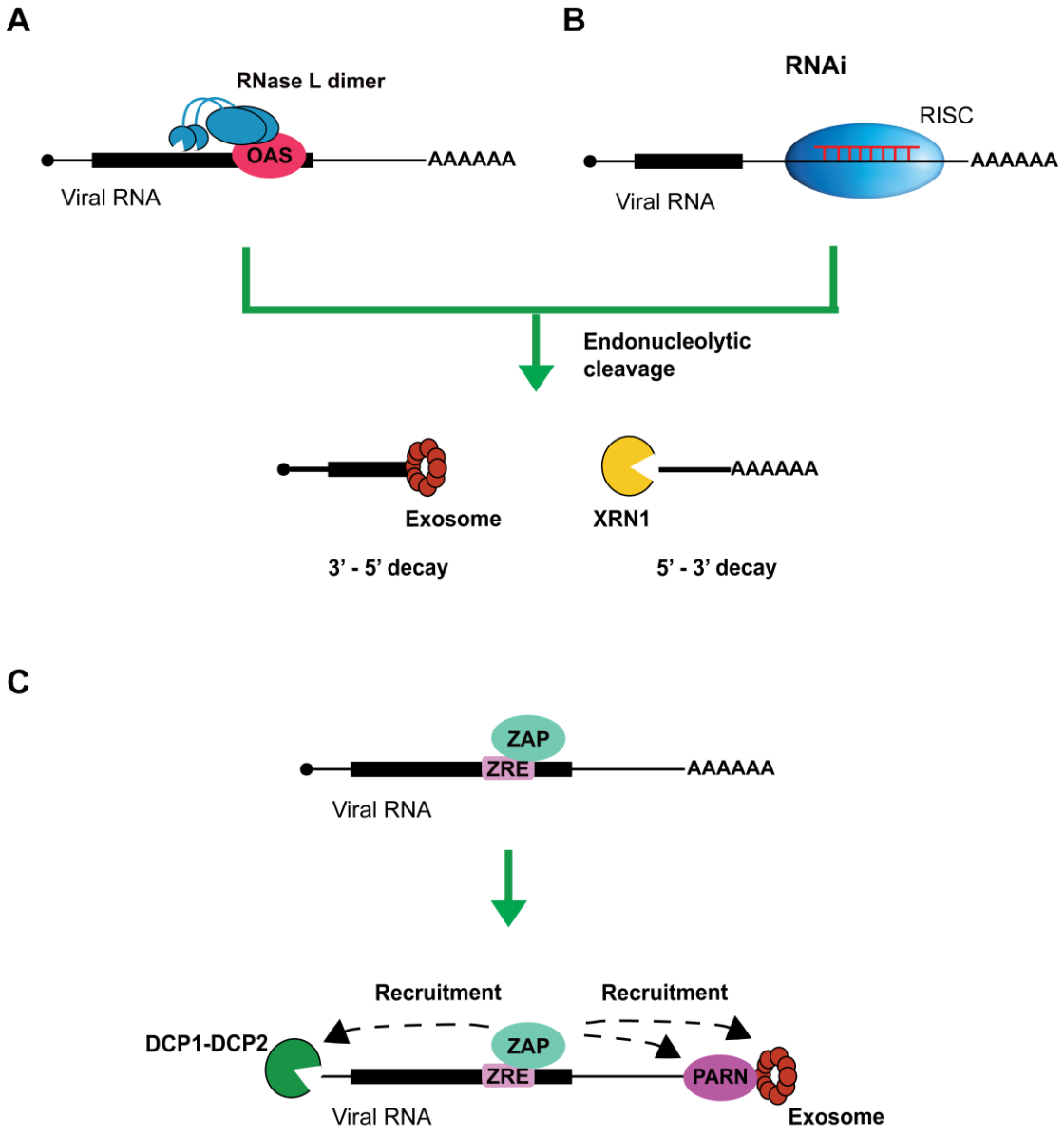

Figure 1.7 Anti-viral response of RNA degradation

***A*)** The IFN-activated 2'-5' OAS binds and activates RNase L, resulting in the dimerisation of RNase L. Subsequently, RNase L dimer cleaves the viral RNAs using its endonucleolytic activity. The two fragments then undergo the degradation in a 3' – 5' decay and a 5' – 3' decay. This pathway non-specifically degrades both viral and host RNAs. ***B*)** The viral dsRNA is proceeded to siRNA by the host's RNAi machinery. siRNA then complementarily binds the target viral RNA, leading to the endonucleolytic cleavage by RISC complex. The two fragments consequently undergo the degradation in a 3' – 5' decay and a 5' – 3' decay. This pathway is specific to the viral RNAs due to the RNAi machinery. ***C*)** The viral RNA contains ZRE which allows ZAP interaction. ZAP then recruits DCPs, deadenylation enzymes and exosome to degrade the viral RNAs from both 5' – 3' direction and 3' – 5- direction.

RNAi is another anti-viral defence mechanism evoked by the viral infection. The host cell utilises the RNAi machinery (details in **Chapter 1.3**) to degrade viral RNAs. The long dsRNA induced by viruses is processed to short interfering RNAs (siRNAs), which complementary target viral RNAs, resulting in the endonucleolytic cleavage. Consequently, it specifically inhibits the viral replication without destructing the infected cells. This pathway is mainly found in plants and invertebrates, and its existence in vertebrates was uncertainty until the recent studies demonstrated the existence of RNAi pathway contributing to anti-viral response in mammalian cells [47, 48]. Depletion of key components of RNAi machinery (Dicer and Drosha) increased HIV-1 replication [49]. The B2 protein for Flock house virus has high affinity to dsRNA and inhibits the host RNAi-based anti-viral response. It was demonstrated that the depletion of B2 protein resulted in the abundant viral siRNAs and consequently increased host RNAi-based anti-viral response to eliminate viruses [48]. In fact, for human, the somatic cells mainly utilise IFN-based anti-viral innate immunity, whereas the embryonic stem cells utilise RNAi to defence viruses [44, 48].

1.3 RNAi mediates gene silencing at the post-transcriptional level

RNAi, also known as post-transcriptional gene silencing, is a biological phenomenon found in fungi, plants, animals, and mammalians that efficiently and specifically regulates the gene expression. RNAi is initiated or triggered by non-coding small dsRNA which contains three types: miRNAs, siRNA and PIWI-interacting (piRNA). piRNAs are 24-30 nt long and the main function of piRNAs is to silence transposable elements in germline cells [50]. As its difference in biogenesis and associated mRBPs to miRNAs and siRNAs, hereafter the introduction and discussion of piRNAs will be excluded in this project. Both siRNA and miRNA are endogenously generated from non-coding RNAs; siRNA can also be introduced into the cells by transfection. miRNAs and siRNAs have approximately 22-nt long with 2-nt overhang at the 3’ end (**Figure 1.8**). miRNA contains the bulge structure within the duplex, whereas siRNA does not. The seed region (nucleotide position 2-8 at the 5’ end) is responsible for complementary binding to the target mRNA. siRNA-induced endonucleolytic cleavage occurs on the target mRNA at the relative site between 10 and 11 nt of siRNA (**Figure 1.8**). miRNAs induce translational

repression and mRNA degradation, and it also leads to the endonucleolytic cleavage when it perfect match to the target mRNA. As the gene regulatory function, RNAi has become a standard experimental tool to silence a gene of interest for biological research. Its potential therapeutic applications are under investigation. The fate of target mRNA undergoes either translational repression or degradation. Therefore, to be relevant to the main goal of this project, RNAi is described in the following chapters. The main focus will be on miRNA and the miRNA-mediated post-transcriptional gene silencing. In this chapter, the discovery of RNAi and miRNA will be introduced.

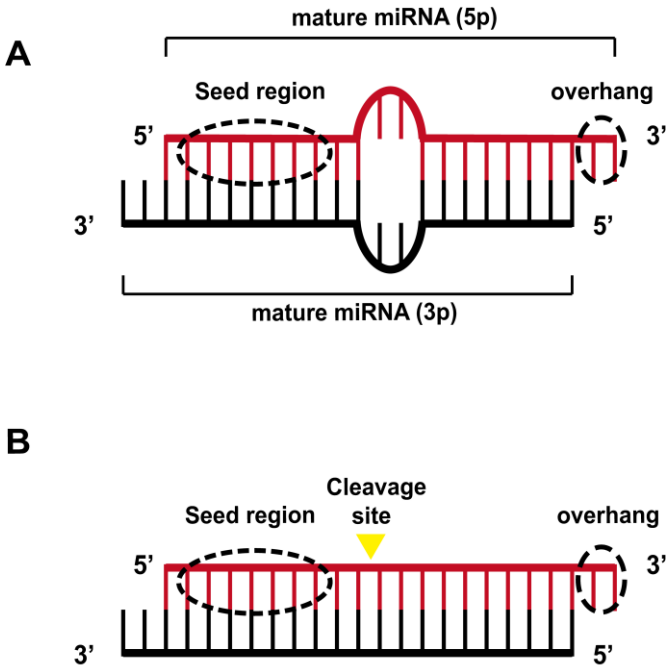

Figure 1.8 Structure of mature miRNA and siRNA
***A*)** The structure of a mature miRNA. The two strands of the miRNA form an approximately 22-nt duplex with the bulge structure (mismatches in the center) and 2-nt overhangs at 3' end. The seed region (2-8 nt), through which the interaction with the target mRNA, is indicated. Both strands (5p and 3p) can cause the silencing of the target mRNA. ***B*)** The structure of a mature siRNA. The two strands of the siRNA form an approximately 22-nt duplex with 2-nt overhangs at 3' end. The endonucleolytic cleavage site of the complementary target mRNA is indicated with a yellow arrowhead (between 10 and 11 nt from 5' end). The seed region (2-8 nt), through which the interaction with the target mRNA is indicated.

1.3.1 The history of miRNA

lin-4 was the first miRNA discovered in 1993 [51]. *LIN-14* is one of the genes to control the temporal post-embryonic development in *C.elegans*, and its expression is negatively regulated by *lin-4* at the first larval stage [51]. Loss of *lin-4* stopped the larval transition from the first to the second larval stage, and it also caused some missing structures in the adult [51, 52]. No start and stop codons are found in *lin-4*, indicating *lin-4* does not encode a protein [51]. In addition, two small transcripts of *lin-4* (61nts and 22nts in length) were found, whose sequences are complementary to the 3'UTR of *lin-14* mRNA. These findings indicated *lin-4* negatively regulates the *LIN-14* translation by RNA-RNA interaction [51].

Seven years later, in 2000, the second miRNA, *let-7* (21nt in length) was discovered in *C.elegans* [53]. Similar to *lin-4*, *let-7* is also one of the heterochronic genes which temporally regulate the developmental timing, controlling the transition of the fourth larval stage to adult [53]. Loss of *let-7* caused the reappearance of larval cell fate during the adult development, whereas over-expression of *let-7* leads to precocious expression during the larval development [53]. *let-7* miRNA is complementary to the 3'UTR region of *lin-41*. The mutation of *let-7* and the deletion of 3'UTR of *lin-41* resulted in the ablation of the down-regulation of *lin-41* [53, 54]. This indicated that *let-7* and 3'UTR of the target mRNA are necessary for controlling the gene expression. The *let-7* sequence is highly conserved not only across the species but also detected at different expression levels in the majority of the tissues in humans [55]. *let-7* family members share the seed region for target recognition, which spans 2 to 8 nt at the end of 5' end of the miRNAs [56, 57]. *let-7* family members, therefore, can regulate the same targets.

1.3.2 The biogenesis of miRNA and siRNA

miRNA genes are transcribed by RNA polymerase II, and the long primary transcript has a local stem-loop structure which contains miRNA sequences. The primary transcript is then capped and polyadenylated. Most of miRNAs in human are encoded by introns of non-coding or coding transcripts. Some miRNAs share the same promoter of a gene where they are located in the intron of a protein-coding gene [58]. There are multiple

miRNA loci located genomic contexts, and they often have multiple transcription start sites (TSSs) as well [59, 60]. Some of miRNAs are close to each other forming clusters. Therefore, these miRNAs are transcribed simultaneously. The mature miRNAs with the same seed region belong to the same miRNA family, for example, *let-7* family. There is only one nucleotide in the difference in miR-141 and miR-200c seed region, but they suppress non-overlapping targets [61]. This finding indicated the seed region is essential for miRNA function. The nomenclature of miRNA genes is followed by several rules: **1**) the gene locus and precursor miRNA (pre-miRNA) are referred as *mir*, while the mature miRNA product is referred as *miR*; **2**) if genes encoding miRNAs from the same family, a suffix letter after the number of miRNA is used (for example, *mir-26a* and *mir-26b*); **3**) if the same mature miRNA is generated from multiple loci, numeric suffix is then added (for example, *mir-26a-1* and *mir-26a-2*) and **4**) because two mature miRNAs are produced from each locus, 5p and 3p are used to indicate the mature miRNA originated from 5' strand or 3' strand of the pre-miRNA (for example, *miR-26a-5p* and *miR26a-3p*).

Following the transcription by RNA polymerase II, primary miRNAs (pri-miRNAs) undergo several steps for maturation (**Figure 1.9A**). pri-miRNA contains a stem-loop structure which is different in length from the stem-loop for siRNAs. Initially, pri-miRNAs are trimmed in the nucleus by Drosha, an RNase III family member, to form a small hairpin-shaped ~65-nt RNA with a 2-nt overhang at 3' end, so-called pre-miRNA [62]. The dsRNA-binding domain (dsRBD) protein DGCR8 is the cofactor associating with Drosha to form the microprocessor [63]. Drosha has tandem RNase III domains whose dimerisation forms a processing centre. The dsRBD within Drosha together with DGCR8 bind pri-miRNA. The first RNase III domain precisely cuts the 3' strand, and the second RNase III domain cuts the 5' strand to produce pre-miRNA [64]. With the help of Exportin-5, pre-miRNA enters into the cytoplasm where the terminal loop is cropped by Dicer, generating the mature 22-nt miRNA duplex (**Figure 1.8** and **Figure 1.9A**). Either strand (5p or 3p) can be selected as the guide strand and then associate with Dicer/AGO/GW182 forming the functional miRISC to regulate gene silencing. The guide strand selection is mediated by the cooperation of Dicer and TAR RNA-binding protein (TRBP) and positive regulators of dsRNA-dependent protein kinase R (PKR) (PACT/PRKRA), mainly according to the relative thermodynamic stabilities of the two

duplex ends [65, 66]. The strand with the less stably base-paired at 5'end and the strand with a U at nucleotide position 1 has the high possibility to be the guide strand [67] [68]. The unselected strand then undergoes immediate degradation. However, this unselected strand can also turn to a guide strand and re-load onto AGO within miRISC [69]. Arm switching has been observed depending on different cell types and different mRNA targets [70]. For example, miR-34c-3p inhibited both U251 and U87 proliferation, whereas miR-34c-5p only inhibited U251 proliferation. miR-34c-3p overexpression reduced Notch pathway, whereas miR-34c-5p did not [71]. miRNA biogenesis also arises from the non-canonical pathways which are independent of Drosha or Dicer processing [64].

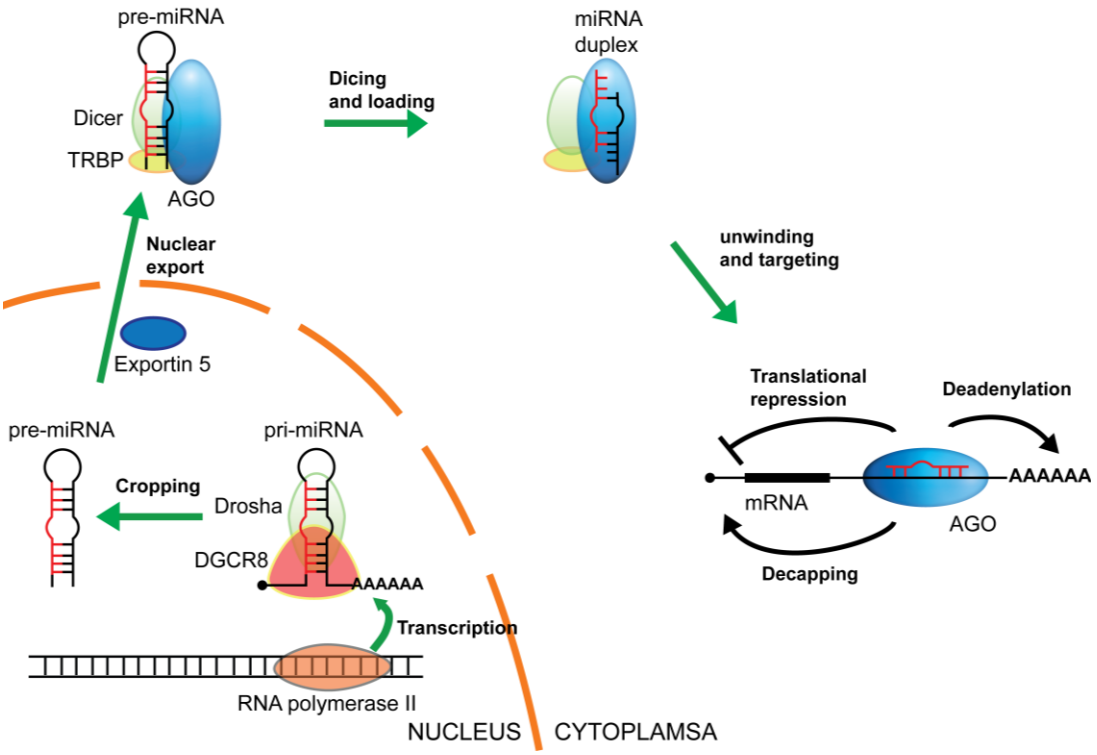

Figure 1.9 The canonical biogenesis of miRNA
The biogenesis of miRNA. pri-miRNA is transcribed from the genome by RNA polymerase II and cropped in the nucleus by Drosha/DGCR8 complex to generate pre-miRNA with the bulged hairpin structure. Pre-miRNA is then exported to the cytoplasm by binding to Exportin 5 on the 5' cap structure. In the cytoplasm, pre-miRNA is further cleaved by Dicer into miRNA duplex, followed by loading onto AGO and unwinding. Either strand (5p or 3p) of miRNA can direct miRISC to the complementary mRNAs for miRNA-mediated gene silencing. The other strand (not bind to the mRNA) is then reloaded onto miRISC. The targeted mRNA undergo either/both the translational repression or/and mRNA decay.

The biogenesis of siRNA is similar to that of miRNA, but there are still some differences, which are listed in **Table 1.1** [69, 72, 73]. Endogenous siRNAs (endo-siRNAs) precursors arise from genomic loci and are derived from transposon transcripts, sense-antisense pairs, pseudogene-derived antisense transcripts and stem-loop-structured RNAs [74, 75]. In *C.elegans* and plant, RNA-dependent RNA polymerases (RdRPs) is required for generation of endo-siRNAs, while *Drosophila* and humans present a RdRPs-independent manner [76]. Exogenous siRNAs (exo-siRNAs) are introduced as the long dsRNA or siRNA duplexes by transfection. In addition, exo-siRNAs can also arise from the viral dsRNA,

resulting in the anti-viral defence. In *Drosophila,* both types of siRNAs are bound and processed by Dicer2 into 21-23nts in length, assembling into pre-RISC. The guide strand of siRNA assembles into the functional RISC with AGO2, whereas the passenger is cleaved by AGO2 resulting in its ejection and degradation [77]. In humans, Dicer, AGO2 and TRBP associate with each other to form the siRISC-loading complex which binds and dices long dsRNAs into siRNAs. The guide strand of siRNAs is then selected to load into AGO2 to form a functional siRISC [78]. The selection of the guide strand depends on the specific duplex parameters (thermodynamics, 5' nucleotide identify). The passenger strand then undergoes the degradation during RISC assembly [73]. Furthermore, the target mRNA cleavage will be impaired if the passenger strand was unable to degrade [73].

Table 1.1 Comparison of the biogenesis of miRNA and siRNA.
Summarised form Guo *et al.*, 2010, Mack *et al.*, 2007, Leuschner *et al.*, 2006 [69, 72, 73].

Small RNA	miRNA	siRNA
Origin	Transcribed from the genome	Exogenous/endogenous dsRNA
Complementarity within the precursor	Partial	Perfect
Configuration	Single stranded	Double stranded
Cytoplasmic processing	Cleaved by Dicer into 21-23nt RNA duplex with 2nt 3'overhangs	
Length	21-23nt ssRNA (guide strand)	
Associated RNP	miRISC	RISC
Fate of the passenger strand	Loading onto another AGO	Cleaved by AGO2 then degradation
Complementarity to target mRNA	Partial	Perfect
Location of silencing occurring	Cytoplasm	
Action	Inhibit translation of mRNA	Cleave mRNA

1.3.3 Key components in miRNA pathway

Although there are differences between miRNA and siRNA with regards to their biogenesis, there are still some in common. For example, they have to associate with RISCs, relying on three important RISC components to regulate the gene expression: Dicer, GW182/TNRC6 and AGO [79-81]. Therefore, these three components will be introduced in this chapter, and the main focus will be on AGO.

1.3.3.1 Dicer

In 2001, because RNase III enzymes were thought to have dsRNA-specific nucleases activity, Bernstein *et al*. took three types of RNase III family members as the candidates to determine which enzyme was responsible for cropping the dsRNA into miRNA/siRNA [82]. One of RNase III enzymes containing a DEXDc ATPase domain, a PAZ domain, two RNase III domains and a dsRBD were identified presenting the cleavage activity and was known as Dicer [82]. Depletion of Dicer caused the loss of dsRNA-induced gene silencing of other genes. This indicated that Dicer is of importance for the initiation of RNAi. In mammals, there is only one Dicer responsible for the biogenesis of miRNA/siRNA, while other organisms have multiple Dicer proteins which have different functions. For example, in *Drosophila* Dicer-1 is responsible for the miRNA biogenesis, while Dicer2 is required for the siRNA pathway [83].

Two domains within Dicer, PAZ and RNase III, are essential for producing siRNAs from dsRNA and processing the maturation of miRNA from precursor stem-loops. Similar to Drosha, the C-terminal tandem RNase III domains of Dicer dimerise to form a catalytic centre. dsRNAs or pre-miRNA are firstly captured by PAZ domain which prefers binding to 2-nt at 3’ end. With the assistance of PAZ and dsRBD, the two RNase III domains then cleave one of the two strands of dsRNAs, generating 2-nt-long 3’ overhang [84]. According to the crystal structure, the region between the PAZ and RNase III domain functions as a molecular ruler so that Dicer cleavage sites are located at a fixed distance (21-25 nts) from the 3’ end, generating the precise cleavage [64]. Additionally, Dicer also cleaves pre-miRNA 22 nts away from the 5’ end [64, 84]. RNase III domain regulates the direct interaction with AGO for loading miRNAs [85, 86].

Dicer contributes the biogenesis of miRNA; deletion of Dicer in human cells resulted in the reduced level of miRNAs [87]. *let-7* miRNA targets human Dicer mRNA which in turn leading to a negative feedback loop between Dicer and *let-7* miRNA [88]. In addition, the Dicer activity can also be regulated by the proteins attached to the terminal loop of pre-miRNA. For instance, LIN-28 binds pre-*let-7* and inhibits Dicer processing by inducing oligouridylation of pre-let-7 [89, 90].

1.3.3.2 GW182/TNRC6

GW182 was first identified in a patient serum in 2002 and was named for the presence of glycine-tryptophan or tryptophan-glycine repeats (GW/WG) and its molecular weight (182 kDa) [91]. There are three paralogs in vertebrates (TNRC6A, TNRC6B and TNRC6C) [92], one homolog (DmGW182/Gawky) in *Drosophila* [93, 94], and one homolog in *C. elegans*, ALG-1 (AIN-1, AIN-2) [95]. They all contain a higher than normal level of GW-repeats. However, for different family proteins, the number of GW-repeats varies. Most GW-repeats lies within the N-terminal region, and few or no GW-repeats lies within the middle- and C-terminal region. The GW182 family proteins are structurally conserved. GW182/AIN-1/Gawky homolog (GAGH) domain is a conserved domain shared in all of this protein family [96]. Except for AIN-1 and AIN-2, GW182 contains an RNA recognition motif (RRM) within C-terminal region for mRNA regulation. TNRC6C and DmGW182 also contain an ubiquitin-association (UBA) domain whose function is under characterisation.

GW182 family proteins are critical miRISC components required for miRNA-mediated silencing. In *Drosophila* cells, Behm-Ansmant *et al.* showed that GW-repeats only within the N-terminal region was necessary for the interaction with PIWI domain of AGO proteins [97-99]. Depletion of GW182 suppressed the silencing of miRNA targets in *Drosophila* [94]. In human cells, depletion of TNRC6A caused the de-repression of the miRNA-targeted gene [100]. These findings indicated that GW182 family proteins associate with AGO to trigger silencing rather than AGO alone. The GW182 family proteins are one component of processing-bodies (p-bodies) (details in **Chapter 1.4**) [101, 102]. The formation of p-bodies is highly dependent on GW182. Knockdown of GW182 in human cells impaired the formation of p-bodies and subsequent miRNA-mediated gene silencing [100]. In miRNA-mediated silencing, GW182 contributes to

target recognition by AGO proteins and recruitment of mRNA decay factors such as DCP2, enhancer of decapping 4 (EDC4), and DEAD box protein 6 (DDX6) [99]. GW182 is an essential component of miRISC to mediate gene silencing [103]. The depletion of GW182 affects the miRNA and AGO2 expression, indicating that GW182 is essential for miRNA-mediated silencing [103].

As mentioned above, GW182 contains the N-terminal GW repeat-containing region which directly interacts AGO proteins [103]. The tryptophan residues contribute to the strength of the interaction. The other essential domain of GW182 is the bipartite silencing domain (SD), consisting of the middle- and C-terminal regions. In *Drosophila* cells, with the depletion of endogenous GW182, silencing cannot be rescued by GW182 lacking the middle- and C-terminal regions, indicating the importance of SD to the translational repression and degradation of miRNA-targeted mRNA [104].

1.3.3.3 Argonaute

Argonaute (AGO) is highly conserved and expressed in all eukaryotes, functioning a key component in the RNAi-mediated gene-silencing process. It was first purified from human HeLa cells in 2002 and found to belong to a highly conserved family across species [105, 106]. The AGO superfamily can be divided into three groups: the Argonaute-like proteins which associate with miRNAs and siRNAs; PIWI-like proteins which associate piRNAs and the third group which lacks the endonuclease domain but is still important for the RNAi pathway [107]. The Argonaute-like proteins are responsible for the regulation of translation by associating with miRNAs and siRNAs in the cytoplasm, while the PIWI-like proteins are related to the transcriptional silencing mainly expressed in germline cells and located in the nucleus. The first two groups present in many species, but most of them are expressed multiple *Ago* genes. In human cells, there are eight *Ago* genes, among which four are Argonaute-like proteins (*AGO1-4*) that are responsible for miRNA and siRNA pathway. In *C. elegans* and *Drosophila*, there are 5 and 27 in total, respectively.

Argonaute-like family proteins (hereafter referred to AGO family proteins/AGOs) (AGO1-4) contain six domains in the order from the amino-to-carboxy terminus: N-

terminal, L1 (Linker 1), PIWI-AGO-ZWILLE (PAZ), L2, middle (MID) and PIWI domains (**Figure 1.10A**). AGO1-4 were shown to associate with miRNAs and regulate translational repression and mRNA decay by interacting with translational initiation machinery and mRNA decay factors [108]. AGO2 is well characterised for its role in binding to small RNA and its crystal structure (**Figure 1.10B**) [109]. Six domains within AGOs form a bilobal architecture: the N-terminal lobe is formed with N and PAZ domains, and the C-terminal lobe is composed of MID and PIWI domains (**Figure 1.10B**) [109]. Both miRNAs and siRNAs require Dicer to excise, generating 2-nt-long 3' overhang on the products. The 5'-monophosphate of RNA is anchored by the pocket structure within the MID domain with the preference for U or A [110, 111]. The small RNA threads along the channel between MID and PIWI to reach the PAZ domain which tightly binds the 2nt-long 3' overhang of small RNA (**Figure 1.10B**) [109]. For the machinery of miRNA-mediated translational repression, it was reported that the MID domain contained an MC sequence region that was believed to be homology to the cap structure binding motif of eIF4E [112]. This indicated that AGO might bind to the cap structure to competitively inhibit eIF4E binding and then represses the translation [112]. However, the further sequencing and mapping of this MC sequence region indicated that there are no compatible similarities not only in sequence but also in local structure [113].

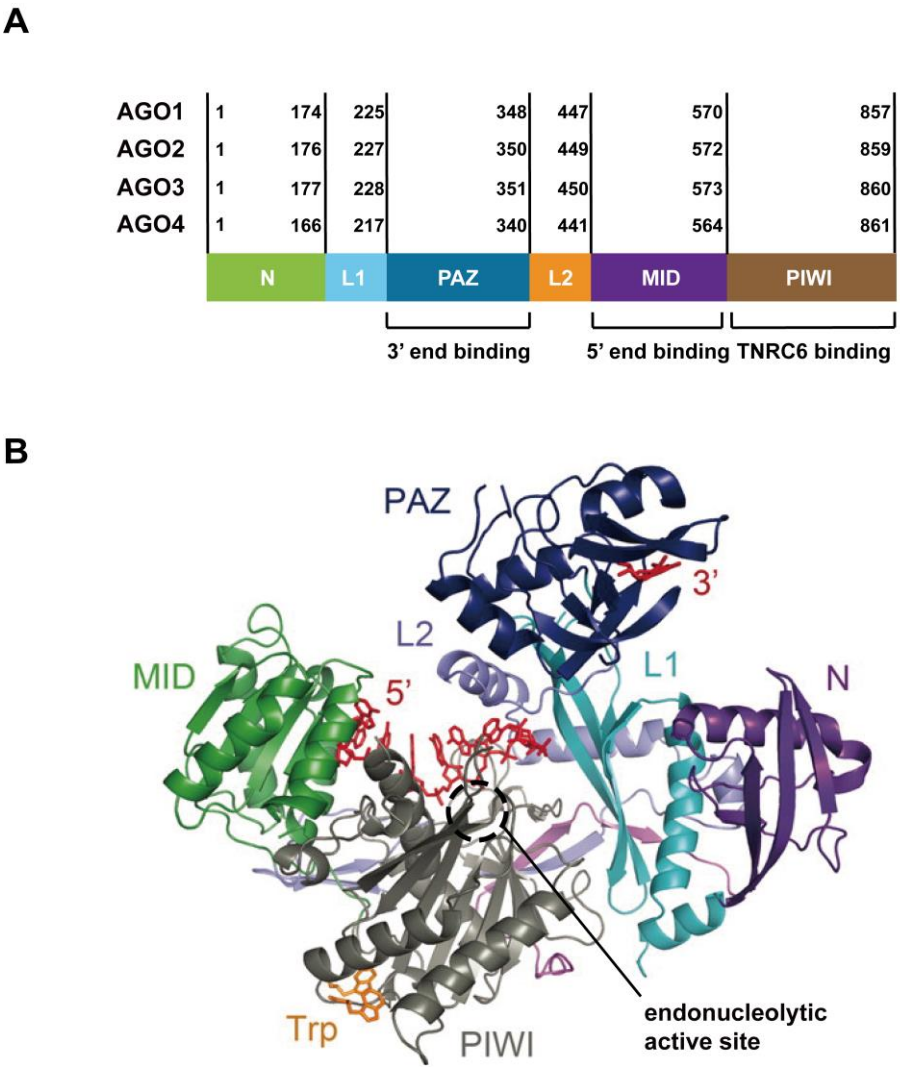

Figure 1.10 Structure of human AGO1-4

A) Human AGO1-4 compose of six domains from N-terminus to C-terminus: the N, L1, PAZ, L2, MID and PIWI domains. The PAZ domain is responsible for binding to the 3' end of guide RNA, and the MID domain binds to the 5' end of guide RNA. The PIWI domain has multiple functions. The two tandem tryptophan-binding pockets within the PIWI domain binds to GW182/TNRC6, resulting in the miRNA-mediated silencing. The PIWI domain also contributes to Dicer binding for loading of small RNAs. Moreover, the PIWI domain has an RNase H-like fold, and the slicer activity is mainly observed in AGO2. ***B)*** The crystal structure of AGO2 (PDB ID: 4OLA) and the guide RNA. AGO2 contains two lobes: the N-PAZ lobe and the MID-PIWI lobe. The 5' end of guide RNA binds to the MID domain and threads along the channel between MID and PIWI to bind to the PAZ domain. The bound guide RNA is coloured as red. The back dashed circle indicates the endonucleolytic active site within the PIWI domain. Figure part ***B*** is adapted from Schirle *et al.*, 2012 [109]

As the key component in the biogenesis of small RNAs, the conserved PIWI box within PIWI domain has been shown to interact with Dicer [85]. The loading of small RNAs onto AGOs requires the interaction between Dicer and AGO. In addition, the phosphorylation of tyrosine 393 (Y393) within L2 domain abolished the Dicer-AGO2 interaction, resulting in the reduced mature miRNAs [114]. This study implied L2 domain might also be responsible for Dicer binding. In *Drosophila*, a strict small-RNA-sorting system exists. After Dicer processing, miRNA duplexes are sorted into AGO1, while siRNA duplexes are sorted into AGO2. miRNAs with a 5' U preferably loads onto AGO1, while siRNA with a 5' C preferably loads onto AGO2. In addition, the structure of miRNA (central mismatches) prevents being sorted into AGO2 (**Figure 1.8**) [115]. However, there is no such strict sorting system existing in humans. AGO1-4 can incorporate miRNAs and siRNAs. The small RNA duplex loading depends on the heat shock cognate 70 (Hsc70)-heat shock protein 90 (Hsp90) chaperone complex which binds to AGO and hydrolyses ATP to change the AGO conformation. The conformational change opens AGO for small RNAs duplex loading and unwinding.

AGO2 directly interacts with TNRC6A through its C-terminal half and recruits TNRC6A to the 3'UTR of mRNA for gene silencing [116]. The crystal structure study showed the tandem tryptophan-binding pockets within the PIWI domain are responsible for binding TNRC6A or other GW-rich proteins [109]. The structure of PIWI domain is similar to RNase H and presents endonucleolytic activity which cleaves the target mRNA [117]. Among AGO1-4, AGO2 was believed to be the only human AGO that can slice the target mRNA with a perfect complementary match of miRNAs. The cleavage takes place between nucleotide position 10 and 11 (relative to the 5' end of miRNA) [64]. The recent study demonstrated that AGO3 also has slicer activity which depends on the guide RNA. For example, it showed AGO3 associated with miR-20a cleaved the target mRNAs, while let-7a or miR-19b did not [118]. Loading with miRNAs converts AGO3 into a catalytically active conformation; the crystal structure was showed AGO3 mimics the endonucleolytic active site of AGO2. Swapping of PIWI domain from AGO3 to AGO2 did not abolish the slicer activity, indicating that AGO3 contains all residues for slicer activity in its PIWI domain [119]. However, crystal structure showed the nucleic acid-binding channel within AGO3 is incomplete. The disordered N domain within AGO3 results in the

channel exit between the N and PIWI domain wider than that within AGO2 (**Figure 1.11**) [118]. The disordered N domain causes a looser packing region between N and L1/L2 domains, which is critical for cleavage [118, 120]. Swapping N domain of AGO3 to AGO2 inhibited AGO2 slicer activity [119]. By contrast, the well-ordered N domain of AGO2 is critical for slicer activity. Once swapping N domain of AGO2 to AGO3, AGO3 showed the detectable slicer activity [119]. Similar to AGO3, a looser packing region between N and L1/L2 was also found in AGO1 [118], indicating the disordered N domain and misarranged catalytic domain leads to the deficient in cleavage activity. In fact, AGO1 cleaved the target when mutations were introduced to the N and PIWI domain, which re-arrange these two domains [119].

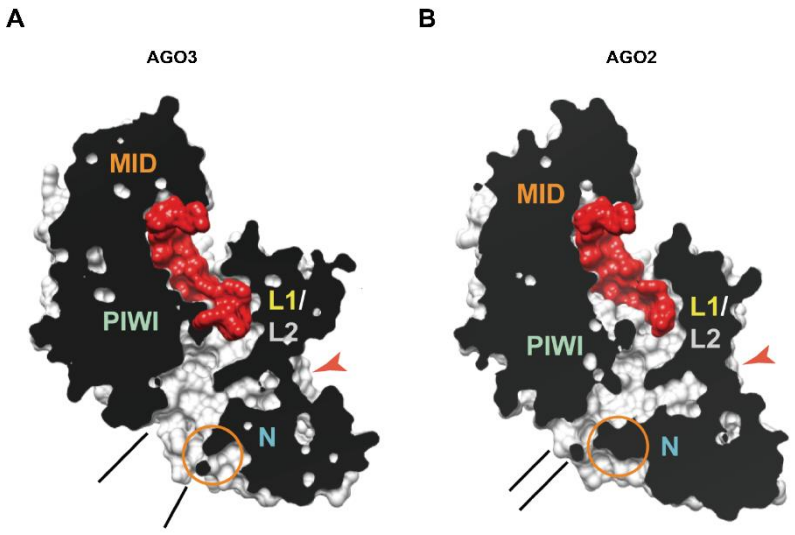

Figure 1.11 The crystal structures of human AGO3 and AGO2 [118]
The crystal structure of **(*A*)** human AGO3 (PDB ID: 5VM9) and **(*B*)** AGO2 (PDB ID: 4OLA). The bound guide RNAs are coloured in red. Compared with the structure of AGO3 and AGO2, the disordered N domain (highlighted in orange circle) within AGO3 leads to a wider channel exit (highlighted in black lines) and a looser connection between the N and L1/L2 domain (highlighted in orange arrowheads). These structural differences within AGO3 result in the abolished endonucleolytic activity. Figure adapted from Park *et al*., 2017 [118].

The post-translational modifications of AGO2 affect the functions (**Table 1.2**) [121]. For instance, the stability of AGO2 is affected by the hydroxylation of proline (P) 700 within the PIWI domain [122]. The hydroxylation of P700 also increased miRNA activity under

the hypoxic condition [123]. Moreover, the phosphorylation of Y529 within the MID domain, which is responsible for the small RNAs binding, reduced the amount of small RNAs bound to AGO2 [124]. Besides, the phosphorylation of the multi-site (S824-S834) was demonstrated to impair the small RNAs binding [125]. The phosphorylation of serine (S) 387 within the L2 domain of AGO2 is mediated by mitogen-activated protein kinase (MAPK)-activated protein kinase 2 (MAPKAPK2) or ATK3, promoting AGO2 localisation to P-bodies and thus translational repression [126, 127]. In addition, another phosphorylation site within the L2 domain, Y393, was reported to contribute the biogenesis of miRNAs. The phosphorylated AGO2 at Y393 residue resulted in the dissociation from Dicer, the reduced loading of miRNA and the reduced level of long-loop mature miRNAs [114, 128]. Under viral infection or stress, AGOs is modified by poly (ADP-ribose) polymerase so that the miRNA-mediated gene silencing is relieved [121, 129]. AGO2 stability is positively regulated by the cellular availability of mature miRNAs and the ubiquitin-proteasome system, and the loading of siRNAs can rescue the stability of AGO2 in the absence of miRNA biogenesis [121, 130].

Table 1.2 The post-translational modification of AGO2.

Modification	Site	Function	Reference
Hydroxylation	P700	Increases AGO2 stability and miRNA levels	[122, 123]
Phosphorylation	S387	Increases P-body localization and translational repression	[126, 127]
	Y393	Dissociates the interaction between Dicer and inhibited the maturation of long-loop miRNAs under hypoxia;	[114, 128]
	Y529	Impairs miRNA loading	[124]
	S824-S834	Impairs miRNA target binding	[125]
Poly ADP-ribosylation		Suppresses RNA silencing during stress or viral infection	[121, 129]
Ubiquitination		AGO2 turnover	[121, 130]

1.3.4 Gene silencing mediated by miRNA

The mature miRNA complementarily binds the 3'UTR of the target mRNA. For silencing, two different pathways are involved: translational repression and mRNA degradation. The machinery of translational repression will be presented in **Chapter 1.5**. For the degradation pathway, TNRC6, a key component of the miRISC complex, recruits PAN2-PAN3 and CCR4-NOT for deadenylation of the target mRNA, followed by decapping process [79]. In addition, AGO2 slices the target mRNA when there is perfect or near-perfect complementary binding between the miRNA and the target mRNA. After cleavage, the mRNA decay machinery factors (exosome, XRN1 and DCPs) degrade the 5' and 3' fragments.

1.3.5 Gene silencing mediated by siRNA

Post-transcriptional siRNA silencing mostly occurs in the cytoplasm. In the siRNA pathway, the siRNA guide strand binds to the target mRNA with perfect complementarity to deliver RISC to the target. The PIWI domain of AGO has the target-cleavage activity. This precisely occurs between the 10^{th} and 11^{th} position on the target nucleotides when counting from the first base-paired nucleotide at 5' end with siRNAs [131]. After cleavage, the cellular decay machinery factors then degrades the fragments, and the functional siRISC is regenerated. In some cases, siRNA can also bind the target with imperfect complementarity, resulting in miRNA-like silencing pathway which is considered as the "off-target" effects of siRNAs [132]. This is due to the seed region on 5'-end of siRNAs targeting the mRNA and mismatches make it indistinguishable from miRNA silencing pathway [133, 134].

1.4 The formation of P-bodies is the consequence of RNAi-mediated silencing

1.4.1 P-body is a distinct cytoplasmic ribonucleoprotein granule

In eukaryotic cells, translationally repressed mRNA (by both mRNA surveillance pathway and RNAi mediation) accumulate in the cytoplasmic mRNA ribonucleoprotein (mRNP) granules, so-called P-bodies. The P-bodies were first discovered in 1997 when 5'-3' XRN1 was found to be localised in small cytoplasmic granular structures, which were later

observed to be localised with DCP1-DCP2 [135, 136]. The formation of P-bodies is revealed to be dependent on and proportional to the non-translated mRNAs; the treatment of ribonuclease A led to P-bodies loss [137]. Lsm1-7 complex, which binds to 3' end of mRNA and enhances the decapping complex for mRNA degradation, is one of the components found in P-bodies [138, 139]. As a result, the assembly of P-body is believed to initiate from the formation of the 'closed loop' structure of mRNA by the interaction between the decapping complex and the Lsm1-7 complex [139]. The aggregation into larger structures are then dependent on the interaction between two TNRC6 proteins bound onto the different mRNAs through their glutamine/asparagine (Q/N) domain [140]. Evidence showed the depletion of TNRC6A diminished P-bodies [141].

1.4.2 The formation of P-bodies is the consequence of RNAi-mediated silencing

A number of proteins involved in miRNA-mediated silencing have been found to be co-localised to P-bodies including AGO2 [142], TNRC6A [91], eIF4E [143], Lsm1-7 complex [144], RCK/p54 [144] and LIMD1 [1], indicating the importance of P-bodies in mRNA-mediated gene silencing. RCK/p54, is required for miRNA-mediated translational repression and facilitates P-bodies formation [144]. Chu *et al*. demonstrated that the depletion of RCK/54 resulted in P-bodies loss and diffusion of AGO2 throughout the cytoplasm, but the depletion of RCK/p54 did not affect miRNA- or siRNA-mediated silencing [144]. Their findings revealed that the integrity of P-bodies is not necessary for RNAi-mediated silencing. Indeed, Ana *et al*. confirmed that the biogenesis of miRNA is connected to P-body formation: the depletion of Drosha reduced P-body sizes and numbers [145]. The depletion of Dicer-1 and dmAgo1 (Drosophila Argonaute only functions in miRNA-mediated silencing) could also reduce P-body formation [145]. Furthermore, studies have shown that the P-body sizes and numbers depended on the amount of de-capped mRNAs [146, 147]. Taken together, these studies concluded that P-body formation indicates the occurrence of RNAi-mediated silencing.

1.4.3 Relationship between P-bodies and stress granules

There is another cytoplasmic mRNP granule, referred to stress granules (SGs), which also aggregate the non-translated mRNAs and whose assembly is also proportional to the non-translated mRNAs. However, studies have shown the differences between P-bodies and SGs in the following aspects: **1**) differences in the shape and size under the microscope (P-bodies perform the compact, dense and droplet like structure, whereas SGs exhibit the larger, irregular, looser and rather granular structure (**Figure 1.12**)) and **2**) differences in aggregated proteins (**Table 1.3**) (P-bodies contain mRNA decay proteins, whereas SGs contain translation initiation proteins). Although P-bodies also contain eIF4E which is one of the translation initiation factors, it was believed that eIF4E-T binds and inhibits eIF4E function resulting in the association between eIF4E and non-translated mRNAs in P-bodies. As a result, mRNAs in P-bodies are specifically for decay, while mRNAs in SGs are not subject to decay immediately. Although XRN1 is found in SGs, it has no function on degrading mRNAs due to no DCPs found within SGs. Therefore, this property makes SGs as protection of mRNA degradation.

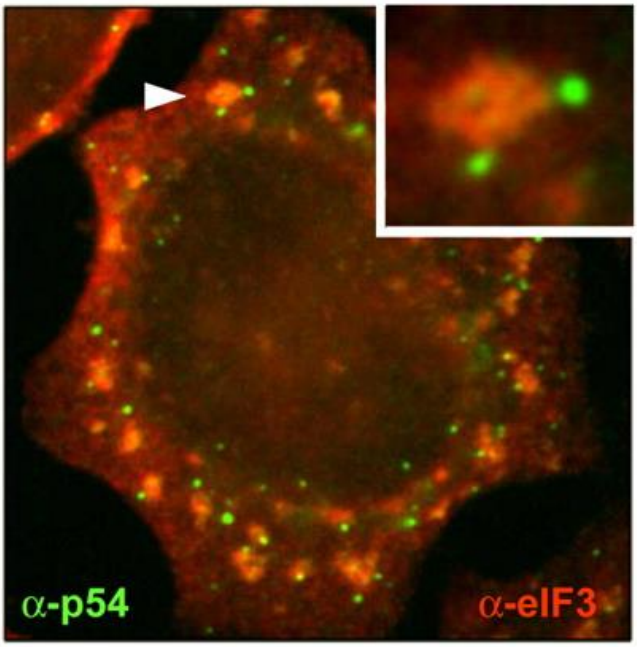

Figure 1.12 Structural differences between P-bodies and SGs [148]
Immunofluorescence image for HeLa cells submitted to an oxidative stress. P-bodies and SGs were detected with anti-p54 (green) and anti-eIF3 (red) antibodies, respectively. P-bodies are frequently associated with SGs, as indicated by the arrowhead and enlarged in the up-right corner. Figure is adapted from Souquere *et al.*, 2009 [148]

Table 1.3 The list of components of P-bodies and stress granules..
Summarized from Decker *et al*., 2012 and Luo *et al*., 2018 [140, 149]

Name	Function	P-bodies	Stress granules
Agonaute proteins	miRNA function	+	+
Ataxin-2	Translation		+
CCR4-NOT complex	Deadenylase	+	
DCP1	Decapping enzyme subunit	+	
DCP2	Decapping enzyme	+	
DDX3	RNA helicase		+
EDC1	Decapping activator	+	
EDC2	Decapping activator	+	
EDC3	Decapping activator	+	
eIF2α	Translation initiation		+
eIF3	Translation initiation		+
eIF4A	Translation initiation		+
eIF4B	Translation initiation		+
eIF4E	Translation initiation	+	+
eIF4G	Translation initiation		+
eIF4E	Translation initiation	+	
eIF4E-T	Translation repressor	+	
eRF1	Translation termination	+	
eRF3	Translation termination	+	
FMBP	Translation, repression/miRNA function		+
Hedls	Decapping activator	+	
Lsm1-7 complex	Decapping activator	+	
Pat1	Translation repressor	+	
PUM1 [150, 151]	Translation repressor	+	+
PUM2 [151, 152]	Translation repressor	+	+
STAU2 [151, 153]	Translation repressor	+	+
Rap55	Translation repressor	+	+
RCK/p54	Translation repressor/decapping activator	+	+
TIA-1	Translation repressor		+
TNRC6A	miRNA function	+	
Upf1	Nonsense-mediated decay	+	
XRN1	5’ – 3’ exonuclease	+	+
YTHDF2 [154, 155]	mRNA stability	+	+
40S ribosomal subunit	Translation		+

P-bodies were shown to have a dual role as mRNA decay sites and storage areas [156]. However, the recent study had a conflict that mRNA segregated within P-bodies are not decayed [151]. Another independent study also showed that mRNA decay products are in cytoplasm not in P-bodies. These findings are very intriguing because the majority mRNA decay proteins are found within P-bodies. This raised a question that how mRNA decay proteins are inhibited within P-bodies to protect mRNAs from degradation. In addition, this recent study implied that mRNA decay would be activated in the cytoplasm, which agrees with the previous independent study that depletion of RCK/p54 resulted in P-bodies lose, but had no effects on RNAi-mediated silencing [144]. The mechanisms remain to be investigated.

For the perspective of mRNA storage, the repressed mRNAs (not all repressed mRNAs) within P-bodies are able to re-engage in translation [156-158]. In fact, mRNAs are observed to cycle between polysomes (where translations take place), P-bodies and SGs. Inhibiting translation initiation resulted in the loss of mRNAs in polysomes and increased mRNAs in P-bodies and SGs [140]. Observations demonstrated that there is a physical interaction between P-bodies and SGs; they can dock together for a short period. The movement of P-bodies and SGs rely on the microtubule network [159, 160]. Given that, the docking can be achieved by the microtubule network. AGO2 with miRNA was showed to travel from P-bodies to SGs, indicating the exchange of components between P-bodies and SGs [161]. The overexpression of cytoplasmic polyadenylation element binding protein (CPEB), which mediates polyadenylation of mRNA, increased docking and fusing from one to another [162]. CPEB was shown to be localised to P-bodies and might re-adenylate mRNAs and transfer to SGs. Moreover, Tristetraprolin (TTP) contributes to increasing the flux of mRNPs from SGs to P-bodies by promoting deadenylation. These findings indicated the re-distribution of mRNPs between P-bodies and SGs, and it also provides a model of mRNA cycle (**Figure 1.13**). Depending on the fusion, mRNPs within P-bodies and SGs undergo the rearrangement; degradation machinery proteins can be replaced with initiation factors by competition which allows the repressed mRNAs return to translation. Similarly, mRNPs within SGs can also be replaced by degradation machinery proteins, resulting in the mRNA decay.

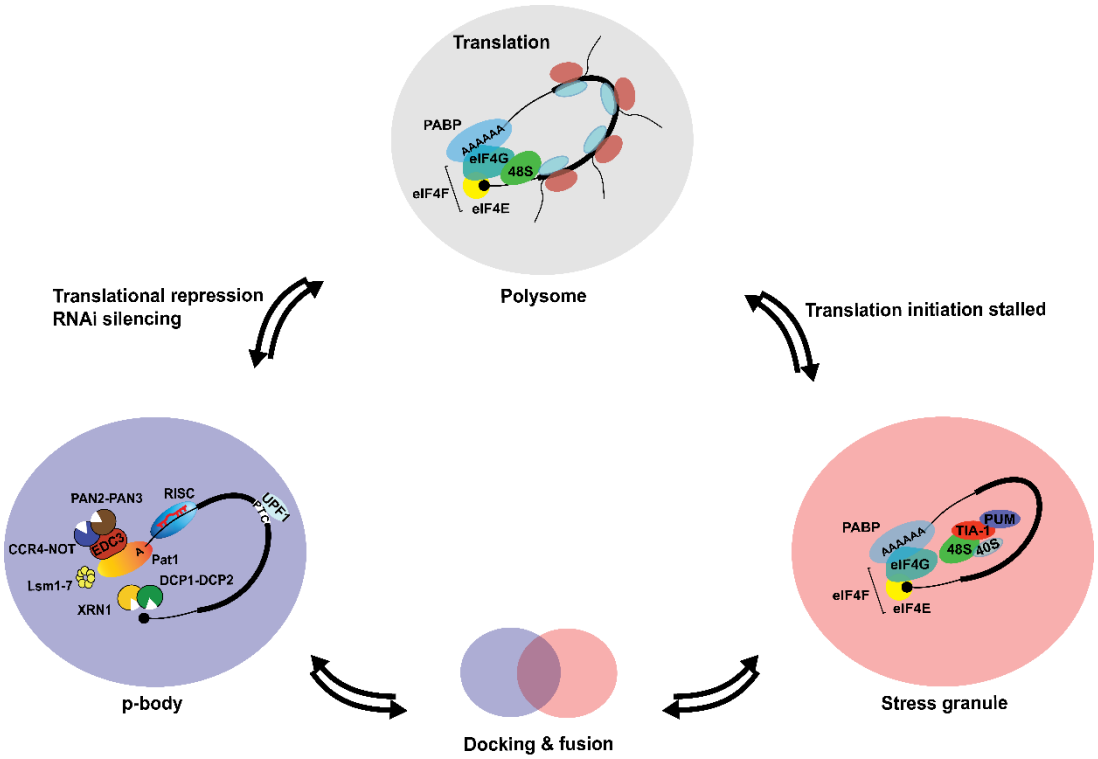

Figure 1.13 The dynamic movement of mRNA between polysomes, P-bodies and stress granules
The translation of normal mRNAs takes place in the polysome, including repeated rounds of translation initiation, elongation and termination. Once the surveillance machinery detects the defective mRNAs or non-coding RNAs bind their complementary targets, which results in the translational repression, the ribosomes drop off and these non-translated mRNAs associated with mRNPs aggregate into the larger structure, so-called P-bodies. Therefore, P-bodies mainly contain mRNA decay proteins. On the other hand, when the translation initiation is stalled under stresses, mRNAs tend to aggregate into stress granules which mainly contain initiation factors. Non-translated mRNAs either in P-bodies or stress granules are able to re-enter to polysome for translation once the degradation machinery is replaced with the initiation factors. The physical interaction (docking) between P-bodies and stress granules is frequently observed. Overexpression of certain proteins can lead to the fusion between P-bodies and stress granules, resulting in the re-arrangement of mRNPs.

1.5 Mechanism of translational repression by miRNAs

In addition to the mRNA decay pathway, miRNA-mediated gene silencing triggers the translational repression on the target mRNAs during the translation initiation or post-initiation [163, 164]. Therefore, to understand the machinery of translational repression, the mechanism of mammalian translation initiation is introduced first, followed by the translational repression models.

1.5.1 The mechanism of mammalian translation initiation

The maturation of mRNAs is required for the post-transcriptional modification on the precursor mRNA in the nucleus, adding a 5' 7-methylguanosine (m^7G) cap structure and a 3'polyadenosine (poly(A)) tail to prevent from exonucleolytic degradation [165, 166]. The mature mRNA is then translocated into the cytoplasm ready for translation [166, 167]. The translation consists of three major steps: **1**) translation initiation which requires ribosomes assembly and the binding to the start codon; **2**) peptide elongation which creates peptide chain by the translocation of the ribosomes and **3**) translation termination which releases the ribosome when it reaches the stop codon [168].

The translation initiation is the process of assembly of elongation-competent 80S ribosomes, in which the initial codon is base-paired bound with transfer RNA (tRNA) in the ribosome. The 80S complex consists of the 48S initiation complexes and 60S ribosomal subunit. The 48S initiation complexes can be further broken down into the assembly of multiple eukaryotic initiation factors (eIFs), which play important roles in translation initiation (**Table 1.4**), to form 43S preinitiation complex [168].

Table 1.4 The list of eIFs involved in the translation initiation.
Adapted from Jackson *et al.*, 2010 [168].

Name	Function	Reference
eIF1	Accelerates the rate of eIF2-GTP-Met-tRNA binding to 40S; promotes ribosomal scanning	[169]
eIF1A	Stabilizes the interaction between eIF2-GTP-Met-tRNA and 40S; cooperates with eIF1 in promoting the ribosomal scanning	[169]
eIF2	Forms the eIF2-GTP-Met-tRNA ternary complex	[170]
eIF2B	Promotes GDP-GTP exchange on eIF2	[171]
eIF3	Binds 40S subunits, eIF1, eIF4G and eIF5; promotes ribosome dissociation for the recycle of 40S subunits; prevents the re-association of 40S to 60S; facilitates binding of eIF2-GTP-Met-tRNA to 40S subunits; and promotes the attachment of 43S complexes to mRNA	[172]
eIF4A	Unwinds 5'cap-proximal region of mRNA for ribosome attachment by DEAD-box ATPase and RNA helicase activity	[173]
eIF4B	Enhances the helicase activity of eIF4A	[174]
eIF4E	Binds to the m^7G 5'cap structure of mRNA	[175-177]
eIF4F	Consists of eIF4A, eIF4E and eIF4G, forming a cap-binding complex	[178]
eIF4G	Functions as a scaffold protein to bind eIF3, eIF4A, eIF4E and PABP, and enhances the binding of 4E to the 5'cap structure of mRNA	[173]
eIF4H	Enhances the helicase activity of eIF4A	[174]
eIF5	Induces the hydrolysis of eIF2-bound GTP	[179]
eIF5B	A ribosome-dependent GTPase that mediates ribosomal subunit joining	[180]
eIF6	Binds 60S subunits to prevent 60S joining to 40S subunits	[181, 182]

1.5.1.1 The initiation of translation requires multiple factors

Translation initiation requires the 40S and 60S ribosomal subunits. Translation is a cyclical process, and thus the ribosomal subunits that are required for the translation initiation are derived by recycling of the post-termination ribosomal complexes (post-TCs) [183]. The post-TCs consists of the 80S ribosome, tRNA and eukaryotic release factors (eRF1 and eRF3) [184]. The main function of eRFs is to release the ribosome from mRNA when it reaches the stop codon. eIFs (eIF1, eIF1A and eIF3) dissociate the post-TCs into the free 60S ribosomal subunits, mRNAs, tRNA and the 40S subunit (**Figure 1.14**). eIF1, eIF1A and eIF3 remain associated with the 40S subunit to prevent its re-association with the 60S subunit. Meanwhile, methionine-tRNA (Met-tRNA) is associated with eIF2

and GTP form the eIF2-GTP-Met-tRNA ternary complex. Subsequently, 43S preinitiation complex is then formed by the assembly of eIF1-eIF1A-eIF3-associated 40S (**Figure 1.14**).

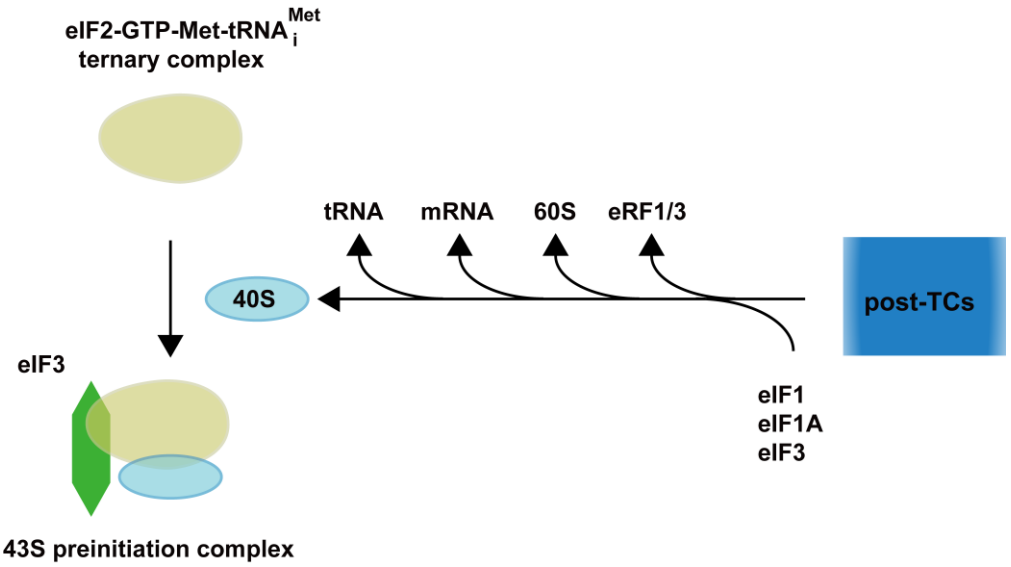

Figure 1.14 The formation of the 43S preinitiation complex by recycling 40S
eIFs (eIF1, eIF1A and eIF3) dissociate the post-TCs into the free 60S ribosomal subunits, mRNAs, tRNA and 40S subunits. The recycled 40S then associates with eIF2-GTP-Met-tRNA^{Met} ternary complex to form the 43S preinitiation complex.

The formation of the 48S complex requires the attachment of the 43S preinitiation complex with 5'UTR of mRNA. Due to the secondary structure of 5'UTR, the 5'cap structure needs modifications for the sufficient loading of the 43S preinitiation complex. eIF4F is a complex consisting of eIF4E, eIF4G and eIF4A, facilitating the association of mRNA with the ribosome [178]. eIF4E binds to the 5'cap structure [175, 176]. eIF4G, as a scaffold protein, provides a platform for the binding of eIF4E, poly(A)-binding protein (PABP), eIF4A and eIF3. Binding to eIF4E, eIF4G is capable of stabilising the 5'cap structure [177]. Consequently, the eIF4E-eIF4G-PABP interaction leads mRNA to a closed-loop structure [185] (**Figure 1.15A**). eIF4A, the DEAD-box RNA helicase, with eIF4B and eIF4H unwind the 5'cap-proximal region of mRNA for ribosomal attachment [174, 178]. Evidence showed that the activity of eIF4A was stimulated by eIF4B and eIF4H, preventing mRNA re-annealing, indicating the 5'cap proximal region of mRNA is always kept prepared for ribosomal attachment [173]. The attachment of 43S

preinitiation complex to mRNA depends on the interaction between eIF4G and eIF3 [168]. Subsequently, the 48S complex is formed by the cap-eIF4E-eIF4G-eIF3-43S chain of interaction (**Figure 1.15B**).

After assembly, with the cooperation by eIF4A, eIF4G and eIF4B, the 43S complex starts scanning mRNAs downstream of the cap to the initiation codon (AUG) [168, 186]. Once the 43S complex encounters the initiation codon (AUG), the 60S ribosomal subunit is recruited mediated by eIF5B [180], resulting in the translation elongation (**Figure 1.15**). For the normal translational machinery, the elongation continues until the ribosome reaches the stop codon, and the ribosome then releases from the mRNA to start the next round of translation. The translation can be stalled if there are defectives within the translated mRNA, which is reviewed in the mRNA degradation pathways (**Chapter 1.2**).

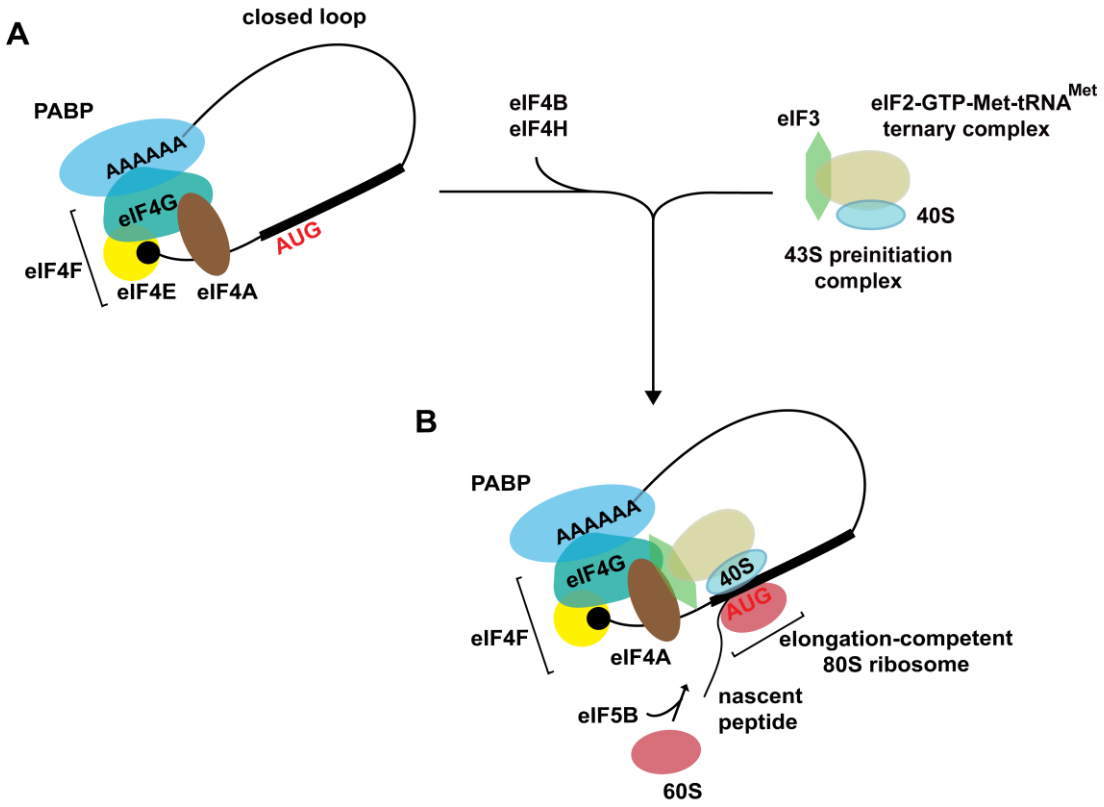

Figure 1.15 The formation of the 48S complex and translation elongation
A) The modification of 5'cap structure of mRNA is processed by binding to eIF4F complex (eIF4A, eIF4E and eIF4G). The closed-loop structure is then formed by the binding of eIF4F to PABP; ***B)*** With the assistance of eIF4B and eIF4H, eIF4G functions as a platform for the assembly of the closed-loop mRNA, and the 43S preinitiation complex to form the 48S complex. The 43S complex then starts scanning the start codon (AUG). eIF5B subsequently mediates 60S recruitment to 40S, forming 80S subunits for translation elongation.

1.5.1.2 Internal ribosome entry sites (IRESs)-mediated translation

In addition to the cap-dependent initiation reviewed above, an alternative mode of translation initiation, which bypasses the requirement for cap-dependent machinery, directly recruits the 40S subunit to the start codon. The IRES elements located in the 5'UTR of mRNA mediate the recruitment of the 40S subunit, therefore so-called IRES-mediated translation or internal initiation [187]. The long and highly structured 5'UTR is not efficient for eIFs binding and scanning, leading to the low level of cap-dependent initiation and thus the low level of translated products [188, 189]. Therefore, the function of IRES-mediated translation is to support for more translational products. In addition, IRES-mediated translation also supports the robust translation of mRNAs when the cap-dependent machinery is compromised under physiological, pathophysiological and stress conditions [187, 189].

The IRES elements are diverse in their sequences and/or structures within different mRNAs: different mRNAs contain different IRES elements in the sequence and structure. Therefore, to determine the existence of an IRES element within in a particular mRNA, it requires the experiments for each mRNA. Alternatively, the IRES element of one mRNA can be predicted by the online IRES prediction tool, but it needs experiments for further determination. The activity of IRES to mediate the internal initiation is with the assistance of eIFs or IRES trans-acting factors (ITAFs) [190]. With the assistance of ITAFs, IRES changes the conformation which is sufficient for recruitment and preparing a landing platform for the ribosomes. In most cases of internal initiation, for example, the internal initiation of *c-myc* and *N-myc* do not require eIF4E and eIF4G (**Figure 1.16A**) [191]. The two ITAFs, Y-box binding protein 1 (YB-1) and polypyrimidine tract-binding protein 1 (PTB-1), bind c-myc IRES and enhance c-myc expression and cell proliferation [192]. A different mechanism of IRES-mediated initiation is to stall the cap-initiated ribosomes in a short upstream ORF (uORF) (**Figure 1.16B**) [193]. For example, uORF embedded within the IRES of cationic 1 (*CAT1*) mRNA can activate IRES activity. Under the amino acid stress, it enables the structural remodelling of the IRES which results in the translation of the main ORF [194]. By contrast, uORF can also inhibit the IRES activity. For instance, the expression of human fibroblast growth factor 9 (FGF9) remains at the

low level due to uORF-mediated translational repression under the normoxic condition (normal level of oxygen), but the expression was up-regulated *via* IRES-mediated translation under the hypoxic condition (low level of oxygen) (**Figure 1.16C**) [195]. Furthermore, RNA G-quadruplex (RG4) structure, which inhibits the cap-dependent translation by compromising 5' cap recognition [196], has been demonstrated to regulate IRES-mediated translation (**Figure 1.16D**) [197]. Inhibiting or stabilising the conformation of RG4 within the vascular endothelial growth factor (*VEGF*) IRES repressed the IRES-mediated translation [197].

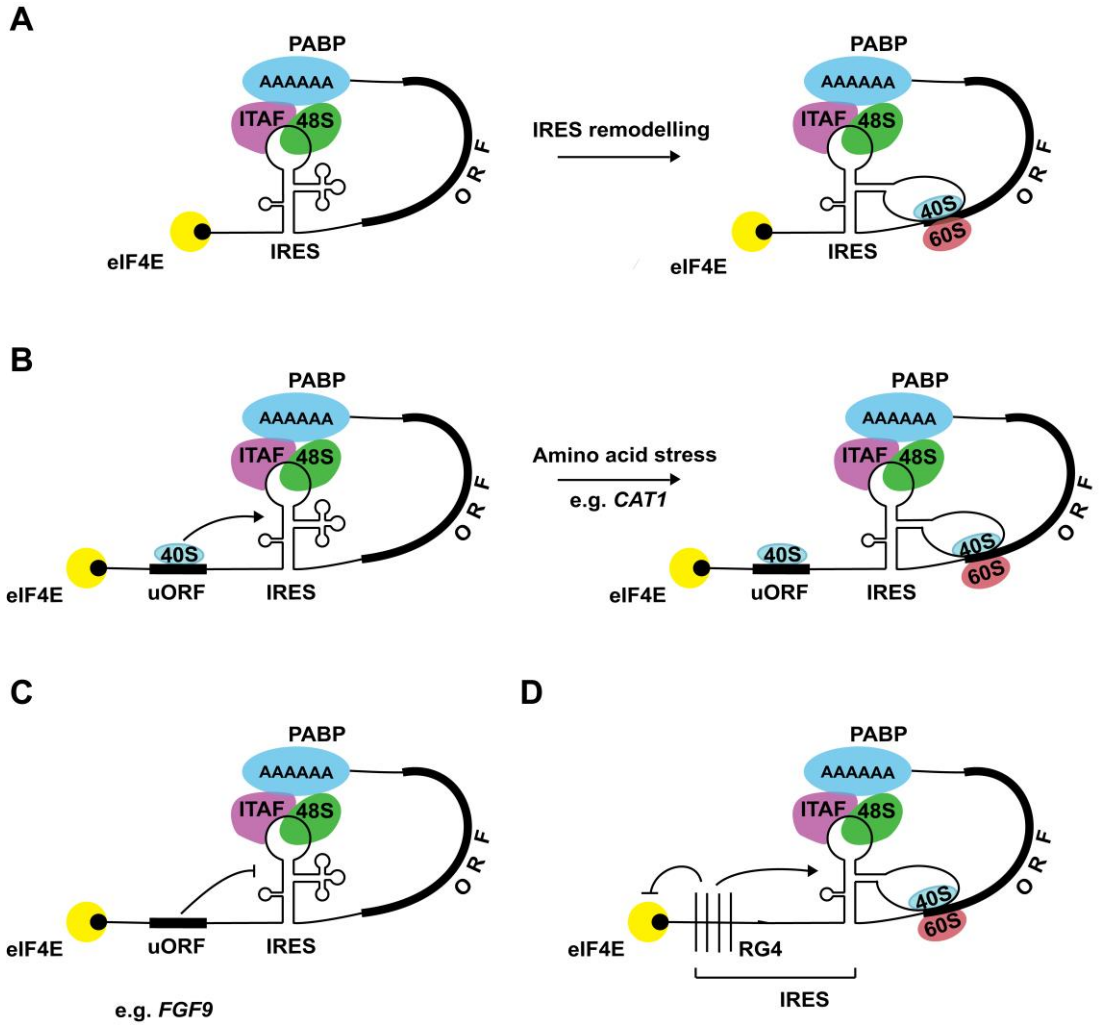

Figure 1.16 The different mechanisms for IRES-mediated translation
The IRES-mediated translation requires the closed-loop structure of mRNA. In the most cases, eIF4E and eIF4G are dispensable. ***A*)** ITAFs assist IRES to remodel into an active conformation, providing a landing platform for the ribosomes. ***B*)** The uORF can promote IRES for ribosomes recruitment. For example, under amino acid stress, the uORF embedded within 5'UTR of *CAT1* mRNA stalls the 40S subunit and thus open the inhibitory structure of IRES. Subsequently, IRES changes its conformation and enables the ribosomes recruitment. ***C*)** The uORF can also inhibit IRES-mediated initiation. For example, the expression of FGF9 keeps at the low level due to the inhibitory function of uORF embedded. However, FGF9 expression is induced by IRES-mediated translation under the hypoxic condition. ***D*)** RG4 embedded within IRES (e.g. VEGF) inhibits cap-dependent initiation and promotes the 40S subunit recruitment and thus IRES-mediated translation.

1.5.2 Translational repression mediated by miRNA

miRNA-mediated gene silencing controls the expression of the target by the translational repression and/or mRNA degradation. Studies have shown that the gene repression occurs either at translation initiation or post-initiation [163, 164]. There are currently several models for how miRNAs repress the initiation or post-initiation stages of translation. The first model proposed the dissociation of ribosomes after the initiation of translation, and ribosomes exit prematurely from their associated mRNAs to terminate the peptide elongation [164] (**Figure 1.17**). The research team observed that ribosomes associated with the repressed mRNAs dropped off more rapidly than those on active mRNAs [164]. In addition, Nottrott *et al.* showed when *let-7a* miRNA was used to regulate the expression of lin-41 in HeLa cells, the polypeptide elongation in repressed mRNAs is at the same rate as it in unrepressed mRNA [198]. This suggested that although ribosome dropped off, the translation continued on the repressed mRNAs. However, no proteins were detected. Therefore, the translation repression occurs during the peptide elongation. During the polypeptide elongation, the components of repressed mRNAs (probably miRISCs) initiate the destruction of the peptide by recruiting proteases [198] (**Figure 1.17**).

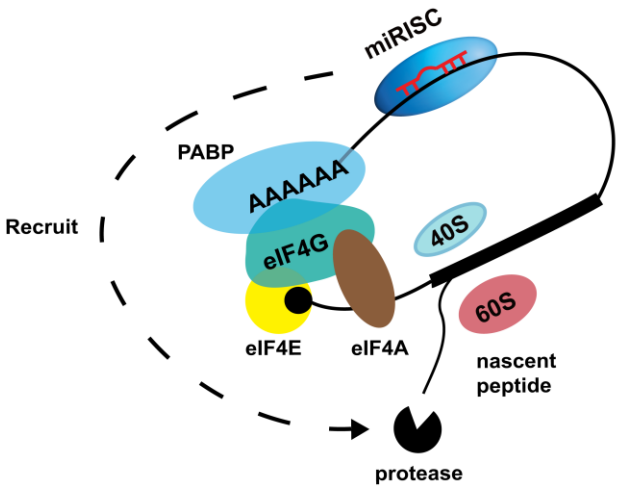

Figure 1.17 The translation repression is caused by ribosome drop-off and protease recruitment by miRISC
miRISC recruits the protease to degrade the nascent peptide during translation elongation. Meanwhile, the ribosomes drop off from the repressed mRNA.

The second model proposed that the miRISC prevent the assembly of the ribosomes (**Figure 1.18**). In a cell-free system, the amount of 60S subunits was found to decrease in miRNA-targeted mRNAs. This indicated translationally repressed mRNAs blocked the association of 60S with 40S subunit [199]. In addition, eIF6, which is involved in the biogenesis of maturation of the 60S subunit, prevents the assembly of 60S with 40S [182]. Depletion of eIF6 ablated the reduction of mRNAs mediated by miRNA-mediated silencing in human cells [181]. The evidence also suggested that AGO2 has the direct interaction with eIF6 and 60S [181]. Therefore, by competing with 40S ribosomal subunits, miRISC binds eIF6-associated 60S subunit and prevents the assembly of ribosomes to initiate the translation (**Figure 1.18**).

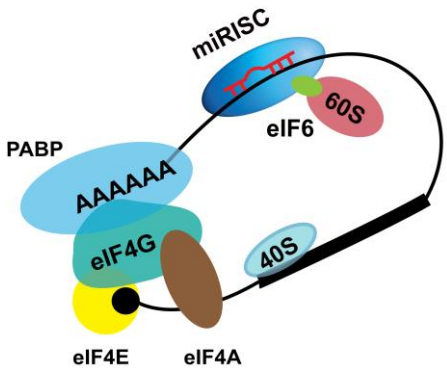

Figure 1.18 miRISC prevents the assembly of the ribosomes
miRISC competes with the 40S subunit to bind to eIF6 and 60S subunit. This prevents the maturation of 60S subunits so that translation is repressed.

The third model addressed the hypothesis that the initiation is repressed by deadenylation of mRNA stimulated by miRISC (**Figure 1.19**). GW182/TNRC6, an important component in miRISC, was reported to compete with eIF4G for binding to PABP1 [200]. In this case, PABP1 along with poly (A) tail is set for free, and the initiation of translation is repressed. Simultaneously, TNRC6A recruits the deadenylase complex (CCR4-NOT) and triggers the deadenylation process so that the translational closed-loop structure cannot be formed through poly(A) tail [99, 201]. By contrast, for those non-polyadenylated mRNAs can still be silenced by miRNA, which highly depends on both

AGO and GW182 functions [103]. Depletion either will cause the ablation of miRNA silencing, while depletion of a component of the deadenylase enzyme causes little effects on translation repression [103].

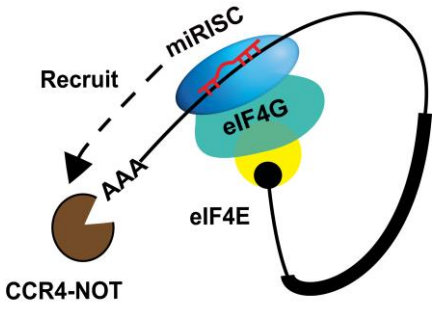

Figure 1.19 miRISC regulates the deadenylation of mRNA
miRISC competes with PABP (not shown) to bind to eIF4G, forming a closed-loop structure. Meanwhile, miRISC recruits (CCR4-NOT) complex to degrade poly(A) tail.

Translation is initiated by eIF4E binding to mRNA 5' cap structure. The methylated base of the cap is stacked between two tryptophan residues on eIF4E. A fourth model suggested that repression of initiation was due to the formation of an inhibitory closed-loop by the competition between AGO2 and eIF4E for binding to the 5' cap structure [112]. The two phenylalanine residues (MC sequence region) within the MID domain of AGO2 was reported to mimic the eIF4E tryptophan [112]. Mutation of either or both phenylalanine caused the abolishment of AGO2 silencing ability. This cap-binding function of AGO2, therefore, repressed the initiation by releasing eIF4E from the 5' cap. However, sequence and structural analysis indicated that AGO2 does not contain such region that was compatible with eIF4E [113]. The explanation for AGO2 losing silencing ability could be that the MID domain structure is destabilised resulted by the mutation of both phenylalanine [113]. In fact, the mutation of these residues disrupted the interaction between Ago1 and GW182 in *Drosophila*, resulting in the ablation of silencing [103]. The findings from James *et al.* support this model of an inhibitory complex repressing initiation [1]. James *et al.* demonstrated that LIMD1 is involved in miRNA-mediated gene silencing [1] (**Figure 1.20**). LIMD1 was found to interact miRISC

complex and initiation factors with 7-Methylguanosine-5'-triphosphate (m^7GTP) Sepharose which is used for purification of mRNA cap binding proteins [1]. Therefore, the translational repression is caused by the formation of the closed-loop structure through a scaffold protein, LIMD1.

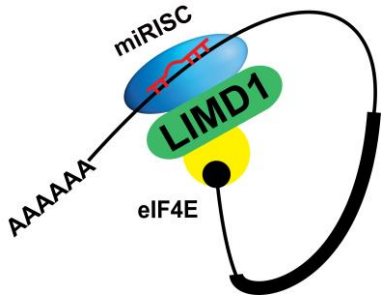

Figure 1.20 LIMD1 bridges miRISC and eIF4E, repressing the initiation of translation
An inhibitory complex is formed by the scaffold protein, LIMD1, linking 5' cap structure and miRISC.

1.6 LIM-domain containing proteins

LIM-domain containing protein was first identified within in Mechanosensory protein 3 (MEC-3) in C.elegans in 1988, where a novel cysteine/histidine-rich domain along with homeodomain was noticed [202]. Further investigations identified such cysteine-rich domain is common to that within cell-lineage protein (lin-11) in *C.elegans* [203] and insulin gene-enhancer-binding protein (Isl1) in rats [204]. Therefore, LIM domain was named after the first three **LIM** domain-containing proteins (**l**in-11, **I**sl1 and **M**EC3). LIM domain was initially believed to bind both zinc and iron [205]. However, the further studies showed LIM domain only binds to zinc [206]. LIM domain contains a broad consensus sequence $C(X)_2C(X)_{16\text{-}23}H/C(X)_{2/4}C/H/E(X)_2C(X)_2C(X)_{14\text{-}21}C/H(X)_{2/1/3}(C/H/D)X$, forming two zinc fingers (X presents any amino acid; '/' represents 'or'; numbers at the right bottom corner represent the number of amino acid in the sequence) [207, 208] (**Figure 1.21**). Eight highly conserved residues (most are cysteine and histidine) and contribute to binding to two zinc atoms forming two zinc fingers. LIM domain was first thought to be involved in DNA or RNA recognition due to its zinc-binding motifs [209]. But it was then proved to be responsible for protein-protein interaction, rather than

protein-DNA/RNA interaction [210, 211]. Therefore, four models of LIM-domain-regulated biological processes were established: **1**) a molecular adaptors, **2**) competitor, **3**) conformer and **4**) localiser [207].

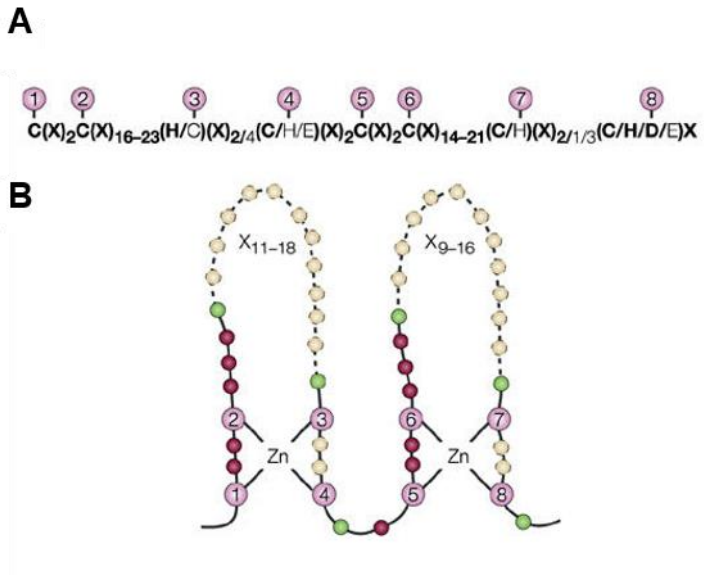

Figure 1.21 Schematic structure of the LIM-domain
***A*)** Amino acid sequences within the one LIM-domain, containing eight residues (numbered) contributing to zinc binding. Frequently observed amino acid for zinc-binding present in **bold**. ***B*)** Schematic structure of the LIM-domain**.** Eight numbered residues are responsible for the zinc-binding, forming two zinc fingers for protein-protein interaction. X represents any amino acid. Figure is adapted from Kadrmas *et al.,* 2004 [207].

By comparison of amino acid (a.a) sequences among 58 genes containing LIM domains, LIM domains can be classified into four broad categories: **1**) the nuclear LIM only, which acts as transcription factors or co-factors; **2**) LIM-homeodomain protein, which is similar to the first group but can locate in the nucleus and the cytoplasm; **3**) actin-binding LIM protein, which contains various protein-protein binding motifs and **4**) LIM kinase, which shares the similarities with the third group and contains kinase catalytic motif [207, 212]. LIMD1 belongs to the ZYXIN family of LIM-domain containing proteins, which belongs to the third group. According to the phylogenetic relationships (**Figure 1.22**), ZYXIN family can be further broken down into two sub-family (AJUBA and ZYXIN). AJUBA sub-family consists of **L**IMD1, **A**JUBA and **W**TIP. To avoid the confusion caused by using AJUBA as a

specific protein or as a sub-family name, **LAW** (initials for three family members) is used throughout this study to refer AJUBA family. ZYXIN sub-family consists of ZYXIN, LPP and TRIP6. As from the same family, all family members contain a variable proline/serine-rich pre-LIM region (25.42% sequence identity), followed by a highly conserved C-terminal region containing three LIM domains (63% sequence identity) (**Figure 1.22**). The ZYXIN sub-family members are localised at focal adhesions and involved in the cytoskeletal arrangement by docking actin-bundling proteins [213-215]. LAW family members were shown as a molecular adaptor (scaffold) to regulate multiple biological processes including regulating miRNA-mediated silencing, HIF hypoxia response pathway, repressing E2F-driven transcription, and tumour necrosis factor (TNF) receptor associated-factor 6 (TRAF6)-mediated signalling [1, 216-218].

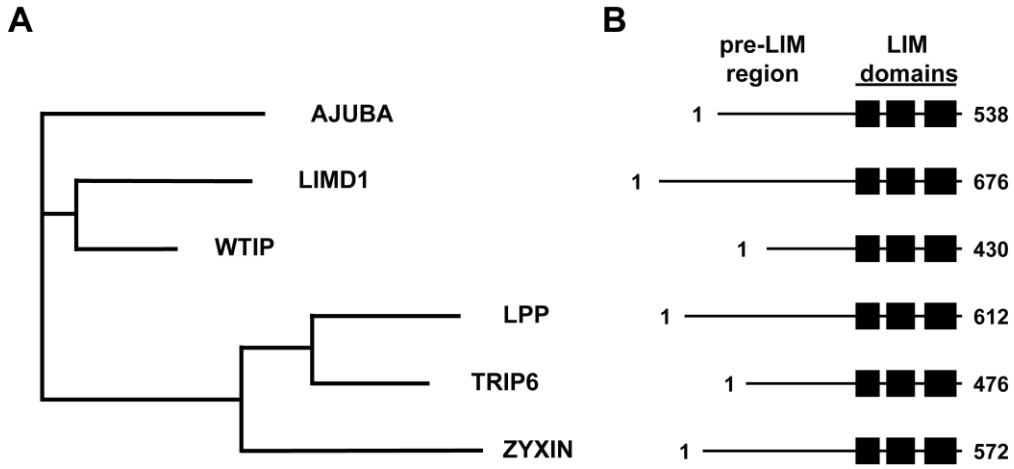

Figure 1.22 The ZYXIN family of LIM proteins
***A*)** The phylogenetic tree shows ZYXIN family can be sub-divided into two groups, AJUBA (AJUBA, LIMD1, and WTIP) and ZYXIN (LPP, TRIP6, and ZYXIN). The phylogenetic tree is generated by DNAMAN Windows 6.0 (Lynnon Biosoft) using default parameters. ***B*)** Each family member contains an N-terminal proline/serine-rich pre-LIM region and three C-terminal LIM domains in a tandem array.

1.6.1 LIMD1 is a tumour suppressor

LIM domain-containing protein 1 (*LIMD1*) gene was first identified to be located within chromosome 3 common eliminated region 1 (C3CER1) which is frequently eliminated on 3p21.3 (Mb 43.32 – 45.74) [219]. Chromosome 3p is frequently deleted in 100 % small cell lung cancers (SCLCs) and 90% non-small cell lung cancer (NSCLCs) [220]. Furthermore, chromosomal deletions and loss of heterozygosity (LOH) of 3p21.3 have been reported in the majority of solid tumours, ranging from 70 to 94 % [221]. More importantly, these genetic alterations occur at the early stage of lung cancers and show the histologic changes of pre-malignant lesions in normal respiratory epithelium [222]. In addition, this region contains several tumour suppressor genes (TSGs) such as FUS1 [223], Ras association domain family member 1 (RASSF1) and BLU [224, 225]. These results indicate that chromosome 3p21.3 is responsible for tumour suppression.

The retinoblastoma (pRB) protein regulates the transcription of multiple genes [226]. The transcription factors of the E2F family are the best-known targets of pRB [227]. E2F controls the transition from G1 to S phase of cell cycle. pRB binds E2F family proteins to repress the initiation of DNA replication by cell cycle progression (G1/S transition) and cell proliferation [227]. LIMD1 was reported to bind pRB (**Figure 1.23**) to increase the repression of E2F in the presence of pRB [217]. In addition, LIMD1 was found to inhibit cell proliferation when plasmids expressing LIMD1 cDNA were transfected into the LIMD1-negative cancer cell line MDA-MB-435 [217]. Over-expression of LIMD1 also inhibits the tumour growth when A9 mouse fibrosarcoma cells were injected into nude mice [217]. As pRB frequently presents loss-of-function in the early stage of lung cancer [228], loss of LIMD1 was postulated to be involved in lung tumourigenesis [217].

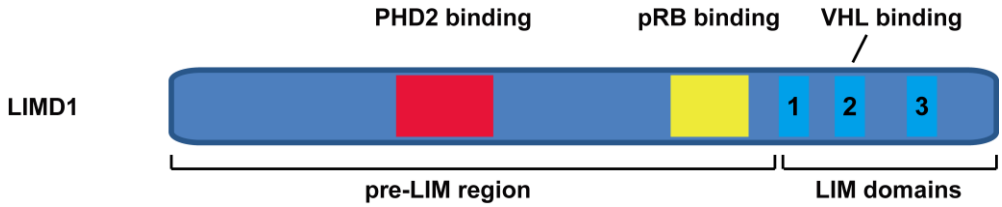

Figure 1.23 Schematic of the structure of LIMD1 and the binding domains for different partners
LIMD1 functions as a scaffold protein to bind to PHD2 and VHL through a.a 186-260 (indicated in red) and LIM2 (indicated by line) domain respectively, regulating the stability of HIF-1α. Additionally, LIMD1 binds pRB through a.a 404-442 (indicated in yellow) to repress E2F.

Further research on LIMD1 has also shown loss of LIMD1 increases tumour incidence and sizes of a tumour *in vivo* [229]. When LIMD1$^{-/-}$ mice were bred with oncogenic K-Ras^{G12D} expressing mice which are an induced lung cancer model, LIMD1$^{-/-}$: K-Ras^{G12D} mice developed more and larger tumours than LIMD1$^{+/+}$: K-Ras^{G12D} (wide type) mice did [229]. In addition, over the 12-month period, it also exhibited much higher mortality rate in LIMD1$^{-/-}$: K-Ras^{G12D} mice (90 %) than LIMD1$^{+/+}$: K-Ras^{G12D} (30%). Therefore, this evidence strongly supported that LIMD1 as a *bona fide* lung tumour suppressor which has reduced expression in 80 % of human lung cancers (most on squamous cell carcinoma) [217, 229].

The LIMD1 expression in human breast cancer is in contrast to that in lung which presents a frequent loss of LIMD1 [217, 230, 231]. LIMD1 is expressed in the majority of breast cancers [230, 231]. However, when compared to the adjacent normal and distant normal tissue, Ian *et al.* found breast cancer tissue presented a significant reduction of LIMD1 expression [230]. LIMD1 expression significantly reduced a significant correlation between high cytoplasmic LIMD1 expression with high nuclear LIMD1 expression [230]. The further investigation proposed LIMD1 as a prognostic marker for breast cancer that low LIMD1 expression correlates with poor prognosis and higher mortality rate [230]. In addition, a high frequency of LIMD1 alteration (deletion, methylation, and mutation) was found in head and neck squamous cell carcinoma, and its alterations contributed to

poor prognosis [232, 233]. Nevertheless, it also revealed a potential tumour suppressive function of LIMD1 in the oesophageal cancer cell, the depletion of which caused the abnormal cell division [234]. Taken together, these findings demonstrated LIMD1 as a tumour suppressor.

1.6.2 LIMD1 is a negative regulator for the hypoxia-induced factor (HIF)

Prolyl hydroxylases (PHDs) regulate the HIFs which are transcriptional factors that respond to the oxygen tension [235, 236]. In high oxygen tension, PHDs hydroxylate HIF-1α and allow HIF-1α to bind the von Hippel-Lindau (VHL) as a result that HIF-1α undergoes the ubiquitylation and degradation [237, 238]. LIMD1 was found to be a scaffold between PHDs and VHL [216]. Forming this PHD-LIMD1-VHL complex, the hydroxylation of VHL is promoted, and thus it activates the ubiquitylation and degradation of HIF-1α by 26S proteasome (**Figure 1.24**). Loss of LIMD1 causes the stabilisation of HIF-1α and causes pseudo-hypoxia with the enhanced HIF-1α expression and activity [216].

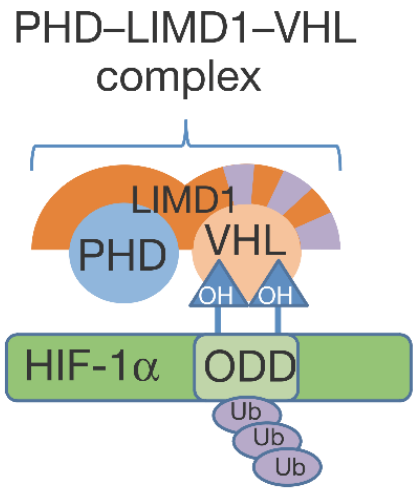

Figure 1.24 LIMD1 bridges PHD and VHL to regulate the expression of HIF-1α
A PHD2-LIMD1-VHL complex is formed by the interaction of LIMD1, as a scaffold, with PHD through its pre-LIM region (a.a 186-260) and VHL through its LIM2 domain. Thus, LIMD1 promotes the hydroxylation by PHD and ubiquitylation by VHL, consequently leading the degradation of HIF-1α by 26S proteasome (not shown). The figure is adapted from Foxler *et al.*, 2012 [216]

1.6.3 LIMD1 is an important regulator of miRNA-mediated silencing

James *et al.* demonstrated that LIMD1 is an important regulator of miRNA-mediated silencing [1]. Co-expression of fluorescently-tagged LIMD1 with DCP2, AGO2, DDX6/RCK and eIF4E in U2OS cells showed LIMD1 has potential interactions with these proteins. This indicated LIMD1 is also a component of P-bodies, suggesting LIMD1 is involved in miRNA-mediated silencing pathway. The co-immunoprecipitation of endogenous LIMD1 confirmed LIMD1 has the physical interactions between the above proteins [1]. Then using a reporter assay, LIMD1 was noticed have a regulatory function in miRNA pathway but not in siRNA pathway [1]. Finally, using the m^7GTP Sepharose affinity resin, LIMD1 was purified with m7G-bound eIF4E. This indicated and provided the evidence for alternative miRNA silencing model that LIMD1 binds 5'cap structure and miRISC (AGO2/TNRC6A) to form an inhibitory complex for translational repression [1].

1.7 Aims and objectives

Upon the 2010 publication from Dr Sharp's group [1], this study therefore aims to investigate and characterise the interaction between LIMD1 and AGO2 for a deeper understanding of the mechanism of how LIMD1 regulates miRNA-mediated silencing in humans. Therefore, the two key aims of this study are as follows:

- **Aim 1:** Recombinant LIMD1 and AGO2 proteins carrying point mutations will be constructed for investigation of the direct binding between LIMD1 and AGO2. As the phosphorylation of S387 was reported to enhance silencing and thus translational repression [127], the interaction of AGO2 and LIMD1 with regards to the phosphorylation of S387 will be investigated. (**Chapter 3**)
- **Aim 2:** Given that LAW (LIMD1, AJUBA, and WTIP) and AGOs (AGO1-4) are involved in miRNA-mediated silencing [1, 108], the co-localisation of each AGO family member with LAW will be observed to investigate their associations with regards to the phosphorylation within AGOs. (**Chapter 4**)

Chapter 2

Materials and methods

2 Materials and methods

2.1 Materials

2.1.1 Bacterial media

Luria Bertani (LB) broth The powder (Sigma-Aldrich, L3022-1KG) was dissolved in the distilled water (2.5% w/v) and autoclaved at 121°C for 20min. The broth was then stored at room temperature, and the required antibiotics were added immediately prior to use.

LB Broth with agar The powder (Sigma-Aldrich, L2897-1KG) was dissolved in the distilled water (3.5% w/v) and autoclaved at 121°C for 20min. After the agar cool to around 50 °C, the required antibiotic was added and mixed thoroughly. 20ml LB-Agar was then poured into each sterile petri dish and allowed to set at room temperature. The plates were then stored at 4°C for up to 1 month.

Agarose The powder (Sigma-Aldrich, A4718-100G) was stored at room temperature.

2.1.2 Plasmids

2.1.2.1 Protein expression plasmids for bacterial cells

pETFPP_2 The pETFPP_2 vector (**Figure 2.1**) allows for ligation independent cloning (LIC). The pETFPP_2 vector provides a 6xHis tag and MBP (maltose binding protein) tag at N-terminus, and another 6xHis tag at C-terminus. The vector has an HRV 3C (Human Rhinovirus 3C) protease recognition site between the tag and the first codon of the sub-cloned CDS of interest. The C-terminal 6xHis tag no longer exists once CDS of interest is subcloned by LIC. Expression of the recombinant protein is driven by the T7 viral promoter, and the kanamycin resistance is to select the successfully transformed colonies.

pMCSG10 The pMCSG10 vector (**Figure 2.2**) allows for LIC. The pMCSG10 vector provides a 6xHis tag and a GST tag at the N-terminus. The vector has a TEV (tobacco etch virus) protease recognition site between the tag and the first codon of the sub-cloned CDS of interest. Expression of the recombinant protein is driven by the T7 viral promoter, and the ampicillin resistance is to select the successfully transformed colonies.

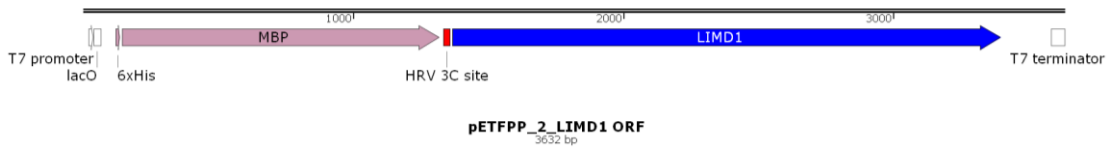

Figure 2.1 Vector map of pETFPP_2-LIMD1
The pMETFPP_2-LIMD1 vector provides a 6xHis tag and an MBP tag at the N-terminus. The vector has an HRV3C protease recognition site between the tags and the first codon of LIMD1 (or LIMD1 deletion mutants). The expression of the recombinant protein is driven by the T7 viral promoter, and the ampicillin resistance (not shown here) is to select the successfully transformed colonies.

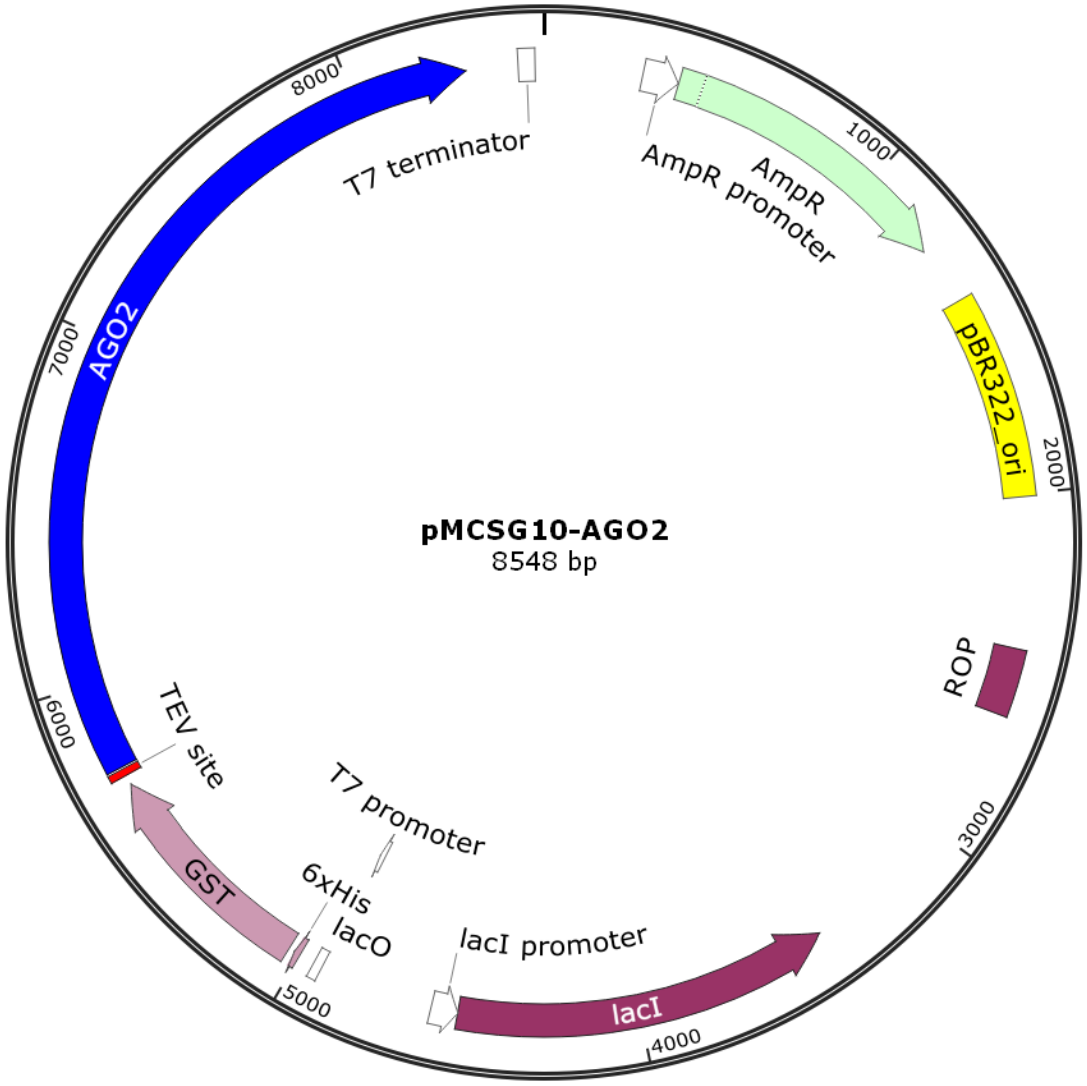

Figure 2.2 Vector map of pMCSG10-AGO2
The pMCSG10-AGO2 vector provides a 6xHis tag and a GST tag at the N-terminus. The vector has a TEV protease recognition site between the tags and the first codon of AGO2. The expression of the recombinant protein is driven by the T7 viral promoter, and the ampicillin resistance is to select successfully transformed colonies.

2.1.2.2 Protein expression plasmids for mammalian cells

pEYFP-C1 The pEYFP-C1 vector provides an N-terminal yellow variant of the EGFP tag (EYFP). The constitutive and high-level expression in mammalian cells of the ORF is driven by a human CMV (cytomegalovirus) promoter. The kanamycin resistance is to select the bacterial successfully transformed colonies, and the neomycin resistance is to select the successfully transfected mammalian cells.

pAsRed2-C1 (mTan) The pAsRed2-C1 vector provides an N-terminal red fluorescent protein tag (mTangerine, short ofr mTan). The constitutive and high-level expression in mammalian cells of the ORF is driven by a CMV promoter. The kanamycin resistance is to select the bacterial successfully transformed colonies, and the neomycin resistance is to select the successfully transfected mammalian cells.

psiCHECK-2 The psiCHECK-2 vector (**Figure 2.3**) contains the Renilla and Firefly luciferase elements. The Renilla luciferase is driven by a SV40 (simian virus 40) promoter, and Firefly luciferase is driven by HSV TK (Herpes simplex virus thymidine kinase) promoter. The ampicillin resistance is to select the bacterial successfully transformed colonies.

2.1.3 Cell culture media

Dulbecco's Modified Eagle's Medium (DMEM) DMEM (Sigma-Aldrich, D6429), containing 4500mg/L glucose, 2mM L-glutamine and 100mg/L sodium pyruvate, was supplemented with 10% (v/v) FBS (Fetal Bovine Serum) and 1% (v/v) Penicillin-Streptomycin) and stored at 4°C. The media was pre-warmed in a water bath at 37°C prior to use. The selection drugs were added immediately prior to use if required.

2.1.4 Primers for DNA Polymerization

The primers used in this study for cloning LIMD1 and AGO2 mutants, STK39 3' reporter constructs and qRT-PCR are listed in

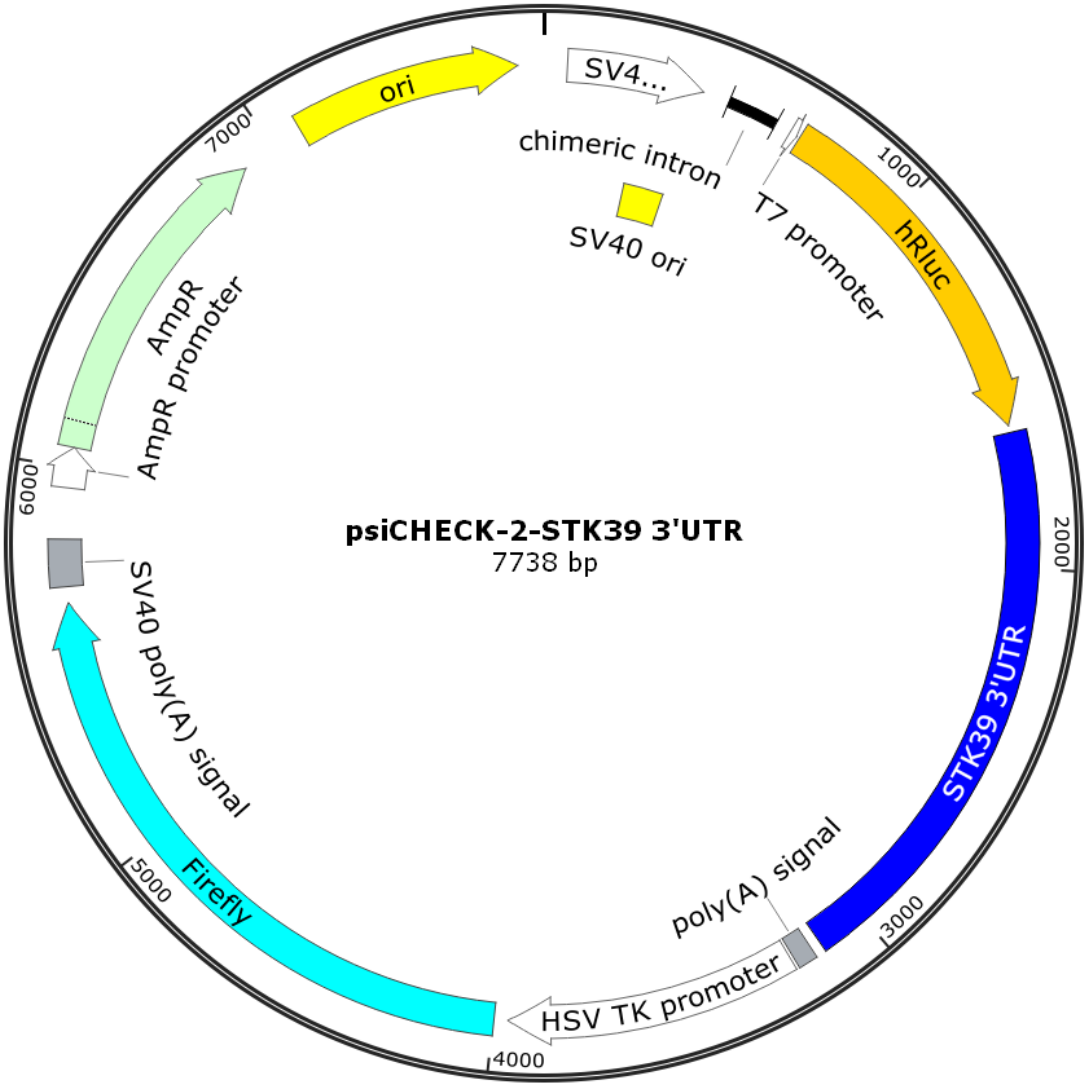

Figure 2.3 Vector map of psiCHECK-2-STK39 3'UTR
The psiCHECK-2 vector contains Renilla and Firefly luciferase elements. The Renilla luciferase is driven by a SV40 promoter, and Firefly luciferase is driven by HSV TK promoter. The ampicillin resistance is to select the bacterial successfully transformed colonies.

Table 2.1 Table of primers used in this study

Highlighted in **Bold** represents 12-nt overhangs on each pair which complementarily matched the backbone sequences for LIC. The lowercase letters represent the substitution for site-directed mutagenesis.

Primers for PCR		
AGO2 N-PAZ (for pMCSG10)	Forward	TAACATTGGAAGTGGATAACG
	Reverse	TTGTCCTGCCACAATGTTAC
AGO2 N-PAZ-L2 (for pMCSG10)	Forward	**TACTTCCAATCCAATGCC**ATGTACTCGGGAGCCGGC
	Reverse	**TTATCCACTTCCAATGTTA**TTATCCACTTCCAATG
AGO2 L2 (for pMCSG10)	Forward	**TACTTCCAATCCAATGCC**AGATGTATTAAAAAATTAACGGA
	Reverse	**TTATCCACTTCCAATGTTA**CCACACCTTGATCTCGA
EYFP-AGO2 Y393D	Forward	TTGGAATCATGGTCAAAGATG
	Reverse	ATTCACGGACGTCTGGATCTGTG
EYFP-AGO2 Y393E	Forward	TTGGAATCATGGTCAAAGATG
	Reverse	ATTCACGGACCTCTGGATCTGTGTTG
EYFP-AGO2 Y393F	Forward	TTGGAATCATGGTCAAAGATG
	Reverse	ATTCACGGACGAATGGATCTGTG
LIMD1 (for pETFPP_2)	Forward	**CCAGGGACCAGCAATCGGC**ATGGATAAGTATGACGACCTGG
	Reverse	**GAGGAGAAGGCGCGTTA**CTAGAAGTGGTGCTGGTGAA
LIMD1 a.a 110-166	Forward	**CCAGGGACCAGCAATCGGC**TCGACAGGGGCACCT
	Reverse	**GAGGAGAAGGCGCGTTA**GCCTGGCTGGTGGA
LIMD1 a.a 120-166	Forward	**CCAGGGACCAGCAATCGGC**CTCGCTGCTGGGCA
	Reverse	**GAGGAGAAGGCGCGTTA**GCCTGGCTGGTGGA
LIMD1 a.a 130-166	Forward	**CCAGGGACCAGCAATCGGC**CAGGAGCAGAGATCCAGG
	Reverse	**GAGGAGAAGGCGCGTTA**GCCTGGCTGGTGGA
LIMD1 a.a 140-166	Forward	**CCAGGGACCAGCAATCGGC**GGCACGAGGCATGG
	Reverse	**GAGGAGAAGGCGCGTTA**GCCTGGCTGGTGGA
STK39 (for psiCHECK2)	Forward	ATGCCTCGAGTGTATGTCCCTTGATGTCACC
	Reverse	ATGCGTTTAAACTCTCATTGTGCAATACACTTTTAT
miR26 mutant site 1 (for psiCHEKC-2)	Forward	aatTTCTAGTTTTAAAACTGACTGTG
	Reverse	ttagTTGGCTAATAAATCTTAATTTTATAAG
miR26 mutant site 2 (for psiCHEKC-2)	Forward	aatAATATCAGAATCTGAGTTTTACTTG
	Reverse	ttagTTATCACCTTTAGAATAACAATC
miR26 mutant site 3 (for psiCHEKC-2)	Forward	aatATTTTGCAGAATACCCAGG
	Reverse	ttagAAAACTCAGATTCTGATATTTTCAAG
miR26 mutant site 1+3 (for psiCHEKC-2)	Forward	aatATTTTGCAGAATACCCAGG
	Reverse	ttagAAAACTCAGATTCTGATATTTTCAAG
miR26 mutant site 1+2+3 (for psiCHEKC-2)	Forward	aataTCAGAATCTGAGTTTTCTAA
	Reverse	ttagTTATCACCTTTAGAATAACAATC

Table 2.2 Table of primers used in this study
Primers used for colony PCR and qRT-PCR in this study.

Primers for colony PCR		
T7 promoter	Forward	TAATACGACTCACTATAGGG
	Reverse	GCTAGTTATTGCTCAGCGG
Primers for qRT-PCR		
RPII	Forward	GACACAGGACCACTCATGAAGT
	Reverse	GTGCGGCTGCTTCCATAAG
STK39 [239]	Forward	TGGAATTAGCAACAGGAGCAGCG
	Reverse	TTTCCAAAGTGGGTGGATCATTT
has-miR-26	Forward	GTCGTATCCAGTGCAGGGTCCGAGGTATTCGCACTGGATACGACACCTAT
	Reverse	N.A.
RNU6	Forward	CGCAAGGATGACACGCAAAT
	Reverse	N.A.

1xTrypsin/EDTA Solution The solution (Sigma-Aldrich, T4299-100ML) contained 500 BAEE units porcine trypsin, 0.2g/100ml EDTA per litre of Dulbecco's PBS without calcium and magnesium. The working solution was stored at 4°C and pre-warmed in a water bath at 37°C prior to use.

Fetal Bovine Serum (FBS) The solution (Gibco, 1050) was aliquoted in 50ml and stored at -20°C. FBS was filtered and added to cell medium by using a syringe and a 0.2µm filter in a cell culture fume hood.

1xOpti-MEM® reduced serum medium (Opti-MEM®) Opti-MEM® (GIBCO, 31985-062), containing L-glutamine and 2.4g/L sodium bicarbonate, was stored at 4°C and pre-warmed in a water bath at 37°C prior to use.

Cell freezing mix sterile dimethyl sulfoxide (DMSO, Sigma-Aldrich, D2438) was mixed with FBS 20% (v/v) and stored at -20°C.

2.1.5 Antibiotics and selection drugs

Ampicillin The stock solution (Sigma-Aldrich, A2804-50MG) was prepared at a concentration of 100mg/ml in the distilled water and the aliquots were stored at -20°C. The standard working concentration was 100µg/ml.

Kanamycin The stock solution (Bioline, BIO-87028) was prepared at a concentration of 33mg/ml in the distilled water and the aliquots were stored at -20°C. The standard working concentration was 33µg/ml.

Puromycin The stock solution (Sigma-Aldrich, A2804-50MG) contained 33 mg/ml Ampicillin in the distilled water and was stored at -20°C. The standard working concentration was 33µg/ml.

Penicillin/Streptomycin The solution (Sigma-Aldrich, P4333-100ML) contained 10,000 units of Penicillin and 10mg/ml Streptomycin in 0.9% NaCl. The working aliquots were stored at 4°C. The standard working concentration was 1% (v/v).

2.1.6 Buffers and solutions

2.1.6.1 Stock solutions

Ethylenediaminetetraacetic acid (EDTA) The stock solution (0.2M) was prepared by dissolving 5.845g EDTA (Sigma-Aldrich, E9884) in the distilled water to a final volume of 100ml and stored at room temperature.

Imidazole The stock solution (1M) was prepared by dissolving 1.702g imidazole (Sigma-Aldrich, I202) in the distilled water to a final volume of 100ml. The solution was adjusted to pH 8.0 with NaOH and stored at 4 °C.

NaCl The stock solution (2M) was prepared by dissolving 58.44g NaCl (Sigma-Aldrich, S3014-5KG) in the distilled water to a final volume of 500ml and stored at room temperature.

Sodium Phosphate buffer (pH 8.0) The stock solution (0.1 M) was prepared by dissolving 1.65g NaH_2PO_4 (Sigma-Aldrich, S0751) and Na_2HPO_4 (Sigma-Aldrich, S5136) in the

distilled water to a final volume of 500ml and pH was adjusted to pH 8.0. The stock solution was stored at 4°C for up to 1 month.

Phosphate buffered saline (PBS, 1x) The powder (Severn, 20-7461-01) was dissolved in 10L distilled water and autoclaved at 121°C for 20min for cell culture purpose. The 1xsolution was stored at room temperature.

Paraformaldehyde (PFA, 4%) The solution was prepared by diluting 16% PFA (Pierce, 28908) with 30 ml 1xPBS and stored at room temperature

Tris-HCl (pH 8.0) 1M stock solution (pre-autoclaved) was obtained from Severn Biotech Ltd. (20-7901-01) and stored at room temperature.

Tris-HCl (pH 6.8) 1M stock solution (pre-autoclaved) was obtained from Severn Biotech Ltd. (20-7901-10) and stored at room temperature.

His binding buffer 50mM Tris-HCl (pH 8.0), 500mM NaCl and 5mM imidazole were dissolved in the distilled water to make the final volume to 50ml and stored at 4°C.

His elution buffer 50mM Tris-HCl (pH 8.0), 500mM NaCl and 50mM imidazole were dissolved in the distilled water to make the final volume to 50ml and stored at 4°C.

2.1.6.2 DNA buffers

Tris-borate-EDTA (TBE, 50x) The stock solution (Severn, 206000) was stored at room temperature. The working solution was prepared by diluting the stock into 1x, and the unused solution was stored at room temperature.

DNA Agarose Gel Loading Buffer (10x) 50% (v/v) glycerol and 0.25% (w/v) Bromophenol Blue were dissolved in 1xTBE and stored at room temperature. The working concentration was 1x.

DNA Agarose Gel 0.8-1.2% (w/v) agarose was added to 1xTBE and dissolved by heating in a microwave till the solution changed from cloudy to clear. The agarose was then left to cool to approximately 50°C, and RedSafe^{TM} (iNtRON, 21141) was added and mixed.

The mixture was poured into the module and left to set. The percentage weight of agarose was varied depending on the size of DNA to be analysed. The smaller the percentage is, the better and the bigger size of DNA can be analysed.

2.1.6.3 Cell lysis/washing buffers

Passive Lysis Buffer (PLB) (5x): 5x PLB (Promega, E1941) was stored at -20°C and diluted to 1x with the distilled water immediately prior to use.

NP-40 Lysis buffer 50mM Tris-HCl pH 8.0, 150mM NaCl, 1% (v/v) and IGEPAL CA-630 (Sigma-Aldrich, I8896) were dissolved in the distilled water to make the final volume to 500ml.

RIPA Lysis buffer 50mM Tris-HCl pH 8.0, 150mM NaCl, 0.5% (w/v) sodium deoxycholate (Sigma-Aldrich, D6750), 0.1% (w/v) sodium dodecyl sulphate (SDS, Thermo Fisher BP166), and 1% (v/v) IGEPAL CA-630 were dissolved in the distilled water to make the final volume to 500ml. The buffer was stored at 4°C.

Buffer A 150mM NaCl, 20mM Tris (pH 8.0), 1mM $MgCl_2$ (Severn Biotech Ltd., 20-xxxx-01), 0.1% (v/v) IGEPAL CA-630 and 10% (v/v) glycerol (VWR, 200-289-5) were dissolved in the distilled water to make the final volume to 500ml. The buffer was stored at 4°C.

Bovine serum albumin (BSA) solution 5% (w/v) of BSA (ACROS, 268131000) was dissolved in the distilled water prior to use.

Protease & phosphatase inhibitor cocktail (1x) The working solution was prepared by dissolving one cOmplete ULTRA Mini EDTA-free protease inhibitor cocktail tablet (Roche, 05892791001) and one PhosSTOP phosphatase inhibitor cocktail tablet (Roche, 04906837001) per 10ml of any lysis buffers for mammalian and bacterial cell lysis immediately prior to use. The unused buffer was aliquoted and stored at -20°C for up to 1 month.

MG-132 proteasome inhibitor (1000x) 10mM stock solution was prepared by dissolving 1mg MG-132 (Calbiochem, 474790) in the distilled water. The stock aliquots were stored

at -20°C and diluted to 1x in any lysis buffers for the mammalian cell lysis immediately prior to use.

2.1.6.4 Protein purification buffers

Isopropyl β-D-1-thiogalactopyranoside (IPTG) The stock solution (1M) was prepared by dissolving 2.383g IPTG (ICN, 102101) in 10ml distilled water and stored at -20°C.

Glutathione resin for the capture of GST-tagged proteins Glutathione Sepharose® 4B resin (GE Healthcare, 17-0756-01) was washed once in PBS by vortex gently and centrifuged for 1 min at 800g, 4°C to remove any ethanol in the storage buffer. The supernatant was discarded after centrifugation.

Nickel resin for the capture of His-tagged proteins HIS-Select® Nickel Affinity Gel (Sigma-Aldrich, P6611-5ML) was washed once in PBS by vortex gently and centrifuged for 1 min at 800g, 4°C to remove any ethanol in the storage buffer. The supernatant was aspirated after centrifugation.

anti-MBP magnetic resin for the capture of MBP-tagged proteins anti-MBP Magnetic Resin (New England Biolabs, E8037S) was washed in 0.1M Sodium phosphate buffer (pH 8.0), and the magnet was then applied for 30s to pull resin to the side of the tube. The supernatant was aspirated.

2.1.6.5 Solutions for sodium dodecyl sulphate-polyacrylamide gel electrophoresis (SDS-PAGE) and western blotting

SDS-PAGE Sample buffer (5x) Tris-HCl (pH 6.8), 50% (v/v) glycerol, 5% (w/v) SDS, 5% (v/v) β-mercaptoethanol (Sigma-Aldrich, M7522) and 0.5% (w/v) Bromophenol Blue (Sigma-Aldrich, 204-086-2) were dissolved in the distilled water to make the final volume to 500ml. The preparation of this buffer should be performed in the fume hood. The dry components were allowed to fully dissolve before the addition of glycerol. The buffer was aliquoted and stored at -20 °C.

SDS-PAGE resolving gel ProtoGel® 30% acrylamide: bisacrylamide (37.5: 1) solution (National Diagnostics, EC-890), 4xresolving buffer (1.5M Tris-HCl, pH 8.8, National

Diagnostics, EC-892), 0.1% (w/v) ammonium persulphate (APS, Sigma-Aldrich, A3678) and 0.1% (v/v) N,N,N',N'-tetramethylethylenediamine (TEMED, Sigma-Aldrich, T9281) were dissolved in the distilled water to make a gel containing 8-12% acrylamide. APS and TEMED were immediately added and inverted gently before pouring into Mini-PROTEAN® casting plates (Bio-Rad), leaving around 1cm space on the top for the stacking gel. 100% ethanol was added to cover the top of the gel solution in the casting plates to eliminate bubbles and ensure a horizontal edge. The gel was allowed to set around 20min at room temperature. The ethanol was then completely removed by using filter paper.

SDS-PAGE stacking gel ProtoGel® 30 % acrylamide: bisacrylamide (37.5:1) solution, 4xstacking buffer (1.0 M Tris-HCl, pH 6.8, National Diagnostics #EC-893), 0.1% (w/v) APS and 0.2% (v/v) TEMED were dissolved in the distilled water to make a gel containing 4% acrylamide. APS and TEMED were immediately added and inverted gently before pouring into casting plates. The comb was then immediately inserted before the gel began to set. The gel was allowed to set around 30min at room temperature. The gels were used immediately or stored at 4°C by wrapping with damp tissue paper and cling film to prevent drying out.

Precision Plus Protein™ all blue molecular weight marker The marker (Bio-Rad, 1610373) was stored at -20°C.

Tris/glycine/SDS Running Buffer (10x) 1xworking solution was made by diluting 10xTris Glycine SDS (Severn Biotech Ltd., 20-6400-50). Unused 1xsolution was stored at room temperature.

Tris/glycine Transfer Buffer (10x) 1xworking solution was made by diluting 10xTris Glycine (Severn Biotech Ltd., 20-6300-50). Unused 1xsolution was stored at room temperature.

PBS-Tween (1x) 0.05% (v/v) Tween® 20 (Sigma-Aldrich, P1379-250ml) was added to 1xPBS and stored at room temperature.

Blocking Solution 5% marvel skim milk powder (Sigma-Aldrich, 70166-500G) was immediately dissolved in 1xPBS-Tween prior to use and stored at 4°C for up to 1 day.

Coomassie Blue Protein Staining 0.12% (w/v) Coomassie Brilliant Blue R (Sigma-Aldrich, 6104-59-2), 50% (v/v) methanol (Fisher, M/3950/17) and 20% (v/v) acetic acid (Sigma-Aldrich, 33209-2.5L) were dissolved in the distilled water to make the final volume to 1L. The solution was then filtered through 3mm filter paper and stored at room temperature.

Coomassie Blue de-staining solution 20% (v/v) methanol and 10% (v/v) acetic acid were dissolved in the distilled water to make the final volume to 1L and stored at room temperature.

2.1.6.6 Dual-luciferase reporter assay solutions

Dual-Luciferase Reporter Assay System The kit (Promega, E1960) contains a Luciferase Assay Buffer and Stop&Glo® Reagent for the measurement of firefly and renilla luciferase signals respectively. The kit was stored at -20°C. The reagent was mixed with the distilled water at 1:1 ratio prior to use. The Luciferase assay buffer was firstly used for detection of Firefly luciferase activity. The Stop&Glo reagent was then added for detection of renilla luciferase activity.

2.2 Methods

2.2.1 Bacterial culture methods

2.2.1.1 PCR amplification

Purified plasmid DNA was used as a template in the 25µl reaction for PCR amplification. Phusion® Hot Start Flex 2xMaster Mix (NEB, M0536S), 3% DMSO [240] and the pair of DNA primers (

Table *2.1*) were mixed. PCR protocols for thermocycler were set according to the manufacturer's guidelines. dsDNA templates were initially denatured for 30s at 98°C. 30

cycles of denaturation (10s at 98°C), annealing (30s at a primer-dependent temperature), and extension (periods according to the product size at 72°C). A final extension step was 10min at 72°C. The extension time was set to 30s/kb for the target gene.

2.2.1.2 Sequence specific digestion of DNA by restriction enzymes

The purified plasmid DNA or PCR products were digested in a total volume of 20µl, using 1µl of each required restriction enzyme in the appropriate buffer and incubated at 37°C for 2h, no longer than 4h. The enzyme was inactivated by incubating at 80°C for 20min (**Table 2.3**).

BseRI (New England Biolabs, R0581S) and SspI (New England Biolabs, R3132) was stored at -20°C.

Table 2.3 Table of conditions of restriction enzyme digestions used in this study
BseRI was used to linearise pETFPP_2 vector, and SspI was used to linearise pMCSG10 vector. Heat inactivation time was 20min for both enzymes

Enzyme	Buffer	Incubation time	Inactivation temperature
BseRI	1x CutSmart® Buffer	2h	80°C
SspI	NEBuffer2	2h	65°C

2.2.1.3 Agarose gel electrophoresis and gel extraction of DNA fragments

Agarose gel contains 0.7-1.2% agarose and 1xRedSafe. The percentage of gels depends on the size of the desired separation DNA. Gels were run at a constant voltage of 100V in TBE buffer until the desired DNA was separated detected by G: Box system (SYNGENE). For gel extraction, DNA bands were visualised and excised on a UV-light box under the proper protection. DNA then was extracted and purified by following the manufacturer's instructions (Qiagen, 28704).

2.2.1.4 Ligation independent cloning (LIC)

LIC is an alternative technique allowing efficient creation of various recombinant plasmids. Due to the long 3' complementary overhangs on the insert and vector, it

maximises the specificity of annealing and correction of insertion with a lower chance of self-circularization of vector [241]. Compared to ligation dependent cloning, the procedure does not require the use of T4 ligase, or alkaline phosphatase. It depends on the action of endo (3'-5') of T4 DNA polymerase with the presence of the single dNTP to generate the complementary overhangs between the target vector and PCR products.

For generating LIMD1 mutants constructs in this project, gene of interest was PCR amplified using the pair of primers designed to contain 12nts on 5' end (**Figure 2.4A**). This 12-nt overhang is the same as to the sequence on the vector backbone. After PCR amplification, the products were treated with T4 DNA polymerase (New England Biolabs, M0203S) with the presence of dATP (Bioline, BIO-39036) (**Figure 2.4A**). In the presence of dATP, the polymerase activity and the 3'-5' exonuclease activity of T4 DNA Polymerase are balanced and generate long overhangs on the 5'ends (**Figure 2.4A**). The pETFPP_2 vector was linearised by BseRI and then was treated with T4 DNA polymerase with the presence of dTTP (Bioline, BIO-39039), generating long overhangs on the 3'ends (**Figure 2.4B**). On the other hand, for pMCSG10 vector, SspI was used for vector linearization, and dCTP (Bioline, BIO-39038) and dGTP (Bioline, BIO-39037) were used for T4 DNA polymerase treatment. The reaction was performed at room temperature for 90min, followed by 75°C for 20min to deactivate T4 DNA polymerase. The treated vector and PCR products were then mixed for annealing (**Figure 2.4C**) at room temperature for 5min, followed by an optional procedure that 5-min incubation at room temperature with 25mM EDTA (Severn, 20-5300-01). EDTA is a metal chelator to diminish the metal reactivity on which the activity of metal-dependent enzymes such as polymerase relies. Although heat deactivation was carried out before annealing, the trace polymerase activity might still exist. Therefore, by adding EDTA, it can decrease the likelihood of unsuccessful annealing. Besides, it can also protect DNA from being damaged by potential nuclease contamination. The annealing mixture was then performed for transformation.

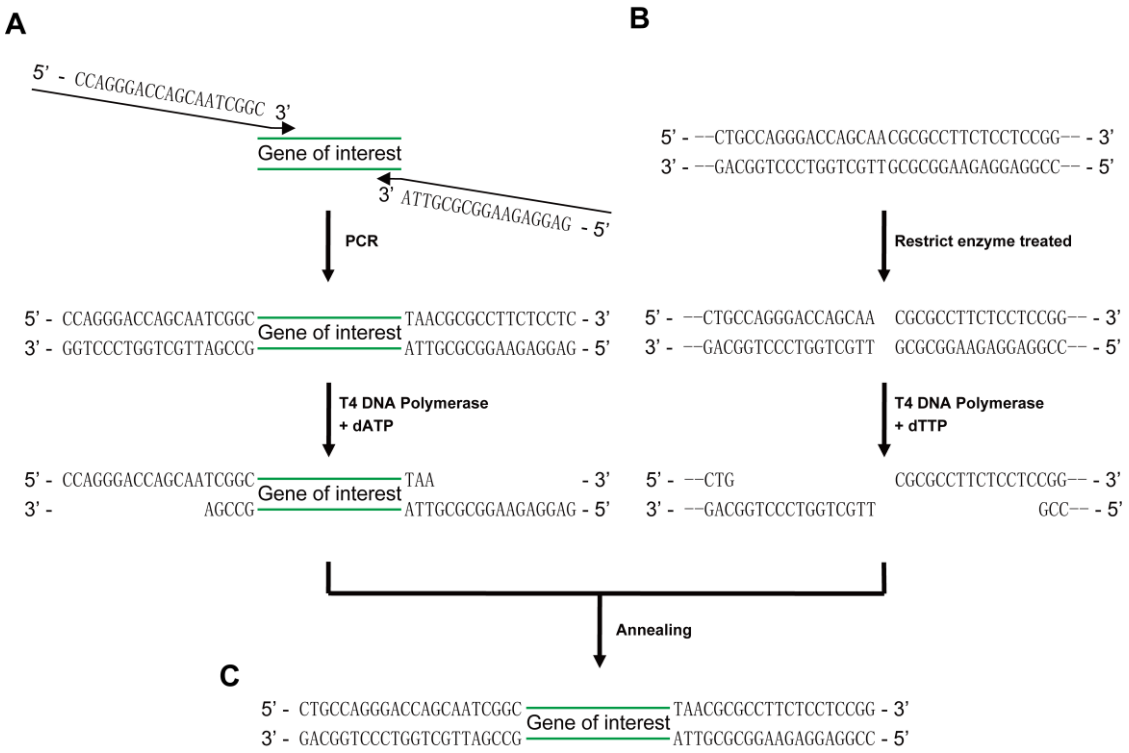

Figure 2.4 A flowchart for Ligation independent cloning
***A*)** Gene of interest was PCR amplified using the pair of primers designed to contain the additional nucleotides on the 5' end, which was the same as to the sequence on the vector backbone. The PCR product was then treated with T4 DNA polymerase in the presence of dATP, creating long overhangs on the 5'ends. ***B*)** The vector was linearised by a restriction enzyme and then treated with T4 DNA polymerase in the presence of dTTP, creating long overhangs on the 3'ends. ***C*)** The overhangs generated by the T4 DNA polymerase on both PCR product and vector are complementarty. The treated vector and PCR product were then mixed for annealing in the presence of EDTA.

2.2.1.5 Site-directed mutagenesis of plasmids

Q5® Site-Directed Mutagenesis was used to generate the internal deletion mutants and the point mutation in this project. To create pMCSG10-AGO2 N-L1-PAZ truncation mutant, a pair of DNA primers flanking the CDS of L2-MID-PIWI was designed and used PCR for amplifying the linear DNA sequences without the undesired sequences (**Figure 2.5A**). To create a point mutation in this project (EYFP-AGO2 Y393), the desired nucleotide changes are designed in the forward primer, including long complementary nucleotides on the downstream of the mutation to allow a sufficient annealing (**Figure**

2.5C). PCR was used to amplify the linear DNA sequences with the desired point mutation. After PCR amplification, a small portion of the linear PCR product was visualised by agarose gel electrophoresis to check a single product of the expected size of the band was amplified, and the majority was applied for column purification to remove any polymerase. The purified DNA was then treated with KLD Mastermix for 5min at room temperature (**Figure 2.5B and Figure 2.5D**). Under the treatment of KLD, kinase phosphorylates the 5'-hydroxyl terminus and in turn allows 5'-phosphate group for ligation by ligase to circularise the linear PCR product. DpnI degrades the methylated template DNA produced by *E.coli*. The mixture was then prepareded for transformation.

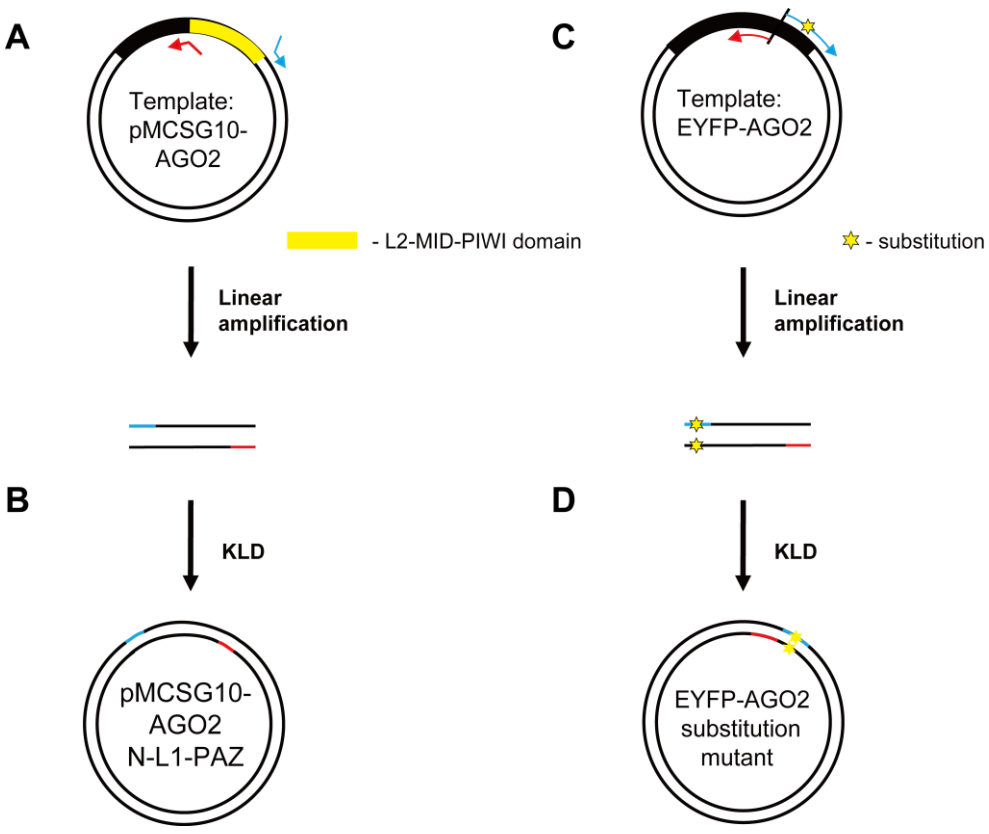

Figure 2.5 A flowchart for site-directed mutagenesis
***A*)** The sequence of pMCSG10-AGO2 N-L1-PAZ and the vector bone were linearly amplified by using a pair of DNA primers flanking the undesired CDS of L2-MID-PIWI (highlighted in yellow). ***B*)** The PCR product was treated with KLD to circularise the linear DNA and remove the circular template DNA. ***C*)** The sequence of EYFP-AGO2 point mutation was linear amplified. The desired point mutation is indicated in a yellow star. ***D*)** The PCR product was treated with KLD to circularise the linear DNA and remove the circular template DNA.

2.2.1.6 Transformation of *E.coli* strains for plasmid DNA production

Chemically competent DH5α bacteria (NEB, C2988J) were thawed on ice immediately prior to use and gently tapped to ensure complete resuspension (avoid pipetting). 5µl of annealed DNA or 1µl of plasmid DNA was added to 40µl bacteria and gently tapped again to ensure mix well, followed by the incubation on ice for 30min. The bacteria were then heat shocked in a water bath (42°C, 35s) and placed on ice to recover for 2min. 500µl of sterile SOC broth (New England Biolabs, B9020S) was added before the incubation at 37°C with vigorous shaking (220rpm) for 60min. 100µl of the bacteria were spread onto LB-agar plates containing the appropriate antibiotic and incubated overnight at 37°C. Plates were removed from the incubator on the following morning (no more than 16h incubation) and stored at 4°C for up to 1 month. The individual bacterial colony was picked by a sterile 10µl pipette tip and inoculated in 5ml of LB broth containing the same appropriate antibiotic overnight at 37°C with vigorous shaking (220rpm). The bacterial pellet was collected on the following morning by centrifugation (5000g, 5min).

To store the inoculated *E.coli,* 800µl solution was mixed with 200µl glycerol and stored at -20°C. For recovery, a sterile 10µl pipette tip was used to pick the frozen solution and spread onto LB-agar plates.

2.2.1.7 Preparation of plasmid DNA

The inoculated *E.coli* solution was centrifuged at 5000rpm, 4°C for 5min to collect the bacterial pellet. The plasmid DNA was then extracted from the bacterial pellet by using High Pure Plasmid Isolation Kit (Roche, 11754785001), or Genopure Plasmid Midi Kit (Roche, 03143414001) on different experimental purpose by following the manufacturer's instruction.

2.2.1.8 Quantification of DNA concentrations

DNA concentration was measured using a NanoDrop® ND-1000 spectrophotometer (NanoDrop Technologies Inc.). The pedestals were wiped with 100% ethanol and the distilled water after each measurement. The instrument was blanked with 1µl of the

same buffer in which DNA eluted. 1µl of the DNA sample was used per measurement with both a 260nm and 280nm light absorbance values. The ratio of 260/280 between 1.8-2.0 means DNA is pure. The ratio 260/230 between 2.0-2.2 means no protein contamination. The concentration was measured twice for each DNA sample, and an average value was taken.

2.2.1.9 DNA sequencing

DNA sequencing was performed by Source BioScience on an Applied Biosystems 3730 DNA Analyzer. The sequencing result was analysed by Multiple Sequence Comparison by Log-Expectation (MUSCLE) [242].

2.2.1.10 Transformation of *E.coli* strains for protein production and expression of the recombinant proteins

Rosetta™ (DE3) pLysS cells (Novagen, 70956) were thawed on ice and gently tapped to ensure complete resuspension. 0.5µl of plasmid DNA was added to 2µl the bacteria and gently tapped again to ensure mix well, followed by the incubation on ice for 5min. The bacteria were heat shocked in a water bath (42°C, 35s) and then incubated on ice to recover for 2min. 500µl of sterile SOC broth was added to the bacteria before being incubated at 37°C with vigorous shaking (220rpm) for 60min. 100µl of the bacteria were spread onto LB-agar plates containing the appropriate antibiotic and incubated overnight at 37°C. Plates were removed from the incubator on the following morning (no more than 16h incubation) and stored at 4°C for up to 1 month.

The individual bacterial colony was picked by a sterile 10µl pipette tip and inoculated in 5ml of LB broth containing the same appropriate antibiotic overnight at 37°C with vigorous shaking (220rpm). For large-scale culture, the inoculated culture was diluted (1: 50) into sterile LB broth containing the same appropriate antibiotic on early afternoon. The culture was incubated at 37°C with vigorous shaking (150rpm) for 90min, followed by incubation at 18°C with vigorous shaking (130rpm) for 17 h. About 60min later, the optical density at 600nm reached 0.6-0.8. IPTG, which is an allolactose mimic negatively regulating the *lac* repressor, was then added to reach a final concentration of 1mM to

induce the protein expression for overnight. The cultures were held at 4°C after the overnight incubation.

After overnight inoculation, the bacterial pellets were collected and frozen on dry ice. The pellets were then thawed on ice and dissolved in 2.8ml/g of RIPA buffer (50mM Tris-HCl, pH 8.0, 150mM NaCl, 0.5% (w/v) SDS, 1% (v/v) IGEPAL CA-630) with protease inhibitor and phosphatase inhibitor. The suspension was frozen on dry ice and thawed again, followed by sonication in a 30s burst for three times until the suspension became watery. The 10s pause was taken between each burst to prevent the suspension overheat. The lysates were then centrifuged at 4°C for 15min at 21,500g, and the supernatant was collected and stored at -80°C for later use.

2.2.1.11 Recombinant protein purification and elution of His-tagged proteins

MBP-tagged protein expressed in pETFPP_2 vector system also has His tags. As a result, HIS-Select® Nickel Affinity Gel can be used to purify and elute the protein for later use. 25µl of pre-washed gel was incubated with 500µl cell lysates at 4°C with rotation for at least 30min. The gel was then washed three times with His binding buffer with vortex and centrifugation at 4°C for 1min, 500g, followed by eluting with His elution buffer with rotation at 4°C overnight. After overnight incubation, the supernatant was collected after centrifugation at 4°C for 1min at 500g. The imidazole in the eluted proteins was removed by Amiconultra (Amicon, UFC501024). The purified protein was then stored at -20°C for later use.

2.2.2 Cell culture methods

2.2.2.1 Cell culture

All cell lines used in this study and their regular cultures are listed in the **Table 2.4**. Human lung epithelial cancer cell line A549 (shSCR and shLIMD1) and Human breast cancer cell line MDA-MB-435 (FH-VO and FH-LIMD1) were lentivirally-transduced for stable knowdown or re-expressing LIMD1, respectively. Human cervical epithelial cancer cell line HeLa (Cas9 Control and LIMD1$^{-/-}$) LIMD1 knockout CRISPR-Cas9 edited cell lines were generated using the lenti-CRISPR v2 plasmid (**Appendix Figure 11.1**) [243],

acquired from Addgene (plasmid, 52961). Therefore, three pairs of isogenic cell lines with regards to expressing LIMD1 or not were generated. Besides all cell lines mentioned above, human bone osteosarcoma U2OS, human bronchoalveolar lung carcinoma cell line H358M, human lung adenocarcinoma cell line H838 and H522, human squamous cell carcinoma H520, human biphasic mesothelioma MSTO-211H, and human lung mesothelioma H28 were cultured in the humidified incubator with 5% CO_2, 20% O_2 using DMEM with required selective drugs. DMEM was supplemented with 10% (v/v) FBS) and 1% (v/v) Penicillin-Streptomycin. Human small airway epithelial cell (SAEC) was cultured in the humidified incubator with 5% CO_2, 20% O_2 using a specific media.

Table 2.4 Table of cells used in this study

Cell	Organism	Tissue	Cell type	Disease	Mycoplasma tested or not
A549	Human	Lung	Epithelial	Carcinoma	Yes
MDA-MB-435	Human	Breast	Epithelial	Carcinoma	Yes
HeLa	Human	Cervix	Epithelial	Adenocarcinoma	Yes
U2OS	Human	Bone	Epithelial	Osteosarcoma	Yes
H358M	Human	Lung	Epithelial	Carcinoma	Yes
H838	Human	Lung	Epithelial	Adenocarcinoma	Yes
H522	Human	Lung	Epithelial	Adenocarcinoma	Yes
H520	Human	Lung	Epithelial	Carcinoma	Yes
MSTO-211H	Human	Lung	Fibroblast	Mesothelioma	Yes
H28	Human	Lung	Epithelial	Mesothelioma	Yes
SAEC	Human	Lung	Epithelial		Yes

2.2.2.2 Splitting and seeding of the cells

Only adherent cell lines were used in this project. Once the adherent cells form a confluent monolayer, the colour of the media, indicating pH, changes from red to yellow. The old media was removed, and the cells were washed gently with 5ml auto-cleaved PBS. 3ml (for T75 flask) of trypsin-EDTA was added, and the cells were incubated at 37°C for 5min to detach the cells from the bottom of the culture flask. 7ml pre-warmed DMEM was added to neutralise trypsin-EDTA, and the cell suspension was transferred into a 15ml Falcon tube, followed by centrifugation at 1200rpm for 3min. The supernatant was then discarded, and the cell pellet was re-suspended in 5-13ml DMEM.

1/5-1/20 of the cell suspension was transferred to a new flask depending on the proliferation rate of the cell line and then topped with pre-warmed DMEM to 10ml.

To seed an exact number of cells, the concentration of cell suspension was then counted using a TC10™ Automated Cell Counter (Bio-Rad).

2.2.2.3 Freezing the cells for storage

After the routine split, the leftover of cell suspension was centrifuged at 1200rpm for 3min, to remove the supernatant. The pellet was then washed with PBS and centrifuged at 1200rpm for 3min. The supernatant was discarded. The pellet was then re-suspended in the cell freezing mix and aliquoted into a 1ml vial, stored at -80°C for short-term storage and in liquid nitrogen for long-term storage.

2.2.2.4 Hypoxic treatment of the cells

The proper number of cells was seeded in 12-well plate to reach 80% confluent after 72h incubation. One plate of cells was left in normoxia (20% O_2) for 72h. The second plate was moved to the hypoxia (1% O_2) at 68h and allowed to set in hypoxia for 4h. The third plate was moved to the hypoxia (1% O_2) at 48h and allowed to set in hypoxia for 24h. All plates of cells were collected at the endpoint (72h). The protein was extracted for the downstream analysis.

2.2.2.5 General transfection of DNA

The proper number of cells was seeded 24h before transfection to achieve 30-50% confluent. For DNA transfection, Viafect (Promega, E2692) was used, and the ratio was 3µl Viafect per µg of plasmid DNA. For each well of 12-well plate, 100µl of Opti-MEM was mixed well with the proper amount of Viafect by vortex and pulse centrifugation. The transfection reagent mixture was then incubated at room temperature for 5min, followed by adding the plasmid DNA. The mixture was then mixed well and incubated at room temperature for 20min. After incubation, the transfection complexes were gently added dropwise to the cells. The cells were then incubated for 48h for the downstream usage.

2.2.2.6 Preparation of mammalian cell lysates for direct binding

2 hours before lysing the cells, MG-132 (Sigma-Aldrich, 1211833-36-9), a reversible and cell-permeable proteasome inhibitor, was added to the cell media to make the final concentration to 10mM. After 2h incubation with MG-132, the cells were washed three times with ice cold PBS and lysed in 500µl NP-40 with the protease inhibitor and phosphatase inhibitor. The cells were then scraped by the reverse end of P1000 pipette tip, and cell lysates were transferred to 1.5ml Eppendorf, followed by vortex 3s for three times. Between each vortex, cell lysates were incubated on ice for 3s. Cell debris was discarded after centrifugation at 4°C, 13,000rpm for 10min and the supernatant was transferred into new Eppendorf and stored on ice for immediate use for the MBP pull-down assay.

2.2.2.7 Human Kinome siRNA Library screening and cell viability assay

Mock transfection and optimisation INTERFERin and Lipofectamine RNAiMAX (hereafter refer to Lipofectamine) were used for the mock transfections to evaluate and optimise the cytotoxicity and transfection efficiency. Both INTERFERin and Lipofectamine are non-liposomal cationic transfection reagents whose activity depend on the basic structure of cationic lipids containing a positively charged head group. Nucleic acids are negatively charged because of the polyphosphate backbone, resulting in the interaction with the positively charged cationic lipids to form transfection complexes. These transfection complexes are positively charged due to the structure of lipids, allowing to interact with the negatively charged cell membrane. Once interacted, cells uptake these complexes into the cytoplasm *via* an endocytosis process. These transfection complexes then release nucleic acids which diffuse through the cytoplasm and function.

Library screening For library screening, cell viability assay for validation and investigation, the seeding number (**Table 2.5**) for the cells was optimised to achieve 90-100% confluent at the endpoint (Day 5). To achieve 50µM siRNA for the final concentration, the cells were seeded on 96-well plate on Day 1. Transfection was performed after 24h seeding the plate. 0.5µl of transfection reagents was mixed well

with 50µl of Opti-MEM by vortex and pulse centrifugation. The transfection reagent mixture was then incubated at room temperature for 5min, followed by mixing well with the proper amount of siRNA to meet the experiment requirement. For library screening, the final concentration of SMARTPool siRNA (**Table 2.6**). The mixture was then incubated at room temperature for 20min. Because the screening was to find out the synthetic lethality, the isogenic pair of each cell line was used. To keep the same siRNA was transfected into two cell lines, 50µl of transfection complexes was aliquoted to each cell line after the cells media was removed, followed by adding 75µl cell media. The cells were then incubated in the incubator for 24h before the cell media was changed on Day 3. The cells were then incubated for another 48h (Day 5) for endpoint measurement and analysis.

Table 2.5 Table of seeding numbers of each cell line in 96 well plate format in this study
The exact seeding number in 96 well plate of each cell line used in this study for target validation and cell viability assay.

Cell line	Seeding number (96well plate)	Cell line	Seeding number (96well plate)
A549 isogenic pair	1500 cells/well	MDA-MB-435 isogenic pair	3500 cells/well
HeLa isogenic pair	1000 cells/well	SAEC	2000 cells/well
A549	2000 cells/well	H28	2000 cells/well
H520	2000 cells/well	H522	2000 cells/well
H838	3000 cells/well	H358M	1500 cells/well
MSTO-211H	2000 cells/well		

Cell viability was measured five days after transfection using the 96-well plate CellTiter-Glo Luminescent Cell Viability Assay kit (Promega, G7570) according to the manufacturer's instructions. Luminescence readings from each well were log transformed and normalised according to the median signal on each plate and then standardised by use of a Z-score statistic (details in **Chapter 2.3**).

Table 2.6 Table of siRNAs used the library screening and target validation

Kinome library siRNA screen was used siGENOME® SMARTPool® siRNA Library targeting Human Protein Kinase. siNTC is non-targeting siRNA control pool. All siRNAs are for Homo sapiens.

Target Gene Symbol	Gene ID	Gene Accession	Alias	Sequence	Length	Pool Catalog Number	Manufactory
Human Protein Kinases	-	-	-	-	19	G-003505	Dharmacon
-	-	-	siNTC/siSCR	-	19	D-001206-13-20	Dharmacon
PLK1	5347	NM_005030	siPLK1 SMARTPool	Pool of the following 4	19	M-003290-01	Dharmacon
AAK1	22848	NM_014911	siAAK1 SMARTPool	Pool of the following 4	19	M-005300-01	Dharmacon
AAK1	22848	NM_014911	siAAK1 #1	GACAUGCACUGCCUAAUUA	19	D-005300-01	Dharmacon
AAK1	22848	NM_014911	siAAK1 #2	GUACAGAACUCUCCCAUUC	19	D-005300-02	Dharmacon
AAK1	22848	NM_014911	siAAK1 #3	GAUGAAAUGUGCCUUGAAA	19	D-005300-03	Dharmacon
AAK1	22848	NM_014911	siAAK1 #4	GAAGGUGGAUUUGCUAUUG	19	D-005300-04	Dharmacon
ACVR2B	93	NM_001106	siACVR2B SMARTPool	Pool of the following 4	19	M-004927-01	Dharmacon
ACVR2B	93	NM_001106	siACVR2B #1	GAACGAACUGUGUCAUGUA	19	D-004927-01	Dharmacon
ACVR2B	93	NM_001106	siACVR2B #2	AAAGAUCACUGGUUGAAAC	19	D-004927-02	Dharmacon
ACVR2B	93	NM_001106	siACVR2B #3	ACGAGAACCUGCUACAGUU	19	D-004927-04	Dharmacon
ACVR2B	93	NM_001106	siACVR2B #4	CUGAAUAGGCAAAGCGAUU	19	D-004927-17	Dharmacon
AURKB	9212	NM_004217	siAURKB SMARTPool	Pool of the following 4	19	M-003326-08	Dharmacon
AURKB	9212	NM_004217	siAURKB #1	CAGAAGAGCUGCACAUUUG	19	D-003326-07	Dharmacon
AURKB	9212	NM_004217	siAURKB #2	CCAAACUGCUCAGGCAUAA	19	D-003326-08	Dharmacon
AURKB	9212	NM_004217	siAURKB #3	ACGCGGCACUUCACAAUUG	19	D-003326-09	Dharmacon
AURKB	9212	NM_004217	siAURKB #4	UGGGACACCCGACAUCUUA	19	D-003326-10	Dharmacon
BMPR1A	657	NM_004329	siBMPR1A SMARTPool	Pool of the following 4	19	M-004933-04	Dharmacon
BMPR1A	657	NM_004329	siBMPR1A #1	GGACUCAGCUCUAUUUGAU	19	D-004933-03	Dharmacon
BMPR1A	657	NM_004329	siBMPR1A #2	CAGCUACGCCGGACAAUAG	19	D-004933-07	Dharmacon
BMPR1A	657	NM_004329	siBMPR1A #3	CGAGUGAUCCGUCAUACGA	19	D-004933-08	Dharmacon
BMPR1A	657	NM_004329	siBMPR1A #4	CCGCAAUUGCUCAUCGAGA	19	D-004933-24	Dharmacon
DCK	1633	NM_000788	siDCK SMARTPool	Pool of the following 4	19	M-006710-00	Dharmacon
DCK	1633	NM_000788	siDCK #1	CCAGAGACAUGCUUACAUA	19	D-006710-01	Dharmacon
DCK	1633	NM_000788	siDCK #2	GCAGGGAAGUCAACAUUUG	19	D-006710-02	Dharmacon
DCK	1633	NM_000788	siDCK #3	UGAAUUGGAUGGAAUCAUU	19	D-006710-03	Dharmacon
DCK	1633	NM_000788	siDCK #4	GAGACAGAGUGGACAAUUU	19	D-006710-04	Dharmacon

DUSP21	63904	NM_022076	siDUSP21 SMARTPool	Pool of the following 4	19	M-007893-02	Dharmacon
DUSP21	63904	NM_022076	siDUSP21 #1	GGGAACAGCUCAUCAAUUA	19	D-007893-01	Dharmacon
DUSP21	63904	NM_022076	siDUSP21 #2	UUGCGUACCUCAUGAAAUA	19	D-007893-03	Dharmacon
DUSP21	63904	NM_022076	siDUSP21 #3	CAAAUAACCAGAAGCUUGU	19	D-007893-04	Dharmacon
DUSP21	63904	NM_022076	siDUSP21 #4	CGGUGGAAGUGGUCAACGU	19	D-007893-18	Dharmacon
EFNB3	1949	NM_001406	siEFNB3 SMARTPool	Pool of the following 4	19	M-011261-00	Dharmacon
EFNB3	1949	NM_001406	siEFNB #1	CAAACCUCCUUCUCACUUG	19	D-011261-01	Dharmacon
EFNB3	1949	NM_001406	siEFNB #2	GUAUAGCCCUAAUCUCUGG	19	D-011261-02	Dharmacon
EFNB3	1949	NM_001406	siEFNB #3	GCUCGCACCACGAUUACUA	19	D-011261-03	Dharmacon
EFNB3	1949	NM_001406	siEFNB #4	CUCCAAACAUCUACUACAA	19	D-011261-04	Dharmacon
ERBB4	2066	NM_001042599	siERBB4 SMARTPool	Pool of the following 4	19	M-003128-03	Dharmacon
ERBB4	2066	NM_001042599	siERBB4 #1	GCAGGAAACAUCUAUAUUA	19	D-003128-06	Dharmacon
ERBB4	2066	NM_001042599	siERBB4 #2	GAUCACAACUGCUGCUUAA	19	D-003128-07	Dharmacon
ERBB4	2066	NM_001042599	siERBB4 #3	GCUCUGGAGUGUAUACAUU	19	D-003128-09	Dharmacon
ERBB4	2066	NM_001042599	siERBB4 #4	GGAAUUCCAACGCGAGAAA	19	D-003128-22	Dharmacon
HIPK2	28996	NM_022740	siHIPK2 SMARTPool	Pool of the following 4	19	M-003266-03	Dharmacon
HIPK2	28996	NM_022740	siHIPK2 #1	GAGAAUCACUCCAAUCGAA	19	D-003266-06	Dharmacon
HIPK2	28996	NM_022740	siHIPK2 #2	AGACAGGGAUUAAGUCAAA	19	D-003266-07	Dharmacon
HIPK2	28996	NM_022740	siHIPK2 #3	GGACAAAGACAACUAGGUU	19	D-003266-08	Dharmacon
HIPK2	28996	NM_022740	siHIPK2 #4	GCACACACGUCAAAUCAUG	19	D-003266-09	Dharmacon
MAGI3	260425	NM_152900	siMAGI3 SMARTPool	Pool of the following 4	19	M-009453-02	Dharmacon
MAGI3	260425	NM_152900	siMAGI3 #1	GGACAGAAGUGCCCUAGAA	19	D-009453-01	Dharmacon
MAGI3	260425	NM_152900	siMAGI3 #2	GAAGAUAAACCACCAAACA	19	D-009453-04	Dharmacon
MAGI3	260425	NM_152900	siMAGI3 #3	CCUGACCAGUCUAUAUAUA	19	D-009453-05	Dharmacon
MAGI3	260425	NM_152900	siMAGI3 #4	GCUGAUGUACCAUUGCUUA	19	D-009453-06	Dharmacon
NEK1	4750	NM_012224	siNEK1 SMARTPool	Pool of the following 4	19	M-004864-01	Dharmacon
NEK1	4750	NM_012224	siNEK1 #1	GAAAUAAACCCAUCAGCUA	19	D-004864-01	Dharmacon
NEK1	4750	NM_012224	siNEK1 #2	GAGAGAAGUUGCAGUAUUG	19	D-004864-02	Dharmacon
NEK1	4750	NM_012224	siNEK1 #3	GAAUUUGGCUUAUCAGAAU	19	D-004864-03	Dharmacon
NEK1	4750	NM_012224	siNEK1 #4	GGGAAGCUAUGCAGAAUAA	19	D-004864-04	Dharmacon
NRBP2	340371	NM_178564	siNRBP2 SMARTPool	Pool of the following 4	19	M-005340-02	Dharmacon
NRBP2	340371	NM_178564	siNRBP2 #1	UCAUGGAGCUGGACAAAUU	19	D-005340-02	Dharmacon

NRBP2	340371	NM_178564	siNRBP2 #2	GGAAUCUACCCACUGAUGA	19	D-005340-05	Dharmacon
NRBP2	340371	NM_178564	siNRBP2 #3	AUGCGGGAGUUCAUCCUUU	19	D-005340-06	Dharmacon
NRBP2	340371	NM_178564	siNRBP2 #4	GGUCACAGAGGAGGCCAUU	19	D-005340-07	Dharmacon
STK39	27347	NM_013233	siSTK39 SMARTPool	Pool of the following 4	19	M-004875-02	Dharmacon
STK39	27347	NM_013233	siSTK39 #1	GAACAGAGAGUACCUGAUU	19	D-004875-01	Dharmacon
STK39	27347	NM_013233	siSTK39 #2	GCACGACUGUUGCUCAUUU	19	D-004875-02	Dharmacon
STK39	27347	NM_013233	siSTK39 #3	CAGGUGGUCUUAUUUAUUG	19	D-004875-04	Dharmacon
STK39	27347	NM_013233	siSTK39 #4	AAACAGGGGUAGAGGAUAA	19	D-004875-05	Dharmacon
TSSK1B/STK22D	83942	NM_032028	siTSSK1B/STK22D SMARTPool	Pool of the following 4	19	M-005038-02	Dharmacon
TSSK1B/STK22D	83942	NM_032028	siTSSK1B/STK22D #1	GGACGAAGCUCGCAAGAAG	19	D-005038-05	Dharmacon
TSSK1B/STK22D	83942	NM_032028	siTSSK1B/STK22D #2	GGAUGACAGUGGUCGAAUG	19	D-005038-07	Dharmacon
TSSK1B/STK22D	83942	NM_032028	siTSSK1B/STK22D #3	CCAGCAAGCCGUCGACUAU	19	D-005038-08	Dharmacon
TSSK1B/STK22D	83942	NM_032028	siTSSK1B/STK22D #4	CAUCACAUGGCAAGGUCUA	19	D-005038-09	Dharmacon
TWF2/PTK9L	11344	NM_007284	siTWF2/PTK9L SMARTPool	Pool of the following 4	19	M-003169-01	Dharmacon
TWF2/PTK9L	11344	NM_007284	siTWF2/PTK9L #1	AGAGAGAGCUCCAGCAGAU	19	D-003169-05	Dharmacon
TWF2/PTK9L	11344	NM_007284	siTWF2/PTK9L #2	UUAACGAGGUGAAGACAGA	19	D-003169-06	Dharmacon
TWF2/PTK9L	11344	NM_007284	siTWF2/PTK9L #3	ACACAGAGCCCACGGAUGU	19	D-003169-07	Dharmacon
TWF2/PTK9L	11344	NM_007284	siTWF2/PTK9L #4	GCUGGGAUCAGGACUAUGA	19	D-003169-08	Dharmacon
WEE1	7465	NM_003390	siWEE1 SMARTPool	Pool of the following 4	19	M-005050-02	Dharmacon
WEE1	7465	NM_003390	siWEE1 #1	GCAGAACAAUUACGAAUAG	19	D-005050-01	Dharmacon
WEE1	7465	NM_003390	siWEE1 #2	UAGAACAUCUCGACUUAUU	19	D-005050-02	Dharmacon
WEE1	7465	NM_003390	siWEE1 #3	GAUCAUAUGCUUAUACAGA	19	D-005050-03	Dharmacon
WEE1	7465	NM_003390	siWEE1 #4	GGGAAUUUGAUGUGCGACA	19	D-005050-22	Dharmacon
WNK1	65125	NM_018979	siWNK1 SMARTPool	Pool of the following 4	19	M-005362-01	Dharmacon
WNK1	65125	NM_018979	siWNK1 #1	GCAGGAGUGUCUAGUUAUA	19	D-005362-01	Dharmacon
WNK1	65125	NM_018979	siWNK1 #2	UAUCGAAGAUGAAGACUUA	19	D-005362-02	Dharmacon
WNK1	65125	NM_018979	siWNK1 #3	GGAAGGCGGUUUAUAGUGA	19	D-005362-03	Dharmacon
WNK1	65125	NM_018979	siWNK1 #4	GCAGUUGUCUCAAUAUCUA	19	D-005362-04	Dharmacon

2.2.2.8 Protein extraction

The cells were washed three times with ice cold PBS and lysed in RIPA with the protease inhibitor and phosphatase inhibitor. The cells were then scraped, and the cell lysates were transferred to 1.5ml Eppendorf, followed by the 3s vortex for three times. Between each vortex, cell lysates were incubated on ice for 3s. Cell debris was discarded after centrifugation at 4°C, 13,000rpm for 10min, and the supernatant was transferred into the new Eppendorf and stored on ice for immediate use for western blot or stored at -80°C.

2.2.3 Direct binding assay

2.2.3.1 MBP pull-down of exogenously expressed proteins in mammalian cell

Cell lysates were incubated with 20µl of pre-washed anti-MBP magnetic resin at 4°C with rotation for 30min to conjugate the MBP-tagged proteins onto the resin. The resin was then washed three times with 200µl of 0.1M sodium phosphate buffer (pH 8.0) with vortex and applied to a magnet for 30s to pull resin to the side of the tube, followed by the incubation with mammalian cell lysates at 4°C with rotation for 2h. After incubation, the resin was washed three times with 500µl RIPA with vortex and applied to a magnet for 30s to pull resin to the side of the tube. Proteins were eluted in 20µl 2xSDS-PAGE sample loading buffer and then analysed by Western Blot.

2.2.3.2 GST pull-down with bacterial expressing recombinant proteins

Glutathione Sepharose 4B resin was blocked in 200µl of 5% BSA at 4°C with rotation for overnight. Bacterial cell lysates were incubated with 20µl of the resin at 4°C with rotation for 30min. The resin was then washed three times with 200µl RIPA with gentle vortex and centrifugation at 4°C for 1min, 500g, followed by incubating with the purified MBP-tagged protein in buffer A at 4°C with rotation for 2h. After incubation, the resin was washed five times with 500µl the binding buffer with vortex and centrifugation at 4°C for 1min, 500g. Proteins were eluted in 20µl 2xSDS-PAGE sample loading buffer and then analysed by Western Blot.

2.2.3.3 MBP pull-down with bacterial expressing recombinant proteins

Cell lysates were incubated with 10µl of pre-washed anti-MBP magnetic resin at 4°C with rotation for 30min to conjugate the MBP-tagged proteins onto the bead. The resin was then washed three times with 200µl RIPA buffer with vortex and applied to a magnet for 30s to pull resin to the side of the tube. The supernatant was then removed, followed by incubating with required protein lysates at 4°C with rotation for 2h. After incubation, the resin was washed three times with 500µl binding buffer with vortex. Proteins were eluted in 20µl 2xSDS-PAGE sample loading buffer and then analysed by Western Blot.

2.2.4 Cell viability assay

Cells were seeded in the 96well plates on Day 1 (**Figure 2.6**). Cells were transfected with siRNAs from Human Kinome siRNA library on Day 2. The cell media was changed on Day 3 or changed at 4h post-transfection if there were a dramatic cell death. Transfected cells were allowed to grow for 2 days till the endpoint (Day 6, **Figure 2.6**). On day 6, the cells were measured the cell viability by using CellTiter-Glo® Luminescent Cell Viability Assay (Promega, G7573). The cells were washed with 100ml PBS and then 100ml of diluted CellTiter-Glo® solution (1:3 with ddH_2O) was added. The cells were then shaken for 2min and allowed to incubate for 10min, followed by the measurement of luminescence using plate reader (PerkinElmer, 1420).

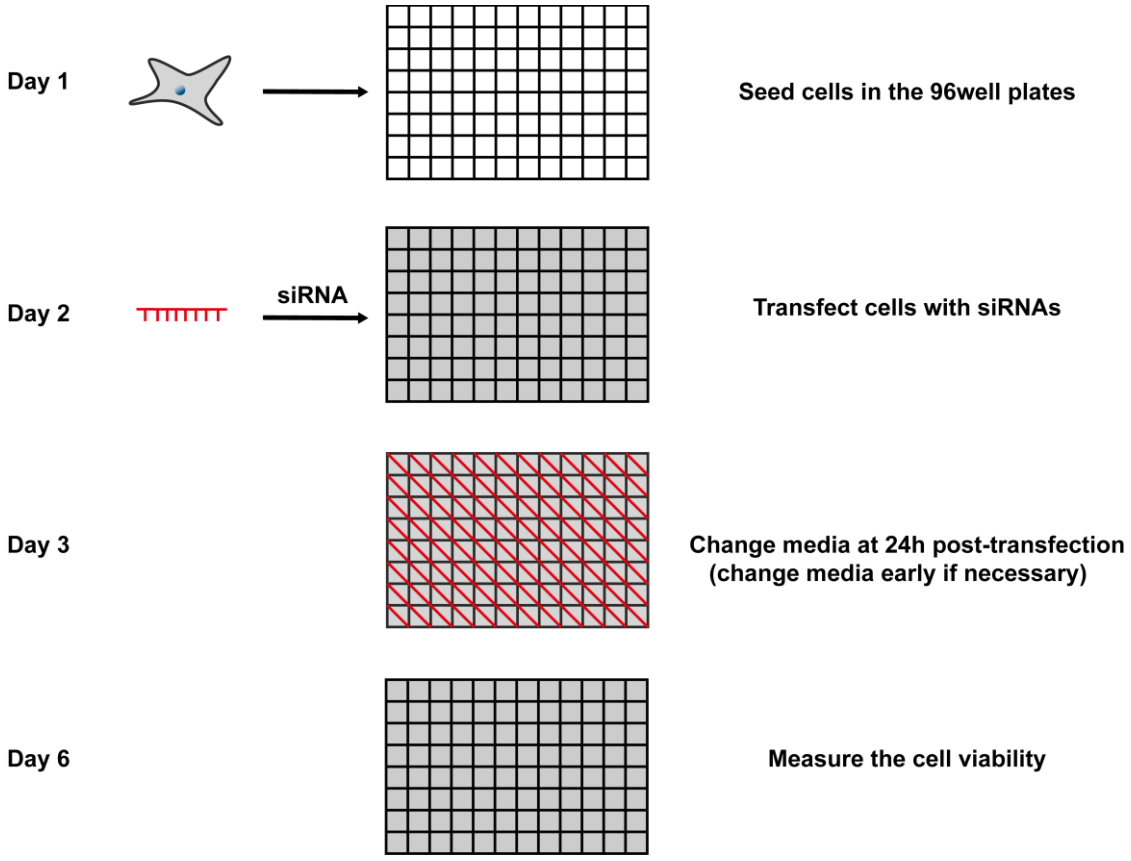

Figure 2.6 A flowchart of measuring the cell viability under the siRNAs treatment.
Cells were seeded in 96well plate on Day 1 and treated with siRNAs from Human Kinome siRNA library on Day 2. The media was then changed at 24h post-transfection or 4h post-transfection if dramatic cell death was caused. The cell viability of each well was measured using the commercial assay kit after two-day growth.

2.2.5 Clonogenic assay for validation siRNA targets from the screening

After 24h transfection in a 96-well-plate format, the cells were trypsinised with 50µl trypsin and incubated for 3min in the incubator. 200µl media was added to neutralise the activity of trypsin. 20µl of complete suspended cell suspension was transferred to one well of 6-well plate. Triplicate on 6-well plate was made for each siRNA transfected sample. 2ml media was added to each well of 6-well plate, and the cells were incubated for ten days. After ten days, the cells were washed once with PBS and fixed with 100% ice cold ethanol overnight at 4°C. The cells were then stained with 10% (v/v) crystal

violet at room temperature for 40min, followed by washed with tap water and allowed to dry at room temperature. The colony number was counted manually.

2.2.6 RNA extraction and quantification

RNA was extracted from the cells by using Reliaprep RNAminiprep (Promega, Z6012), following the manufacturer's instruction. RNA concentration was measured using a NanoDrop® ND-1000 spectrophotometer (NanoDrop Technologies Inc.).

2.2.7 Total RNA extraction

The cells were allowed to grow to confluent in monolayer. The culture media was removed. 1ml/1x10^7 cells of TRIzol reagent (Sigma-Aldrich, T9424-100ML) was directly added to the culture dis. The cell lysate was transferred to a 1.5ml Eppendorf and then was passed through a sterile, disposable 21g needle for three times to fragment the high-molecular weight cellular components, which minimise their presence in the aqueous phase. The homogenate was incubated at room temperature for 5min. 200ml chloroform (Sigma-Aldrich, C2432-25ML) was added and mixed vigorously. The homogenate was then incubated at room temperature for 3min, followed by centrifugation at 4°C for 15min, 12,000g. The homogenate was then equilibrated to the room temperature. The upper aqueous RNA solution was transferred to a new 1.5ml Eppendorf. 1 volume of isopropanol was added to the aqueous RNA solution and mixed gently. The mixture was incubated on ice for 1h, followed by the centrifugation at 4°C for 30min, 12,000g. The supernatant was then carefully discarded to prevent perturbing the RNA pellet. The RNA pellet was then washed with 1 volume of 70% chilled ethanol and mixed well. The solution was centrifuged at 4°C for 15min, 12,000g and incubated at room temperature for 15min. The solution was then centrifuged at 4°C for 5min, 12,000g and the supernatant was discarded carefully. The RNA pellet was air-dried at room temperature for 10min and dissolved in 200ml RNase-free water. The extracted RNA was stored at -80°C for the downstream assays.

2.2.8 RNA quantification

The pedestals were wiped clean 100% ethanol and the distilled water after each measurement. The instrument was blanked with 1µl of the same buffer in which RNA eluted. 1µl of the DNA sample was used per measurement with both a 260nm and 280nm light absorbance values. The ratio of 260/280 between 1.8-2.0 means RNA is pure. The ratio 260/230 between 2.0-2.2 means no protein contamination. The concentration was measured twice for each RNA sample, and an average value was taken.

2.2.9 Reverse transcription and qRT-PCR for miRNA

The total RNA (1ug) was first treated with DNase 1 (Sigma-Aldrich, AMPD1-1KT) to eliminate the residue DNA during the extraction and precipitation processes. 500ng DNase-treated total RNA was then reverse transcribed to cDNA with 20µl of the following reaction system using miScript II RT Kit (QIAGEN, 218161): 4µl 5xmiScript HiFlex Buffer, 10xmiScript Nucleics Mix, 7µl RNase-free water and 2µl miScript Reverse Transcriptase Mix. The reaction mixture was incubated at 37°C for 60min, followed by the incubation at 95°C for 5min to inactivate miScript Reverse Transcriptase Mix.

2.5ng of cDNA was used for 25µl of the following qRT-PCR reaction system: 12.5µl 2xQuantiTect SYBR Green PCR Master Mix (QIAGEN, 218073), 2.5µl 10xmiScript Universal Primer, 2.5µl 10xmiScript miR-26 Primer and RNase-free water. The initial denaturation was performed for 15min at 95°C. 30 cycles of denaturation (15s at 94°C), annealing (30s at 55°C), and extension (30s at 70°C). Data were normalised to the reference non-coding small nuclear RNA (U6), and the relative amount of targets were quantified using the $2^{-\Delta\Delta Ct}$ method.

2.2.10 qRT-PCR for mRNA

RNA was diluted to 10ng for each sample and added to GoTaq 1-step qRT-PCR (Promega, A6020) reactions along with the specific primers. qRT-PCR was performed in triplicate on the Applied Biosystems 7500 Real-Time PCR System. Data were normalised to the

housekeeping gene RNA polymerase II (RPII), and the relative amount of targets were quantified using the $2^{-\Delta\Delta Ct}$ method.

2.2.11 Annexin V/PI staining for FITC apoptosis detection by the flow cytometry

Apoptotic cells can be identified based on the phosphatidylserine transition on the cell surface-chromosomal and the DNA fragmentation. Annexin V is used to stain the cells to indicate cell membrane changes which occur in the early stage of apoptosis. Once apoptosis is initiated, the phosphatidylserine present in the inner cell membrane migrates through the cell membrane of the lipid bilayer. Annexin V specifically binds to phosphatidylserine in the presence of protein-dependent Ca ion. Propidium iodide (PI) bind with DNA and is only permeant to dead cells. Therefore, by using fluorescent labelled Annexin V and PI, it is possible to perform double staining simultaneously and identify the living cells and apoptotic cells by the flow cytometry (**Figure 2.7**).

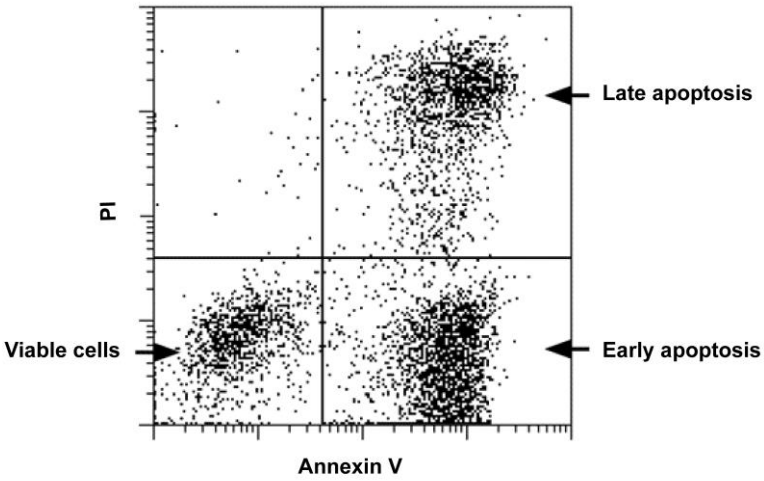

Figure 2.7 An example of apoptosis detection by Annexin V/PI staining using the flow cytometry
One example to demonstrate in which area that the cells represent viable, early apoptosis, or late apoptosis using Annexin V/PI double staining.

The cells were seeded in 6well plate and transfected with 50nM siRNAs. After 48h, the supernatant was discarded. The cells were washed with 1ml PBS twice, followed by detaching with Trypsin-EDTA. The cells pellets were collected by centrifugation at

1200rpm for 3min and were washed with PBS twice. 1xAnnexin V binding solution (Dojindo, AD01-02) was used to make final cell concentration of $1x10^6$ cells/ml. 100ul of cell suspension was transferred, and 5µl PI was added for incubation at room temperature for 15min, protected from light. 400µl 1xAnnexin V was added and applied for flow cytometry analysis.

2.2.12 Western blot protein expression analysis

2.2.12.1 SDS-PAGE

SDS-PAGE gels were assembled into a mini-PROTEAN® Tetra Cell (Bio-Rad) and filled with 1xrunning buffer. 5µl protein marker and samples were carefully loaded into the bottom of each well of the gel. Gels were then run at a constant voltage of 80V until the blue dye reached and concentrated at the top of the resolving gel, which usually takes 15min. A constant voltage of 120V-180V was then used until the blue dye front reached the bottom of the resolving gel.

2.2.12.2 Coomassie Staining and Destaining

The SDS-PAGE gel was stained with Coomassie blue staining solution at room temperature with shaking gently for 1-2h. The gel was washed with tap water for three times and then destained in Coomassie blue de-staining solution for overnight at room temperature.

2.2.12.3 Immunoblot

During SDS-PAGE, PVDF membrane (Roche, 0301004001) were completely soaked in 100% methanol with shaking at room temperature for 5min, followed by gradually diluting 100% methanol to 0% methanol by adding the distilled water. The membrane was then soaked in the transfer buffer with shaking at room temperature until use. After the electrophoresis, SDS-PAGE gels along with the membrane and filter paper were assembled according to the manufactory's instruction and transferred at a constant 20V for 20min using Trans-Blot® Turbo™ transfer cell (Bio-Rad). The membrane was then incubated in the blocking solution at room temperature for at least 1h. Membranes can

be cut into small size if multiple antibodies were applied. The required primary antibody was diluted in the blocking solution (**Table 2.7**). After blocking, the membrane was incubated in the antibody solutions overnight with gentle agitation at 4°C. The membrane was then washed with PBS-T three times for 5min at room temperature with shaking. Horseradish peroxidase (HRP)-conjugated secondary antibodies were diluted at a ratio of 1:5000 in blocking solution. The membranes were incubated with the secondary antibody with shaking at room temperature for 1h. The membrane was then washed with PBS-T for three times for 5min at room temperature with shaking before incubation with an Enhanced Chemi-luminescence Reagent (ECL2) Western Blotting Detection Solution (Thermo Scientific, PI80196) for 5min to initiate an HRP-catalysed luminescent reaction. The membrane was finally exposed to Chemi-luminescent Detection Film (Roche Applied Science) for different time according to the intensity of the signals. Alternatively, the membrane can be analysed under G: Box system (SYNGENE).

Table 2.7 Table of the primary and secondary antibodies used for immunoblotting in this study
The table contains the information of the working dilutions, host species, predicted molecular weight, manufacturing company and catalogue number indicated.

Primary antibodies					
Antigen	**Dilution**	**Host species**	**Size of antigen (kDa)**	**Company**	**Catalogue Number**
AGO1	1: 1000	Rabbit	97	Cell Signalling	5053S
AGO2	1: 1000	Rabbit	97	Cell Signalling	2897S
AGO3	1: 1000	Rabbit	97	Cell Signalling	5054S
AGO4	1: 1000	Rabbit	97	Cell Signalling	6913S
β-actin	1: 25,000	Mouse	42	Sigma-Aldrich	A1978
DnaK (hHSP70)	1: 1000	Mouse	70	Cell Signalling	ab69617
EGFP/EYFP tag	1: 2,000	Mouse	26.9	Roche	11814 460001
GW182	1: 1000	Mouse	182	Santa Cruz	sc-56314
HIF-1α	1: 1000	Mouse	120	BD Biosciences	610959
LIMD1 (N-terminus)	1 : 500	Mouse	72	Sharp *et al*.(2004) Clone 3F2/C6	N/A
MBP	1: 50,000	Mouse	42.5	New England Biolabs	E8032S
Phospho-S387-AGO2	1: 200	Rabbit	97	Prof. Paμl Graves	N/A
p38	1:1000	Rabbit	43	Cell Signalling	9212S
Phospho-p38	1:1000	Mouse	43	Cell Signalling	9216S
STK39	1:1000	Rabbit	65	Cell Signalling	2281S
HRP-conjugated Secondary antibodies					
Antigen	**Dilution**	**Host species**		**Company**	**Catalogue Number**
Mouse	1: 5,000	Goat		Dako	P0447
Rabbit	1: 5,000	Goat		Dako	P0448

2.2.13 Immunofluorescence assay

Immunofluorescence assay (IFA) was employed to investigate the co-localisation between two proteins, detected by the confocal microscope. The assay normally uses the specificity of antibody conjugated with fluorescent dyes against the endogenous proteins and allows to visualise and analyse the distribution of the endogenous proteins [244]. Two or more proteins of interest respectively bind their specific antibody conjugated with different colours of fluorophores. Because different fluorophores have their fluorescence emission wavelengths, the confocal microscope measures these

different wavelengths by using temporally separated laser sources. Consequently, different colours for each labelled protein will be observed, which in turn provide the localisation of each protein within the cells. Therefore, if there is an association between different proteins, it will be observed that these different proteins are within proximate distant and subsequently causing the merged colour to be captured by the microscope.

U2OS was used for IFA due to its large shape. The cells are ideally approximately 60% confluent at the end point. 2.5 x 10^4 cells/well were seeded in 12-well plate with polylysine-coated coverslips (Corning, 354085) in it. After 24h incubation, the cells were co-transfected with two plasmids DNA containing genes of interest (500ng/well for each). The cells were then incubated at 37°C, 5% CO_2 for 48h. Media was changed if the cells were dying because of the toxicity of transfection reagent or DNA to be transfected. After 48h incubation, the cells were washed three times with PBS and fixed in 1ml 4% paraformaldehyde at room temperature for 3min. The cells were then washed for three times with PBS. 10µl of mounting medium with DAPI (Biotium, 23004) was added onto a microscope slide. The coverslips were removed from the 12 well plate using a blade and tweezers and flipped over onto the mounting medium. The coverslips were then allowed to set at room temperature and stored at 4°C without light. The cells can be analysed under a confocal microscope.

The quantification of each pair of co-localisation in this study (in **Chapter 4**) was generated from two or three independent biological repeats (n=2 or 3). For each individual repeat, the number of co-localised foci out of 80-100 cells was counted manually under the microscope, and then the percentage of co-localisation was calculated.

2.3 Statistical Analysis

Standard score (Z-score) was calculated according to the cell viability in Human Kinome siRNA Library screening. The formula is $z_i = \frac{x_i - \overline{x}}{S}$, where x_i represents each value in the data set; $\overline{x}$ represents the mean of all values in the data set and S represents the standard deviation of the dataset. Z-score, which represents the distance between the raw value and the population mean in units of the standard deviation, was calculated

for each kinase for each cell line according to the cell viability [245]. In the library screening, Z-score described that how many standard deviations of cell viability treated with one siRNA lies above or below the mean of all cell viability treated with the whole Human Kinome siRNA library. A Z-score above the mean had a positive value, whereas it bellow the mean had a negative value. The positive value indicated the increasing growth of the cells, while the negative value indicated an inhibitory or cytotoxicity on the cells. Therefore, the greater the absolute Z-score value was, the greater effect on the cells due to the depletion of the gene by siRNAs. ΔZ-score was the difference in Z-score between the isogenic pair of cell lines: $\Delta Z = Z_{-} - Z_{+}$, where Z_{-} represents LIMD1 negative cell line and Z_{+} represents LIMD1 positive cell line. The smaller ΔZ-score was, the more potent synthetic lethality the siRNA caused.

Statistical significance was calculated using the Student's t-test unless otherwise

Chapter 3 Results

Characterisation of the interaction interfaces between LIMD1 and AGO2

3 Characterisation of the interaction interfaces between LIMD1 and AGO2

To initiate miRNA-mediated silencing, AGO proteins recruit TNRC6 proteins and the downstream effector proteins (DCPs), DDX6, and CCR4-NOT4 to form miRISC [99]. It has been reported that the depletion of LIMD1 reduced the efficacy of miRNA-mediated gene silencing through disruption of miRISC [1]. It was demonstrated that LIMD1 is a critical component required for miRNA-mediated silencing, binding to AGO2 through the unstructured the pre-LIM region (amino acid (a.a) 1-464) [1]. Pre-LIM domain has been reported to interact with multiple protein partners, including PHD2 *via* a.a 186-260 and pRB between *via* 404-442 (**Figure 1.23**) [216, 217]. However, the precise interaction region for AGO2 binding remained unknown. Moreover, the specific domain within pre-LIM domain for AGO2 binding was also required to be investigated. The characterisation of the interaction interfaces on both AGO2 and LIMD1 would help for deep understanding the role and function of LIMD1 in miRISC assembly, and thus the mechanism of miRNA-mediated silencing.

Initially, to map the interaction interface on LIMD1, a set of internal deletion mutants within pre-LIM domain together with Xpress (Xpr)-tagged LIMD1 FL (full-length) were expressed and subjected to co-immunoprecipitation (co-IP) with EYFP-AGO2 from HEK293T cells. The co-IP result showed that the deletion of a.a 140-166 within pre-LIM region abrogated the interaction with AGO2 (**Figure 3.1**). This result suggested that a.a 140-166 within LIMD1 is a critical domain that contributes to the interaction with AGO2.

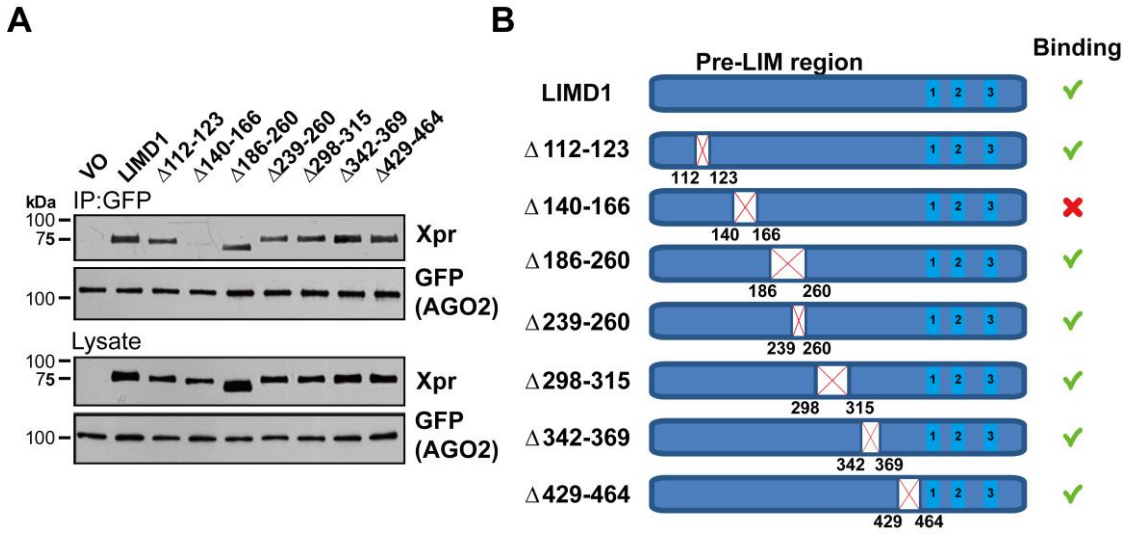

Figure 3.1 Amino acids 140-166 within LIMD1 are required for association with AGO2 *in vitro*
***A*)** Co-IP of Xpr-LIMD1 and the internal deletion mutants with EYFP-AGO2 from HEK293T lysate. The deletion of a.a 140-166 within LIMD1 abolishes association with EYFP-AGO2. Experiments were performed by Dr Katherine S. Bridge. ***B*)** Schematic of LIMD1 internal deletion mutants and summary of binding to EYFP-AGO2. Xpr, Xpress.

3.1 Construction of the expression plasmids to investigate the interaction interfaces between LIMD1 and AGO2

Given that a.a 186-260 is responsible for the binding to PHD2, the deletion of which does not affect the association between LIMD1 and AGO2(**Figure 3.1A**), it implied in addition to a.a.140-166, a.a 112-140 may also may also contribute to AGO2 binding. As a result, not only a.a 140-166 but also the larger specific domains of pre-LIM were designed for the fusion-tag technology to investigate the direct interaction region with AGO2 (**Figure 3.2A**).

AGO2 contains six domains as depicted in **Figure 1.10**: the N, L1, PAZ, L2, MID and PIWI domains. Therefore, to map the interaction domain on AGO2, truncation mutants with each domain sequentially deleted from either the N- or C-terminus were designed (**Figure 3.2B**). Because bacteria (*E.coli*), as a host, has the unparalleled fast growth

leading to a high cell density [246], bacterial recombinant expression plasmids were used for the production of the purified proteins required for *in vitro* identification of the interaction interfaces on LIMD1 and AGO2.

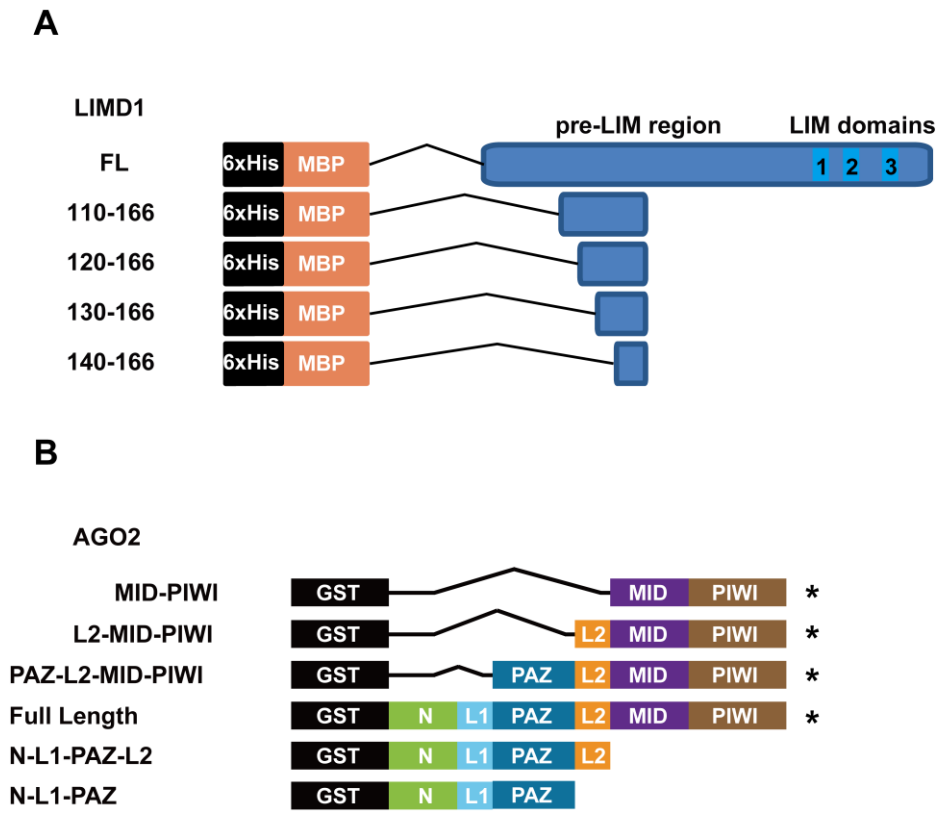

Figure 3.2 Schematic of LIMD1 and AGO2 constructs used in this project
A) LIMD1 FL (full length) or the truncation mutants was designed to fuse with an N-terminal HisMBP-tag. ***B)*** Full length of AGO2 or a serial set of sequential truncation mutants from either the N- or C-terminus were designed to fuse with an N-terminal GST-tag. *, the constructs were made by Dr Sybil C.K. Wong.

3.1.1 Construction of expression plasmids for LIMD1 FL and truncation mutants by LIC

Maltose-binding protein (MBP) is a common protein expression tag that natively expresses in *E.coli*. Because MBP, as a molecular chaperone, prevents the aggregation of the incompletely folded fusion protein, fusion of a target protein to MBP allows to significantly increase the expression level and solubility [247]. In addition, MBP-tagged proteins can be readily purified for the downstream analysis and experiments. The

pETFPP_2 vector system was selected because it provides an N-terminal MBP-tag (**Figure 2.1**) and utilises ligation independent cloning (LIC) (details described in **Chapter 2.2.1.4**). Moreover, due to the long 3' complementary overhangs on the insert and vector, LIC maximises the specificity of annealing and correction of insertion with a lower chance of self-circularisation of the vector [241].

The required cDNA sequence of LIMD1 encoding a.a 110-166 was prepared by PCR amplification using Xpr-LIMD1 as a template. A single PCR product of the expected size was successfully amplified (**Figure 3.3A**). The empty parental pETFPP_2 vector (pETFPP-VO) was linearised by the treatment of BseRI (**Figure 3.3B**). The PCR product and the purified linearised vector were annealed after the treatment of T4 DNA Polymerase (details described in **Chapter 2.2.1.4**). The colony PCR was performed by using T7 primers for verifying whether there was an insert to the parental vector backbone. The results showed the size of the PCR product of the colony #4 was bigger than that in the empty parental vector (**Figure 3.3C**). However, the colony #1 showed a PCR product at the same size of the empty parental vector (**Figure 3.3C**). The results indicated only colony #4 had an insert due to a larger size of the PCR product (with the required sequences). The alignment of the experimental DNA sequence of the colony #4 to the NCBI Database CDS for LIMD1 (NM_014240.2) then confirmed the insert was in frame with the tag sequences (**Figure 3.3D**). The same procedure was used to insert the CDS of LIMD1 a.a 120-166, 130-166, 140-166, and FL into pETFPP_2-VO for expressing MBP-LIMD1 120-166, 130-166, 140-166, and LIMD1 FL (**Figure 3.2A**). The sequencing results showed coding sequences of the desired cDNAs in all plasmids were in frame with the tag sequences (**Figure 3.4 and Figure 3.5**).

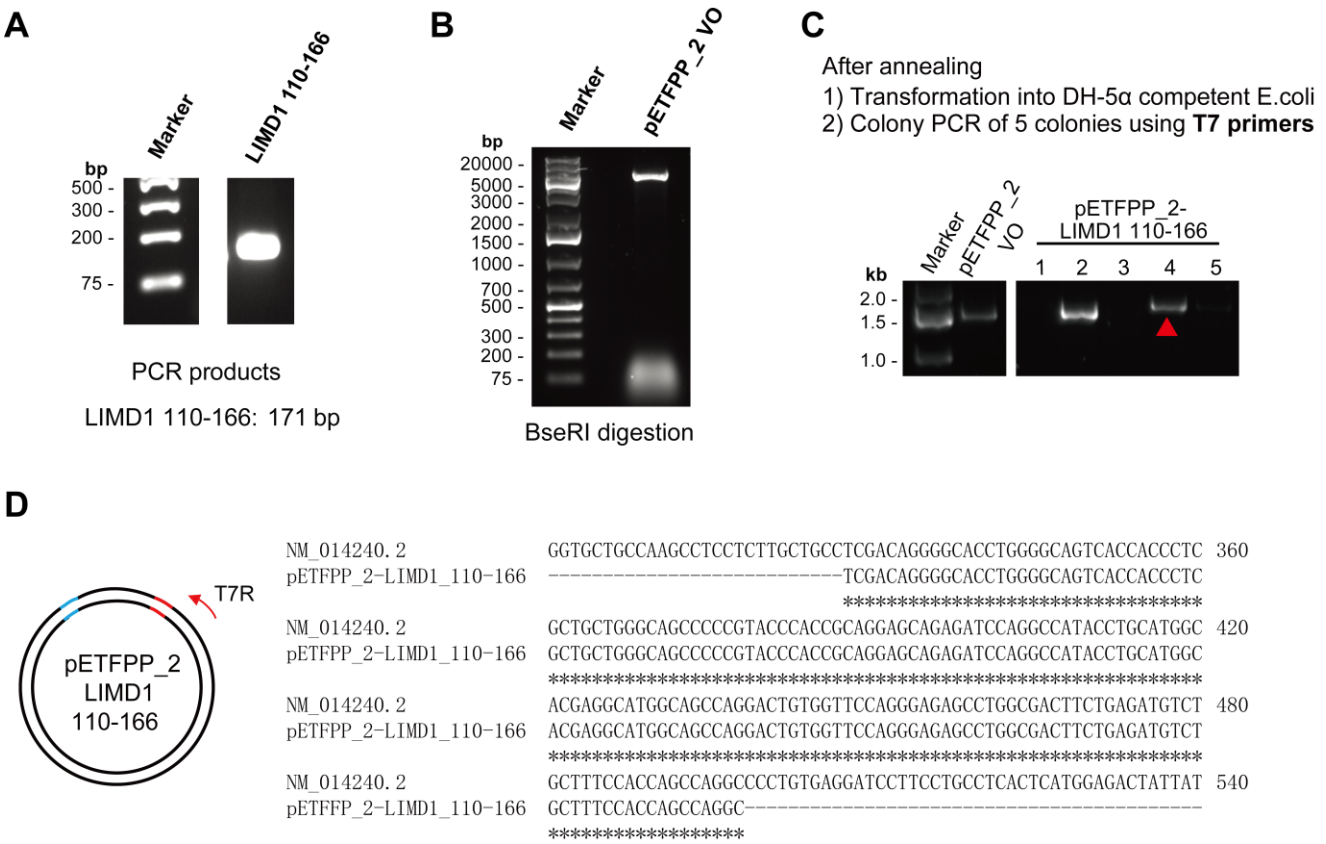

Figure 3.3 Cloning of bacterial expression plasmid for MBP-LIMD1 110-166 from Xpr-LIMD1 and empty pETFFP_2 vector by LIC

A) The CDS of a.a 110-166 was successfully PCR amplified from Xpr-LIMD1 and was visualised by agarose gel electrophoresis. ***B)*** BseRI-linearised vector was visualised by agarose gel electrophoresis. ***C)*** The colony PCR of 5 colonies was performed to indicate the successful insertion using T7 primers. The PCR product of pETFPP_2 VO was used as a reference. PCR band chosen for sequencing was highlighted by the red arrowhead. ***D)*** The alignment of the Sanger sequencing read to the database LIMD1 CDS (NM_014240.2) performed by MUSCLE. Only CDS of LIMD1 110-166 were displayed

Figure 3.4 Verification of bacterial expression plasmids for pETFPP_2-LIMD1 120-166 and 130-166, prepared from Xpr-LIMD1

A&C) The colony PCR of numbers of colonies was performed to indicate the successful insertion using T7 primers. The PCR product of pETFPP_2 VO was used as a reference. PCR band chosen for sequencing was highlighted by the red arrowhead. ***B&D***) The alignment of the Sanger sequencing read to the database LIMD1 CDS (NM_014240.2) performed by MUSCLE. Only CDS of LIMD1 120-166 and 130-166 were displayed.

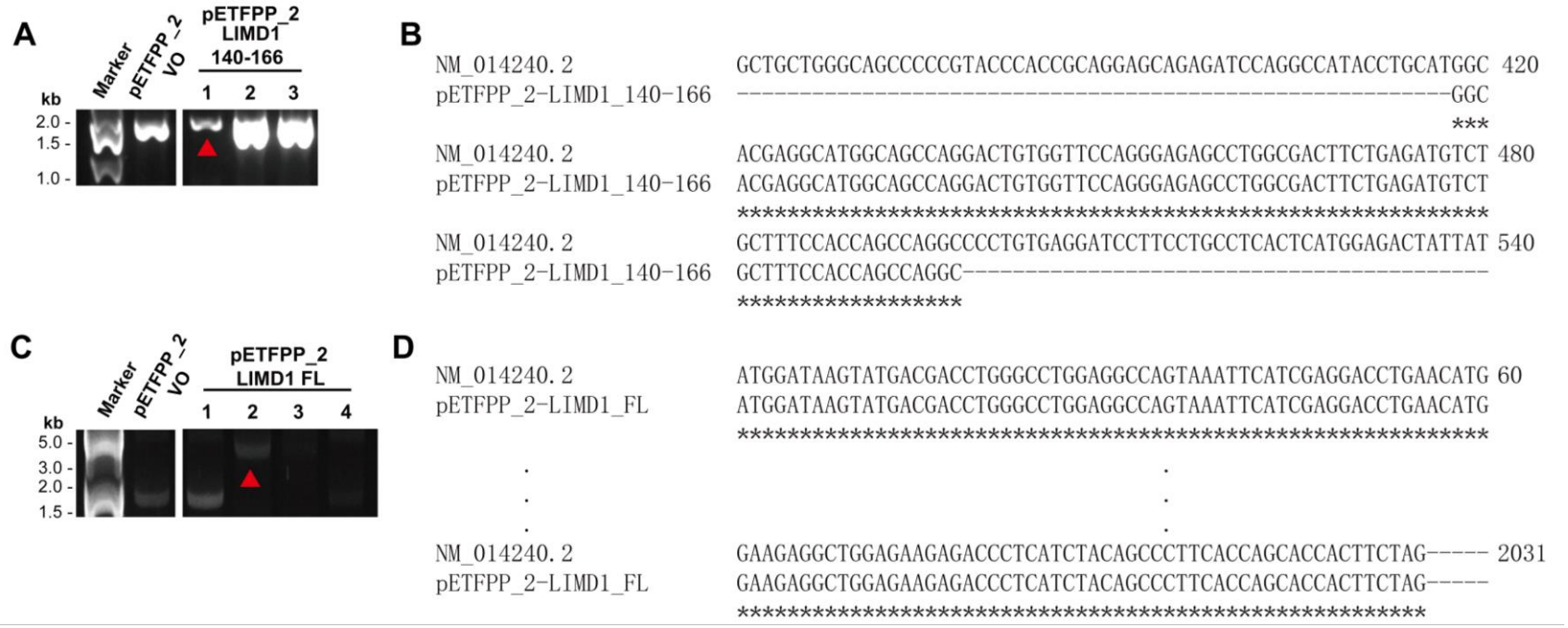

Figure 3.5 Verification of bacterial expression plasmids for pETFPP_2-LIMD1 140-166 and FL, prepared from Xpr-LIMD1

A&C) The colony PCR of numbers of colonies was performed to indicate the successful insertion using T7 primers. The PCR product of pETFPP_2 VO was used as a reference. PCR band chosen for sequencing was highlighted by the red arrowhead. ***B&D***) The alignment of the Sanger sequencing read to the database LIMD1 CDS (NM_014240.2) performed by MUSCLE. Only CDS of LIMD1 120-166 and 130-166 were displayed.

The pETFPP_2-VO plasmid expressing MBP-VO and MBP-tagged LIMD1 plasmids with the correct insert described above were transformed into *E.coli*. Isopropyl β-D-1-thiogalactopyranoside (IPTG) was used to induce the expression of MBP-VO and MBP-tagged LIMD1 proteins (**Chapter 2.2.1.10**). The constructs also encode an N-terminal poly-histidine tag (**Figure 2.1**). Hence the recombinant proteins can be purified by Ni-NTA resin, which provides high specificity and affinity to histidine residues. The purified proteins were eluted from the resin by using imidazole, which is a competitive inhibitor for His-tag [248], and analysed by both Coomassie staining and Western blot. All desired recombinant proteins were expressed at the correct molecular weight (**Figure 3.6**). For MBP-VO, there were double bands detected by Western blot (**Figure 3.6A**). The sequencing result of the parental pETFPP_2-VO showed there was no stop codon after MBP, and thus gives an additional 45 amino acids which in turn causes the size of the product is bigger than the actual size (larger size of the band in **Figure 3.6D**). The smaller size of the band for MBP-VO is degradation product but still encodes MBP. As a result, the difference in the size of bands between MBP-VO and MBP-tagged LIMD1 truncation mutants in Western blot did not represent the real difference in predicted molecular weight between MBP-VO and MBP-tagged LIMD1 truncation mutants (**Figure 3.6A and Figure 3.6E**).

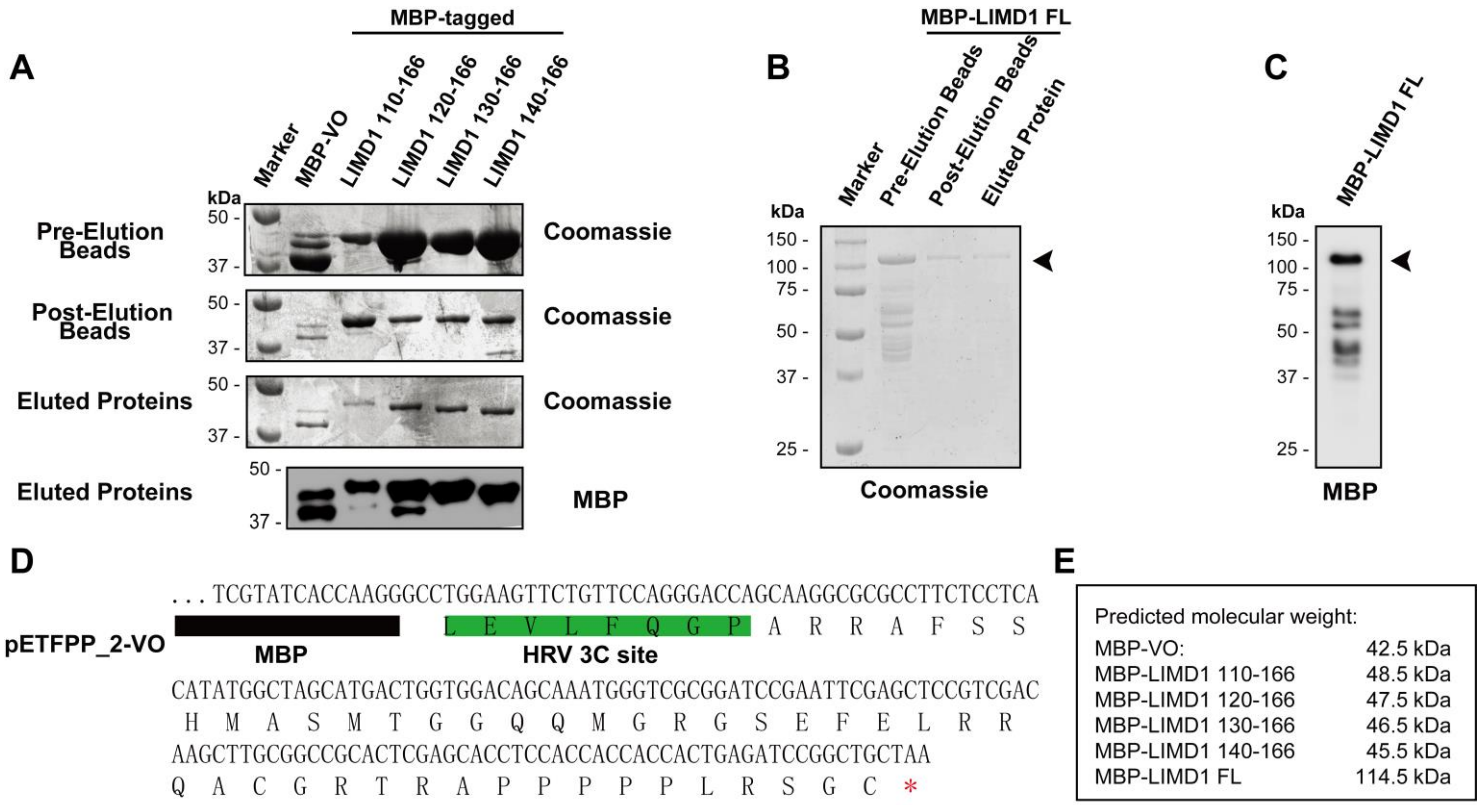

Figure 3.6 Verification of the expression of MBP-tagged LIMD1 truncation mutants and FL

A) pETFPP_2 VO expressing MBP-VO and pETFPP_2 LIMD1 truncation mutants were transformed and induced by IPTG to overexpress the recombinant MBP-tagged proteins. The purified and eluted proteins were analysed by Coomassie staining and Western blot. ***B)*** pETFPP_2 LIMD1 FL were transformed and induced by IPTG for overexpression. The purified and eluted proteins (highlighted by **black** arrowhead) were analysed by Coomassie staining. ***C)*** Western blot analysis for the eluted MBP-LIMD1 FL (highlighted by **black** arrowhead). ***D)*** The sequencing result of the parental pETFPP_2-VO. The part of MBP sequencing is highlighted in **black**. HRV 3C site is highlighted in green. ***E)*** The predicted molecular weight of MBP-VO and MBP-tagged LIMD1 FL and truncation mutants.

3.1.2 Construction of expression plasmids for AGO2 C-terminal truncation mutants

To investigate the interaction domain on AGO2, a serial set of constructs expressing sequential truncation mutants of AGO2 were designed (**Figure 3.2B**). Glutathione S-transferase (GST) is a widely used tag due to its positive influence of the GST-tagged proteins on solubility, expression and purification for the study of protein-protein interaction [249]. Therefore, the pMCSG10 vector expressing an N-terminal GST-tag was selected (**Figure 2.2**). The FL and N-terminal truncations MID-PIWI, L2-MID-PIWI and PAZ-L2-MID-PIWI of AGO2 were previously cloned into pMCSG10 vector by Dr Sybil C.K. Wong. The LIC method was used to generate N-L1-PAZ-L2 truncation mutant in the pMCSG10 vector. pMCSG10-AGO2 was used as a template for PCR amplification of the CDS of N-L1-PAZ-L2. For colony PCR verifying the correct insert, the size of colony PCR product of truncation mutant should be smaller than that of pMCSG10-AGO2 FL. The colony #1 and #3 were not successfully cloned because of their sizes of PCR products were the same as that of pMCSG10-AGO2 FL, while the highlighted band indicated a successful cloning of colony 5 (**Figure 3.7A**), indicating there was no internal deletion. The plasmid DNA of the highlighted colony was sequenced by using pGEX5 forward primer or T7 reverse primer (**Figure 3.7B and Figure 3.7C**). The sequencing result confirmed that the insert matched to the CDS of AGO2 (NM_012154.3) and was in frame with GST sequences (**Figure 3.7D**).

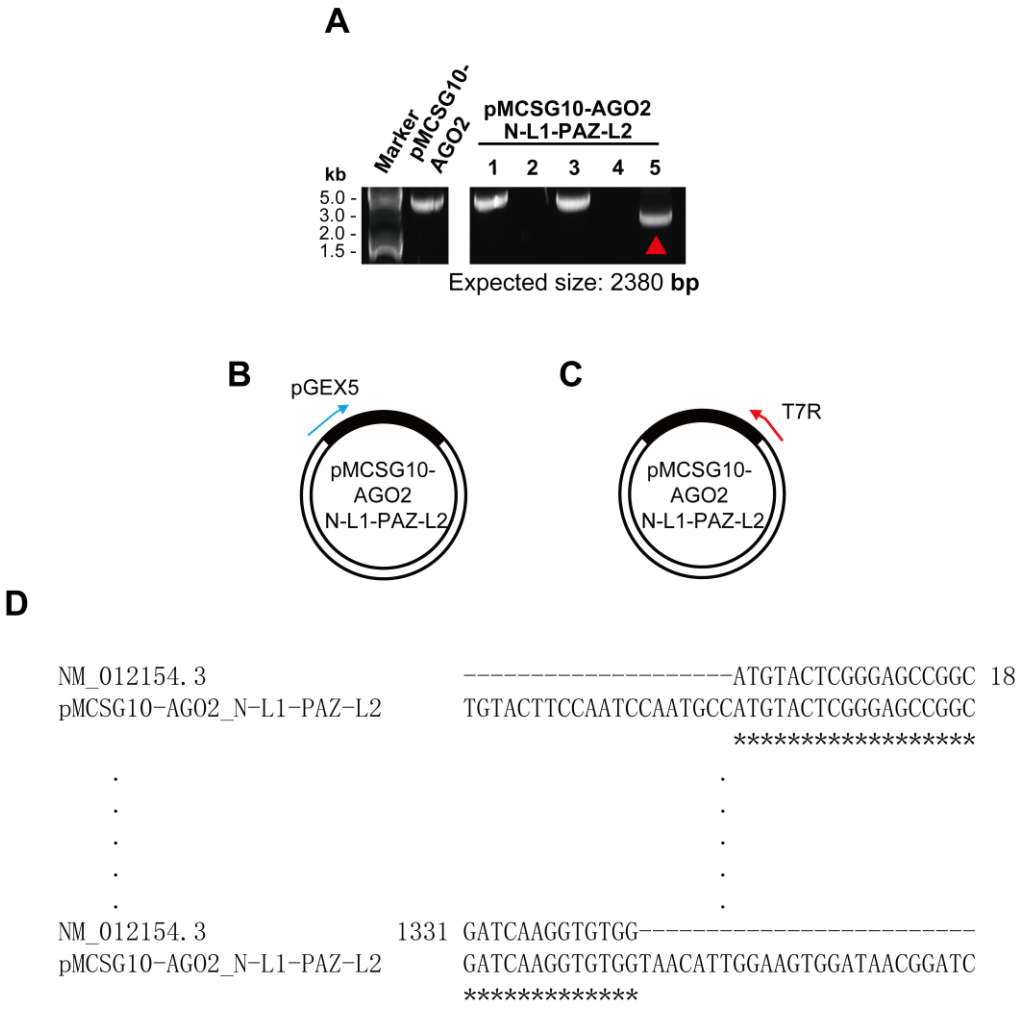

Figure 3.7 Cloning of bacterial expression plasmids for pMCSG10-AGO2 N-L1-PAZ-L2 by LIC
***A*)** The colony PCR of 5 colonies was performed to indicate the successful cloning using T7 primers. The expected size of the correct insert is 3607bp. PCR band chosen for sequencing was highlighted by the red arrowhead. ***B&C*)** pGEX5 forward primer or T7 reverse primer was used for sequencing. ***D*)** The alignment of the Sanger sequencing read to the database AGO2 CDS (NM_012154.3) performed by MUSCLE. Only partial of codons downstream or upstream of the CDS start or stop were displayed.

Site-directed mutagenesis was used to generate the pMCSG10-AGO2 N-L1-PAZ truncation mutant (details described in **Chapter 2.2.1.5**). A pair of DNA primers flanking the CDS of L2-MID-PIWI of AGO2 were designed for PCR amplification of the linearised DNA sequencing of N-L1-PAZ (**Figure 3.8A**). The single PCR product of the expected size

(7021bp) of AGO2 N-L1-PAZ was successfully amplified, analysed by agarose gel electrophoresis (**Figure 3.8A**). The colony PCR was then performed to confirm the mutagenesis worked. PCR product from pMCSG10-AGO2 FL was used as a reference for no internal deletion. The result showed both colony #2 and #3 had PCR products whose size are the same as to pMCSG10-AGO2 FL (**Figure 3.8B**). This indicated the mutagenesis did work on colony #2 and #3 to delete the undesired cDNA sequence (L2-MID-PIWI). In contrast, the mutagenesis successfully worked on colony #1; the PCR product showed a smaller size at 2083bp (**Figure 3.8B**). The sequencing result and alignment confirmed the cDNA sequences matched to the CDS of AGO2 and was in frame with GST sequences (**Figure 3.8E**).

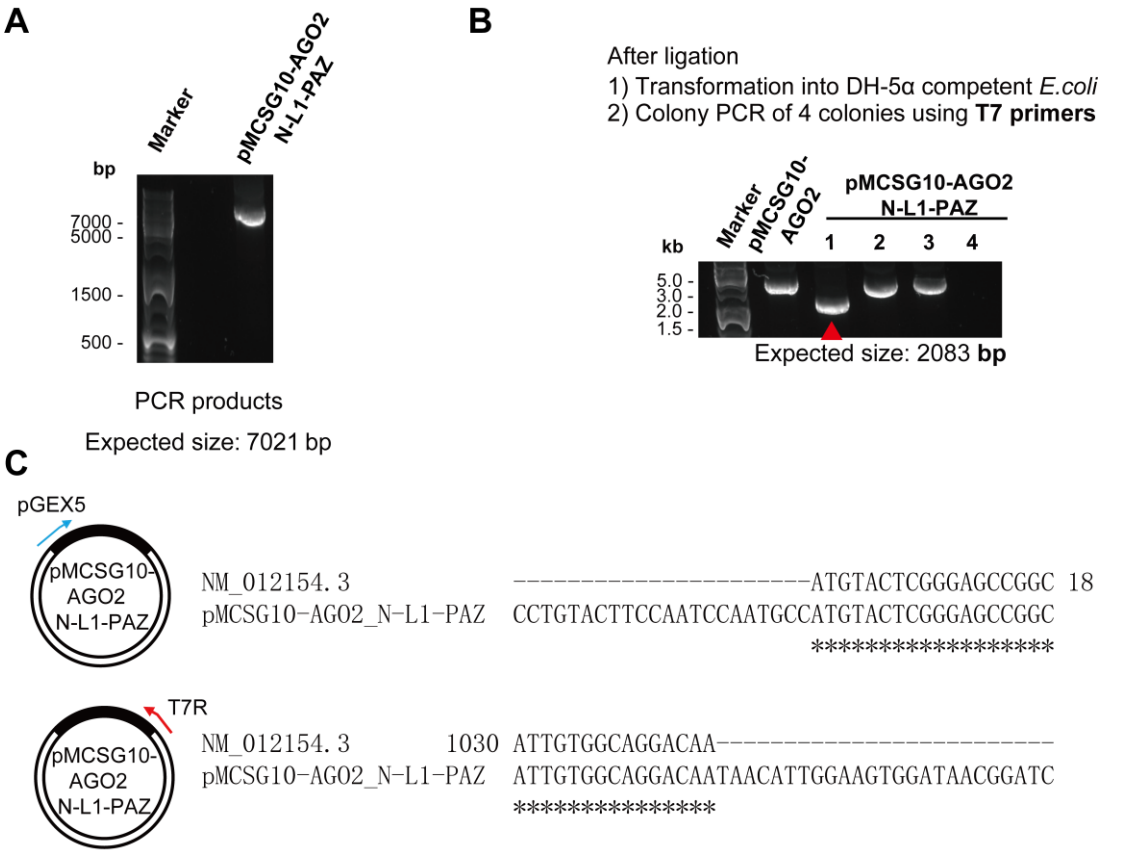

Figure 3.8 Cloning of bacterial expression plasmid for pMCSG10-AGO2 N-L1-PAZ truncation mutant from pMCSG10-AGO2 by Q5® site-directed mutagenesis
A) Agarose gel electrophoresis for visualising the PCR product of the required DNA sequence of pMCSG10-AGO2 N-L1-PAZ, amplified using pMCSG10-AGO2 as a template and a pair of primers flanking the region L2-MID-PIWI. ***B)*** The colony PCR of 4 colonies was performed to indicate the successful cloning using T7 primers. The PCR product of pETFPP_2 VO was used as a reference for the expected size of the backbone band. PCR band chosen for sequencing was highlighted by the red arrowhead. ***C)*** pGEX5 forward primer or T7 reverse primer was used for sequencing. The alignment of the Sanger sequencing read to the database AGO2 CDS (NM_012154.3) performed by MUSCLE. Only partial of codons downstream of the CDS start or upstream of L2 domain were displayed.

To check the expression of the GST-AGO2 constructs generated above, plasmids were transformed in *E.coli,* and the expression of the recombinant proteins was induced by IPTG. The recombinant proteins were purified using the glutathione resin from the bacterial cell lysates and adjusted to the similar concentration of protein purified on the resin. The result showed the desired GST-AGO2 N-L1-PAZ-L2 and N-L1-PAZ were

successfully expressed and confirmed by Western blot, and the similar concentration of the indicated recombinant proteins was purified on the glutathione resin (**Figure 3.9**).

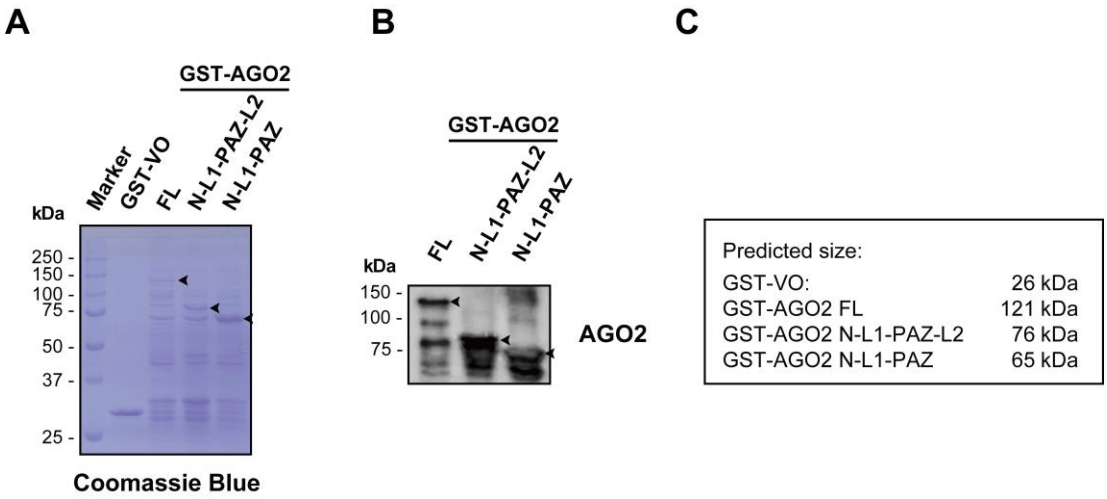

Figure 3.9 Verification of GST-tagged AGO2 full length (FL) and truncation mutants expression
pMCSG10-VO and pMCSG10-AGO2 truncation mutants were transformed and induced by IPTG to overexpress the recombinant GST-tagged proteins. The Glutathione agarose resin was used for purification, analysed by ***A*)** Coomassie staining and ***B*)** Western blot. ***C*)** The predicted molecular weight of GST-AGO2 FL and its C-terminal truncation mutants.

3.1.3 Optimisation of the conditions and reagents for *in vitro* direct binding assays

The pull-down assay, which is an *in vitro* direct binding assay to confirm the existence physical interaction between two proteins, was employed to determine the minimal binding domains within both AGO2 and LIMD1. GST-VO and MBP-VO were used as the negative controls for the pull-down assay to examine whether there was any non-specific binding between GST-VO and MBP-VO. The pilot pull-down assay showed a non-specific interaction between GST-VO and MBP-VO by incubating both proteins either on the MBP magnetic resin or the glutathione resin (**Figure 3.10A and Figure 3.10B**). However, MBP-VO could not be immobilised on the glutathione resin (**Figure 3.10C**). Therefore, these results indicated that the non-specific interaction was between GST-VO and MBP-VO rather than the affinity between MBP-VO with the glutathione resin.

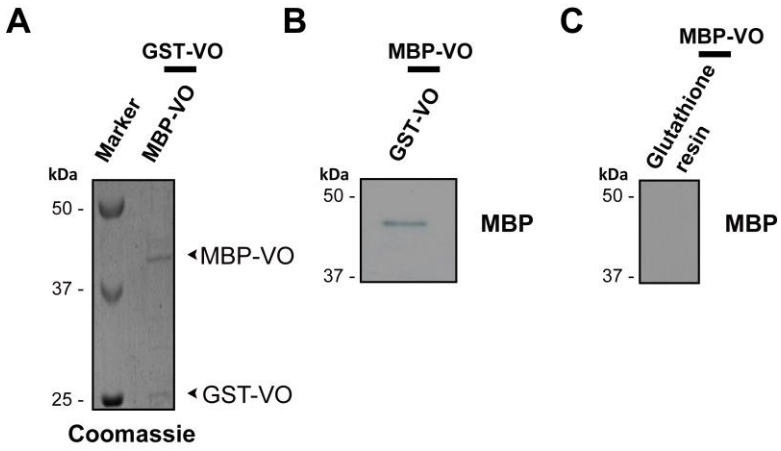

Figure 3.10 A pilot pull-down assay to examine the non-specific binding between negative controls
***A*)** MBP-VO was immobilised on the MBP magnetic resin and incubated with GST-VO, detected by Coomassie staining. Two highlighted bands represent for MBP-VO (42.5 kDa) and GST-VO (26 kDa) respectively. ***B*)** GST-VO was immobilised on the glutathione resin and incubated with MBP-VO, detected by Western blot. ***C*)** MBP-VO was incubated with glutathione resin to confirm that there was no interaction between MBP and the glutathione resin, detected by Western blot.

To reduce/remove this non-specific binding between GST-VO and MBP-VO, further optimisations of pull-down were carried out. Initially, the effect of different incubation times (1, 2, 4h, and O/N) were investigated. Through optimisations of time, the result showed 1, 2, and 4h incubations were optimal for reducing the non-specific binding (**Figure 3.11A**). To allow sufficient time for detecting the specific binding, 4h was used throughout this project. Given that the protein-protein interaction can be affected by the buffer conditions (salt concentration and/or the type of detergent), three different conditions of the incubation buffers were optimised (conditions described in **Chapter 2.1.6.3**). The optimisation showed Buffer A was optimal for reducing the specific interaction between AGO2 and LIMD1 140-166 (**Figure 3.11B**). Taken together, 4h incubation and Buffer A were optimal for GST pull-down in this project.

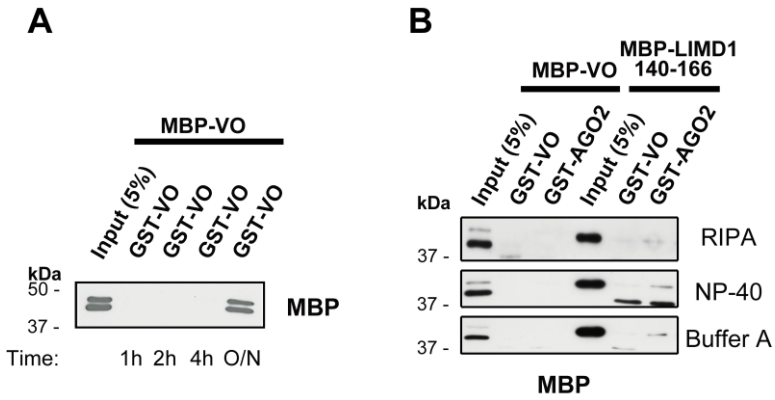

Figure 3.11 Optimisation of conditions for reducing the non-specific binding in GST pull-down assay ***A*****)** GST-VO was incubated with immobilised GST-VO on the glutathione resin with different incubation time periods: 1h, 2h, 4h, and O/N. The sample was assayed by Western blot. O/N: overnight. ***B*****)** Western blot analysis for the GST pull-down in different binding/washing buffers. GST-tagged proteins were purified on the glutathione resin and incubated with the pre-purified and eluted MBP-VO or MBP-LIMD1 140-166 respectively.

3.2 Investigation of the direct interaction between AGO2 and LIMD1

3.2.1 LIMD1 binds to AGO2 *via* LIMD1 140-166

The deletion of LIMD1 140-166 caused the loss of binding with AGO2 according to the co-IP results (**Figure 3.1**). Because co-IP from cell extracts does not necessarily indicate a direct interaction, an *in vitro* direct binding assay (GST pull-down) was employed to investigate the direct interaction. Bacterial proteins GST-VO and GST-AGO2 were purified on the glutathione resin. It was adjusted that the concentration of GST-VO, as an experimental control for non-specific binding, no less than that of GST-AGO2 (**Figure 3.12A**). GST-AGO2 FL is highlighted, and the smaller bands were degradation products, as confirmed by Western blot (**Figure 3.12B**). The eluted MBP-VO and MBP-LIMD1 140-166 were then incubated using the optimal conditions, which are 4h incubation and buffer A as binding/washing buffer. The result indicated GST-AGO2 directly bound to

MBP-LIMD1 140-166, suggesting a.a 140-166 within LIMD1 was sufficient for AGO2 binding.

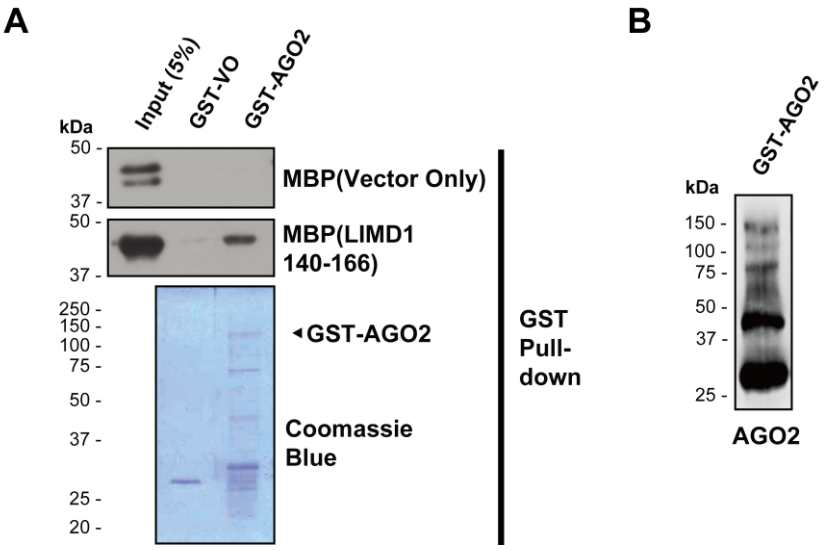

Figure 3.12 LIMD1 binds AGO2 *via* a.a 140-166
***A*)** GST-VO and GST-AGO2 were purified on the resin and incubated with MBP-VO and MBP-LIMD1 140-166 respectively, analysed by Western blot. The purified GST-VO and GST-AGO2 were analysed by Coomassie staining to visualise the concentration of GST-tagged protein for pull-down. ***B*)** The purified GST-AGO2 was analysed by Western blot to confirm the smaller size of bands as the degradation products of GST-AGO2.

GST-AGO2 purified from *E.coli* underwent extensive degradation. The research group of Ian J.MacRae kindly provided the purified untagged crystallography grade human AGO2 (hAGO2), which has been used for the study of the crystal structure of hAGO2 [109]. hAGO2 [250] purified from *Spodoptera Frugiperda* cell sf-9 was stabilised, showing there were not any degradation products even large amount of protein was loaded (**Figure 3.13**). To rule out the possibility that the impurities in the homemade AGO2 in *E.coli* affected the interaction with LIMD1, hAGO2 was then used in the MBP pull-down. MBP-VO, MBP-LIMD1 and MBP-LIMD1 140-166 were expressed in *E.coli* and purified on the MBP magnetic resin. hAGO2 was then added for the incubation, analysed by Western blot. The purified MBP-tagged proteins were visualised by Coomassie staining to confirm the concentration of protein for the pull-down assay (**Figure 3.13**). The result of MBP

pull-down matched the previous co-IP data from our group that there was an interaction between AGO2 and LIMD1 [1]. By using different tags for direct binding assay, the robust result showed that 140-166 is a specific interaction domain for AGO2 binding (**Figure 3.12 and Figure 3.14**).

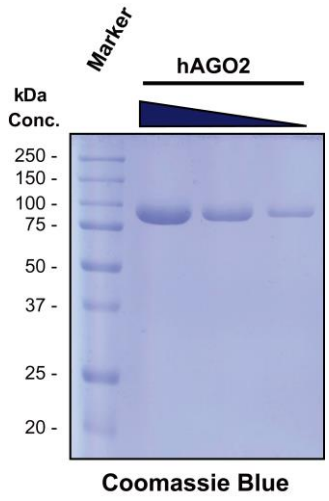

Figure 3.13 A serial dilution of the crystallography grade hAGO2
Purified untagged crystallography grade hAGO2 kindly provided from Dr Ian J.MacRae's research group [250], showss no degradation products compared to that in **Figure 3.12A**. 18ug, 9ug, and 4.5ug hAGO2 were analysed by Coomassie staining.

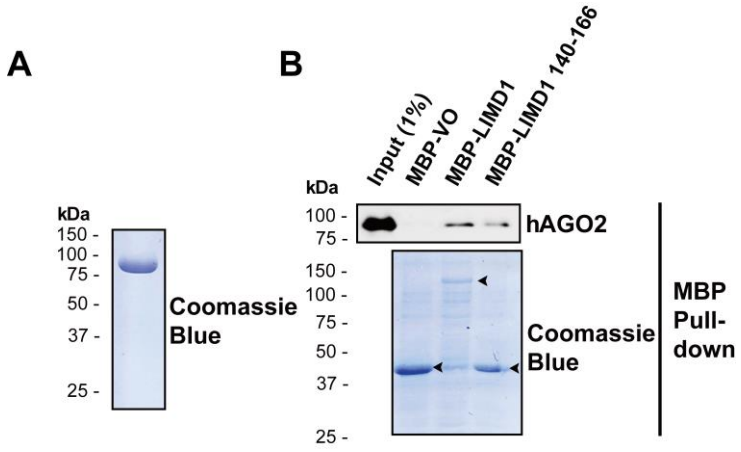

Figure 3.14 MBP pull-down with MBP-VO, MBP-LIMD1, or MBP-LIMD1 140-166
***A*)** The purified untagged crystallography grade hAGO2 was used for MBP pull-down. ***B*)** MBP-VO, MBP-LIMD1, and MBP-LIMD1 140-166 were purified on the MBP magnetic resin and incubated with hAGO2, analysed by Western blot (highlighted by **black** arrowheads).

3.2.2 LIMD1 binds to the L2 domain of AGO2.

To map the precise interaction interface on AGO2 with LIMD1, the sequential truncation mutants from either N- or C-terminus was fused to GST and expressed in *E.coli* highlighted by black arrowheads in **Figure 3.15A**. The truncation mutations made within AGO2 systematically removed one domain at a time. Thus, these could be used to identify the domain required for the binding to LIMD1 140-166. The expression and the concentration of GST-VO and GST-AGO2 truncation mutants purified on the glutathione resin were analysed by Coomassie staining. The concentration of protein was adjusted to the similar level (**Figure 3.15A**). The GST pull-down showed that GST-AGO2 FL and all AGO2 truncation mutants with the L2 domain binding to MBP-LIMD1 140-166 (**Figure 3.15A**). Either N- or C-terminal truncation mutants without the L2 domain abolished the interaction with LIMD1 (**Figure 3.15B**). The result indicated that L2 domain was necessary for the direct interaction between GST-AGO2 and MBP-LIMD1 140-166 (**Figure 3.15**). As a result, the L2 domain of AGO2 was revealed to be responsible for the direct interaction with LIMD1.

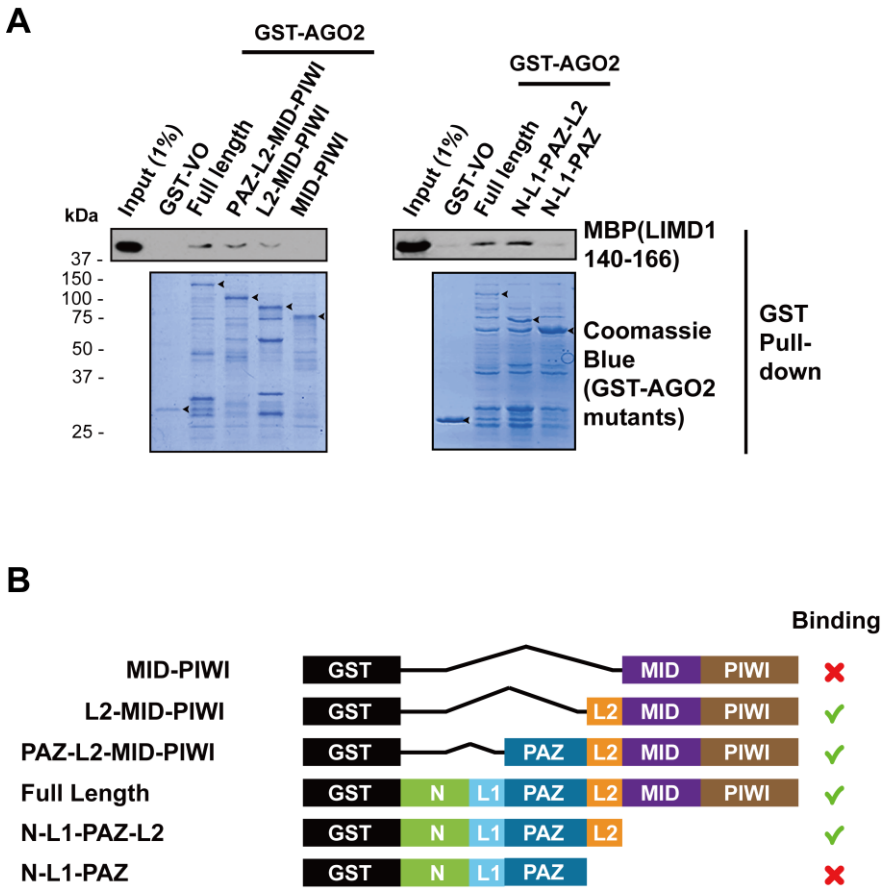

Figure 3.15 LIMD1 binds to the L2 domain of AGO2
A) GST-VO and GST-AGO2 truncation mutants were purified on the resin and incubated with MBP-VO and MBP-LIMD1 140-166 respectively, analysed by Western blot. The purified GST-VO and GST-AGO2 truncation mutants were analysed by Coomassie staining to visualise the concentration of the purified GST-tagged protein for pull-down. ***B)*** Schematic of GST-AGO2 truncation mutants and a summary of binding to LIMD1 140-166.

3.3 Phosphorylation status of S387 within the L2 domain affects the direct interaction with LIMD1

It has been proposed that Akt3-dependent phosphorylation of S387 within the L2 domain of AGO2 diverts its activity from mRNA cleavage to (or toward) miRNA-mediated silencing [127]. Therefore, it raised the question as to whether the phosphorylation of S387 within the L2 domain would trigger the association between AGO2 and LIMD1.

According to the chemical structure of amino acids (**Figure 11.2**), the constructs expressing phospho-deficient (unphosphorylatable alanine mutant AGO2 S387A) or phospho-mimic (AGO2 S387E) of EYFP-AGO2 FL version were generated by Dr Sybil C.K. Wong. The point mutation of S387 represents the ability to be phosphorylated, which inferred the phosphorylation status of S387.

3.3.1 Construction of expression plasmids for GST-AGO2 L2 domain only

It has shown that the loss of L2 domain abrogated the interaction between AGO2 and LIMD1 (**Figure 3.15**). To corroborate this mapping result, the construct expressing GST-AGO2 L2 domain was generated using LIC. In addition, to investigate how the phosphorylating ability on S387 within L2 domain would affect the interaction with LIMD1, the construct expressing GST-AGO2 L2 S387E was also generated using site-directed mutagenesis. The colony PCR results showed the colony #1 and #3 containing potential correct L2 domain inserts, and the sequencing results confirmed the cDNA sequences matched to the database and all inserts were in frame with GST sequences (**Figure 3.16A and Figure 3.16B**). The construct expressing GST-AGO2 L2 was then used a template to generate S387E mutant of GST-AGO2 L2 version. The sequencing results of the colony #3, which has a potential correct L2 S387E insert, showed serine was substituted by glutamic acid (**Figure 3.16C and Figure 3.16D**).

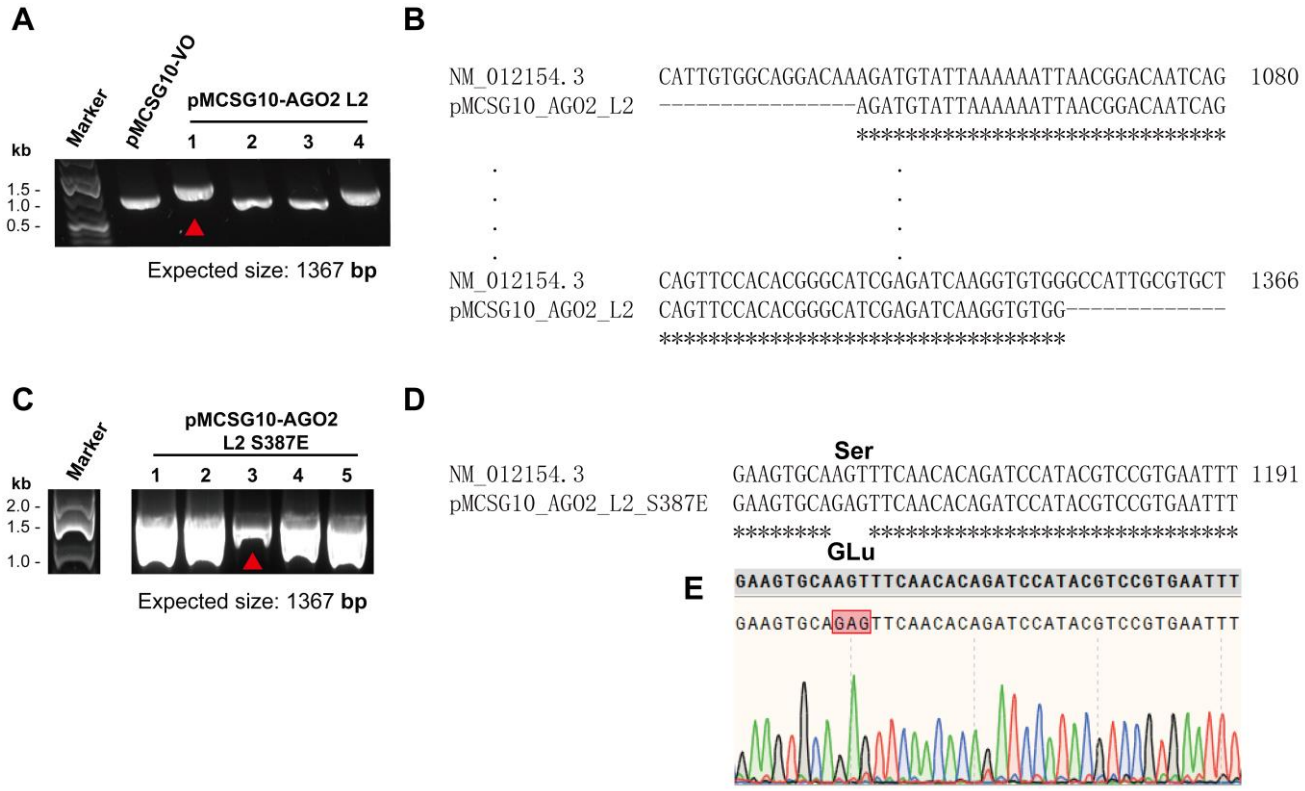

Figure 3.16 Cloning of bacterial expression plasmids for pMCSG10-AGO2 L2 and L2 S387E

A) Colony PCR of 4 colonies was performed to indicate the successful cloning using the T7 primer. PCR band chosen for sequencing was highlighted by the red arrowhead. ***B)*** The alignment of the Sanger sequencing read to the database AGO2 CDS (NM_012154.3) performed by MUSCLE. Only partial of codons downstream or upstream of the CDS start or stop were displayed. ***C)*** Colony PCR of 5 colonies was performed to indicate the successful cloning using the T7 primer. PCR band chosen for sequencing was highlighted by the red arrowhead. ***D)*** The alignment of the Sanger sequencing read to the database AGO2 CDS (NM_012154.3) performed by MUSCLE. Only partial of codons of the CDS within L2 domain were displayed. ***E)*** The chromatograms showed distinct peaks for each nucleotide in the corresponding region, indicating the required point mutation.

To examine the expression of GST-AGO2 L2 and GST-AGO2 L2 S387E, both plasmids, as well as GST-VO, were transformed in *E.coli,* and the protein expression was induced by IPTG. The recombinant proteins were purified by the glutathione resin and analysed by Coomassie staining (**Figure 3.17A**). The predicted size of GST-AGO2 L2 and L2 S387E are 37kDa (highlighted in **Figure 3.17A**). However, there were additional larger bands (band 2 and 6 in **Figure 3.17A**), indicating impurities were co-purified. The mass spectrometric analysis was performed upon the purified GST-Ago2 L2/L2 S387E, which confirmed that the majority of lower bands (band 4, 5, 8 and 9) were GST-AGO2 degradation products. This analysis also identified that the purified samples contained the bacterial version of chaperone protein Hsp70 (DnaK). As the heat shock proteins were demonstrated to chaperone AGOs and facilitate the loading of small RNA duplexes [251], DnaK may function in the same mechanism to associate with and be co-purified with the recombinant AGO2 proteins.

A

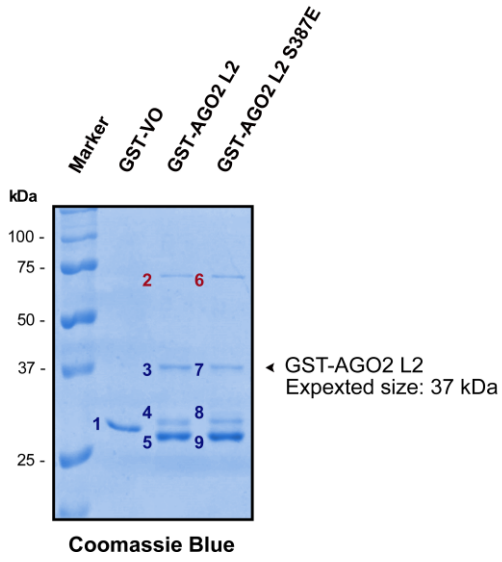

B

Band	Protein ID	#peptides	Score	Peptide sequences
1	GST	6	563	LTQSMAIIRAEISMLE GAVLDIRLLLEYLEEK YEEHLYERYIAWPLQ GWQATFGGGDHPPK KFELGLEFPNLPYYID GDVK
2	*E.Coli* Chaperone protein DnaK	5	626	TAEDYLGEPVTEAVIT VPAYFNDAQRAKLES LVEDLVNRVALQDAG LSVSDIDDVILVGGQT RHSQVFSTARDNQSA VTIHVLQGERSLGQFN LDGINPAPR
3	GST	4	427	AEISMLEGAVLDIRLLL EYLEEKYEEHLYERYI AWPLQGWQATFGGG DHPPK
	AGO2	3	289	SASFNTDPYVRVLQPF SILYGGRAIATPVQGV WDMR
4	GST	6	624	YEEHLYERAEISMLEG AVLDIRLLLEYLEEKYE EHLYERYIAWPLQGW QATFGGGDHPPKKFE LGLEFPNLPYYIDGDV K
5	GST	6	565	LTQSMAIIRAEISMLEG AVLDIRLLLEYLEEKYE EHLYERYIAWPLQGW QATFGGGDHPPKKFE LGLEFPNLPYYIDGDV K
6	*E.Coli* Chaperone protein DnaK	9	928	TAEDYLGEPVTEAVIT VPAYFNDAQRLINYLV EEFKKAKLESLVEDLV NRVALQDAGLSVSDID DVILVGGQTRHSQVFS TAEDNQSAVTIHVLQG ERSLGQFNLDGINPAP RKFEELVQTRNQGDH LLHSTR
7	GST	5	477	YEEHLYERAEISMLEG AVLDIRLLLEYLEEKYE EHLYERYIAWPLQGW QATFGGGDHPPK
	AGO2	2	180	VLQPPSILYGGRAIATF VQGVWDMR
8	GST	6	543	LTQSMAIIRAEISMLEG AVLDIRLLLEYLEEKYE EHLYERYIAWPLQGW QATFGGGDHPPKKFE LGLEFPNLPYYIDGDV K
9	GST	5	579	AEISMLEGAVLDIRLLL EYLEEKYEEHLYERYI AWPLQGWQATFGGG DHPPKKFELGLEFPNL PYYIDGDVK

Figure 3.17 Verification of the expression of GST-AGO2 L2 and GST-AGO2 L2 S387E
***A*)** GST-AGO2 L2 and L2 S387E were purified on the glutathione resin and analysed by Western blot. The expected size of GST-AGO2 L2/ L2 S387) is 37kDa (highlighted by the arrowhead). Degradation products of GST-AGO2 L2/ L2 S387E were identified by ***B*)** Mass spectrometry analysis. The Mass spectrometry analysis was performed by the group of Dr Michael Plevin.

3.3.2 DnaK does not affect the interaction between LIMD1 and AGO2

As shown in **Figure 3.17**, DnaK was co-purified from the lysates made from *E.coli*. There were 70kDa bands shown by Coomassie staining (**Figure 3.15**) across all GST-AGO2 truncation mutants, resulting in the impurities in GST-AGO2 purified samples. In addition, the heat shock proteins have been shown to associate with AGO2 for loading small RNA onto AGO2 [251, 252]. Therefore, it raised a question whether the LIMD1-AGO2 interaction would be indirect (bridged by DnaK). To prove this is not a case, Western blot was performed to analyse the samples of GST pull-down. The result demonstrated that DnaK levels were equal across the samples, including the AGO2 truncation mutants that did and did not interact with LIMD1 (**Figure 3.18**). This result indicated that the presence of DnaK was thus not conferring any interaction between AGO2 and LIMD1.

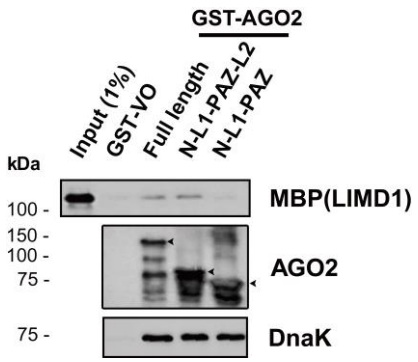

Figure 3.18 DnaK identified as present in purified GST-AGO2 truncation mutants does not affect binding to LIMD1

The purified GST-AGO2 C-terminal truncation mutants were blot with the indicated antibodies. DnaK levels were equal across samples, and the DnaK present did not affect the interaction between AGO2 and LIMD1.

3.3.3 The interaction of AGO2 and LIMD1 depends on the phosphorylating ability of S387 within the L2 domain.

The phosphorylation of S387 within AGO2 increased the association with TNRC6A to promote its miRNA silencing, but the mechanism of this association remained unknown [127]. As S387 is located within the L2 domain of AGO2, which is required for LIMD1 interaction (**Figure 3.15**), it was examined whether the phosphorylation of S387 could affect the interaction with LIMD1. To address this, EYFP-AGO2,-AGO2-S387A, or -AGO2-S387E was co-expressed with Xpr-LIMD1 respectively in HEK293T cells, and co-IPs were performed to investigate their interacting ability with LIMD1. AGO2 S387A reduced the interaction with LIMD1 by 74%, whereas the phospho-mimic version of AGO2 (AGO2 S387E) rescued/enhanced the interaction with LIMD1 (**Figure 3.19**).

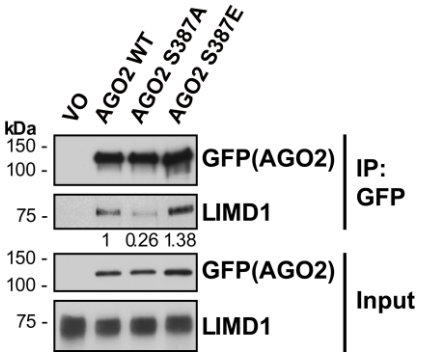

Figure 3.19 Interaction between LIMD1 and AGO2 is dependent on S387 phosphorylation
Co-IP of Xpr-LIMD1 with EYFP-AGO2 WT, -AGO2 S387A (phospho-deficient), and -AGO2 S387E (phospho-mimic) point mutants from HEK293T lysate. Quantification of LIMD1 binding relative to co-IP with EYFP-AGO2 was shown in numbers. This experiment was performed by Dr Katherine S. Bridge.

The importance of S387 phosphorylation for LIMD1 binding was further confirmed by the GST pull-down. GST-AGO2 WT and -AGO2 S387E were overexpressed in *E.coli* and purified on the glutathione resin. MBP-LIMD1 140-166, which was previously identified as a minimal interaction interface for AGO2 (**Figure 3.11**), was then added. The result revealed an enhanced interaction by 3-fold between the AGO2 S387E (phospho-mimic)

and LIMD1 140-166 (**Figure 3.20**). This result corroborated the co-IP result (**Figure 3.19**) that the phospho-mimic version of AGO2 (S387E) enhanced the interaction with LIMD1.

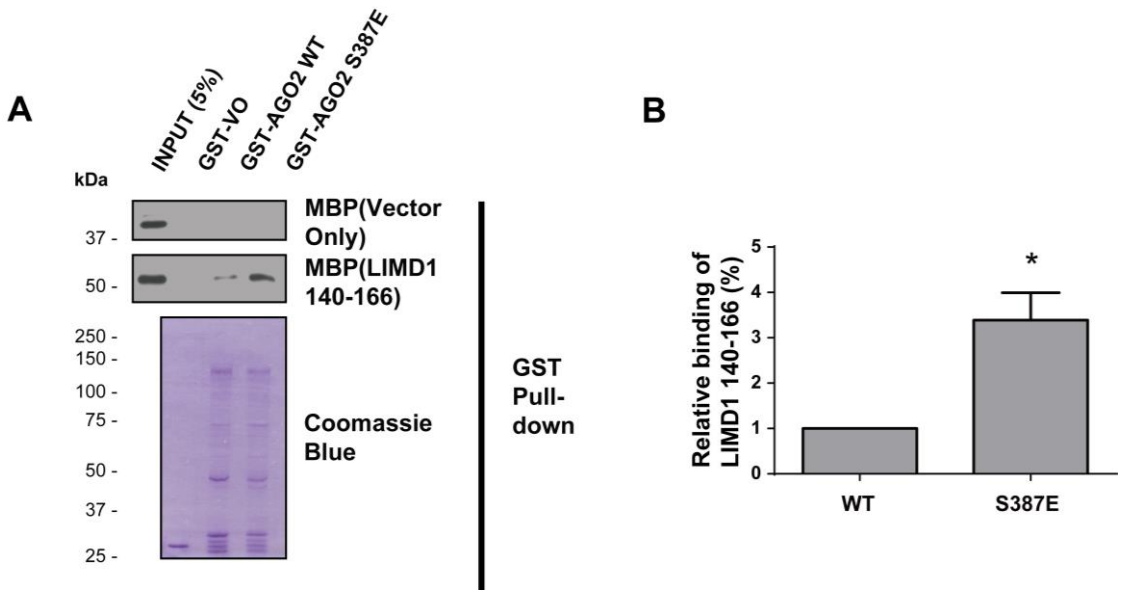

Figure 3.20 Phospho-mimic mutation of S387 enhances the interaction with MBP-LIMD1 140-166
***A*)** GST-VO, -AGO2 and -AGO2 S387E point mutants were purified on the resin and incubated with MBP-VO and MBP-LIMD1 140-166 respectively, analysed by Western blot. The purified GST-VO, -AGO2 WT and -AGO2 S387E point mutants were analysed by Coomassie staining. ***B*)** Quantification of LIMD1 binding relative to AGO2 WT. Data shown are mean ±SEM, n=3, * $p<0.05$.

It has been revealed that the L2 domain of AGO2 was the binding domain for LIMD1 (**Figure 3.15**) and the phosphorylation of S387 within the L2 domain increases the interaction with LIMD1 (**Figure 3.20**). To further confirm these findings, the recombinant protein AGO2 L2 domain only and the S387E point mutant were generated and performed for the GST pull-down with MBP-LIMD1 FL and MBP-LIMD1 140-166 (**Figure 3.21**). The result confirmed that L2 domain was responsible for the interaction with LIMD1, and the phospho-mimic mutation, S387E, enhanced the interaction.

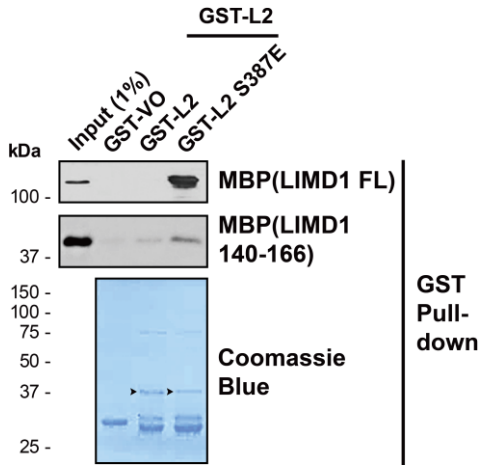

Figure 3.21 S387 phosphorylation within the L2 domain only mutants enhances the interaction with MBP-LIMD1 140-166

GST-VO, -AGO2 L2 and -AGO2 L2 S387E point mutant were purified on the resin and incubated with MBP-VO and MBP-LIMD1 140-166 respectively, analysed by Western blot. The purified GST-VO, -AGO2 L2 and -AGO2 L2 S387E point mutants were analysed by Coomassie staining to visualize the concentration of GST-tagged protein for pull-down. The expected size of GST-AGO2 L2 is 37kDa, which is highlighted by **black** arrowheads.

The phospho-mimic version of AGO2 (S387E) enhanced the interacting ability with LIMD1 (**Figure 3.20** and **Figure 3.21**). In addition, as S387 was reported to be phosphorylated by Akt3 and was Akt3-signalling dependent [127], HA-Akt3 was co-expressed with EYFP-AGO2 in HEK293T cells to facilitate Akt3-driven phosphorylation at S387 residue on EYFP-AGO2 WT. The pull-down assays were then performed to examine whether MBP-LIMD1 140-166 could interact with Akt3-driven phosphorylated AGO2. The optimisation of the binding buffer showed NP-40 was the optimal buffer for detecting the interaction between the phosphorylated EYFP-AGO2 and MBP-LIMD1 140-166 (**Figure 3.22**).

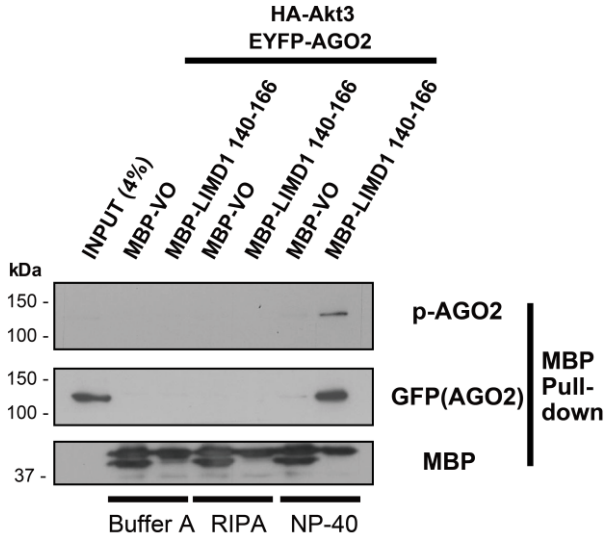

Figure 3.22 Optimisation of binding/washing buffers for MBP pull-down
MBP-VO and MBP-LIMD1 140-166 were purified on the MBP resin and incubated with HEK293T cell lysates, which were co-transfected with HA-Akt3 and EYFP-AGO2. Buffer A, RIPA, and NP-40 were used to optimise the binding and washing buffer. The samples were analysed by Western blot.

To examine the binding ability of Akt3-driven phosphorylation at S387, three pairs of constructs (HA-VO/EYFP-AGO2, HA-Akt3/EYFP-AGO2, and HA-VO/ EYFP-AGO2 S387E) were co-expressed in HEK293T cells. Without over-expressing Akt3, the endogenous Akt3 was not sufficient to phosphorylate EYFP-AGO2, resulting in S387 on EYFP-AGO2 remaining hypo-phosphorylated (**Figure 3.23A**). Therefore there was no interaction between EYFP-AGO2 and MBP-LIMD1 140-166 observed. Not surprisingly, once S387 was phosphorylated by over-expressed HA-Akt3, EYFP-AGO2 interacted with MBP-LIMD1 140-166 (**Figure 3.23B**). Over-expressing the phospho-mimic version of EYFP-AGO2 (S387E) also facilitated the interaction between AGO2 and LIMD1 140-166 (**Figure 3.23C**). These results indicated S387 phosphorylation was of importance to regulate the AGO2-LIMD1 interaction. Intriguingly, there was no interaction between EYFP-AGO2 and MBP-LIMD1 110-166 (**Figure 3.23**).

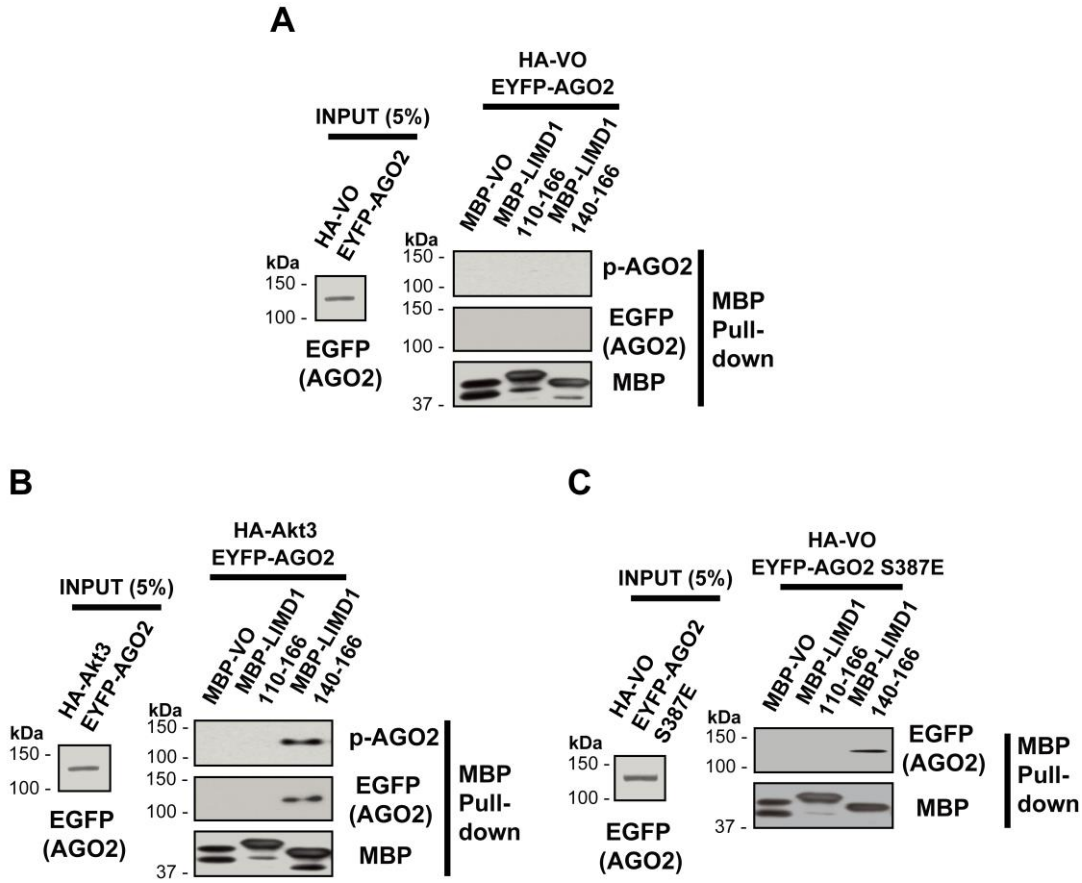

Figure 3.23 MBP pull-down assay for Akt3-driven phosphorylation of EYFP-AGO2
***A*)** MBP-VO and MBP-LIMD1 140-166 were purified on the MBP resin and incubated with HEK293T cell lysates, which were co-transfected with HA-VO and EYFP-AGO2. ***B*)** MBP-VO and MBP-LIMD1 140-166 were purified on the MBP resin and incubated with HEK293T cell lysates, which were co-transfected with HA-Akt3 and EYFP-AGO2. ***C*)** MBP-VO and MBP-LIMD1 140-166 were purified on the MBP resin and incubated with HEK293T cell lysates, which were co-transfected with HA-VO and EYFP-AGO2 S387E.

3.4 Summary

Within the pre-LIM region of LIMD1, loss of a.a 140-166 completely abrogated the association with AGO2 (**Figure 3.1**). The further investigation identified and corroborated that a.a 140-166 was an essential domain and was sufficient for the direct interaction with AGO2 (**Figure 3.12**). Within AGO2, loss of L2 domain abolished the direct interaction with LIMD1 a.a 140-166 (**Figure 3.15**). This observation was

corroborated by the result of *in vitro* direct binding assay that L2 domain was sufficient for interaction with LIMD1 (**Figure 3.21**). Although DnaK was identified to be co-purified with GST-AGO2, it did not contribute to the direct binding of AGO2 to LIMD1 (**Figure 3.18**). The direct interaction between AGO2 and LIMD1 depended on the phosphorylating ability of S387 within the L2 domain of AGO2 (**Figure 3.20** and **Figure 3.21**). Akt3-mediated phosphorylation on S387 of AGO2 enhanced the interaction with LIMD1 (**Figure 3.23**). These results demonstrated that the phosphorylation at S387 regulated the direct interaction with LIMD1 *via* the L2 domain and a.a 140-166 on both proteins, providing a novel aspect that LIMD1-involved miRNA-mediated silencing was signalling pathway dependent.

Chapter 4 Results

Investigation of the co-localisation between AGOs and LAW

4 Investigation of the co-localisation between AGOs and LAW

The human AGOs (AGO1-4) are evolutionally conserved, and AGOs have been demonstrated as large redundant with regards to miRNA loading and target recognition [108]. Therefore, the AGO2-LIMD1 interaction might anticipate all four human AGOs could bind to LIMD1. To address this hypothesis, GST-AGO1, -AGO3, and -AGO4 were respectively immobilised and incubated with MBP-LIMD1 140-166 (**Figure 4.1**). The result showed that MBP-LIMD1 140-166 had the direct interaction with all four AGOs (**Figure 4.1A**), whose expressions were confirmed by Western blot using the specific antibodies (**Figure 4.1B**). This implied that all four human AGOs had the direct interaction with LIMD1.

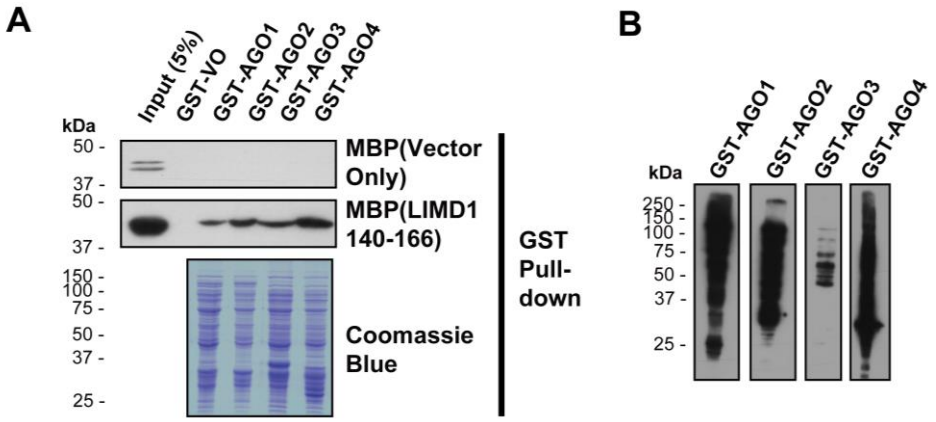

Figure 4.1 LIMD1 binds four AGOs through LIMD1 140-166
***A*)** GST-VO and GST-AGOs were performed GST pull-down with MBP-VO and MBP-LIMD1 140-166 respectively, analysed by Western blot. The purified GST-VO and GST-AGOs proteins were analysed by Coomassie staining and **(*B*)** Western blot.

The alignment analysis of the L2 domain within human AGOs showed the existence of a significant structural homology (84.6% identity) (**Figure 4.2**). In addition, L2 domain of AGO2 has been revealed to be responsible for the interaction with LIMD1 (**Chapter 3.2.2**). Therefore, it required investigating whether the L2 domain of other AGOs contributes to LIMD1 binding. To address this question, GST-AGO1 N-terminal

truncation mutants were made and performed for GST pull-down. As with AGO2, all truncation mutants, except the mutants without L2 domain had the direct interactions with LIMD1 (**Figure 4.3**). This indicated that the L2 domain on AGO1 was a critical domain for the interaction with LIMD1. The investigation was only performed on AGO1, but it was inferred that L2 domain within the other AGO proteins (AGO3 and AGO4) could also be essential for LIMD1 interaction. It will be demonstrated in **Chapter 4.1.2** that how the phosphorylating ability of the conserved S387 residue within L2 domain affects the association of AGO proteins with LIMD1.

```
AGO1_L2   349  RCIKKLTDNQTSTMIKATARSAPDRQEEISRLMKNASYNL--DPYIQEFGIKVKDDMTEV  405
AGO2_L2   351  RCIKKLTDNQTSTMIRATARSAPDRQEEISKLMRSASFNT--DPYVREFGIMVKDEMTDV  408
AGO3_L2   352  RCIKKLTDNQTSTMIKATARSAPDRQEEISRLVRSANYET--DPFVQEFQFKVRDEMAHV  409
AGO4_L2   341  RCIKKLTDNQTSTMIKATARSAPDRQEEISRLVKSNSMVGGPDPYLKEFGIVVHNEMTEL  400
               ***************.***************.*:.. .      **::.** : *.::*: :

AGO1_L2   406  TGRVLPAPILQYGGRNRAIATPNQGVWDMRGKQFYNGIEIK  447
AGO2_L2   409  TGRVLQPPSILYGGRNKAIATPVQGVWDMRNKQFHTGIEIK  449
AGO3_L2   410  TGRVLPAPMLQYGGRNRTVATPSHGVWDMRGKQFHTGVEIK  449
AGO4_L2   401  TGRVLPAPMLQYGGRNKTVATPNQGVWDMRGKQFYAGIEIK  441
               ***** .* : *****.::*** :******.***: *:***
```

Identity = 84.6%

Figure 4.2 Multiple sequence alignment of the L2 domain of human AGOs
The alignment of the protein sequences for the L2 domain of AGO1 (NP_036331.1), AGO2 (NP_036286.2), AGO3 (NP_079128.2) and AGO4 (NP_060099.2) was performed by DNAMAN Windows 6.0 (Lynnon Biosoft) using default parameters, and the identity was also calculated by DNAMAN. The conservation symbols were added manually. *, positions with complete identity; :, positions with strongly conserved residues (PAM250 score > 0.5); ., positions with weakly conserved residues (0 < PAM250 ≤ 0.5). The conserved serines were highlighted in red; the glutamic acid which is 2-a.a downstream of the conserved serine within AGO3 was highlighted in green.

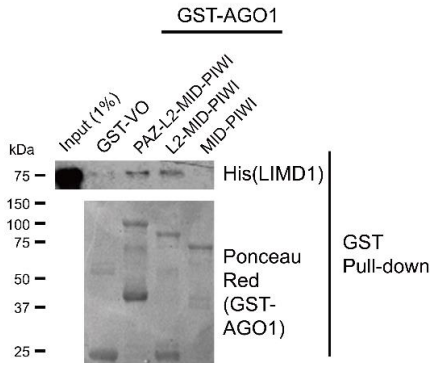

Figure 4.3 AGO1 binds LIMD1 *via* L2 domain
GST-VO and GST-AGO1 N-terminal truncation mutants were purified on the resin and incubated with His-LIMD1 FL, analysed by Coomassie staining. The purified GST-VO and GST-AGO1 N-terminal truncation mutants were analysed by Ponceau staining to visualise the concentration of GST-tagged protein for pull-down. This experiment was performed by Dr Sybil C.K. Wong.

4.1 Investigation of the co-localisation of AGO proteins and LIMD1

Akt3-mediated phosphorylation of AGO2 (S387) within L2 domain promoted a phospho-dependent interaction with LIMD1 (**Chapter 3.3**). The alignment of the L2 domain of all four human AGOs revealed that a conserved serine residue also present in AGO1 (S385) and AGO4 (S377) (Highlighted in Red, **Figure 4.2**). AGO3 lacks this conserved serine residue but instead contains a phospho-mimic glutamic acid residue (E390) (Highlighted in Green, **Figure 4.2**). Therefore, it was hypothesised whether the interaction/association of AGOs with LIMD1 was also phospho-dependent within the L2 domain.

To address the question whether the conserved serine residue was responsible for LIMD1 association, immunofluorescence co-localisation experiments were employed to visualise the subcellular localisation of EGFP-AGO2 (including the version of point mutations on the conserved serine) and mTangerine (mTan)-LIMD1. P-bodies, which are cytoplasmic foci where mRNA storage, decapping or decay can take place [101, 102], contains key components of miRNA silencing pathway: AGOs. The formation of P-bodies is the consequence of the miRNA-mediated silencing [145]. LIMD1 was previously demonstrated to regulate miRNA-mediated silencing and revealed as a P-body component interacting with AGO2 [1]. Therefore, by using fluorescently tagged proteins and the confocal microscope, the degree of co-localisation of AGO2 with LIMD1 could be visualised and calculated.

4.1.1 Optimisation of the reagents and conditions for immunofluorescence assay

To investigate the co-localisation, U2OS cell line was selected as it expresses characteristics of monolayer and larger shape which offer a clear vision of the cell context, especially for the co-localisation. Therefore, U2OS cells were co-transfected with the pair of EYFP-tagged protein and mTan-tagged protein using ViaFect™ Transfection Reagent, which is a cationic delivery reagent in aqueous solution. Given that the amount of DNA, DNA: ViaFect™ ratio, incubation time, and type of cells are

critical aspects for transfection efficiency, the ratio of DNA: ViaFect™ and the amount of DNA were optimised to achieve a successful transfection for the optimal results for co-localisation to be observed. The detail of optimisation was listed in **Table 4.1**.

Table 4.1 Table of the optimisations for DNA amount and the ratio of DNA: ViaFect™

Primary optimisation for the ratio of DNA: ViaFect™				
	Ratio of DNA: ViaFect™			
	1:2		1:3	
DNA amount	750ng		750ng	
Volume of ViaFect™	1.5µl		2.25µl	
Secondary optimisation for the amount of DNA				
	Ratio of DNA: ViaFect™			
	1:3	1:3	1:3	1:3
DNA amount	500ng	750ng	1000ng	1500ng
Volume of ViaFect™	1.5µl	2.25µl	3µl	4.5µl

The primary optimisation was performed in U2OS transfected with the same amount of mTan-LIMD1 (750ng) using different DNA: ViaFect™ ratio (1:2 and 1:3), and the fluorescent signals were visualised to determine the transfection efficiency (**Figure 4.4**). Cells were transfected with mTan-LIMD1 resulting in cells expressing the fluorescent signals under the microscope. Depending on the transfection efficiency, more cells would show red signals if the transfection efficiency was higher. Therefore, the more the number of cells expressing red signals, the higher transfection efficiency is (**Figure 4.4**). The result indicates that the ratio 1:3 of DNA: ViaFect™ provided a higher transfection efficiency when transfected with the same amount of DNA (**Figure 4.4B**).

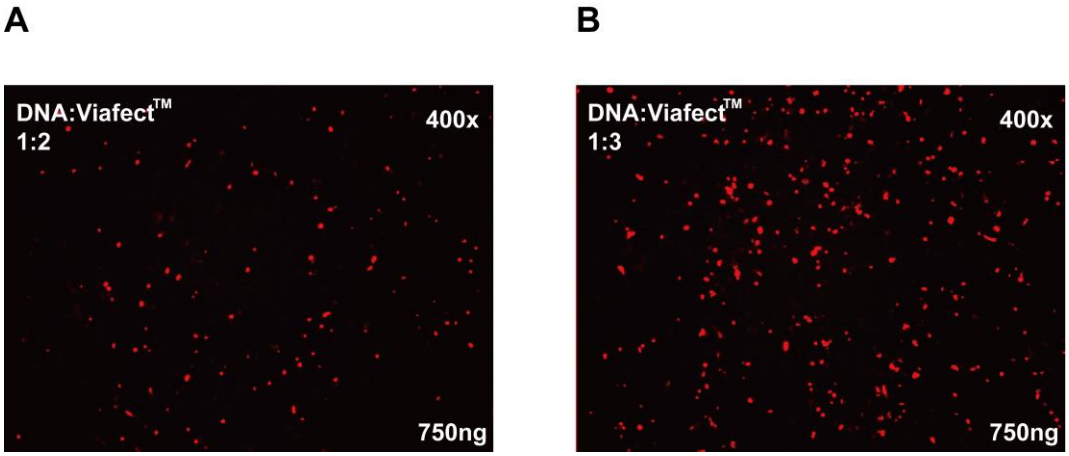

Figure 4.4 The primary optimisation of the ratio of DNA: ViaFect™ using the same amount of DNA
U2OS was transfected with 750ng of mTan-LIMD1 using the ratio **(*A*)** 1:2 or **(*B*)** 1:3of DNA:ViaFect™. The amount of fluorescent signals were used to determine the transfection efficiency. The magnification was **400x.**

Then for the secondary optimisation, the ratio 1:3 was used to optimise the amount of DNA. Four amounts of DNA (500ng, 750ng, 1000ng, and 1500ng) were transfected into the cells respectively. As expected, increasing the amount of DNA transfected correlated to an increase in transfected cells (amount of the red signals), up to 1000ng (**Figure 4.5**). Above this (1500ng), the DNA/transfection reagent complex was toxic to cells, resulting in cells that were fluorescent but not viable (**Figure 4.5C and Figure 4.5D**). Therefore, 1000ng of DNA was considered as an optimal amount of DNA transfected into U2OS with the ratio 1:3 of DNA: ViaFect™ for immunofluorescence assay in this project.

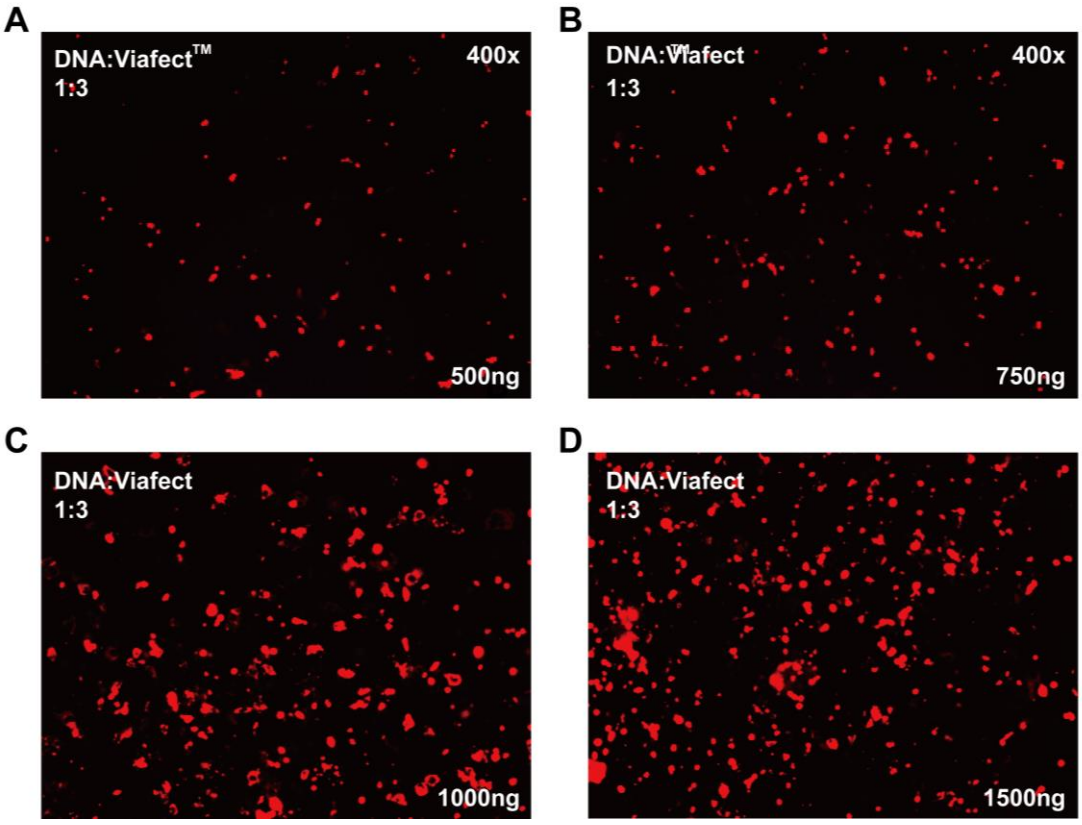

Figure 4.5 The secondary optimisation of the amount of DNA using the same ratio of DNA: ViaFect™
U2OS was transfected with **(*A*)** 500ng mTan-LIMD1, **(*B*)** 750ng mTan-LIMD1, **(*C*)** 1000ng mTan-LIMD1 and **(*D*)** 1500ng mTan-LIMD1, using the same ratio of DNA: ViaFect™. The amount of fluorescent signals were used to determine the transfection efficiency. Although **(*D*)** shows the greatest number of the fluorescent signals, the cells were dying as they started floating. The magnification was **400x.**

4.1.2 Phosphorylation of the conserved serine within L2 domain affects the co-localisation of AGO proteins with LIMD1

To corroborate the direct binding studies between LIMD1 and AGO proteins (**Figure 4.1** and **Figure 4.3**) and the phosphorylation-dependent interaction between AGO2 and LIMD1 (**Chapter 3.3.3**), EYFP-AGO2 and mTan-LIMD1 were over-expressed in U2OS cells with the siRNA-mediated knockdown of Akt3. The result showed a 9-fold reduction in co-localisation between EYFP-AGO2 and mTan-LIMD1 (**Figure 4.6A** and **Figure 4.6B**). The dependency on S387 for LIMD1 association was also examined in U2OS cells transfected

with mTan-LIMD1 and the EYFP-AGO2 constructs expressing the point mutations on S387. Compared to AGO2 WT, AGO2 S387A and S387E showed a 9.4-fold decrease and 2.1-fold increase in co-localisation with LIMD1, respectively. These data indicated that the interaction between AGO2 with LIMD1 was dependent on the phosphorylating ability of AGO2 S387.

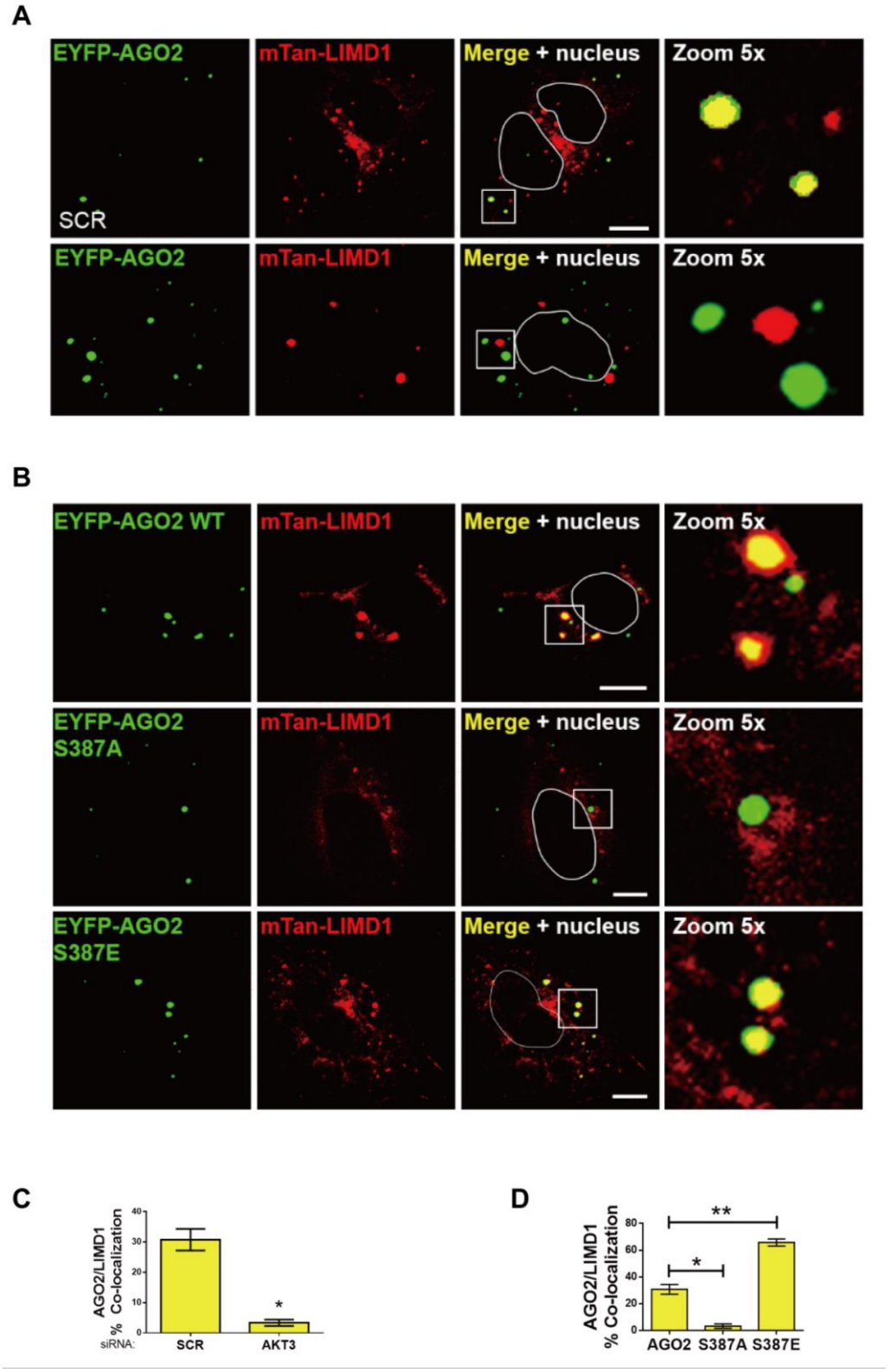

Figure 4.6 The co-localisation of LIMD1 and AGO2 depends on Akt3-mediated phosphorylation
***A*)** Co-expression of EYFP-AGO2 with mTan-LIMD1 in U2OS cells treated with non-targeting (SCR) or Akt3 siRNA. ***B*)** Co-expression of EYFP-AGO2 S387 point mutants with mTan-LIMD1 in U2OS cells. ***C*)** Quantification of number of AGO2 P-bodies co-localised with LIMD1 in (*A*). ***D*)** Quantification of number of AGO2 P-bodies co-localised with LIMD1 in (*C*). Data shown are mean ±SEM, n=3, * p<0.05, ** p<0.001. Nuclear outlines in white. Scale bars are 10µm. This experiment was performed by Dr Katherine S.Bridge.

To investigate whether the interaction between AGO proteins and LIMD1 was dependent on the phosphorylation of the equivalent conserved serine, the point mutants of EYFP-AGO1 (S385A and S385E) and -AGO4 (S377A and S377E) were generated. However, AGO3 does not have an equivalent serine but contains a glutamic acid residue two amino acids downstream (**Figure 4.2**). Therefore, E390 residue was substituted by alanine as a phospho-deficient mutant (E390A) to evaluate whether E390 was responsible for the association with LIMD1. The results demonstrated that with the treatment of Akt3 siRNA, there was a trend of disassociation of AGO1 and LIMD1 (**Figure 4.7A** and **Figure 4.7B**). These data implied that Akt3-mediated phosphorylation contributed to AGO1-LIMD1 association. For the point mutants of AGOs, as with AGO2 that the phospho-deficient mutants of AGO1 and AGO4 significantly decreased the association with LIMD1, whereas the phospho-mimic mutants of AGO1 and AGO4 enhanced the co-localisation with LIMD1 (**Figure 4.7C, Figure 4.7D and Figure 4.8**). Interestingly, as AGO3 containing a naturally existing phospho-mimic residue E390, the AGO3-LIMD1 interaction was not affected by the treatment of Akt3 siRNA (**Figure 4.9A** and **Figure 4.9B**). This indicated that AGO3-LIMD1 association was not Akt3 signal-dependent. In addition, E390A mutants showed a significant reduction in co-localisation (**Figure 4.9C** and **Figure 4.9D**). Therefore, AGO3-LIMD1 interaction was independent on Akt3 signalling due to the naturally existing phospho-mimic residue E390. Taken together, these data revealed a fundamental mechanism of the interaction between AGO proteins and LIMD1, which depended on Akt3-mediated phosphorylation on the conserved serine within L2 domain. For the naturally existing phospho-mimic residue on AGO3, the interaction with LIMD1 was not Akt3-dependent.

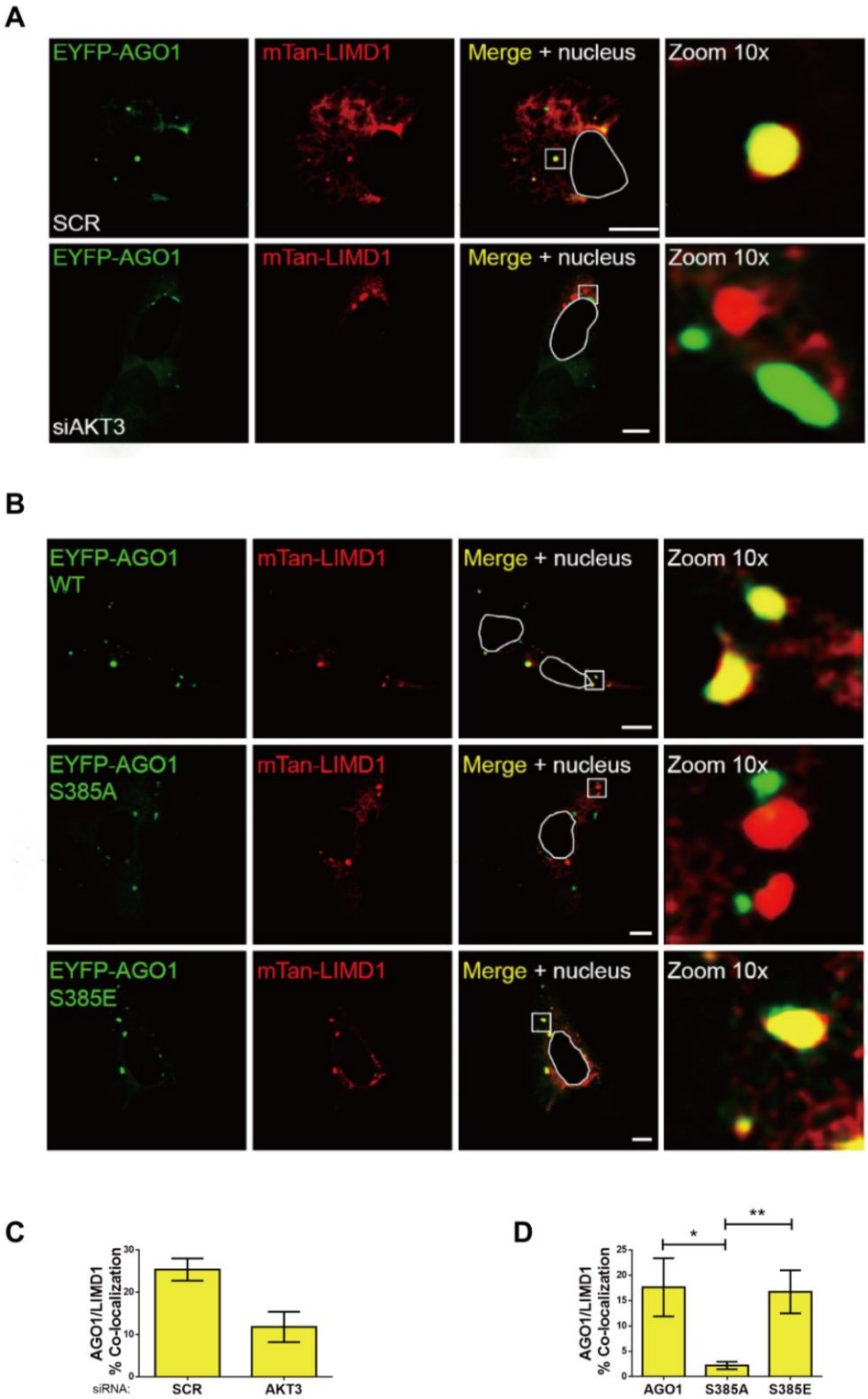

Figure 4.7 The co-localisation of LIMD1 and AGO1 depends on Akt3-mediated phosphorylation
***A*)** Co-expression of EYFP-AGO1 with mTan-LIMD1 in U2OS cells treated with non-targeting (SCR) or Akt3 siRNA. ***B*)** Co-expression of EYFP-AGO1 S385 point mutants with mTan-LIMD1 in U2OS cells. ***C*)** Quantification of number of AGO1 P-bodies co-localised with LIMD1 in (*A*). ***D*)** Quantification of number of AGO1 P-bodies co-localised with LIMD1 in (*C*). Data shown are mean ±SEM, n=3, * $p<0.05$, ** $p<0.001$. Nuclear outlines in white. Scale bars are 10µm.

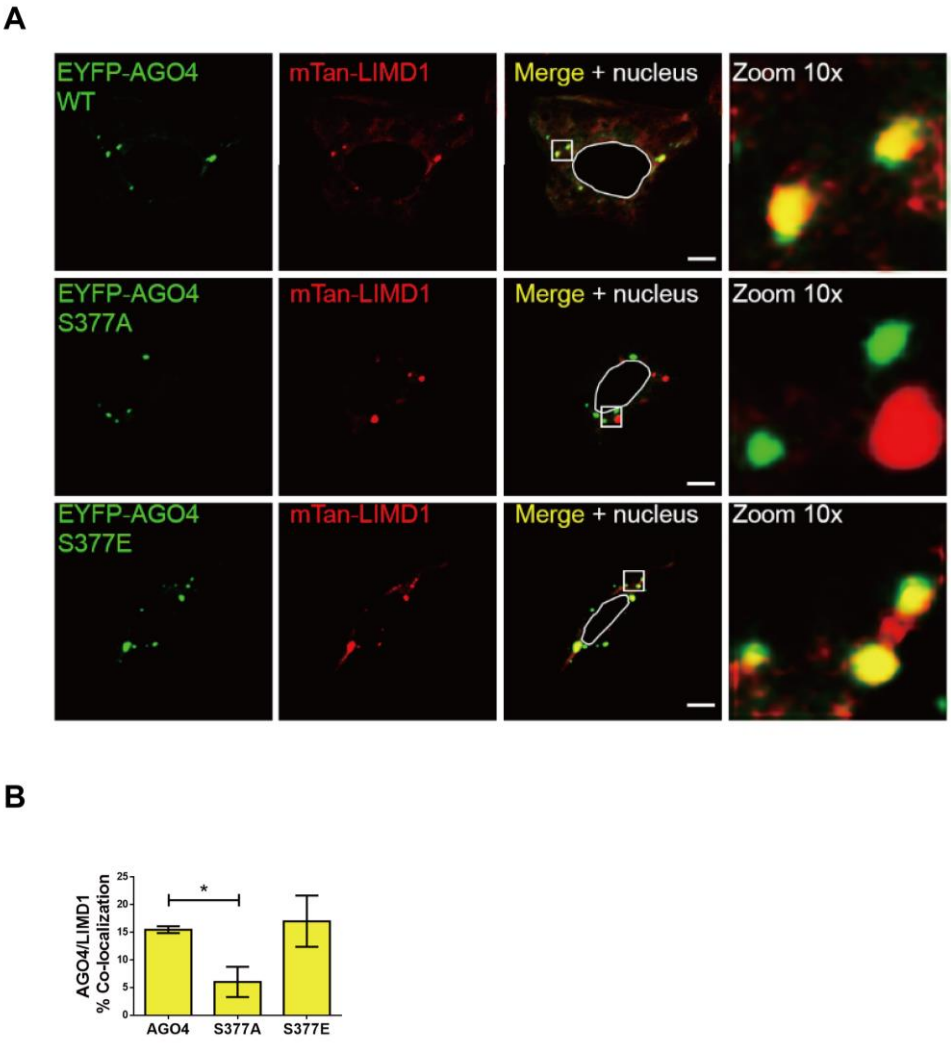

Figure 4.8 The co-localisation of LIMD1 and AGO4 depends on the phosphorylation of S377
***A*)** Co-expression of EYFP-AGO4 S377 point mutants with mTan-LIMD1 in U2OS cells. ***B*)** Quantification of number of AGO4 P-bodies co-localised with LIMD1 in (*A*). Data shown are mean ±SEM, n=3, * $p<0.05$. Nuclear outlines in white. Scale bars are 10µm.

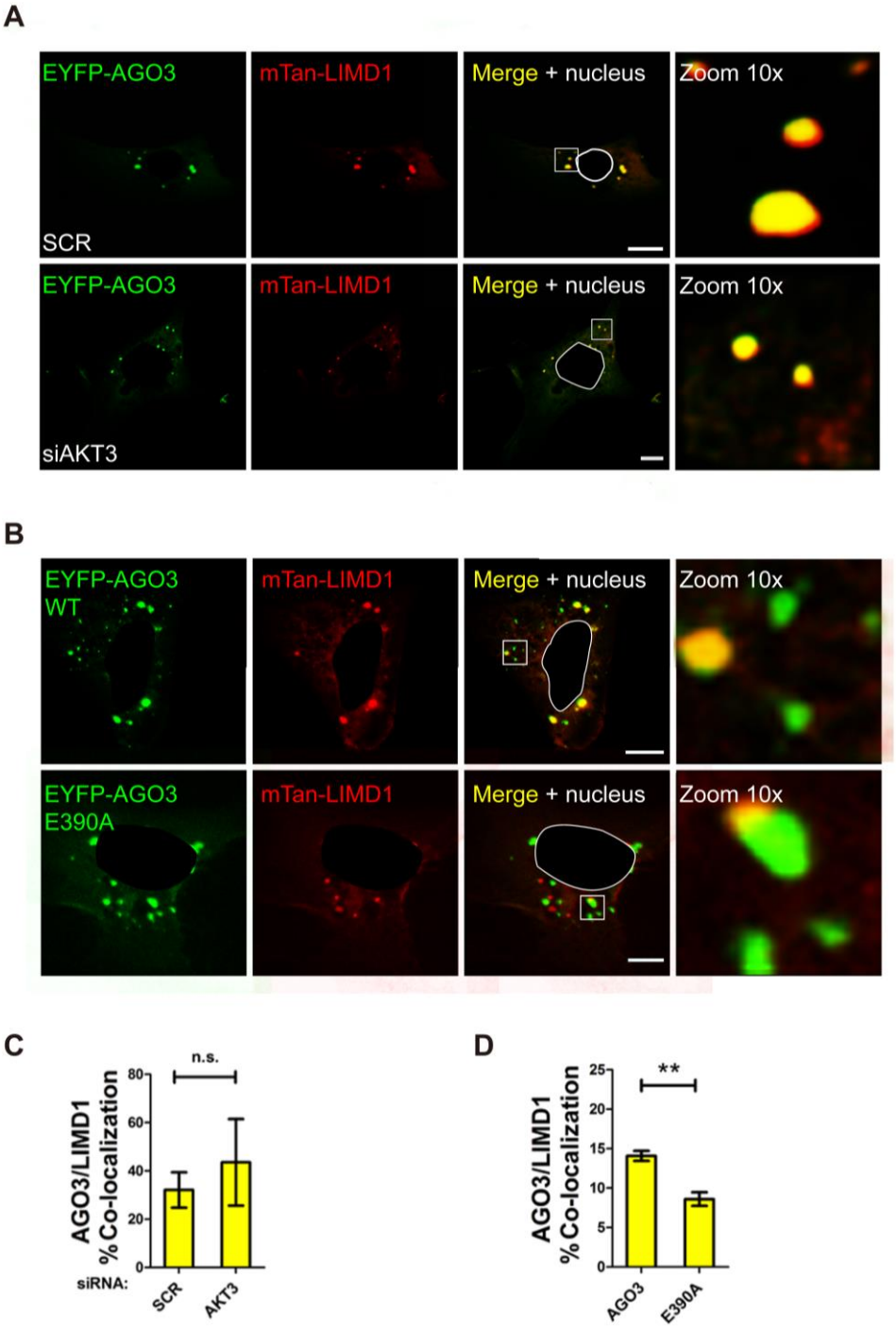

Figure 4.9 The co-localisation between AGO3 E390, a natural phospho-mimic, and LIMD1 is not Akt3 dependent.

***A*)** Co-expression of EYFP-AGO3 with mTan-LIMD1 in U2OS cells treated with non-targeting (SCR) or Akt3 siRNA. ***B*)** Co-expression of EYFP-AGO3 E390 point mutant with mTan-LIMD1 in U2OS cells. ***C*)** Quantification of number of AGO3 P-bodies co-localised with LIMD1 in (*A*). ***D*)** Quantification of number of AGO3 P-bodies co-localised with LIMD1 in (*C*). Data shown are mean ±SEM, n=3, ** p<0.001. Nuclear outlines in white. Scale bars are 10µm.

4.2 Characterisation of the association between AGOs and LAW

It has been demonstrated that LAW family members (LIMD1, AJUBA and WTIP) were critical regulators for miRNA-mediated silencing [1]. To date, the focus of miRNA-mechanism has been focused on the role of LIMD1 within miRISC. Our attention was next turned to the family member proteins AJUBA and WTIP to examine whether they co-localise with the AGOs and whether the S387 point mutations within AGO2 and the conserved serine within AGO proteins were important for the association. Therefore, mTan-AJUBA was co-expressed with EYFP-AGOs (containing serine point mutants) in U2OS cells to examine the co-localisation. The results confirmed the hypothesis that there was an association between AJUBA and AGOs (AGO1-3). The AGO1 S385A mutant showed a significant 7-fold reduction in co-localisation with AJUBA, while it showed an increasing trend when it was S385E mutant (**Figure 4.10**). For AGO3, the same results as LIMD1 were observed; E390A abolished the most of the co-localisation with AJUBA (**Figure 4.11**). Compared to AGO2 WT, AGO2 S387A and S387E showed an increasing trend (2-fold and 1.5-fold respectively) in co-localisation with AJUBA, although the increase was no statistically significance.

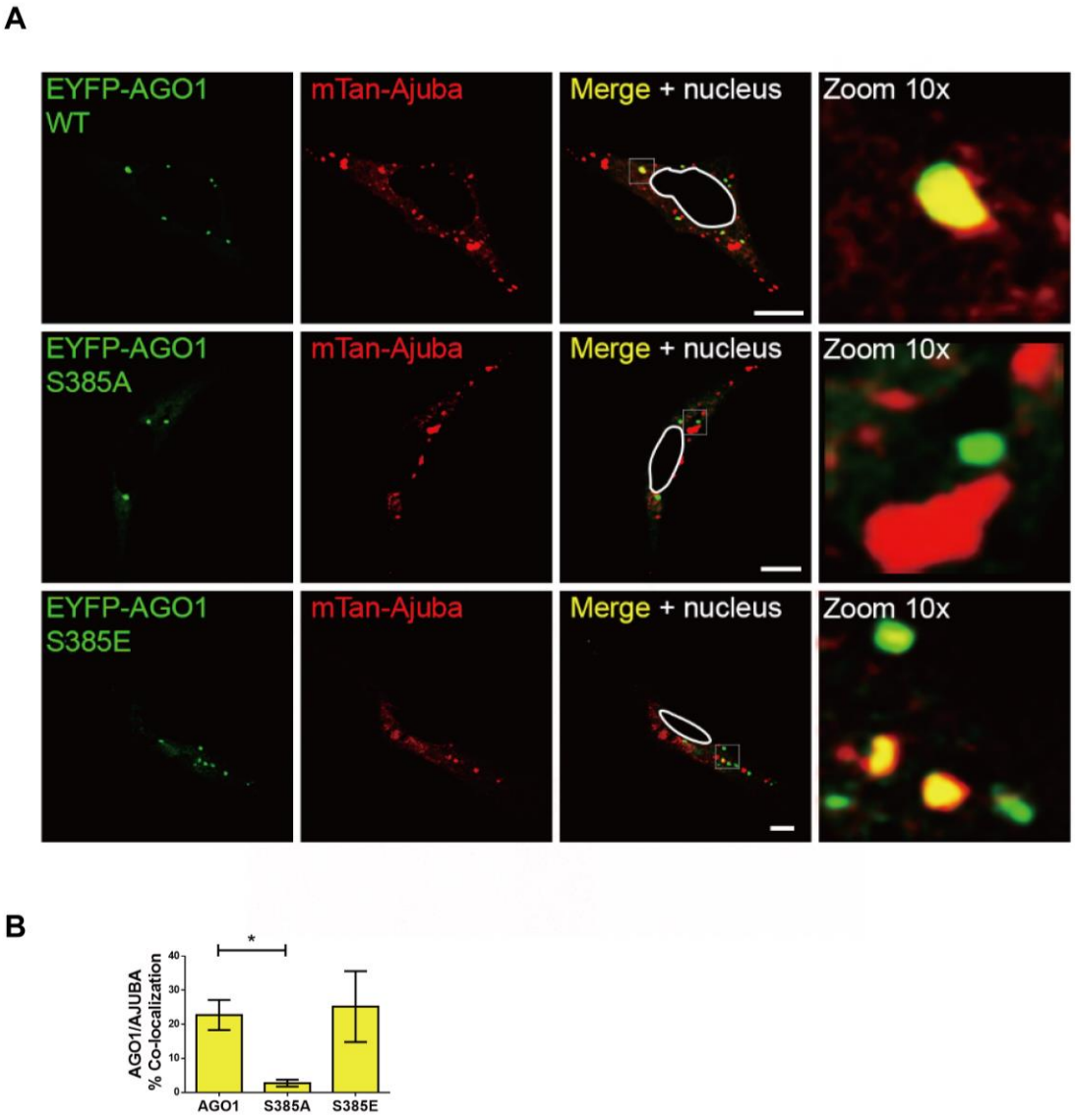

Figure 4.10 The co-localisation of AGO1 and AJUBA depends on the phosphorylation of S385
***A*)** Co-expression of EYFP-AGO1 S387 point mutants with mTan-AJUBA in U2OS cells. ***B*)** Quantification of number of AGO1 p-bodies co-localised with AJUBA in (*A*). Data shown are mean ±SEM, n=2, * $p<0.05$. Nuclear outlines in white. Scale bars are 10µm.

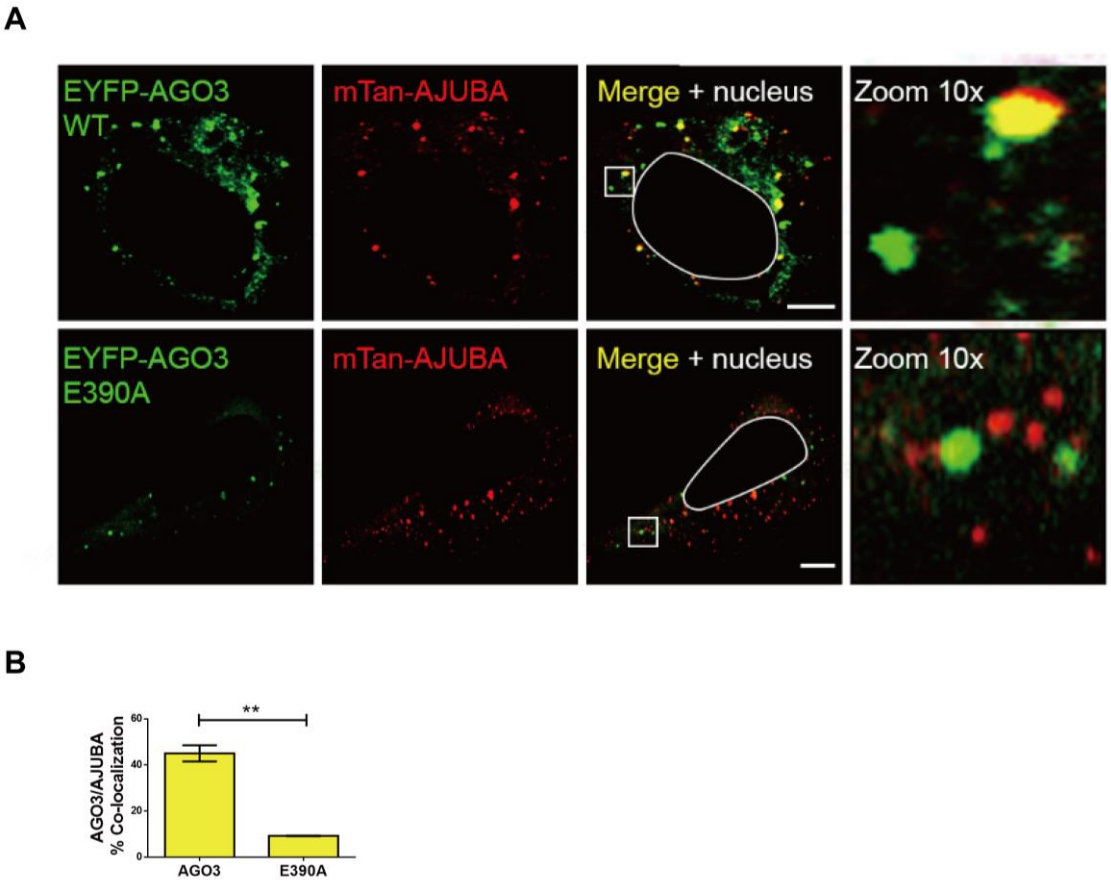

Figure 4.11 The co-localisation of AGO3 and AJUBA depends on E390, a natural phospho-mimic
***A*)** Co-expression of EYFP-AGO3 E390 point mutants with mTan-AJUBA in U2OS cells; ***B*)** Quantification of number of AGO3 p-bodies co-localised with AJUBA in (*A*). Data shown are mean ±SEM, n=2, ** p<0.001. Nuclear outlines in white. Scale bars are 10µm. Published data.

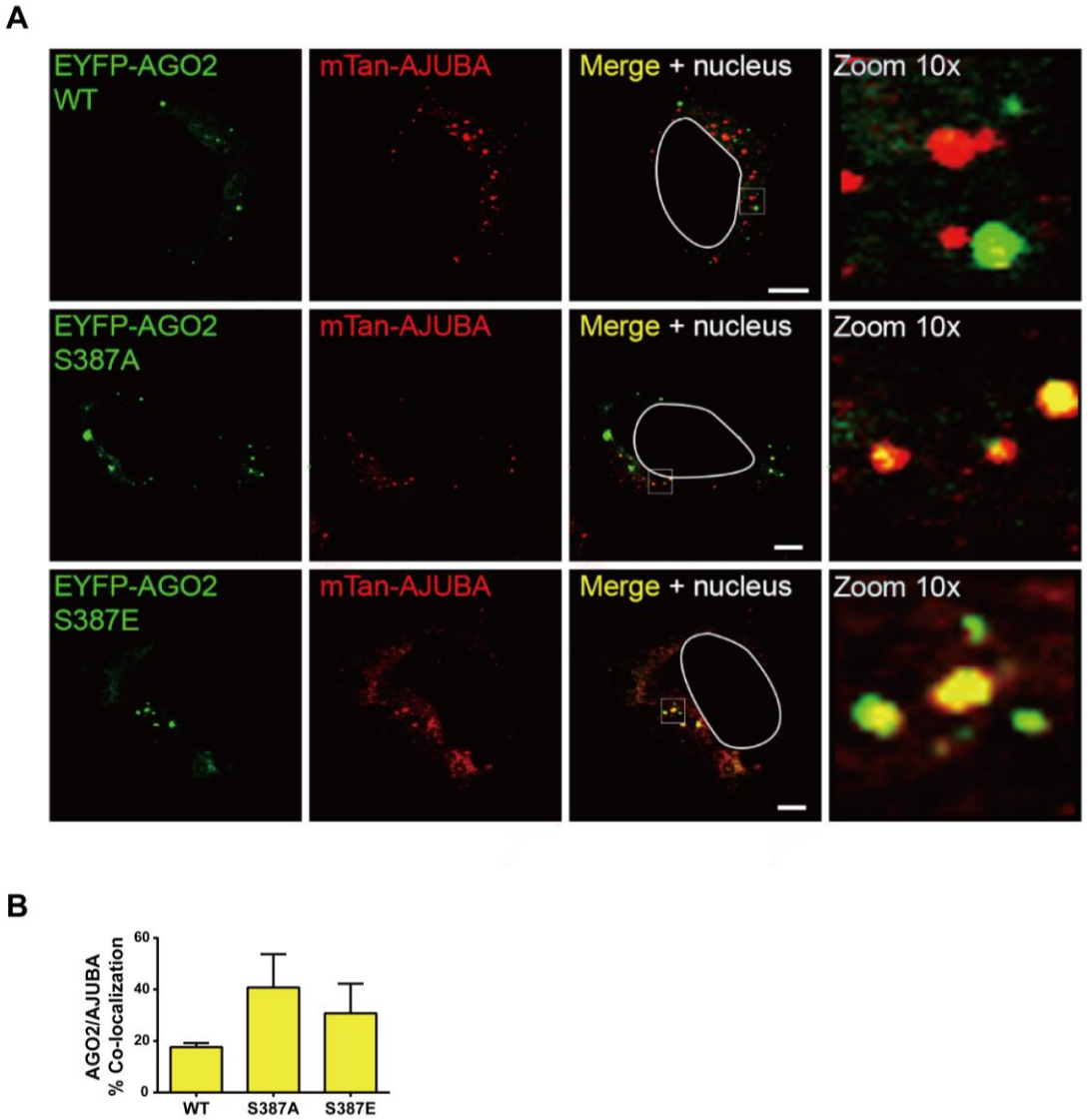

Figure 4.12 The co-localisation of AGO2 and AJUBA is affected by the phosphorylation of S387
***A*)** Co-expression of EYFP-AGO2 S387 point mutants with mTan-AJUBA in U2OS cells. ***B*)** Quantification of number of AGO2 p-bodies co-localised with AJUBA in (*A*). Data shown are mean ±SEM, n=2. Nuclear outlines in white. Scale bars are 10µm.

The association between WTIP and AGOs (AGO1-3) was then examined with regards to the point mutants of the conserved serine. The co-localisation data showed AGO1-WTIP association was dependent on the conserved S385. Compared to AGO1 WT, the phospho-deficient mutant (S385A) showed a reduction on the co-localisation, whereas the phospho-mimic mutant (S385E) increased the AGO1-WTIP co-localisation (**Figure 4.13**). In addition, the association between AGO3 and WTIP decreased if the point mutation was introduced (E390A) (**Figure 4.14**). Unlike AGO1-WTIP association regulated by the point mutations on the conserved serine, either S387A or S387E mutations showed the increased co-localisation of AGO2 and WTIP (**Figure 4.15**).

In summary, these data demonstrated that the association between AGO proteins (AGO1 and AGO2) and LAW depended on the ability of the conserved serine to be phosphorylated (**Figures 4.10, 4.12, 4.13, and 4.15**). Lacking of the conserved serine on AGO3, the naturally existing phospho-mimic residue E390 contributed to AGO3 constitutive association with LAW (**Figure 4.11 and 4.14**).

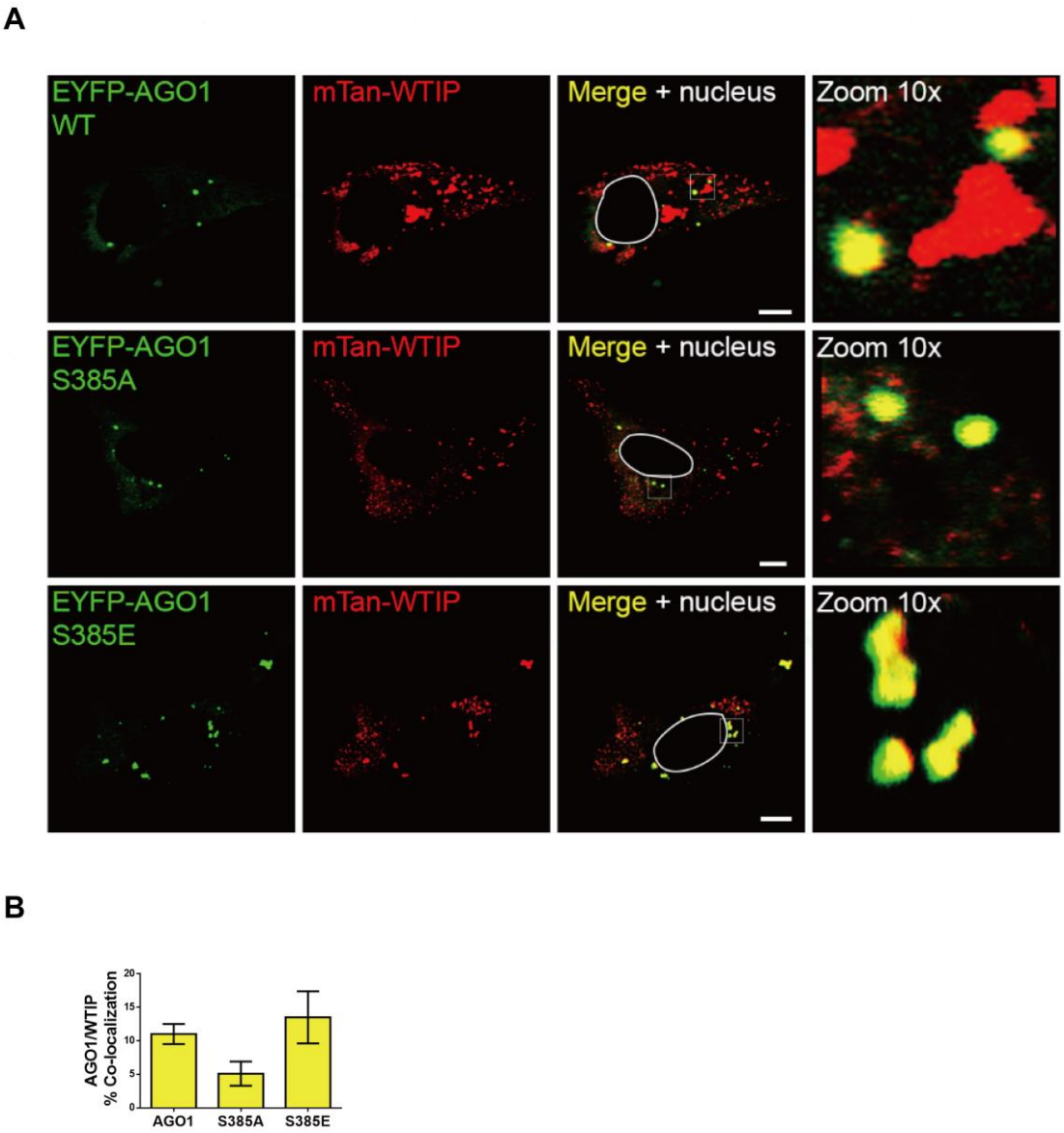

Figure 4.13 The co-localisation of AGO1 and WTIP depends on the phosphorylation of S385
***A*)** Co-expression of EYFP-AGO1 S385 point mutants with mTan-WTIP in U2OS cells. ***B*)** Quantification of number of AGO1 p-bodies co-localised with WTIP in (*A*). Data shown are mean ±SEM, n=2. Nuclear outlines in white. Scale bars are 10µm.

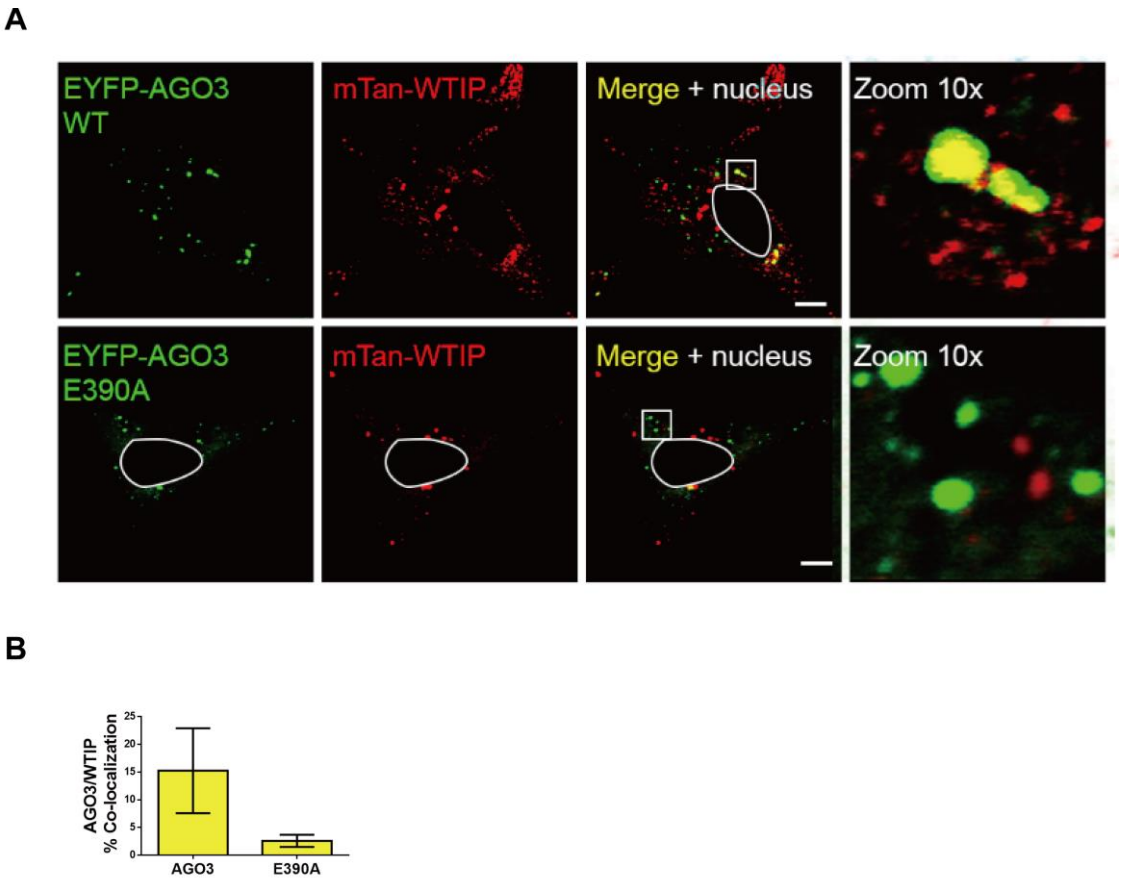

Figure 4.14 Co-localisation of AGO3 and WTIP depends on the E390, a natural phospho-mimic
***A*)** Co-expression of EYFP-AGO3 E390 point mutants with mTan-WTIP in U2OS cells. ***B*)** Quantification of number of AGO3 P-bodies co-localised with WTIP in (*A*). Data shown are mean ±SEM, n=2. Nuclear outlines in white. Scale bars are 10µm.

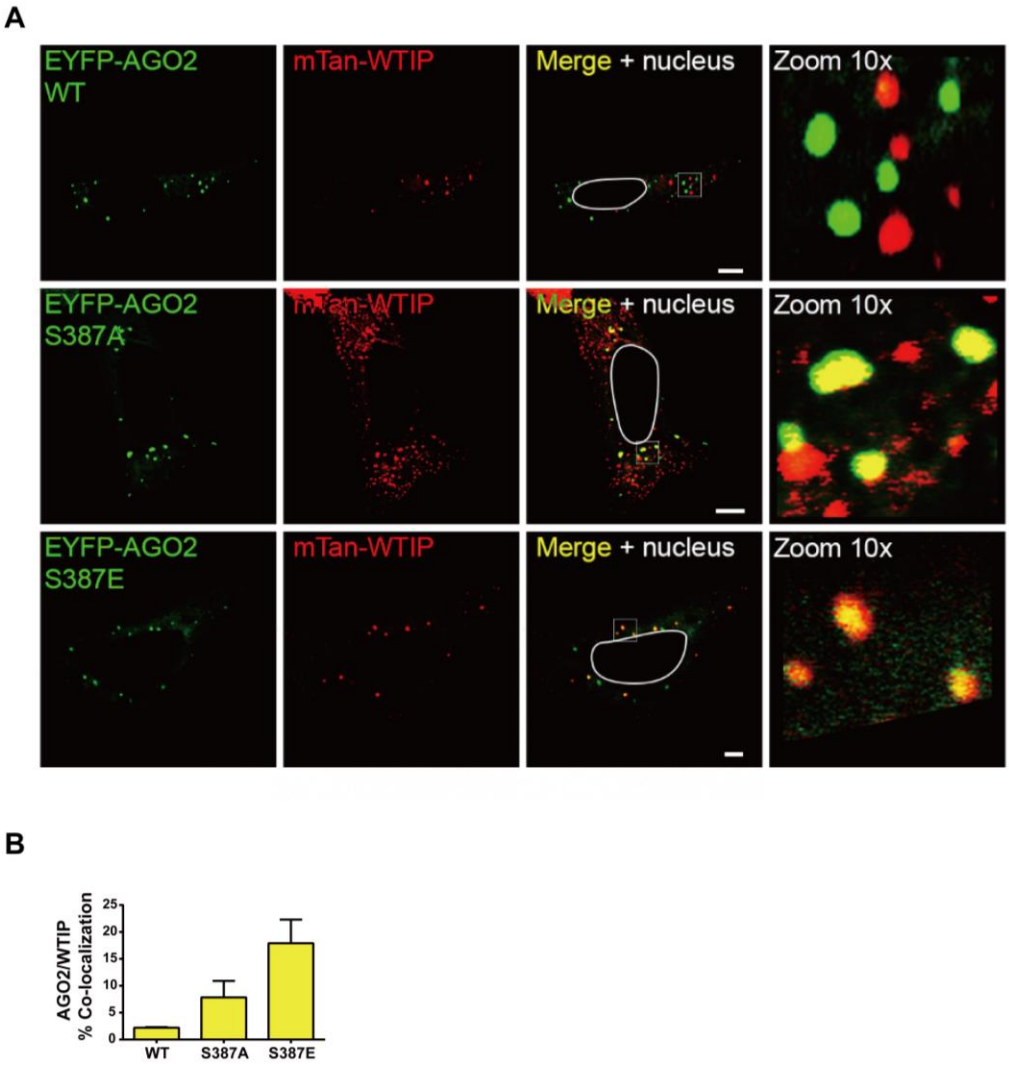

Figure 4.15 The co-localisation of AGO2 and WTIP is affected by the phosphorylation of S387
***A*)** Co-expression of EYFP-AGO2 S387 point mutants with mTan-WTIP in U2OS cells. ***B*)** Quantification of number of AGO2 P-bodies co-localised with WTIP in (*A*). Data shown are mean ±SEM, n=2. Nuclear outlines in white. Scale bars are 10µm.

4.3 Investigation of the co-localisation of AGO2 and LIMD1 with regards to the phosphorylating ability of Y393 within L2 domain

In addition to S387, EGFR-mediated phosphorylation at tyrosine 393 (Y393) on AGO2 was reported to reduce the interaction with Dicer to inhibit the biogenesis of miRNAs [114]. The phosphorylation at Y393 was also reported to inhibit miRNAs loading onto AGO2 and in turn resulted in the inhibition of miRNA-mediated silencing [128]. These reports suggested that Y393 was another important phosphorylation site involved in miRNA-mediated silencing pathway. Given that Y393 is also located within the L2 domain, it raised a question whether the phosphorylation at Y393 affected the association with LIMD1.

4.3.1 Construction of the expression plasmids for EYFP-AGO2 Y393 point mutants

To examine whether the residue Y393 was also important and could contribute to AGO2-LIMD1 association, one set of constructs expressing phospho-mimic (Y393D) or phospho-deficient (Y393F) of EYFP-AGO2 S387 version needed to be generated according to the chemically-similarity of amino acids (**Figure 11.3**). In addition, the interaction of AGO2 and LIMD1 depended on Akt3-mediated phosphorylation of S387 (**Chapter 3.3**). To rule out the effect by S387, another set of constructs expressing the point mutation at Y393 residue (Y393D and Y393F) of EYFP-AGO2 S387A version were also required. Therefore, to generate two sets of EYFP-AGO2 Y393 point mutants with regards to S387/S387A, site-directed mutagenesis was performed by using EYFP-AGO2 S387 or EYFP-AGO2 S387A as a template (details described in **Chapter 2.2.1.5**). The sequencing was directly performed after mutagenesis treatment. The results showed except for EYFP-AGO2 Y393F, other constructs including EYFP-AGO2 Y393D and EYFP-AGO2 S387A contained the required substitutions on Y393 (**Figure 4.16 and Figure 4.17**). The sequencing result showed there were two peak readings at Y393 (highlighted by a red arrowhead, **Figure 4.16**). This indicated that there was a technique error on picking colonies sent to sequencing, resulting in the vial of this construct contains two plasmids, EYFP-AGO2 Y393 and EYFP-AGO2 Y393F.

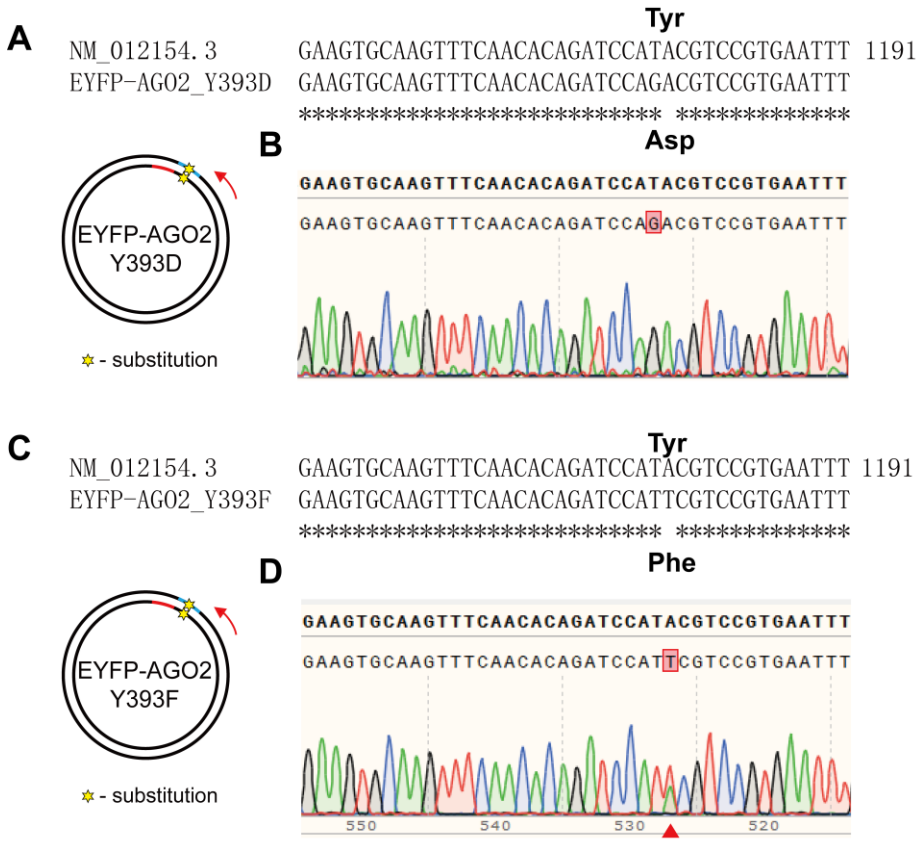

Figure 4.16 The preparation of Y393 point mutations on EYFP-AGO2 S387 WT by Q5® site-directed mutagenesis

***A&C*)** The alignment of the Sanger sequencing read to the database AGO2 CDS (NM_012154.3) performed by MUSCLE. ***B&D*)** The chromatograms showed distinct peaks for each nucleotide in the corresponding region, indicating the required point mutations. The Red arrowhead indicates that there are two readings at the required mutagenesis site.

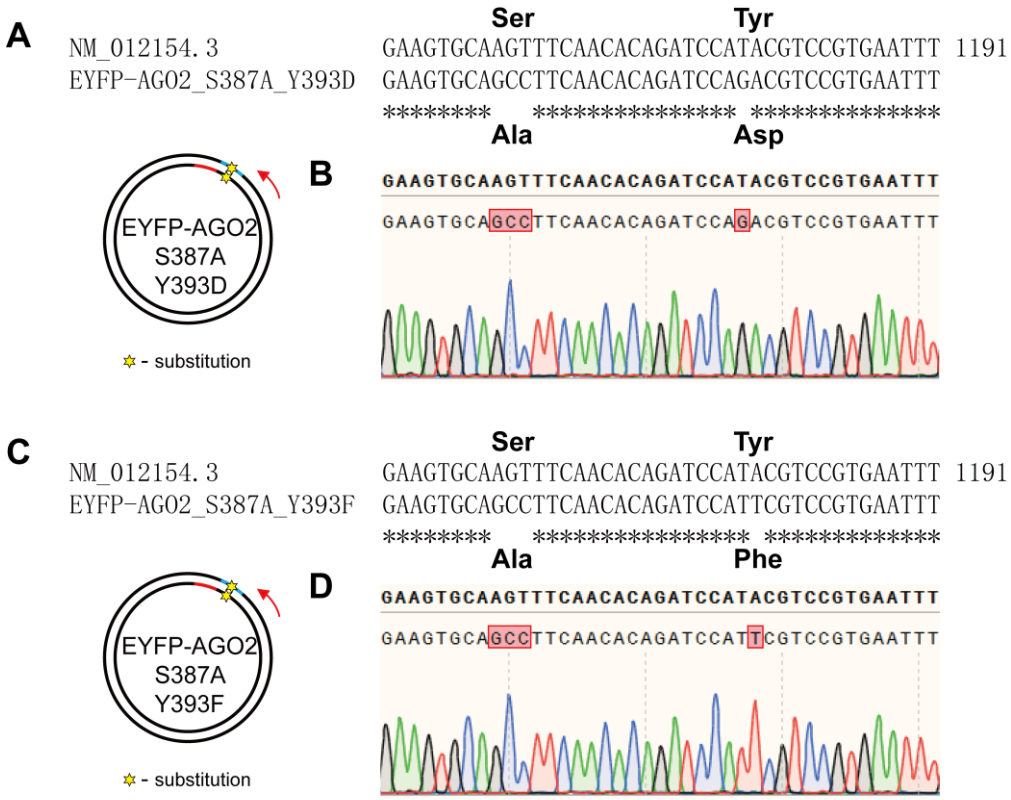

Figure 4.17 Preparation of Y393 point mutations on EYFP-AGO2 S387A by Q5® site-directed mutagenesis

***A&C*)** The alignment of the Sanger sequencing read to the database AGO2 CDS (NM_012154.3) performed by MUSCLE. ***B&D*)** The chromatograms showed distinct peaks for each nucleotide in the corresponding region, indicating the required point mutations.

4.3.2 Phosphorylating ability of Y393 within the L2 domain of AGO2 affects the co-localisation with LIMD1

It is of note that the mutated AGO2 was over-expressed to investigate its co-localisation with LIMD1 according to the ability of phosphorylation on Y393. Therefore, the co-localisation experimental results did not directly examine the phosphorylation status of Y393. By co-transfecting EYFP-AGO2 WT set of Y393 point mutants with mTan-LIMD1, the results showed that EYFP-AGO2 Y393D (phospho-mimic) had 6-fold less co-localisation with LIMD1 compared to EYFP-AGO2 WT, whereas the co-localisation between EYFP-AGO2 Y393F (phospho-deficient) with LIMD1 increased (**Figure 4.18**). These results implied the association with LIMD1 was dependent on the phosphorylation of Y393. Unlikely with the function of S387 examined in **Chapter 4.1** that the phosphorylation enhances the interaction with LIMD1, the phosphorylation of Y393 might inhibit the association with LIMD1 and hypo-phosphorylation of Y393 enhanced this association. With regards to the technique error on EYFP-AGO2 Y393F, this would underestimate the effect of Y393F on enhancing the association with LIMD1, and this could explain the high error bar on Y393F among the independent biological repeats (**Figure 4.18**).

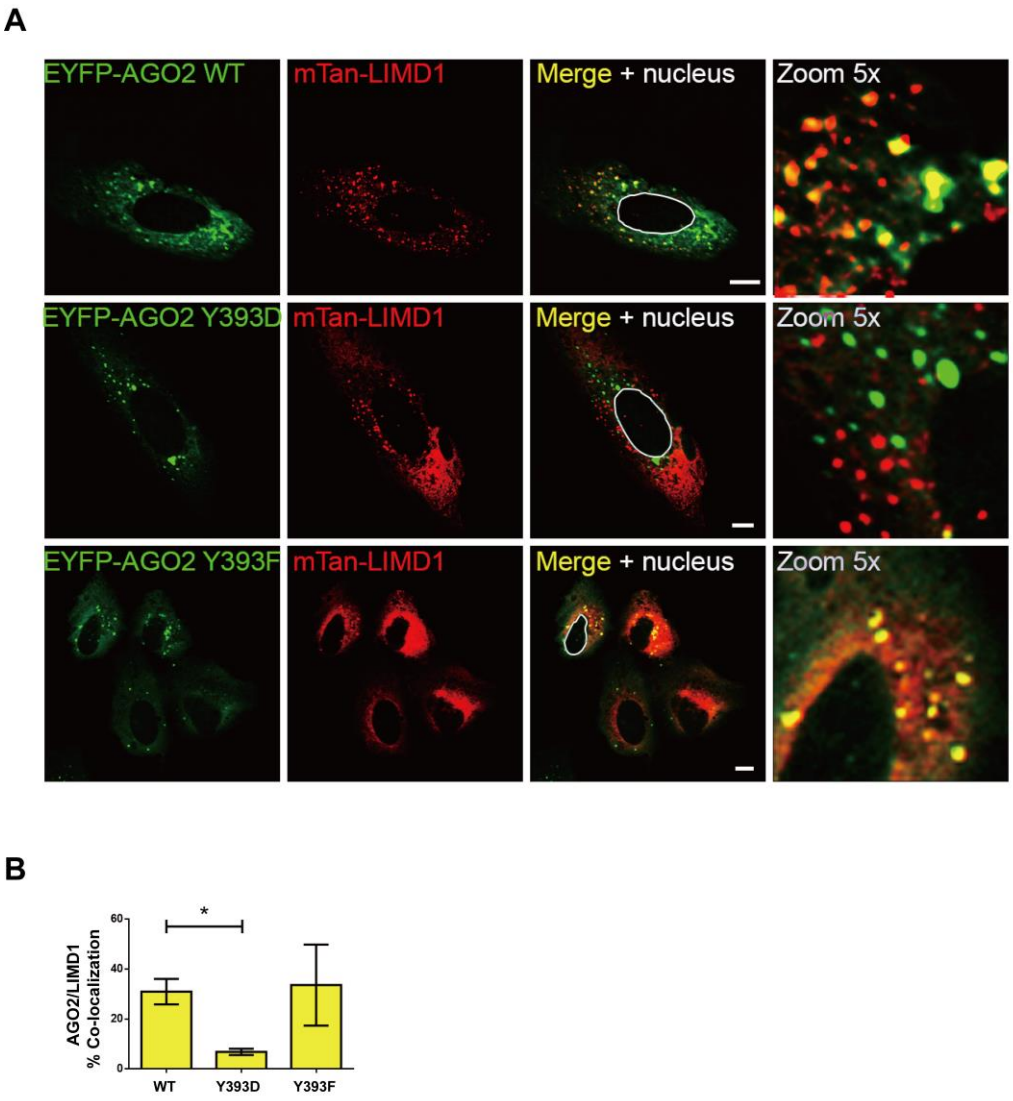

Figure 4.18 The point mutation of Y393 within L2 domain affects the association with LIMD1
***A*)** Co-expression of EYFP-AGO2 Y393 point mutants with mTan-LIMD1 in U2OS cells. ***B*)** Quantification of number of AGO2 P-bodies co-localised with LIMD1 in (*A*). Data shown are mean ±SEM, n=2, *, p<0.05. Nuclear outlines in white. Scale bars are 10µm.

Given that S387A within AGO2 abrogated the association with LIMD1 (**Figure 4.6**), it raised the question how it affected AGO2-LIMD1 interaction with regards to the combined phosphorylation at these two resides. By examining the co-localisation of EYFP-AGO2 S387A/Y393 point mutants, S387A mutant was found to achieve a low co-localisation with LIMD1 (**Figure 4.19**), which agreed with our previous observations above where hypo-phosphorylation at S387 disrupted the interaction with LIMD1 (**Chapter 3.3**). With the dual-mutation on S387A/Y393D, the co-localisation could not be rescued and remained low (10%) at a similar level to the S387A mutation only. S387A/Y393F dual-mutation, however, increased the co-localisation with LIMD1 (**Figure 4.19**). Within AGO2 S387A set, the phospho-mimic mutant Y393D did not change the association with LIMD1, but as observed previously the phospho-deficient mutant Y393F increased the association with LIMD1. This further confirmed the association of AGO2 and LIMD1 was also dependent on the phosphorylation of Y393.

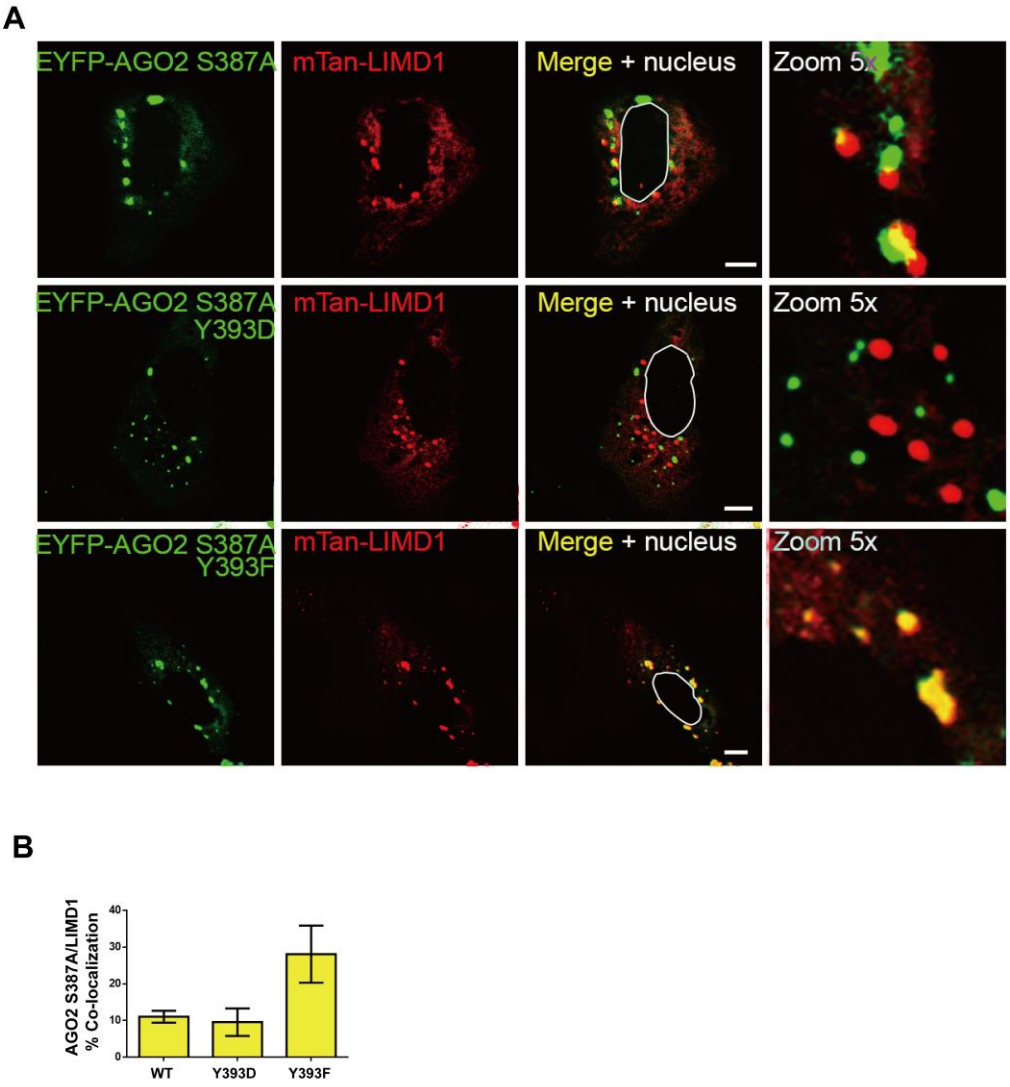

Figure 4.19 The point mutation of Y393 within L2 domain affects the association with LIMD1
***A*)** Co-expression of EYFP-AGO2 S387A Y393 point mutants with mTan-LIMD1 in U2OS cells. ***B*)** Quantification of number of AGO2 P-bodies co-localised with LIMD1 in (*A*). Data shown are mean ±SEM, n=2. Nuclear outlines in white. Scale bars are 10µm.

4.4 Summary

In summary, the conserved serine within the L2 domain of all four human AGOs was demonstrated to be responsible for LIDM1 association (**Chapter 4.1**). Moreover, it showed there were associations between AGOs and LAW family members. These associations were regulated by the phosphorylation at the conserved serine (expect AGO3 with naturally existing glutamic acid (**Figure 4.11** and **Figure 4.14**)) (**Chapter 4.2**). In addition to S387 contributing to regulating the AGO2-LIMD1 interaction, the AGO2-LIMD1 association might also depend on another phosphorylation site (Y393) within the L2 domain (**Figure 4.18 and Figure 4.19**). The phosphorylation of S387 and Y393 function as a molecular 'switch' to regulate the association of AGO2 with LIMD1. For simplicity, '**ON**' or '**OFF**' was used to define whether there is an association or not, respectively (**Table 4.2** and **Figure 4.20**). For example, S387/Y393 (EYFP-AGO2 WT) was considered as an '**ON**' model that LIMD1 and AGO2 showed a high co-localisation (**Figure 4.19C, Figure 4.20** and **Table 4.2**). Phospho-mimic mutant Y393D decreased the interaction ('**OFF**'), whereas phospho-deficient mutant Y393F rescued the association ('**ON**'). On the other hand, S387A/Y393 resulted in a low co-localisation ('**OFF**') between AGO2 and LIMD1 (**Table 4.2, Figure 4.19C** and **Figure 4.20**). Phospho-mimic mutant Y393D remained the low degree of interaction, whereas phosphor-deficient mutant Y393F rescued the degree of interaction (**Table 4.2** and **Figure 4.20B**). These observations provided a potential fundamental mechanism through which the phosphorylation of Y393 regulated AGO2-LIMD1 association, which was not addressed in the previous studies. It helped to understand how AGO2 is regulated to interact with LIMD1 (also with WTIP and AJUBA) and function in miRNA-mediated silencing.

Table 4.2 Simplified AGO2-LIMD1 association with regards to different combinatorial point mutants on S387 and Y393

Combined point mutations		LIMD1 association ('ON' or 'OFF')
S387	Y393	ON
	Y393D	OFF
	Y393F	ON
S387A	Y393	OFF
	Y393D	OFF
	Y393F	ON

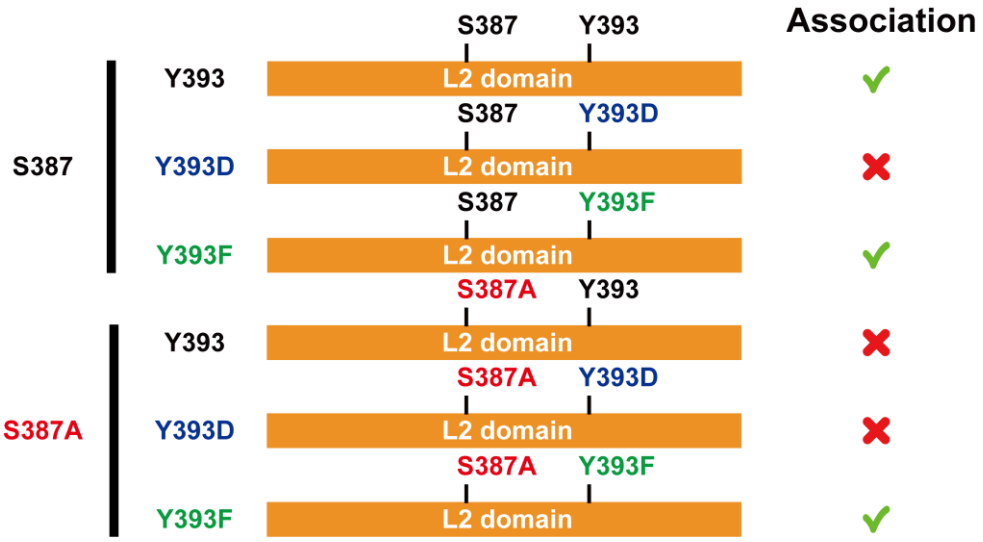

Figure 4.20 Summary of AGO2-LIMD1 association with regards to the combined point mutations of S387 and Y393

AGO2-LIMD1 association was regulated by the combined point mutations of S387 and Y393. S387A mutation shown in Red; Y393D mutation shown in Blue; Y393F mutation shown in Green.

Chapter 5

Discussion

5 Discussion

This study was designed to **1**) characterise the direct binding interfaces between LIMD1 and AGO2 for a better understanding for the role of LIMD1 as a regulator in miRNA-mediated silencing and **2**) investigate the association between AGOs and LAW to expand our knowledge of AGOs utilisation with regards to different LAW family proteins. Therefore, this chapter will discuss the overall mechanistic implications of the findings presented so far and postulate the proposed/hypothesised model of the pathway that LIMD1 involved in the above study.

5.1 The specific domains responsible for the AGO2-LIMD1 interaction

The previously published study from our group demonstrated that LIMD1 associates with miRISC to facilitate the miRNA-mediated silencing [1]. This present study not only determined that LIMD1 binds directly to AGO2, one of the key component of miRISC, but also revealed their specific interaction domains: a.a 140-166, which was defined as an AGO-binding motif (AB-motif) of LIMD1 in our latest publication [253], binds to the L2 domain of AGO2 (**Chapter 3.2**). It is of note that the crystal structure analysis revealed the PIWI domain of AGO2 with tandem tryptophan-binding pockets is responsible for direct binding with TNRC6A tryptophan residues [109]. This present study confirmed that this domain does not interact with LIMD1 (**Figure 3.15**). LIM domains were determined by our latest publication to directly interact with TNRC6A, another key component of miRISC, *via* the Argonaute-binding domain (ABD) (**Figure 5.1A**). The loss of LIMD1 significantly impaired AGO2-TNRC6A/miRISC association and miRNA-mediated silencing activity (Figures 1A-1C and 2 of [253], p269-p270).

The phosphorylation has been demonstrated to contribute to the protein-protein interaction, and the phosphorylation site tend to be located on the interaction interfaces [254]. A previous study has shown that the phosphorylation of S387 on AGO2 by Akt3 increased miRNA-mediated silencing and decrease siRNA-mediated

endonucleolytic activity [127]. Evidence has been showed that the N and L1/L2 domain on AGO3 is looser than that on AGO2 (**Figure 1.11**), and thus AGO3 lacks its endonucleolytic activity [118]. Therefore, it is reasonable to postulate the phosphorylation of S387 or the phospho-mimic mutant, S387E might change the conformation of AGO2: open the space between the N and L1/L2 domain. This not only increased the interaction with LIMD1 and miRNA-mediated silencing.

This present study indicated that the Akt3-mediated phosphorylation on S387 promotes AGO2-LIMD1 interaction (**Figure 4.6 and Figure 5.1B**). The phosphorylation may modulate the binding energy and thus change the molecular structure [254], which ultimately enhance the binding of AGO2 with LIMD1. Our latest publication has elaborated this finding that phosphorylation at S387 subsequently enhances miRNA-mediated silencing. In agreement with our findings, La Rocca *et al*. recently identified phosphorylation-dependent activation of miRNA silencing by PI3K, a kinase that lies upstream of Akt3 [255]. In addition, the interaction between AGO2 and TNRC6A is independent of LIMD1 binding [256], suggesting AGO2 can interact TNRC6A without LIMD1. Taken all together, the phosphorylation of S387 on AGO2 enhances the interaction with LIMD1, and in turn, LIMD1 is proposed to function as a molecular 'clamp' by binding to both AGO and TNRC6A proteins simultaneously. Therefore, the enhanced AGO2-LIMD1 interaction secure the association among three proteins, which subsequently facilitates miRNA-mediated silencing.

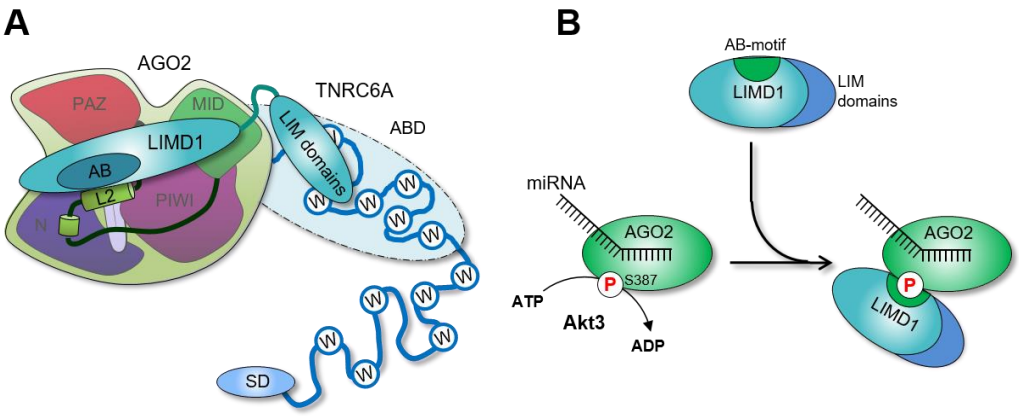

Figure 5.1 Schematic of the interfaces of LIMD1, AGO2 and TNRC6A for binding to each other
A) The graphical representation of domain interaction of AGO2, LIMD1, and TNRC6A. The AB-motif of LIMD1 (a.a 140-166) directly binds to the L2 domain of AGO2, and the LIM domains of LIMD1 bind to the N-terminal ABD of TNRC6A. ***B)*** The phosphorylation of S387 on AGO2 facilities its interaction with AB-motif of LIMD1. ABD, Argonaute-binding domain. SD, silencing domain.

5.2 AGO-LAW association occurs *via* a common phosphorylation-dependent mechanism

The L2 domain connecting the PAZ and MID domains is evolutionally conserved across all four human AGOs with 84.6% sequence identity (**Figure 4.2**). This study suggested the direct interaction of human AGO1-4 with LIMD1 *via* the L2 domain (**Figure 4.1** and **Figure 4.3**). In addition, the S387 residue within the L2 domain of AGO2, which is phosphorylated by Akt3, is conserved in human AGO1 and 4 (highlighted in **Figure 4.2**). This study showed that the association of LIMD1 with AGO1 and 4 is also dependent on the phosphorylation at this conserved serine residue (**Figure 4.7** and **Figure 4.8**). Given that a previous study demonstrating that AGO1 can be phosphorylated [124], these data imply a hypothesis of a common AGO-activating mechanism whereby the conserved serine residue is phosphorylated by Akt3 and/or other unidentified kinases. AGO3 does not contain this conserved serine residue but contains a phospho-mimic glutamic acid residue (E390) instead (**Figure 4.2**). E390 on AGO3 directs the association with LIMD1

independently of Akt signalling (**Figure 4.9**). Horman *et al*. postulated that the phosphorylation of S387 represented a molecular switch between the siRNA and miRNA function of AGO2 [127]. To expand upon this concept, this study indicates the Akt3-mediated phosphorylation on AGO1, 2 (and possibly AGO4) could also be considered as a switch from OFF to ON for miRNA-silencing function. Furthermore, this study also suggests LAW family members (LIMD1, AJUBA and WTIP) can associate with all human AGOs (**Chapter 4.1**) and were previously demonstrated to be required for the miRNA-mediated silencing [1, 253]. The co-localisation results do not imply that all four AGOs associating with LAW depend on the same 'phospho-serine-switch-ON/OFF' mechanism as with AGO2-LIMD1. However, it is similar that the presence of a glutamic acid residue (E390) within the L2 domain allows AGO3 to associate with LAW irrespective of Akt-signalling. As a result, this study reveals a possible compensatory silencing pathway *via* AGO3-LAW when there is no Akt3 signalling to activate any or all of the other AGOs by phosphorylation.

Although Wang *et al*. demonstrated that AGO2 is the most abundant and in turn most contributes to miRNA-mediated silencing [257], LAW family proteins are important determinants of AGO utilisation [253]. By cross-comparing all co-localisation results in **Chapter 4** with regards to the wild-type conserved serine within L2 domain of AGO1-3, AGO3-AJUBA is the dominant complex in U2OS (**Figure 5.2**).

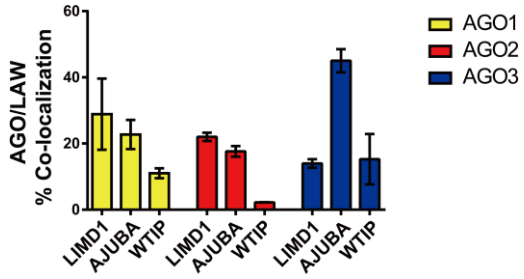

Figure 5.2 Cross comparison of AGO-LAW association
Data summarised from the previous IFA results and focused on AGO with the wild-type serine. Quantification of the number of AGOs P-bodies co-localised with LAW in U2OS cells co-expressed EYFP-AGOs (1-3) with mTan-LAW. Data shown are mean ±SEM, n=2.

Taken together with the result that AGO3-WTIP complex switches to function in miRNA-mediated silencing when AGO2-LIMD1 complex is depleted [253], this present study implied the common existence of a differential AGO-LAW complexes (AGO3-AJUBA) and were involved in miRNA-mediated silencing. Furthermore, in the *LIMD1*$^{-/-}$ HeLa cell line, it was WTIP rather than AJUBA that forms a complex with AGO3 and resulted in significant repression of the miR-99/100 reporter [253]. Such results are not contradictive to the dominant AGO3-AJUBA complex observed in this present study (**Figure 5.2**), but instead, it proved that the differential AGO-LAW complexes exist and are dependent on the context of the cell type and abundance of each AGO. As discussed previously, LIMD1 as a molecular 'clamp' to secure AGO2-LIMD1-TNRC6A complexes to facilitate miRNA-mediated silencing. The recent study demonstrated that one molecule of TNRC6A can recruit up to three human AGO proteins *via* its GW motifs [258]. The cooperative repression was observed by different miRNAs when their seeding sites are within 13-35 nts [259]. In addition, it has shown that AGOs function cooperatively to silence the target mRNA by the cooperativity in binding: the recruitment of the first miRISC to the 3'UTR of mRNA enhances the recruitment of the other miRISC complexes through the physical interaction between miRISCs [260]. Recently, Flamand *et al*. revealed the interaction interfaces between AGOs within two miRISCs in *C.elegans* (**Figure 5.3A**), and such interaction allowed the conformation change of AGO and TNRC6, resulting in the recruitment of CCR4-NOT deadenylases complex [261]. Therefore, taken together with these studies, this present study would put forward the proposed model for miRNA-mediated silencing with regards to AGO-LAW-TNRC6 complex (**Figure 5.3B**). If the miRNA seed sites are within a close distance, one molecule of TNRC6 can bind to three different AGOs. The interaction between AGOs and TNRC6 is clamped by the association with LAW and AGO-AGO interaction. Consequently, it results in the cooperative repression of the target mRNA. This present study elaborates the theory that the determination of AGO utilisation, the cooperation of different AGO proteins and the specific pairing with LAW maybe context-dependent with regards to the distribution of a particular miRNA among AGO proteins [108, 262], the abundance of AGO proteins and differential LAW expression in the cells. Further investigations need

to clearly define the regulation of miRNA-dependent silencing with regards to AGO-LAW association.

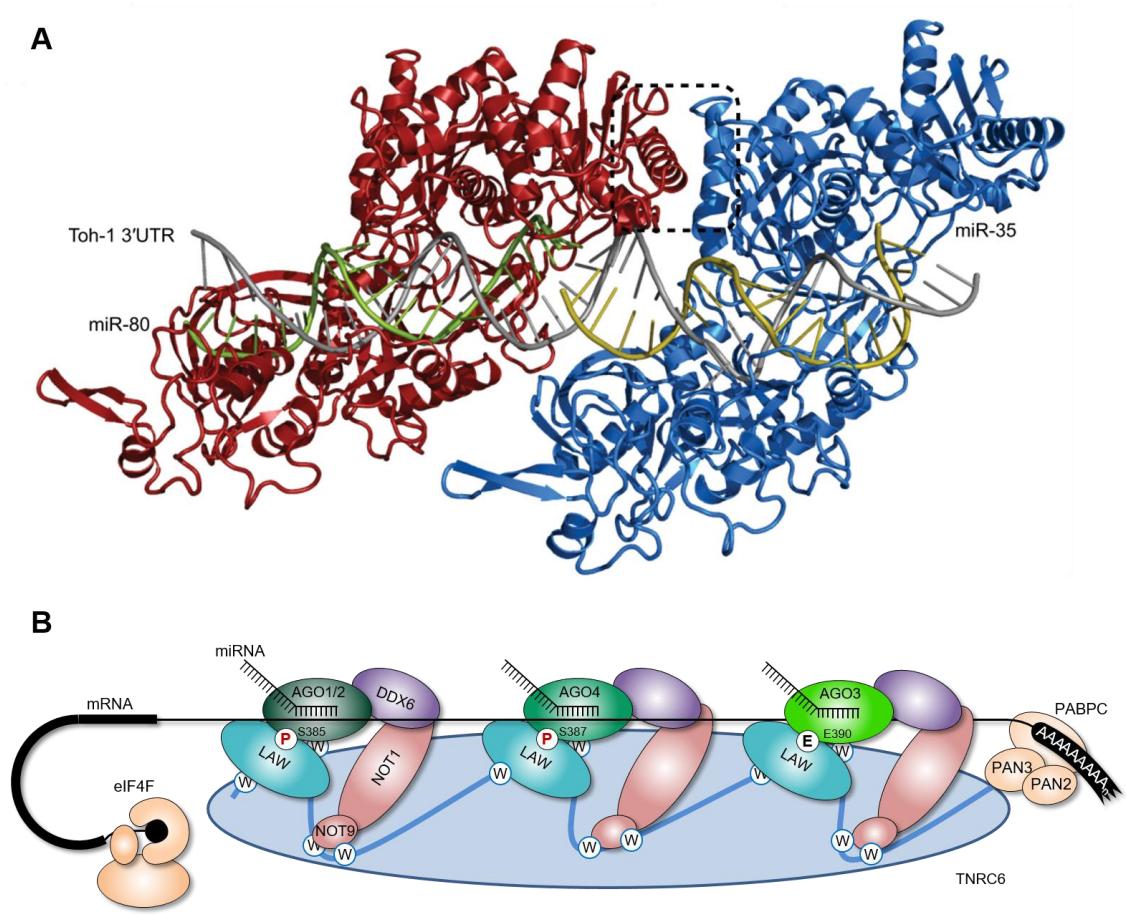

Figure 5.3 Proposed model of AGO-LAW-TNRC6 association regulating miRNA-mediated silencing
A) Interaction between tow ALG-2 (the homology of human AGO2) within two miRISCs (not shown) loaded with *miR-80* (indicated in green) and *miR-35* (indicated in yellow), which target the 3'UTR of *Toh-1* (indicated in grey). The dashed box indicates the proposed interaction interface. ***B)*** *One* molecule of TNRC6 (indicated in light blue) can interact up to three AGO proteins. The determination of AGO utilisation and its specific pairing with LAW depend on the distribution of miRNA among AGO proteins, the abundant of AGO proteins and LAW expression in the cells. Figure part **(*A*)** is adapted from Flamand *et al.*, 2017 [261].

It is of note that this study has examined only the phosphorylating ability but not the phosphorylation status of the conserved serine within the L2 domain. Although AGO1 can be phosphorylated [124], there is no specific evidence to show the conserved serine

on AGO1 and 4 can be phosphorylated. Therefore, the results were based on the assumption that the conserved serine is phosphorylated by Akt3 and/or other unidentified kinases. Further investigations are required to examine the possible phosphorylation. In addition, all the co-localisations observed in this study was conducted by the confocal microscope. Although the confocal microscope scans across the sample and generates high-resolution images, the diffraction limit is less than 240nm. Therefore, proteins within 240nm are visualised as co-localised. Proximity ligation assay (PLA) [263], is an immunohistochemical tool for the precise protein analysis, including protein-protein interactions and protein modifications. The principle of PLA is to use one pair of short DNA oligonucleotides labelled antibodies which bind to different epitopes of two proteins. If two proteins are in close proximity (40nm apart), DNA oligonucleotides on the antibodies then form a circular ssDNA molecule and continue the rolling cycle amplification. Therefore, the amplified signals can be detected by the confocal microscope. PLA has been employed to show AGO2-LIMD1, LIMD1-TNRC6A and TNRC6A-CNOT9 signals, but not TNRC6A-CNOT1 signal [253]. As a result, PLA is necessary to reveal the AGO-LAW association accurately.

5.3 The residue Y393 also regulates AGO2-LIMD1 association

Besides S387, this study also reveals another residue, Y393, within the L2 domain of AGO2, the phosphorylation of which can also regulate AGO2 association with LIMD1; phospho-mimic mutant (Y393D) impairs the AGO2-LIMD1 association, whereas phospho-deficient mutant (Y393F) restores/enhances the AGO2-LIMD1 association. In agreement with the previous study demonstrating the dephosphorylation of Y393 on AGO2 is required to promote miRNAs loading onto AGO2 and thus miRNA-mediated silencing [128], this present study implied LIMD1 participates in this pathway that the dephosphorylation of Y393 results in the interaction of AGO2 with LIMD1 and thus miRNA-mediated silencing. In addition, as similar to the conserved serine (S387 in AGO2), Y393 is also conserved across all four human AGOs (**Figure 5.4**). More interestingly, AGO3 not only contains a naturally existing phospho-mimic (E390) residue which is

independent of Akt3-signalling but also contains a naturally existing phospho-deficient (F394) residue. Therefore, AGO3 may be the most dominant AGO required for miRISC complexes, which is in agreement with the IFA data (**Figure 5.2**). However, the endogenous AGO3 expression is extremely low due to the high proportion of rarely used codons in its mRNA [264]. Maunoury *et al.* demonstrated that AGO1 and AGO2 are redundant in miRNA-mediated silencing [265], and thus the redundant AGO1 and AGO2 function in miRNA-mediated silencing. Therefore, based on our latest publication [253], this present study indicates AGO3 can function in miRNA-mediated silencing and specific functions as a compensatory miRNA-silencing pathway in the absence of the Akt3-AGO2^{S387}-LAW signalling axis or other AGO2^{Y393} signalling axes due to its two naturally existing residue within L2 domain.

```
AGO1   375 EEISRLMKNASYNL--DPYIQE 394
AGO2   377 EEISKLMRSASFNT--DPYVRE 396
AGO3   376 EEISRLVRSANYET--DPFVQE 397
AGO4   367 EEISRLVKSNSMVGGPDPYLKE 388
```

Figure 5.4 Multiple sequence alignment of the human AGO family
AGO proteins contain a highly conserved Tyrosine residue: AGO1 Y391, AGO2 Y393 and AGO4 385. AGO3 contains a phosphor-deficient phenylalanine residue (F394).

5.4 Which residue functions dominantly, S387 or Y393?

When considering the S387 phosphorylation-dependent mechanism on regulating AGO2-LIMD1 interaction, it raises a question of which residue (S387 or Y393) has the dominant role in inducing the association with LIMD1, and thus the miRNA-mediated silencing; whether the phosphorylation of S387 and dephosphorylation of Y393 occur simultaneously or sequentially. It was shown that Y393F (phospho-deficient) enhanced AGO2-LIMD1 association even when S387 was not able to be phosphorylated (S387A) (**Figure 4.20** and **Table 4.2**). By considering the role of Y393 in miRNA maturation and loading ability on AGO2, this present study hypothesises a model for miRISC assembly

whereby AGO2 is initially dephosphorylated at Y393 residue by the specific phosphatases (such as protein tyrosine phosphatase 1B (PTP1B)) to bind to Dicer and process the miRNA maturation and thus promotes miRNA loading (**Figure 5.5A**). Meanwhile, the dephosphorylated AGO2 recruits LIMD1. S387 is then (or simultaneously with the dephosphorylation of Y393) phosphorylated by the Akt3-signalling to secure the AGO2-LIMD1-TNRC6A association within miRISC complexes (**Figure 5.5A**).

Smibert *et al.* demonstrated that AGO2 stability is positively regulated by the cellular availability of mature miRNAs and the ubiquitin-proteasome system, and the loading of siRNAs can rescue the stability of AGO2 in the absence of miRNA biogenesis [130]. Therefore, the phosphorylated Y393 reduces the maturation of miRNAs and in turn decreases AGO2 stability. To compensate/self-rescue this instability, siRNAs may be forced to load on AGO2 more efficiently and subsequently achieves the siRNA-mediated silencing (**Figure 5.5B**). This present study opens up the possibility for the functional differences in the combined phosphorylation status of S387/Y393 in AGOs with respects to the miRISC assembly. To elaborate the 'switch-ON/OFF' theory on S387 mentioned in the previous section, Y393 along with S387 collaborate as a molecular switch to determine whether AGO2 undergoes miRNA- or siRNA-mediated gene silencing. The phosphorylation of Y393 switches AGO2 to function in siRNA-mediated silencing and abrogates the association with LIMD1. Therefore this hypothesis would fit with the published data demonstrating that LIMD1 is exclusively involved in miRNA-mediated silencing but not siRNA-mediated silencing [1].

Nevertheless, the phosphorylation of Y393 abolishes the interaction of AGO2 with Dicer [128]. Considering Dicer binds to PIWI domain of AGO2, it raises a question whether Dicer binds L2 domain, or LIMD1 might be a scaffold regulating their interaction.

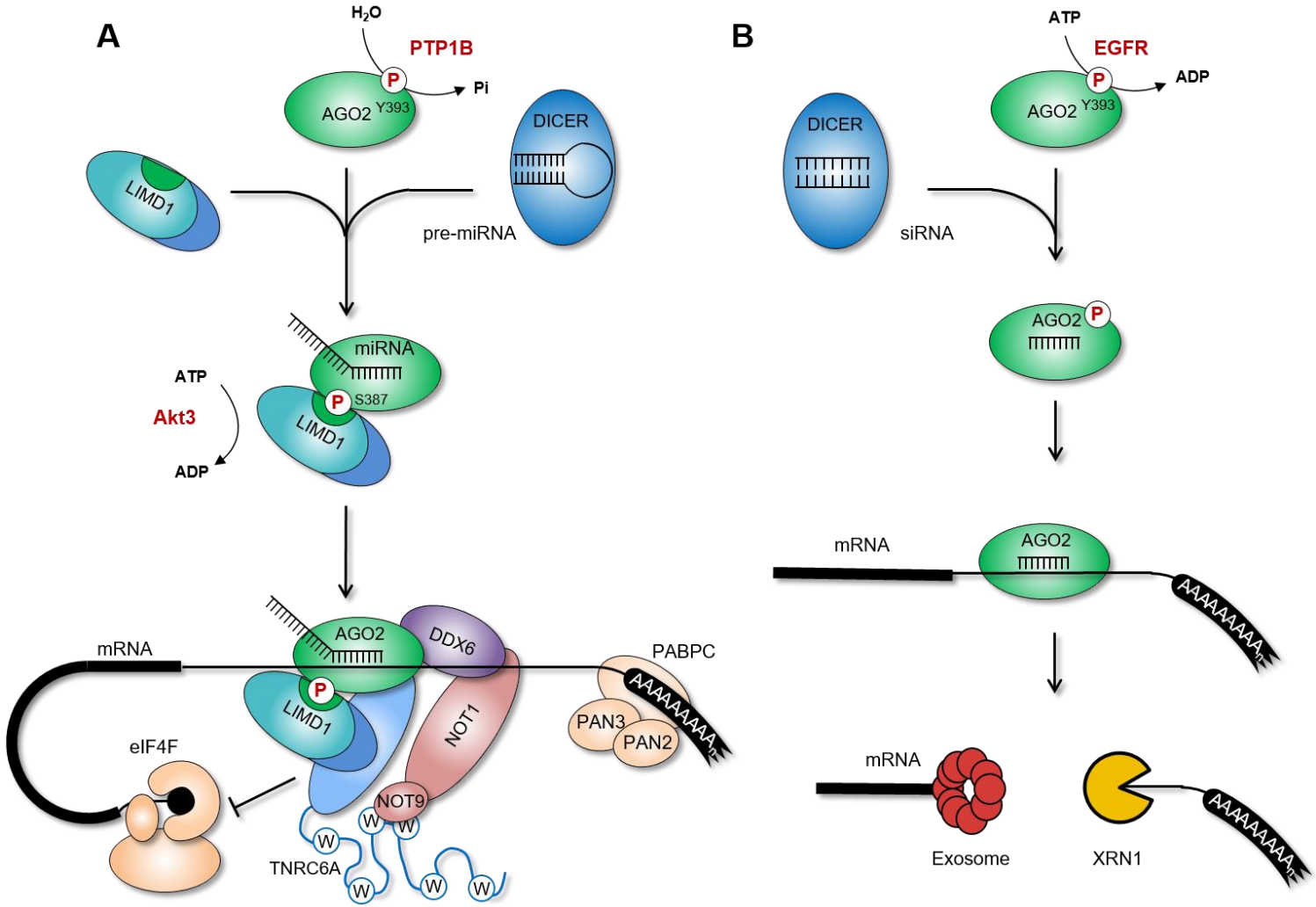

Figure 5.5 The hypothesis model that the phosphorylation of S387/Y393 regulates the miRNA- and siRNA-mediated silencing

A) The dephosphorylation Y393 on AGO2 (by PTP1B) is able to bind Dicer and LIMD1 and to process the maturation of miRNA. S387 is phosphorylated to secure the AGO2-LIMD1-TNRC6A association, which recruits downstream effector complexes for miRNA-mediated silencing. ***B)*** The phosphorylation on Y393 of AGO2 by EGFR abolishes the association of AGO2 with Dicer to inhibit the maturation of a subclass of miRNA. siRNAs are forced to load on AGO2 more efficiently to rescue the stability of AGO2 and subsequently siRNA silencing.

Chapter 6

Project 2

Introduction

6 Introduction

Given that LIMD1 is frequent down-regulated, targeting LIMD1 faces lots of challenges. By using the synthetic lethality approach, serine/threonine kinase 39 (STK39) was revealed a synthetic lethality function with LIMD1 loss in the **Results Chapter 7**. Therefore, this chapter will firstly introduce the kinase family that STK39 belongs to, followed by the overview of STK39 including its history of discovery, the structures and domains, binding partners, signalling cascades, the mammalian physiological roles and the role in cancer.

6.1 The overview of STK39

6.1.1 STK39 belongs to Ste20-related kinases

The function of serine/threonine kinases is to hydrolyse ATP and transfer the inorganic phosphate to the side chain of the serine and threonine residues. This leads to the phosphorylation of the target protein, resulting in the regulation of cellular processes. The Sterile 20 (Ste20)-related kinases are a relatively large family of proteins highly conserved in fungi, plants, *Drosophila, C.elegans* and mammals, whose function is to regulate mitogen-activated protein kinase (MAPK) cascades [266, 267]. According to whether the catalytic domain is located at the N- or C-terminal, Ste20-related kinase family can be sub-grouped into the germinal centre kinases (GCKs) presenting a N-terminal catalytic domain and the p21-activated kinases (PAKs) presenting a C-terminal catalytic domain [267]. GCKs can be further broken down into eight sub-groups (GCKI-VIII). Indeed, GCK family has been demonstrated as MAP4Ks in MAPK signalling cascades function and thus regulates signalling transduction [267] (**Table 6.1**). STK39 belongs to GCK-VI sub-family and regulates several cellular processes, which will be elaborated in the next section.

Table 6.1 List of GCK family members which regulate MAPK signalling pathway
Summarised from Dan *et al*., and Gagnon *et al*., 2012[267, 268]

Name	Sub-family of GCKs	Function	Reference
MAP4K5	GCK-I	Wnt-mediated JNK activation	[267]
Mst2	GCK-II	Positive role in Raf-1/ERK pathway	[269]
Mst4	GCK-III	Modulation of ERK pathway	[270]
NIK, NRK	GCK-IV	Activation of JNK pathway	[271]
STK39	GCK-VI	Activation of p38	[272]
TAO1/2/3	GCK-VIII	Activation of p38; Inhibition of JNK pathway	[273]

6.1.2 PASK, SPAK and STK39 are referred to the same protein

The current literature is using two widely-accepted names to refer to the same protein (STK39). This inconsistently used name would confuse the researchers. Therefore, it is necessary to clarify how and where the name is derived from. A novel protein with the molecular weight of 66kDa was identified from rat brain tissue. This novel protein contained the similar catalytic domain with the Ste20 protein kinases and the abundance of proline and alanine residues. As a result, this novel protein was named proline-alanine-rich Ste20-related kinase (PASK) [274]. Two years later, based on the characterisation of a novel kinase which was previously identified in rat pancreatic beta cells containing the similar sequence with Ste20 serine/threonine kinases, this protein was named Ste20/SPS1-related proline alanine-rich kinase (SPAK) [272, 275]. The comparison of amino acid then showed that PASK and SPAK were the same protein. In addition, the National Centre for Biotechnology Information also assigned the name *STK39* to human SPAK. Therefore, to be consistent and avoid confusion, STK39, as the same name for its encoded gene, is referred in this thesis.

6.1.3 The structure and domains of STK39

STK39 contains the main domains in the order from the N- to C-terminus: PAPA box, catalytic domain, PF1 domain and PF2 domain (**Figure 6.1**). PAPA box is a region of proline and alanine repeats. A colonic STK39 variant was identified and analysed to show the lack of PAPA box upstream of the catalytic domain [276]. However, evidence has shown that the absence of PAPA box does not impair the binding and phosphorylation of its target [277]. Although this result indicated that PAPA box is not essential for the kinase activity, it does not rule out the possibility that it has the unknown functions for the kinase.

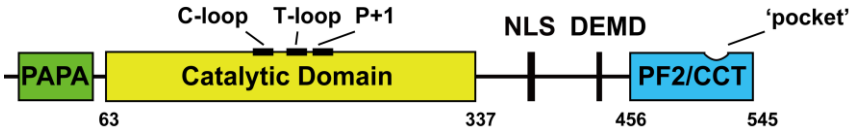

Figure 6.1 Schematic of the structure of STK39
STK39 contains proline/alanine-rich (PAPA) box, catalytic domain, PF1 (not shown) and PF2 (also called CCT). C-loop, catalytic loop. T-loop, activation loop. P+1, after activation loop for substrate binding. NLS, nuclear localisation signal. DEMD, a putative caspase cleave site. The pocket structure recognises the binding other proteins containing the RFxV motif.

The activation segment consists of the activation loop and P+1 loop. The phosphorylation of the activation loop activates the kinase activity. P+1 loop is after the activation loop, whose function is to bind the substrate for phosphorylation. The swap of activation segment is critical for STK39 function; mutating the threonine residue within the P+1 loop into an alanine residue (T237A) inhibits STK39 from phosphorylating and activating its target [277]. The PF1 domain is just after the catalytic domain, which contains a conserved serine-motif (S-motif) [268, 278]. S-motif is targeted by with-no-lysine kinase 1 (WNK1) on S373 for the activation of STK39 [279]. Within the PF1 domain, there are three identified regions: nuclear localisation signal (NLS), a tryptophan-glutamic acid-tryptophan motif (WEW motif), and DEMD [268]. NLS's function has not

been determined. WEW motif is capable of binding with Calcium-binding protein 39 (Cab39) to regulate the activation of Na-K-Cl cotransporters (NKCCs) [280]. DEMD is a putative caspase cleavage site. The study showed that TRAIL-induced cleavage occurred two amino acids downstream of this site, leading to inactivation of SPAK and subsequently increased cell sensitivity to apoptosis [281].

The PF2 domain, also known as conserved C-terminal (CCT) domain, is the last 90 amino acids of STK39 [268, 282]. The phenylalanine (F481), leucine (L497), alanine (A499) and leucine (L502) residues form a 'pocket' structure for the binding of the benzyl side chain of the phenylalanine residue (**Figure 6.1**). F481A mutation resulted in the decreased NKCC1 activation by WNK4-STK39 axis pathway [268]. An important binding motif, RFxV (where x stands for any amino acid), was identified in STK39 binding partners for the interaction with this pocket structure [283]. The mutation of the phenylalanine residue within RFxV motif impairs the kinase-substrate interaction. In addition, it has been demonstrated that the protein with both PF2-like domain and RFxV binding motif can achieve self-regulation, contributing to auto-inhibition [284]. Taken together, PF2 of STK39 is of importance in regulating protein interaction.

6.1.4 The biological functions of STK39

STK39 expression is widely expressed in different tissues. The well-established pathway for STK39 is to regulate the cotransporters. Therefore, the function of STK39 will be reviewed in the following section with regards to the cotransporter and the role in the cancers.

6.1.4.1 WNK-STK39-NKCC/KCC axis pathway regulates blood pressure

The RFxV motif is responsible for the binding to STK39. Therefore it can be used to predict potential proteins interacting with STK39. Studies have been done and successfully identified multiple proteins containing this RFxV motif and expanded this binding motif sequence to [V/S/G]RFx[V/I/T/S] [283, 285]. Sodium chloride cotransporter 12 (SLC12) family is one of the cation-chloride cotransporters that

regulates the cellular secretion of salt and protects cells from damage by osmotic stress [286]. The family contains three sub-groups based on their regulated ions: N-K-Cl cotransporters (NKCCs), K-Cl cotransporters (KCCs) and N-Cl cotransporters (NCCs). The first co-transporter found to interact with STK39 was NKCC1, which controls the cell volume and keep the osmotic balance between the external and internal cellular environments by taking up Na^+, K^+ and Cl^-[287]. The interaction takes place through PF2 domain on STK39 and two RFxV motifs located within the N-terminal cytosolic domain of NKCC1 [288]. The mutation of these motifs caused the inhibition of the binding to STK39 and the inactivation of NKCC1 [288]. A cluster of conserved threonine within the cytosolic domain of NKCC1 was reported to be phosphorylated by STK39 [288]. This cluster is highly conserved within NKCC2 and NCC, which is phosphorylated by STK39 as well. Therefore, evidence has been shown that STK39 can interact with NKCC2 and NCC through the single RFxV motif [287, 289]. As NKCC2 and NCC only express in the kidney, they, therefore, regulate renal salt re-absorption and subsequently hypertension [290]. After phosphorylation by STK39, a conformational change takes place on cotransporters to induce their activities [291].

WNKs belong to serine-threonine kinases and are named after the lack of lysine residue in the catalytic domain [292]. The mutation of WNKs has been demonstrated to be correlated to hypertension [293]. The overexpression of WNK decreases K^+ excretion and in turn increases salt re-absorption in the kidney, leading to salt-sensitive hypertension. All four WNK isoforms (WNK1-4) contain the putative RFxV motif at the N-terminal for the interaction with STK39. It has been demonstrated that co-expression of human NKCC1 with wild-type STK39 in *Xenopus laevis* oocytes did not cause cotransporter activation, but co-expression of NKCC, wild-type STK39 and wild-type WNK4 resulted in the activation of NKCC1 activity [294]. This indicated the activation of NKCC required both WNK4 and STK39. Variety of independent studies have demonstrated that WNKs bind STK39 and regulate STK39-mediated NKCCs activity [283, 294-296]. The activation of WNKs depends on either hyperosmotic stress or hypotonic low-Cl^- conditions but is not stimulated by signal-transduction pathway activators and

non-osmotic cellular stresses [297, 298]. The serine located within T-loop for regulating the protein kinase activity is phosphorylated by hyperosmotic stress or hypotonic low-Cl^- conditions. The phospho-deficient mutation (alanine) on S382 abolished WNK activity, whereas the glutamic acid substitute enhanced the activity [299].

The thick ascending limb (TAL) and distal convoluted tubule (DCT) in the kidney re-absorb the filtered salt to preserve salt homeostasis and regulate blood pressure. The reabsorption is based on the expression of specific ion transport proteins. In general, in the epithelial cells of the TAL, the Na^+ and Cl^- reabsorption are achieved by the combination of the NKCC2 and the renal outer medullary potassium channel (ROMK) on the apical membrane with Na^+-K^+ ATPase and chloride on the basolateral membrane [300]. In the epithelial cells of the DCT, NCCs are expressed along the entire DCT segment. The general mechanism for Na^+ absorption is achieved by the NCC expression on the apical to influx Na^+ and Cl^-. The basolateral expression Na^+-K^+ ATPase effluxes Na^+ for reabsorption. STK39 and NKCC2 are expressed and co-localised in the TAL [301]. Carmosino *et al*. demonstrated that the increased phosphorylation of STK39 and NKCC2 presented in the Milan hypertensive rat strain, in which the Na^+ reabsorption increased due to the mutation for Na^+-K^+ ATPase. Taken together with the study demonstrating a significant increase of STK39 and NCC found in WNK4 knockin in hypertension mice[302], the improper salt homeostasis (for example, the increased salt reabsorption) was contributed to hypertension. In addition, WNK-STK39-NKCC1 has also been demonstrated to express in vascular smooth muscle and regulate contractility of blood vessels and blood pressure [303, 304]. Angiotensin II (ANGII), which causes vascular constriction and subsequently increase blood pressure, was reported to induce the activation of WNK-STK39 cascade [305]. The *STK39* null mice demonstrate hypotension, presenting an increased expression of total NKCC1 but a decreased amount of the phosphorylated NKCC1 [306].This observation indicated STK39 is the predominant regulatory kinase of NKCC1 activity. Taken together, these findings demonstrated that STK39 functions predominantly in regulating blood pressure. The overexpression of

STK39 causes hypertension by the over-phosphorylation of the downstream sodium chloride cotransporters to increase salt reabsorption.

Genome-wide association studies (GWAS) provides a promising way to identify the association of genes with the single nucleotide polymorphisms (SNPs) with the particular disease. GWAS has identified that the strong association between *STK39* and hypertension [307]. In two large cohorts of Swedish patients, the rs35929607 A/G polymorphism was revealed to correlate with hypertension, and the female carrying the G-allele had a higher prevalence of hypertension [308]. However, one of Chinese cohort demonstrated that male presented the significant association of *STK39* with hypertension [309]. Nevertheless, another Chinese cohort along with another individual cohort of African Americans argued that none of the *STK39* SNPs was associated with hypertension [310, 311]. Despite these contradictions, from the biological function aspect, STK39 is a vital protein that links WNKs and sodium-chloride cotransporters to regulate sodium absorption and hypertension.

6.1.4.2 The role of STK39 in human cancers

Little is known about the role of STK39 in the cancers. However, based on the fact that cancers present aberrant cell proliferation and migration, it is indicated that there are connections with cation-chloride cotransporters due to their regulation of cell volume. Indeed, Shen *et al.* have demonstrated that KCC3 mRNA was abundant in human cervical cancer and was associated with the process of cervical malignancy [312]. They also observed the enhanced cell growth in KCC3-transfected cells [313]. An increasing number of studies have been shown that that cation-chloride cotransporters play an important role in tumour biology proliferation and migration [314]. The brain tumour originating from glial cells intend to modify the cell volume by releasing K^+ and Cl^- to migrate and invade into the neighbouring brain parenchyma rather metastasis [315, 316]. NKCC1 expression was highly expressed in glioblastoma, the depletion of which resulted in the decreased cell migration and invasion [317]. Haas *et al*. revealed the physical interaction between WNK3 and NKCC1 stimulates the invasion by regulating

cell volume. The malignant glioblastoma showed the increased WNK3 but decreased WNK2 and STK39 [318]. It is of note that this study did not preclude that STK39 as an adaptor protein to facilitate the physical interaction between WNK3 and NKCC1.

Receptor expressed in lymphoid tissues (RELT), which is a member of tumour necrosis factor-α (TNF-α) superfamily, was reported to interact with STK39 through RFxV motif. The interaction then activates p38 mitogen-activated protein kinase (MAPK) [272]. Recently, studies have been revealed the role of STK39 in tumourigenesis [319, 320]. Chiu *et al.* demonstrated that STK39 promoted cervical cancer aggressiveness and tumour formation *via* p38 MAPK, suggesting STK39 may be a potential target for pharmacological intervention [319]. In addition to this study, another independent study on the non-small cell lung cancer (NSCLC) defined STK39 as a novel oncogene [320]. This study showed the high expression of STK39 significantly positively correlated to the advanced tumour stage, large tumour size, metastasis and poor prognosis [320]. The depletion of STK39 led to the decreased cell proliferation by inducing apoptosis through the inactivation of p38 MAPK and decreased migration and invasion [320]. Besides, this study also showed a significant correlation to p38 MAPK.

Little is known about the association between STK39 with breast cancer, but STK39 is expressed at high level in most of breast cancer cell lines investigated in one study [321]. For breast cancer, Fos-related antigen 1 (Fra-1) is a member of the Fos family that forms the heterodimer with the Jun family members. This heterodimerisation forms the activating protein (AP-1) which is a transcription factor regulating cell proliferation and tumorigenesis [322]. Belguise *et al.* demonstrated that the aberrantly hyper-phosphorylated Fra-1 found in the invasive breast cancer cell lines was due to the protein kinase C (PKC) θ activity regulated by STK39 [323]. The normal human prostate and the prostate cancer cell lines express a significantly increased STK39 as a response to androgen treatment in a dose- and time-dependent manner [321]. This suggested that androgen presents a positive regulation of STK39. On the other hand, the prostate cancer cells would disable the STK39-related stress responses resulting in the cancer

metastasis and the primary prostate tumour relapse [324]. It has shown that the reduced STK39 contributed to the breast cancer presenting the resistance to doxorubicin and cyclophosphamide [325]. These studies suggested the importance of STK39 in the development of cancers, treatment resistance and tumour relapse. More importantly, STK39 shows differential biological effects in various malignant tumours, suggesting STK39 (or related signalling pathway) might have differential roles.

6.2 The overview of MAPK

STK39 was defined as an oncogene contributing to the activation of p38 MAPK and regulated apoptosis, and several studies have demonstrated that the sodium chloride cotransporters are associated with MAPK [326, 327]. Additionally, with regards to be relevant to **Chapter 7** in this thesis, the role of MAPK in cancer and apoptosis will be reviewed in this section.

6.2.1 Conventional regulation of MAPK pathways

MAPKs are ubiquitous and evolutionarily conserved kinases that phosphorylate their own and substrates to control fundamental cellular processes such as growth, proliferation, differentiation, migration and apoptosis. The activation of MAPK cascade is initiated by the multiple stimuli [328, 329]. There are three-tiered core signalling modules to subsequently activate MAPK signalling cascade. A MAP kinase kinase kinase (MAP3K) phosphorylates MAP2K on the serine and threonine in the activation loop [330, 331]. Sequentially, MAP2K catalyses MAPK on the tyrosine and threonine within the conserved TxY motif located in the T-loop [330, 331].

MAPKs consist of three family members, the extracellular signal-regulated kinase (ERK1 and ERK2), the p38 MAPK (p38α, p38β, p38δ and p38γ), and the c-Jun NH2-terminal kinase (JNK1, JNK2 and JNK3) (**Figure 6.2**). Raf-MEK1/2-ERK1/2, MLK-MKK4/7-JNK and ASK1/2-MEK3/6-p38 are classical axes in MAPK signalling pathway. Assembly of MAPK cascade components by scaffold proteins is important for efficient phosphorylation and pathway activation. Kinase suppressor of Ras (KSR) has no kinase activity due to the lack of

catalytic lysine residue, but it direct interacts with Raf-1, MEK1/2 and ERK1/2 to form a complex and subsequently facilitates the activation of ERK1/2 (**Figure 6.2**) [332]. In the JNK signalling pathway, it is JNK interacting proteins (JIPs) that functions as a scaffold protein associating with mixed lineage kinases (MLKs), MEK4/7, JNK [333]. JIPs also function as a scaffold in the p38 signalling pathway [334, 335]. p38 family contains four members, whose sequences only show 60% identity within the same family [333]. This property suggests that each family members has highly diverse functions. After activation by ASK1/2, MEK3/6 is allowed to selectively phosphorylate p38 isoforms. p38α, p38δ and p38γ isoforms can be phosphorylated by both MEK3 and MEK6, while p38β is phosphorylated by MEK6 [336]. As the activation of MAPK signalling pathway depends on the phosphorylation at TxY motif within the T-loop, the activity of MAPK can be negatively regulated by the activation of MAPK phosphatases (MKPs) or dual-specificity phosphatase (DSP) [331, 337].

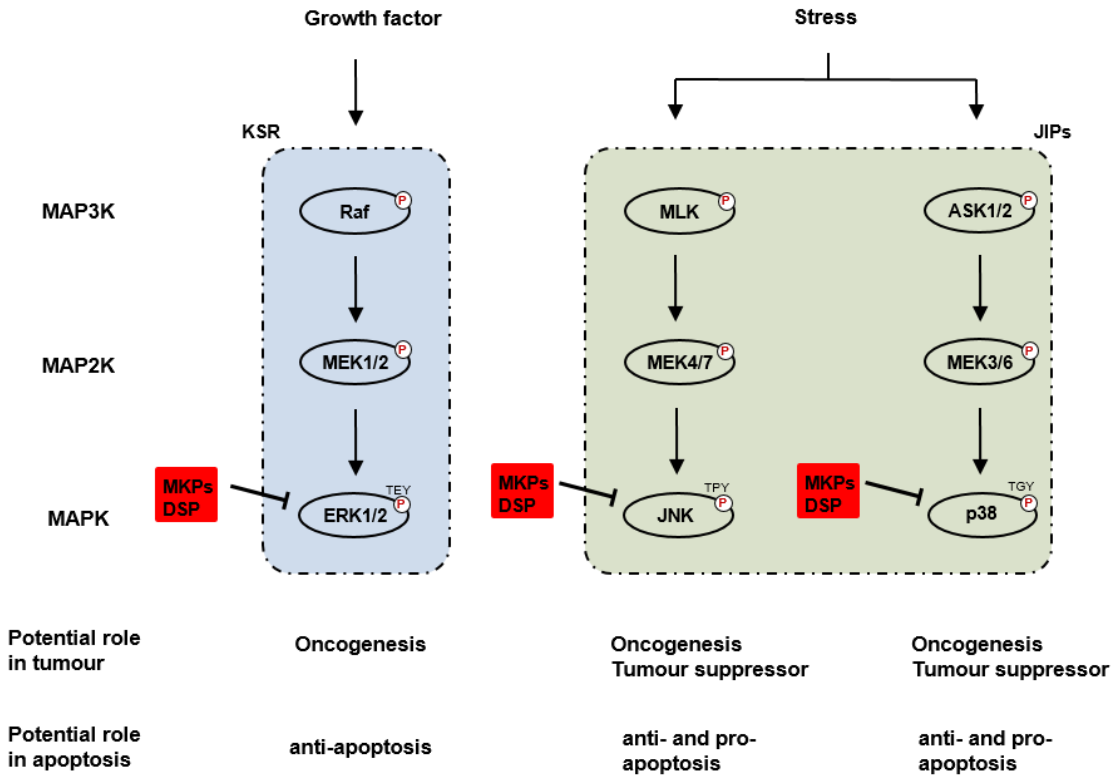

Figure 6.2 Simplified MAPK signalling pathways related to the role in tumour and in apoptosis
Three modules of MAPK signalling cascade. ERKs are activated by growth factors, initiating the signalling axis. KSR (Blue) functions as a scaffold protein to facilitate the phosphorylation. JNK/p38 are preferable to be activated by stress. JIPs (Green) functions as a scaffold protein to facilitate the phosphorylation. The activation of ERK/JNK/p38 depends on the dual-phosphorylation at tyrosine and threonine within the conserved TxY motif. MKPs and DSP functions phosphatase to negatively control the MAPK signalling cascade. The role of each module in tumour and apoptosis is indicated. Summarized from Raman *et al*., 2007, Soares-Silon *et al*., 2016 and Wada *et al*., 2004 [333, 338, 339].

6.2.2 The role of MAPK in human cancers

MAPK pathways convert the extracellular stimuli into a wide range of cellular responses such as immunity [340], apoptosis [339] and cell cycle progression [341]. The deregulation of these cellular responses has been demonstrated as hallmarks of cancer [342], suggesting the importance of MAPK pathways in tumourigenesis and the development of cancer [343]. Cancer cells can utilise these pathways to facilitate their

proliferation, survival and invasion. The deregulation of MAPK pathways has been correlated with human cancer. The ERK signalling pathway is up-regulated and constitutively activated in most human cancers (30%) [344], due to the overexpression of growth factors, *B-Raf* mutations [343, 345, 346]. It has been shown that B-raf presented V600E mutation in the T-loop leading to the constitutive activation of catalytic activity and contributed to the malignant melanoma, colorectal and thyroid cancers [346]. The V600E mutation dramatically enhanced B-raf activity and subsequent MEK-ERK activity. Therefore, ERK pathway is considered as an oncogenic pathway that promotes tumourigenesis [347].

The JNK pathway presents dual functions as either oncogenic or tumour suppressive. For example, JNK1 functions as oncogenic in hepatocellular carcinoma (HCC) with the increased activity to proliferate tumour cells caused by the downregulation of p21, a cell cycle inhibitor [348]. The gene expression analysis confirmed the oncogenic function of JNK in prostate cancer [349]. By contrast, the loss-of-function mutation of JNK3 has been demonstrated to promote the brain tumour [350]. Similar to JNK, the p38 signalling pathway also presents dual functions in apoptosis, and the precise mechanism remains unclear [351]. Lyoda *et al.* revealed that the decreased p38 was associated with HCC, and it showed that p38 had pro-apoptotic function [352]. This study indicated p38 had a tumour suppressive function. However, a number of cancers have been demonstrated to be correlated with the increased phosphorylated p38. [353, 354], indicating its oncogenic function. Nevertheless, the mutations of these pathways result in the inflammatory disorders, which are important for cancer cell survival [355]. In summary, the role of MAPK pathways, especially for JNK/p38 pathways, in human cancers shows the complexity and the precise mechanism is unclear (simplified summarised in **Figure 6.2**). The oncogenic role and the apoptosis controlled by MAPK pathways are dependent on tumour cells.

6.3 Aims and objectives

Considering the frequent down-regulation of LIMD1 in cancers [229], this study aims to identify the synthetic lethal gene encoded the human kinase with LIMD1 loss to provide a novel target for specifically treating LIMD1 negative cancers. Therefore, the key aim of this study is as follows:

- **Aim 1:** Using the concept of synthetic lethality, a screening on Human Kinome siRNA library will be conducted to identify the synthetic lethal target with LIMD1 loss. The investigation of the validated target will be carried on to understand the potential unknown function of LIMD1 and may subsequently represent a novel target for therapy in LIMD1 negative cancers. (**Chapter 7**)

Chapter 7

Identification and investigation of synthetic lethal genes to LIMD1

7 Identification and investigation of synthetic lethal genes to LIMD1

LIMD1, as a tumour suppressor gene, is frequently down-regulated in more than 80% human lung tumours [229]. The loss of LIMD1 enables the cancer cells to grow rapidly and aggressively [229]. Genetic mutations causing the gain-of-function are often druggable, whereas loss-of-function mutations or deletions of tumour suppressors such as LIMD1 often proves much more difficult to target. A synthetic lethality, therefore, was employed to identify the potential protein kinases (or related pathways), whose loss could cause the specific cell death in LIMD1 negative cells.

7.1 Identification of synthetic lethal targets in LIMD1 negative cells

The concept of synthetic lethality is defined as a simultaneous loss of function of two genes causing cell death, while the loss of function of either gene alone does not [356, 357] (**Figure 7.1A**). Therefore, a number of techniques to alter LIMD1 expression in cancer cell lines were employed in this study to generate screening platforms on which the strategy of synthetic lethality was applied to identify protein kinase targets. The isogenic pairs of cell lines with regards to LIMD1 expression were seeded in the format of 96-well plate and treated with Human Kinome siRNA library (**Figure 7.1B**). A synthetic lethal target (kinase) will cause cell death in LIMD1$^{-/-}$ cells rather than LIMD1$^{+/+}$ cells (**Figure 7.1B**).

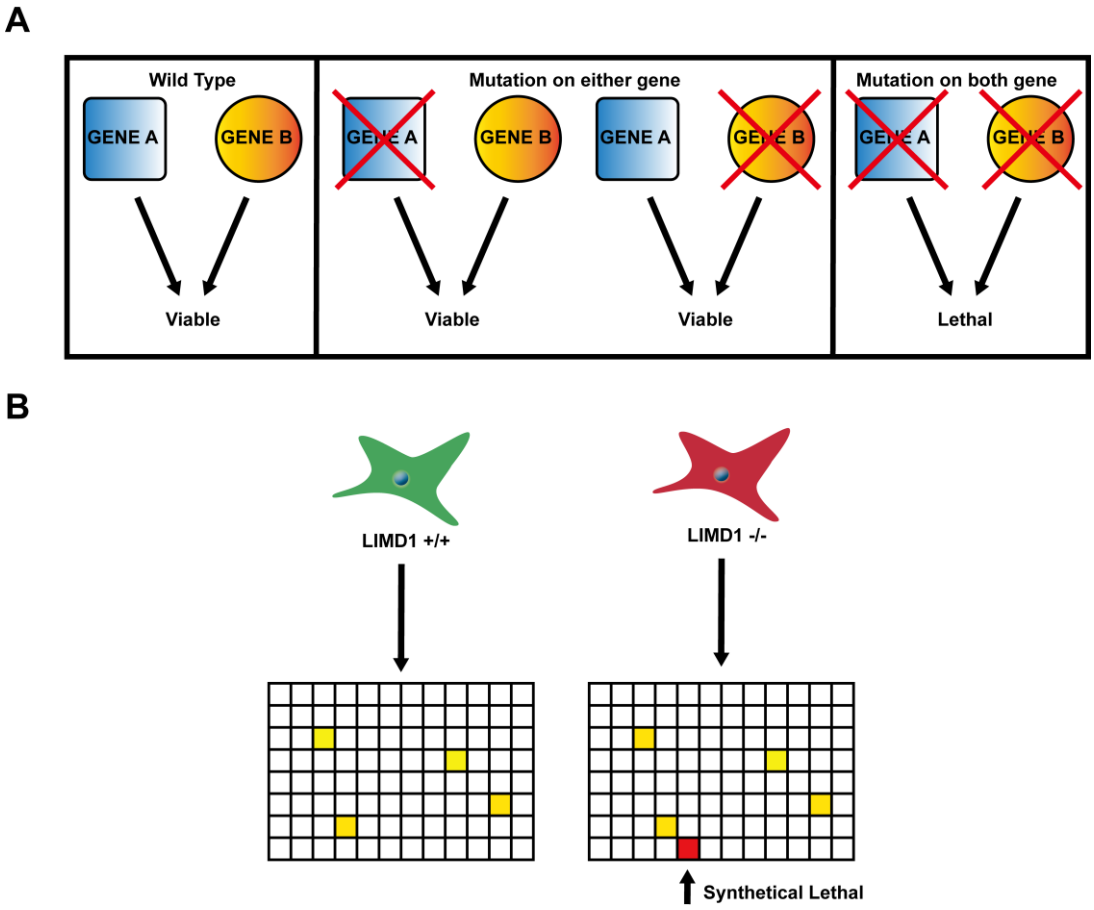

Figure 7.1 The concept of synthetic lethality
A) Simultaneous loss of function of two genes causes cell death, while mutation of either gene alone does not. (Adapted from Sebastian *et al.,* 2011 [357]). ***B)*** An isogenic pair of cell lines expressing LIMD1$^{+/+}$ or LIMD1 $^{-/-}$ was used as the screening platform treated with the individual siRNA targeting the specific human kinase. The ablation of target causing synthetic lethality is highlighted in red. This represents the cytotoxicity to cells with the loss of LIMD1, whereas it spares LIMD1$^{+/+}$ cells.

The initiation of cancer is a process by which a series of genetic mutations drive normal cells to acquire the hallmarks of cancer over time and gradually results in uncontrolled growth, inappropriate invasion, and, ultimately, metastasis. Lung cancer is the leading cause of cancer mortality as a result of late diagnosis and recurrence. Although the well-studied first-line chemotherapy drugs, for example, cisplatin, which interferes with DNA repair mechanisms, has been approved to be clinically successful, cancer cells could

develop resistance to such broad-spectrum drugs. The resistance arises from the alteration of a number of genes and the redundant pathways due to secondary mutations caused by cisplatin [358]. Furthermore, the genetic alteration of cancer cells differs not only between cancer types but also between individuals. Therefore, it is necessary to develop drugs for patients who acquire resistance to the first line drugs or broad-spectrum drugs.

For the screening of the synthetic lethality, the siKinome library which targets the Human Kinome, which is the complete set of protein kinases encoded in the human genome [359]. Protein kinases and phosphatases are responsible for conducting the majority of signal transduction in the cells, regulating the function of proteins by the phosphorylation [359]. Phosphorylation events, therefore, regulate a host of cellular processes such as metabolism, transcription, apoptosis, cellular proliferation, survival and migration. Mutation and dysregulation of human protein kinases correlate to many human diseases, including cancers [360]. In addition, it was revealed in 2004 according to the Cancer Gene Census that the most common protein domain encoded by oncogenes was the protein kinase domain [361]. Two individual studies defined 120 protein kinase mutations in a cohort of 210 specimens, and 157 mutations within 230 kinases in a 441 specimen cohort, respectively [362, 363]. These studies indicated that protein kinases play the crucial roles in the development of cancers. Therefore, there is significant scope and president to develop new therapies by targeting these dysfunctions and mutated protein kinases.

7.1.1 Generation of the screening platforms

To identify synthetic lethal genes with LIMD1, different molecular techniques were used to generate isogenic pairs of cell lines to knockdown, knockout or re-express LIMD1. Lung cancer cell line A549 and cervical cancer cell line HeLa were selected to be the screening platforms in this study due to the original aim (lung cancer treatment), the rapid growth and widely used in anti-cancer studies. In addition, breast cancer cell line MDA-MB-435 was also selected as a screening platform as the result of the lack of LIMD1

expression. Stable knockdown of LIMD1 in A549 was generated by Dr John Foster, using lentiviral plasmid system depending on the short hairpin RNA (shRNA) [1, 364]. The shRNA system results in some of the target RNA remaining at low levels, creating an incomplete knockdown of LIMD1 in A549 shLIMD1 (**Figure 7.2A**). Therefore, the residual LIMD1 expression may affect the cellular processes. As a result, for a total knockout platform for the study of the synthetic lethality with LIMD1 loss, CRISPR-Cas9 gene editing was employed to generate HeLa with the complete knockout of LIMD1 (**Figure 7.2B** and **Figure 11.1**). Furthermore, to study the possible effects on the synthetic lethality with the gain-of-function of LIMD1, the isogenic pair of MDA-MB-435, which was previously reported to not express LIMD1 due to the hyper-methylation of the promoter region [217, 229], lentivirally expressing lentivirus only and LIMD1 were generated (**Figure 7.2C**).

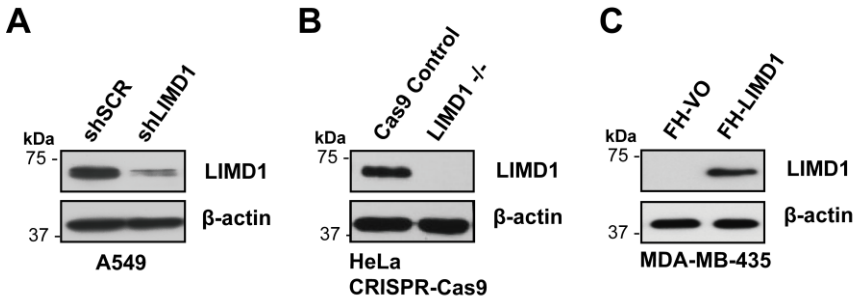

Figure 7.2 Three isogenic pairs of cell lines as the screening platforms were generated with regards to LIMD1 expression by different molecular techniques
Western blot analysis of LIMD1 expression in A549 (made by Dr John Foster), MDA-MB-435 and HeLa (made by Dr Daniel Foxler) isogenic pairs with regards to LIMD1 expression. shSCR, non-targeting scramble shRNA; FH-VO, FlagHis-tagged lentivirus only.

7.1.2 Transfection optimisation

To ensure the transfection reagents were not cytotoxic to the cells, mock transfection was performed to use different transfection reagents in the absence of siRNA (Mock). Besides the cytotoxicity, the transfection efficiency is another important parameter for consideration. PLK1 locates to centrosomes and regulates mitosis, which is an early

trigger for G2/M transition [365, 366]. siRNA targeting *PLK1*, depletion of which induces apoptotic pathway and inhibits cell growth [367], was employed to assess the transfection efficiency according to the inhibitory of cell growth. In addition, the cytotoxicity and transfection efficiency are reagent type- and cell type-dependent [368]. Therefore, the mock transfection and optimisation were conducted on the three isogenic pairs of cell lines (A549, MDA-MB-435 and HeLa).

Two transfection reagents, INTERFERin and Lipofectamine RNAiMAX (hereafter refer to Lipofectamine), were used. More than 80% relative cell viability was considered as an acceptable cytotoxicity, and less than 20% treated with siPLK1 was considered as a good transfection efficiency. The results showed no reagents cytotoxicity on three isogenic pairs according to the relative cell viability of mock (only transfection reagents used) compared with that in Media (**Figure 7.3A-F**). Although the depletion of PLK1 inhibited more than 80% cell growth, which indicated both transfection reagents worked and had the similar transfection efficiency on A549 and HeLa, INTERFERin showed higher toxicity when HeLa was treated with the non-targeting siRNA control (<80%) (**Figure 7.3C**). As a result, both reagents were suitable for the A549 isogenic pair, and Lipofectamine was suitable for HeLa isogenic pair. For MDA-MB-435, to reduce the cytotoxicity caused by Lipofectamine (**Figure 7.3F**), media was changed after 4h post-transfection and achieved a reduction of cytotoxicity (**Figure 7.3G**). Taken together, according to the mock transfection and optimisation of two transfection agents, Lipofectamine showed lower cytotoxicity and higher transfection efficiency in three different cell lines. Therefore, it was used for the library screening.

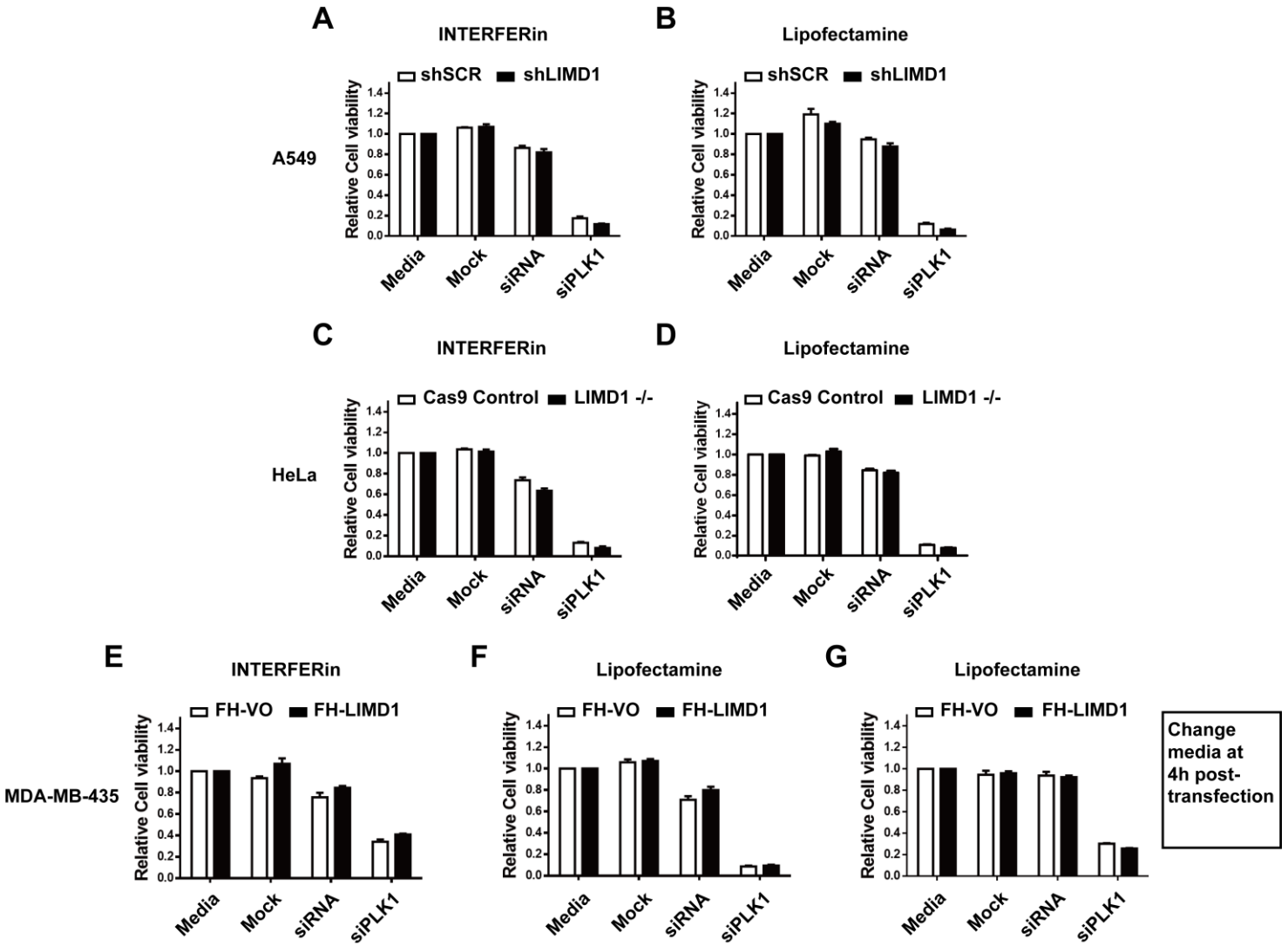

Figure 7.3 Optimisation of transfection using two transfection reagents on three isogenic pairs of cell lines

Cells were maintained in **Media**, transfected without siRNA (**Mock**), or transfected with the indicated siRNA, non-targeting (**siSCR**), or **PLK1** siRNA (**siPLK1**). ***A***, ***C&F)*** INTERFERin was optimised. ***B***, ***D***, ***E&G)*** Lipofectamine was optimised. Media was only changed after 4h post-transfection in ***G)***. Data shown are mean ±SEM, n=3.

7.1.3 Human Kinome siRNA Library screening on three different cell-based platforms

Human Kinome siRNA library (G-003505, Dharmacon) contains 720 kinases and pseudokinases for sufficient silencing of the target gene expression, which was previously used for identification of early regulators of cell proliferation [369]. Three pairs of isogenic platforms A549, MDA-MB-435 and HeLa were applied to screen Human Kinome siRNA Library using the optimal transfection reagents (Lipofectamine). Z-score was calculated for each well treated with the individual siRNA in each cell line according to the cell viability (details described in **Chapter 2.3**). It describes the difference in cell viability between cells treated with the individual siRNA and the median of the whole population. The individual dot in **Figure 7.4** implied how great effect on the cell growth with the depletion of each gene. The positive value indicated the increasing growth of the cells, while the negative value indicated an inhibitory or cytotoxicity to the cells (**Figure 7.4** and **Table 11.1**). However, most of the dots located in the range from -1 to 1 (**Figure 7.4**). This was considered as no effects on the cells when treated with the specific siRNA. Therefore, with the aim of this project that finds the specific siRNA would cause cell death in LIMD1$^{-/-}$ but not in LIMD1$^{+/+}$ cell line, the siRNAs that present the z-score with the greater negative value in LIMD1$^{-/-}$ and the greater positive value in LIMD1$^{+/+}$ are required to be investigated.

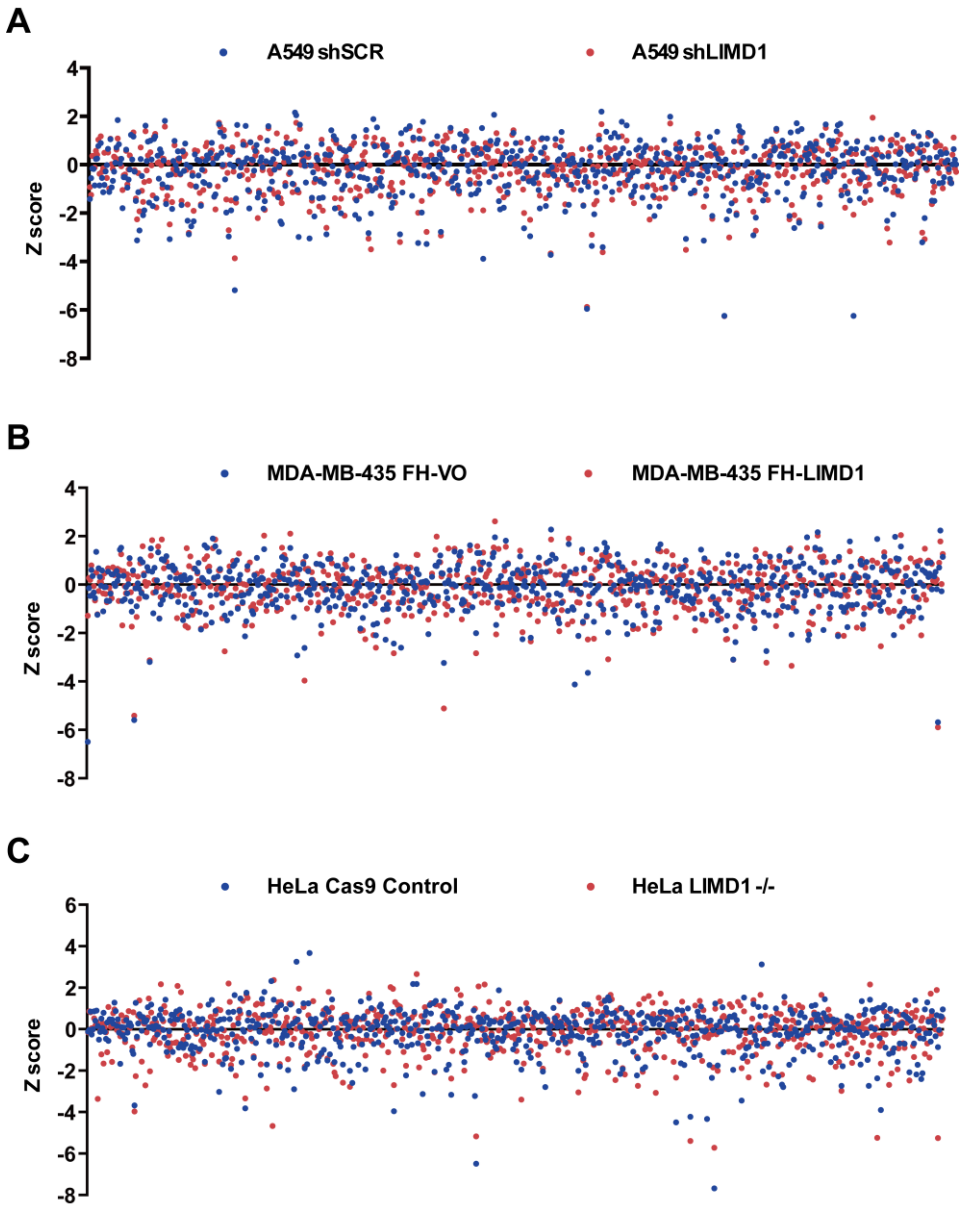

Figure 7.4 Z-score of the human kinome siRNA library screening on three isogenic pairs of cell lines
A) A549 isogenic pair (shSCR and shLIMD1), ***B***) MDA-MB-435 isogenic pair (FH-VO and FH-LIMD1) and ***C***) HeLa CRISPR-Cas9 isogenic pair (Cas9 Control and LIMD1$^{-/-}$) were screened against the Human Kinome siRNA Library containing 720 kinases at 50nM concentration in 96-well plate format. Z-score of individual siRNA targeting the specific kinase on each cell line was calculated. Z-score was considered as a measurement of cell growth (positive value) or cell death (negative value). The positive value indicated the increasing growth of the cells, while the negative value indicated an inhibitory or cytotoxicity on the cells

To identify the synthetic lethal protein kinase with LIMD1 that only kill LIMD1 negative cell line, ΔZ-score, which is the difference in Z-score between LIMD1 negative cell line and LIMD1 positive cell line, was generated (**Figure 7.5** and **Table 11.1**)**.** Therefore, the greater of ΔZ-score in the negative direction, the greater of the synthetic lethality with LIMD1 was. According to ΔZ-score in the negative direction, the top 10 'hits' were ranked on three isogenic pairs (**Figure 7.6**). STK39, AAK1, and DCK respectively showed the greatest synthetic lethality with LIMD1 in A549, MDA-MB-435, and HeLa isogenic pairs (**Figure 7.6**). However, there was no overlapping 'hit(s)', and as a result, further investigation and data analysis were required.

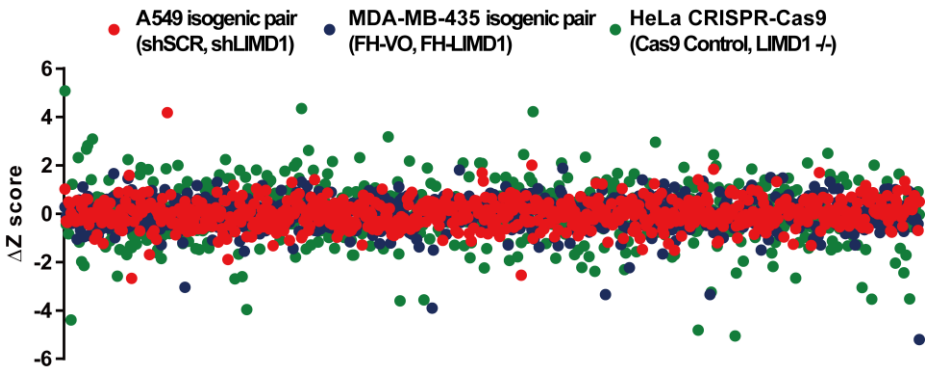

Figure 7.5 ΔZ-score was generated to identify the potential 'hits' from the screening on three isogenic pairs of cell lines
ΔZ-score is the difference in the Z-score of the LIMD1 negative cell line and LIMD1 positive cell line, indicating the level of the synthetic lethality according to how great the value of ΔZ-score is in the negative direction.

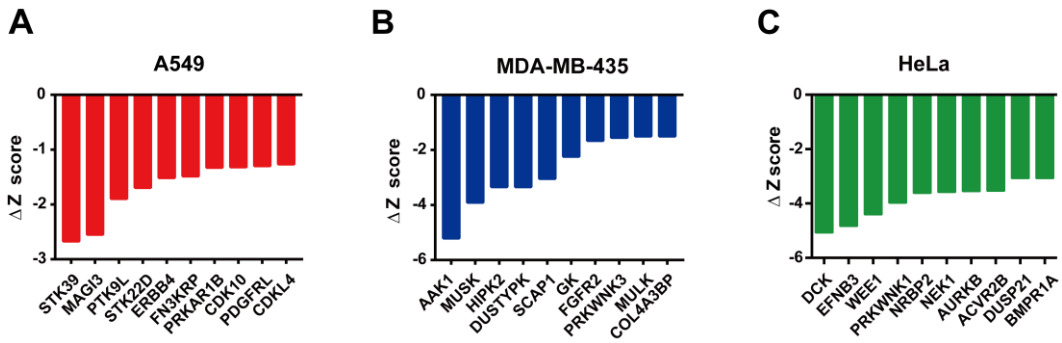

Figure 7.6 Top 10 'hits' are ranked by ΔZ-score on each isogenic pair of cell lines
The top 10 'hits' identified according to ΔZ-score on ***A)*** A549 isogenic pair; ***B)*** MDA-MB-435 isogenic pair; ***C)*** HeLa isogenic pair.

7.2 Target validation from Human Kinome siRNA Library screen

As no common synthetic lethal 'hits' to LIMD1 were identified in all three isogenic pairs of cell lines (**Figure 7.6**), it was decided to investigate whether there were any common synthetic lethal pathways. DAVID pathway analysis was therefore employed to identify enriched functionally-related gene groups [370, 371]. The complete results of DAVID analysis are shown in

Table 11.2-11.4. In addition to the DAVID pathway analysis, cell-based target validation was also conducted for the top 'hits' from the screening.

7.2.1 Investigation of the common synthetic lethal pathways by the DAVID pathway analysis

The results of DAVID analysis were presented based on two databases (KEGG and BioCarta). Upon KEGG database, there were some overlapping pathways from top 100 'hits' across three cell platforms. The following pathways occurred in any two or all cell types according to the statistical significance (PValue): MAPK signalling pathway (A549 and HeLa, **Figure 7.7A** and **Figure 7.7E**), neurotrophin signalling pathway (A549 and HeLa, **Figure 7.7A** and **Figure 7.7E**) and ErbB signalling pathway (MDA-MB-435 and HeLa, **Figure 7.7C** and **Figure 7.7E**). By considering the number of genes involved in the pathways, the common pathways were MAPK signalling pathway (A549 and HeLa, **Figure 7.7A, Figure 7.7B** and **Figure 7.7F**), Rap1 signalling pathway (A549 and MDA-MB-435, **Figure 7.7A, Figure 7.7B** and **Figure 7.7D**) and neurotrophin signalling pathway (A549 and HeLa, **Figure 7.7B and Figure 7.7F**). Therefore, MAPK signalling pathway, Rap1 signalling pathway and neurotrophin signalling pathway were two common enriched pathways containing the most significance and highest number of genes among top 100 'hits' from the library screening.

According to BioCarta database, MAPK signalling pathway occurred in all three cell platforms with not only the greatest significance but also the most enriched pathway

(**Figure 7.8**). Taken together, the combined result of KEGG and BioCarta showed MAPK signalling pathway is the most enriched pathway (**Figure 7.7** and **Figure 7.8**), indicating the most synthetically lethal kinases across the three screening platforms were involved in the MAPK signalling pathway (**Figure 7.9**).

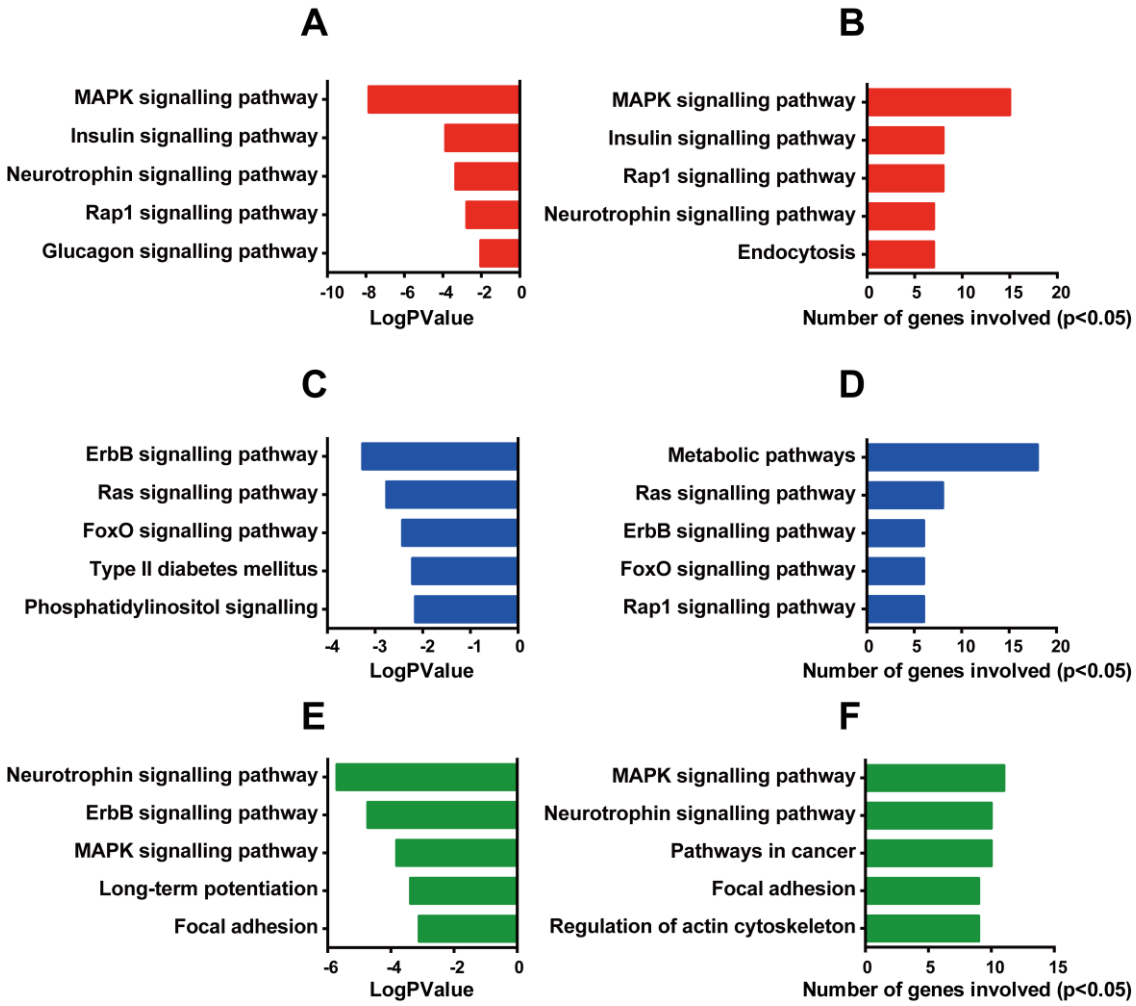

Figure 7.7 KEGG data-based DAVID analysis of top 100 'hits' from three isogenic pairs of cell lines. Top 5 enriched pathways from top 100 'hits' of screening were ranked by LogPValue on ***A*)** A549 isogenic pair, ***C*)** MDA-MB-435 isogenic pair and ***E*)** Hela isogenic pair. Top 5 enriched pathways from top 100 'hits' of screening was ranked by the number of genes involved in ***B*)** A549 isogenic pair, ***D*)** MDA-MB-435 isogenic pair and ***F*)** HeLa isogenic pair.

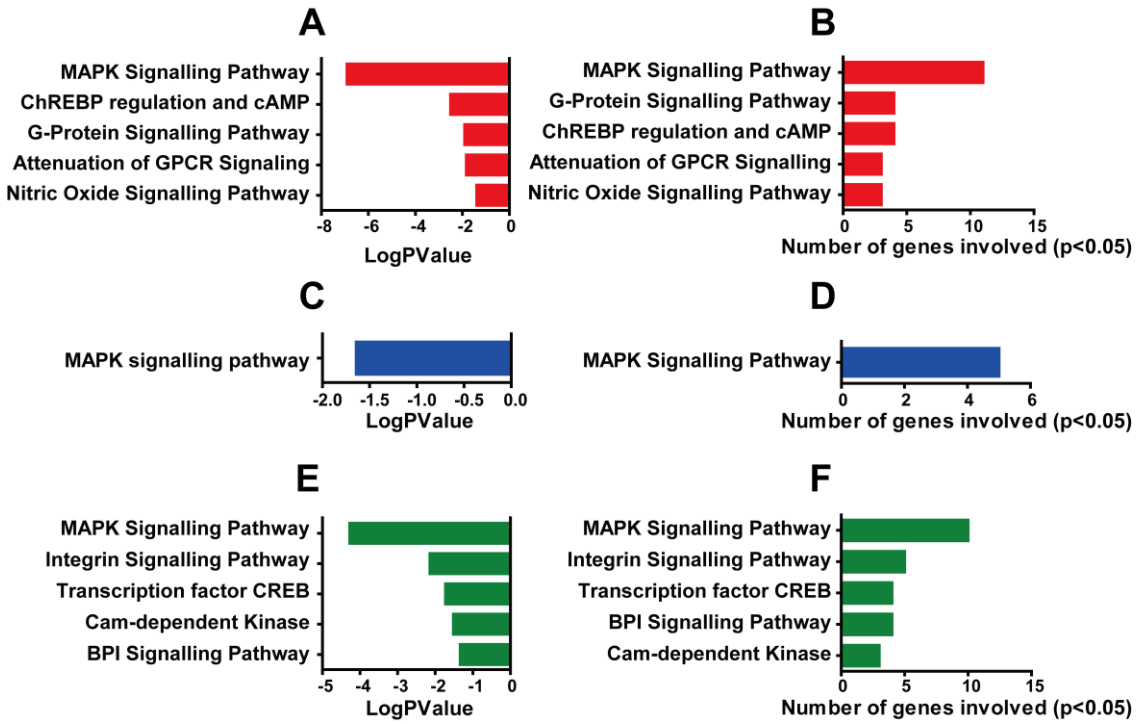

Figure 7.8 BioCarta data-based DAVID analysis of top 100 'hits' from three isogenic pairs of cell lines. Top 5 enriched pathways from top 100 'hits' of screening were ranked by LogPValue on ***A*)** A549 isogenic pair, ***C*)** MDA-MB-435 isogenic pair and ***E*)** Hela isogenic pair. Top 5 enriched pathways from top 100 'hits' of screening was ranked by the number of genes involved in ***B*)** A549 isogenic pair, ***D*)** MDA-MB-435 isogenic pair and ***F*)** HeLa isogenic pair.

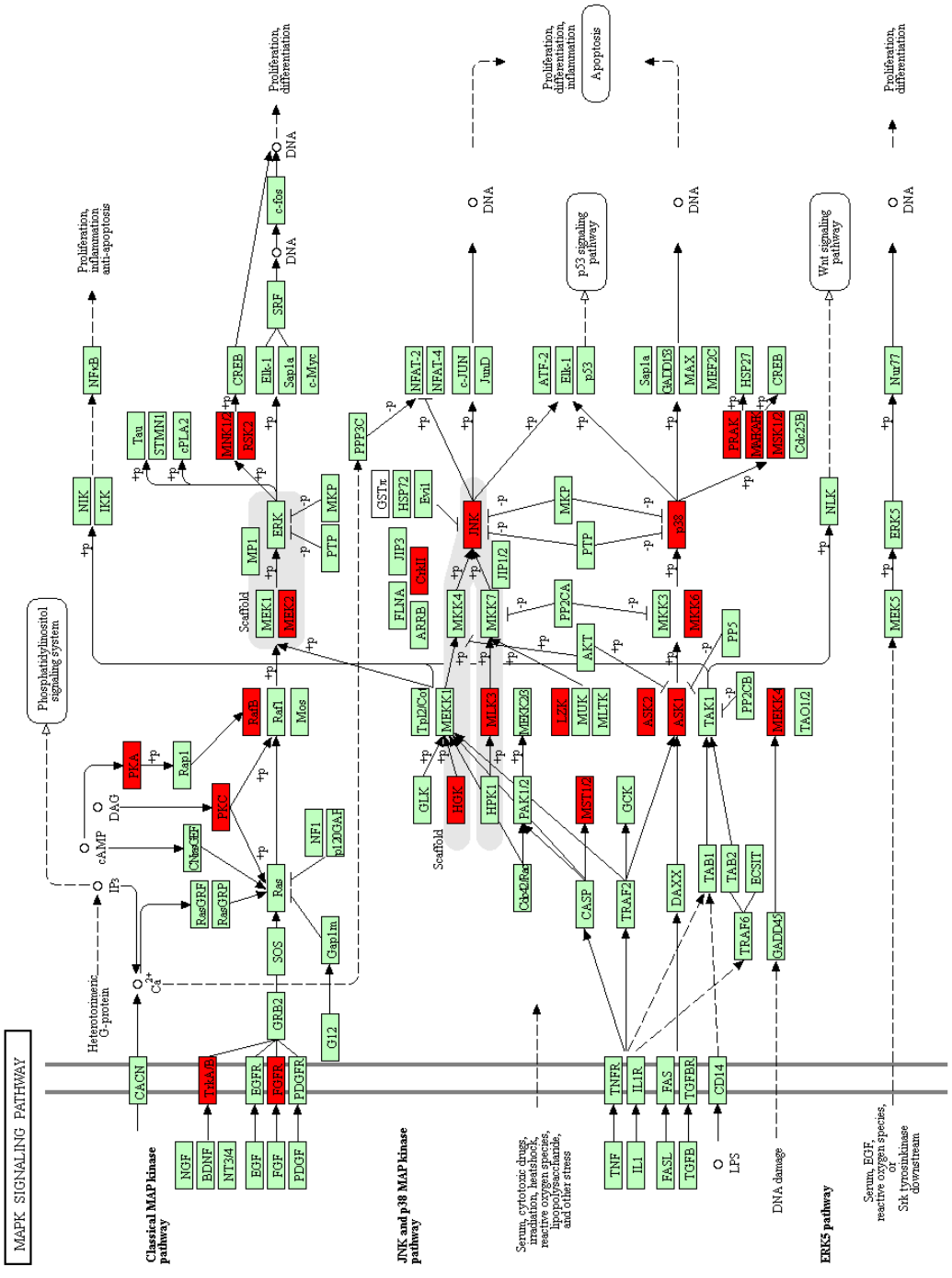

Figure 7.9 Most kinases from top 100 'hits' were involved in the MAPK signalling pathway
The kinases from the top 100 'hits' involved in the MAPK signalling pathway were highlighted in red. The pathway map was obtained from (KEGG) [372].

7.2.2 Knockdown of STK39 is synthetic lethal to LIMD1 negative cells

The identification of multiple kinases within the MAPK signalling pathway as synthetically lethal with LIMD1 was therefore investigated. MAPK signalling contains p38 signalling pathway which is activated by STK39 [272]. STK39 was a top 'hit' on A549 from the screen (**Figure 7.6A**). STK39 therefore within this pathway was targeted in validation experiments in the HeLa CRISPR isogenic cell line pair, as this conferred the cleanest mechanistic platform for interrogating LIMD1 ablation. SMARTPool (SP) of each kinase was used in Kinome siRNA Library screening. Therefore, four individual siRNAs contained in the SMARTPool were also used in target validation to minimise the off-target effects. To define the synthetic lethality with LIMD1 in the target validation, two basic rules were followed: **1**) more than 25% difference in the relative cell viability between isogenic cell lines with statistical significance was considered to be synthetic lethal and **2**) SMARTPool must cause the synthetic lethality with LIMD1. The validation on HeLa isogenic pair showed that all four individual siRNA (#1-4) targeting STK39 could cause the synthetic lethality with LIMD1 loss, and the SMARTPool and siRNA #1 showed the least cell viability on LIMD1$^{-/-}$ cell line (**Figure 7.10**). Therefore, the SMARTPool and siRNA #1 were used in the whole project.

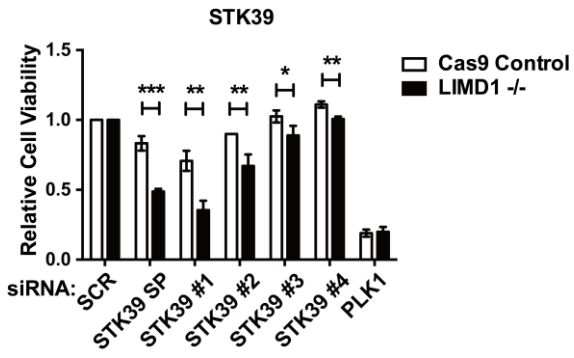

Figure 7.10 STK39 validation on HeLa isogenic pair of cell lines
Cells were transfected with the indicated siRNAs: Non-targeting (siSCR); SMARTPool, (SP) and individual siRNA, (#1, #2, #3, and #4). Cell viability was measured by CellTiter-Glo Luminescent Cell Viability Assay. Data shown are mean ±SEM, n=3. *, p<0.05. **, p<0.01. ***, p<0.001

The further validation of STK39 was performed on A549 isogenic pair. The results showed a significant difference in cell viability with LIMD1 loss in A549 isogenic pair not only for the SMARTPool but siRNA #1 as well (**Figure 7.11A**). The result also showed STK39 mRNA was repressed by 80% when treated with STK39 siRNAs in A549 isogenic pair (**Figure 7.11B**). This indicated a good knockdown efficiency of STK39 in A549 isogenic pair. Taken together, STK39 was validated to be synthetically lethal for LIMD1 in A549.

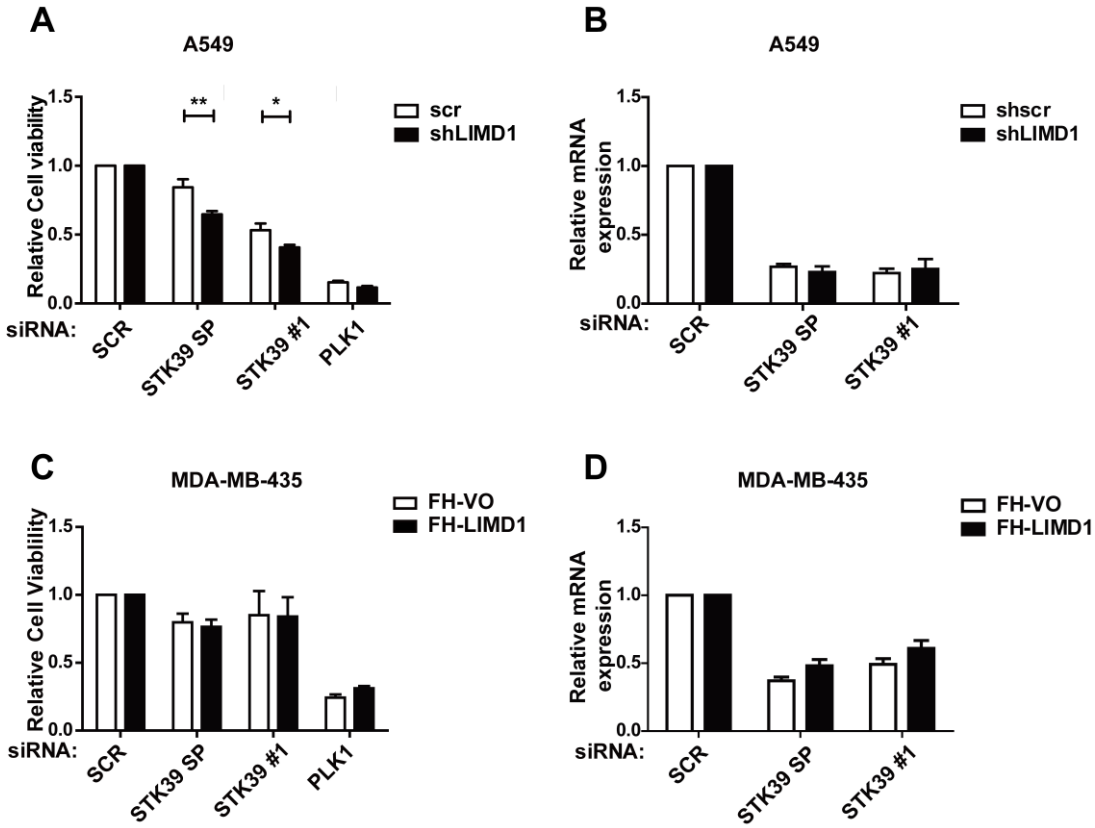

Figure 7.11 Further validation of STK39 siRNAs on A549 and MDA-MB-435 isogenic pairs
***A*)** A549 isogenic pair of cell lines were transfected with the indicated siRNAs. Cell viability was measured by CellTiter-Glo Luminescent Cell Viability Assay and relative to the value of SCR. ***B*)** qRT-PCR analysis of STK39 siRNA knockdown efficiency. ***C*)** MDA-MB-435 isogenic pair of cell lines were transfected with the indicated siRNAs. Cell viability was measured by CellTiter-Glo Luminescent Cell Viability Assay and relative to the value of SCR. ***D*)** qRT-PCR analysis of STK39 siRNA knockdown efficiency. SCR, non-targeting siRNA. SP, SMARTPool. siRNA #1, the individual siRNA of STK39 contained in the SMARTPool. Data shown are mean ±SD, n=3. *, p<0.05. **, p<0.01.

The validation on MDA-MB-435 showed the knockdown of STK39 did not kill both cell lines; the relative cell viability did not significantly change when treated with the SMARTPool and siRNA #1 (**Figure 7.11C**). In addition, the qRT-PCR result showed the knockdown efficiency of SKT39 siRNAs in MDA-MB-435 isogenic pair was poor (**Figure 7.11D**). For example, the poorest transfection efficiency was 50% repression of SKT39 mRNA in FH-LIMD1 line (**Figure 7.11D**). These results indicated there might be no synthetic lethality with LIMD1 in MDA-MB-435 treated with STK39 siRNAs, which may be due to the poor transfection efficiency.

To elaborate the synthetic lethality of STK39, HeLa CRISPR-Cas9 isogenic pair was treated with STK39 siRNAs. The results confirmed that knockdown of STK39 by the SMARTPool, and siRNA #1 caused a synthetic lethality with LIMD1 loss (**Figure 7.12A**). The knockdown efficiency of STK39 mRNA was around 75% (**Figure 7.12B** and **Figure 7.12C**). STK39 siRNAs resulted in a rounding-up effect on the adherent cells (**Figure 7.12D**). This morphologic change by STK39 siRNAs was observed more in the LIMD1 negative cells, which directly represented the significant synthetic lethality with LIMD1 loss.

The clonogenic assay is to assess the effectiveness on the survival and proliferation of cells under the specific treatment. Therefore, it was employed to investigate the effects on the survival and proliferation caused by the knockdown of STK39. For Cas9 Control, knockdown of STK39 by the SMARTPool and siRNA #1 inhibited the cell colony formation by 45% and 40% respectively, whereas they inhibited the colony formation by70-80% when there was no LIMD1 expression (**Figure 7.12E and F**). This indicated the ablation of STK39 dramatically ($p<0.001$) reduced the proliferation rate in LIMD1$^{-/-}$ cell line, which supports its synthetic lethality to LIMD1.

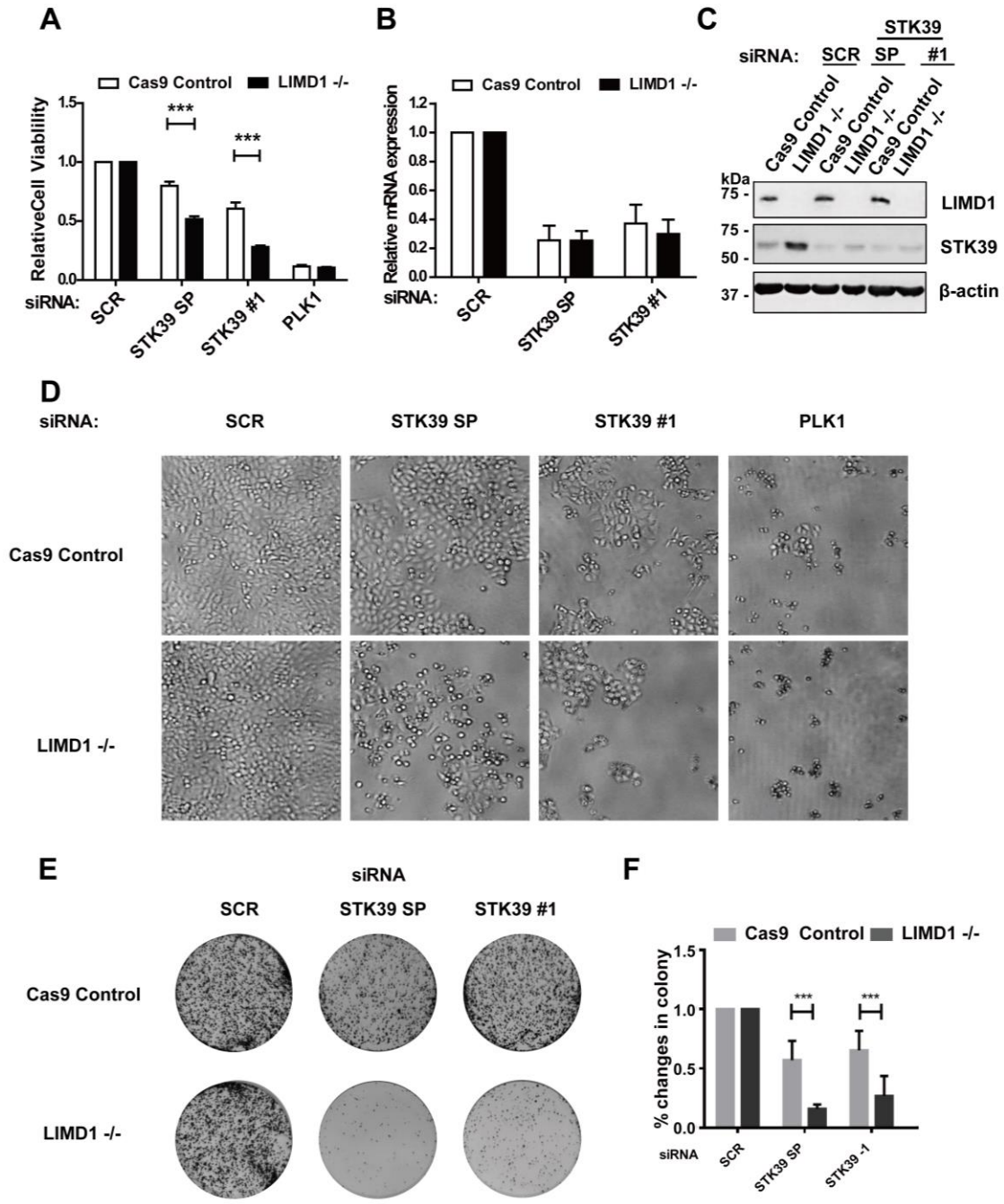

Figure 7.12 Further validation of STK39 on HeLa CRISPR-Cas9 isogenic pair

***A*)** Cells transfected with the indicated siRNAs were measured by CellTiter-Glo Luminescent Cell Viability Assay. ***B*)** qRT-PCR analysis of STK39 siRNAs knockdown efficiency. ***C*)** Western blot analysis of STK39 siRNAs knockdown efficiency. ***D*)** Cells morphological changes treated with the indicated siRNAs were observed by the bright field microscope (400x). ***E*)** Clonogenic assay of HeLa isogenic pair treated with the indicated siRNAs. ***F*)** The percentage of the change in colony numbers in the indicated siRNAs-treated cells. SCR, non-targeting siRNA. SP, SMARTPool. STK39 #1, the individual siRNA contained in the SMARTPool. Data shown are mean ±SD, n=3. ***, p<0.001.

7.2.2.1 Knockdown of STK39 caused the reduction of p38 activity and induced apoptosis in LIMD1 negative cells

DAVID pathway analysis showed MAPK signalling was enriched for the synthetic lethality with LIMD1 loss (**Chapter 7.2.1**). p38 signalling pathway was previously reported to be activated by STK39 [272]. In addition, according to the KEGG pathway (**Figure 7.7**), p38 along with its three downstream effectors were in the top 100 'hits'. Therefore, to investigating whether p38 MAPK signalling pathway was altered with the depletion of STK39, the expression of p38 and phospho-p38 (p-p38) were examined in HeLa isogenic pair. These experiments/analysis showed that LIMD1 knockout caused an increased STK39 expression and in turn increased p-p38 expression, but not the total p38 expression (**Figure 7.13A**). These data were in agreement with the previous report that p38 is activated by STK39 [272]. Intriguingly, knockdown of STK39 showed a different pattern in p-p38 expression between HeLa CRISPR-Cas9 isogenic pair. In LIMD1 expressing line (Cas9 Control), p-p38 remained unchanged with the depletion of STK39, whereas p-p38 expression decreased in LIMD1$^{-/-}$ line (**Figure 7.13B**). This indicated the validated synthetic lethality of STK39 with LIMD1 might be due to the dephosphorylation of p38 and therefore possible inactivation of p38 and its downstream signalling.

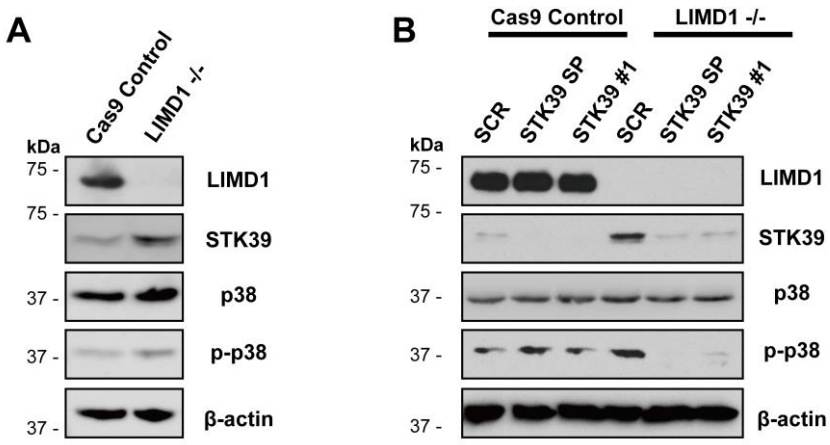

Figure 7.13 p38 and p-p38 expression in HeLa CRISPR-Cas9 isogenic pair altered
***A*)** Western blot analysis of the indicated proteins in HeLa CRISPR-Cas9 isogenic pair. ***B*)** Western blot analysis of the indicated proteins in HeLa CRISPR-Cas9 isogenic pair treated with the indicated siRNAs. SCR, non-targeting siRNA. SP, SMARTPool.

p38 signalling is involved in modulating and regulating apoptosis [339, 373]. Depending on the cell type and stimuli, p38 can function as a pro-apoptotic mediator or an anti-apoptotic mediator; for example, p38 induces apoptosis in HCT-116 (colon cancer), whereas p38 presents anti-apoptosic function in LNCap (prostate cancer). Therefore, Annexin V/(PI) staining was used to investigate whether knockdown of STK39 leads to the apoptosis in HeLa isogenic pair. Compared to Cas9 Control line, there was a significant apoptotic induction in LIMD1$^{-/-}$ line (**Figure 7.14**). This indicated the synthetic lethal caused by knockdown of STK39 in HeLa CRISPR-Cas9 isogenic pair resulted from the apoptosis.

In summary, loss of LIMD1 in HeLa cell line altered the expression of STK39 and in turn caused the dephosphorylation of p38. The synthetic lethality of STK39 to LIMD1 loss was caused by apoptosis according to these observations.

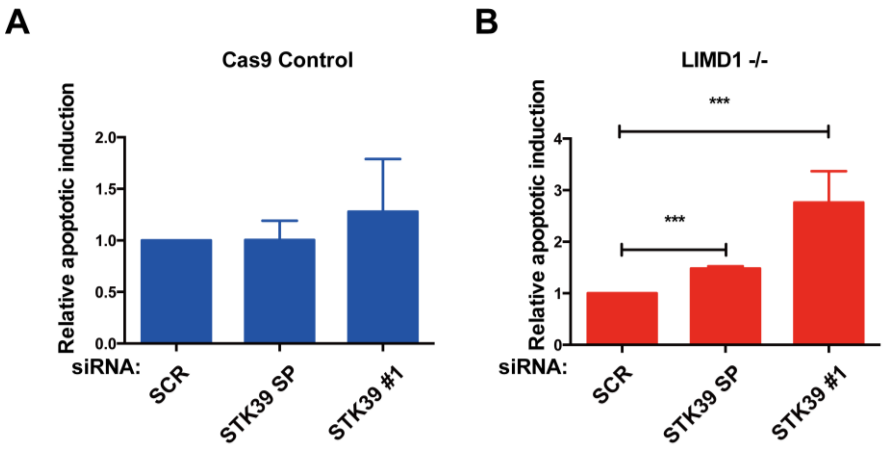

Figure 7.14 Apoptotic induction of HeLa CRISPR-Cas9 treated with STK39 siRNAs
A) Annexin V/PI analysis of the apoptotic induction of HeLa Cas9 control cell line treated with STK39 siRNA (SMARTPool and siRNA). ***B)*** Annexin V/PI analysis of the apoptotic induction of HeLa LIMD1$^{-/-}$ cell line treated with STK39 siRNA (SMARTPool and siRNA #1). SCR, non-targeting siRNA. SP, the SMARTPool of STK39 siRNAs. STK39 #1, the individual siRNA of STK39 contained in the SMARTPool. Data shown are mean ±SEM, n=3. ***, p<0.001.

7.2.3 Validation of the top 'hits' from the screening by the cell-based assay

Apart from the DAVID pathway analysis, cell-based target validation was also employed using HeLa isogenic pair with the complete LIMD1 knockout. AAK1 and HIPK2 from the screening of MDA-MB-435, the top 5 'hits' from the screening of A549, and the top 10 'hits' from the screening of HeLa CRISPR-Cas9 were validated. AAK1, which was the top 'hit' in MDA-MB-435 (**Figure 7.6B**), showed a significant difference in cell viability (**Figure 7.15A**), but it did not result in the sufficient synthetical lethality (referred to the basic rules described in **Chapter 7.2.2**). Therefore, AAK1 was not validated as a synthetic lethal with LIMD1 loss.

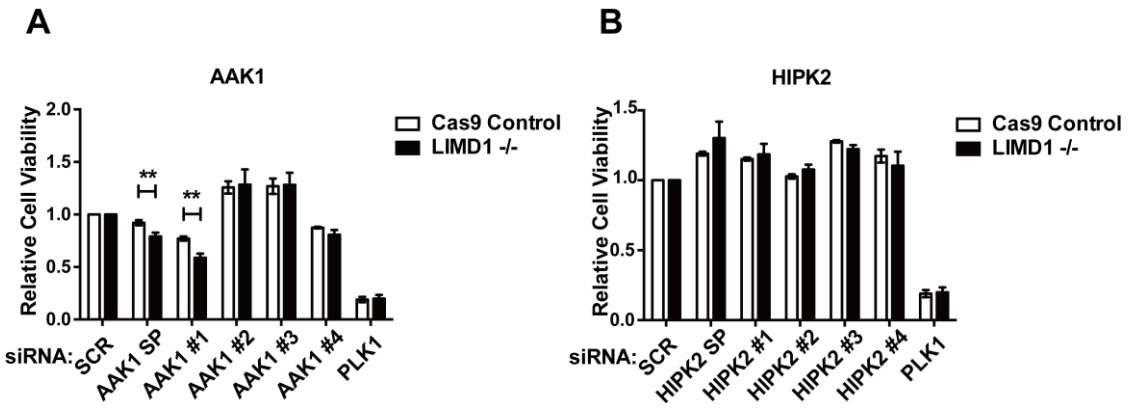

Figure 7.15 Target validation on HeLa isogenic pair of cell lines
Cells were transfected with the indicated siRNAs. SCR, Non-targeting. SP, the SMARTPool of siRNAs. #1, #2, #3, and #4 represent the individual siRNA. Cell viability was measured by CellTiter-Glo Luminescent Cell Viability Assay. ***A)*** AAK1. ***B)*** HIPK2. Data shown are mean ±SEM, n=3. **, p<0.01.

For the 'hits' screened from A549 (**Figure 7.6A**), although MAGI3, TWF2/PTK9L, TSSK1B/STK22D and ERBB4 showed the statistically significant difference in cell viability, they did not cause lethal to LIMD1 negative cells (**Figure 7.16**). The validation results of the top 10 'hits' from HeLa isogenic pair showed that only ACVR2B presented a significant synthetic lethality with LIMD1 loss (**Figure 7.17 and Figure 7.18**). Taken together, ACVR2B was validated as a synthetic lethal target with LIMD1 loss due to that

more than 25% difference in cell viability with significance and synthetic lethality in SMARTPool were observed (**Figure 7.17**)

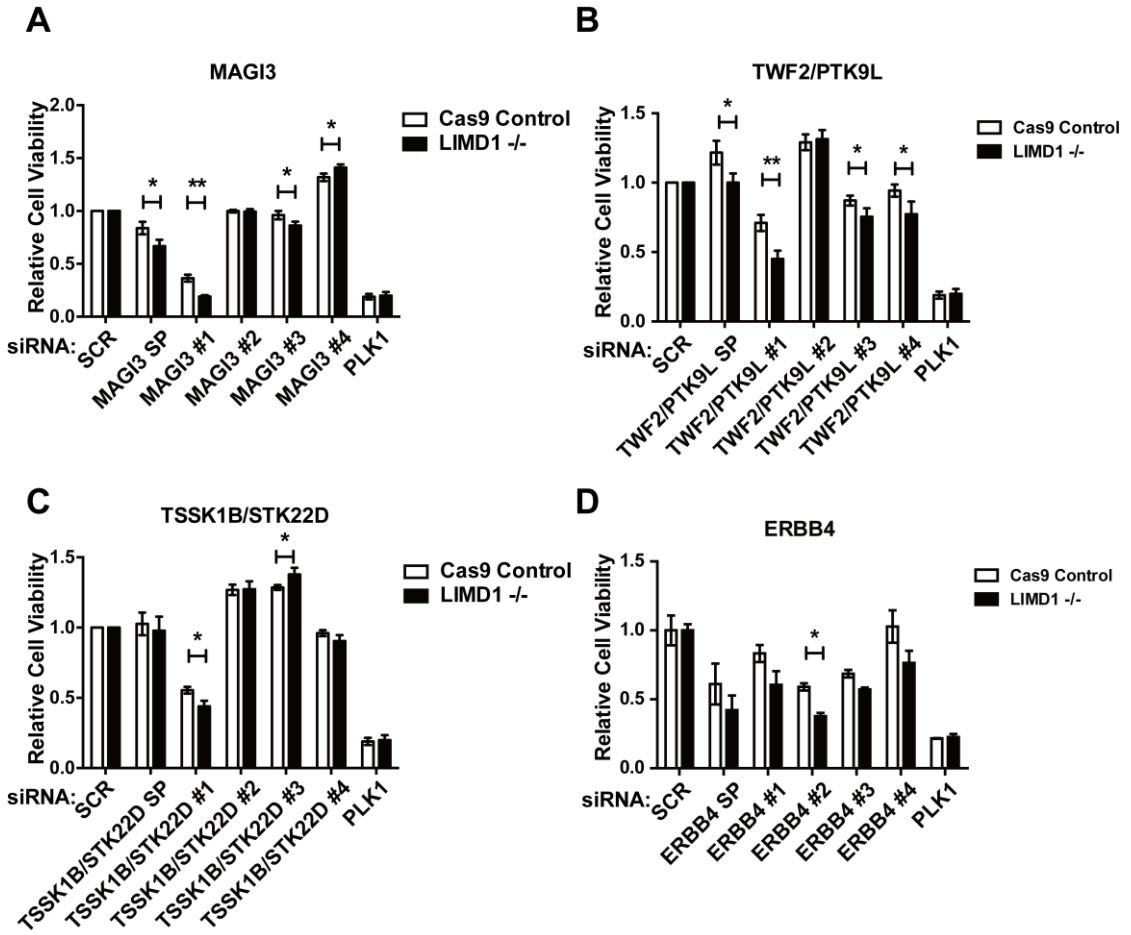

Figure 7.16 Target validation on HeLa isogenic pair of cell lines
Cells were transfected with the indicated siRNAs. SCR, Non-targeting. SP, the SMARTPool of siRNAs. #1, #2, #3, and #4 represent the individual siRNA. Cell viability was measured by CellTiter-Glo Luminescent Cell Viability Assay. ***A*)** MAGI3. ***B*)** TWF2/PTK9L. ***C*)** TSSK1B/STK22D. ***D*)** ERBB4. Data shown are mean ±SEM, n=3. *, p<0.05. **, p<0.01. ***, p<0.001.

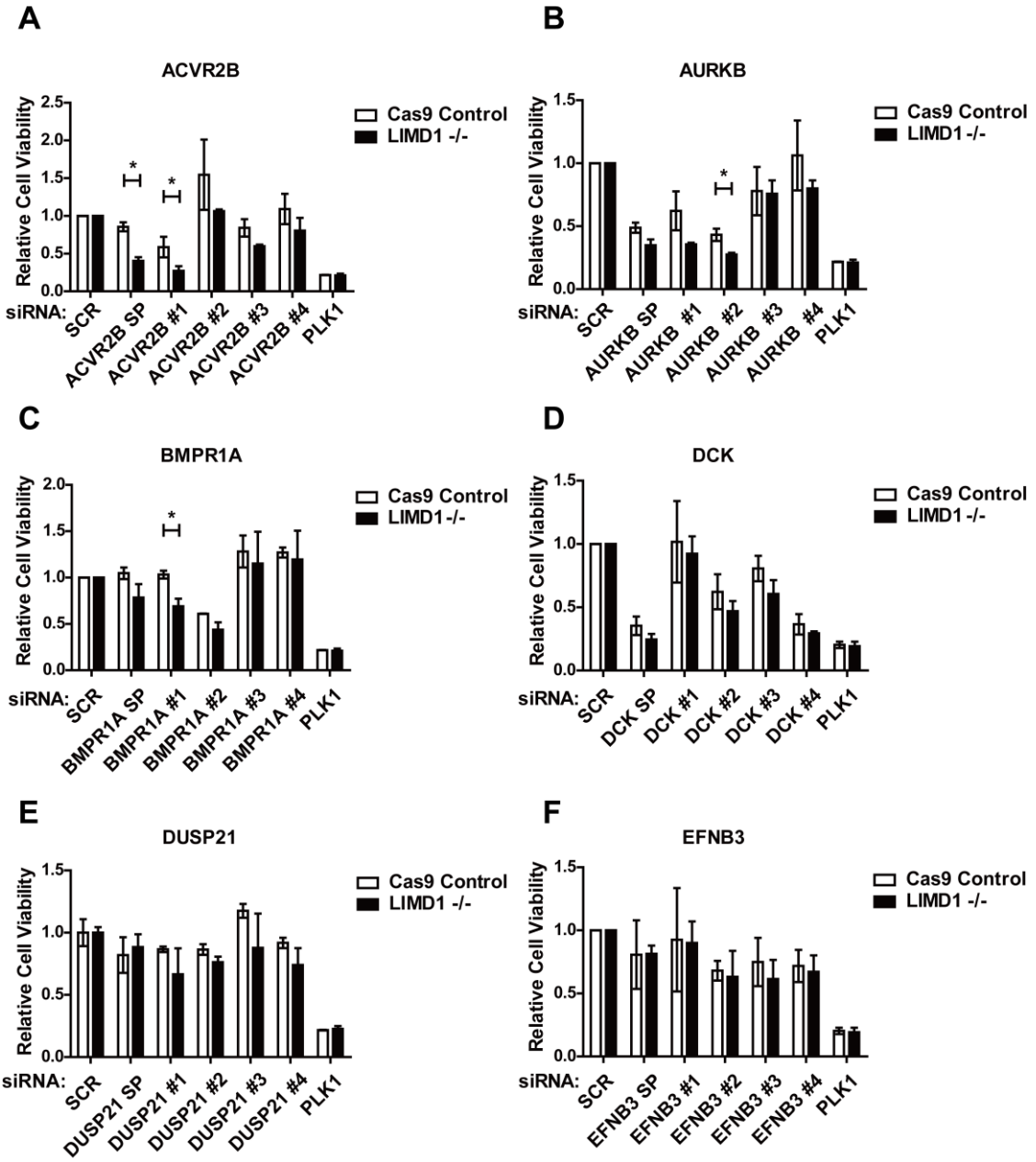

Figure 7.17 Target validation on HeLa isogenic pair of cell lines

Cells were transfected with the indicated siRNAs. SCR, Non-targeting. SP, the SMARTPoolof siRNAs. #1, #2, #3, and #4 represent the individual siRNA. Cell viability was measured by CellTiter-Glo Luminescent Cell Viability Assay. ***A***) ACVR2B. ***B***) AURKB. ***C***) BMPR1A. ***D***) DCK. ***E***) DUSP21. ***F***) EFNB3. Data shown are mean ±SEM, n=3. *, p<0.05. **, p<0.01. ***, p<0.001.

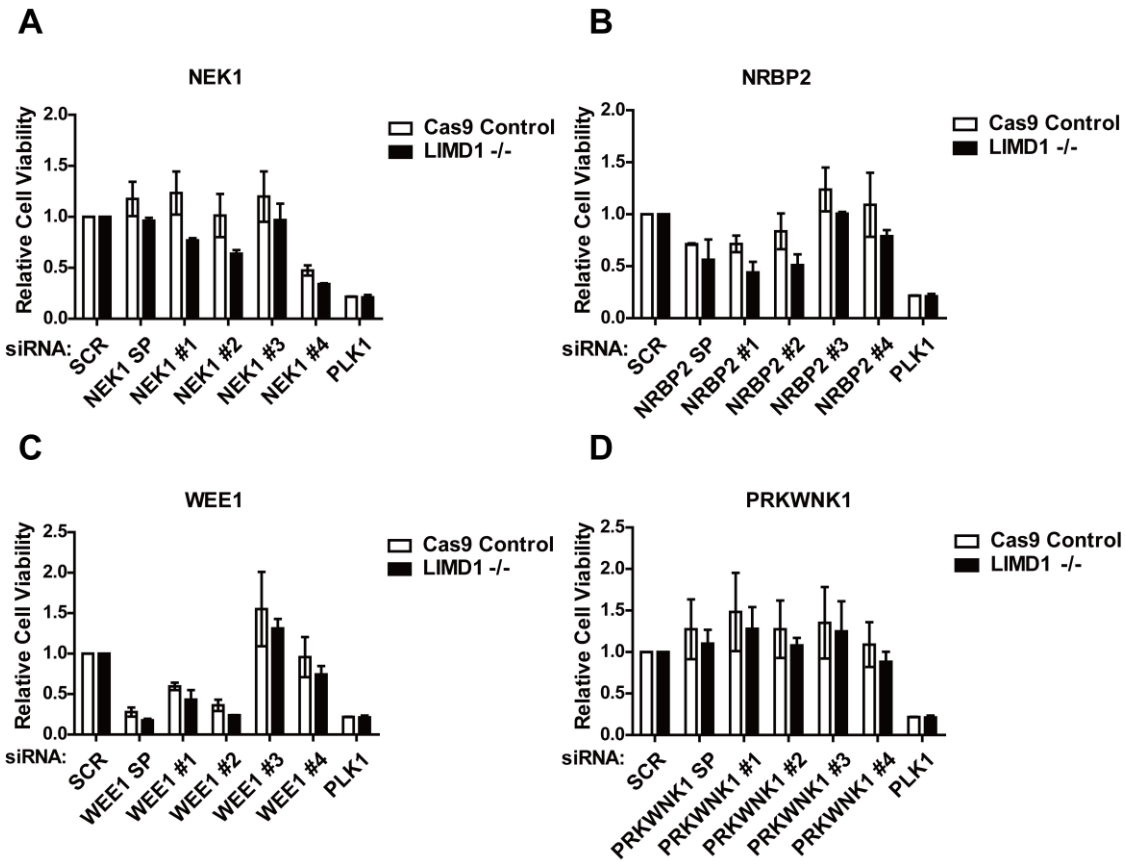

Figure 7.18 Target validation on HeLa isogenic pair of cell lines

Cells were transfected with the indicated siRNAs. SCR, Non-targeting. SP, the SMARTPoolof siRNAs. #1, #2, #3, and #4 represent the individual siRNA. Cell viability was measured by CellTiter-Glo Luminescent Cell Viability Assay. ***A*)** NEK1. ***B*)** NRBP2. *C*) WEE1. ***D*)** PRKWNK1. Data shown are mean ±SEM, n=3. *, p<0.05. **, p<0.01. ***, p<0.001.

7.2.4 Knockdown of ACVR2B is synthetic lethal to LIMD1 negative cells

To further confirm the synthetic lethality with LIMD1, HeLa CRISPR-Cas9 isogenic pair were treated with ACVR2B SMARTPool and the individual siRNA #1. The results showed non-targeting siRNA did not cause any cell death observed by the bright field microscope (**Figure 7.19**). Knockdown of ACVR2B using the SMARTPool siRNA did not cause dramatical cell death (~25%) in HeLa Cas9-Control line, whereas it led to significant cell death (60%) in HeLa LIMD1$^{-/-}$ line (**Figure 7.19A**). However, ACVR2B siRNA #1 caused a more lethal effect on both cell lines. (**Figure 7.19A**).

To investigate the survival and proliferation under the treatment of ACVR2B siRNAs, the clonogenic assay was performed. For the non-targeting siRNA, LIMD1$^{-/-}$ showed an increased proliferation rate as more colonies were formed than Cas9 Control (**Figure 7.19C**), which agrees with the function of LIMD1 as a tumour suppressive gene [217]. When treated with ACVR2B SMARTPool siRNAs, HeLa Cas9 Control cell line survived and proliferated, whereas LIMD1$^{-/-}$ cell line was very sensitive causing cell death (**Figure 7.19C** and **Figure 7.19D**). Treatment with ACVR2B siRNA #1 resulted in a significant reduction in colony formation in both cell lines (**Figure 7.19C** and **Figure 7.19D**). By corroborating the cell viability assay, the results indicated that the SMARTPool of ACVR2B was synthetic lethal to LIMD1 in HeLa isogenic pair. However, the individual siRNA #1 was too lethal to conclude the synthetic lethality. These results suggested the further investigations were required on individual siRNAs with regards to transfection efficiency and off-target effects.

To sum up, using DAVID pathway analysis, MAPK signalling was an overlapping synthetic lethal pathway among three individual screenings. STK39 was validated on the cell-based validation. In addition, STK39 is an oncogene, and the inhibition of it causes cell death [320]. Furthermore, as STK39 has been reported to activate p38, which is a canonical signalling protein kinase in MAPK signalling pathway [272]. Taken together, STK39 was the main focused of the synthetic lethality aspect of this study. On the other hand, ACVR2B is involved in the transforming growth factor-beta (TGF-β) signalling

pathway [374]. Although this pathway did not come up as an enriched signalling pathway in DAVID analysis, it has also shown that ACVR2B presented some degree of specific synthetic lethality with LIMD1 loss. As a result, the further investigations of ACVR2B are required.

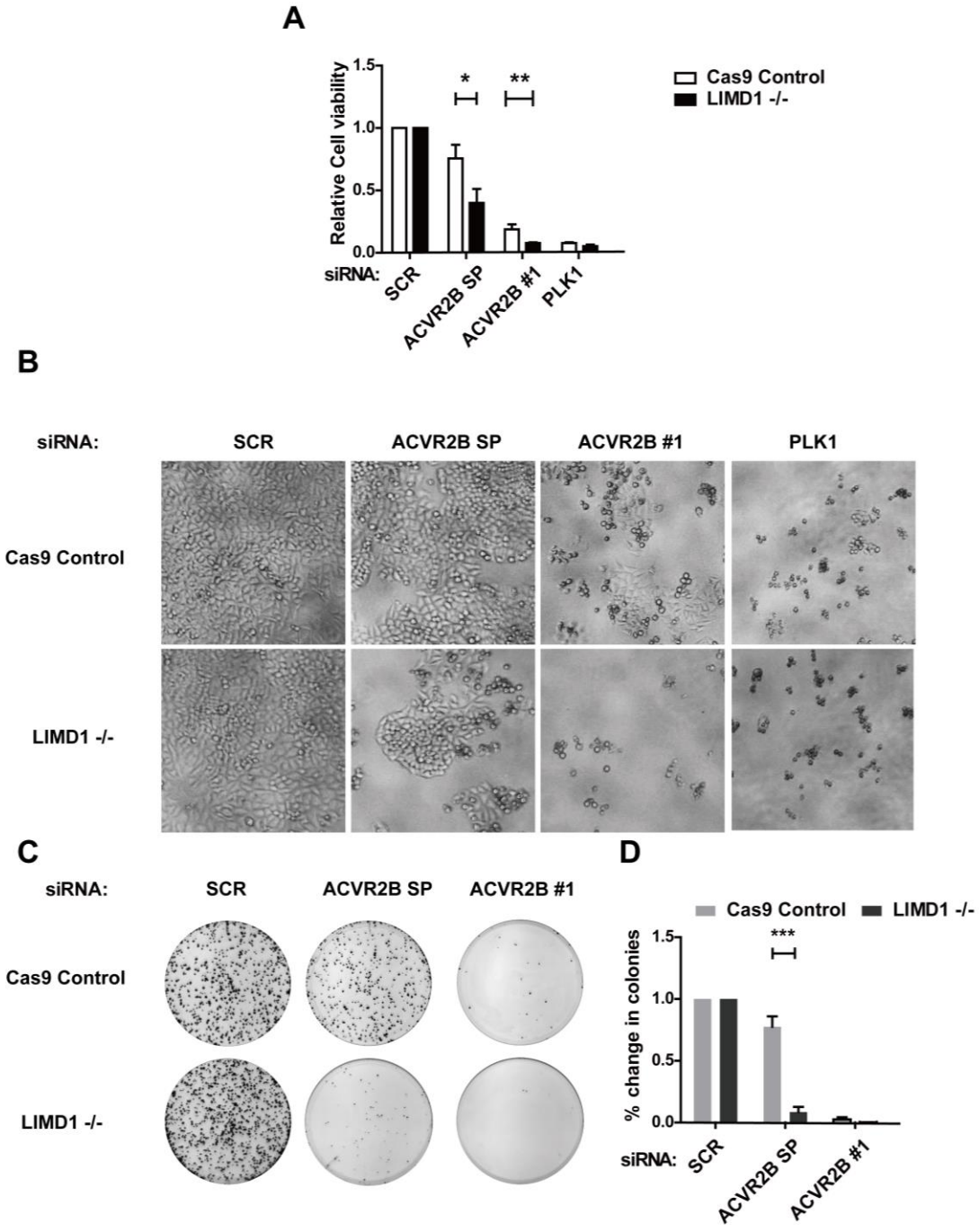

Figure 7.19 Further validation of ACVR2B siRNAs on HeLa CRISPR-Cas9 isogenic pair of cell lines
***A*)** Cells transfected with the indicated siRNAs were measured the cell viability by CellTiter-Glo Luminescent Cell Viability Assay and relative to the value of SCR. ***B*)** Cells morphology treated with the indicated siRNAs was observed by the bright field microscope (400x). ***C*)** Clonogenic assay for HeLa isogenic pair treated with the indicated siRNAs. ***D*)** The percentage of the change in colony numbers in the indicated siRNAs-treated cells. SCR, non-targeting siRNA. SP, the SMARTPoolof siRNAs. siRNA #1, the individual siRNA contained in the SMARTPool. Data shown are mean ±SEM, n=3. *, $p<0.05$. **, $p<0.01$.

7.3 Investigation of the inverse relationship between LIMD1 and STK39

7.3.1 LIMD1 regulates STK39 via miRNA-mediated silencing

During the target validation, the increased expression of STK39 was observed with LIMD1 knockout. It showed a dramatically increased expression not only in protein level but also in mRNA level (increased by ~2.7-fold) (**Figure 7.20**). Considering the biological functions of LIMD1 that regulates the gene expression *via* miRNA-mediated gene silencing pathway [1] (**Figure 7.21A**), it was reasonable to examine whether the increased expression of STK39 resulted from this pathway. The results showed knockdown of LIMD1 in HeLa WT contributed to an increased STK39 expression (**Figure 7.21A**), which corroborated the observation in HeLa isogenic pair. Besides, STK39 expression increased when two key miRISC components, AGO2 and TNRC6A, were depleted (**Figure 7.21B**). These results suggested that the impairment of miRISC increased STK39 expression.

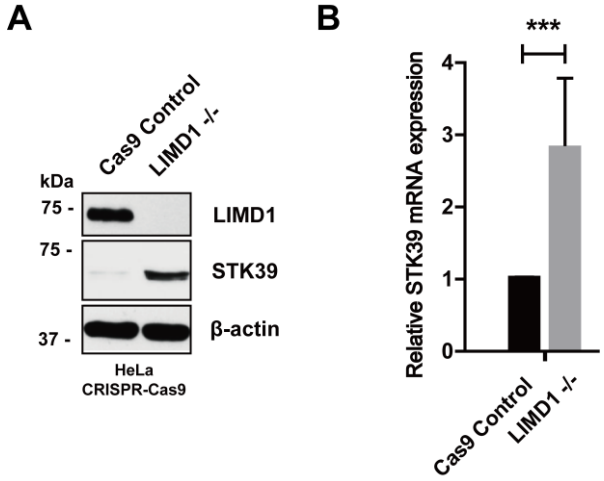

Figure 7.20 STK39 expression increases with LIMD1 knockout
A) Western blot analysis of the indicated proteins in HeLa isogenic pair. ***B)*** qRT-PCR analysis of STK39 mRNA in HeLa CRISPR-Cas9 isogenic pair. Data shown are mean ±SEM, n=3. ***, p<0.001.

To further investigate the regulation of STK39, the 3'UTR (1476bp) of STK39 was cloned into a reporter system construct (psiCHECK-2) by Dr Kunal Shah (**Figure 2.3** and **Figure 7.21C**). The reporter assay results showed the luciferase activity significantly increased in LIMD1$^{-/-}$ line (**Figure 7.21D**), indicating the change of luciferase activity was controlled by the 3'UTR of STK39. This implied that STK39 mRNA is regulated by miRNA-mediated gene silencing in a LIMD1-dependent manner.

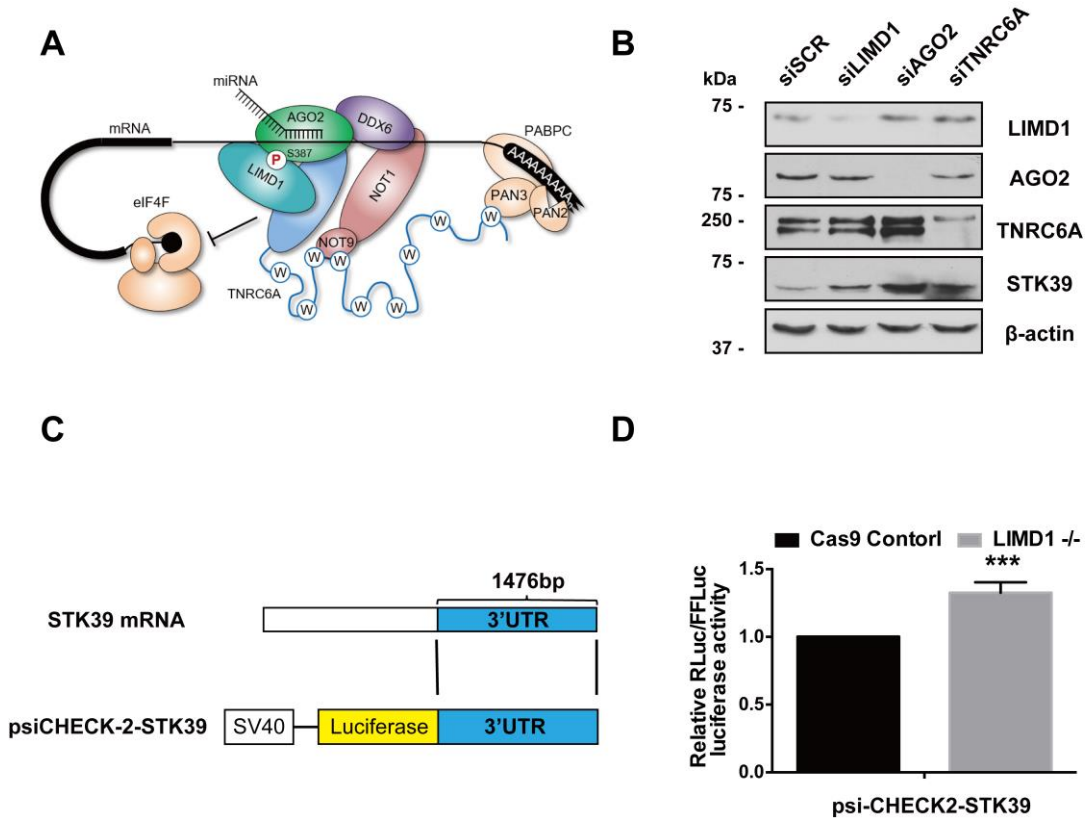

Figure 7.21 STK39 expression is regulated by 3'UTR *via* miRNA-mediated silencing
***A*)** Proposed model of LIMD1-regulated miRNA-mediated silencing**.** LIMD1 interacts AGO2 and TNRC6A simultaneously to repress mRNA translation. ***B*)** Western blot analysis of the indicated proteins in HeLa (wild type) with the depletion of LIMD1, AGO2 and TNRC6A, which are key components of miRISC. siSCR, non-targeting control. ***C*)** Schematic of the cloning of 3'UTR of STK39 into the reporter construct (psiCHECK-2). ***D*)** The reporter construct was transfected into HeLa CRISPR-Cas9 isogenic pair. Relative luciferase activity increased with LIMD1 knockout. Data shown are mean ±SEM, n=3. ***, p<0.001.

In the 1476bp 3'UTR of STK39, there are three miR-26 binding sites (**Figure 7.22A**). It was reported that *miR-26* regulates STK39 expression by targeting these three seed sequences in its 3'UTR [375]. Therefore, the mature *miR-26* expression level was examined in HeLa isogenic pair to investigate the reasons for the inverse relationship between LIMD1 and STK39. Total mRNA was extracted from HeLa isogenic pair of cell line and reverse-transcribed into cDNA, followed by qRT-PCR for quantification *miR-26* and STK39 mRNA (**Chapter 2.2.9** and **Chapter 2.2.10**). The result showed the abundance of *miR-26* was significantly down-regulated in LIMD1$^{-/-}$ line (**Figure 7.22B**). In addition, STK39 mRNA was significantly up-regulated in LIMD1$^{-/-}$ line (**Figure 7.22C**). As a result, these results would suggest that the increased STK39 mRNA expression was due (in part) to the down-regulated mature *miR-26* level *via* miRNA-mediated gene silencing pathway and subsequent mRNA degradation.

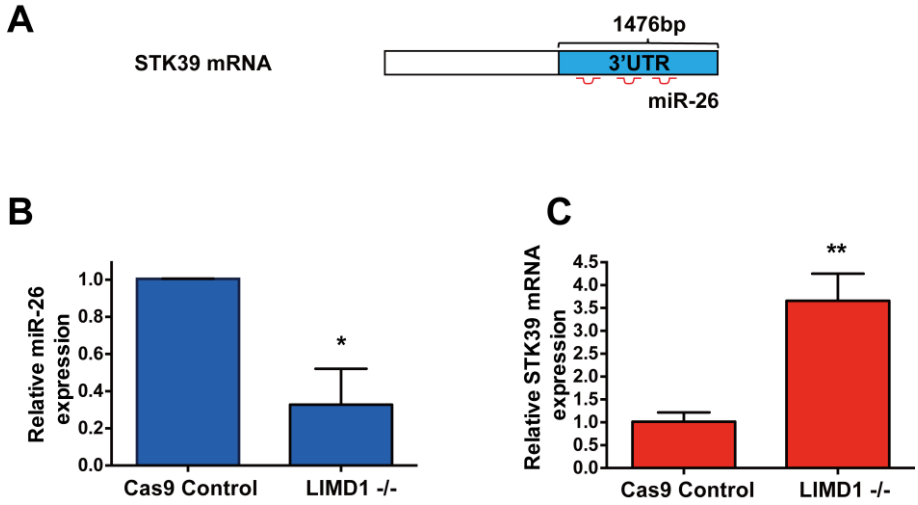

Figure 7.22 *miR-26* reduction might cause the increase expression of STK39 in HeLa CRISPR-Cas9 isogenic pair

***A*)** The sequence of 3'UTR of STK39, containing three miR-26 seed sequences. ***B*)** qRT-PCR analysis of *miR-26* expression in HeLa CRISPR-Cas9 isogenic pair. ***C*)** qRT-PCR analysis of STK39 mRNA expression in HeLa CRISPR-Cas9 isogenic pair Data shown are mean ±SD, n=3. *, $p<0.05$. ***, $p<0.001$.

7.3.2 LIMD1-STK39 inverse relationship commonly occurs in various of cancers

The inverse relationship between LIMD1 and STK39 was observed in HeLa isogenic pair (**Figure 7.20**). Considering STK39 as an oncogene [320] and LIMD1 as a tumour suppressor gene [217], an inverse relationship between LIMD1 and STK39 might fundamentally exists. To test this hypothesis, western blot analysis was performed in a panel of lung cancer cell lines to check the expression of LIMD1 and STK39. The result revealed ~45% lung cancer cell lines presenting an inverse relationship (**Figure 7.23A**). The cancer cell lines, therefore, were divided into two groups: high LIMD1 expression with low STK39 expression and low LIMD1 expression with high STK39 expression. For example, in high LIMD1 with low STK39, there were A549, H838, H1299, HCC193, H2951 and H28 (**Figure 7.23A**). There were Hop62, H358, H358M, H520, H2170 and H69 expressing low LIMD1 and high STK39 (**Figure 7.23A**). Notably, SAEC and HBEC are non-transformed cell controls for adenocarcinoma and squamous cancer cell respectively. The expression of STK39 was up-regulated in both lung adenocarcinoma and squamous cancer cells (**Figure 7.23A**). The bioinformatics was then performed to analyse the RNA expression (FPKM, fragments per kilobase million) across different types of cancer cell lines. The result showed a significant inverse correlation between LIMD1 and STK39 (**Figure 7.23B**). This demonstrated a fundamental inverse relationship between LIMD1 and STK39 existed in cancer cell lines.

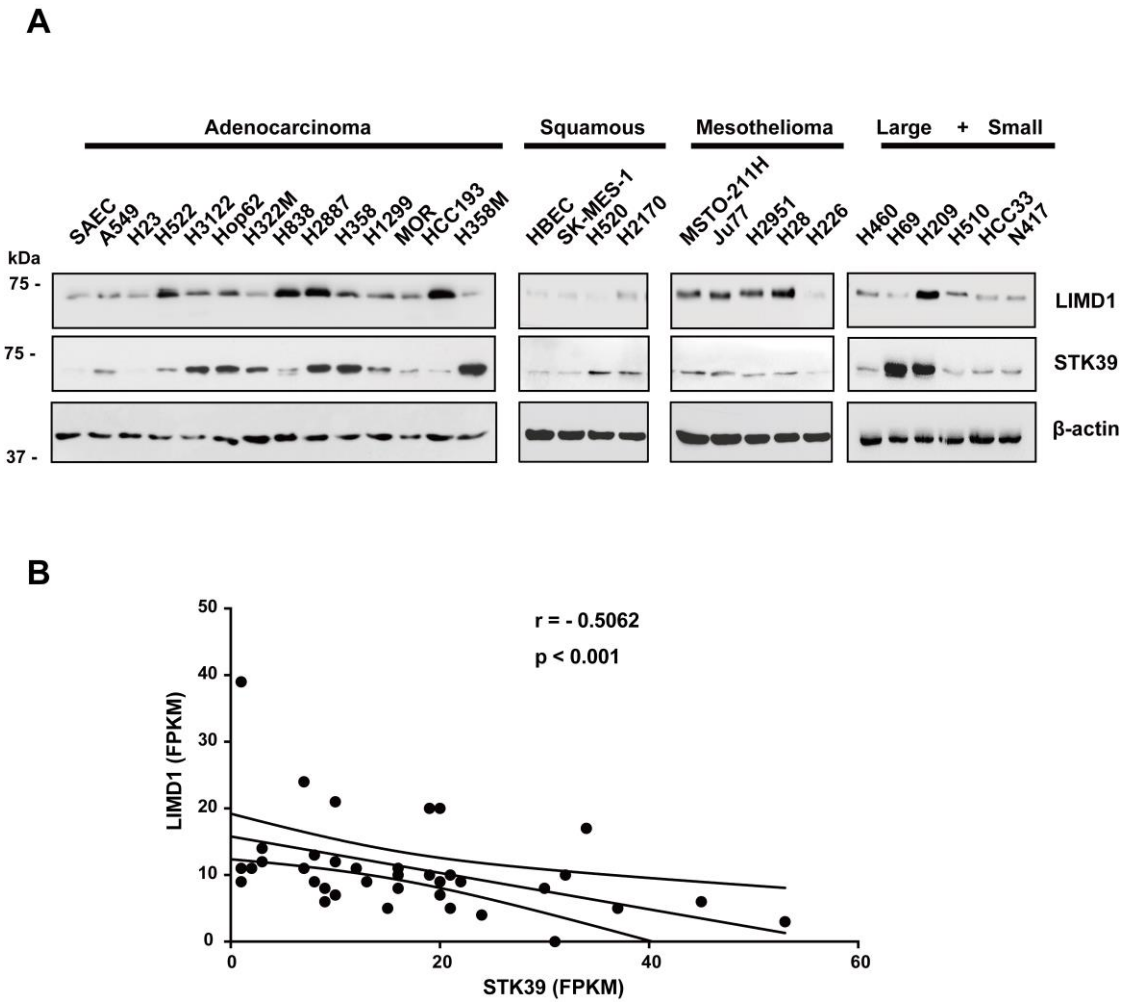

Figure 7.23 An inverse relationship between LIMD1 and STK39 exists across different cancer cell lines ***A*****)** Western blot analysis of LIMD1 and STK39 expression in lung cancer cell lines. ***B*****)** The bioinformatics showed a significant inverse relationship ($p<0.001$) between LIMD1 and STK39. Data of FPKM were obtained from Human Protein Atlas. The Spearman's correlation was performed. FPKM, fragments per kilobases million.

The cell viability assay indicated knockdown of STK39 caused synthetic lethality in LIMD1 negative cancer cell lines (**Chapter 7.2.2**). To test whether such synthetic lethality with LIMD1 loss exists in the lung cancer cell lines, a number of lung cancer cell lines were selected to represent the two groups of cells with regards to the LIMD1-STK39 inverse relationship. The lines selected had low STK39 with high LIMD1 (SAEC, A549, H838 and H28) and high STK39 with low LIMD1 (H522, H358M, H520 and MSTO-211H) (**Figure**

7.24A). Knockdown of STK39 in these lung cancer cell lines caused the differential cell viability regarding the differential expression ratio of LIMD1 and STK39. SAEC expressing low STK39 showed no significant cell death when STK39 was depleted (**Figure 7.24B**). H358M, H520 and MSTO-211H expressing low LIMD1 with high STK39 showed significant cell death upon the STK39 depletion (**Figure 7.24B**). For high expression of LIMD1 and relative low STK39, H28 and H838 did not have much cell death in STK39 siRNA-treated lines compared to that in SCR siRNA-treated lines (**Figure 7.24B**). These results showed a potential phenotype that the high ratio of LIMD1 and STK39 expression did not respond to the depletion of STK39, whereas cells expressing the low ratio of STK39 and LIMD1 expression were sensitive, resulting in significant cytotoxicity.

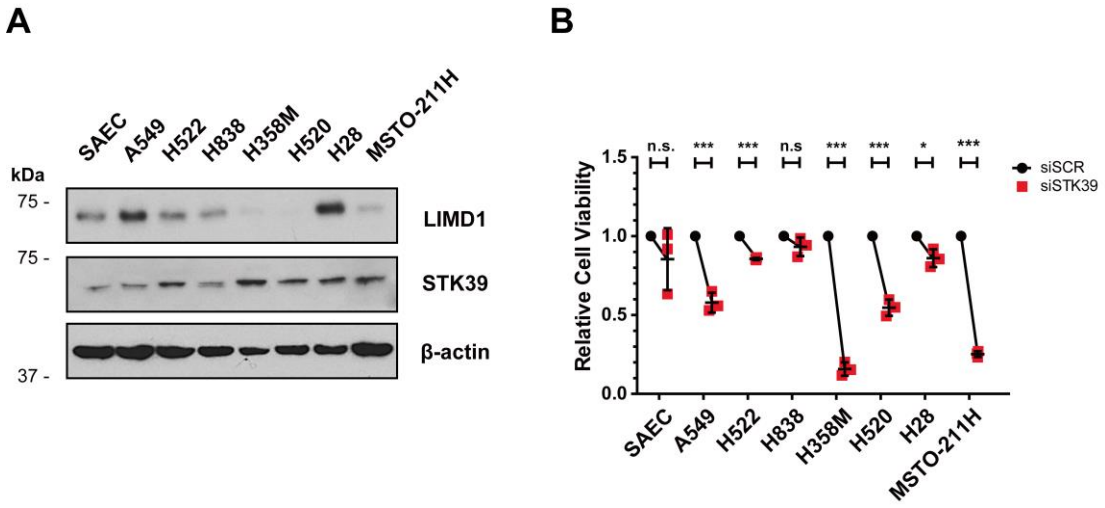

Figure 7.24 Targeting STK39 in lung cancer cells with differential expression of LIMD1 and STK39
A) A number of lung cancer lines were selected for STK39 siRNA treatment with regards to LIMD1-STK39 expression, analysed by Western blot. ***B)*** Cells transfected with STK39 siRNA was measured the cell viability by CellTiter-Glo Luminescent Cell Viability Assay and relative to the value of SCR. SAEC is small airway epithelial cell. Data shown are mean ±SEM, n=3. n.s, not significant. *, $p<0.05$. ***, $p<0.001$.

To be clinical relevant, a cohort of patients with lung cancers was examined for the expression of LIMD1 and STK39. The result showed a significant correlation of STK39 with tumour size and stage ($p=0.022$) and metastasis ($p=0.024$) (**Figure 7.25A**). Patients with high STK39 suffered from a larger tumour (T2+T3) than those with low STK39. The

cancer cells are localised not metastasis with high STK39. The prognosis analysis showed that lower expression of STK39 correlated to the poor prognosis (p=0.097, approaching significance). Taken together, high expression of STK39 caused the localised but larger tumour with high prognosis, whereas low STK39 contributed more invasive which showed more fatal to the patients.

A

Variable	STK39		
	low	high	P value
Age			
<70	31 (16.4%)	61 (32.2%)	0.176
>70	24 (12.7%)	73 (38.6%)	
Gender			
Male	27 (14.0%)	64 (33.2%)	0.850
Female	29 (15.0%)	73 (37.8%)	
Tumour type			
Adenocarcinoma	46 (21.2%)	122 (56.2%)	0.351
Adenosquamous Carcinoma	10 (4.6%)	14 (8.3%)	
Other	7 (3.2%)	18 (8.3%)	
Tumour stage and size			
T1a + T1b	10 (5.2%)	39 (20.3%)	0.022*
T2a + T2b	24 (12.5%)	69 (35.9%)	
T3 + T4	22 (11.5%)	28 (14.6%)	
Metastasis			
Yes	19 (12.6%)	31 (20.5%)	0.024*
No	21 (13.9%)	80 (53.0%)	

B

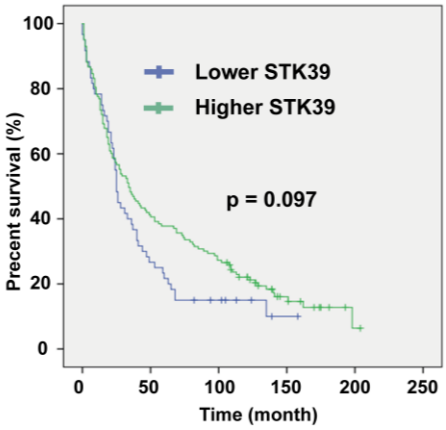

Figure 7.25 IHC analysis of STK39 in a cohort of 276 patients with lung cancers
***A*)** Correlation of STK39 protein expression with patients' features**. *B*)** Kaplan-Meier survival analysis showed that patients with low STK39 expression level had a worse prognosis than that of patients with higher STK39 expression (p=0.097).

7.4 Summary

Upon the screening on Human Kinome siRNA Library and cell-based validation, *STK39* was validated as a synthetic lethal gene with LIMD1 loss (**Figure 7.12**). Taken together with the previous study demonstrating that STK39 activates p38 [272], this present result corroborated the database-validation that MAPK signalling pathway is an enrich pathway for synthetic lethality with LIMD1 loss (**Figure 7.7 and Figure 7.8**). The depletion of STK39 in LIMD1$^{-/-}$ negative cell lines inactivated p38 and caused cell death

by apoptosis (**Figure 7.13** and **Figure 7.14**). In addition, LIMD1 loss resulted in an increased STK39 expression *via* miRNA-mediated silencing (**Figure 7.21** and **Figure 7.22**). To sum up, with regards to synthetic lethality, LIMD1 and STK39 function normally in the normal healthy cells (**Figure 7.26A**). Cells use two pathways for survival. The loss of LIMD1 led to a decreased in mature *miR-26* level and in turn, increased STK39 expression mediated *via* miRNA-mediated silencing (**Figure 7.26B**). This further increased p38 activity and cells keep proliferating. By targeting STK39, p38 function was inactivated resulting in apoptosis which caused cells death (**Figure 7.26C**). Furthermore, the regulation of STK39 by LIMD1 resulted in an inverse relationship between LIMD1 and STK39 which was showed to exist in numbers of cancer cell lines (**Figure 7.23**). Upon such inverse relationship, lung cancer cell lines expressing high STK39 with low LIMD1 were sensitive to STK39-targeted treatment, whereas those expressing low STK39 with high LIMD1 did not (**Figure 7.24**).

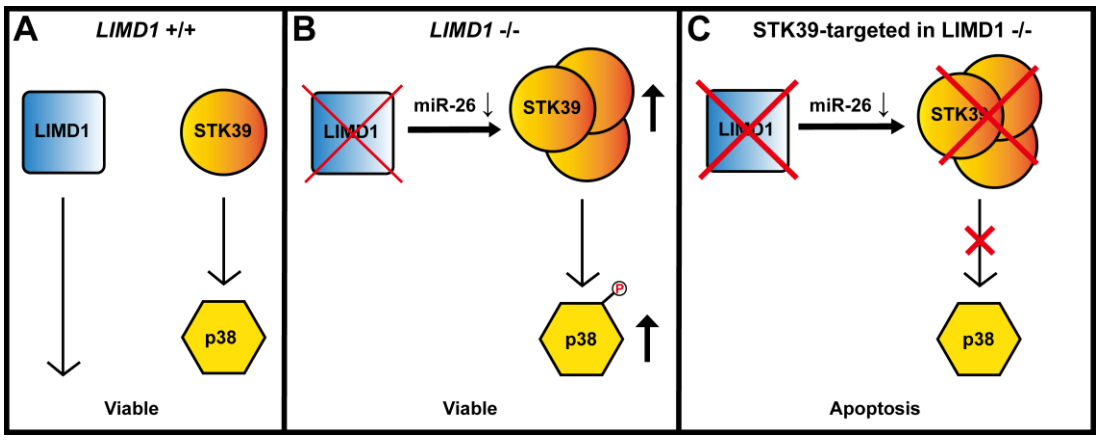

Figure 7.26 Summary for the synthetic lethality of STK39 with LIMD1
***A*)** LIMD1 and STK39 function normally in healthy cells and cell survive. ***B*)** In *LIMD1*$^{-/-}$ cells, mature *miR-26* was up-regulated. This led to the increased STK39 expression and subsequently increased p38 activity. Cells use STK39-p38 axis for survival. ***C*)** When targeting STK39, it inhibited STK39-p38 axis, which induced apoptosis resulting in cell death.

Chapter 8

Discussion

8 Discussion

This study was to investigate the novel synthetic lethal kinase to LIMD1 loss for cancer treatment. Therefore, this chapter will discuss the overall mechanistic implications of the findings presented so far and postulate the proposed/hypothesised model of the pathway that LIMD1 involved in the above study.

8.1 STK39-p38 signalling pathway is synthetic lethal with LIMD1 loss *via* apoptosis

By screening the Human Kinome siRNA library, this study discovered *STK39* is a synthetic lethal gene with LIMD1 loss. Johnston *et al.* demonstrated that STK39 interacts with RELT to activates p38 [272], and Zhao *et al*. showed that *STK39* is an oncogene highly expressed in cancers and inhibits cell apoptosis *via* STK39-activated p38 signalling [320]. However, this present study suggested STK39-activated p38 and the apoptosis caused by the depletion of STK39 could only occur in *LIMD1*$^{-/-}$ cells rather than *LIMD1*$^{+/+}$ cells (**Figure 7.14**). It is of note that this present study has not examined whether it altered the downstream effectors of p38 related to the apoptosis pathway (for example Bcl2 and Bax). Indeed, Zhao *et al.* provided the evidence that the depletion of STK39 results in an increased Bax (pro-apoptotic function) and a decreased Bcl2 (anti-apoptotic function), indicating the activation of the apoptosis pathway [320]. Therefore, this present study is with the agreement with Zhao's. In addition, it has shown that TRAF6 interacts with LIMD1 to mediate receptor activator of NF-κB (RANK) signalling [218]. The depletion of LIMD1 resulted in the decreased p38 activation, indicating TRAF6-LIMD1 complex activated p38 signalling. Taken together with the DAVID analysis that p38 pathway was an enriched synthetic lethal pathway with LIMD1 loss, it suggested that p38 signalling may be a compensatory pathway for the cells survive when LIMD1 lose its function. Therefore, this present study proposed a model for the synthetic lethal pathway of STK39 with LIMD1 loss related to p38 signalling (**Figure 8.1**). Binding of the ligand, RANK is initiated and activates p38 *via* the TRAF6-LIMD1 complex in *LIMD1*$^{+/+}$ cell [218] (**Figure 8.1A**). When LIMD1 is depleted or down-regulated, it enhances STK39 expression (**Figure 8.1B**). The enhanced STK39 interacts with RELT to positively control

p38 activity, resulting in the activation of STK39-p38 signalling, which subsequently causes the activation of anti-apoptotic protein Bcl-2 and apoptotic protein Bax (**Figure 8.1B**). This drives the cells to become more dependent on the STK39-p38 axis to protect the cells from apoptosis and therefore survive. Once STK39 is depleted in *LIMD1*$^{-/-}$ cells, it inactivates p38 signalling (**Figure 7.13**) to induce apoptosis, and subsequently, the cells die.

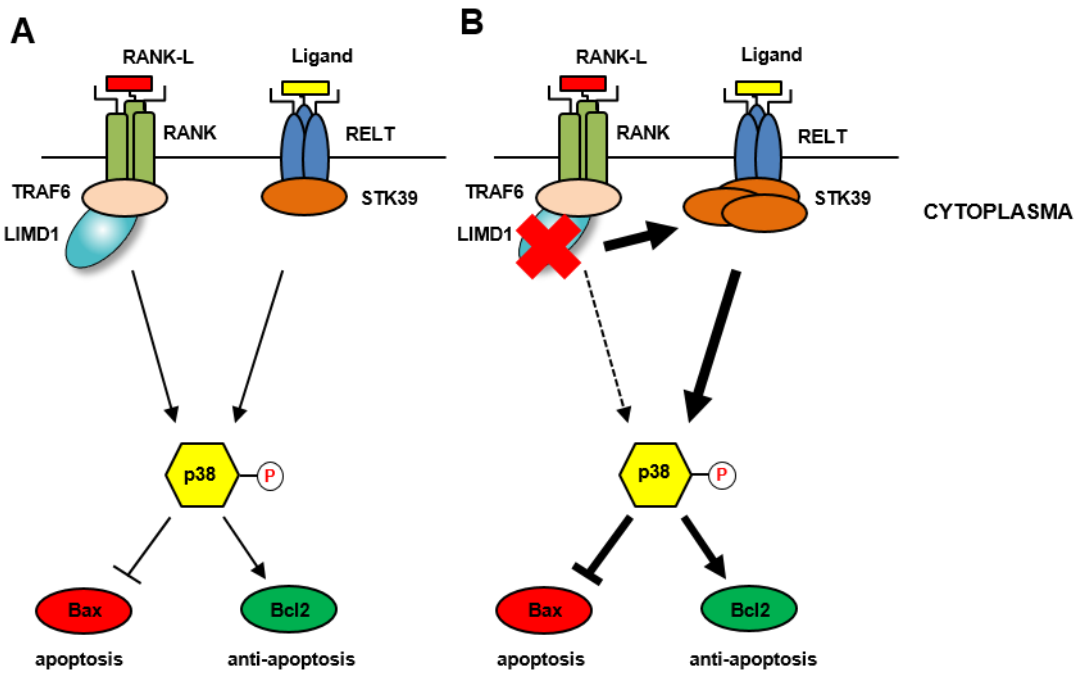

Figure 8.1 Schematic model of LIMD1-STK39 synthetic lethal pathway
***A*)** In *LIMD1*$^{+/+}$ cells, RANK-mediated TRAF6-LIMD1 complex activates p38 MAPK signalling pathway. ***B*)** In *LIMD1*$^{-/-}$*cells*, the STK39 expression is up-regulated, and the cells become addicted to the STK39-p38 axis for survival. The enhanced p38 activates Bcl2 to increase p38-mediated anti-apoptotic function and inhibits Bax to decrease p38-mediated apoptotic function. The cells are protected from the apoptosis and thus keep proliferating. The dashed line represents the decreased effect. The thick line represents the increased effect.

8.2 TGF-β signalling pathway may also be synthetic lethal to LIMD1

Besides STK39, this study also found *ACVR2B* as a potential synthetic lethal gene with LIMD1 loss. ACVR2B belongs to TGF-β superfamily. Binding of the ligand causes bridging of the pre-formed dimers of TGF-β type I receptors and dimers of type II receptors to

form hetero-tetrameric receptor complexes. The type II receptor kinase is constitutively active and phosphorylates the type I receptor, which in turn recruits SMADs and phosphorylate SMADs to allow them to form homomeric complexes [376]. Two pieces of evidence have shown that the activin family binds to the TGF-β type I receptor, Nodal, to activate p38 signalling in a SMAD-dependent manner, and the apoptosis induced by TGF-β signalling is mediated by p38 [377, 378]. Therefore, these studies suggested that ACVR2B may function on the activation of p38 (**Figure 8.2A**). Alternatively, p38 activation can also be activated by a SMAD-independent manner *via* the interaction of LIMD1 with TRAF6 [218, 379] (**Figure 8.2B**). Taken together, the results of the present study along with these previous findings suggest that a potential synthetic lethal pathway in TGF-β signalling was generated (**Figure 8.2**). We hypothesised that loss of LIMD1 and the depletion of ACVR2B induces cell death, while *LIMD1*$^{+/+}$ cells survive by using the compensatory TRAF6-LIMD1-p38 axis signalling [218].

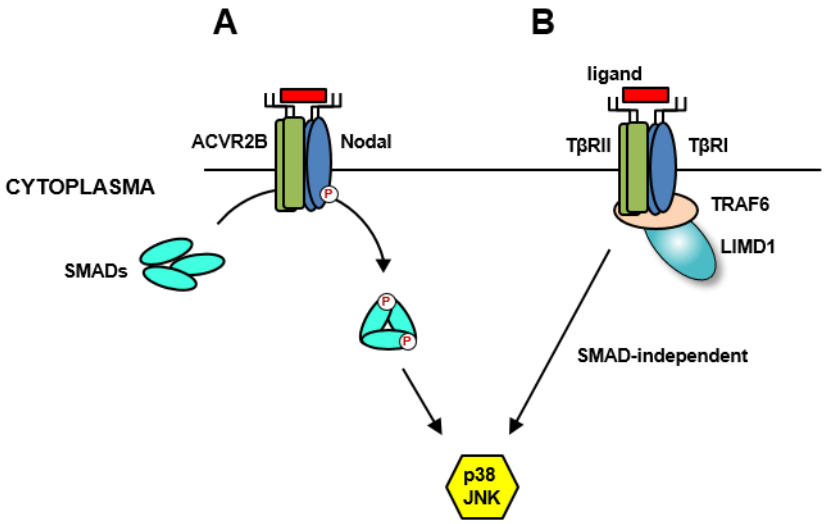

Figure 8.2 Potential synthetic lethal pathway with regards to LIMD1 and ACVR2B within TGF-β signalling
Binding with type I receptor initiates TGF-β signalling pathway which subsequently activates SMAD complexes to regulate gene transcription. ***A)*** ACVR2B interacts with Nodal to activate p38 *via* SMAD complexes. ***B)*** LIMD1 has an interaction between TRAF6, which binds the hetero-tetrameric receptor complexes to activate p38 signalling in a SMAD-independent manner. The loss of LIMD1 and ACVR2B simultaneously is fatal to the cells.

8.3 LIMD1 regulates STK39 expression

LIMD1 binds AGO2 and TNRC6A simultaneously to regulate miRNA-mediated silencing to control mRNA expression [253]. This present study revealed that LIMD1 controls STK39 expression by miRNA-mediated silencing pathway (**Chapter 7.3.1**); by the transient impairment of key components of miRISC, it leads to the increased STK39 expression (**Figure 7.21**). Our latest publication suggested the long term of LIMD1 loss does not affect the miRNA-mediated silencing pathway because of the compensatory silencing pathway *via* AGO-LAW association (**Chapter 3** and **Chapter 4**) [253]. However, previously published data has shown that the maturation of *miR-26* reduces in response to the phosphorylation at Y393 on AGO2 in hypoxia [114]. This present study did not examine the amount of mature *miR-26* in hypoxia but found a decreased amount of the mature *miR-26* in normoxia (**Figure 7.22**). This could be explained by one of the biological functions of LIMD1 that the loss of LIMD1 stabilises HIF-1α, resulting in the pseudo-hypoxia [216]. Interestingly, HIF-1α was reported to negatively regulate PTP1B activity for dephosphorylation of Y393 on AGO2 [128, 380]. The maturation of *miR-26* is then down-regulated and subsequently decrease the post-transcriptional repression of STK39. Therefore, a potential mechanism on how STK39 is regulated by LIMD1 is hypothesised. Firstly, the regulation of STK39 is mediated by LIMD1-HIF-1α-PTP1B-miR-26 axis (**Figure 8.3**). The loss of LIMD1 loss stabilises HIF-1α expression, which in turn inhibits the dephosphorylation of Y393 on AGO2 by PTP1B activity and keep AGO2 hyper-phosphorylated at Y393 residue. Therefore, the hyper-phosphorylation of AGO2 reduce the maturation of *miR-26* and consequently, increase STK39 *via* miRNA-mediated silencing.

HIF-1α regulates the transcription of multiple genes by binding hypoxia response element (HRE) in the promoter region. STK39 transcription was reported to be regulated by NF-κB [239]. Evidence has shown that the depletion of HIF-1α increased NF-κB activity [381], which is contradictive to the observation in this present study, suggesting STK39 increase in *LIMD1*$^{-/-}$ may not be caused by NF-κB activity. As a result, this present study did not examine STK39 expression with regards to NF-κB activity. Except for the

NF-κB binding site within the promoter region of STK39, bioinformatics analysis showed it contains HRE in the promoter region. Taken together, this present study postulates the second potent pathway for regulation of STK39 by HIF-dependent transcription (**Figure 8.3**).

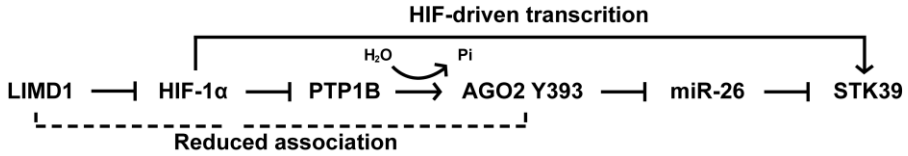

Figure 8.3 Investigation of the regulation of STK39
The loss of LIMD1 stabilises HIF-1α. Y393 on AGO2 cannot be dephosphorylated by HIF-1α-repressed PTP1B activity [380], resulting in the inhibition of maturation of *miR-26* [128]. This results in the increase of STK39. Alternatively, the stabilised HIF-1α may enhance the transcription of *STK*39 gene.

8.4 LIMD1-STK39 inverse relationship exists across variety of cancer cells and is a potential predictive marker for STK39-targeted therapy

This study revealed a common inverse relationship between LIMD1 and STK39 exists across different types of cancers. According to the cohort (276 patients with lung cancers) in this study, the high expression of STK39 significantly correlates with tumour stage and size (**Figure 7.25A**). It also showed that lower expression of STK39 correlates to poor prognosis (**Figure 7.25B**). These results are partially in agreement with the previous study from another independent cohort (135 patients with lung cancers) that STK39 correlated with tumour size, tumour stage and lymph node metastasis [320]. However, it showed a contradictive result to this present study that patients with high expression have a worse prognosis than that of patients with lower STK39 [320]. One possible explanation for the contradictive prognosis results between the two individual cohorts would be the ethnic genetic variation of STK39. It has been observed that STK39 correlates to hypertension in Caucasian populations, but not in Chinese populations regarding differential SNPs [307, 310, 382]. It is of note that lung cancers contain two SNPs (rs10176669 and rs4438452) located within intron 1 [383], implying that STK39

expression regarding the clinical significance may be different. Therefore, a cohort containing Chinese patients are under-investigation for the expression of LIMD1, STK39 as well as p38 (phospho-p38) to examine whether there is the difference in correlation between different ethnic populations. Furthermore, this study finds cancers cells expressing high STK39 with low LIMD1 are more sensitive to the depletion of STK39 (**Figure 7.24**). It defines a subgroup of *LIMD1*$^{-/-}$ cancers that can benefit from STK39-targeted (possibly p38-targeted) therapy.

Chapter 9

Conclusion

9 Conclusion

The first study has put forward the current knowledge of the interactions between LIMD1 and miRISC components AGO2 into the next level, understanding how LIMD1 regulates the miRNA-mediated silencing pathway in humans. The two key aims of this study were achieved as follows:

- **Aim 1: Characterisation of the direct binding domains on LIMD1 and AGO2**

  The recombinant LIMD1 and AGO2 proteins (with mutants) have been constructed and expressed. The direct binding assay (GST pulldown and MBP pulldown) were optimised for the investigation of the direct binding between LIMD1 and AGO2. The precise interaction domains on LIMD1 (a.a 140-166) and AGO2 (L2 domain) were determined. In addition, the interaction of AGO2 and LIMD1 enhanced by a phospho-mimic glutamic acid substitution (S387E). This suggests that the phosphorylation of S387 enhances the interaction with LIMD1. (**Chapter 3**)
- **Aim 2: Investigation of the association between AGOs and LAW**

  By over-expressing phospho-deficient (alanine) and phospho-mimic (glutamic acid) point mutants on the S387, the co-localisation data corroborated the direct binding assay that the phosphorylation of S387 on AGO2 enhanced the binding to LIMD1, while the binding to LIMD1 abrogated when S387A was unable to be phosphorylated. In addition, this interaction was shown to be Akt3-dependent. The conserved serine exists in AGO1 and AGO4. Therefore this study elaborates the Akt-dependent association to all human AGOs and LAW. AGO3 contains the naturally existing glutamic acid was not shown to rely on the Akt3 signalling, suggesting AGO3-LAW is a compensatory complex for miRNA-mediated silencing. Furthermore, the phosphorylation of Y393 on AGO2 can also regulate the association with LIMD1, indicating S387/Y393 cooperate together for the regulation of its binding to LIMD1 and determine whether to undergo miRNA- or siRNA-mediated silencing. (**Chapter 4**)

The second study has revealed the synthetic lethal gene (pathway) with LIMD1 loss, and investigated the relationship between such gene and LIMD1. This provided a deeper understanding of the function of the tumour suppressor protein LIMD1 with regards to tumourigenesis. In addition, this study provided a novel concept for target therapy. The key aim of this study was achieved as follows:

- **Aim 1: Investigation of the novel synthetic lethal kinase to LIMD1 loss**

  STK39 and *ACVR2B* were identified as synthetic lethal genes with LIMD1 loss. STK39 expression is regulated by LIMD1 *via* miRNA-mediated silencing, and the synthetic lethality was achieved by apoptosis *via* dephosphorylation of p38. The synthetic lethality of ACVR2B with LIMD1 may be within TGF-β signalling to activate p38. The inverse relationship between LIMD1 and STK39 commonly exists, and by using such inverse relationship, patients stratification with low LIMD1 and high STK39 can be predicted for benefits from STK39-target therapy. (**Chapter 7**)

The following chapter will briefly discuss the future directions to extend the present findings in this study.

Chapter 10

Future plans

10 Future plans

This final chapter puts forward the perspective based on the present findings in this study to highlight areas of the potential interests and improvements for the future work within the group.

10.1 Characterisation of the eIF4E-LIMD1-AGO2 interaction

As a scaffold protein, LIMD1 interacts with not only AGO2-TNRC6A but also eIF4E, forming an inhibitory loop for miRNA-mediated silencing [1]. James *et al.* demonstrated that the induction of LIMD1 resulted in an increase in the co-immunoprecipitation of AGO2 with eIF4E [1]. Bioinformatics shows a putative 4E binding motif (a.a 144-155) within LIMD1 AB-motif (a.a 140-166). The preliminary data showed LIMD1 AB-motif (a.a 140-166) could also interact with eIF4E (**Figure 10.1**). Further investigations are required to confirm this interaction and if so, to identify the precise domain within AB-motif for eIF4E interaction as well as AGO2 interaction. LIMD1 may be a molecular 'clamp' for eIF4E-LIMD1-AGO2 as same as that for AGO2-LIMD1-TNRC6A, which will help to answer the previous observation that LIMD1 facilities the eIF4E-AGO2 association [1]. Furthermore, according to PhosphoSitePlus® [384], two putative phosphorylation sites (S145 and S150) within AB-motif are indicated. Whether these sites are responsible for the interaction with AGO2 (probably eIF4E) are required for further investigation.

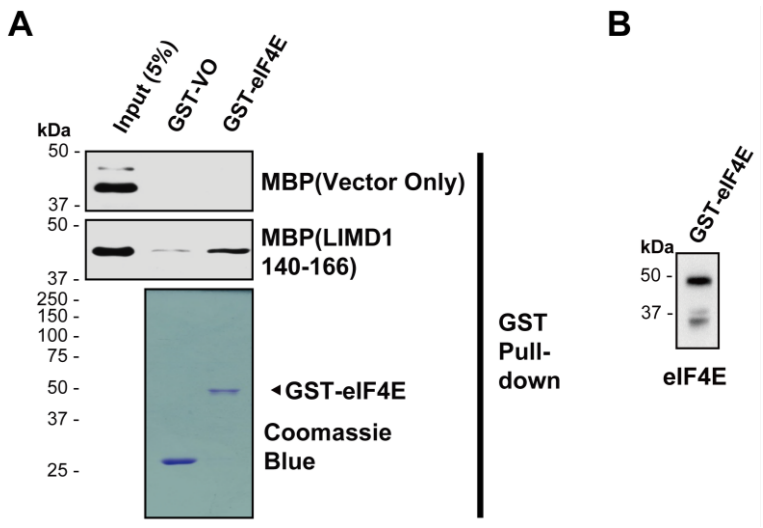

Figure 10.1 The preliminary data shows LIMD1 binds eIF4E *via* a.a 140-166
A) GST-VO and GST-eIF4E were purified on the resin and incubated with MBP-VO and MBP-LIMD1 140-166 respectively, analysed by Western blot. Coomassie staining was performed to visualise the concentration of the GST-tagged protein for pull-down. **B)** Western blot analysis of the purified GST-eIF4E.

10.2 Investigation of the combined phosphorylation at S387/Y393 with regards to the AGO2-LIMD1 interaction

The phosphorylation status of S387 and Y393 regulate the association of AGO2 and LIMD1. The interaction of AGO2 with LIMD1 with regards to Y393 residue needs to be confirmed by the direct binding assay (GST pull-down) and/or PLA. In addition, it requires the examination whether the dephosphorylated Y393 involved in miRNA-mediated silencing. This present study has defined a 'Switch ON/OFF' function for the interaction of AGO2 with LIMD1 for simplicity (**Figure 4.20** and **Table 4.2**). Therefore, the different combinatorial phosphorylation of both S387 and Y393 are required for understanding which residue is dominant in regulating LIMD1 binding and thus miRNA-mediated silencing. It is also of interest and importance to examine whether the phosphorylation of Y393 affects the siRNA silencing, which will indicate the role of S387

and Y393 of AGO2 along with LIMD1 in switching the functions in miRNA/siRNA pathways.

Furthermore, there is no evidence so far to preclude the interaction between LIMD1 and Dicer. Dicer-AGO2 and AGO2-LIMD1 interaction are impaired by the phosphorylation of Y393. Therefore, it is reasonable and of interest to investigate whether there is an interaction between Dicer and LIMD1 and if so, it will help for introduce a novel LIMD1 function in miRNA biogenesis.

10.3 Investigation of LAW-AGO association

Although this present study revealed that the AB-motif is responsible for the interaction between AGO2, LAW family members contain the sequence variations within the pre-LIM region where the AB-motif locates. Therefore, it requires revealing the precise interaction domain within both AJUBA and WTIP. In addition, the specific antibody against the phospho-serine on each AGO protein is required to further confirm the mechanism whether the association between AJUBA/WTIP with AGOs is phosphorylation-dependent.

10.4 Potential dual-regulation of STK39 by LIMD1

STK39 contains HRE in its promoter region, indicating the regulation of STK39 might also be regulated by HIF-driven transcription. Here, the preliminary data showed STK39 expressions in HeLa isogenic pair increased at 4h hypoxic induction, and then they decreased at 24h hypoxic induction (**Figure 10.2A**). The STK39 expression was demonstrated to be regulated by miRNA-mediated silencing, and *miR-26* was reported to target the 3'UTR of STK39 and responds to hypoxia, respectively [375, 385]. In agreement with these studies, the preliminary study confirms *miR-26* abundance increased in the hypoxic condition (1% O_2) (**Figure 10.2B**). These observations implied the alteration of STK39 expression observed in hypoxia might be regulated by HIF-driven transcription which dominantly functions at 4h hypoxic induction and with the increase of hypoxia, miRNA-mediated silencing starts to take over the responsibility to negatively

control STK39 expression. The balance and dynamic process of regulating STK39 is also required for further investigation.

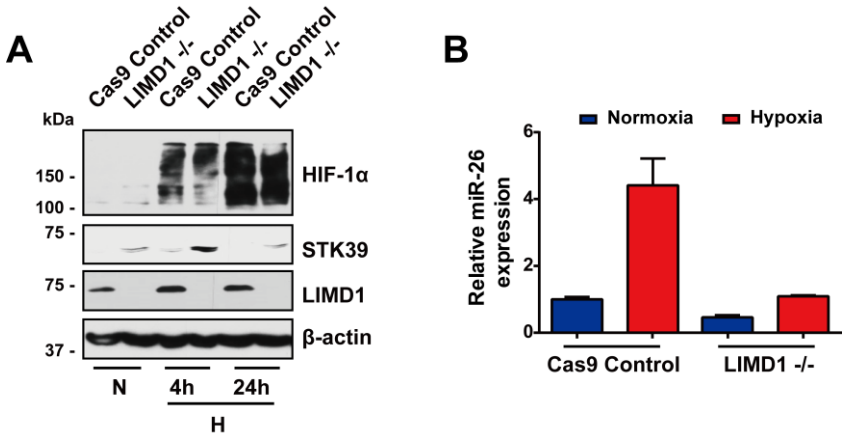

Figure 10.2 Potential dual-regulation of STK39 by LIMD1
***A*)** Western blot analysis of the indicated proteins in HeLa isogenic pair under the normoxic and hypoxic conditions (n=1). ***B*)** qRT-PCR analysis of the relative expression of *miR-26* in HeLa isogenic pair under the normoxic and hypoxic conditions**.** Data shown are mean ±SEM, n=1. N, Normoxia (20% O_2). H, hypoxia (1% O_2).

According to the bioinformatics, there are two SMAD binding elements (SBEs) within the promoter region of STK39, indicating the transcription of *STK39* might be driven by SMADs. Nevertheless, TGF-β induces HIF-1α accumulation and its DNA binding activity [386]. Therefore, the synthetic lethality of ACVR2B with LIMD1 observed in this study could also result from the down-regulated STK39 caused by the depletion of ACVR2B. To link two separate pathway together, it is of interest to investigate whether the depletion of ACVR2B diminishes the STK39 expression. If so, mutating the SBE sites would suggest whether SBE is involved in regulating the transcription of *STK39*.

In summary, this present study opens the possibility whether there is a specific group of genes like *STK39* whose expression are synergistically dual-regulated by LIMD1 *via* miRNA-mediated silencing pathway and gene transcription pathway (probably other

unknown LIMD1 biological functions). This would matches the biological function of LIMD1 as a tumour suppressor, which lose function in the early stage of lung cancer [229]. The down-regulated LIMD1 may contribute to the over-expression of oncogenes such as STK39 observed in this study. This will provide a better understanding of tumourigenesis with regards to the biological consequences caused by LIMD1 loss and develop effective approaches for the cancer treatment.

10.5 STK39-LIMD1 inverse relationship predicts the benefits of STK39-target therapy on cancers

The depletion of STK39 was demonstrated to be lethal in low LIMD1 and high STK39 cells. The future work will focus on applying the ratio of LIMD1 and STK39 upon other cancer cells to investigate the threshold of this ratio that the cells would respond to the depletion of STK39. In addition, the genetic alteration of cancer cells differs not only from cancer types but also from individuals. The cohort with regards to LIMD1, STK39 p38 expressions is under investigation. It is of importance to examine whether there is an inverse relationship between STK39 and LIMD1. Therefore, this ratio would be a predictive parameter for the personalised cancer treatment.

Chapter 11

Appendix

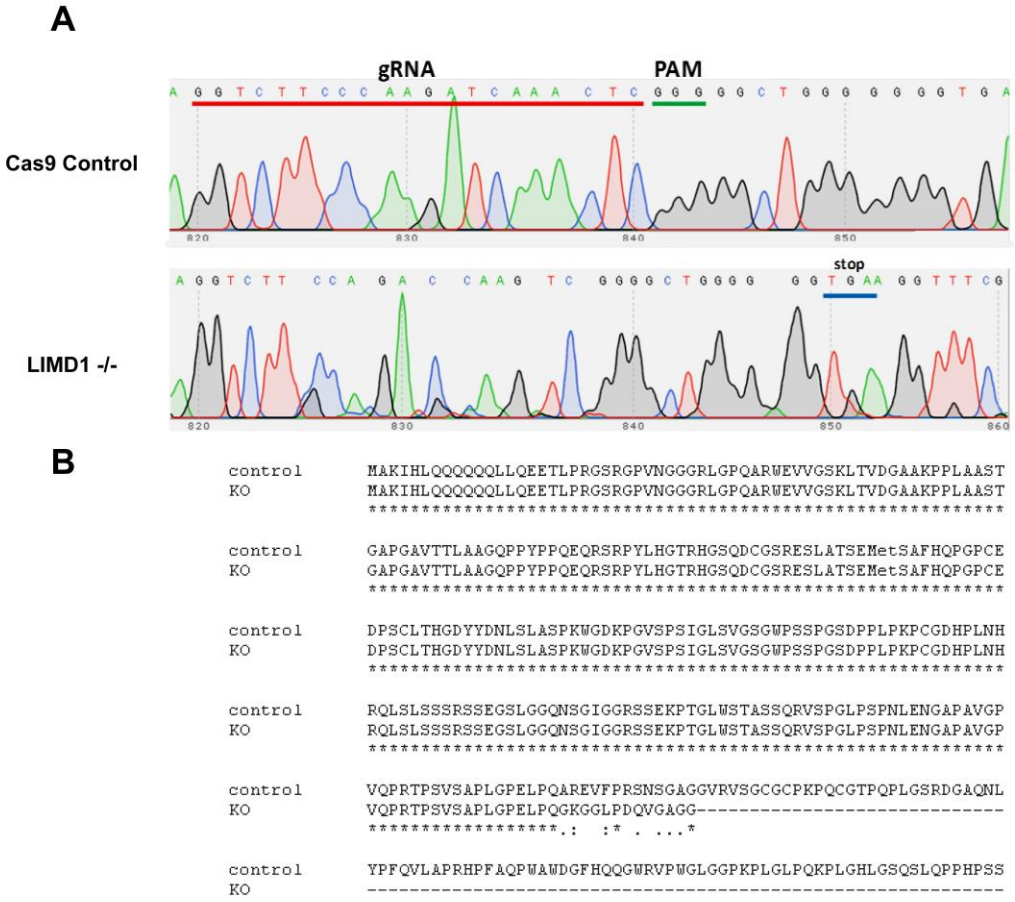

Figure 11.1 Sequencing results for CRISPR-Cas9 edited HeLa to knockout LIMD1

***A*)** Chromatograms of Cas9 control (*LIMD1*$^{+/+}$) and *LIMD1*$^{-/-}$ HeLa cells surrounding the gRNA target sequence. Erroneous non homologous end joining surrounding the PAM motif results in the frameshift mutations and premature stop codon formation leading to LIMD1 knockout. ***B*)** Amino acid alignment of the WT and LIMD1$^{-/-}$ cell line. The frameshift mutation and premature stop codon disrupts normal LIMD1 protein expression.

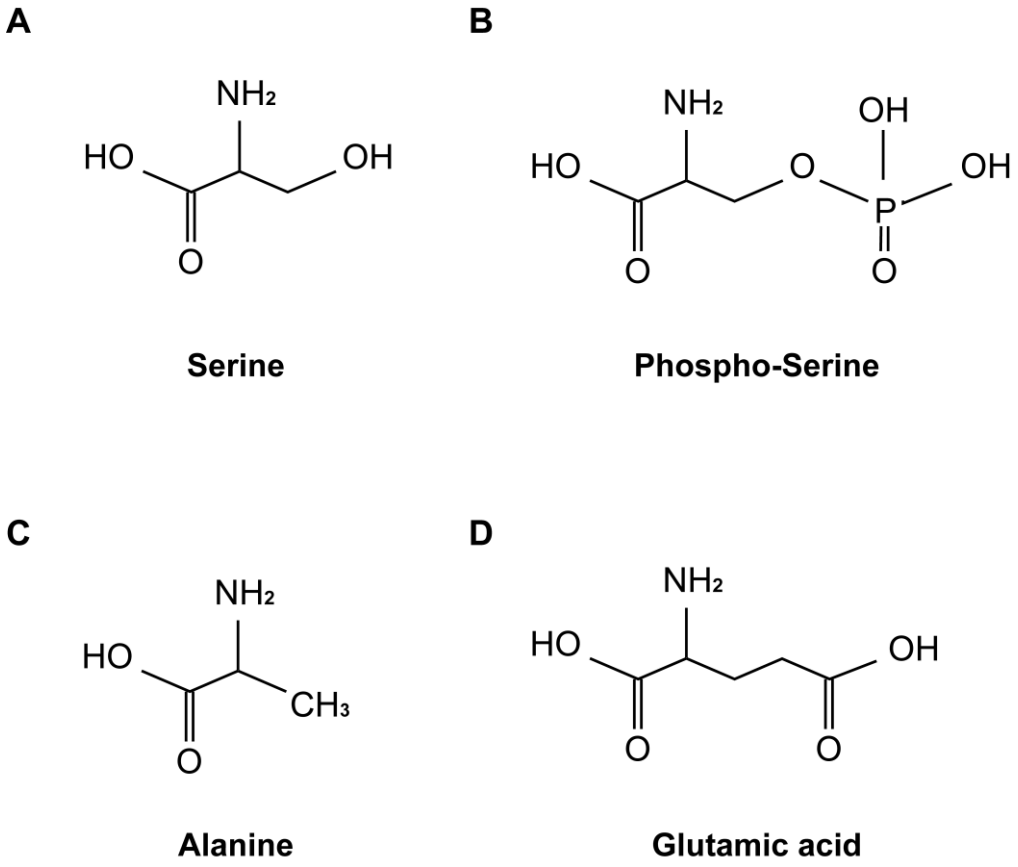

Figure 11.2 Chemical structure of amino acids

***A*)** The chemical structure of serine. ***B*)** The chemical structure of phospho-serine. ***C*)** The chemical structure of alanine. ***D*)** The chemical structure of glutamic acid.

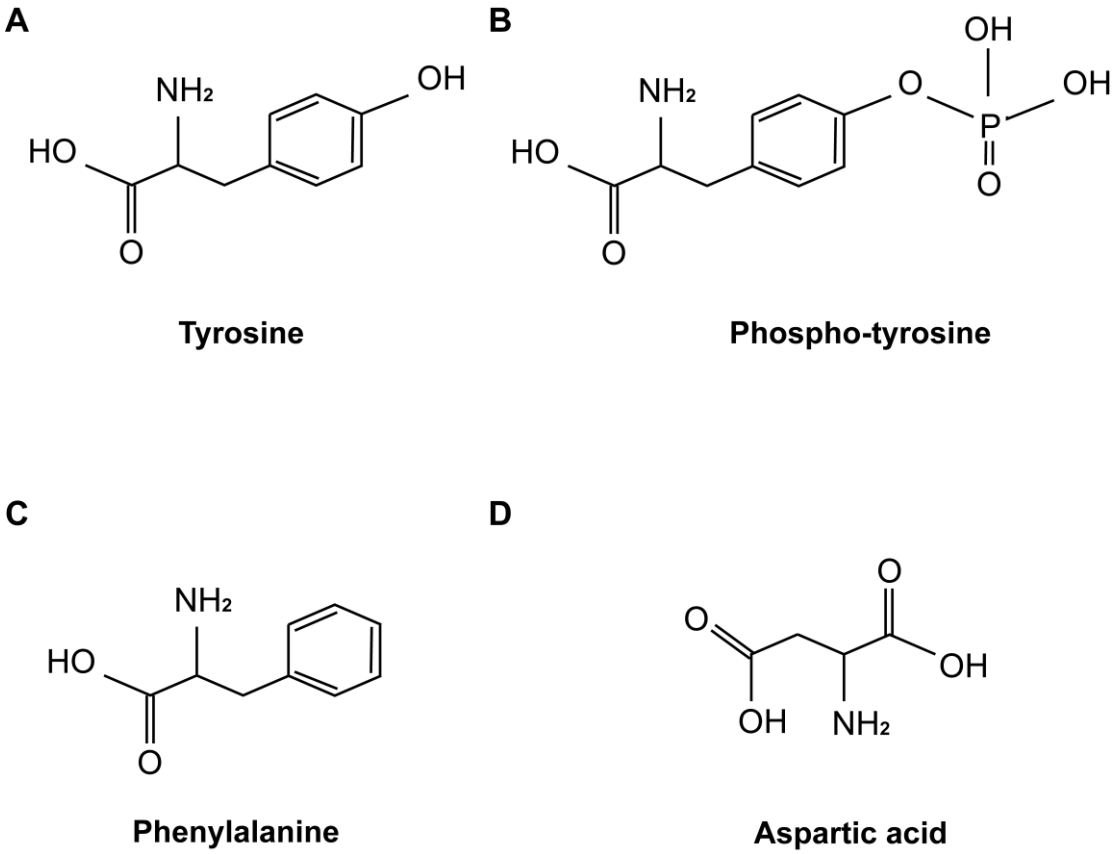

Figure 11.3 Chemical structure of amino acids
***A*)** The chemical structure of tyrosine. ***B*)** The chemical structure of phospho-tyrosine. ***C*)** The chemical structure of phenylalanine. ***D*)** The chemical structure of aspartic acid.

Table 11.1 Table of Z-score and ΔZ of the full list of genes targeting the specific kinase from Human Kinome siRNA Library.

Gene Symbol	A549			MDA-MB-435			HeLa CRISPR-Cas9		
	Z score		ΔZ	Z score		ΔZ	Z score		ΔZ
	shSCR	shLIMD1		FH-VO	FH-LIMD1		Cas9 Control	Knock-out	
AAK1	-1.414	-0.923	0.491	-6.495	-1.287	-5.208	-0.118	-0.148	-0.030
AATK	-0.554	-1.244	-0.690	-0.148	0.278	-0.426	-0.041	0.860	0.901
ABL1	-0.150	0.370	0.520	-0.465	0.193	-0.658	0.852	0.809	-0.043
ABL2	-0.177	0.364	0.541	0.604	0.799	-0.196	-0.262	0.044	0.306
ACVR1	-0.858	-0.117	0.741	0.353	-0.401	0.755	0.002	-0.015	-0.016
ACVR1B	0.230	0.573	0.343	-0.328	-0.069	-0.259	0.861	0.525	-0.337
ACVR1C	0.255	0.415	0.161	-0.553	-0.658	0.105	0.411	0.168	-0.243
ACVR2	0.772	1.033	0.262	1.359	0.494	0.865	0.891	0.351	-0.541
ACVR2B	-0.855	-0.376	0.479	-1.242	-1.225	-0.017	0.153	-3.368	-3.521
ACVRL1	0.891	1.172	0.281	0.671	-0.264	0.935	-0.510	0.147	0.657
ADCK1	-0.541	-0.292	0.249	0.328	0.120	0.208	-0.131	-0.090	0.042
ADCK2	-1.135	-0.149	0.985	-0.047	0.083	-0.131	0.506	-1.211	-1.716
ADCK4	-0.838	0.492	1.330	0.590	0.275	0.315	0.053	0.282	0.229
ADCK5	-0.277	-0.260	0.017	-1.103	-0.367	-0.736	0.788	-1.655	-2.442
ADK	-0.018	-0.544	-0.526	-0.103	0.461	-0.565	-0.129	0.091	0.220
ADP-GK	0.655	0.508	-0.147	-0.091	-0.381	0.289	-0.470	-0.149	0.322
ADRBK1	-1.121	-0.988	0.133	-0.664	-0.723	0.060	0.322	-1.110	-1.432
ADRBK2	1.054	1.071	0.017	0.538	0.676	-0.139	-0.566	1.073	1.639
AIP1	-0.934	0.021	0.954	-0.670	-0.127	-0.544	0.475	0.326	-0.149
AK1	-0.661	-0.172	0.488	-0.375	-0.340	-0.035	0.382	0.105	-0.278

AK2	-0.280	0.332	0.612	0.429	-0.565	0.993	0.468	-1.575	-2.043
AK3	0.082	0.283	0.201	0.421	0.718	-0.297	0.270	0.768	0.499
AK3L1	0.717	0.621	-0.096	0.033	0.395	-0.361	1.280	0.957	-0.323
AK5	1.843	1.081	-0.762	-0.059	0.526	-0.585	0.872	0.179	-0.692
AK7	0.847	0.131	-0.716	0.568	0.063	0.505	0.159	-0.034	-0.193
AKT1	0.052	0.237	0.185	0.155	0.650	-0.495	0.471	0.264	-0.207
AKT2	0.243	-0.064	-0.308	0.352	-0.671	1.022	-0.164	-0.073	0.091
AKT3	-1.795	-1.048	0.746	1.446	0.594	0.852	-1.673	-0.343	1.330
ALK	-0.517	-0.434	0.083	1.523	1.256	0.267	0.102	0.680	0.578
ALS2CR2	-0.518	-0.404	0.113	-0.675	-1.681	1.006	-0.290	-0.240	0.050
ALS2CR7	0.629	0.574	-0.055	0.362	0.551	-0.189	0.074	0.391	0.317
AMHR2	-0.946	-0.817	0.129	-0.607	-0.066	-0.541	-0.481	-0.623	-0.142
ANKK1	-0.616	-0.197	0.419	-0.108	-0.352	0.243	0.440	0.561	0.121
ANKRD3	-0.195	0.388	0.583	-0.362	0.427	-0.789	-0.163	-0.171	-0.009
ARAF1	1.236	1.232	-0.004	0.017	0.219	-0.202	0.212	0.871	0.659
ARK5	0.218	0.213	-0.005	1.098	0.861	0.236	0.286	0.053	-0.233
ASK	1.166	1.332	0.166	-0.695	-0.314	-0.381	0.166	0.164	-0.002
ATM	-0.283	-0.228	0.055	-1.115	-1.735	0.620	-1.057	-0.879	0.178
ATR	-1.499	-1.394	0.106	0.585	0.415	0.170	-1.192	0.809	2.001
AURKA	-3.123	-2.260	0.863	-5.593	-5.418	-0.175	-3.677	-3.969	-0.292
AURKB	-1.131	-0.347	0.783	-0.155	-0.049	-0.106	1.269	-2.270	-3.539
AURKC	-2.716	-1.923	0.793	-0.892	-1.333	0.441	-0.365	-0.444	-0.079
AXL	0.230	0.710	0.480	0.055	0.333	-0.278	0.273	0.650	0.377
BAIAP1	-0.465	-1.070	-0.605	-0.164	-0.586	0.422	0.721	1.382	0.661
BCKDK	-2.087	-1.533	0.554	1.042	0.885	0.157	0.632	0.533	-0.099

BCR	-1.887	-0.719	1.168	-0.351	-0.309	-0.042	-0.077	-1.563	-1.487
BLK	1.616	1.380	-0.236	0.920	1.583	-0.663	0.582	0.388	-0.194
BMP2K	0.159	-0.235	-0.395	0.385	0.456	-0.071	0.364	0.263	-0.101
BMPR1A	0.954	0.380	-0.574	-0.490	0.111	-0.601	0.344	-2.714	-3.058
BMPR1B	-1.569	-0.661	0.908	-0.505	-0.045	-0.460	0.426	-0.154	-0.580
BMPR2	0.997	0.519	-0.478	0.726	0.040	0.686	1.056	0.559	-0.497
BMX	0.211	-0.022	-0.233	0.578	0.067	0.511	0.095	1.475	1.380
BRAF	-1.706	-1.260	0.445	-3.193	-3.121	-0.072	-0.734	-2.030	-1.296
BRD2	1.062	1.147	0.085	1.493	1.199	0.294	1.193	0.804	-0.389
BRD3	1.164	1.278	0.114	0.534	1.834	-1.300	0.126	0.271	0.146
BRD4	-1.395	-1.764	-0.369	-1.188	-0.332	-0.856	0.006	-0.526	-0.532
BRDT	0.374	0.070	-0.304	0.693	0.188	0.505	0.496	-0.409	-0.905
BTK	-0.573	0.116	0.689	-0.304	-0.290	-0.014	0.167	0.321	0.153
BUB1	0.636	0.382	-0.254	0.172	-0.135	0.307	-0.261	-0.119	0.142
BUB1B	0.500	-0.011	-0.511	1.336	1.574	-0.237	0.108	-0.180	-0.288
C10ORF89	-0.807	-0.959	-0.151	-1.408	-1.394	-0.013	0.669	-0.665	-1.334
C14ORF20	0.177	0.248	0.071	-0.815	-0.520	-0.295	0.960	2.170	1.210
C7ORF2	1.811	1.576	-0.235	1.041	1.870	-0.828	0.486	0.002	-0.484
C9ORF12	-1.625	-1.490	0.135	-0.637	-0.112	-0.525	-0.036	0.378	0.414
C9ORF96	-0.939	-1.282	-0.342	0.997	0.674	0.323	-0.415	1.113	1.528
CALM1	-0.422	0.084	0.506	-0.411	-0.008	-0.403	1.418	0.806	-0.612
CALM2	-3.074	-2.467	0.607	1.179	0.948	0.231	-1.103	-0.771	0.331
CALM3	-0.409	-0.958	-0.549	0.003	-0.277	0.279	-0.657	-1.283	-0.626
CAMK1	-1.829	-1.541	0.287	0.743	-0.279	1.022	-0.099	-0.297	-0.199
CAMK1D	0.155	-0.181	-0.336	0.309	-0.166	0.474	0.422	-0.952	-1.375

CAMK1G	0.981	0.804	-0.177	-0.481	-0.042	-0.439	0.701	-0.680	-1.381
CAMK2A	-0.020	-0.391	-0.371	0.788	0.676	0.112	-1.096	0.274	1.370
CAMK2B	-0.225	-0.181	0.045	0.590	-0.446	1.036	0.693	0.245	-0.449
CAMK2D	0.555	0.233	-0.323	0.658	0.660	-0.002	0.488	-0.652	-1.140
CAMK2G	0.263	0.156	-0.107	0.245	0.492	-0.247	0.860	-0.638	-1.498
CAMK4	-0.372	-0.405	-0.033	-0.070	-1.385	1.314	0.467	2.089	1.622
CAMKIINALPHA	-1.669	-1.499	0.170	-0.718	-0.432	-0.285	-0.890	-1.489	-0.599
CAMKK1	0.540	0.585	0.045	-0.216	-0.223	0.007	0.942	0.694	-0.247
CAMKK1	-0.250	0.355	0.606	0.301	0.387	-0.086	-0.709	1.787	2.495
CAMKK2	0.878	0.436	-0.442	0.185	0.174	0.011	0.630	0.450	-0.180
CARKL	0.006	-0.213	-0.219	-1.468	-1.257	-0.211	-0.903	-0.517	0.386
CASK	-2.315	-1.643	0.672	0.385	-0.475	0.860	0.175	0.147	-0.028
CCRK	-2.879	-2.818	0.061	-0.837	-1.705	0.868	-0.729	-1.289	-0.560
CDADC1	-0.103	-0.827	-0.724	0.209	1.502	-1.293	-0.042	-0.285	-0.243
CDC2	-2.550	-0.854	1.696	-1.293	-1.778	0.486	-0.378	0.123	0.501
CDC2L1	-0.458	-0.332	0.126	-0.162	0.769	-0.932	0.770	0.397	-0.372
CDC2L2	-2.332	-1.908	0.424	0.275	1.165	-0.890	-0.961	-1.718	-0.758
CDC2L5	0.430	0.597	0.167	-1.068	-0.544	-0.524	-0.813	-1.281	-0.469
CDC42BPA	-0.897	-0.916	-0.019	-0.124	-1.246	1.122	-1.171	-1.462	-0.291
CDC42BPB	0.205	0.564	0.359	-0.382	0.665	-1.046	-0.043	0.232	0.274
CDC7	-0.449	0.188	0.637	0.665	-0.054	0.718	-0.872	-1.885	-1.013
CDK10	0.154	-1.166	-1.320	-0.727	-1.079	0.352	-0.131	-0.224	-0.093
CDK11	-1.694	-1.632	0.062	0.531	0.460	0.071	0.494	-0.040	-0.534
CDK2	-0.206	0.234	0.440	0.891	0.159	0.732	0.366	-1.061	-1.427
CDK3	-0.711	-1.046	-0.335	-1.135	-0.736	-0.399	-0.959	1.133	2.092

CDK4	-0.759	-0.252	0.507	-1.858	-1.816	-0.042	-0.023	-0.546	-0.523
CDK5	0.160	0.765	0.605	0.273	0.156	0.117	0.491	-0.484	-0.975
CDK5R1	0.388	0.901	0.514	0.201	-0.093	0.293	-0.352	-0.728	-0.377
CDK5R2	0.268	0.306	0.037	1.621	1.051	0.570	-1.572	-1.673	-0.101
CDK6	-0.834	-0.869	-0.035	-1.226	-1.707	0.481	-0.083	0.109	0.192
CDK7	0.488	0.569	0.081	1.523	1.176	0.347	0.151	0.312	0.161
CDK8	0.902	0.596	-0.306	0.097	0.697	-0.600	1.185	-0.007	-1.192
CDK9	0.067	0.255	0.188	0.551	0.744	-0.193	-0.128	-0.278	-0.150
CDKL1	-1.317	-1.324	-0.007	-0.443	-0.072	-0.372	-0.394	0.590	0.984
CDKL2	-1.224	-1.849	-0.625	-1.566	-0.938	-0.629	1.413	-1.250	-2.663
CDKL3	0.271	0.385	0.114	1.902	1.507	0.395	-0.019	0.204	0.223
CDKL4	0.369	-0.897	-1.266	0.286	0.231	0.055	-0.479	0.434	0.912
CDKL5	1.674	1.733	0.059	1.581	1.866	-0.286	0.883	0.732	-0.151
CDKN1A	1.340	1.587	0.248	-0.420	-0.178	-0.242	-0.083	-0.228	-0.144
CDKN1B	0.499	0.738	0.239	0.338	-0.116	0.454	0.398	0.958	0.560
CDKN1C	-0.006	-0.077	-0.071	1.356	0.582	0.774	-3.023	-1.562	1.461
CDKN2B	1.176	1.436	0.260	0.650	0.597	0.052	0.468	0.918	0.449
CDKN2C	-0.607	-0.012	0.594	-0.146	-0.367	0.221	0.013	-0.369	-0.382
CDKN2D	-1.975	-1.432	0.543	-0.751	-1.396	0.645	-1.689	-0.684	1.006
CERK	0.629	-0.336	-0.965	-0.131	-0.235	0.104	0.491	-0.067	-0.558
CHEK1	-2.969	-2.709	0.260	-1.277	-2.751	1.474	-1.423	-1.208	0.215
CHEK2	0.015	0.416	0.401	0.287	-0.039	0.326	-1.386	-1.171	0.215
CHKA	-1.889	-1.477	0.412	-1.471	-0.553	-0.918	-0.756	-0.412	0.345
CHKB	0.540	0.711	0.171	0.236	0.136	0.100	0.813	2.208	1.394
CHUK	-0.073	-0.281	-0.208	0.541	0.754	-0.213	0.487	1.311	0.824

CIB2	-5.186	-3.865	1.322	-1.185	-0.441	-0.743	-1.913	-1.726	0.187
CIT	-1.397	-1.570	-0.173	0.233	-0.460	0.693	-0.248	-1.434	-1.186
CKB	1.643	1.251	-0.393	0.778	0.976	-0.198	0.835	0.178	-0.657
CKM	0.141	0.177	0.036	0.836	0.908	-0.072	1.640	-0.544	-2.184
CKMT1B	-0.469	-0.452	0.017	-0.476	-0.154	-0.322	-0.616	-2.239	-1.622
CKMT2	-0.116	-0.046	0.070	1.007	-0.489	1.496	-0.949	-0.353	0.596
CKS1B	0.076	-0.430	-0.505	-0.999	-0.932	-0.067	0.275	0.526	0.251
CKS2	0.825	0.952	0.128	0.206	1.280	-1.074	0.886	0.940	0.055
CLK1	0.102	0.047	-0.055	0.409	0.078	0.331	1.483	0.753	-0.730
CLK2	1.604	0.811	-0.794	-0.457	-0.332	-0.125	-1.596	-0.461	1.135
CLK3	0.263	-0.221	-0.484	-0.722	-0.763	0.041	-0.026	1.367	1.393
CLK4	-1.049	-0.607	0.442	-0.422	0.010	-0.432	-0.118	-0.589	-0.471
COASY	-1.800	-1.102	0.699	-2.131	-1.682	-0.449	-3.818	-3.345	0.473
COL4A3BP	0.920	0.933	0.013	-1.515	-0.012	-1.502	1.756	1.662	-0.094
COMMD3	0.214	0.093	-0.121	0.766	0.615	0.150	0.413	1.498	1.085
CPNE3	0.187	-0.434	-0.621	-0.360	-0.277	-0.083	0.788	0.714	-0.074
CRIM1	-0.242	0.696	0.937	0.157	0.918	-0.761	0.099	-0.002	-0.101
CRK7	0.577	0.380	-0.197	-0.196	-0.933	0.737	-0.453	0.089	0.542
CRKL	0.816	0.525	-0.291	-1.098	-1.695	0.597	0.409	-0.573	-0.982
CSF1R	-1.353	-2.205	-0.852	-1.216	-0.820	-0.396	-1.375	-1.314	0.061
CSK	-1.160	-1.078	0.082	0.385	0.401	-0.016	0.080	0.689	0.609
CSNK1A1	0.139	1.117	0.978	0.162	-1.013	1.175	-0.665	1.179	1.844
CSNK1A1L	0.302	0.011	-0.291	1.103	0.440	0.663	0.254	1.225	0.971
CSNK1D	-0.106	-0.225	-0.118	-0.017	0.028	-0.046	0.212	0.528	0.316
CSNK1E	-1.817	-1.259	0.557	0.205	-0.746	0.951	-0.118	0.186	0.304

CSNK1G1	-1.503	-1.866	-0.362	-0.475	-0.753	0.278	-2.215	-1.690	0.525
CSNK1G2	0.147	0.100	-0.046	0.286	0.559	-0.273	1.462	1.229	-0.232
CSNK1G3	0.998	0.617	-0.381	0.246	-0.563	0.809	0.683	0.582	-0.102
CSNK2A1	1.592	1.509	-0.083	1.467	2.021	-0.554	1.798	-0.169	-1.967
CSNK2A2	-1.008	-0.244	0.764	-0.378	-0.006	-0.372	0.177	-0.179	-0.357
CSNK2B	0.085	-0.368	-0.454	-0.866	-1.086	0.220	-1.706	-2.862	-1.156
DAPK1	-0.698	-1.041	-0.343	-0.463	-0.111	-0.352	0.684	0.007	-0.677
DAPK2	0.240	0.573	0.333	-0.114	0.169	-0.282	-0.589	0.655	1.244
DAPK3	-0.207	-1.208	-1.001	-0.231	-0.424	0.193	0.701	0.087	-0.614
DCAMKL1	0.530	0.015	-0.515	-0.195	-0.133	-0.062	2.319	-0.135	-2.454
DCK	0.476	1.294	0.818	-0.809	-0.706	-0.103	0.385	-4.674	-5.059
DDR1	-1.343	-1.159	0.184	-0.204	0.395	-0.599	1.415	2.370	0.954
DDR2	-0.074	-0.116	-0.042	0.137	0.144	-0.006	0.882	0.659	-0.223
DGKA	-2.342	-1.386	0.955	-0.625	-0.255	-0.369	-0.766	-0.545	0.221
DGKB	-2.446	-1.585	0.861	-0.943	-1.088	0.145	1.041	0.303	-0.738
DGKD	0.505	0.646	0.141	0.540	0.393	0.148	0.286	1.302	1.016
DGKG	0.305	0.106	-0.199	0.315	0.222	0.093	-1.794	-1.682	0.112
DGKH	-0.876	-0.751	0.124	-0.452	-1.001	0.549	1.169	1.318	0.149
DGKI	0.894	1.135	0.241	1.139	1.527	-0.389	-0.412	-0.657	-0.244
DGKK	0.270	0.237	-0.033	0.787	0.440	0.347	-0.246	0.089	0.335
DGKQ	0.138	-0.389	-0.527	0.225	1.220	-0.995	-0.079	0.187	0.265
DGUOK	-0.324	-0.302	0.022	1.042	1.064	-0.022	0.970	0.319	-0.652
DKFZP434C131	0.879	0.894	0.015	-0.502	-0.231	-0.272	-0.304	0.559	0.863
DKFZP761P0423	-0.787	-1.139	-0.352	0.186	-0.722	0.909	-1.970	-1.444	0.526

DLG1	0.326	-0.818	-1.144	0.195	0.486	-0.291	0.153	1.234	1.081
DLG2	2.160	0.952	-1.208	1.516	2.101	-0.585	1.191	-0.154	-1.344
DLG3	2.045	1.739	-0.306	0.017	0.005	0.012	-0.744	1.230	1.974
DLG4	-1.035	-1.124	-0.089	0.441	0.828	-0.387	0.264	0.288	0.024
DMPK	-2.982	-1.145	1.838	-1.350	-0.563	-0.786	-2.892	-0.456	2.436
DTYMK	1.654	1.490	-0.165	0.678	0.616	0.062	0.360	0.510	0.150
DUSP21	0.438	-0.002	-0.440	0.092	0.047	0.044	3.258	0.017	-3.242
DUSTYPK	0.479	0.158	-0.321	-2.928	0.413	-3.341	0.462	0.464	0.003
DYRK1A	0.152	0.240	0.088	-0.452	-0.175	-0.277	0.875	1.957	1.082
DYRK1B	-0.044	0.463	0.507	0.631	0.104	0.528	0.106	0.193	0.087
DYRK2	-0.731	-0.044	0.686	-0.612	-0.123	-0.489	-0.883	-0.737	0.147
DYRK3	0.750	0.415	-0.335	0.037	-0.066	0.104	-0.641	-0.112	0.530
DYRK4	0.459	0.311	-0.148	0.856	0.939	-0.083	1.247	1.073	-0.174
EEF2K	-3.041	-1.941	1.099	-2.615	-3.962	1.347	-1.888	-1.808	0.080
EFNA3	-0.023	-0.023	0.000	1.169	0.646	0.523	-0.339	-0.206	0.133
EFNA4	-1.361	-1.488	-0.127	-0.320	-0.988	0.668	-1.690	-1.234	0.455
EFNA5	-0.320	-0.027	0.293	0.558	0.654	-0.096	1.240	0.676	-0.564
EFNB3	-2.130	-0.726	1.404	-0.224	-0.163	-0.062	3.667	-1.148	-4.815
EGFR	-0.583	-0.054	0.529	-0.416	-0.732	0.316	0.485	-0.238	-0.723
EIF2AK3	0.281	0.400	0.119	0.198	0.519	-0.321	0.293	-0.446	-0.739
EIF2AK4	0.194	-0.167	-0.361	0.051	0.195	-0.144	0.264	1.350	1.086
EPHA1	-1.386	-1.721	-0.335	-0.147	-0.141	-0.007	0.335	-0.877	-1.212
EPHA10	-0.700	-0.622	0.078	0.039	-0.018	0.058	0.497	0.187	-0.311
EPHA2	0.858	1.037	0.179	0.868	0.860	0.008	-0.327	0.286	0.612
EPHA3	-1.358	-1.893	-0.534	-1.057	-0.406	-0.650	-1.559	-1.298	0.261

EPHA4	-0.772	-0.217	0.555	-0.946	-0.747	-0.199	-1.334	-0.008	1.325
EPHA5	0.421	0.211	-0.210	0.850	1.251	-0.401	0.129	0.189	0.059
EPHA6	-2.873	-2.609	0.265	-1.686	-2.030	0.344	-1.146	-1.209	-0.064
EPHA7	-0.419	-0.327	0.093	0.789	-0.118	0.906	0.721	0.262	-0.458
EPHA8	0.392	0.648	0.256	0.037	0.544	-0.507	-1.000	0.910	1.910
EPHB1	0.403	0.169	-0.234	-0.741	-0.213	-0.527	0.309	0.680	0.371
EPHB2	1.429	0.502	-0.926	-0.194	-0.139	-0.055	0.998	0.422	-0.576
EPHB3	-0.062	-0.353	-0.292	-0.630	-0.637	0.007	-1.504	-1.419	0.085
EPHB4	1.187	1.032	-0.155	1.068	0.397	0.671	0.839	1.790	0.951
EPHB6	-1.807	-1.381	0.426	-0.958	-1.092	0.134	-1.215	-0.229	0.985
ERBB2	1.034	0.893	-0.142	1.077	1.291	-0.214	0.461	0.549	0.088
ERBB3	-0.377	-0.691	-0.314	-0.240	0.881	-1.121	1.434	1.030	-0.404
ERBB4	-0.263	-1.778	-1.515	-0.457	-1.551	1.094	0.038	-1.671	-1.710
ERK8	0.682	0.714	0.033	-0.008	-0.094	0.085	-1.594	-2.092	-0.498
ERN1	-2.008	-1.401	0.607	-0.895	-0.230	-0.666	-0.472	-2.265	-1.793
ERN2	-1.009	-1.033	-0.024	0.777	0.435	0.343	-0.223	0.049	0.272
ETNK1	0.600	0.208	-0.393	0.772	0.261	0.511	-0.204	-0.364	-0.160
EXOSC10	-0.856	-2.104	-1.248	-0.532	-0.171	-0.362	-0.642	-0.286	0.356
FASTK	0.553	0.337	-0.215	-0.283	0.063	-0.346	-0.840	-0.549	0.291
FER	0.150	-0.137	-0.287	-0.375	-1.235	0.860	0.492	0.273	-0.220
FES	-0.443	-0.378	0.065	0.619	0.366	0.253	-1.704	-2.579	-0.876
FGFR1	0.645	-0.194	-0.838	0.248	-0.973	1.221	0.575	0.654	0.079
FGFR2	-0.391	-1.051	-0.660	-0.810	0.853	-1.663	0.287	-0.071	-0.359
FGFR3	-0.055	0.786	0.841	1.043	0.731	0.313	0.596	0.697	0.101
FGFR4	-0.127	-0.453	-0.326	0.250	-0.488	0.738	-0.002	-0.349	-0.347

FGFRL1	1.151	0.915	-0.236	-1.269	-0.616	-0.654	0.136	0.406	0.270
FGR	-2.078	-1.403	0.675	0.122	-0.601	0.723	-2.014	-2.780	-0.767
FLJ10761	-1.475	-0.931	0.544	-1.007	-0.975	-0.032	-0.364	0.067	0.431
FLJ13052	-0.106	0.018	0.124	0.658	1.207	-0.549	-2.592	0.362	2.953
FLJ23074	-2.231	-0.999	1.233	-0.349	-0.572	0.223	-0.852	-0.474	0.378
FLJ23356	-0.509	-1.296	-0.787	-1.019	0.008	-1.027	0.452	0.432	-0.020
FLJ23356	0.018	-0.164	-0.182	-0.252	0.105	-0.357	0.255	0.245	-0.010
FLJ25006	0.014	0.385	0.371	-0.023	-0.301	0.278	0.563	0.084	-0.479
FLJ32685	-0.531	0.134	0.666	0.035	-0.764	0.799	-1.722	-0.479	1.242
FLJ34389	0.854	0.515	-0.339	-0.073	-0.019	-0.055	-0.066	-0.717	-0.651
FLT1	1.431	1.145	-0.286	-1.818	-1.909	0.091	1.339	0.490	-0.849
FLT3	-0.581	-1.082	-0.501	0.207	-0.467	0.674	-0.742	-0.561	0.181
FLT4	-2.826	-3.060	-0.234	-1.375	-1.888	0.513	0.533	0.077	-0.456
FN3K	-0.864	-0.030	0.834	0.521	0.999	-0.478	0.633	0.516	-0.117
FN3KRP	-2.011	-3.495	-1.484	-0.861	-2.253	1.392	-1.939	-1.271	0.668
FRAP1	-1.060	-1.041	0.019	0.412	0.720	-0.308	-0.281	-0.471	-0.190
FRDA	1.888	0.867	-1.021	0.019	-0.474	0.493	0.280	0.854	0.573
FRK	0.764	1.112	0.348	0.743	0.013	0.730	1.502	1.714	0.212
FUK	-0.955	-0.590	0.364	-0.112	0.236	-0.347	0.002	0.200	0.198
FYN	1.542	0.781	-0.762	-0.685	-0.388	-0.297	1.007	-0.573	-1.580
GAK	-0.231	-0.770	-0.539	-0.017	0.264	-0.281	0.092	-0.006	-0.098
GALK1	-0.721	-0.795	-0.075	-1.655	-2.082	0.427	-0.715	0.934	1.649
GALK2	-0.559	-1.284	-0.725	-0.531	-0.777	0.246	-0.274	0.368	0.642
GCK	-0.890	-0.270	0.619	-2.098	-2.607	0.509	0.355	0.675	0.320
GK	0.823	1.032	0.209	-1.608	0.630	-2.239	0.200	0.467	0.267

GK2	0.717	0.770	0.053	-0.267	0.332	-0.599	-0.637	0.692	1.329
GNE	0.399	0.701	0.302	-0.065	0.523	-0.588	1.077	-0.080	-1.157
GOLGA5	0.740	0.807	0.067	0.644	0.650	-0.006	1.191	0.686	-0.505
GRK1	0.071	0.539	0.468	0.675	0.142	0.533	0.858	-0.771	-1.629
GRK4	-1.242	-1.309	-0.067	-1.024	-0.521	-0.503	0.315	-2.001	-2.317
GRK5	0.116	-0.905	-1.021	0.477	0.488	-0.012	0.428	0.465	0.036
GRK6	-1.776	-0.742	1.034	-2.275	-1.001	-1.274	0.580	-0.351	-0.931
GRK7	-1.580	-1.057	0.522	-0.830	-1.519	0.689	0.151	-0.152	-0.303
GSG2	0.224	0.312	0.088	-0.999	-1.477	0.478	-0.264	-1.109	-0.845
GSK3A	-1.309	-1.574	-0.265	-0.324	-0.735	0.412	0.028	0.107	0.079
GSK3B	0.405	0.443	0.038	-0.090	-0.047	-0.043	0.355	2.023	1.668
GTF2H1	0.297	0.158	-0.139	0.473	0.111	0.362	-0.153	0.766	0.919
GUCY2C	0.480	0.324	-0.156	0.326	-0.330	0.656	0.828	1.950	1.122
GUCY2D	-2.878	-3.200	-0.321	-2.431	-2.834	0.403	-3.957	-2.693	1.264
GUCY2F	1.306	0.843	-0.463	0.586	0.452	0.134	0.382	1.307	0.925
GUK1	-1.148	-0.736	0.412	1.212	0.815	0.397	-0.604	0.008	0.612
HAK	0.226	-0.003	-0.229	0.677	0.198	0.479	0.019	1.167	1.148
HCK	0.128	-0.047	-0.174	-1.008	-0.744	-0.264	0.920	0.749	-0.171
HIPK1	1.454	0.271	-1.183	0.167	0.126	0.040	0.957	1.095	0.138
HIPK2	0.509	0.153	-0.356	-2.603	0.739	-3.342	-0.779	0.619	1.397
HIPK3	-0.158	-0.021	0.137	-0.734	-0.127	-0.607	-0.187	-0.483	-0.296
HIPK4	1.596	1.519	-0.078	-0.600	-0.755	0.155	0.303	-1.099	-1.402
HK1	-0.229	-0.418	-0.189	-0.302	-1.264	0.963	0.705	0.081	-0.625
HK2	-1.284	-0.055	1.229	0.156	0.720	-0.564	-2.232	-1.761	0.471
HK3	1.123	1.015	-0.108	-0.393	-0.236	-0.156	-0.829	0.346	1.175

HRI	-0.005	0.255	0.260	0.653	0.474	0.179	0.472	-0.028	-0.500
HSMDPKIN	-0.278	0.359	0.637	-0.961	-0.663	-0.298	-0.293	-0.254	0.039
HSPB8	-0.439	-0.343	0.096	0.322	0.703	-0.381	0.023	-0.117	-0.140
HUNK	-3.232	-1.982	1.250	-0.652	-1.296	0.644	-0.746	0.561	1.307
HUS1	1.071	1.407	0.336	0.095	0.264	-0.169	2.180	-0.210	-2.390
ICK	0.472	0.222	-0.250	-0.042	-0.302	0.260	0.833	0.721	-0.112
IGF1R	-1.978	-1.492	0.486	-0.125	-0.070	-0.054	0.207	-0.061	-0.268
IGF2R	1.777	1.060	-0.717	0.639	1.239	-0.599	2.185	2.661	0.477
IHPK1	-0.455	-0.019	0.437	0.464	1.228	-0.764	-0.681	0.202	0.883
IHPK2	0.195	0.048	-0.148	0.423	-0.057	0.480	-0.071	-1.844	-1.773
IHPK3	-3.274	-2.776	0.497	-1.094	-0.844	-0.251	-0.096	-0.413	-0.317
IKBKAP	0.205	0.184	-0.021	0.092	-0.189	0.281	-0.083	0.627	0.710
IKBKB	-0.089	-0.488	-0.400	-0.359	-0.922	0.563	-3.135	-0.799	2.336
IKBKE	-1.069	-1.204	-0.135	0.116	0.048	0.068	0.356	-0.978	-1.334
IKBKG	0.857	0.389	-0.468	-0.748	-0.760	0.013	0.660	1.054	0.393
ILK	-0.402	-1.112	-0.711	0.145	-0.098	0.243	0.842	-1.384	-2.226
ILK-2	0.206	0.915	0.708	0.085	0.029	0.057	-0.343	0.342	0.684
INSR	-0.545	-0.698	-0.153	-2.047	-1.443	-0.604	-0.688	-1.344	-0.655
INSRR	0.204	-0.711	-0.915	-0.598	-0.436	-0.162	1.165	-0.337	-1.502
IPMK	1.173	0.872	-0.301	-0.464	-0.477	0.013	0.755	1.249	0.494
IRAK1	-0.089	-0.609	-0.519	0.328	0.453	-0.125	0.006	-0.311	-0.317
IRAK2	0.413	0.510	0.097	-0.730	-0.508	-0.222	1.254	-0.441	-1.695
IRAK3	-2.771	-2.928	-0.157	-0.847	-1.178	0.331	-2.060	-2.084	-0.024
IRAK4	0.237	-0.215	-0.452	0.785	1.434	-0.649	1.364	1.203	-0.161
ITK	0.715	0.977	0.263	0.763	1.989	-1.226	0.062	0.013	-0.048

ITPK1	-0.300	0.100	0.400	-0.495	-0.640	0.146	-0.939	-0.613	0.326
ITPKA	0.621	1.217	0.595	0.937	0.927	0.010	0.133	0.184	0.051
ITPKB	0.651	1.105	0.454	1.206	0.930	0.277	-0.363	1.124	1.487
ITPKC	0.020	-0.772	-0.792	0.475	0.338	0.137	-0.015	-0.304	-0.289
JAK1	0.021	0.022	0.001	0.449	0.466	-0.017	0.627	-0.216	-0.843
JAK2	1.529	1.384	-0.145	-3.238	-5.112	1.874	1.366	0.744	-0.622
JAK3	-0.688	-0.650	0.037	0.053	-0.794	0.846	0.433	0.457	0.024
JIK	-0.965	-0.546	0.419	-0.291	-1.243	0.952	-1.949	0.145	2.094
KALRN	0.724	0.607	-0.118	-0.562	-0.898	0.337	0.872	0.663	-0.209
KCNH2	-0.548	-0.470	0.078	0.174	1.497	-1.323	-1.713	-0.556	1.158
KCNH8	-0.285	-0.963	-0.678	0.594	0.353	0.241	-0.163	-0.456	-0.293
KDR	-0.853	-1.054	-0.201	0.012	0.012	-0.001	-3.169	-2.387	0.782
KHK	-1.083	-1.196	-0.112	-1.058	-0.047	-1.010	0.791	-1.054	-1.845
KIAA0999	1.268	0.317	-0.951	0.018	-0.109	0.127	0.154	0.353	0.199
KIAA1361	0.247	0.341	0.094	1.361	1.483	-0.122	0.618	0.358	-0.260
KIAA1639	0.579	0.580	0.000	-0.059	-0.514	0.455	0.563	0.124	-0.439
KIAA1765	0.973	0.595	-0.378	0.617	0.409	0.209	1.070	1.918	0.848
KIAA1804	1.170	1.182	0.011	0.805	0.813	-0.008	-0.006	0.600	0.607
KIAA1811	1.088	1.399	0.311	1.206	0.933	0.273	-0.048	0.002	0.050
KIAA1811	-0.039	0.413	0.453	1.342	1.123	0.220	1.236	1.645	0.408
KIAA2002	-0.262	-0.711	-0.450	-0.787	-1.435	0.648	0.100	-1.134	-1.234
KIT	-0.797	-0.640	0.157	-0.629	-0.830	0.201	-1.080	-1.074	0.005
KSR	-1.233	-1.871	-0.638	-0.719	-0.102	-0.618	-1.587	-1.998	-0.411
KSR2	0.099	0.157	0.058	-1.084	-0.692	-0.392	-1.042	-0.764	0.278
KUB3	0.609	0.863	0.254	-0.076	-0.013	-0.063	0.104	0.196	0.093

LAK	0.507	-0.291	-0.798	-1.099	0.289	-1.388	-0.461	0.490	0.951
LATS1	-1.185	-0.769	0.416	0.194	-0.841	1.035	0.173	-0.241	-0.413
LATS2	0.689	0.407	-0.281	1.628	1.421	0.207	0.177	0.523	0.346
LCK	-1.044	-0.495	0.549	-0.134	-0.321	0.187	-0.222	0.281	0.503
LIMK1	-0.773	-0.207	0.566	-0.939	0.112	-1.051	-0.035	0.271	0.306
LIMK2	0.456	0.641	0.185	0.654	0.490	0.165	0.903	0.073	-0.830
LMTK2	1.514	0.487	-1.027	-0.477	0.180	-0.657	-3.218	0.993	4.211
LMTK3	-3.889	-1.885	2.004	-2.001	-2.837	0.835	-6.495	-5.170	1.325
LOC340156	0.039	-0.293	-0.332	1.304	1.585	-0.281	-0.565	0.184	0.749
LOC390226	0.695	0.895	0.200	0.166	-0.400	0.565	0.567	2.061	1.494
LOC91461	0.642	0.340	-0.303	1.304	0.918	0.386	0.341	0.256	-0.085
LRRK1	0.637	0.295	-0.342	0.617	0.809	-0.193	0.480	-0.534	-1.014
LRRK2	-0.713	0.030	0.743	0.068	-0.745	0.813	0.019	-0.038	-0.057
LTK	0.986	0.804	-0.182	0.913	1.321	-0.408	0.348	0.705	0.358
LYK5	-0.146	0.027	0.173	-0.184	-0.420	0.236	-0.288	2.155	2.443
LYN	-0.146	0.131	0.277	-0.040	0.330	-0.369	-0.517	-0.002	0.515
MAGI-3	2.064	-0.485	-2.549	-0.169	0.442	-0.611	0.575	-0.615	-1.190
MAK	-0.497	0.135	0.632	-0.070	-0.744	0.674	-1.241	-0.450	0.790
MAP2K1	0.872	1.306	0.434	0.831	0.580	0.251	0.246	1.318	1.072
MAP2K2	1.016	0.561	-0.455	-0.222	0.001	-0.222	0.403	-1.382	-1.786
MAP2K3	-1.507	-1.000	0.508	-0.517	-0.478	-0.039	-0.320	-0.204	0.116
MAP2K4	-1.841	-1.063	0.778	1.133	1.292	-0.159	-0.611	-1.107	-0.497
MAP2K5	0.164	-0.402	-0.566	1.314	1.534	-0.219	0.357	0.398	0.041
MAP2K6	0.296	0.439	0.142	1.952	2.613	-0.661	-0.852	0.447	1.299
MAP2K7	-1.772	-1.340	0.432	-1.663	-2.058	0.395	-0.944	-0.568	0.376

MAP3K1	-0.885	-0.018	0.867	-0.748	-0.956	0.209	-0.428	-0.994	-0.566
MAP3K10	0.511	0.857	0.346	0.177	1.472	-1.295	1.879	-0.060	-1.939
MAP3K11	-1.147	-1.214	-0.066	-0.138	-0.477	0.339	0.306	-0.938	-1.244
MAP3K12	-0.838	-0.866	-0.028	0.356	-0.757	1.113	0.348	0.514	0.166
MAP3K13	0.253	-0.370	-0.624	-0.806	-1.257	0.451	-0.566	0.937	1.503
MAP3K14	0.297	0.117	-0.180	-0.101	0.034	-0.135	-0.435	-1.050	-0.616
MAP3K15	0.567	1.235	0.668	0.766	0.578	0.188	-0.176	-0.204	-0.027
MAP3K2	1.316	1.420	0.104	1.818	1.566	0.252	0.095	0.602	0.506
MAP3K3	0.029	0.256	0.226	-0.119	0.049	-0.167	0.098	-0.289	-0.387
MAP3K4	0.892	-0.048	-0.940	0.852	0.885	-0.033	0.517	1.242	0.725
MAP3K5	0.352	-0.293	-0.645	-0.125	-0.659	0.534	0.701	0.390	-0.312
MAP3K6	0.048	-0.723	-0.771	0.218	-0.295	0.513	0.147	0.750	0.603
MAP3K7	-0.006	-0.265	-0.259	0.029	-0.214	0.243	0.229	-0.386	-0.616
MAP3K7IP1	0.583	0.914	0.331	0.456	-0.333	0.789	-0.969	0.508	1.477
MAP3K8	-0.080	0.154	0.234	-0.665	-0.550	-0.115	0.256	-0.342	-0.599
MAP3K9	-0.562	-1.028	-0.466	-0.146	0.461	-0.607	-0.730	-0.508	0.223
MAP4K1	-2.628	-1.999	0.629	-0.194	-1.036	0.843	-1.592	-1.047	0.545
MAP4K2	0.047	0.063	0.016	0.609	0.314	0.295	0.338	-0.012	-0.350
MAP4K3	-0.323	-0.560	-0.237	-0.451	-0.620	0.169	-0.519	-0.202	0.316
MAP4K4	1.081	0.251	-0.830	1.165	1.406	-0.241	0.958	0.318	-0.640
MAP4K5	-0.682	-0.518	0.164	0.458	0.260	0.198	-1.955	-3.400	-1.445
MAPK1	-2.951	-2.279	0.672	-2.257	-1.962	-0.295	-0.082	0.152	0.234
MAPK10	0.613	0.354	-0.259	-0.041	0.649	-0.689	0.581	-1.663	-2.244
MAPK11	-0.654	0.687	1.341	0.145	0.338	-0.193	0.457	0.543	0.086
MAPK12	-0.763	0.919	1.682	-0.093	-0.544	0.452	-0.816	1.255	2.070

MAPK13	0.254	-0.525	-0.778	0.827	0.537	0.290	0.991	0.644	-0.347
MAPK14	-0.534	-0.497	0.037	0.502	0.555	-0.053	-1.137	0.954	2.091
MAPK3	-0.334	-0.323	0.011	-0.866	-1.237	0.371	-0.513	-0.320	0.193
MAPK4	-1.045	-0.760	0.285	-2.198	-2.342	0.143	-1.376	-1.044	0.332
MAPK6	-1.807	-1.276	0.531	-0.261	-0.694	0.433	0.474	0.249	-0.225
MAPK7	0.505	1.047	0.542	-0.059	0.067	-0.126	0.353	0.053	-0.300
MAPK8	1.091	0.500	-0.592	0.703	0.232	0.471	0.796	0.674	-0.123
MAPK9	0.146	0.463	0.317	0.453	0.806	-0.353	0.686	0.488	-0.198
MAPKAPK2	0.718	-0.414	-1.132	-0.369	-0.557	0.188	0.632	-0.569	-1.201
MAPKAPK3	-1.706	-1.381	0.325	-0.794	-1.520	0.725	0.582	-1.242	-1.824
MAPKAPK5	1.081	0.265	-0.816	1.114	0.782	0.332	-1.667	-0.142	1.524
MARK1	-0.264	-0.427	-0.164	0.113	0.326	-0.213	-0.848	-0.694	0.154
MARK2	-1.254	-1.001	0.253	0.529	0.173	0.356	0.723	0.385	-0.338
MARK3	-3.728	-3.670	0.058	0.009	-0.565	0.574	-2.050	-1.909	0.141
MARK4	-0.094	-0.324	-0.230	-0.124	0.051	-0.175	0.618	-0.702	-1.320
MAST2	-0.392	-0.152	0.240	-1.029	-1.187	0.158	-2.793	-0.697	2.096
MAST3	-0.458	-0.022	0.436	0.525	0.886	-0.361	0.428	0.444	0.016
MAST4	1.069	0.801	-0.268	0.918	-0.886	1.804	0.343	0.466	0.124
MASTL	-0.833	-0.203	0.630	-0.440	-0.682	0.242	0.032	0.007	-0.025
MATK	0.174	-0.628	-0.802	0.987	0.561	0.426	-0.194	-0.129	0.064
MELK	0.227	0.097	-0.130	2.276	1.862	0.413	0.138	0.167	0.029
MERTK	0.722	0.001	-0.722	1.230	1.231	-0.001	-0.483	0.221	0.704
MET	1.358	0.993	-0.365	-1.114	-0.836	-0.278	1.025	-0.283	-1.309
MGC16169	-0.484	-0.213	0.271	-1.051	-1.059	0.008	0.539	0.354	-0.185
MGC42105	0.409	0.012	-0.397	1.071	0.401	0.670	0.380	0.321	-0.059
MGC45428	-1.931	-1.637	0.294	-0.368	-0.789	0.421	0.114	0.641	0.527

MGC4796	-0.621	-0.490	0.131	-1.447	-1.372	-0.075	-0.656	-1.017	-0.361
MGC4796	0.152	0.299	0.146	-1.597	-1.923	0.326	1.393	1.347	-0.046
MGC8407	-1.652	-0.836	0.816	-0.438	0.414	-0.852	0.308	0.371	0.063
MIDORI	0.018	0.396	0.378	-0.758	-1.056	0.298	0.109	-0.131	-0.239
MINK	-0.828	-0.265	0.563	0.029	-0.692	0.721	-0.415	-0.528	-0.113
MKNK1	0.254	0.402	0.148	0.380	0.748	-0.368	0.573	-0.326	-0.899
MKNK2	0.095	-1.014	-1.109	0.164	0.265	-0.101	-0.643	-0.717	-0.075
MLCK	-0.318	-0.058	0.259	0.358	0.036	0.322	0.450	0.259	-0.191
MOS	-0.321	-0.455	-0.135	-1.089	-1.648	0.559	-0.366	-1.140	-0.774
MPP1	-0.256	-0.750	-0.494	1.671	1.900	-0.230	0.321	0.036	-0.284
MPP2	-0.467	-0.460	0.007	0.526	0.066	0.461	0.057	-0.572	-0.629
MPP3	-0.001	-0.292	-0.290	-0.151	-0.212	0.061	-0.187	0.069	0.256
MST1R	-1.054	-1.050	0.003	-0.935	-1.516	0.581	-0.303	0.836	1.139
MULK	0.184	0.642	0.458	-1.032	0.471	-1.503	0.635	0.649	0.013
MUSK	-1.696	-1.672	0.025	-4.127	-0.221	-3.906	0.312	0.364	0.052
MVK	-0.707	-0.216	0.491	0.634	0.469	0.165	0.220	0.163	-0.057
MYLK	-0.503	-0.638	-0.135	-0.228	-0.724	0.496	-0.326	0.926	1.252
MYLK2	-5.959	-5.878	0.081	-2.118	-2.124	0.006	-2.003	-3.047	-1.043
MYO3A	-0.901	-0.744	0.157	-0.373	-0.742	0.369	-0.391	-0.001	0.390
MYO3B	0.139	0.666	0.527	-0.338	-0.393	0.055	-1.203	0.683	1.886
N4BP2	0.719	0.379	-0.339	1.450	1.316	0.134	-0.398	-0.102	0.296
NAGK	-3.353	-2.893	0.460	-1.535	-1.590	0.054	-1.413	-1.518	-0.105
NEK1	-0.202	-0.070	0.132	0.681	0.587	0.095	1.203	-2.365	-3.567
NEK11	-2.050	-1.639	0.410	0.008	0.055	-0.047	-1.732	-2.207	-0.475
NEK2	-0.450	-0.758	-0.308	-1.290	-1.327	0.036	0.338	1.122	0.783

NEK3	-1.136	-1.490	-0.355	-3.640	-2.267	-1.373	1.192	0.400	-0.792
NEK4	-0.290	-0.060	0.230	-0.805	-0.483	-0.322	-0.507	-0.156	0.351
NEK5	1.040	1.200	0.160	-0.011	1.053	-1.065	0.394	0.958	0.564
NEK6	0.502	0.341	-0.161	0.253	0.355	-0.102	0.731	0.155	-0.576
NEK7	2.196	1.676	-0.520	-0.347	0.277	-0.625	-0.507	0.011	0.518
NEK8	-3.409	-3.618	-0.210	-1.533	-2.236	0.703	-0.690	-0.755	-0.065
NEK9	-0.253	-0.571	-0.317	-0.239	0.601	-0.840	0.115	-0.083	-0.197
NLK	-0.915	-0.034	0.880	1.459	0.923	0.535	-0.332	0.058	0.390
NME1	1.365	0.718	-0.648	-0.128	0.660	-0.788	0.372	0.845	0.473
NME2	-0.292	0.444	0.735	-0.050	-0.786	0.736	-0.657	1.519	2.176
NME3	0.278	0.639	0.360	0.753	0.014	0.739	0.090	-0.657	-0.747
NME4	-0.378	0.217	0.595	-0.852	-0.719	-0.133	0.586	1.236	0.650
NME5	1.125	0.607	-0.518	0.999	1.219	-0.220	0.625	0.407	-0.219
NME6	-1.123	-1.443	-0.320	-1.021	-1.225	0.204	0.161	0.796	0.635
NME7	-0.200	-0.399	-0.199	1.730	1.072	0.658	1.358	1.393	0.035
NPR2	1.302	0.676	-0.626	1.343	1.127	0.216	1.026	0.690	-0.336
NRBP	0.376	0.246	-0.129	1.521	0.979	0.542	0.831	0.254	-0.577
NRBP2	0.296	-0.367	-0.663	-1.978	-3.080	1.102	1.541	-2.063	-3.604
NRK	1.141	0.346	-0.796	0.818	1.186	-0.368	1.390	-0.275	-1.665
NTRK1	-0.772	-1.032	-0.260	-0.208	0.089	-0.297	0.342	1.660	1.318
NTRK2	0.466	-0.219	-0.684	0.776	0.384	0.392	0.746	1.441	0.695
NTRK3	1.775	1.172	-0.602	-1.011	-0.284	-0.727	0.122	0.004	-0.118
NUCKS	0.676	-0.230	-0.905	-0.022	-0.147	0.125	0.778	0.331	-0.446
NUP62	-0.190	-0.750	-0.559	-1.277	-0.979	-0.298	-1.594	-2.456	-0.862
NYD-SP25	0.008	-0.858	-0.866	-0.400	0.820	-1.219	0.528	0.899	0.370

OSR1	1.630	0.998	-0.632	1.259	0.769	0.490	-0.295	0.437	0.732
P101-PI3K	-0.630	-0.414	0.216	0.919	0.571	0.348	-0.600	-0.648	-0.048
PACE-1	0.471	0.156	-0.315	0.160	-0.153	0.313	-2.159	1.021	3.180
PACSIN1	-0.447	-0.508	-0.060	0.192	-0.365	0.557	0.987	0.395	-0.591
PAK1	-1.266	-1.337	-0.070	0.723	0.056	0.667	-1.922	-1.878	0.044
PAK2	-0.324	-0.115	0.209	-0.276	-0.657	0.381	-0.238	0.081	0.319
PAK3	-1.103	-1.581	-0.478	0.136	0.593	-0.456	-0.726	-2.185	-1.460
PAK4	-0.888	0.124	1.013	-1.568	-0.829	-0.739	0.751	0.793	0.042
PAK6	0.623	0.105	-0.518	-2.041	-0.800	-1.241	-0.328	0.313	0.641
PAK7	-0.270	0.074	0.344	0.399	0.158	0.241	-0.656	-0.081	0.575
PANK1	0.702	0.372	-0.330	0.231	-0.669	0.900	0.554	0.593	0.039
PANK2	1.019	0.345	-0.675	-0.193	-0.254	0.062	-0.043	-0.590	-0.546
PANK3	0.346	-0.016	-0.361	0.421	0.061	0.360	0.416	0.814	0.398
PANK4	-1.366	-0.903	0.463	-1.687	-1.838	0.151	-1.091	-0.030	1.061
PAPSS1	0.530	0.188	-0.341	-0.003	0.891	-0.893	0.052	0.219	0.167
PAPSS2	0.701	0.055	-0.646	0.227	0.317	-0.091	-0.429	-0.065	0.364
PASK	0.784	0.734	-0.050	-0.207	-0.310	0.103	-2.230	-1.330	0.901
PCK1	-0.916	-0.848	0.068	-0.863	-1.821	0.958	-1.405	-2.738	-1.333
PCK2	-0.471	0.161	0.632	-0.023	-0.061	0.038	0.696	1.202	0.505
PCTK1	-1.731	-2.266	-0.535	0.307	-0.067	0.374	-0.180	-0.054	0.126
PCTK2	0.074	0.662	0.588	0.237	0.459	-0.222	0.796	0.239	-0.557
PCTK3	-0.189	-0.300	-0.111	-0.055	-0.805	0.750	-1.931	-2.058	-0.127
PDGFRA	-1.289	-0.849	0.439	-1.170	-1.051	-0.119	0.325	1.473	1.148
PDGFRB	-2.112	-1.351	0.761	-1.261	-1.682	0.421	-1.840	-0.978	0.862
PDGFRL	0.273	-1.023	-1.296	0.152	-0.069	0.221	0.035	-0.786	-0.821

PDIK1L	0.455	0.696	0.242	0.976	0.522	0.454	0.596	0.625	0.029
PDK1	-0.232	0.148	0.380	0.097	-0.313	0.410	-0.717	1.599	2.316
PDK2	-1.722	-1.397	0.324	-0.033	0.486	-0.519	-0.681	-0.963	-0.281
PDK3	0.078	0.131	0.052	-0.292	0.417	-0.709	0.504	0.587	0.083
PDK4	-0.511	-0.981	-0.470	0.445	0.125	0.320	0.368	1.276	0.908
PDPK1	0.001	-0.348	-0.350	-1.864	-2.007	0.143	0.251	0.732	0.481
PDXK	1.026	0.482	-0.543	0.800	0.363	0.437	0.438	-1.274	-1.713
PFKFB1	-0.930	-1.370	-0.440	-1.549	-1.152	-0.397	-1.355	-3.069	-1.714
PFKFB2	0.498	-0.197	-0.694	-0.952	0.215	-1.166	0.522	-0.583	-1.105
PFKFB3	0.018	0.291	0.273	1.482	1.409	0.073	-0.492	-0.149	0.344
PFKFB4	0.445	-0.277	-0.722	-1.568	-1.802	0.234	0.214	0.588	0.373
PFKL	1.981	1.701	-0.279	1.666	1.379	0.287	0.823	1.713	0.890
PFKM	0.060	0.147	0.088	0.155	-0.041	0.196	0.514	0.861	0.347
PFKP	-0.601	-0.780	-0.179	-0.332	-0.043	-0.289	0.459	-0.249	-0.708
PFTK1	-0.523	-0.990	-0.467	-0.130	0.251	-0.381	-0.370	-1.350	-0.980
PGK1	-0.950	-0.363	0.587	0.715	0.312	0.403	0.835	1.254	0.419
PGK2	0.651	0.844	0.193	0.800	1.377	-0.576	0.097	0.738	0.640
PHKA1	0.316	0.090	-0.225	-0.642	-0.287	-0.354	0.198	0.340	0.142
PHKA2	0.286	-0.463	-0.750	-0.143	-0.077	-0.065	-0.067	0.328	0.395
PHKB	0.929	0.532	-0.397	-0.339	-0.476	0.137	0.814	0.531	-0.283
PHKG1	0.671	-0.304	-0.975	0.105	-0.103	0.208	0.752	0.583	-0.168
PHKG2	-0.352	-0.309	0.043	0.569	1.214	-0.645	0.240	0.054	-0.185
PI4K2B	-0.637	-0.207	0.430	0.616	0.795	-0.179	-0.135	-1.574	-1.440
PI4KII	0.276	0.065	-0.211	-0.356	-0.716	0.360	0.201	0.252	0.051
PIK3C2A	-3.068	-3.510	-0.443	-0.476	-1.356	0.881	-4.492	-2.341	2.150

PIK3C2B	-0.203	-0.113	0.090	-0.269	0.307	-0.576	0.944	0.567	-0.377
PIK3C2G	-0.008	-0.394	-0.386	-0.008	0.242	-0.250	-0.246	-0.302	-0.057
PIK3C3	0.757	0.687	-0.070	0.194	0.740	-0.546	0.420	-0.562	-0.982
PIK3CA	-1.187	-0.334	0.854	0.633	0.381	0.251	-1.651	-0.002	1.649
PIK3CB	-0.391	-0.056	0.335	-0.607	-0.728	0.122	0.897	1.323	0.426
PIK3CD	0.021	0.190	0.169	0.714	0.390	0.325	-0.537	0.692	1.229
PIK3CG	-1.069	-1.159	-0.091	-0.646	-0.948	0.303	-1.728	-0.711	1.017
PIK3R1	0.488	0.697	0.210	1.002	0.772	0.230	0.508	0.530	0.022
PIK3R2	0.064	0.702	0.638	-0.480	0.157	-0.636	0.052	-0.412	-0.464
PIK3R3	1.048	1.276	0.228	-0.078	-0.991	0.913	1.004	0.289	-0.715
PIK3R4	-0.426	-0.745	-0.319	-0.486	-1.045	0.559	-0.968	0.017	0.984
PIK4CA	-0.729	-0.381	0.348	-0.664	0.054	-0.718	-4.222	-5.393	-1.171
PIK4CB	0.282	0.709	0.427	0.150	0.507	-0.357	0.268	0.353	0.084
PIM1	-0.451	-0.133	0.318	-0.763	-0.068	-0.695	-0.328	-0.616	-0.288
PIM2	-3.138	-1.734	1.404	-0.595	-0.983	0.388	-1.344	-0.754	0.590
PIM3	-0.073	-0.152	-0.079	-1.391	-1.897	0.505	-0.656	1.139	1.795
PINK1	-1.285	-1.002	0.283	-0.009	-0.449	0.440	-0.298	0.093	0.391
PIP5K1A	-0.275	0.414	0.689	-0.175	-0.124	-0.052	0.844	-0.447	-1.291
PIP5K1B	-0.050	-0.579	-0.528	-0.279	-0.711	0.432	0.632	0.452	-0.180
PIP5K1C	1.144	0.446	-0.698	0.445	-0.701	1.146	-1.261	1.357	2.618
PIP5K2A	0.759	0.376	-0.384	1.444	0.619	0.825	1.098	0.473	-0.625
PIP5K2B	-2.115	-2.239	-0.124	-1.239	-1.450	0.211	-0.067	-1.529	-1.462
PIP5K2C	0.688	0.828	0.141	0.314	0.490	-0.176	0.569	0.914	0.345
PIP5K3	-0.038	-0.338	-0.299	1.083	0.986	0.097	-0.115	-0.365	-0.250
PIP5KL1	0.452	-0.431	-0.883	-0.189	-1.492	1.303	-0.062	0.343	0.405

PKIA	1.370	0.374	-0.996	0.153	-0.090	0.242	-4.335	0.008	4.342
PKIB	0.240	0.568	0.327	0.201	0.928	-0.727	0.367	-0.419	-0.786
PKLR	-0.159	0.665	0.824	0.473	0.152	0.321	-1.724	-0.263	1.461
PKM2	-0.504	-0.066	0.439	0.279	-0.601	0.880	0.423	0.164	-0.258
PKMYT1	0.123	0.498	0.375	-1.243	-1.100	-0.143	-2.344	-0.250	2.093
PKN3	-1.282	-0.562	0.720	-0.503	-0.573	0.069	-0.051	-1.849	-1.799
PLK1	-6.247	-6.253	-0.006	-10.546	-11.193	0.647	-7.677	-5.714	1.962
PLK2	0.217	0.219	0.003	-0.776	0.668	-1.444	1.232	0.992	-0.241
PLK3	-2.266	-0.966	1.300	-0.808	-0.789	-0.018	0.175	-0.245	-0.420
PLK4	-0.459	-0.421	0.038	-1.476	-1.196	-0.280	-1.749	-2.005	-0.256
PMVK	-1.902	-3.009	-1.107	-0.978	-0.617	-0.361	-0.136	0.107	0.243
PNCK	-0.012	-0.268	-0.256	0.240	0.081	0.158	0.366	1.345	0.979
PNKP	-1.597	-1.065	0.532	-1.083	-1.409	0.326	-0.106	-0.041	0.065
PRKAA1	-0.262	-0.080	0.182	0.897	0.493	0.405	1.056	0.572	-0.483
PRKAA2	0.967	0.532	-0.435	0.143	0.153	-0.010	-1.112	0.639	1.750
PRKAB1	-0.768	-1.475	-0.707	-0.334	-0.308	-0.027	0.140	0.040	-0.100
PRKAB2	-2.071	-2.009	0.062	-1.885	-2.267	0.382	0.068	0.012	-0.056
PRKACA	0.005	-0.105	-0.110	-1.284	-2.245	0.962	0.390	0.490	0.101
PRKACB	1.596	0.981	-0.614	1.242	0.893	0.349	-0.002	-1.082	-1.080
PRKACG	1.410	1.166	-0.244	-0.368	-0.612	0.244	0.601	1.205	0.604
PRKAG1	0.955	0.905	-0.050	0.492	0.424	0.068	0.038	0.030	-0.007
PRKAG2	1.336	0.534	-0.802	-0.066	0.083	-0.149	0.589	1.071	0.482
PRKAG3	-0.726	-0.992	-0.265	-3.096	-3.108	0.012	-1.963	-1.113	0.850
PRKAR1A	-0.018	-0.030	-0.012	0.323	0.158	0.164	0.675	0.581	-0.094
PRKAR1B	0.684	-0.642	-1.326	-2.374	-1.736	-0.638	0.050	0.090	0.040

PRKAR2A	0.114	-0.484	-0.598	1.200	0.860	0.340	0.435	0.156	-0.280
PRKAR2B	-0.939	-0.826	0.113	-0.042	-0.169	0.126	-0.066	1.313	1.379
PRKCA	-0.828	-1.464	-0.636	-1.292	-0.730	-0.562	-0.307	-0.861	-0.554
PRKCB1	-0.590	-0.893	-0.303	0.584	0.199	0.384	-0.134	1.142	1.277
PRKCD	-0.852	-0.338	0.514	-1.373	-1.029	-0.344	-3.449	-1.875	1.573
PRKCE	-2.915	-1.947	0.968	-0.967	-0.267	-0.700	-1.393	-0.758	0.635
PRKCG	0.351	0.344	-0.006	0.737	0.710	0.027	1.527	0.864	-0.663
PRKCH	-2.183	-2.730	-0.547	-0.683	-0.786	0.103	-1.277	-0.521	0.756
PRKCI	-0.673	-0.519	0.154	0.128	-1.036	1.164	-0.926	-0.195	0.732
PRKCL1	-0.316	-0.470	-0.153	-0.015	-0.157	0.142	-0.864	-1.565	-0.701
PRKCL2	-0.736	-1.029	-0.293	-1.103	-0.269	-0.834	-0.859	-2.328	-1.469
PRKCM	-0.552	0.194	0.746	0.753	0.489	0.263	-0.129	-0.093	0.036
PRKCN	-0.445	-1.077	-0.633	-0.828	-0.587	-0.241	0.088	-0.659	-0.747
PRKCQ	-1.473	-0.441	1.032	-0.111	-0.406	0.295	-1.292	0.508	1.801
PRKCSH	0.760	0.398	-0.362	-1.245	-1.476	0.231	1.207	1.399	0.192
PRKCZ	-1.221	-0.813	0.408	-1.797	-1.507	-0.291	-0.322	-0.249	0.073
PRKD2	0.952	0.455	-0.497	1.141	1.444	-0.303	-0.519	-1.232	-0.714
PRKDC	-0.481	-1.450	-0.969	-0.502	-0.086	-0.415	-0.786	0.078	0.864
PRKG1	0.106	0.195	0.090	0.197	0.440	-0.243	1.066	0.208	-0.858
PRKG2	0.377	0.555	0.177	0.692	0.955	-0.262	0.058	-0.037	-0.095
PRKR	1.050	0.967	-0.083	0.776	0.156	0.620	0.624	1.651	1.028
PRKWNK1	0.958	0.002	-0.956	-0.214	-0.001	-0.213	3.128	-0.832	-3.961
PRKWNK2	0.585	0.755	0.170	-0.580	-0.417	-0.162	-2.031	-0.529	1.502
PRKWNK3	0.700	0.639	-0.061	-1.140	0.412	-1.552	-0.697	-0.502	0.194
PRKX	1.482	1.407	-0.075	0.737	1.276	-0.539	1.055	0.665	-0.390

PRKY	-1.135	-0.378	0.757	-2.746	-3.230	0.483	-0.072	-2.679	-2.607
PRPF4B	-0.092	-0.441	-0.349	-0.429	-0.647	0.218	-0.690	-0.092	0.598
PRPS1	0.364	0.776	0.412	-1.266	-0.136	-1.131	-1.818	-0.021	1.797
PRPS1L1	0.453	0.406	-0.047	1.158	0.943	0.216	0.026	-1.648	-1.674
PRPS2	0.999	0.817	-0.182	0.064	-0.114	0.178	0.277	0.594	0.317
PSKH1	0.726	0.441	-0.285	0.308	0.721	-0.413	0.475	-0.050	-0.524
PSKH2	0.348	-0.397	-0.745	0.379	0.725	-0.346	0.520	-2.173	-2.693
PTK2	-1.445	-0.271	1.174	-0.060	-0.014	-0.046	-0.266	-0.129	0.137
PTK2B	-0.755	-0.008	0.746	-1.265	-1.718	0.453	0.998	0.241	-0.757
PTK6	0.809	0.591	-0.217	0.653	0.613	0.040	0.423	0.777	0.354
PTK7	-2.115	-2.254	-0.140	-0.445	-1.083	0.638	-2.282	-0.836	1.445
PTK9	1.338	0.865	-0.473	1.175	1.016	0.160	-0.281	0.077	0.358
PTK9L	0.226	-1.669	-1.895	-0.231	-1.150	0.919	-0.731	0.720	1.451
PXK	0.552	-0.505	-1.057	0.123	-0.600	0.723	-2.669	-2.199	0.470
PYCS	-2.612	-2.088	0.524	-0.883	-0.063	-0.820	-2.793	-0.558	2.235
RAF1	-0.156	0.385	0.542	0.301	0.720	-0.419	1.559	1.269	-0.290
RAGE	1.718	0.847	-0.871	0.905	0.050	0.856	0.093	0.442	0.349
RBKS	1.384	0.767	-0.616	-0.110	0.414	-0.524	-0.203	0.417	0.620
RELA	-2.391	-2.310	0.081	-0.935	-0.925	-0.010	-0.366	-0.459	-0.093
RET	0.178	0.039	-0.138	1.433	1.389	0.044	-1.715	-0.108	1.607
RFK	1.471	0.292	-1.179	0.933	1.500	-0.567	0.926	1.069	0.143
RFP	-1.319	-0.438	0.881	-2.060	-3.358	1.298	-0.238	0.088	0.326
RIOK1	-1.187	-0.946	0.241	-0.332	-0.957	0.626	0.742	0.424	-0.318
RIOK2	0.398	0.538	0.140	-0.741	-0.677	-0.064	-1.471	-0.485	0.986
RIOK3	0.687	0.611	-0.076	0.721	0.575	0.146	-0.019	0.896	0.915

RIPK1	0.214	-0.311	-0.526	-1.103	-0.008	-1.095	-0.135	0.296	0.431
RIPK2	0.440	0.126	-0.314	-0.334	-0.434	0.099	-0.322	-0.867	-0.545
RIPK3	0.871	0.674	-0.197	0.759	0.329	0.430	0.312	1.151	0.839
RNASEL	-0.452	-0.271	0.181	0.387	0.248	0.139	0.671	-0.757	-1.428
ROCK1	0.741	0.488	-0.253	1.124	1.167	-0.044	0.786	-0.423	-1.209
ROCK2	-0.275	-0.794	-0.519	-0.083	-0.098	0.015	-0.245	1.048	1.293
ROR1	0.596	0.305	-0.291	0.870	0.185	0.685	-1.068	-0.079	0.988
ROR2	0.865	0.968	0.103	-0.457	-0.109	-0.348	0.568	-0.075	-0.643
ROS1	-0.046	-0.670	-0.624	-0.256	-0.211	-0.044	-0.061	-0.763	-0.701
RP6-213H19.1	0.227	0.675	0.448	1.959	1.514	0.445	0.109	-0.148	-0.257
RPS6KA1	-1.647	-1.351	0.296	-2.283	-1.934	-0.350	-0.048	-0.165	-0.117
RPS6KA2	-2.553	-2.454	0.099	-2.067	-1.566	-0.502	-0.846	-2.335	-1.489
RPS6KA3	1.204	0.580	-0.624	0.674	0.064	0.610	0.297	0.157	-0.140
RPS6KA4	-0.434	0.113	0.547	-0.008	-1.174	1.166	1.121	0.427	-0.694
RPS6KA5	-0.626	-0.528	0.098	-1.120	-1.632	0.512	-0.985	-2.435	-1.450
RPS6KA6	1.662	1.527	-0.135	0.518	0.064	0.454	0.708	0.798	0.090
RPS6KB1	-0.360	-0.697	-0.337	1.521	1.436	0.085	1.169	0.570	-0.599
RPS6KB2	0.425	-0.267	-0.692	-0.262	-0.376	0.114	0.442	0.104	-0.338
RPS6KC1	0.995	0.890	-0.105	2.160	2.021	0.139	0.714	0.695	-0.019
RPS6KL1	-0.484	-0.304	0.181	-0.426	-0.915	0.489	0.490	0.001	-0.489
RYK	0.814	0.658	-0.155	1.447	1.133	0.313	-0.100	-1.249	-1.149
SAST	0.973	0.228	-0.745	0.397	-0.445	0.842	0.323	1.653	1.329
SBK1	-0.298	-0.199	0.100	0.922	0.282	0.640	-0.721	0.210	0.931
SCAP1	0.170	0.670	0.500	-1.879	1.165	-3.043	0.767	0.489	-0.278
SCYL1	1.381	0.955	-0.426	-0.259	-0.239	-0.020	1.445	0.619	-0.826

SGK	1.634	1.018	-0.616	-0.267	0.934	-1.200	0.568	-0.665	-1.234
SGK2	-0.059	-0.067	-0.008	0.167	0.211	-0.044	0.463	0.395	-0.068
SGKL	1.693	1.252	-0.441	0.352	0.056	0.296	0.436	0.944	0.508
SIK2	-1.263	-1.060	0.203	-1.196	-1.407	0.210	-0.396	0.629	1.025
SLK	0.386	-0.062	-0.447	-0.936	-0.152	-0.784	-1.589	0.404	1.994
SMG1	0.039	-0.441	-0.480	0.393	-0.227	0.620	-0.171	-0.813	-0.643
SNARK	-0.898	-1.776	-0.878	-0.388	-0.382	-0.006	0.474	0.014	-0.460
SNF1LK	0.894	0.524	-0.371	0.936	0.403	0.533	0.364	0.240	-0.124
SNRK	-1.187	-1.116	0.072	-0.402	0.095	-0.498	-1.386	-1.815	-0.429
SPEG	0.502	0.100	-0.403	-0.388	0.074	-0.462	0.425	0.341	-0.084
SPHK1	-1.472	-0.684	0.788	-2.129	-2.064	-0.064	-0.002	-0.225	-0.223
SPHK2	0.656	0.443	-0.213	1.142	1.019	0.123	-0.759	-1.582	-0.823
SRC	0.127	0.097	-0.030	-0.436	0.008	-0.444	0.114	0.376	0.262
SRMS	-6.241	-2.065	4.176	-0.923	-0.462	-0.461	-2.729	-2.974	-0.245
SRP72	-0.305	-0.272	0.033	0.291	0.382	-0.092	-1.790	0.068	1.857
SRPK1	0.641	0.445	-0.197	-1.118	-2.116	0.998	-0.660	0.165	0.825
SRPK2	0.960	0.976	0.017	-0.214	-0.347	0.133	-0.035	-0.449	-0.414
SSTK	-0.281	-0.602	-0.321	-0.936	-1.140	0.204	0.632	-1.218	-1.850
SSTK	-1.395	-0.767	0.628	-1.758	-0.477	-1.282	0.284	-0.632	-0.916
STK10	-0.606	-0.326	0.279	-0.836	-0.205	-0.631	-0.025	0.017	0.042
STK11	-0.395	-0.501	-0.106	1.784	1.371	0.413	0.107	-0.271	-0.379
STK16	0.473	0.506	0.033	0.746	0.132	0.614	0.546	-0.941	-1.487
STK17A	-0.510	-1.572	-1.062	-0.845	-0.989	0.144	-0.006	-1.621	-1.615
STK17B	-1.094	-0.905	0.189	0.176	0.282	-0.105	0.059	0.332	0.274
STK19	0.701	-0.006	-0.707	0.384	0.239	0.146	-0.059	-0.398	-0.339

STK22B	0.236	-0.539	-0.776	-0.042	0.456	-0.498	-1.321	-0.004	1.317
STK22C	0.037	-0.817	-0.854	-0.815	-1.773	0.958	-1.287	-1.209	0.077
STK22D	0.239	-1.455	-1.694	0.305	-0.324	0.629	0.271	0.142	-0.129
STK22D	0.192	0.629	0.437	-0.296	0.287	-0.584	-0.126	0.653	0.779
STK23	1.041	1.949	0.908	0.989	0.847	0.143	-1.703	0.117	1.820
STK24	0.072	0.318	0.246	0.829	1.064	-0.235	1.352	0.259	-1.093
STK25	-0.151	0.186	0.337	-1.654	-1.818	0.164	-0.293	-0.642	-0.349
STK29	0.412	0.641	0.230	-1.216	-0.960	-0.256	0.709	0.023	-0.686
STK3	-0.353	0.523	0.876	0.369	0.701	-0.332	0.939	0.335	-0.605
STK31	-0.336	-0.279	0.057	0.937	0.101	0.836	-0.184	-0.013	0.171
STK32A	-0.797	-0.345	0.452	0.320	-0.010	0.330	-1.489	0.420	1.909
STK32B	1.104	0.392	-0.712	-0.054	-0.271	0.217	-2.733	-1.118	1.615
STK32C	0.337	1.064	0.727	-0.813	-0.949	0.137	1.423	2.156	0.733
STK33	-0.594	-0.702	-0.108	-0.872	-0.455	-0.417	0.105	-0.771	-0.876
STK35	-0.455	-0.355	0.100	0.716	0.990	-0.274	0.920	-0.334	-1.254
STK36	-1.017	-0.242	0.775	-0.506	-0.056	-0.450	0.835	0.527	-0.308
STK38	-2.312	-2.637	-0.326	-0.225	-0.792	0.567	0.002	-0.269	-0.271
STK38L	0.347	0.484	0.138	0.088	-0.340	0.428	0.963	0.070	-0.893
STK39	-0.541	-3.213	-2.672	1.883	0.895	0.988	-0.988	-2.390	-1.402
STK4	0.794	1.013	0.219	-0.526	-0.442	-0.085	1.026	-0.304	-1.330
STYK1	-0.549	1.036	1.585	-0.844	-0.312	-0.532	-0.435	-0.814	-0.379
SYK	-2.059	-1.138	0.922	-1.083	-2.542	1.459	-3.904	-1.664	2.240
TAF1	-0.602	-0.902	-0.300	0.576	0.700	-0.123	1.032	-0.660	-1.692
TAF1L	0.030	0.543	0.513	-0.718	-0.079	-0.639	0.160	-0.219	-0.378
TAO1	1.230	0.891	-0.340	1.156	1.334	-0.179	1.149	0.844	-0.305

TBK1	-1.087	-1.239	-0.152	0.831	0.638	0.193	-0.893	-0.254	0.639
TEC	0.447	-0.254	-0.700	0.723	0.802	-0.079	0.614	0.389	-0.225
TEK	0.519	0.693	0.174	-0.211	-1.037	0.826	0.251	0.559	0.308
TESK1	-0.629	-1.286	-0.658	-0.428	-1.147	0.718	-1.197	-2.684	-1.487
TESK2	0.175	1.047	0.872	0.571	0.977	-0.406	0.975	0.882	-0.094
TEX14	-0.043	-0.296	-0.253	0.484	-0.021	0.505	0.457	-2.133	-2.590
TGFBR1	0.136	0.054	-0.082	0.522	-0.107	0.629	-1.130	-1.002	0.128
TGFBR2	-0.126	-0.460	-0.335	-2.082	-1.085	-0.996	-0.927	-0.175	0.751
TGFBR3	0.757	0.626	-0.130	1.978	0.324	1.654	0.054	0.235	0.182
THNSL1	0.629	0.579	-0.050	1.087	0.412	0.675	0.864	0.010	-0.854
TJP2	-0.014	-0.430	-0.416	0.577	0.976	-0.399	-1.583	-1.943	-0.361
TK2	0.025	0.460	0.435	1.056	0.563	0.493	0.201	-0.927	-1.128
TLK1	0.764	0.788	0.024	-1.297	-0.693	-0.604	-0.686	0.700	1.385
TLK2	1.348	1.308	-0.039	1.579	2.046	-0.467	0.117	0.304	0.187
TNIK	-0.567	-0.602	-0.035	-1.151	-1.749	0.598	0.275	0.350	0.075
TNK1	-0.386	-0.250	0.136	-0.299	0.139	-0.438	0.696	-0.679	-1.376
TNK2	0.102	0.658	0.556	-0.991	-1.088	0.096	-0.700	-0.896	-0.196
TNNI3K	1.173	-0.062	-1.234	0.355	0.685	-0.330	0.617	0.811	0.194
TOPK	0.505	0.131	-0.374	0.079	0.701	-0.622	0.555	0.305	-0.250
TP53RK	0.838	0.843	0.005	-0.012	-0.060	0.048	0.507	1.166	0.659
TPK1	-3.209	-2.809	0.401	-1.106	-1.507	0.401	-2.076	-2.475	-0.399
TRIB1	0.290	0.584	0.293	0.179	1.083	-0.904	0.411	-0.101	-0.513
TRIB2	-2.208	-3.077	-0.870	0.033	0.057	-0.024	0.084	0.779	0.695
TRIB3	-0.135	-0.129	0.006	-1.116	-1.324	0.208	0.115	-0.811	-0.927
TRIO	0.840	-0.217	-1.057	-0.259	-0.511	0.252	-0.695	-1.340	-0.645

TRPM6	1.316	1.175	-0.140	0.466	0.920	-0.454	1.387	0.582	-0.805
TRPM7	0.272	0.159	-0.113	-0.525	-0.547	0.022	-2.182	0.902	3.084
TSKS	1.229	1.263	0.034	0.767	0.942	-0.175	-1.718	-0.315	1.403
TTBK1	-1.485	-1.626	-0.142	-0.948	-0.603	-0.345	-0.062	-0.292	-0.231
TTBK2	-0.685	-1.136	-0.451	0.086	0.996	-0.910	-0.429	0.019	0.448
TTK	-1.495	-0.902	0.594	-1.378	-2.094	0.716	-2.408	0.408	2.815
TYK2	0.971	0.720	-0.251	0.600	0.006	0.594	-2.124	0.543	2.667
TYRO3	0.312	0.913	0.601	-0.055	-0.419	0.365	-0.453	0.029	0.482
UCK1	-0.128	-0.042	0.086	0.534	1.484	-0.950	0.953	-1.191	-2.144
UHMK1	-0.768	-0.347	0.421	0.479	-0.621	1.100	-0.195	-0.133	0.063
ULK1	0.520	0.785	0.265	0.897	0.933	-0.035	1.292	-0.695	-1.987
ULK2	0.431	0.151	-0.280	0.310	0.994	-0.683	0.355	0.477	0.121
ULK4	-0.739	-0.973	-0.234	0.460	-0.103	0.563	-0.189	-1.365	-1.175
UMP-CMPK	-0.511	0.047	0.558	0.904	0.926	-0.021	-0.595	1.717	2.312
UMPK	0.095	0.637	0.543	-0.193	0.858	-1.052	0.875	0.691	-0.184
URKL1	0.481	0.156	-0.326	0.368	0.157	0.211	0.414	0.303	-0.111
VRK1	0.184	-0.114	-0.298	0.345	0.184	0.161	0.195	0.406	0.212
VRK2	-0.182	-0.303	-0.121	0.526	0.111	0.415	-0.343	-0.015	0.328
VRK3	-0.584	-0.731	-0.146	-0.189	0.216	-0.405	0.674	1.887	1.213
WEE1	-0.761	-0.732	0.029	-5.688	-5.893	0.204	-0.864	-5.255	-4.391
WNK4	0.013	0.411	0.399	0.706	0.904	-0.199	-0.032	-0.103	-0.071
XYLB	0.641	1.121	0.480	2.232	1.782	0.450	0.625	-0.211	-0.836
YES1	0.204	-0.157	-0.361	-0.278	0.029	-0.307	0.609	0.413	-0.197
ZAK	0.012	-0.297	-0.309	1.147	1.261	-0.114	0.959	0.512	-0.447
ZAP70	-1.616	-0.603	1.013	-0.792	-1.065	0.272	-5.877	-0.802	5.075

Table 11.2 Table of DAVID data analysis of top 100 'hits' from the screening on A549 isogenic pair
The table indicates the number of genes analysed by DAVID belong to each signalling pathway.

A549		
KEGG_PATHWAY		
Term	**Count**	**PValue**
MAPK signalling pathway	15	1.44E-08
Insulin signalling pathway	8	1.40E-04
Neurotrophin signalling pathway	7	4.69E-04
Rap1 signalling pathway	8	0.001746356
Glucagon signalling pathway	5	0.009311845
Calcium signalling pathway	6	0.016694189
AMPK signalling pathway	5	0.018855997
Endocytosis	7	0.020387447
Proteoglycans in cancer	6	0.025616618
Ras signalling pathway	6	0.040315077
GnRH signalling pathway	4	0.040541457
Oxytocin signalling pathway	5	0.043036799
T cell receptor signalling pathway	4	0.055043129
Purine metabolism	5	0.059620005
Insulin resistance	4	0.061727743
Sphingolipid signalling pathway	4	0.079229892
mTOR signalling pathway	3	0.084924424
VEGF signalling pathway	3	0.092553458
Osteoclast differentiation	4	0.096967392
BIOCARTA		
Term	**Count**	**PValue**
MAPK Signalling Pathway	11	1.23E-07
ChREBP regulation by carbohydrates and cAMP	4	0.003164398
Signalling Pathway from G-Protein Families	4	0.012548636
Attenuation of GPCR Signalling	3	0.014769915
Nitric Oxide Signalling Pathway	3	0.040345274
Stathmin and breast cancer resistance to anti-microtubule agents	3	0.051009907
Transcription factor CREB and its extracellular signals	3	0.058626058
g-Secretase mediated ErbB4 Signalling Pathway	2	0.099090004

Table 11.3 Table of DAVID data analysis of top 100 'hits' from the screening on MDA-MB-435 isogenic pair.

The table indicates the number of genes analysed by DAVID belong to each signalling pathway.

MDA-MB-435		
KEGG_PATHWAY		
Term	**Count**	**PValue**
ErbB signalling pathway	6	5.49E-04
Ras signalling pathway	8	0.001743635
FoxO signalling pathway	6	0.003758183
Type II diabetes mellitus	4	0.006088059
Phosphatidylinositol signalling system	5	0.006995986
Toll-like receptor signalling pathway	5	0.009190165
Metabolic pathways	18	0.010026357
Glycerolipid metabolism	4	0.010282067
Neurotrophin signalling pathway	5	0.014028033
Axon guidance	5	0.01695745
Insulin signalling pathway	5	0.022290181
Rap1 signalling pathway	6	0.023393265
Aldosterone-regulated sodium reabsorption	3	0.036942815
Inflammatory mediator regulation of TRP channels	4	0.04077648
Choline metabolism in cancer	4	0.043960432
T cell receptor signalling pathway	4	0.04615065
Chagas disease (American trypanosomiasis)	4	0.047265885
TNF signalling pathway	4	0.049536338
Insulin resistance	4	0.051859733
Toxoplasmosis	4	0.064253619
Regulation of actin cytoskeleton	5	0.081896263
Osteoclast differentiation	4	0.082214376
Biosynthesis of antibiotics	5	0.083004747
Colorectal cancer	3	0.084229879
Central carbon metabolism in cancer	3	0.0889285
Pancreatic cancer	3	0.091306894
Renal cell carcinoma	3	0.091306894
Fc epsilon RI signalling pathway	3	0.098553247
BioCarta		
Term	**Count**	**PValue**
MAPK Signalling Pathway	5	0.022784798
Agrin in Postsynaptic Differentiation	3	0.080783813
p38 MAPK Signalling Pathway	3	0.092459319

Table 11.4 Table of DAVID data analysis of top 100 'hits' from the screening on HeLa CRISPR-Cas9 isogenic pair

The table indicates the number of genes analysed by DAVID belong to each signalling pathway.

HeLa		
KEGG_PATHWAY		
Term	**Count**	**PValue**
Neurotrophin signalling pathway	10	1.95E-06
ErbB signalling pathway	8	1.85E-05
MAPK signalling pathway	11	1.52E-04
Long-term potentiation	6	4.17E-04
Focal adhesion	9	7.84E-04
Oxytocin signalling pathway	8	7.87E-04
Regulation of actin cytoskeleton	9	9.17E-04
FoxO signalling pathway	7	0.0018
Phosphatidylinositol signalling system	6	0.002497
Proteoglycans in cancer	8	0.003062
Renal cell carcinoma	5	0.003507
Inositol phosphate metabolism	5	0.004819
Axon guidance	6	0.007538
Aldosterone synthesis and secretion	5	0.007677
Chemokine signalling pathway	7	0.008982
Progesterone-mediated oocyte maturation	5	0.009837
Wnt signalling pathway	6	0.010594
Insulin signalling pathway	6	0.010594
GnRH signalling pathway	5	0.011477
cAMP signalling pathway	7	0.012004
Pathways in cancer	10	0.012945
Glucagon signalling pathway	5	0.015262
Oocyte meiosis	5	0.020996
Glioma	4	0.024827
Vascular smooth muscle contraction	5	0.027902
Adherens junction	4	0.031187
Herpes simplex infection	6	0.031767
Chronic myeloid leukemia	4	0.032323
Gastric acid secretion	4	0.03348
Fructose and mannose metabolism	3	0.038111
Measles	5	0.039618
Prion diseases	3	0.04032
Salmonella infection	4	0.046221
Prostate cancer	4	0.053371
Bladder cancer	3	0.059618
Circadian entrainment	4	0.06422

Ras signalling pathway	6	0.067378
Inflammatory mediator regulation of TRP channels	4	0.069161
Melanogenesis	4	0.072548
Endometrial cancer	3	0.090154
Tuberculosis	5	0.092128
Cholinergic synapse	4	0.092461
Calcium signalling pathway	5	0.095058
BIOCARTA		
Term	**Count**	**PValue**
MAPK Signalling Pathway	10	5.35E-05
Integrin Signalling Pathway	5	0.007193
Transcription factor CREB and its extracellular signals	4	0.018795
Ca++/Calmodulin-dependent Protein Kinase Activation	3	0.030299
Bioactive Peptide Induced Signalling Pathway	4	0.046138
Regulation of PGC-1a	3	0.092561
Stathmin and breast cancer resistance to antimicrotubule agents	3	0.099286

Article

Cell Reports

Argonaute Utilization for miRNA Silencing Is Determined by Phosphorylation-Dependent Recruitment of LIM-Domain-Containing Proteins

Graphical Abstract

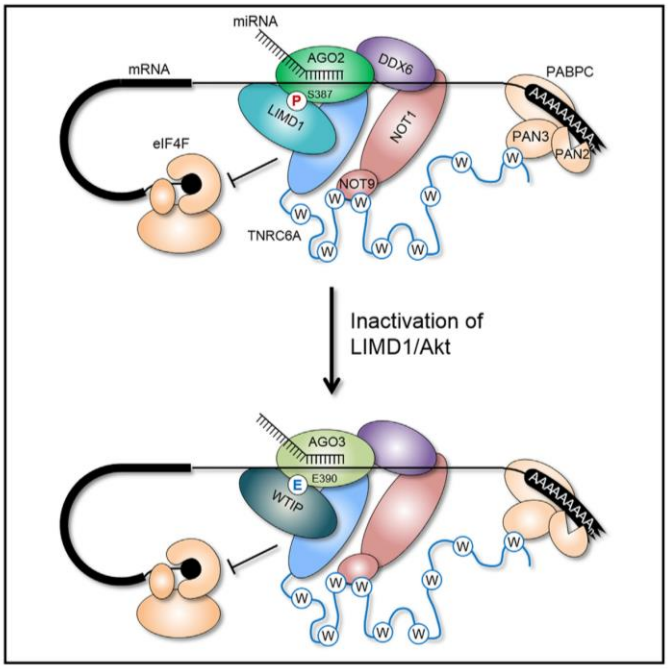

Authors

Katherine S. Bridge, Kunal M. Shah, Yigen Li, ..., Michael J. Plevin, Dimitris Lagos, Tyson V. Sharp

Correspondence

t.sharp@qmul.ac.uk

In Brief

Argonaute (AGO) proteins mediate post-transcriptional gene silencing through formation of the microRNA-induced silencing complex (miRISC). Bridge et al. identify LIM-domain-containing proteins as essential for miRISC formation through a phosphorylation-dependent mechanism. This is critical for post-transcriptional gene silencing and reveals that miRISC functionality is maintained by "AGO switching."

Highlights

- LIMD1 is necessary for the Akt3-dependent assembly of an AGO-TNRC6A functional miRISC
- AGO1, 2, and 4 recruit LIMD1 in a phospho-dependent manner
- AGO2 to AGO3 switching occurs upon LIMD1 ablation in HeLa cells
- AGO3-WTIP replaces AGO2-LIMD1 for miRNA silencing in an Akt3-independent manner

Bridge et al., 2017, Cell Reports *20*, 173–187
July 5, 2017
http://dx.doi.org/10.1016/j.celrep.2017.06.027

CellPress

Cell Reports
Article

OPEN ACCESS
CellPress

Argonaute Utilization for miRNA Silencing Is Determined by Phosphorylation-Dependent Recruitment of LIM-Domain-Containing Proteins

Katherine S. Bridge,[1,10] Kunal M. Shah,[1,10] Yigen Li,[1,10] Daniel E. Foxler,[1] Sybil C.K. Wong,[1] Duncan C. Miller,[1] Kathryn M. Davidson,[1] John G. Foster,[1] Ruth Rose,[2] Michael R. Hodgkinson,[3] Paulo S. Ribeiro,[4] A. Aziz Aboobaker,[5] Kenta Yashiro,[9] Xiaozhong Wang,[7] Paul R. Graves,[6] Michael J. Plevin,[3] Dimitris Lagos,[8] and Tyson V. Sharp[1,11,*]

[1]Centre for Molecular Oncology, Barts Cancer Institute, Queen Mary University of London, John Vane Science Centre, Charterhouse Square, London EC1M 6BQ, UK
[2]School of Biological and Chemical Sciences, Queen Mary University of London, Fogg Building, Mile End Road, London E1 4NS, UK
[3]Department of Biology, University of York, Heslington, York YO10 5DD, UK
[4]Centre for Tumour Biology, Barts Cancer Institute, Queen Mary University of London, John Vane Science Centre, Charterhouse Square, London EC1M 6BQ, UK
[5]Department of Zoology, University of Oxford, The Tinbergen Building, South Parks Road, Oxford OX1 3PS, UK
[6]Department of Radiation Oncology, New York-Presbyterian Brooklyn Methodist Hospital, 506 6th Street, Brooklyn, NY 11215, USA
[7]Department of Biochemistry, Molecular Biology and Cell Biology, Northwestern University, Evanston, IL 60208, USA
[8]Centre for Immunology and Infection, Hull York Medical School and Department of Biology, University of York, Heslington, York YO10 5DD, UK
[9]Cardiac Regeneration and Therapeutics, Osaka University Graduate School of Medicine, 2-2 Yamada-oka, Suita, Osaka 565-0871, Japan
[10]These authors contributed equally
[11]Lead Contact
*Correspondence: t.sharp@qmul.ac.uk
http://dx.doi.org/10.1016/j.celrep.2017.06.027

SUMMARY

As core components of the microRNA-induced silencing complex (miRISC), Argonaute (AGO) proteins interact with TNRC6 proteins, recruiting other effectors of translational repression/mRNA destabilization. Here, we show that LIMD1 coordinates the assembly of an AGO-TNRC6 containing miRISC complex by binding both proteins simultaneously at distinct interfaces. Phosphorylation of AGO2 at Ser 387 by Akt3 induces LIMD1 binding, which in turn enables AGO2 to interact with TNRC6A and downstream effector DDX6. Conservation of this serine in AGO1 and 4 indicates this mechanism may be a fundamental requirement for AGO function and miRISC assembly. Upon CRISPR-Cas9-mediated knockout of LIMD1, AGO2 miRNA-silencing function is lost and miRNA silencing becomes dependent on a complex formed by AGO3 and the LIMD1 family member WTIP. The switch to AGO3 utilization occurs due to the presence of a glutamic acid residue (E390) on the interaction interface, which allows AGO3 to bind to LIMD1, AJUBA, and WTIP irrespective of Akt signaling.

INTRODUCTION

MicroRNAs are ~22 nucleotide non-coding RNA molecules that silence gene expression post-transcriptionally (Bartel, 2004). Their loading onto Argonaute (AGO) proteins facilitates base-pairing to mRNA targets with partial complementarity and ultimately translational repression and mRNA degradation (Huntzinger and Izaurralde, 2011; Hutvagner and Simard, 2008). Repression is executed by the microRNA-induced silencing complex (miRISC), a large multi-subunit complex assembled by AGO-mediated recruitment of GW182/TNRC6 proteins and downstream effector complexes (Behm-Ansmant et al., 2006; Chekulaeva et al., 2011; Lian et al., 2009; Liu et al., 2005). TNRC6 proteins facilitate translational repression, mRNA destabilization, and ultimately degradation of target mRNAs via recruitment of effector proteins to the miRISC, such as those involved in decapping (DCP1/2), RNA unwinding (DDX6), and deadenylation (CCR4-NOT) (Bazzini et al., 2012; Chen et al., 2014; Chu and Rana, 2006; Rouya et al., 2014).

Despite significant advances in our understanding of the terminal effects of miRNAs on their targets, the early steps of miRISC assembly and its functional activation remain poorly understood. Recent studies have explored the role of post-translational modification of AGO proteins (Jee and Lai, 2014; Rüdel et al., 2011). For example, phosphorylation of AGO2 Y529 inhibits loading of small RNAs (Rüdel et al., 2011), while EGFR-dependent phosphorylation of AGO2 Y393 prevents processing of looped precursor RNAs into mature miRNAs (Shen et al., 2013). Additionally, Akt3-mediated phosphorylation of AGO2 S387 reduces the mRNA cleavage activity of AGO2 and drives it toward translational repression associated with miRNA-mediated silencing (Horman et al., 2013; Zeng et al., 2008). It has also recently been shown that primary T cells display a signaling-dependent shift in miRISC configuration. While the majority of miRNAs were found in low-molecular-weight miRISC complexes in resting T cells, stimulation of phosphatidylinositol 3-kinase (PI3K) signaling caused an increased association of miRNAs with high-molecular-weight miRISC complexes and an enhancement of miRNA-mediated silencing (La Rocca et al., 2015). These data

indicate that miRISC assembly into an active complex and the protein-protein interactions therein are highly dynamic processes, controlled by signal transduction cascades.

To date, the four human AGO proteins (AGO1–4) have been demonstrated to function largely redundantly with regards to miRNA loading and target recognition, with the functionally dominant AGO currently attributed to the expression levels of these proteins (Dueck et al., 2012; Su et al., 2009; Wang et al., 2012). How these overlapping functions are facilitated in light of recent findings demonstrating the role of signaling pathways in the regulation of miRNA biogenesis and function is unclear. Interestingly, plasticity in AGO usage following genetic ablation has been observed (Wang et al., 2012), although the mechanism underpinning this switch remains unknown.

The discovery that AGO2 activity is regulated by phosphorylation, and indeed other post-translational modifications, raises the question as to whether all four human AGO proteins are subject to regulation by signaling, and whether, through differential signal transduction and phosphorylation, may not exhibit complete redundancy (Golden et al., 2017; Lopez-Orozco et al., 2015; Patranabis and Bhattacharyya, 2016; Sahin et al., 2014; Shen et al., 2013; Zeng et al., 2008). Horman and colleagues suggest that the AGO2 S387 phosphorylation diverts its activity from mRNA cleavage to (or toward) miRNA-mediated silencing (Horman et al., 2013). However, this study did not consider the high homology within the S387-containing L2 domain between AGO2 and other human AGO proteins, which are not involved in small interfering RNA (siRNA) silencing. We therefore sought to determine whether signaling regulates miRISC assembly and function across the entire AGO family and whether this regulation would identify an additional dimension of AGO family member functional specificity.

LIMD1 is a component of miRISC required for silencing (James et al., 2010). However, its precise function in miRISC and miRNA silencing is poorly understood. Here, we demonstrate that LIMD1 is crucial for AGO2 miRNA function and that loss of AGO2-LIMD1-mediated miRNA silencing reveals a previously unknown mechanism of AGO selection, with LIMD1 association being a key determinant of AGO utilization. LIMD1 is required for the recruitment of TNRC6A and downstream effectors (DDX6) to AGO2. We show that Akt3-mediated phosphorylation of AGO2 (S387) promotes a phospho-dependent interaction with LIMD1 that is vital for enabling engagement of AGO2 with TNRC6A, revealing the mechanism by which AGO-S387 phosphorylation regulates miRISC function. The phosphorylation-dependent interaction with LIMD1 also extends to the other human AGO family members, with a conserved serine also present in AGO1 and AGO4. AGO3 lacks this conserved serine residue but instead contains a phospho-mimic glutamic acid residue (E390), which facilitates signaling-independent binding to LIMD1 family members. Our findings demonstrate that loss of LIMD1 abolishes AGO2-mediated miRNA silencing and results in redistribution of AGO utilization for miRNA silencing to AGO3.

RESULTS

AGO Utilization Is Determined by LIMD1

Members of the LIMD1 family (LIMD1, AJUBA, and WTIP) of LIM-domain-containing proteins associate with miRISC and are required for miRNA-mediated silencing (James et al., 2010). To examine the role of LIMD1 on AGO2 function, we designed a Renilla luciferase reporter containing five targeted or non-targeted miR-99/100 binding sites in its 3′ UTR. We observed significant de-repression of the targeted reporter upon AGO2, TNRC6A, or LIMD1 siRNA-mediated knockdown in HeLa cells, whereas little or no de-repression was seen with depletion of AGO1, 3, or 4 (Figure 1A and S1A). The high specificity of this reporter for AGO2 is surprising as a previous study did not find evidence for miRNA sorting into AGO1, 2, or 3 in HeLa cells and concluded that association of a particular miRNA with a particular AGO solely reflected AGO protein abundance (Dueck et al., 2012). Moreover, mRNA levels of the targeted reporter were unchanged, indicating that, at the time points analyzed, the reporter is subject to miRNA-mediated translation inhibition rather than target cleavage (Figure S1B).

To investigate the mechanistic function of LIMD1 in miRNA silencing independently of engagement of the RNAi machinery, we genetically ablated *LIMD1* in HeLa cells using CRISPR-Cas9 technology (Figure S1C). Unexpectedly, we found that repression of the miR-99/100 reporter was equivalent in $LIMD1^{+/+}$ and $LIMD1^{-/-}$ cell lines (~50% repression of the targeted reporter), although expression of exogenous LIMD1 enhanced silencing in the $LIMD1^{-/-}$ line (Figure S1D). To explore the mechanism underlying the maintenance of silencing in the $LIMD1^{-/-}$ line, we analyzed reporter activity when this isogenic HeLa CRISPR pair was treated with siRNAs targeting AGO1–4 (Figures 1B and 1C). We observed a switch in the requirement for AGO proteins in this pair of HeLa lines. AGO2 depletion only led to de-repression of miRNA silencing in the $LIMD1^{+/+}$ line, whereas, in the $LIMD1^{-/-}$ line, AGO3 depletion produced a de-repression. As AGO2 comprises the majority (~60%) of the AGO pool in HeLa cells (Petri et al., 2011) and its levels remained unchanged upon LIMD1 loss (Figure S1C), the switch in AGO utilization may reflect the importance of LIMD1 specifically for AGO2 function in HeLa.

In order to interrogate the generality of this switch in AGO utilization, we employed a *let-7a*-targeted reporter. Similarly, we observed that loss of LIMD1 ($LIMD1^{-/-}$) rendered AGO2 unable to contribute to silencing, whereas in $LIMD1^{+/+}$ cells, de-repression was induced upon AGO2 knockdown (Figures S1E and S1F). In contrast to the miR-99/100 reporter, however, AGO1 and AGO3 knockdown resulted in de-repression of the *let-7a*-targeted reporter, regardless of *LIMD1* genotype, indicating this reporter and miRNA demonstrated a broader specificity for AGO and LIMD1 family proteins. To rule out the possibility that the observed switch in AGO use was due to the use of a synthetic 3′ UTR miRNA reporter, we also examined whether LIMD1 loss resulted in a switch in AGO requirement of two natural 3′ UTRs reporters—FGFR3 and MTOR, which each contain, in addition to other miRNA sites, single miR-99/100 sites (Figures 1H, 1I, S1G, and S1H). Both reporters showed a switch from AGO1/2 dependency, to AGO1/3 and AGO4, respectively, in the absence of LIMD1.

LIMD1 Is Critical for the Interaction of AGO2 with TNRC6A and DDX6

We next examined the binding partners and function of LIMD1 in miRISC in more detail to shed light on why loss of LIMD1

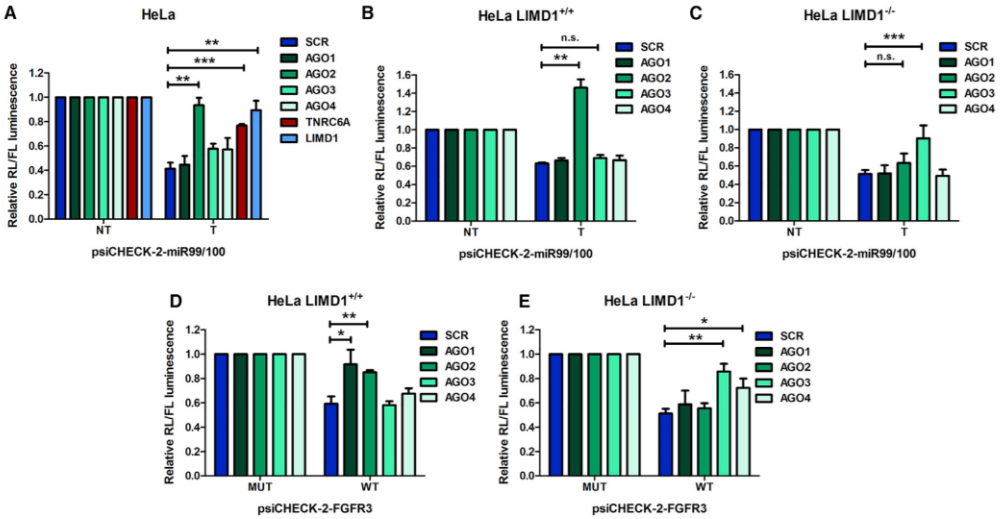

Figure 1. Genetic Ablation of LIMD1 Switches Dependency upon Argonaute Species for miRNA Silencing

(A) psiCHECK-2-miR-99/100 luciferase reporter (NT, non-targeting reporter; T, targeting reporter; mean ± SEM; n = 4 treated with indicated siRNAs (SCR, non-targeting control).

(B and C) (B) psiCHECK-2-miR99/100 reporter in CRISPR-Cas9 gene-edited HeLa cells with Cas9 alone control (LIMD1$^{+/+}$) or (C) LIMD1 knockout (LIMD1$^{-/-}$) cells, treated with the indicated siRNAs.

(D and E) (D) psiCHECK-2-FGFR3 (endogenous mutant [MUT] or wild-type [WT] 3′ UTR) reporter in CRISPR-Cas9 gene-edited HeLa cells with Cas9 alone control (LIMD1$^{+/+}$) or (E) LIMD1 knockout (LIMD1$^{-/-}$) cells, treated with the indicated siRNAs.

appeared to render AGO2 unable to contribute to silencing of both synthetic and natural 3′ UTRs and how the switch in AGO utilization was facilitated. Immunofluorescence (IF) staining of endogenous LIMD1, AGO2, and TNRC6A showed triple colocalization to processing bodies (P-bodies) (Figure 2A). To investigate direct endogenous association of AGO2 and TNRC6A with LIMD1 in situ, we performed proximity ligation assays (PLA) (Söderberg et al., 2006) for AGO2:LIMD1 and TNRC6A:LIMD1 (Figures 2B and S2A). We observed PLA signal for LIMD1 with both AGO2 and TNRC6A. In agreement with recent reports (Chen et al., 2014; Mathys et al., 2014), our PLA analysis demonstrated TNRC6A directly associated with CNOT9 (CNOT9 contains W-binding pockets to accommodate tryptophan residues from TNRC6A). By contrast CNOT1 did not exhibit PLA signal with TNRC6A; these data may be reflective of the lack of direct binding evidence between these proteins and the absence of a structurally resolved binding interface (Chen et al., 2014; Mathys et al., 2014). This supports the validity and specificity of the endogenous LIMD1 direct interactions with AGO2/TNRC6A.

LIM-domain-containing proteins are characterized by their ability to act as scaffolds in multi-protein complexes (Koch et al., 2012). We therefore reasoned that the close proximity and association observed between LIMD1, AGO2, and TNRC6A could indicate a scaffolding role for LIMD1 within the miRISC. We examined the endogenous colocalization of AGO2 with TNRC6A and miRISC component DDX6 by IF in HeLa cells upon treatment with siRNA targeting *LIMD1* (Figures S2B–S2D). LSM1 is required for the assembly of P-bodies but does not affect miRNA-silencing function; we therefore included siRNA targeting LSM1 as a control for P-body disruption. LIMD1 depletion did not disrupt the colocalization of AGO2 with TNRC6A or DDX6. By contrast, and as described in the literature, LSM1 knockdown caused a decrease in visible AGO2/TNRC6A/DDX6 P-bodies (Chu and Rana, 2006).

To rule out a possible false-negative effect due to the limited resolution of confocal microscopy (240 nm) (Nature Photon, 2009), we repeated our analysis using PLA, which detects proteins within 40 nm of each other (Figures 2C–2F). PLA analysis demonstrated that interaction of AGO2 with TNRC6A and DDX6 was significantly reduced upon LIMD1 knockdown, whereas LSM1 knockdown did not reduce this interaction, and in fact increased interaction of AGO2 with TNRC6A. In agreement with these data, reporter assays performed in cells treated with the same siRNAs demonstrated significant de-repression of a miR-99/100 reporter upon loss of LIMD1 but not LSM1 (Figure S2E). These findings confirm that assembly of P-bodies is a consequence rather than a cause of miRNA silencing (Eulalio et al., 2007) and demonstrate that the de-repressive effect of LIMD1 depletion on miRNA silencing is not dependent on the disassembly of P-bodies. Together, our data show that LIMD1 contributes to maintaining the interactions of AGO2 with TNRC6A and DDX6.

OPEN ACCESS CellPress

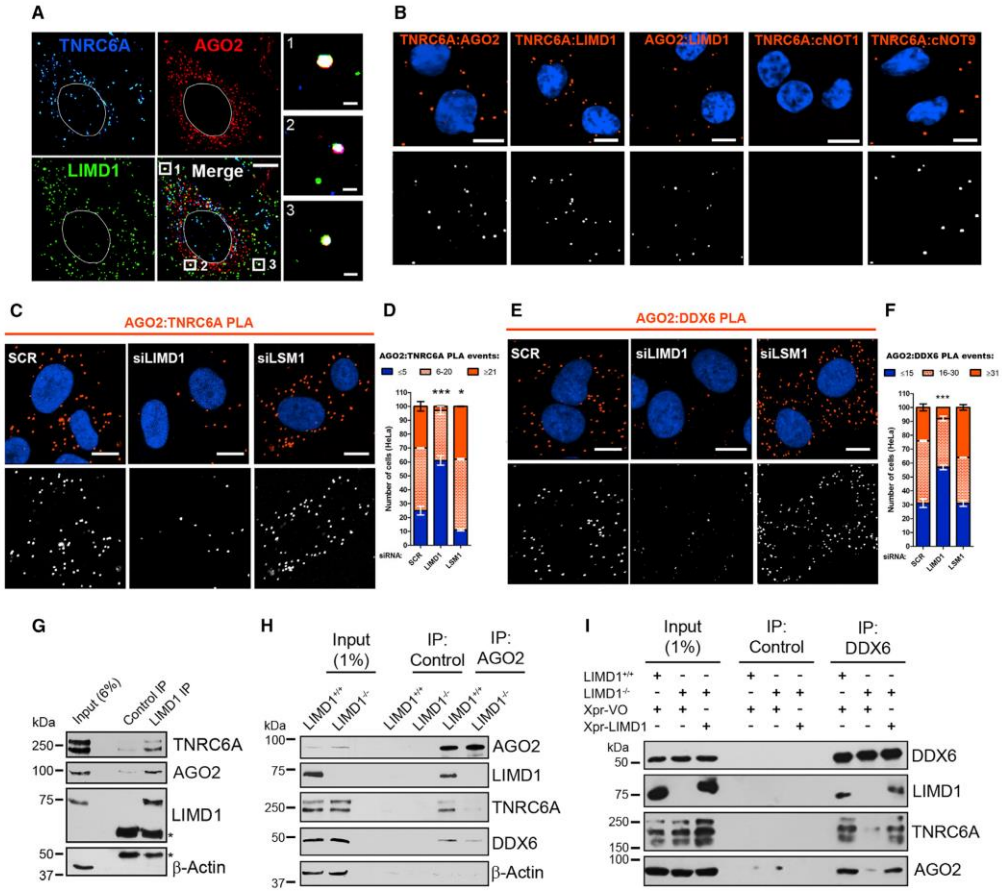

Figure 2. LIMD1 Interacts with miRISC Components AGO2 and TNRC6A and Promotes Their Association

(A) Endogenous IF of the indicated proteins in HeLa cells.

(B) Endogenous in situ interaction determined by proximity ligation assay (PLA) of the indicated proteins. PLA signal orange, cells stained with DAPI (top); PLA signal white for visual clarity (bottom). Scale bars, 10 μm.

(C) PLA analysis of endogenous AGO2 and TNRC6A interaction in HeLa cells treated with SCR (non-targeting), LIMD1, or LSM1 siRNA. PLA signal orange, cells stained with DAPI (top); PLA signal white for visual clarity (bottom).

(D) Quantification of PLA interaction events in (C), displayed as a stacked histogram. Data are mean ± SEM, n = 3, $^{**}p < 0.001$, $^{***}p < 0.0001$, determined using the chi-square test.

(E) PLA analysis of endogenous AGO2 and DDX6 interaction, as in (C).

(F) Quantification of (E) as in (D).

(G) Endogenous co-immunoprecipitation of LIMD1 with the indicated proteins from HeLa cells (*IgG heavy chain).

(H) Endogenous coIP of indicated miRISC components with AGO2 from CRISPR-Cas9 gene-edited HeLa LIMD1$^{+/+}$ or LIMD1$^{-/-}$ cells.

(I) Endogenous coIP of indicated miRISC components with DDX6 from CRISPR-Cas9 gene-edited HeLa LIMD1$^{+/+}$ or LIMD1$^{-/-}$ cells expressing Xpress (Xpr) vector only (VO) or LIMD1.

In order to further pursue the discrepancy between protein localization to P-bodies and the interaction between miRISC proteins, we performed endogenous IF for AGO1, 2, 3, and 4 with both TNRC6A and DDX6 in the isogenic *LIMD1*$^{-/-}$ HeLa CRISPR pair (Figures S3A and S3B). Loss of LIMD1 had no visible effect on AGO1, 2, or 3 colocalization with TNRC6A or

DDX6 in P-bodies (AGO4 did not colocalize with TNRC6A/DDX6 in either cell line). Furthermore, we did not detect any change in colocalization of EYFP-tagged AGO2 with endogenous TNRC6A upon inhibition of Akt3 by siRNA, treatment with Akt inhibitor MK-2206, or overexpression of AGO2 S387A point mutant (Figure S4A). We therefore performed complementary PLA and endogenous immunoprecipitation experiments and observed strikingly that *LIMD1* knockout caused significant impairment of endogenous AGO2 interaction with TNRC6A and DDX6 (Figures S4B–S4G), in agreement with functional reporter assays performed in these lines (Figure 1). Furthermore, re-expression of Xpress (Xpr)-tagged LIMD1 in the *LIMD1*$^{-/-}$ line restored the interaction of DDX6 with AGO2 and TNRC6A (Figure 2I), potentially explaining the enhancement of silencing observed when LIMD1 is overexpressed in a *LIMD1*-null background (Figure S1D). These data therefore demonstrate that endogenous interaction assays, including PLA and IP, are more accurate methods of determining endogenous miRISC protein-protein interaction, as opposed to visible colocalization within P-bodies. In summary, loss of LIMD1 profoundly impaired the ability of AGO2 to interact with TNRC6A and downstream effectors within miRISC required for miRNA-mediated silencing.

LIMD1 Interacts with AGO2 and TNRC6A via Specific Domains

Having demonstrated that LIMD1 is required to scaffold the interaction of AGO2 and TNRC6A, we next sought to map the interaction interfaces on all three proteins. LIMD1 contains three tandemly arrayed LIM domains (protein-protein interacting zinc fingers) in its C-terminal region and a preceding proline/serine-rich unstructured domain referred to as the pre-LIM (residues 1–471). Our previous work demonstrated that AGO2 bound to the pre-LIM portion of LIMD1 (James et al., 2010). To identify the precise AGO Binding (AB) motif in the pre-LIM, we co-immunoprecipitated Xpr-tagged full-length LIMD1 or a series of LIMD1 internal deletion mutants with EYFP-tagged AGO2. We found that deletion of amino acids 140–166 within LIMD1 abrogated the interaction with AGO2 (Figure 3A). The identification of amino acids 140–166 as the AB motif in LIMD1 was confirmed by direct binding assays using purified un-tagged AGO2 (hAGO2) (De and Macrae, 2011) (Figure 3B) and maltose binding protein (MBP)-tagged full-length LIMD1 or AB motif (Figure 3C). Generation of a set of HeLa lines lentivirally transduced to express sh-SCR (non-targeting) or sh-LIMD1 RNA and RNAi-resistant wild-type (WT) LIMD1 (rr-LIMD1) or LIMD1 deletion mutants (Figure S5A) demonstrated loss of silencing of the miR-99/100 reporter in sh-LIMD1 and rr-Δ140–166 lines (Figure 3D). In contrast, we observed that cells expressing the larger adjacent rr-Δ186–260 LIMD1 deletion mutant (which retains AGO2 binding, Figure 3A) displayed equivalent levels of silencing to that seen in rr-LIMD1 cells, thus providing an additional control for the impact of internal deletions on the secondary structure of the pre-LIM domain. These data indicate that, as predicted, the ability of LIMD1 to bind AGO2 via its AB motif is critical for its miRNA-silencing function.

We next performed complementary direct binding assays to identify the corresponding LIMD1-binding domain within AGO2, using a series of GST-AGO2 N- and C-terminal truncation mutants (Figures S5B and S5C). We determined that the Linker 2 (L2) domain of AGO2, which lies between the PAZ and MID domains, was necessary for direct interaction with the AB motif of LIMD1 (MBP-LIMD1 140–166) and full-length LIMD1 (Figure 3E). We note that the additional bands present in these purified AGO2 mutants are either degradation products (as determined by western blot and mass spectrometry (Figures S5D–S5G) or bacterial Hsp70 (DnaK), which did not affect binding to LIMD1 (Figure S5H).

As our PLA experiments also indicated a close association of LIMD1 with TNRC6A, we sought to confirm whether this occurred independently of AGO2. We found that deletion of the LIM domains (C-terminal) of LIMD1 resulted in loss of interaction with EGFP-tagged TNRC6A in co-immunoprecipitation experiments (Figure 3F). Deletion of the LIMD1 AB motif did not affect interaction with TNRC6A, demonstrating that the interaction of LIMD1 with TNRC6A is not dependent upon LIMD1 interaction with AGO2. Next, we determined that the N-terminal AGO-binding domain (ABD) of TNRC6A (Eulalio et al., 2009b) was responsible for binding to LIMD1; coIP experiments in HEK293T cells using EGFP-tagged TNRC6A truncations and Xpr-LIMD1 revealed that deletion of TNRC6A amino acids 1–883 resulted in complete loss of binding to LIMD1 (Figure 3G).

In summary, the pre-LIM region of LIMD1 is responsible for interaction with AGO L2 (via the AB, aa 140–166), and the C-terminal LIM domains interact with the N-terminal portion of TNRC6A. Therefore, we provide evidence that LIMD1 functions as a central scaffold protein and a core component of miRISC, forming an integral link between AGO2 and TNRC6A through simultaneous direct contacts with each (Figure 3H).

Akt3-Mediated Phosphorylation of S387 in the AGO2 L2 Domain Is Necessary for Interaction with LIMD1

It has been proposed that Akt3-dependent phosphorylation of AGO2 S387 promotes its miRNA function and opposes its target cleavage activity (Horman et al., 2013). AGO2 S387 phosphorylation was suggested to increase the association of AGO2 with TNRC6A via an unknown mechanism. As S387 is located within the L2 region of AGO2, we tested whether phosphorylation of this residue could trigger the association between AGO2 and LIMD1 and subsequent recruitment of TNRC6A to AGO2. We generated constructs expressing phospho mutant (AGO2 S387A) or phospho-mimic (AGO2 S387E) versions of EYFP-AGO2 and compared their ability to interact with LIMD1 in immunoprecipitation assays. AGO2 S387A had reduced binding to LIMD1, whereas the phospho-mimic version of AGO2 (AGO2 S387E) rescued interaction with LIMD1 (Figures 4A and S6B). The interaction profile of LIMD1 with these AGO2 constructs was mirrored by endogenous TNRC6A and DDX6, which displayed significantly reduced binding to AGO2 S387A, and rescue of binding with AGO2 S387E (Figures S6A and S6B). The importance of S387 phosphorylation for LIMD1 binding was further confirmed by direct binding assays between the AB motif of LIMD1 and GST-AGO2 WT or GST-AGO2 S387E, which revealed enhanced binding of the AGO2 phospho mimic to LIMD1 AB motif (Figure 4B). The dependency on S387 for LIMD1 association was also evident in the degree of colocalization of AGO2 and LIMD1 in U2OS cells transfected with

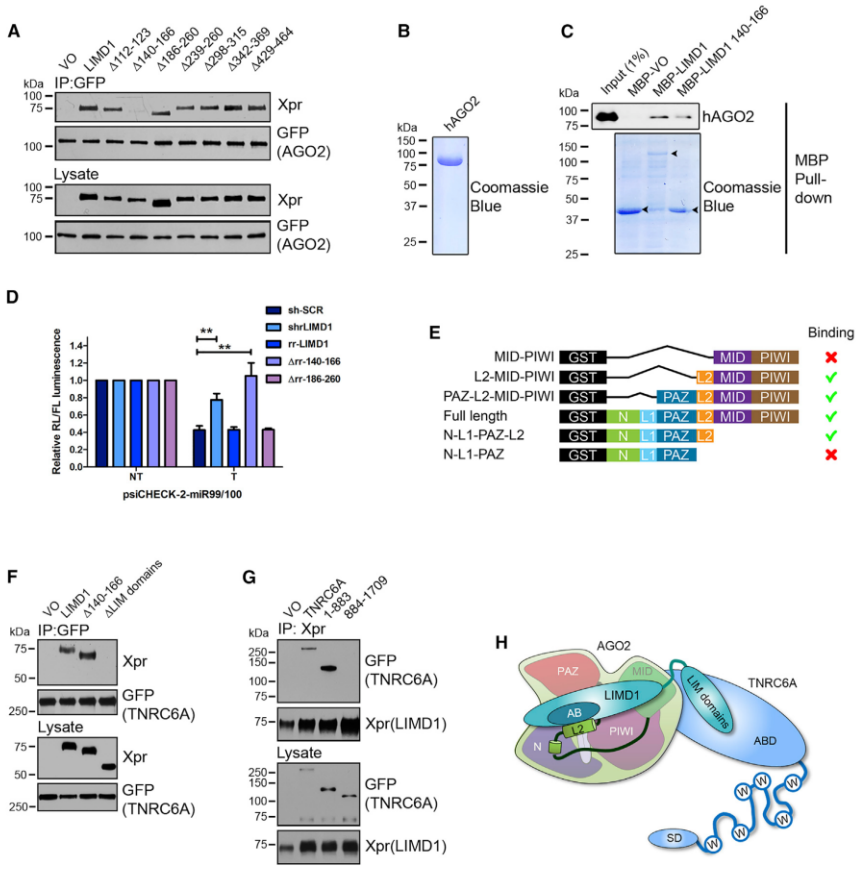

Figure 3. LIMD1 Bridges AGO2 and TNRC6A via Distinct Interaction Sites

(A–C) (A) Co-immunoprecipitation (coIP) of Xpress (Xpr)-LIMD1 and internal deletion mutants with GFP-AGO2 from HEK293T lysate. (B) Purified un-tagged crystallography grade hAGO2 used in (C) direct binding assay with MBP-VO, MBP-LIMD1, or MBP-LIMD1 140 166 (AB motif) (highlighted by arrows).

(D) psiCHECK-2-miR99/100 luciferase reporter (NT [non-targeting], T [targeting]) assay performed in shRNA knockdown and rescue (RNAi resistant [rr]) LIMD1 HeLa cells (mean ± SEM; n = 3).

(E) Schematic of GST-AGO2 truncation mutants and summary of binding to LIMD1 AB motif.

(F) CoIP of Xpr-LIMD1 and deletion mutants with GFP-TNRC6A from HEK293T lysate.

(G) CoIP of TNRC6A and truncation mutants with Xpr-LIMD1 from HEK293T lysate.

(H) Graphical representation of domain interaction of AGO2, LIMD1, and TNRC6A. The AB motif of LIMD1 (aa 140–166) directly binds linker 2 (L2) of AGO2, and the LIM domains of LIMD1 bind the N-terminal AGO-binding domain (ABD) of TNRC6A (SD, silencing domain).

mTan-LIMD1 and the EYFP-AGO2 constructs (Figures 4C, 4D, and S6C). Compared to WT AGO2, AGO2 S387A and S387E showed a 9.4-fold decrease and 2.1-fold increase in colocalization with LIMD1, respectively. These data indicate that the interaction of AGO2 with LIMD1 is dependent on the phosphorylation status of AGO2 S387.

Next, we tested whether the interaction between LIMD1 and AGO2 could be directly promoted by overexpression of Akt3, thought to be the primary kinase responsible for phosphorylation of AGO2 S387 (Horman et al., 2013). We immunoprecipitated endogenous LIMD1 from serum-starved HeLa cells transfected with an empty vector or a constitutively active myristoylated Akt3 (HA-myr-Akt3) (Song et al., 2008) and found that Akt3 significantly enhanced both the levels of phospho-S387 AGO2 (using a phospho-S387-specific antibody (Zeng et al., 2008; Figure S6D) and the interaction of AGO2 with LIMD1 (Figure 4E).

In a complementary assay, treatment of the HeLa CRISPR-Cas9 isogenic pair with the Akt inhibitor MK-2206 demonstrated that interaction of AGO2, LIMD1, and TNRC6A with DDX6 was significantly impaired in *LIMD1*$^{+/+}$ cells upon Akt inhibition (Figure 4F); under these conditions, the interaction of the complex was equivalent to that of the *LIMD1*$^{-/-}$ line (Figure S6E). Treatment of the *LIMD1*$^{-/-}$ cells with MK-2206 entirely abolished the complex interactions, indicating that there is some residual interaction of AGO2 with miRISC in the absence of LIMD1, which is also Akt dependent. In agreement with these assays, siRNA-mediated knockdown of Akt3 in U2OS cells resulted in a 9-fold reduction in colocalization between EYFP-AGO2 and mTan-LIMD1 (Figures 4G, 4H, and S6F). In summary, these data confirm that Akt3-mediated phosphorylation of AGO2 S387 is required for AGO2-LIMD1 interaction.

Activated Phospho-S387-AGO2 Requires LIMD1 for Formation of a Functional AGO2-miRISC

To determine whether phosphorylated AGO2 (S387) is dependent on LIMD1 for miRISC formation and function, we examined the activity of the miR-99/100 reporter in HeLa CRISPR lines treated with siRNA against AGO2, where WT AGO2 or S387 phospho-site mutants were re-expressed (Figures 5A, 5B, and S6G). In *LIMD1*$^{+/+}$ cells, AGO2 knockdown caused the expected de-repression. Re-expression of AGO2 WT and S387E rescued silencing, whereas AGO2 S387A was unable to rescue silencing, in agreement with published data (Horman et al., 2013). In contrast, in the *LIMD1*$^{-/-}$ line, AGO2 knockdown did not cause any de-repression, and re-expression of any AGO2 construct (WT or S387 mutant) similarly had no effect.

We next determined whether the previously established regulation of AGO2 miRNA silencing by Akt3 was in fact mediated by LIMD1 (Horman et al., 2013). Upon siRNA-mediated depletion of Akt3, we observed de-repression of the miR-99/100 reporter in *LIMD1*$^{+/+}$ cells, but this had no effect in the *LIMD1*$^{-/-}$ line, where silencing was maintained (Figures 5C and S6H). Taken together, these data demonstrate that the activating effect of Akt3-mediated phosphorylation on AGO2 is dependent on subsequent interaction with LIMD1. In the absence of LIMD1, miRNA silencing still occurs independently of Akt3. To investigate how LIMD1 loss caused this striking inhibition of phospho-AGO2 activity, we examined the interaction of phospho-AGO2 with TNRC6A and DDX6 upon loss of LIMD1. PLA analysis with the phospho-AGO2 (S387)-specific antibody demonstrated that loss of LIMD1 significantly disrupts the ability of phospho-AGO2 to bind both TNRC6A and DDX6 endogenously (Figures 5D–5G, S6I, and S6J). These data therefore demonstrate that AGO2 phosphorylation by Akt3 has no activating effect on miRNA silencing in the absence of LIMD1 due to the fact that the loss of this scaffold protein dissociates phospho-AGO2 from TNRC6A/miRISC and precludes AGO2-dependent miRNA silencing. These data are in agreement with the functional observations made upon LIMD1 loss (Figure 1), where we observed functional replacement by AGO3. We therefore went on to examine whether this mechanism of phospho-dependent recruitment of LIMD1 family proteins was conserved across all human AGO proteins.

AGO1 and AGO4 Exhibit Phosphorylation-Dependent Interaction with LIMD1 Family Proteins

A significant structural homology exists between the four human AGO proteins; our alignment analysis revealed that AGO2 S387 is conserved in the L2 domains of AGO1 and AGO4 (Figure 6A). We therefore investigated whether there was a conserved phospho-dependent mechanism of AGO1, 2, and 4 interaction with LIMD1 family members. First, we found that LIMD1, Ajuba, and WTIP interacted with all four AGOs (Figures S7A, S7B, and data not shown). LIMD1 also directly bound to the L2 domain of AGO1 (Figure S7C), and, in a similar manner to AGO2, mutation of the conserved serine in AGO1 (S385) to alanine inhibited colocalization with LIMD1, whereas mutation to glutamic acid rescued this colocalization (Figures S7D and S7F). Furthermore, knockdown of Akt3 by siRNA significantly reduced AGO1:LIMD1 colocalization, suggesting that Akt3 may also phosphorylate AGO1 S385 (Figures S7E and S7G). Point mutation of the conserved serine (S377) in AGO4 produced the same disruption and rescue of colocalization with LIMD1 as observed with AGO1 and 2 (Figures S7H and S7J). Taken together these data suggest a common mechanism may exist whereby human AGO 1, 2 and 4 are activated for miRNA-silencing function by phosphorylation of a conserved serine residue, which directs their interaction with LIMD1 and family members and subsequent recruitment to TNRC6A/miRISC. Given the ability of LIMD1 to colocalize with three AGO proteins in a phospho-dependent manner, we also demonstrated that the LIMD1 family member Ajuba, also colocalized with AGO1 and that this was dependent on the phosphorylation status of S385 (Figure S7I). These data support a fundamentally conserved mechanism of phosphorylation-dependent activation of AGO proteins by recruitment and regulation of all three members of this LIM-domain-containing family, LIMD1, Ajuba, and WTIP.

AGO3 Interacts with LIMD1 Family Proteins Independently of Akt3 Phosphorylation

In contrast to AGO1 and AGO4, AGO3 possesses a phosphorylation-mimicking glutamic acid residue at amino acid position 390 (Figure 6A). Given that we found AGO3 can rescue loss of AGO2 miRNA function in the absence of LIMD1, we postulated that this phospho-mimic residue may facilitate interaction with LIMD1 and/or its closely related family members Ajuba/WTIP independently of Akt3 signaling. This could be a mechanism explaining the switch to AGO3 utilization upon deletion of LIMD1 (Figure 1).

To interrogate this hypothesis, we first determined that AGO3 colocalizes with LIMD1, consistent with IP data (Figure S7A), and that this is significantly reduced upon mutation of the phospho-mimic residue to alanine (E390A) (Figures 6B and 6C). Similarly, colocalization of AGO3 with Ajuba was reduced by mutation of E390 to alanine (Figures S7K and S7L). In striking contrast to AGO2, siRNA-mediated knockdown of Akt3 did not affect AGO3/LIMD1 colocalization (Figures 6D and 6E). WTIP interaction with AGO3 was also unaffected by Akt inhibition (MK-2206), as opposed to AGO2, which demonstrated loss of interaction (Figures 6F and 6G), and siRNA-mediated knockdown of Akt3 similar had no effect on AGO3 colocalization with WTIP

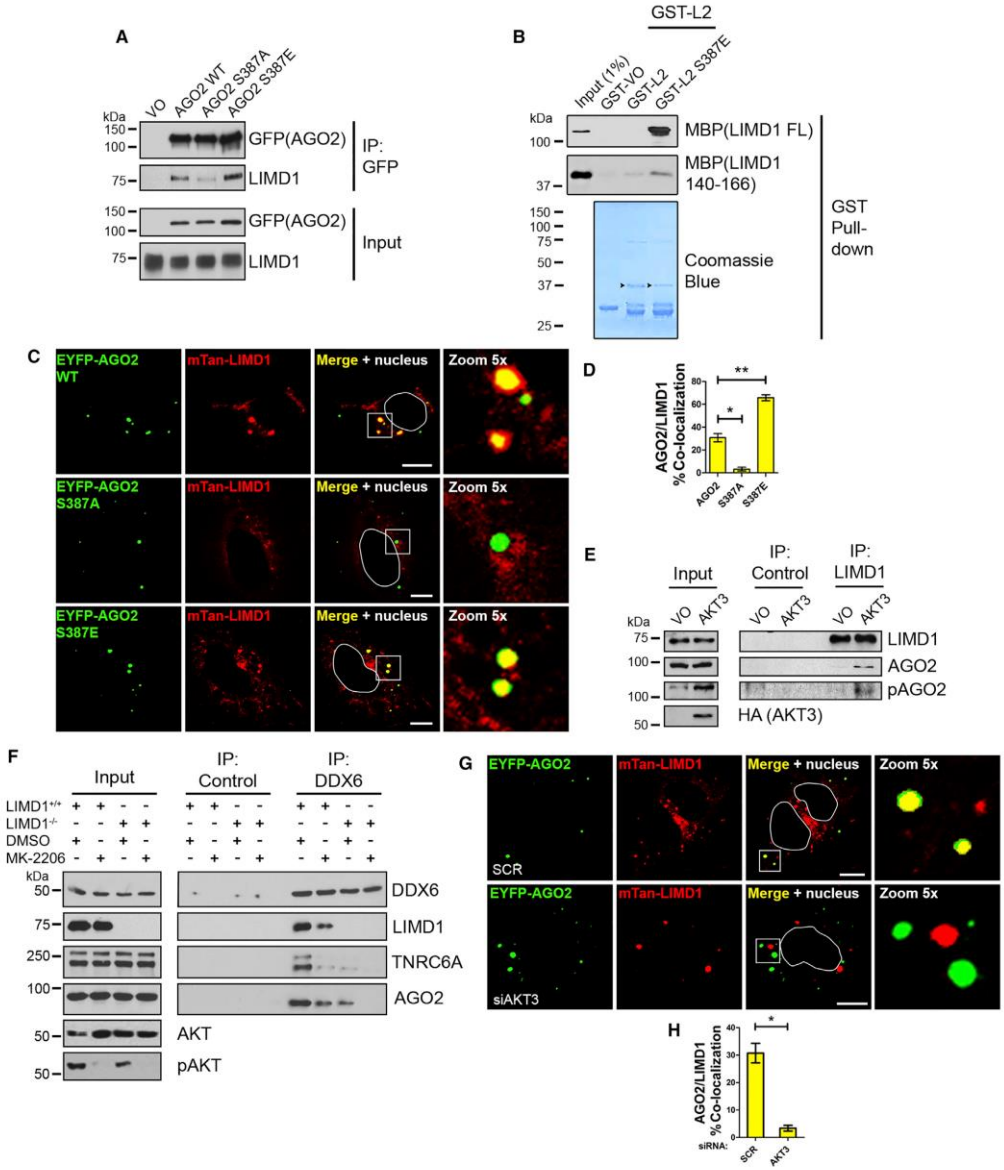

Figure 4. Binding of LIMD1 to AGO2 Is Dependent on Akt3-Mediated S387 Phosphorylation

(A) Co-immunoprecipitation (IP) of Xpr-LIMD1 with EYFP-AGO2 WT, AGO2S387A (phospho-deficient), and AGO2S387E (phospho-mimic) point mutants from HEK293T lysate.

(B) Purified recombinant GST-AGO2 L2 or L2 S387E were used in direct binding assay with MBP-LIMD1 full-length or AB motif (140–166).

(legend continued on next page)

(Figures 6H and 6I). These data therefore demonstrate that AGO3 interaction with LIMD1 family proteins occurs independently of Akt signaling as a result of the naturally occurring phospho-mimic residue E390.

We observed activation of AGO3 miRNA function when LIMD1 protein expression was entirely ablated (Figure 1), and phosphorylated AGO2 was unable to engage with TNRC6A and silencing effectors (Figure 5). In the *LIMD1*$^{-/-}$ HeLa cell line, siRNA depletion of WTIP yielded a significant de-repression of the miR-99/100 reporter, whereas Ajuba knockdown did not (data not shown). Therefore, to determine whether WTIP was responsible for engaging AGO3 in the absence of LIMD1, we performed siRNA knockdown of AGO3 or WTIP, singularly or in combination, in the *LIMD1*$^{-/-}$ HeLa cell line. We discovered that WTIP is required for silencing of a miR-99/100 reporter in these cells (Figure 7A). Furthermore, depletion of WTIP and AGO3 in combination led to an almost complete de-repression of silencing (Figure 7A). Concurrent with this, we discovered an increase in the number of AGO3 P-bodies in the *LIMD1*$^{-/-}$ line compared to *LIMD1*$^{+/+}$ (Figures S7M and S7N), indicating that while a reduction in an AGO miRNA-silencing function is not necessarily associated with dissociation from P-bodies (as is the case with AGO2), an increase in AGO3 silencing function may be associated with an increase in its recruitment to P-bodies. Furthermore, we observed an increase in AGO3:WTIP interaction in the *LIMD1*$^{-/-}$ line compared to *LIMD1*$^{+/+}$ (Figures 7B and 7C).

AGO function in miRNA silencing is critically dependent on association with TNRC6 proteins, which enable recruitment of several effector complexes that mediate target mRNA decapping and deadenylation. We therefore examined whether TNRC6A recruitment to AGO2 and AGO3 was altered in the presence and absence of LIMD1, which would explain the apparent switch in AGO function. Endogenous immunoprecipitation of AGO2 or AGO3 from the HeLa *LIMD1*$^{-/-}$ CRISPR cell line pair demonstrated that, in contrast to the loss of TNRC6A interaction with AGO2, AGO3 interaction with TNRC6A was significantly enhanced upon loss of LIMD1 (Figures 7D and 7E).

These interaction data elucidate the mechanism by which loss of LIMD1 causes a switch in cellular AGO dependency (Figure 1). We have discovered that, in HeLa cells, loss of LIMD1 causes dependency upon AGO2 to switch to AGO3, and this is associated with enhanced (phosphorylation-independent) interaction of AGO3 with LIMD1 family member WTIP, and with TNRC6A as the effector of silencing. These data therefore define the mechanism by which AGO2-S387 phosphorylation is an activating event for silencing. Additionally, as all LIMD1 family proteins interact with AGO1–4 in a phospho-dependent manner, these data suggest a general mechanism whereby specific AGO proteins are activated for miRNA function by their phosphorylation and subsequent recruitment of LIMD1 family proteins, thus enabling miRISC formation.

DISCUSSION

LIMD1 Acts as a Molecular Clamp to Secure Phospho-AGO2 and TNRC6A Together within miRISC

We determined that LIMD1 binds directly to AGO2 and TNRC6A at distinct interfaces: the AGO-binding motif (AB motif) of LIMD1 binds the L2 domain of AGO2, and the C-terminal LIM domains of LIMD1 bind the amino-terminal ABD of TNRC6A, independently of AGO binding (Figure 3) (Eulalio et al., 2009a; Pfaff et al., 2013; Takimoto et al., 2009). It is important to note that our data do not suggest the AGO-TNRC6A association can only occur via LIMD1; the MID/PIWI (P-element induced wimpy testis) domains of AGO2 that directly bind TNRC6A tryptophan residues do not bind to LIMD1 (Figure 3E) (Schirle and MacRae, 2012). Additionally, the association of the C-terminal silencing domain of TNRC6A with PABP/CNOT9/CNOT1/DDX6 does not preclude the binding of LIMD1, which interacts with the N-terminal half of TNRC6A (Figure 3D) (Eulalio et al., 2009a). Therefore, our data indicate that LIMD1 acts as a molecular "clamp" by binding to both AGO and TNRC6A proteins simultaneously to secure their association and commit both proteins and associated effectors to the miRNA-silencing pathway: AGO2 association with TNRC6A/miRISC and its miRNA-silencing activity is significantly impaired upon LIMD1 loss (Figures 1A–1C and 2).

It has been demonstrated that activation of miRNA silencing is dependent on Akt3-mediated phosphorylation of AGO2 at S387 (Horman et al., 2013). We have determined that this phosphorylation promotes association of AGO2 with LIMD1 and subsequent recruitment of TNRC6A and downstream silencing effector complexes (Figures 4 and 5). Our findings therefore reveal the functional consequence of S387 phosphorylation, which underpins an apparent preference of AGO utilization directed by LIMD1 family member proteins. In agreement with our findings, La Rocca et al. recently identified phosphorylation-dependent activation of miRNA silencing by PI3K, a kinase that lies upstream of Akt3 (La Rocca et al., 2015). Although this study did not examine the precise changes in AGO2 phosphorylation, it discovered an increase in the molecular mass of AGO2 upon pathway activation, most likely via the recruitment of other effector proteins, which would include TNRC6A, DDX6, and, from our data, LIMD1.

(C) Co-localization of EYFP-AGO2/S387 point mutants with mTan-LIMD1 in U2OS cells. Nucleus outline in white.
(D) Quantification of percentage of AGO2/S387 P-bodies colocalized with LIMD1 in (C).
(E) Immunoprecipitation of endogenous LIMD1 from HeLa cells transfected with HA-VO or HA-myristolated Akt3, and western blot analysis of the indicated proteins; pAGO2 is S387.
(F) Immunoprecipitation of DDX6 from HeLa LIMD1$^{+/+}$ or LIMD1$^{-/-}$ treated with DMSO or Akt inhibitor MK-2206 and analyzed for the indicated proteins by western blot; pAKT is S473.
(G) Co-expression of EYFP-AGO2 (WT) with mTan-LIMD1 in U2OS cells treated with non-targeting (SCR) or AKT3 siRNA. Nuclear outlines in white.
(H) Quantification of number of AGO2 P-bodies colocalized with LIMD1 in (G).
Data shown are mean ± SEM, n = 3, *p < 0.05, **p < 0.001. Scale bars, 10 mm.

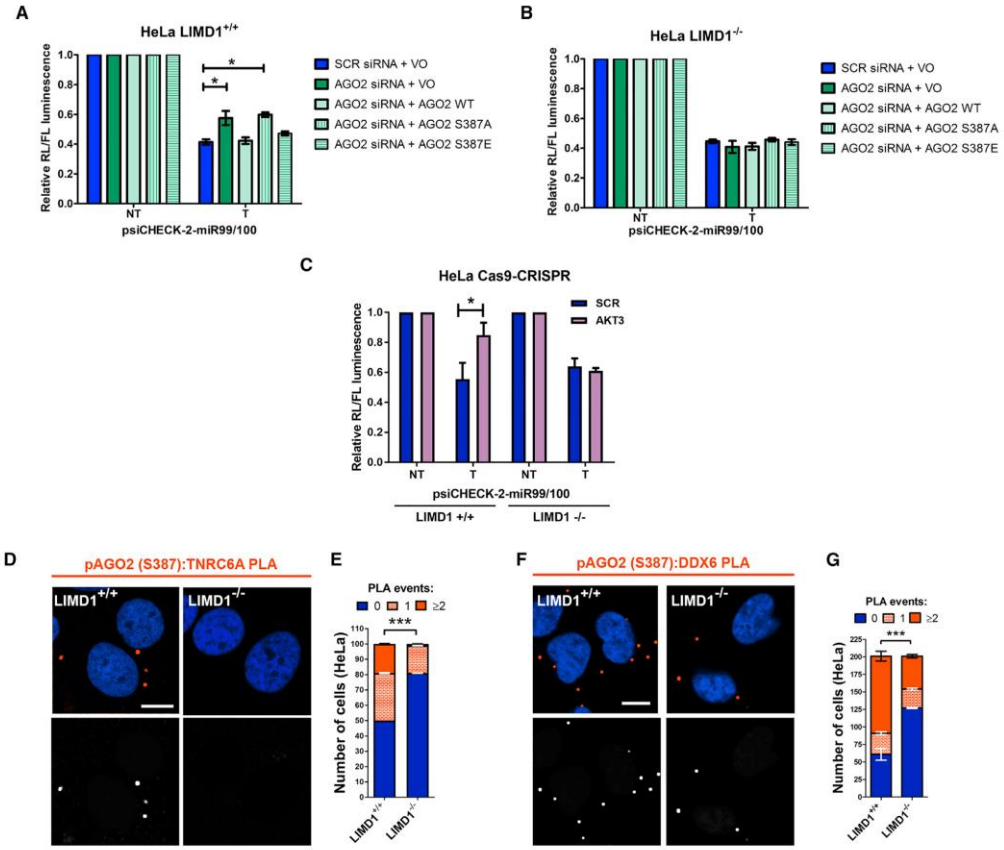

Figure 5. LIMD1 Is Required for Phospho-S387-AGO2 to Engage TNRC6A/DDX6 for miRNA-Mediated Silencing

(A and B) (A) psiCHECK-2-miR99/100 reporter assay in HeLa CRISPR-Cas9 LIMD1$^{+/+}$ or (B) LIMD1$^{-/-}$ cell lines transfected with non-targeting (SCR) or AGO2 siRNA and EYFP-AGO2, EYFP-AGO2S387A, or EYFP-AGO2S387E.

(C) miR99/100 reporter assay in in above HeLa CRISPR-Cas9 cell lines transfected with non-targeting (SCR) or AKT3 siRNA.

(D) PLA analysis of endogenous phospho-AGO2 (S387):TNRC6A interaction in situ in HeLa CRISPR-Cas9 LIMD1$^{+/+}$ or LIMD1$^{-/-}$ lines. PLA signal orange, cells stained with DAPI (top); PLA signal white for visual clarity (bottom). Scale bars, 10 μm.

(E) Quantification of PLA interaction events in (D), displayed as stacked histograms. Data are mean ± SEM, n = 3, total of 200 cells determined using the chi-square test.

(F) PLA analysis of phospho-AGO2 (S387):DDX6 interaction in above HeLa CRISPR-Cas9 cell lines.

(G) Quantification of (F) as in (E).

Unless otherwise stated, data are mean ± SEM, n = 3, *p < 0.05, **p < 0.001, ***p < 0.0001 according to the Student's t test.

AGO Interaction with LIMD1 Family Proteins Occurs via a Common Phosphorylation-Dependent Mechanism

The AGO L2 domain is a 98-residue, extended L-shaped coil that connects the PAZ and MID domains of AGO proteins (Elkayam et al., 2012; Schirle and MacRae, 2012). The AGO3 S387 residue phosphorylated by Akt3 is conserved in human AGO1 and 4 (Figure 6A). Our data demonstrate that LIMD1 can interact with all four AGO proteins (Figure S8A) and that association with AGO1 and 4 is also dependent on the ability of this conserved serine residue to be phosphorylated (Figures S8D–S8I). Taken together with previous studies demonstrating that AGO1 is phosphorylated (Rüdel et al., 2011), these data support a hypothesis of a common AGO-activating mechanism by Akt3 and/or other unidentified kinases. AGO3 does not contain this

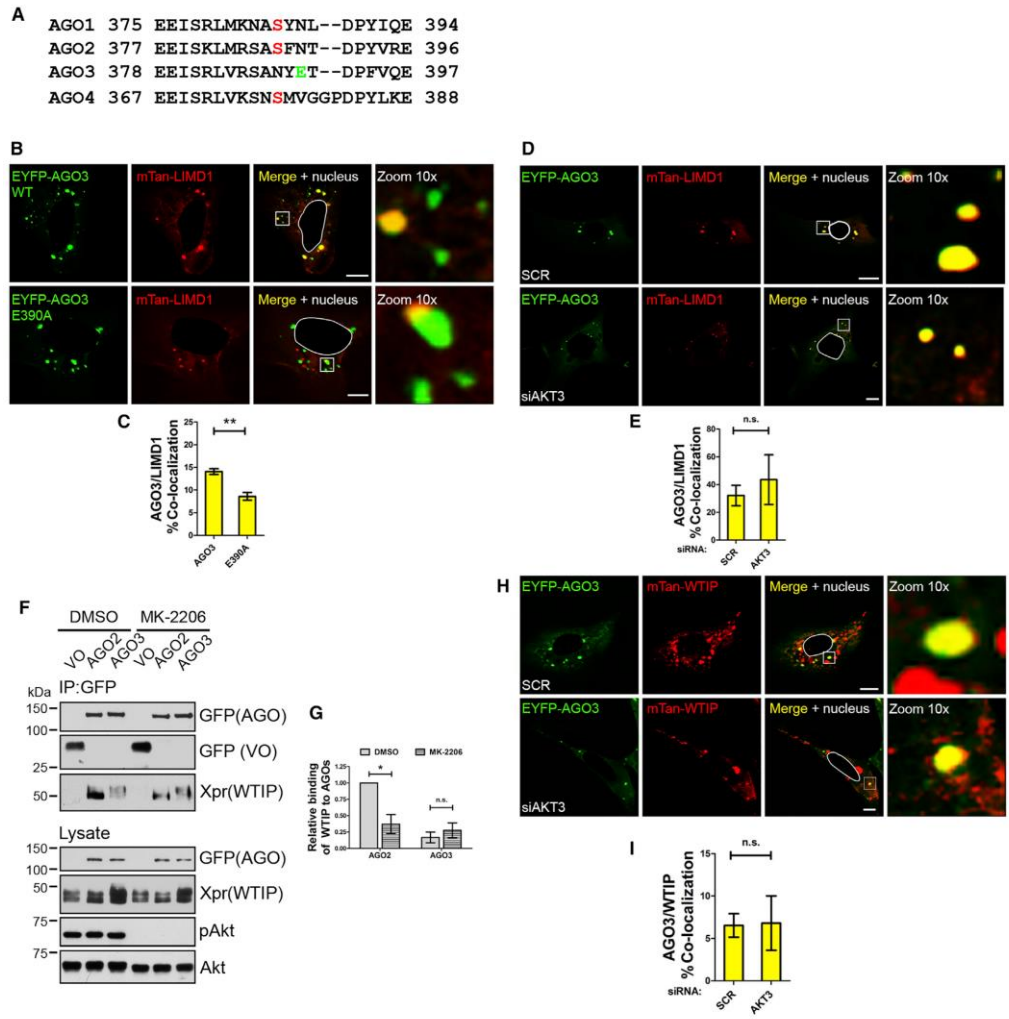

Figure 6. AGO3 E390 Acts as a Phospho-mimic, Facilitating Interaction with LAW Independently of Akt Signaling

A) AGO2 S387 is highly conserved within AGO1 (S385) and AGO4 (S377). AGO3 does not contain an equivalent serine residue but instead an adjacent phospho-mimic glutamic acid residue (E390).

B) Colocalization of EYFP-AGO3/E390 point mutants with mTan-LIMD1 in U2OS cells.

C) Quantification of percentage of AGO3 P-bodies colocalized with LIMD1 in (B).

D) Colocalization of EYFP-AGO3 with LIMD1 in U2OS cells treated with non-targeting (SCR) or AKT3 siRNA.

E) Quantification of percentage of AGO3 P-bodies colocalized with LIMD1 in (D), n = 2.

F) Immunoprecipitation (IP) of EYFP-VO, -AGO2, or -AGO3 from HEK293T lysate co-transfected with Xpress (Xpr)-WTIP and treated with DMSO or Akt inhibitor MK-2206.

G) Quantification of WTIP interaction with AGO2 and 3, in (F). Data are mean densitometry relative to AGO2 (DMSO), ±SEM, n = 3.

H) Colocalization of EYFP-AGO3 with WTIP in U2OS cells treated with non-targeting (SCR) or AKT3 siRNA.

I) Quantification of percentage of AGO3 P-bodies colocalized with WTIP in (H), n = 2.

Unless otherwise stated, quantification data are mean ± SEM, n = 3, *p < 0.05, **p < 0.01, ***p < 0.001, n.s., not significant.

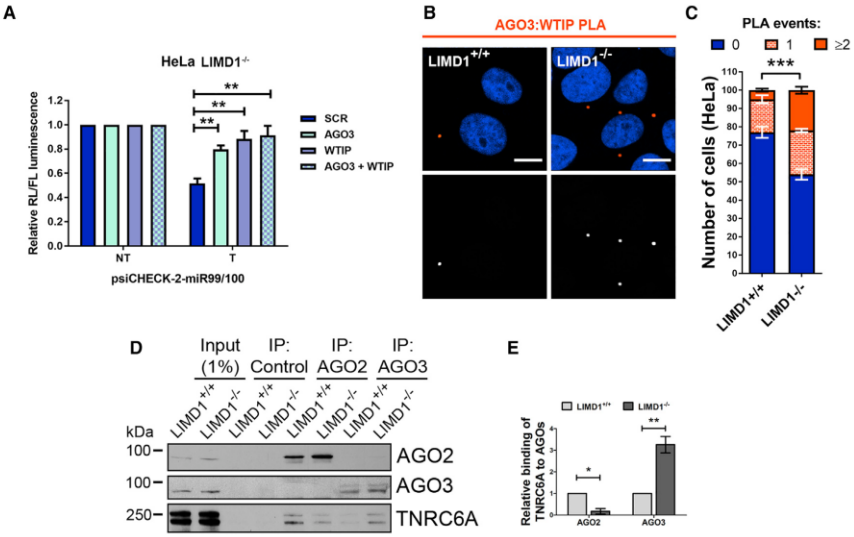

Figure 7. AGO2 miRNA Function Switches to AGO3 with LIM Family Member WTIP in the Absence of LIMD1

(A) LIMD1$^{-/-}$ HeLa cells transfected with non-targeting (SCR) and the indicated siRNAs (**p<0.01 according to student's T-test).

(B) PLA of AGO3 and WTIP in HeLa CRISPR-Cas9 cell lines.

(C) Quantification of PLA interaction events in (B), displayed as a stacked histogram.

(D) IP of endogenous AGO2 or AGO3 from HeLa CRISPR-Cas9 cells, coIP of endogenous TNRC6A.

(E) Quantification of TNRC6A coIP with AGO2 and 3 in HeLa CRISPR-Cas9 cells in (D). Data are mean densitometry relative to LIMD1$^{+/+}$ AGO2/3.

Unless otherwise stated, all data are ±SEM, n = 3, *p < 0.05, **p < 0.001, ***p < 0.0001, n.s., not significant, according to the Student's t test.

conserved serine residue but rather contains a phospho-mimic glutamic acid residue, which directs interaction with LIMD1 family members independently of Akt signaling (Figure 7).

Horman et al. postulated that phosphorylation of S387 represented a molecular switch between the siRNA and miRNA function of AGO2 (Horman et al., 2013). However, our data indicate the Akt3-mediated phosphorylation of AGO1, 2 (and possibly AGO4) could also be considered as a switch from OFF to ON for miRNA-silencing function. Furthermore, if one were to consider the possibility of a cell state with no Akt3 signaling, where silencing may only be possible through AGO3 function, then an activation of Akt3 could activate a switch from the default AGO3 silencing to any or all of the AGO1-, 2-, or 4-dependent mechanisms. Our work also opens up the possibility for functional differences between the four human AGO proteins that have been previously been described to act redundantly in the miRNA pathway (Dueck et al., 2012; Su et al., 2009). Future work will address this possibility.

Although many components and processes of the miRNA pathway are highly conserved between humans and *Drosophila*, an important difference is that, in *Drosophila*, only one of two AGO proteins, AGO1, functions in the miRNA pathway (Förstemann et al., 2007; Tomari et al., 2007). Within the L2 domain of *Drosophila* AGO1, S387 is not conserved. This may suggest that the evolution of S387 in human AGO2 (and equivalent serines in AGO1 and 4) was necessary for coordinating the responses of multiple AGOs to signaling inputs. It remains to be determined whether a protein in *Drosophila* fulfills the role of LIMD1 with regard to promoting interaction between AGO1 and GW182. Recent data from Golden et al. have shown that cyclic phosphorylation at highly conserved serine residues in the PIWI domain of human AGO2 (S824–S834) promotes efficient miRNA silencing (Golden et al., 2017). They noted that these residues are conserved in human AGOs 1–4 and *Drosophila* AGO1 but not in *Drosophila* AGO2, which only functions in the siRNA pathway. Thus, the evolution of several regulatory phospho sites, including S387, may be integral to the expansion of the AGO gene family between fly and human, all of which can function in miRNA-mediated silencing.

LIMD1 Directs AGO Family Member Utilization for miRNA Silencing

While siRNA and shRNA-mediated knockdown of proteins is able to provide functional insights, the complete genetic ablation of a protein can reveal longer-term adaptations in cells and alternative pathways to maintain homeostasis. Through the use of CRISPR-Cas9 technology, we ablated LIMD1 expression and observed a switch in AGO dependency for silencing from AGO2 to AGO3. In the *LIMD1*$^{-/-}$ cell line, we found that phospho-AGO2 S387 and total AGO2 interaction

with TNRC6A and DDX6 was significantly impaired, and AGO2 miRNA function was entirely ablated irrespective of its phosphorylation status (Figure 5). In parallel assays, LSM1, which is required for P-body assembly but not miRNA silencing (Chu and Rana, 2006; Eulalio et al., 2007, 2009a), affected neither AGO2 association with TNRC6A/DDX6 nor AGO2-dependent miRNA silencing (Figures 2C–2F). These data indicate that the effects observed upon LIMD1 loss occur specifically as a result of its scaffold role in the AGO2:TNRC6A association and not as a general effect of loss of P-body structural integrity. Indeed, re-expression of LIMD1 in the *LIMD1*$^{-/-}$ line not only enhanced silencing, but also rescued the interaction of AGO2 with TNRC6A and DDX6 (Figure 2J).

The contributions of each AGO protein to miRNA-mediated silencing has been attributed to their expression levels, with AGO2 being the most abundant and therefore of greatest importance (Wang et al., 2012). However, our data reveal that LIMD1 family proteins are important determinants of AGO utilization and show that AGO levels per se may not necessarily determine functional importance. The typically low AGO3 expression in various tissues and cell types has been ascribed to the high proportion of rarely used codons in its mRNA (Valdmanis et al., 2012). Despite this, we have shown AGO3 does function in miRNA silencing and specifically functions in the absence of the Akt3-AGO2-LIMD1 signaling axis. Determination of AGO utilization and the cooperation of different AGOs may, in addition to specific pairing with LIMD1 family proteins, be context dependent with respect to miRNA site geometry in the 3′ UTR and the distribution of a particular miRNA among AGO proteins expressed in the cell. These considerations warrant further investigation to more clearly define the regulation of miRNA-dependent silencing.

We may speculate that, for our miR-99/100 reporter, in the presence of LIMD1, the majority of targeted sites on the reporter mRNA are occupied by AGO2-LIMD1 with a minor contribution of AGO3-WTIP. Potential interactions between LIMD1 and WTIP may be required for overall stability of the multiple RISCs assembled on this 3′ UTR, and short-term loss of either one (in the context of siRNA knockdown) would lead to significant de-repression of silencing. With LIMD1 loss, AGO3-WTIP may increase in occupancy of remaining/free sites on the reporter thereby rendering silencing highly dependent on AGO3.

Loss of LIMD1 by genetic ablation did not affect silencing of the *let-7a* reporter, but the underlying AGO utilization was altered, with AGO2 no longer contributing to silencing (Figures S1E and S1F). In this respect, as seen with the miR-99/100 reporter, long-term loss of LIMD1 led to functional adaptation to maintain miRNA silencing and also revealed the particular involvement of LIMD1 in AGO2-dependent miRNA silencing. The *let-7a* reporter contained six tandem *let-7a* sites, and its repression was dependent on AGO1, 2, and 3. This result suggests that, for this particular synthetic 3′ UTR, a broad cooperative alliance of AGO1–3 and LIM domain proteins is necessary for silencing and that short-term loss of any component by siRNA knockdown is highly unfavorable.

Post-transcriptional gene silencing involving miRNAs was first discovered over 20 years ago but only now are its precise mechanism and place within the array of cellular signaling networks becoming more clearly defined. There is now intense interest in how post-translational modification of components of miRNA biogenesis and miRISC can regulate and fine-tune both siRNA and miRNA-mediated gene silencing. A particularly active topic in the field is how phosphorylation of miRISC proteins can affect miRNA loading and recruitment to miRISC, ultimately affecting functionality (Golden et al., 2017; Horman et al., 2013; Lopez-Orozco et al., 2015; McKenzie et al., 2016; Rüdel et al., 2011; Shen et al., 2013; Warner et al., 2016; Yang et al., 2014; Zeng et al., 2008). Our findings identify that phosphorylation causes AGO selection for silencing by recruitment of a LIMD1 family member and sequential assembly of AGO-TNRC6A miRISC.

EXPERIMENTAL PROCEDURES

Cell Culture

HEK293T, HeLa, and U2OS cells were routinely cultured in DMEM (Sigma) supplemented with 10% fetal calf serum (FCS), 100 U/mL penicillin, and 100 μg/mL streptomycin. Akt inhibitor MK-2206 was used at a final concentration of 10 μM in complete DMEM, for 16 hr.

Plasmids

The generation of constructs used in this study are detailed in the Supplemental Experimental Procedures.

Luciferase Reporter Assays

Firefly and Renilla luciferase activities were assayed with the Dual-Luciferase Reporter Assay System (Promega) according to the manufacturer's instructions. Further details are provided in the Supplemental Experimental Procedures.

Immunoprecipitation and Western Blotting

Routine methods to immunoprecipitate proteins were employed and detailed in the Supplemental Experimental Procedures. Antibodies used in the study are detailed in Table S2.

Expression of Recombinant Proteins and Purification

Details are provided in Supplemental Experimental Procedures.

MBP Direct Binding Assay

Details are provided in Supplemental Experimental Procedures.

GST-Pull-Down Assays

Details are provided in Supplemental Experimental Procedures.

Real-Time qPCR

Details are provided in Supplemental Experimental Procedures.

Lentiviral Line Generation

To obtain pseudotyped lentivirus (recombinant HIV-1 with vesicular stomatitis virus G [VSV-G] envelope protein), we used the gene delivery and production system developed by Naldini et al. (1996). Details for selection are in the Supplemental Experimental Procedures.

Protein Mass Spectrometry

Details are provided in Supplemental Experimental Procedures.

IF Microscopy

For analysis of miRISC protein localization, cells were fixed with 4% paraformaldehyde and stained according to standard procedures, which are detailed in the Supplemental Experimental Procedures.

PLA

PLAs were performed on HeLa cells prepared as for IF assays, including primary antibody incubation. Subsequently, Duolink In Situ PLA probes (1:10 in 2% BSA/0.025% Tween PBS) and orange detection reagents were used in accordance with the manufacturer's instructions. For negative controls, each of the primary antibodies was added with an immunoglobulin G (IgG) antibody for the corresponding antibody species (rabbit, mouse, or goat, as appropriate). PLA signal in images has been digitally intensified for visual clarity in printed figures.

CRISPR-Cas9 Cell Line Generation

LIMD1 knockout CRISPR cell lines (HeLa) were generated using the lenti-CRISPR v2 plasmid (Sanjana et al., 2014), acquired from Addgene (plasmid 52961). Further details for guide RNA sequence and clonal selection are in the Supplemental Experimental Procedures.

Quantification and Statistical Analysis

PLA interaction events were counted using the ImageJ "Analyze Particles" function. Data were stratified according to quartiles for the control condition and displayed as a stacked histogram. Statistical significance was calculated using chi-square analysis (for grouped data).

Quantification of western blots was performed by densitometric analysis using ImageJ software. For quantification of relative binding in co-immunoprecipitation assays, co-immunoprecipitated proteins were double normalized first against their input levels and second against levels of immunoprecipitated protein species. Binding data displayed are relative to WT or untreated conditions.

Statistical significance was calculated using the Student's t test, unless otherwise specified. Significance is represented as $^{*}p < 0.05$, $^{**}p < 0.001$, or $^{***}p < 0.0001$ throughout.

SUPPLEMENTAL INFORMATION

Supplemental Information includes Supplemental Experimental Procedures, seven figures, and two tables and can be found with this article online at http://dx.doi.org/10.1016/j.celrep.2017.06.027.

AUTHOR CONTRIBUTIONS

K.S.B., K.M.S., Y.L., S.C.K.W., D.E.F., D.C.M., M.R.H., M.J.P., D.L., and T.V.S. designed and performed experiments and analyzed the data. K.M.D., J.G.F., P.R.G., K.Y., R.R., P.S.R., X.W., A.A.A., and M.J.P. provided reagents, experimental advice, and design. All authors contributed to editing and proofreading the manuscript. K.S.B., K.M.S., M.J.P., D.L., and T.V.S. wrote the manuscript. T.V.S. supervised and managed all research.

ACKNOWLEDGMENTS

We thank Prof Ian MacRae and Jessica Sheu-Gruttadauria from The Scripps Research Institute, San Diego for providing purified recombinant AGO2 protein. We also thank Dr. Incheol Shin from Hanyang University in South Korea for providing the Myristoylated-Akt3 construct. K.S.B. is supported by funds from the BBSRC (Grant Code BB/L027755/1). K.M.S. was supported by funds from the BBSRC (Grant Code BB/I007571/1). J.G.F. was supported by funds from CRUK (C8932/A12733). M.J.P. is a BBSRC New Investigator (BB/N018818/1). D.L. is a Medical Research Council New Investigator Research Grant holder (MR/L008505/1) with further funding from The Wellcome Trust through the Centre for Chronic Diseases and Disorders at the University of York (097829). This work was supported by funds awarded to T.V.S. from the BBSRC (Grant Code BB/I007571/1).

Received: December 11, 2015
Revised: April 27, 2017
Accepted: June 9, 2017
Published: July 5, 2017

REFERENCES

Bartel, D.P. (2004). MicroRNAs: Genomics, biogenesis, mechanism, and function. Cell *116*, 281–297.

Bazzini, A.A., Lee, M.T., and Giraldez, A.J. (2012). Ribosome profiling shows that miR-430 reduces translation before causing mRNA decay in zebrafish. Science *336*, 233–237.

Behm-Ansmant, I., Rehwinkel, J., Doerks, T., Stark, A., Bork, P., and Izaurralde, E. (2006). mRNA degradation by miRNAs and GW182 requires both CCR4:NOT deadenylase and DCP1:DCP2 decapping complexes. Genes Dev. *20*, 1885–1898.

Chekulaeva, M., Mathys, H., Zipprich, J.T., Attig, J., Colic, M., Parker, R., and Filipowicz, W. (2011). miRNA repression involves GW182-mediated recruitment of CCR4-NOT through conserved W-containing motifs. Nat. Struct. Mol. Biol. *18*, 1218–1226.

Chen, Y., Boland, A., Kuzuoğlu-Öztürk, D., Bawankar, P., Loh, B., Chang, C.T., Weichenrieder, O., and Izaurralde, E. (2014). A DDX6-CNOT1 complex and W-binding pockets in CNOT9 reveal direct links between miRNA target recognition and silencing. Mol. Cell *54*, 737–750.

Chu, C.Y., and Rana, T.M. (2006). Translation repression in human cells by microRNA-induced gene silencing requires RCK/p54. PLoS Biol. *4*, e210.

De, N., and Macrae, I.J. (2011). Purification and assembly of human Argonaute, Dicer, and TRBP complexes. Methods Mol. Biol. *725*, 107–119.

Dueck, A., Ziegler, C., Eichner, A., Berezikov, E., and Meister, G. (2012). microRNAs associated with the different human Argonaute proteins. Nucleic Acids Res. *40*, 9850–9862.

Editorial. (2009). Beyond the diffraction limit. Nat. Photon *3*, 361–361.

Elkayam, E., Kuhn, C.D., Tocilj, A., Haase, A.D., Greene, E.M., Hannon, G.J., and Joshua-Tor, L. (2012). The structure of human argonaute-2 in complex with miR-20a. Cell *150*, 100–110.

Eulalio, A., Behm-Ansmant, I., Schweizer, D., and Izaurralde, E. (2007). P-body formation is a consequence, not the cause, of RNA-mediated gene silencing. Mol. Cell. Biol. *27*, 3970–3981.

Eulalio, A., Helms, S., Fritzsch, C., Fauser, M., and Izaurralde, E. (2009a). A C-terminal silencing domain in GW182 is essential for miRNA function. RNA *15*, 1067–1077.

Eulalio, A., Tritschler, F., and Izaurralde, E. (2009b). The GW182 protein family in animal cells: New insights into domains required for miRNA-mediated gene silencing. RNA *15*, 1433–1442.

Förstemann, K., Horwich, M.D., Wee, L., Tomari, Y., and Zamore, P.D. (2007). Drosophila microRNAs are sorted into functionally distinct argonaute complexes after production by dicer-1. Cell *130*, 287–297.

Golden, R.J., Chen, B., Li, T., Braun, J., Manjunath, H., Chen, X., Wu, J., Schmid, V., Chang, T.C., Kopp, F., et al. (2017). An Argonaute phosphorylation cycle promotes microRNA-mediated silencing. Nature *542*, 197–202.

Horman, S.R., Janas, M.M., Litterst, C., Wang, B., MacRae, I.J., Sever, M.J., Morrissey, D.V., Graves, P., Luo, B., Umesalma, S., et al. (2013). Akt-mediated phosphorylation of argonaute 2 downregulates cleavage and upregulates translational repression of MicroRNA targets. Mol. Cell *50*, 356–367.

Huntzinger, E., and Izaurralde, E. (2011). Gene silencing by microRNAs: Contributions of translational repression and mRNA decay. Nat. Rev. Genet. *12*, 99–110.

Hutvagner, G., and Simard, M.J. (2008). Argonaute proteins: Key players in RNA silencing. Nat. Rev. Mol. Cell Biol. *9*, 22–32.

James, V., Zhang, Y., Foxler, D.E., de Moor, C.H., Kong, Y.W., Webb, T.M., Self, T.J., Feng, Y., Lagos, D., Chu, C.Y., et al. (2010). LIM-domain proteins, LIMD1, Ajuba, and WTIP are required for microRNA-mediated gene silencing. Proc. Natl. Acad. Sci. USA *107*, 12499–12504.

Jee, D., and Lai, E.C. (2014). Alteration of miRNA activity via context-specific modifications of Argonaute proteins. Trends Cell Biol. *24*, 546–553.

Koch, B.J., Ryan, J.F., and Baxevanis, A.D. (2012). The diversification of the LIM superclass at the base of the metazoa increased subcellular complexity and promoted multicellular specialization. PLoS ONE *7*, e33261.

La Rocca, G., Olejniczak, S.H., González, A.J., Briskin, D., Vidigal, J.A., Spraggon, L., DeMatteo, R.G., Radler, M.R., Lindsten, T., Ventura, A., et al. (2015). In vivo, Argonaute-bound microRNAs exist predominantly in a reservoir of low molecular weight complexes not associated with mRNA. Proc. Natl. Acad. Sci. USA *112*, 767–772.

Lian, S.L., Li, S., Abadal, G.X., Pauley, B.A., Fritzler, M.J., and Chan, E.K. (2009). The C-terminal half of human Ago2 binds to multiple GW-rich regions of GW182 and requires GW182 to mediate silencing. RNA *15*, 804–813.

Liu, J., Rivas, F.V., Wohlschlegel, J., Yates, J.R., 3rd, Parker, R., and Hannon, G.J. (2005). A role for the P-body component GW182 in microRNA function. Nat. Cell Biol. *7*, 1261–1266.

Lopez-Orozco, J., Pare, J.M., Holme, A.L., Chaulk, S.G., Fahlman, R.P., and Hobman, T.C. (2015). Functional analyses of phosphorylation events in human Argonaute 2. RNA *21*, 2030–2038.

Mathys, H., Basquin, J., Ozgur, S., Czarnocki-Cieciura, M., Bonneau, F., Aartse, A., Dziembowski, A., Nowotny, M., Conti, E., and Filipowicz, W. (2014). Structural and biochemical insights to the role of the CCR4-NOT complex and DDX6 ATPase in microRNA repression. Mol. Cell *54*, 751–765.

McKenzie, A.J., Hoshino, D., Hong, N.H., Cha, D.J., Franklin, J.L., Coffey, R.J., Patton, J.G., and Weaver, A.M. (2016). KRAS-MEK Signaling Controls Ago2 Sorting into Exosomes. Cell Rep. *15*, 978–987.

Naldini, L., Blömer, U., Gallay, P., Ory, D., Mulligan, R., Gage, F.H., Verma, I.M., and Trono, D. (1996). In vivo gene delivery and stable transduction of nondividing cells by a lentiviral vector. Science *272*, 263–267.

Patranabis, S., and Bhattacharyya, S.N. (2016). Phosphorylation of Ago2 and subsequent inactivation of let-7a RNP-specific MicroRNAs control differentiation of mammalian sympathetic neurons. Mol. Cell. Biol. *36*, 1260–1271.

Petri, S., Dueck, A., Lehmann, G., Putz, N., Rüdel, S., Kremmer, E., and Meister, G. (2011). Increased siRNA duplex stability correlates with reduced off-target and elevated on-target effects. RNA *17*, 737–749.

Pfaff, J., Hennig, J., Herzog, F., Aebersold, R., Sattler, M., Niessing, D., and Meister, G. (2013). Structural features of Argonaute-GW182 protein interactions. Proc. Natl. Acad. Sci. USA *110*, E3770–E3779.

Rouya, C., Siddiqui, N., Morita, M., Duchaine, T.F., Fabian, M.R., and Sonenberg, N. (2014). Human DDX6 effects miRNA-mediated gene silencing via direct binding to CNOT1. RNA *20*, 1398–1409.

Rüdel, S., Wang, Y., Lenobel, R., Körner, R., Hsiao, H.H., Urlaub, H., Patel, D., and Meister, G. (2011). Phosphorylation of human Argonaute proteins affects small RNA binding. Nucleic Acids Res. *39*, 2330–2343.

Sahin, U., Lapaquette, P., Andrieux, A., Faure, G., and Dejean, A. (2014). Sumoylation of human argonaute 2 at lysine-402 regulates its stability. PLoS ONE *9*, e102957.

Sanjana, N.E., Shalem, O., and Zhang, F. (2014). Improved vectors and genome-wide libraries for CRISPR screening. Nat Methods. *11*, 783–784.

Schirle, N.T., and MacRae, I.J. (2012). The crystal structure of human Argonaute2. Science *336*, 1037–1040.

Shen, J., Xia, W., Khotskaya, Y.B., Huo, L., Nakanishi, K., Lim, S.O., Du, Y., Wang, Y., Chang, W.C., Chen, C.H., et al. (2013). EGFR modulates microRNA maturation in response to hypoxia through phosphorylation of AGO2. Nature *497*, 383–387.

Söderberg, O., Gullberg, M., Jarvius, M., Ridderstråle, K., Leuchowius, K.J., Jarvius, J., Wester, K., Hydbring, P., Bahram, F., Larsson, L.G., and Landegren, U. (2006). Direct observation of individual endogenous protein complexes in situ by proximity ligation. Nat. Methods *3*, 995–1000.

Song, J., Park, S., Kim, M., and Shin, I. (2008). Down-regulation of Notch-dependent transcription by Akt in vitro. FEBS Lett. *582*, 1693–1699.

Su, H., Trombly, M.I., Chen, J., and Wang, X. (2009). Essential and overlapping functions for mammalian Argonautes in microRNA silencing. Genes Dev. *23*, 304–317.

Takimoto, K., Wakiyama, M., and Yokoyama, S. (2009). Mammalian GW182 contains multiple Argonaute-binding sites and functions in microRNA-mediated translational repression. RNA *15*, 1078–1089.

Tomari, Y., Du, T., and Zamore, P.D. (2007). Sorting of Drosophila small silencing RNAs. Cell *130*, 299–308.

Valdmanis, P.N., Gu, S., Schüermann, N., Sethupathy, P., Grimm, D., and Kay, M.A. (2012). Expression determinants of mammalian argonaute proteins in mediating gene silencing. Nucleic Acids Res. *40*, 3704–3713.

Wang, D., Zhang, Z., O'Loughlin, E., Lee, T., Houel, S., O'Carroll, D., Tarakhovsky, A., Ahn, N.G., and Yi, R. (2012). Quantitative functions of Argonaute proteins in mammalian development. Genes Dev. *26*, 693–704.

Warner, M.J., Bridge, K.S., Hewitson, J.P., Hodgkinson, M.R., Heyam, A., Massa, B.C., Haslam, J.C., Chatzifrangkeskou, M., Evans, G.J., Plevin, M.J., et al. (2016). S6K2-mediated regulation of TRBP as a determinant of miRNA expression in human primary lymphatic endothelial cells. Nucleic Acids Res. *44*, 9942–9955.

Yang, M., Haase, A.D., Huang, F.K., Coulis, G., Rivera, K.D., Dickinson, B.C., Chang, C.J., Pappin, D.J., Neubert, T.A., Hannon, G.J., et al. (2014). Dephosphorylation of tyrosine 393 in argonaute 2 by protein tyrosine phosphatase 1B regulates gene silencing in oncogenic RAS-induced senescence. Mol. Cell *55*, 782–790.

Zeng, Y., Sankala, H., Zhang, X., and Graves, P.R. (2008). Phosphorylation of Argonaute 2 at serine-387 facilitates its localization to processing bodies. Biochem. J. *413*, 429–436.

Cell Reports, Volume *20*

Supplemental Information

Argonaute Utilization for miRNA Silencing Is Determined by Phosphorylation-Dependent Recruitment of LIM-Domain-Containing Proteins

Katherine S. Bridge, Kunal M. Shah, Yigen Li, Daniel E. Foxler, Sybil C.K. Wong, Duncan C. Miller, Kathryn M. Davidson, John G. Foster, Ruth Rose, Michael R. Hodgkinson, Paulo S. Ribeiro, A. Aziz Aboobaker, Kenta Yashiro, Xiaozhong Wang, Paul R. Graves, Michael J. Plevin, Dimitris Lagos, and Tyson V. Sharp

Figure S1.

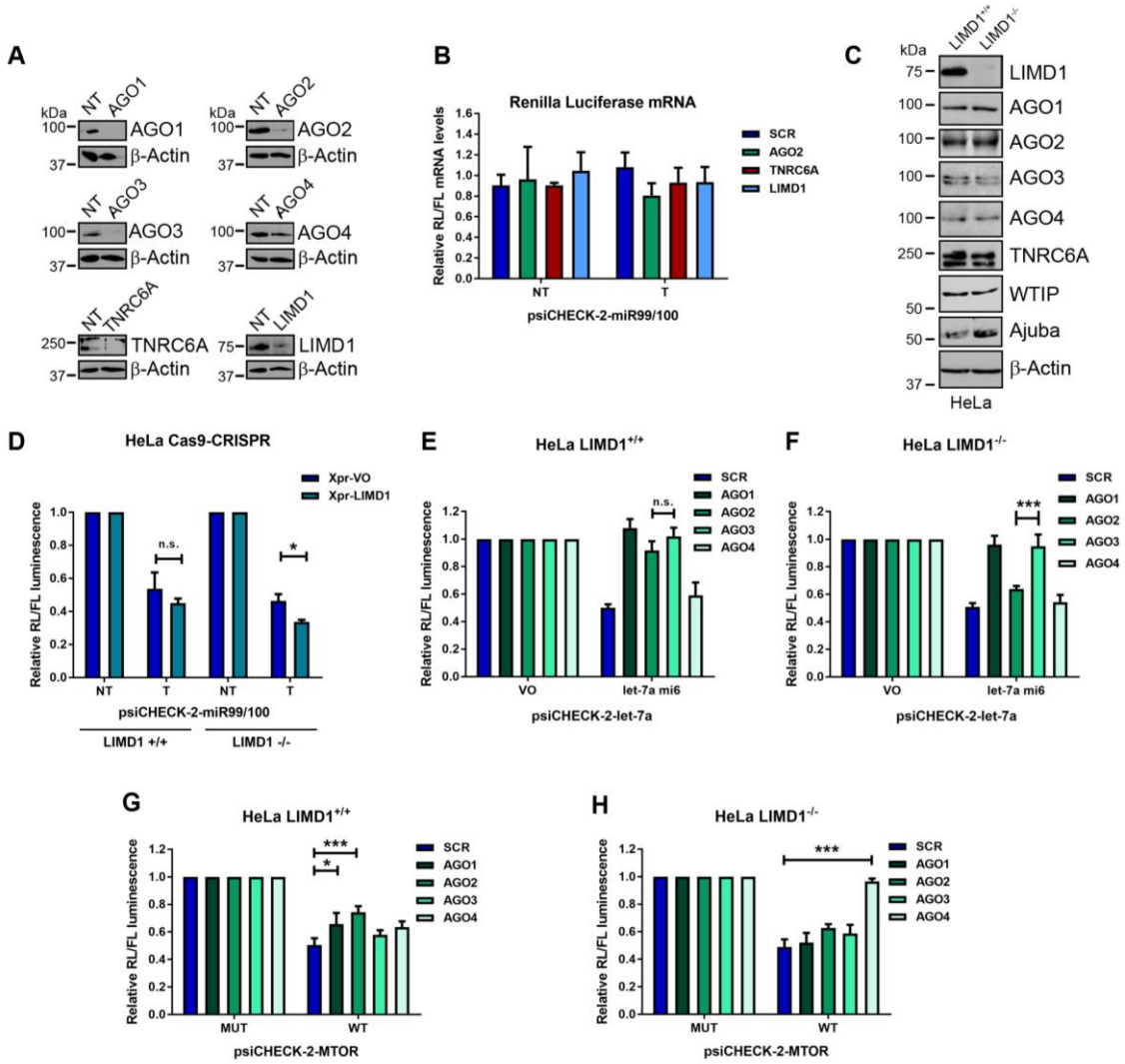

Figure S1. Related to Figure 1. Genetic ablation of LIMD1 switches AGO dependency within miRNA silenci

(A) Western blot analysis of siRNA-mediated knockdown of the indicated proteins of interest in HeLa cells. β-Act loading control. **(B)** Quantitative real-time PCR (qRT-PCR) of Renilla Luciferase (RL) mRNA levels, normalised Firefly Luciferase (FL) mRNA in HeLa cells. **(C)** Western blot analysis of the indicated proteins in CRISPR-Cas gene-edited HeLa cells; LIMD1 +/+ (Cas9 alone control) or LIMD1 -/-. **(D)** psiCHECK-2-miR-99/100 reporter assay CRISPR-Cas9 gene-edited HeLa transfected with Xpress (Xpr)-tagged vector only (VO) or LIMD1. **(** psiCHECK-2-*let-7a* (non-targeting [NT], targeting [T]) reporter in CRISPR-Cas9 gene-edited HeLa cells with Cas alone control (LIMD1$^{+/+}$) or **(F)** LIMD1 knockout (LIMD1$^{-/-}$) cells, treated with the indicated siRNAs. **(** psiCHECK-2-MTOR (endogenous mutant [MUT] or wild type [WT] 3'-UTR) reporter in CRISPR-Cas9 gene-edite HeLa cells with Cas9 alone control (LIMD1$^{+/+}$) or **(H)** LIMD1 knockout (LIMD1$^{-/-}$) cells, treated with the indicate siRNAs. Unless otherwise stated, data shown are mean ±SEM, n=3,* p<0.05, ** p<0.001, *** p<0.0001.

Figure S2.

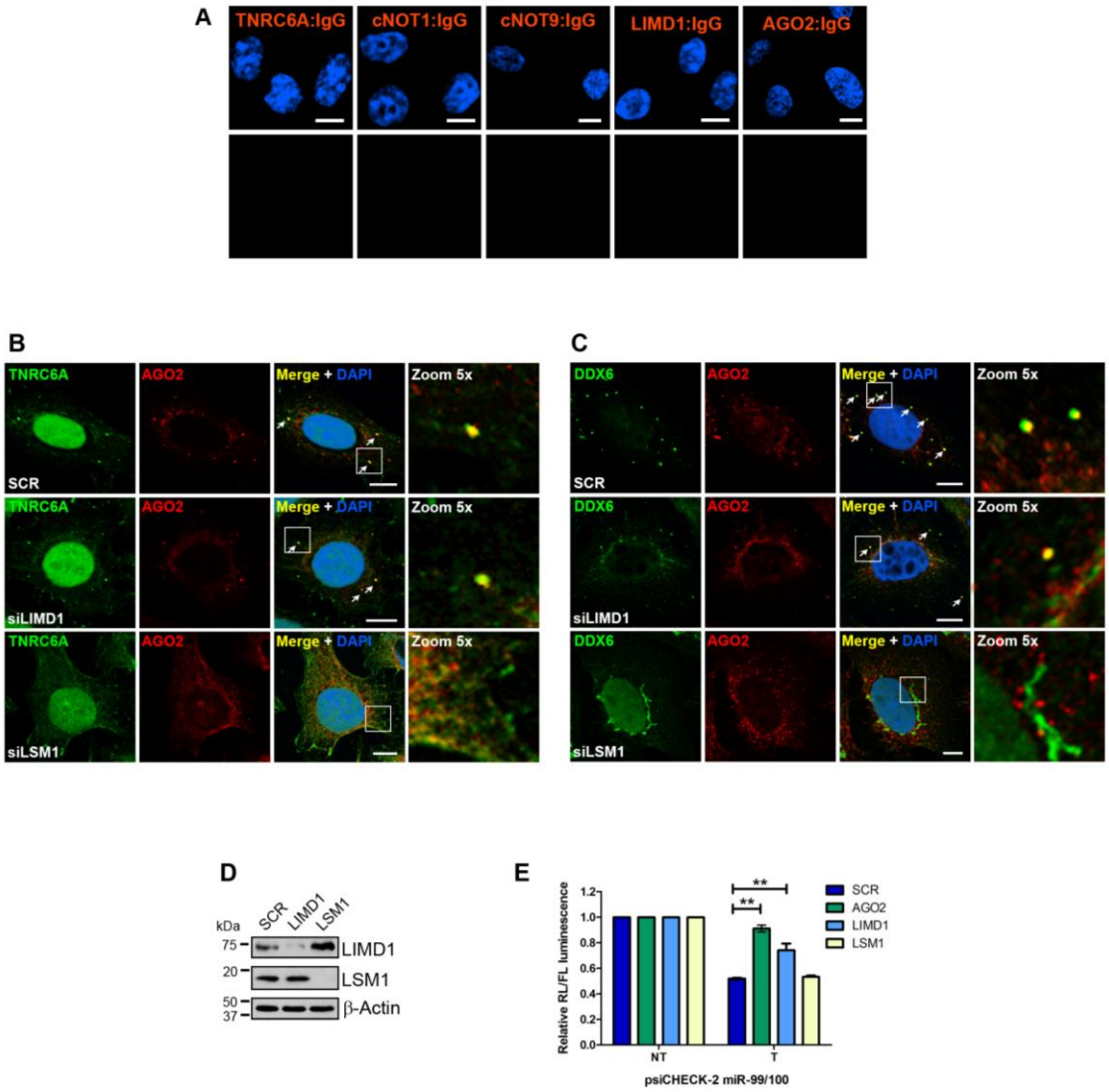

Figure S2. Related to Figure 2. Loss of P-body component LSM1 does not affect AGO2 interaction with TNRC6A/DDX6 or miRNA silencing activity.

(A) Negative control for endogenous *in situ* interaction determined by proximity ligation assay (PLA) of the indicated proteins. Cells stained with DAPI (top). **(B)** Endogenous immunofluorescence analysis of AGO2 with TNRC6A or **(C)** DDX6 in HeLa cells treated with the indicated siRNAs (SCR, non-targeting control). **(D)** Western blot analysis of HeLa cells in (B) and (C). **(E)** psiCHECK-2-miR-99/100 (NT [non-targeting], T [targeting]) reporter assay in HeLa cells treated with the indicated siRNAs. Data shown are mean ±SEM, n=3,* p<0.05, ** p<0.001, *** p<0.0001. Scale bars, 10 μm.

Figure S3.

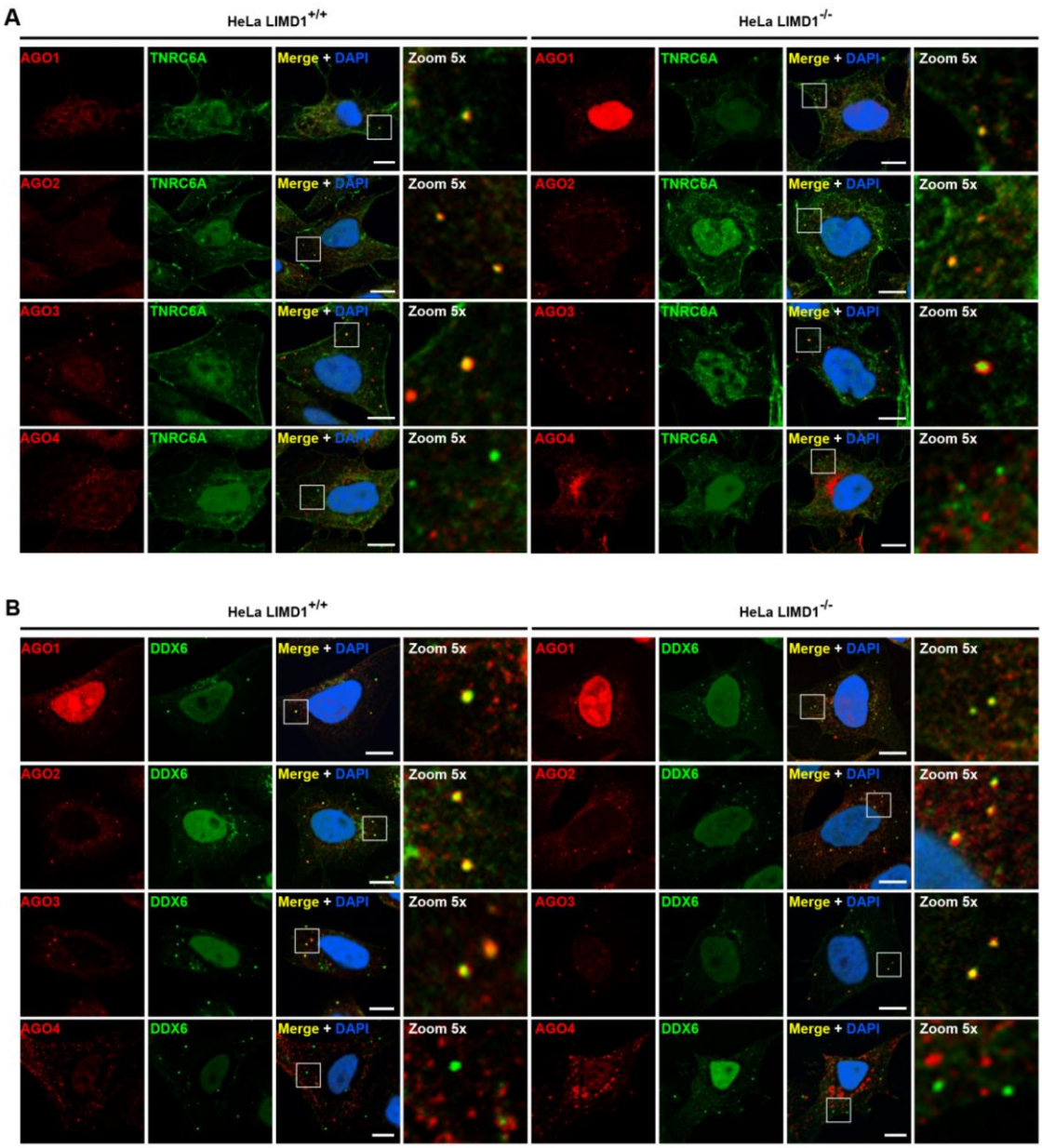

Figure S3. Related to Figure 2. Immunofluorescent colocalization of miRISC components is not a definitive indication of direct interactions.

(A) Endogenous immunofluorescence analysis in HeLa CRISPR LIMD1$^{+/+}$ and LIMD1$^{-/-}$ cells of AGO1, 2, 3 and 4 with TNRC6A and **(B)** DDX6. Scale bars, 10μm.

Figure S4.

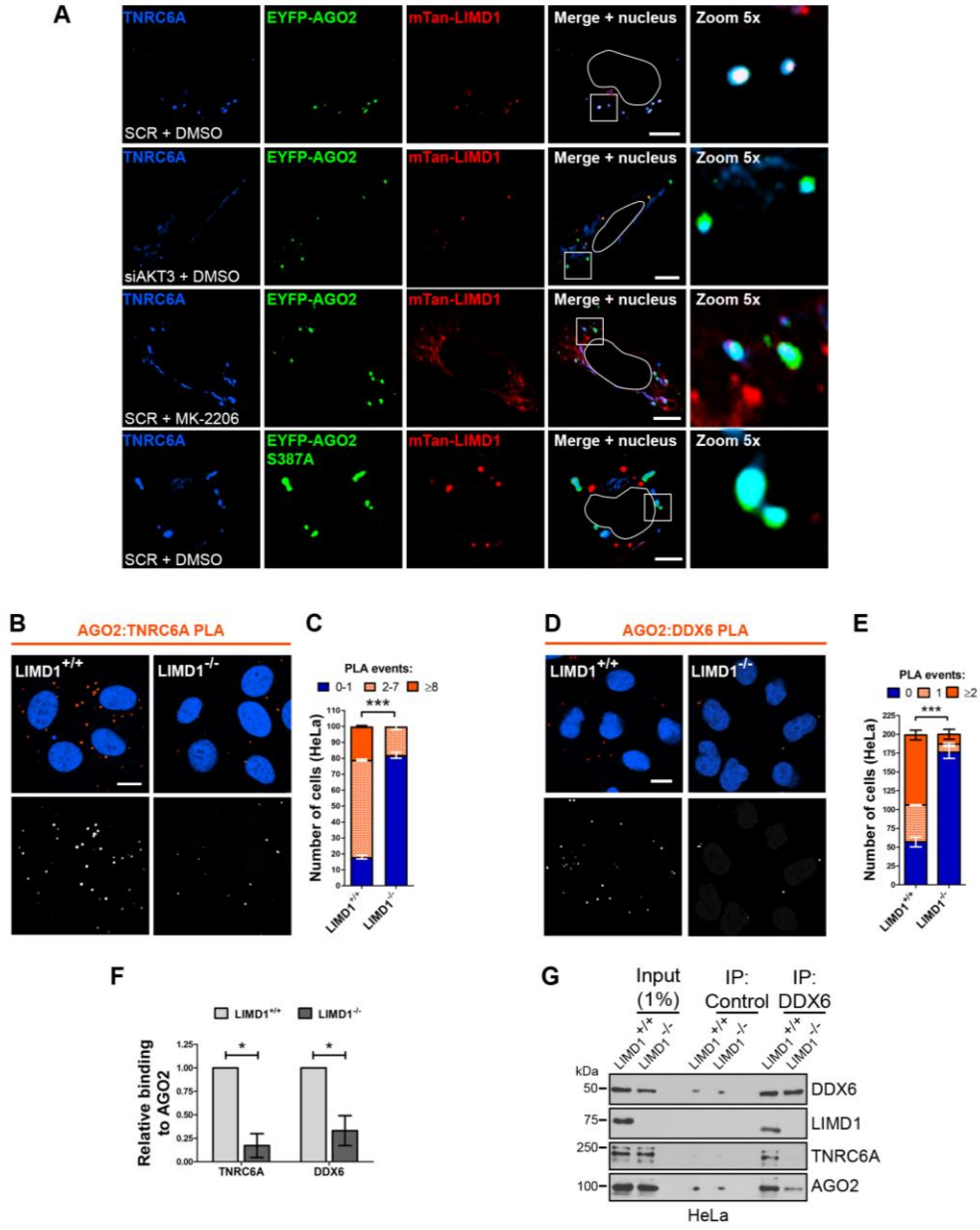

Figure S4. Related to Figure 2. Loss of LIMD1 significantly impairs AGO2 interaction with miRISC components TNRC6A and DDX6

A) Immunofluorescence of endogenous TNRC6A with EYFP-AGO2 or -AGO2 S387A and mTan-LIMD1. Cells treated with the indicated siRNAs (SCR, non-targeting control) or pan Akt-inhibitor (MK-2206). Scale bars, 10µm. **(B)** PLA analysis of endogenous AGO2 and TNRC6A interaction in CRISPR-Cas9 gene-edited HeLa cells. PLA signal orange, cells stained with DAPI (top); PLA signal white for visual clarity (bottom). **(C)** Quantification of PLA interaction events in (B), displayed as a stacked histogram. Data shown is mean ±SEM, n=3, total of 100 cells. ** $p<0.001$, *** $p<0.0001$, determined using the Chi-squared test. Scale bars, 10µm. **(D)** PLA analysis of AGO2:DDX6 interaction in above CRISPR-Cas9 gene-edited HeLa cell lines. **(E)** Quantification of (D) as in (C). **(F)** Quantification of relative binding of TNRC6A and DDX6 to AGO2 from CRISPR-Cas9 gene-edited HeLa LIMD1$^{+/+}$ or LIMD1$^{-/-}$ cells. Data shown is mean ±SEM, n=3, * $p<0.05$, determined using the Student's t-test **(G)** Immunoprecipiration of DDX6 from HeLa LIMD1$^{+/+}$ or LIMD1$^{-/-}$, analysed for the indicated proteins by western blot.

Figure S5.

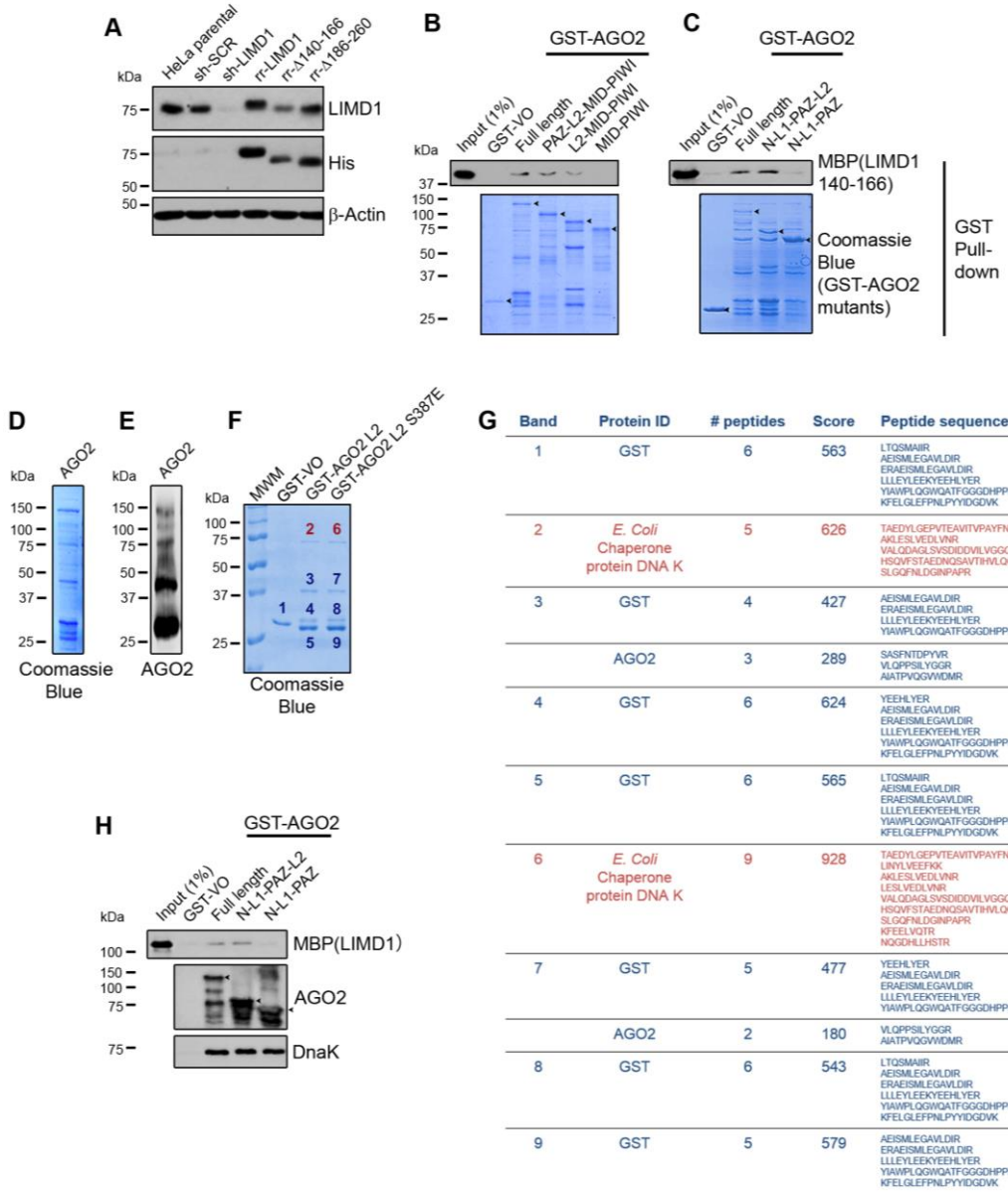

Band	Protein ID	# peptides	Score	Peptide sequences
1	GST	6	563	LTQSMAIIR AEISMLEGAVLDIR ERAEISMLEGAVLDIR LLLEYLEEKYEEHLYER YIAWPLQGWQATFGGGDHPPK KFELGLEFPNLPYYIDGDVK
2	*E. Coli* Chaperone protein DNA K	5	626	TAEDYLGEPVTEAVITVPAYFNDAQR AKLESLVEDLVNR VALQDAGLSVSDIDDVILVGGQTR HSQVFSTAEDNQSAVTIHVLQGER SLGQFNLDGINPAPR
3	GST	4	427	AEISMLEGAVLDIR ERAEISMLEGAVLDIR LLLEYLEEKYEEHLYER YIAWPLQGWQATFGGGDHPPK
	AGO2	3	289	SASFNTDPYVR VLQPPSILYGGR AIATPVQGVWDMR
4	GST	6	624	YEEHLYER AEISMLEGAVLDIR ERAEISMLEGAVLDIR LLLEYLEEKYEEHLYER YIAWPLQGWQATFGGGDHPPK KFELGLEFPNLPYYIDGDVK
5	GST	6	565	LTQSMAIIR AEISMLEGAVLDIR ERAEISMLEGAVLDIR LLLEYLEEKYEEHLYER YIAWPLQGWQATFGGGDHPPK KFELGLEFPNLPYYIDGDVK
6	*E. Coli* Chaperone protein DNA K	9	928	TAEDYLGEPVTEAVITVPAYFNDAQR LINYLVEEFKK AKLESLVEDLVNR LESLVEDLVNR VALQDAGLSVSDIDDVILVGGQTR HSQVFSTAEDNQSAVTIHVLQGER SLGQFNLDGINPAPR KFEELVQTR NQGDHLLHSTR
7	GST	5	477	YEEHLYER AEISMLEGAVLDIR ERAEISMLEGAVLDIR LLLEYLEEKYEEHLYER YIAWPLQGWQATFGGGDHPPK
	AGO2	2	180	VLQPPSILYGGR AIATPVQGVWDMR
8	GST	6	543	LTQSMAIIR AEISMLEGAVLDIR ERAEISMLEGAVLDIR LLLEYLEEKYEEHLYER YIAWPLQGWQATFGGGDHPPK KFELGLEFPNLPYYIDGDVK
9	GST	5	579	AEISMLEGAVLDIR ERAEISMLEGAVLDIR LLLEYLEEKYEEHLYER YIAWPLQGWQATFGGGDHPPK KFELGLEFPNLPYYIDGDVK

Figure S5. Related to Figure 3. LIMD1 AB-motif (a.a. 140-166) directly binds AGO2 L2 domain.
(A) sh-RNA mediated knock-down and rescue of RNAi resistant (rr) LIMD1 or deletion mutants, HeLa cell lines. sh-SCR is non-targeting control. **(B)** Direct binding assay of N-terminal and **(C)** C-terminal truncation mutants of GST-AGO2 with MBP-LIMD1 140-166 (ABD). **(D)** Purified GST-AGO2 analysed by Coomassie Blue staining and **(E)** western blot analysis for AGO2. **(F)** Degradation products of GST-AGO2 L2/ L2 S387E were identified by **(G)** mass spectrometry analysis. **(H)** DnaK identified as present in purified GST-AGO2 samples did not affect binding to LIMD1.

Figure S6.

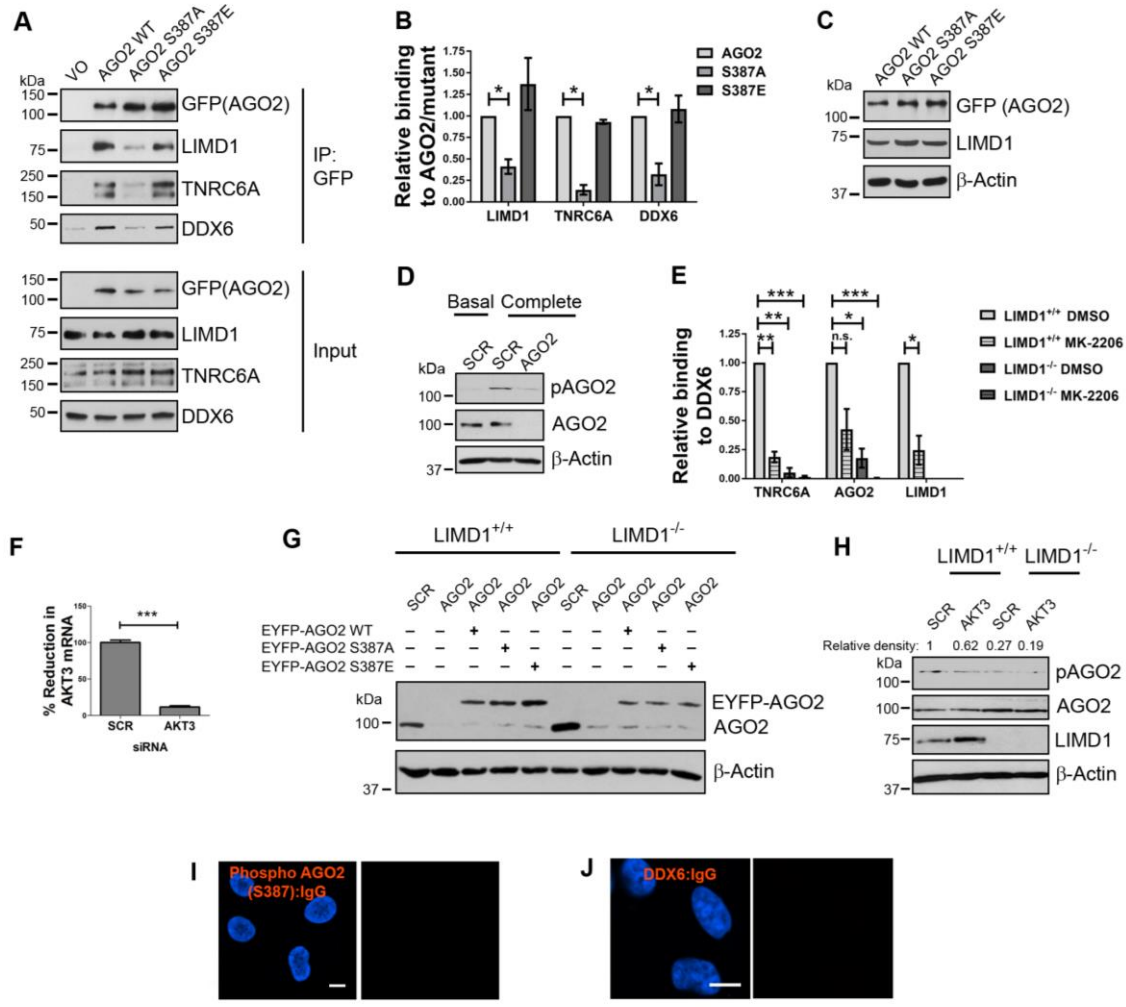

Figure S6. Related to Figures 4 and 5. Akt3-mediated phosphorylation of AGO2 S387 directs interaction with LIMD1 and recruitment of miRISC components TNRC6A and DDX6.

(A) Immunoprecipiration of GFP-VO, AGO2 and S387A/S387E point mutants from HEK293T lysate co-transfected with Xpr-LIMD1, analysed for the indicated proteins by western blot. **(B)** Quantification of co-IP in (A), data shown is mean ±SEM, n=4. **(C)** Western blot analysis of indicated overexpressed proteins in U2OS cells used for immunofluorescence analysis. β-Actin loading control. **(D)** Western blot analysis of phospho-AGO2 (S387) antibody specificity, in serum starved (basal) and complete medium conditions, treated with the indicated siRNAs. **(E)** Quantification of TNRC6A, AGO2 and LIMD1 interaction with DDX6 immunoprecipitated from HeLa LIMD1$^{+/+}$ or LIMD1$^{-/-}$ cells treated with DMSO or MK-2206. **(F)** qRT-PCR analysis of AKT3 mRNA in U2OS upon treatment with non-targeting (SCR) or AKT3 siRNA. **(G)** Western blot analysis of Cas9 control (LIMD1$^{+/+}$) and LIMD1$^{-/-}$ HeLa cell lines transfected with the indicated siRNAs and EYFP-VO/AGO2 constructs. AGO2 antibody detects both endogenous and EYFP-tagged AGO2. β-Actin loading control. **(H)** Western blot analysis of above HeLa CRISPR-Cas9 cell lines transfected with non-targeting (SCR) or AKT3 siRNA. Density of phospho-AGO2 (S387) band is calculated relative to SCR in the LIMD1$^{+/+}$ line. **(I)** Negative control PLA for the Phospho-S387-Ago2 antibody performed with goat IgG. PLA signal orange, cells stained with DAPI (top); PLA signal white for visual clarity (bottom). **(J)** Negative control PLA for the DDX6 antibody performed with rabbit IgG. Unless otherwise stated, data shown is mean ±SEM, n=3, * p<0.05, ** p<0.01, *** p<0.001, n.s. = not significant. Scale bars, 10μm.

Figure S7.

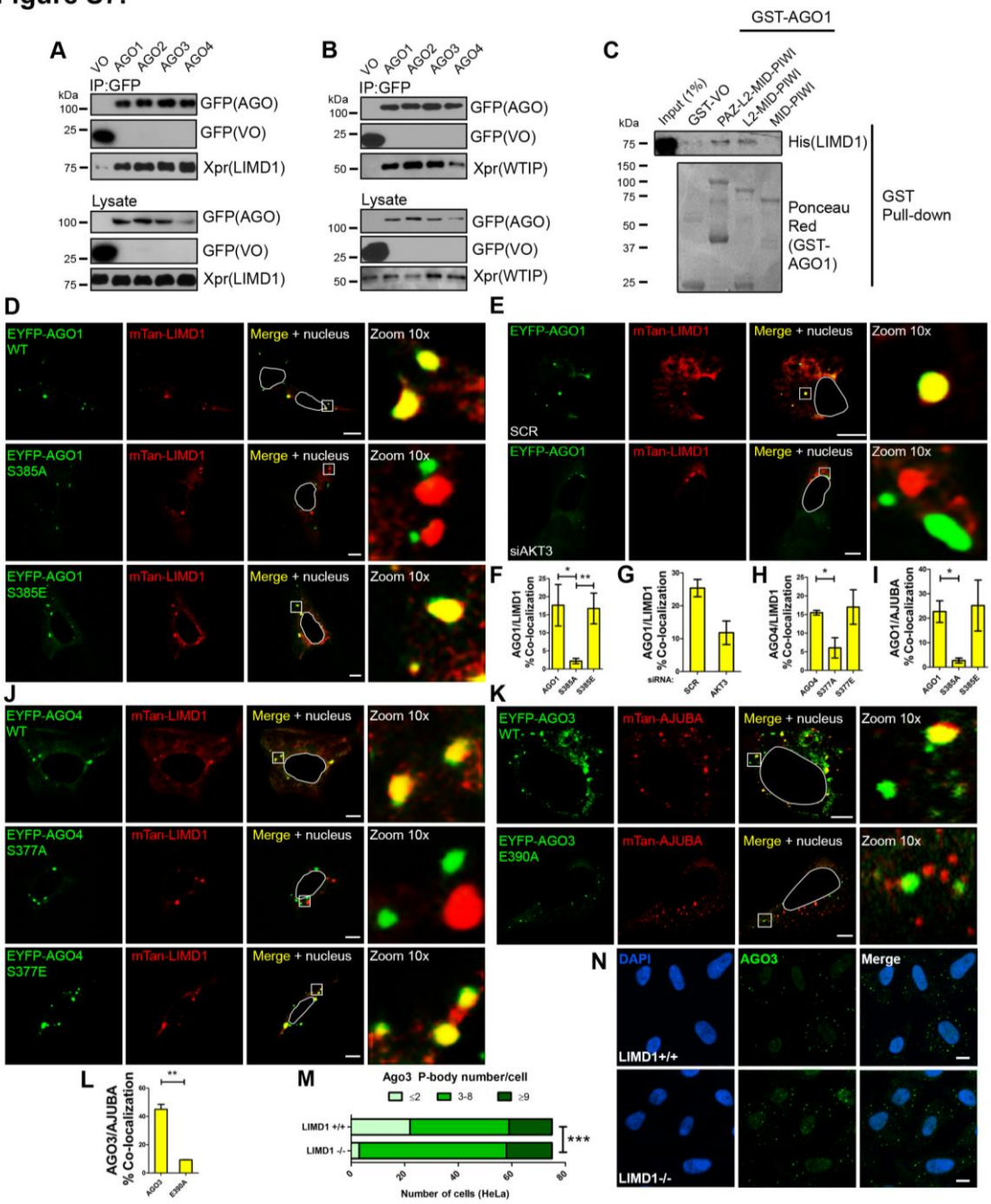

Figure S7. Related to Figures 6 and 7. AGO1-4 interact with LIMD1/Ajuba/WTIP in a phospho-dependent mechanism.

(A) Xpress-tagged (Xpr) LIMD1 co-immunoprecipitates with GFP-AGO1-4 from HEK293T lysate. **(B)** Xpr-WTIP co-IPs with GFP-AGO1-3 from HEK293T lysate. **(C)** The L2 domain of purified GST-AGO1 is required to directly bind His-LIMD1. **(D)** Co-localization of EYFP-AGO1/S385 point mutants with mTan-LIMD1 in U2OS cells. Nucleus outline in white. **(E)** Co-expression of EYFP-AGO1 with mTan-LIMD1 in U20S treated with non-targeting (SCR) or AKT3 siRNA. **(F)** Quantification of (D). **(G)** Quantification of (E). **(H)** Quantification of (J). **(I)** Quantification of Ago1/point mutant colocalization with AJUBA (images not shown). **(J)** Co-localization of EYFP-AGO4/S377 point mutants with mTan-LIMD1 in U2OS cells. **(K)** Co-expression of mTan-AJUBA with EYFP-AGO3 WT/E390 point mutant. **(L)** Quantification of (K). **(M)** Stacked histogram quantification of number of AGO3 P-bodies in (N). **(N)** Immunofluorescence staining for endogenous AGO3 in HeLa CRISPR-Cas9 cell lines. DAPI, nuclear staining. Unless otherwise stated, scale bars, 10μm. $p<0.001$, *** $p<0.0001$.

Supplemental Experimental Procedures

Luciferase Reporter Assays

For siRNA knockdown experiments, cells were reverse transfected in 96 well plates with siRNA at 40 nM using INTERFERin reagent (Polyplus transfection Illkirch, France). After 48h cells were transfected with 20 ng/well of psiCheck2 plasmid using Fugene 6 reagent or Viafect reagent (Promega). After a further 24h cells were harvested in 1x Passive Lysis buffer. Lysates were assayed for Firefly and Renilla luciferase activities with the Dual-Luciferase Reporter Assay System (Promega) according to the manufacturer's instructions on the Wallac Victor2 1420 multilabel counter (Perkin-Elmer, Waltham, MA, USA).

For reporter assays without prior siRNA treatment, cells were plated in 96 well plates and 24h later transfected with the reporter plasmids as above. After 24h cells were harvested in 1x Passive Lysis buffer and assayed as above.

For reporter assays that included co-transfection of miRNA mimic, cells were transfected with reporter plasmids and miRNA mimic at 20 nM using JetPrime Reagent (Polyplus) and harvested 24h later in 1X Passive Lysis buffer.

Plasmids

Annealed oligonucleotides containing five tandem miR-99/100 sites with seed matches (T) or seed mismatches (NT) were cloned into the 3' UTR region of the Renilla luciferase cassette in psiCheck2 (Promega, WI Madison USA) using the XhoI and PmeI restriction sites. Matched sites contained the sequence 5'AGCAAGTGTAACGG**TACGGGT**A-3' (seed sequence in bold). Mismatched sites contained the sequence 5'AGCAAGTGTAACGG**TAATAAC**A-3'. For the artificial let-7a reporter six seed-matched let-7a sites were cloned into the XhoI and NotI sites of psiCheck2 5'-AACTATACAACGT**CTACCTC**A-3' (seed sequence in bold). For FGFR3 and MTOR 3'UTR reporters, the 3'UTRs were PCR amplified using Phusion PCR mastermix using human genomic DNA as a template and primers containing XhoI and PmeI sites. PCR products were cloned into XhoI and PmeI sites of psiCheck2. miR-99/100 site mutants were

generated by site-directed mutagenesis using the Q5 site directed mutagenesis kit (New England Biolabs), according to the manufacturer's instructions. psiCheck2-TGFBR2 3'UTR WT and mutant plasmids were obtained from Addgene (31882 and 31883)

pFLRu *h*LIMD1 shRNA rrLIMD1-FH construct has previously been described (Foxler et al., 2012). Deletion mutants for the rrLIMD1 were made by site directed mutagenesis.

Ligation-independent cloning was carried out as described by Eschenfeldt *et al* (Eschenfeldt et al., 2009). Briefly, PCR products were separated on 1% agarose gels and purified. pMCSG7 or pMCSG10 vectors were linearized by digestion with SspI, and pETFPP_2 by BseRI (for cloning of MBP-LIMD1). Both PCR products and vectors were then treated with T4 DNA polymerase in the presence of the specific single deoxynucleotide. The transformation was followed by the usual protocol. Positive clones were identified with colony PCR, using T7 promoter and T7 terminator primers. Positive colonies were grown in 5 ml of LB media overnight and plasmids were prepared using a Plasmid Miniprep Kit (Roche).

Plasmids expressing mTan-LIMD1, mTan-WTIP and mTan-Ajuba have been described previously (James et al., 2010). pEYFP-C1-Ago1 and Ago2 were obtained from Dr. Tariq Rana (Chu and Rana, 2006) . Ago3 and Ago4 cDNAs were cloned into the EcoRI and XbaI sites of pEYFP-C1.

Expression of recombinant proteins and purification

Recombinant plasmids containing the target clones were transformed into Rosetta (DE3) expression strain. Single colonies from each plate were transferred into 5 ml of LB and incubated at 37^{o}C, 250 rpm for 2.5 h until the optical density at 600 nm reached 0.6-0.8. IPTG was then added to reach a final concentration of 1 mmol/L to induce the protein expression at 25^{o}C overnight. After overnight expression, the bacteria were collected and frozen on dry ice. The pellets were then thawed on ice and re-suspended in RIPA buffer, followed by sonication.

The supernatant was collected after centrifugation at 4°C for 15 min at 21,500 g and stored at -80°C for later use. For MBP-tagged proteins, a small amount of supernatant was incubated with 25 µl of His-Select Nickel Affinity Gel (SIGMA, P6611) and incubated at 4°C rotating for 30 min. The resin was then washed three times with His binding buffer (50 mM Tris-HCL, pH 8.0; 500 mM NaCl; 5 mM imidazole), followed by eluting in elution buffer (50 mM Tris-HCL, pH 8.0; 500 mM NaCl; 50 mM imidazole) by rotating at 4°C overnight. After overnight incubation, the supernatant was collected after centrifugation at 4°C for 1 min at 500 g and the imidazole was reduced by Amicon Ultra (Amicon, UFC501024). The purified lysates was then stored at -20°C for later use.

MBP direct binding assay

10ul of anti-MBP magnetic beads was washed once in PBS and incubated with cell lysates at 4 °C with rotation for 30 min to conjugate the MBP-tagged proteins onto the beads. The beads was then washed three times with 200µl RIPA with vortex and applied to magnet for 30s to remove the supernatant, followed by incubating with crystallography grade un-tagged AGO2 at 4 °C with rotation for 2h. After incubation, the beads were washed three times with 500µl binding buffer with vortex and the supernatant was removed. Proteins were finally eluted in 20µl 2xSDS-PAGE sample loading buffer and then analysed by Western Blot.

GST-pulldown assays

20µl of pre-blocked Glutathione Sepharose 4B resin (GE Healthcare, 17-0756-01) was blocked at 4°C with rotation for overnight. Bacterial cell lysates were incubated with the resin at 4°C with rotation for 30min. The resin was then washed three times with 200µl RIPA with gentle vortex and centrifugation at 4 °C for 1 min, 500 g. The supernatant was carefully removed. The pre-purified MBP-tagged protein in binding buffer (150 mM NaCl, 20 mM Tris (pH 8.0), 1 mM $MgCl_2$, 0.1 % (v/v) IGEPAL CA-630 and 10 % (v/v) glycerol (Fisher Chemical, G/0650/17)) was added and incubated at 4 °C with rotation for 2 h. After incubation, the beads were washed three times with 500µl the binding buffer with vortex and centrifugation at 4 °C

for 1 min, 500 g to remove the supernatant. Proteins were finally eluted in 20µl 2xSDS-PAGE sample loading buffer and then analysed by Western Blot.

Lentiviral Line Generation

HeLa cells were transduced with viral supernatants and after three days, cells were subcultured into medium containing puromycin (1.0 µg/ml) to select for transduced cells. Medium containing puromycin was replaced every two to three days and following ten days of selection frozen stocks were made. Cells were maintained in medium containing puromycin, but when performing experiments with the lines, puromycin was removed. Western blotting was used to validate the lentiviral lines.

Immunofluorescence microscopy

For endogenous protein detection, following fixation cells were permeabilised with 0.3% Triton and blocked with 2% BSA/0.025% Tween. Primary antibodies were diluted in 2% BSA/0.025% Tween in PBS as follows: TNRC6A (1:300), AGO1 (1:400 Millipore) AGO2 (Rabbit 1:200, Goat 1:100, Mouse 1:400), AGO3 (1:400 Millipore), AGO4 (1:400 Millipore) LIMD1 (1:300), cNOT1 (1:100), cNOT9 (1:50), DDX6 (1:200), Phospho-AGO2 (1:100). Cells were washed in PBS and stained with Alexa-Fluor conjugated secondary antibodies (1:500 or 1:2000) (Life Technologies). Images were captured at x40 or x100 magnification with a Zeiss LSM 710 confocal microscope.

Immunoprecipitation

For immunoprecipitation of endogenous proteins, Dynabeads® Co-immunoprecipitation Kit including Dynabeads® M-270 Epoxy beads was used. 1.5mg of beads/IP were conjugated with 7.5µg/mg beads of immunoprecipitating antibody overnight at 37ºC with shaking. Cells were collected, centrifuged, and resuspended in P-body lysis buffer (Chu and Rana, 2006) supplemented with 'Complete' protease inhibitors (Roche) and PhosSTOP phosphatase inhibitors (Roche) at a 1:9 ratio of cell pellet weight (mg) to lysis buffer volume (µl). Lysates

were incubated on ice for 15 minutes and centrifuged at 2,600 rpm for 5 minutes. The cleared lysate was rotated at 4ºC for 30 minutes with the antibody-conjugated Dynabeads®, which were subsequently washed 4 times with unsupplemented P-body lysis buffer. Protein complexes were eluted in 2x SDS-PAGE sample buffer or 0.1M glycine pH 2.5 and analysed by western blot.

For immunoprecipitation of ectopically expressed proteins, transfected HEK293T cells were lysed by the addition of ice-cold RIPA buffer (150mM NaCl, 1%(v/v) IGEPAL-630, 0.5%(w/v) sodium deoxycholate, 0.1%(w/v) SDS, 50mM Tris, pH 8) supplemented with 'Complete' protease inhibitors (Roche) and PhosSTOP phosphatase inhibitors (Roche) and scraped using a cell scraper. Lysates were rotated at 4°C for 20min and centrifuged at 14,800 rpm for 10min to pellet debris. Protein concentration of cleared lysate was determined by Bradford assay and 500 µg of protein was used for IP. The cleared lysate was rotated at 4°C for 4h with immunoprecipitation matrix (Santa Cruz sc-45042) previously conjugated to 2µg of immunoprecipitating antibody (2% BSA/PBS, 4ºC for 2 hours). The immunoprecipitation matrix–antibody complex was then washed three times with ice-cold RIPA, and protein complexes were eluted in 5×SDS–PAGE sample buffer and analysed by Western blot.

Protein Mass Spectrometry

Protein bands were excised from the gel, destained, reduced, alkylated and digested with trypsin following standard protocols. The resulting peptide solutions were desalted using U-C18 ZipTips (Millipore) following the manufacturer's instructions. Samples were spotted directly onto the MALDI target plate in addition to matrix solution (α-Cyano-4-hydroxycinnamic acid).

MS/MS analysis was performed on a Bruker Ultraflex in positive ion, reflector mode. MS spectra were acquired in the mass range m/z 800-4000. The 10 most intense peaks in the MS spectra for each sample were then selected for MS/MS analysis. The MS/MS datawere submitted to database searching against NCBInr, using a locally running copy of the Mascot

software (Matrix Science) through a Biotools (Bruker Daltonics) interface. Scores greater than 62 indicate identity or extensive homology ($p<0.05$).

Real-time quantitative PCR

RNA was extracted from cells using TriReagent (Sigma) or Reliaprep RNA miniprep (Promega) according to manufacturers' instructions. Following treatment with DNase I, RNA was diluted and added to GoTaq 1-step RT-qPCR (Promega) reactions along with specific primers. RT-qPCR was performed on the Applied Biosystems 7500 Real-Time PCR System and relative amounts of targets were quantified using the $2^{-\Delta\Delta Ct}$ method.

CRISPR-Cas9 Cell Line Generation

The gRNA sequence (5'-GGTCTTCCAAGATCAAACTC) targets Exon 1 of LIMD1. Transduced HeLa cells were initially selected with puromycin (1 µg/ml) prior to screening of single cell colonies for LIMD1 knockout by Western blot. Genetic mutation was confirmed by Sanger sequencing of genomic DNA utilising the primers 5' GAGTAGAGGCCCTGTCAATGG and 5' CACAGATCCCAGGCTACCATC.

Chapter 12

Reference

12 Reference

1. James, V., et al., *LIM-domain proteins, LIMD1, Ajuba, and WTIP are required for microRNA-mediated gene silencing.* Proc Natl Acad Sci U S A, 2010. **107**(28): p. 12499-504.
2. Wu, X. and G. Brewer, *The regulation of mRNA stability in mammalian cells: 2.0.* Gene, 2012. **500**(1): p. 10-21.
3. Chen, C.Y. and A.B. Shyu, *Mechanisms of deadenylation-dependent decay.* Wiley Interdiscip Rev RNA, 2011. **2**(2): p. 167-83.
4. Wahle, E. and G.S. Winkler, *RNA decay machines: deadenylation by the Ccr4-not and Pan2-Pan3 complexes.* Biochim Biophys Acta, 2013. **1829**(6-7): p. 561-70.
5. Yamashita, A., et al., *Concerted action of poly(A) nucleases and decapping enzyme in mammalian mRNA turnover.* Nat Struct Mol Biol, 2005. **12**(12): p. 1054-63.
6. Siddiqui, N., et al., *Poly(A) nuclease interacts with the C-terminal domain of polyadenylate-binding protein domain from poly(A)-binding protein.* J Biol Chem, 2007. **282**(34): p. 25067-75.
7. Wolf, J., et al., *Structural basis for Pan3 binding to Pan2 and its function in mRNA recruitment and deadenylation.* EMBO J, 2014. **33**(14): p. 1514-26.
8. Brown, C.E. and A.B. Sachs, *Poly(A) tail length control in Saccharomyces cerevisiae occurs by message-specific deadenylation.* Mol Cell Biol, 1998. **18**(11): p. 6548-59.
9. Boland, A., et al., *Structure and assembly of the NOT module of the human CCR4-NOT complex.* Nat Struct Mol Biol, 2013. **20**(11): p. 1289-97.
10. Collart, M.A., *The Ccr4-Not complex is a key regulator of eukaryotic gene expression.* Wiley Interdiscip Rev RNA, 2016. **7**(4): p. 438-54.
11. Funakoshi, Y., et al., *Mechanism of mRNA deadenylation: evidence for a molecular interplay between translation termination factor eRF3 and mRNA deadenylases.* Genes Dev, 2007. **21**(23): p. 3135-48.
12. Goldstrohm, A.C., et al., *PUF protein-mediated deadenylation is catalyzed by Ccr4p.* J Biol Chem, 2007. **282**(1): p. 109-14.
13. Fabian, M.R., et al., *Structural basis for the recruitment of the human CCR4-NOT deadenylase complex by tristetraprolin.* Nat Struct Mol Biol, 2013. **20**(6): p. 735-9.
14. Siwaszek, A., M. Ukleja, and A. Dziembowski, *Proteins involved in the degradation of cytoplasmic mRNA in the major eukaryotic model systems.* RNA Biol, 2014. **11**(9): p. 1122-36.
15. Liu, Q., J.C. Greimann, and C.D. Lima, *Reconstitution, activities, and structure of the eukaryotic RNA exosome.* Cell, 2006. **127**(6): p. 1223-37.
16. Zinder, J.C. and C.D. Lima, *Targeting RNA for processing or destruction by the eukaryotic RNA exosome and its cofactors.* Genes Dev, 2017. **31**(2): p. 88-100.
17. Chen, N., et al., *Crystal structures of human DcpS in ligand-free and m7GDP-bound forms suggest a dynamic mechanism for scavenger mRNA decapping.* J Mol Biol, 2005. **347**(4): p. 707-18.

18. Taverniti, V. and B. Seraphin, *Elimination of cap structures generated by mRNA decay involves the new scavenger mRNA decapping enzyme Aph1/FHIT together with DcpS.* Nucleic Acids Res, 2015. **43**(1): p. 482-92.
19. Li, Y. and M. Kiledjian, *Regulation of mRNA decapping.* Wiley Interdiscip Rev RNA, 2010. **1**(2): p. 253-65.
20. Charenton, C., et al., *A unique surface on Pat1 C-terminal domain directly interacts with Dcp2 decapping enzyme and Xrn1 5'-3' mRNA exonuclease in yeast.* Proc Natl Acad Sci U S A, 2017. **114**(45): p. E9493-E9501.
21. Klauer, A.A. and A. van Hoof, *Degradation of mRNAs that lack a stop codon: a decade of nonstop progress.* Wiley Interdiscip Rev RNA, 2012. **3**(5): p. 649-60.
22. van Hoof, A., et al., *Exosome-mediated recognition and degradation of mRNAs lacking a termination codon.* Science, 2002. **295**(5563): p. 2262-4.
23. Chiabudini, M., et al., *Release factor eRF3 mediates premature translation termination on polylysine-stalled ribosomes in Saccharomyces cerevisiae.* Mol Cell Biol, 2014. **34**(21): p. 4062-76.
24. Saito, S., N. Hosoda, and S. Hoshino, *The Hbs1-Dom34 protein complex functions in non-stop mRNA decay in mammalian cells.* J Biol Chem, 2013. **288**(24): p. 17832-43.
25. Bracken, C.P., et al., *Global analysis of the mammalian RNA degradome reveals widespread miRNA-dependent and miRNA-independent endonucleolytic cleavage.* Nucleic Acids Res, 2011. **39**(13): p. 5658-68.
26. Tomecki, R. and A. Dziembowski, *Novel endoribonucleases as central players in various pathways of eukaryotic RNA metabolism.* RNA, 2010. **16**(9): p. 1692-724.
27. Matsushita, K., et al., *Zc3h12a is an RNase essential for controlling immune responses by regulating mRNA decay.* Nature, 2009. **458**(7242): p. 1185-90.
28. Wawro, M., et al., *Intact NYN/PIN-Like Domain is Crucial for the Degradation of Inflammation-Related Transcripts by ZC3H12D.* J Cell Biochem, 2017. **118**(3): p. 487-498.
29. Hwang, J. and L.E. Maquat, *Nonsense-mediated mRNA decay (NMD) in animal embryogenesis: to die or not to die, that is the question.* Curr Opin Genet Dev, 2011. **21**(4): p. 422-30.
30. Simms, C.L., L.L. Yan, and H.S. Zaher, *Ribosome Collision Is Critical for Quality Control during No-Go Decay.* Mol Cell, 2017. **68**(2): p. 361-373 e5.
31. Doma, M.K. and R. Parker, *Endonucleolytic cleavage of eukaryotic mRNAs with stalls in translation elongation.* Nature, 2006. **440**(7083): p. 561-4.
32. Gupta, P. and Y.R. Li, *Upf proteins: highly conserved factors involved in nonsense mRNA mediated decay.* Mol Biol Rep, 2018. **45**(1): p. 39-55.
33. Kashima, I., et al., *SMG6 interacts with the exon junction complex via two conserved EJC-binding motifs (EBMs) required for nonsense-mediated mRNA decay.* Genes Dev, 2010. **24**(21): p. 2440-50.
34. Schmidt, S.A., et al., *Identification of SMG6 cleavage sites and a preferred RNA cleavage motif by global analysis of endogenous NMD targets in human cells.* Nucleic Acids Res, 2015. **43**(1): p. 309-23.
35. Huntzinger, E., et al., *SMG6 is the catalytic endonuclease that cleaves mRNAs containing nonsense codons in metazoan.* RNA, 2008. **14**(12): p. 2609-17.

36. Houseley, J. and D. Tollervey, *The many pathways of RNA degradation.* Cell, 2009. **136**(4): p. 763-76.
37. Harigaya, Y. and R. Parker, *No-go decay: a quality control mechanism for RNA in translation.* Wiley Interdiscip Rev RNA, 2010. **1**(1): p. 132-41.
38. Mei, Q., et al., *Regulation of DNA replication-coupled histone gene expression.* Oncotarget, 2017. **8**(55): p. 95005-95022.
39. Mullen, T.E. and W.F. Marzluff, *Degradation of histone mRNA requires oligouridylation followed by decapping and simultaneous degradation of the mRNA both 5′ to 3′ and 3′ to 5′.* Genes Dev, 2008. **22**(1): p. 50-65.
40. Su, W., et al., *mRNAs containing the histone 3′ stem-loop are degraded primarily by decapping mediated by oligouridylation of the 3′ end.* RNA, 2013. **19**(1): p. 1-16.
41. Balistreri, G., et al., *The host nonsense-mediated mRNA decay pathway restricts Mammalian RNA virus replication.* Cell Host Microbe, 2014. **16**(3): p. 403-11.
42. Wang, W., et al., *Activation of innate antiviral immune response via double-stranded RNA-dependent RLR receptor-mediated necroptosis.* Sci Rep, 2016. **6**: p. 22550.
43. DeWitte-Orr, S.J., et al., *Long double-stranded RNA induces an antiviral response independent of IFN regulatory factor 3, IFN-beta promoter stimulator 1, and IFN.* J Immunol, 2009. **183**(10): p. 6545-53.
44. Guo, Y.L., *Utilization of different anti-viral mechanisms by mammalian embryonic stem cells and differentiated cells.* Immunol Cell Biol, 2017. **95**(1): p. 17-23.
45. Chakrabarti, A., B.K. Jha, and R.H. Silverman, *New insights into the role of RNase L in innate immunity.* J Interferon Cytokine Res, 2011. **31**(1): p. 49-57.
46. Zhu, Y., et al., *Zinc-finger antiviral protein inhibits HIV-1 infection by selectively targeting multiply spliced viral mRNAs for degradation.* Proc Natl Acad Sci U S A, 2011. **108**(38): p. 15834-9.
47. Maillard, P.V., et al., *Inactivation of the type I interferon pathway reveals long double-stranded RNA-mediated RNA interference in mammalian cells.* EMBO J, 2016. **35**(23): p. 2505-2518.
48. Li, Y., et al., *RNA interference functions as an antiviral immunity mechanism in mammals.* Science, 2013. **342**(6155): p. 231-4.
49. Triboulet, R., et al., *Suppression of microRNA-silencing pathway by HIV-1 during virus replication.* Science, 2007. **315**(5818): p. 1579-82.
50. Siomi, M.C., et al., *PIWI-interacting small RNAs: the vanguard of genome defence.* Nat Rev Mol Cell Biol, 2011. **12**(4): p. 246-58.
51. Lee, R.C., R.L. Feinbaum, and V. Ambros, *The C. elegans heterochronic gene lin-4 encodes small RNAs with antisense complementarity to lin-14.* Cell, 1993. **75**(5): p. 843-54.
52. Chalfie, M., H.R. Horvitz, and J.E. Sulston, *Mutations that lead to reiterations in the cell lineages of C. elegans.* Cell, 1981. **24**(1): p. 59-69.
53. Reinhart, B.J., et al., *The 21-nucleotide let-7 RNA regulates developmental timing in Caenorhabditis elegans.* Nature, 2000. **403**(6772): p. 901-6.
54. Vella, M.C., et al., *The C. elegans microRNA let-7 binds to imperfect let-7 complementary sites from the lin-41 3'UTR.* Genes Dev, 2004. **18**(2): p. 132-7.

55. Pasquinelli, A.E., et al., *Conservation of the sequence and temporal expression of let-7 heterochronic regulatory RNA.* Nature, 2000. **408**(6808): p. 86-9.
56. Lim, L.P., et al., *The microRNAs of Caenorhabditis elegans.* Genes Dev, 2003. **17**(8): p. 991-1008.
57. Kaufman, E.J. and E.A. Miska, *The microRNAs of Caenorhabditis elegans.* Semin Cell Dev Biol, 2010. **21**(7): p. 728-37.
58. Bartel, D.P., *MicroRNAs: genomics, biogenesis, mechanism, and function.* Cell, 2004. **116**(2): p. 281-97.
59. Ozsolak, F., et al., *Chromatin structure analyses identify miRNA promoters.* Genes Dev, 2008. **22**(22): p. 3172-83.
60. Long, Y.S., et al., *Identification of the transcriptional promoters in the proximal regions of human microRNA genes.* Mol Biol Rep, 2011. **38**(6): p. 4153-7.
61. Kim, Y.K., et al., *TALEN-based knockout library for human microRNAs.* Nat Struct Mol Biol, 2013. **20**(12): p. 1458-64.
62. Lee, Y., et al., *The nuclear RNase III Drosha initiates microRNA processing.* Nature, 2003. **425**(6956): p. 415-9.
63. Han, J., et al., *The Drosha-DGCR8 complex in primary microRNA processing.* Genes Dev, 2004. **18**(24): p. 3016-27.
64. Ha, M. and V.N. Kim, *Regulation of microRNA biogenesis.* Nat Rev Mol Cell Biol, 2014. **15**(8): p. 509-24.
65. Noland, C.L. and J.A. Doudna, *Multiple sensors ensure guide strand selection in human RNAi pathways.* RNA, 2013. **19**(5): p. 639-48.
66. Kok, K.H., et al., *Human TRBP and PACT directly interact with each other and associate with dicer to facilitate the production of small interfering RNA.* J Biol Chem, 2007. **282**(24): p. 17649-57.
67. Tomari, Y. and P.D. Zamore, *Perspective: machines for RNAi.* Genes Dev, 2005. **19**(5): p. 517-29.
68. Ghildiyal, M., et al., *Sorting of Drosophila small silencing RNAs partitions microRNA* strands into the RNA interference pathway.* RNA, 2010. **16**(1): p. 43-56.
69. Guo, L. and Z. Lu, *The fate of miRNA* strand through evolutionary analysis: implication for degradation as merely carrier strand or potential regulatory molecule?* PLoS One, 2010. **5**(6): p. e11387.
70. Guo, L., et al., *Selected isomiR expression profiles via arm switching?* Gene, 2014. **533**(1): p. 149-55.
71. Wu, Z., et al., *Differential effects of miR-34c-3p and miR-34c-5p on the proliferation, apoptosis and invasion of glioma cells.* Oncol Lett, 2013. **6**(5): p. 1447-1452.
72. Mack, G.S., *MicroRNA gets down to business.* Nat Biotechnol, 2007. **25**(6): p. 631-8.
73. Leuschner, P.J., et al., *Cleavage of the siRNA passenger strand during RISC assembly in human cells.* EMBO Rep, 2006. **7**(3): p. 314-20.
74. Ghildiyal, M., et al., *Endogenous siRNAs derived from transposons and mRNAs in Drosophila somatic cells.* Science, 2008. **320**(5879): p. 1077-81.
75. Okamura, K., et al., *The Drosophila hairpin RNA pathway generates endogenous short interfering RNAs.* Nature, 2008. **453**(7196): p. 803-6.

76. Chapman, E.J. and J.C. Carrington, *Specialization and evolution of endogenous small RNA pathways.* Nat Rev Genet, 2007. **8**(11): p. 884-96.
77. Rand, T.A., et al., *Argonaute2 cleaves the anti-guide strand of siRNA during RISC activation.* Cell, 2005. **123**(4): p. 621-9.
78. MacRae, I.J., et al., *In vitro reconstitution of the human RISC-loading complex.* Proc Natl Acad Sci U S A, 2008. **105**(2): p. 512-7.
79. Braun, J.E., E. Huntzinger, and E. Izaurralde, *The role of GW182 proteins in miRNA-mediated gene silencing.* Adv Exp Med Biol, 2013. **768**: p. 147-63.
80. Meister, G., *Argonaute proteins: functional insights and emerging roles.* Nat Rev Genet, 2013. **14**(7): p. 447-59.
81. Wilson, R.C. and J.A. Doudna, *Molecular mechanisms of RNA interference.* Annu Rev Biophys, 2013. **42**: p. 217-39.
82. Bernstein, E., et al., *Role for a bidentate ribonuclease in the initiation step of RNA interference.* Nature, 2001. **409**(6818): p. 363-6.
83. Lee, Y.S., et al., *Distinct roles for Drosophila Dicer-1 and Dicer-2 in the siRNA/miRNA silencing pathways.* Cell, 2004. **117**(1): p. 69-81.
84. Zhang, H., et al., *Single processing center models for human Dicer and bacterial RNase III.* Cell, 2004. **118**(1): p. 57-68.
85. Tahbaz, N., et al., *Characterization of the interactions between mammalian PAZ PIWI domain proteins and Dicer.* EMBO Rep, 2004. **5**(2): p. 189-94.
86. MacRae, I.J., K. Zhou, and J.A. Doudna, *Structural determinants of RNA recognition and cleavage by Dicer.* Nat Struct Mol Biol, 2007. **14**(10): p. 934-40.
87. Kim, Y.K., B. Kim, and V.N. Kim, *Re-evaluation of the roles of DROSHA, Export in 5, and DICER in microRNA biogenesis.* Proc Natl Acad Sci U S A, 2016. **113**(13): p. E1881-9.
88. Tokumaru, S., et al., *let-7 regulates Dicer expression and constitutes a negative feedback loop.* Carcinogenesis, 2008. **29**(11): p. 2073-7.
89. Nam, Y., et al., *Molecular basis for interaction of let-7 microRNAs with Lin28.* Cell, 2011. **147**(5): p. 1080-91.
90. Wang, L., et al., *LIN28 Zinc Knuckle Domain Is Required and Sufficient to Induce let-7 Oligouridylation.* Cell Rep, 2017. **18**(11): p. 2664-2675.
91. Eystathioy, T., et al., *A phosphorylated cytoplasmic autoantigen, GW182, associates with a unique population of human mRNAs within novel cytoplasmic speckles.* Mol Biol Cell, 2002. **13**(4): p. 1338-51.
92. Meister, G., et al., *Identification of novel argonaute-associated proteins.* Curr Biol, 2005. **15**(23): p. 2149-55.
93. Schneider, M.D., et al., *Gawky is a component of cytoplasmic mRNA processing bodies required for early Drosophila development.* J Cell Biol, 2006. **174**(3): p. 349-58.
94. Rehwinkel, J., et al., *A crucial role for GW182 and the DCP1:DCP2 decapping complex in miRNA-mediated gene silencing.* RNA, 2005. **11**(11): p. 1640-7.
95. Ding, L., et al., *The developmental timing regulator AIN-1 interacts with miRISCs and may target the argonaute protein ALG-1 to cytoplasmic P bodies in C. elegans.* Mol Cell, 2005. **19**(4): p. 437-47.

96. Ding, L. and M. Han, *GW182 family proteins are crucial for microRNA-mediated gene silencing.* Trends Cell Biol, 2007. **17**(8): p. 411-6.
97. Till, S., et al., *A conserved motif in Argonaute-interacting proteins mediates functional interactions through the Argonaute PIWI domain.* Nat Struct Mol Biol, 2007. **14**(10): p. 897-903.
98. El-Shami, M., et al., *Reiterated WG/GW motifs form functionally and evolutionarily conserved ARGONAUTE-binding platforms in RNAi-related components.* Genes Dev, 2007. **21**(20): p. 2539-44.
99. Behm-Ansmant, I., et al., *mRNA degradation by miRNAs and GW182 requires both CCR4:NOT deadenylase and DCP1:DCP2 decapping complexes.* Genes Dev, 2006. **20**(14): p. 1885-98.
100. Jakymiw, A., et al., *Disruption of GW bodies impairs mammalian RNA interference.* Nat Cell Biol, 2005. **7**(12): p. 1267-74.
101. Parker, R. and U. Sheth, *P bodies and the control of mRNA translation and degradation.* Mol Cell, 2007. **25**(5): p. 635-46.
102. Valencia-Sanchez, M.A., et al., *Control of translation and mRNA degradation by miRNAs and siRNAs.* Genes Dev, 2006. **20**(5): p. 515-24.
103. Eulalio, A., E. Huntzinger, and E. Izaurralde, *GW182 interaction with Argonaute is essential for miRNA-mediated translational repression and mRNA decay.* Nat Struct Mol Biol, 2008. **15**(4): p. 346-53.
104. Eulalio, A., et al., *A C-terminal silencing domain in GW182 is essential for miRNA function.* RNA, 2009. **15**(6): p. 1067-77.
105. Carmell, M.A., et al., *The Argonaute family: tentacles that reach into RNAi, developmental control, stem cell maintenance, and tumorigenesis.* Genes Dev, 2002. **16**(21): p. 2733-42.
106. Martinez, J., et al., *Single-stranded antisense siRNAs guide target RNA cleavage in RNAi.* Cell, 2002. **110**(5): p. 563-74.
107. Yigit, E., et al., *Analysis of the C. elegans Argonaute family reveals that distinct Argonautes act sequentially during RNAi.* Cell, 2006. **127**(4): p. 747-57.
108. Dueck, A., et al., *microRNAs associated with the different human Argonaute proteins.* Nucleic Acids Res, 2012. **40**(19): p. 9850-62.
109. Schirle, N.T. and I.J. MacRae, *The crystal structure of human Argonaute2.* Science, 2012. **336**(6084): p. 1037-40.
110. Nykanen, A., B. Haley, and P.D. Zamore, *ATP requirements and small interfering RNA structure in the RNA interference pathway.* Cell, 2001. **107**(3): p. 309-21.
111. Frank, F., N. Sonenberg, and B. Nagar, *Structural basis for 5′-nucleotide base-specific recognition of guide RNA by human AGO2.* Nature, 2010. **465**(7299): p. 818-22.
112. Kiriakidou, M., et al., *An mRNA m7G cap binding-like motif within human Ago2 represses translation.* Cell, 2007. **129**(6): p. 1141-51.
113. Kinch, L.N. and N.V. Grishin, *The human Ago2 MC region does not contain an eIF4E-like mRNA cap binding motif.* Biol Direct, 2009. **4**: p. 2.
114. Shen, J., et al., *EGFR modulates microRNA maturation in response to hypoxia through phosphorylation of AGO2.* Nature, 2013. **497**(7449): p. 383-7.

115. Czech, B., et al., *Hierarchical rules for Argonaute loading in Drosophila.* Mol Cell, 2009. **36**(3): p. 445-56.
116. Lian, S.L., et al., *The C-terminal half of human Ago2 binds to multiple GW-rich regions of GW182 and requires GW182 to mediate silencing.* RNA, 2009. **15**(5): p. 804-13.
117. Liu, J., et al., *Argonaute2 is the catalytic engine of mammalian RNAi.* Science, 2004. **305**(5689): p. 1437-41.
118. Park, M.S., et al., *Human Argonaute3 has slicer activity.* Nucleic Acids Res, 2017. **45**(20): p. 11867-11877.
119. Hauptmann, J., et al., *Turning catalytically inactive human Argonaute proteins into active slicer enzymes.* Nat Struct Mol Biol, 2013. **20**(7): p. 814-7.
120. Kwak, P.B. and Y. Tomari, *The N domain of Argonaute drives duplex unwinding during RISC assembly.* Nat Struct Mol Biol, 2012. **19**(2): p. 145-51.
121. Jee, D. and E.C. Lai, *Alteration of miRNA activity via context-specific modifications of Argonaute proteins.* Trends Cell Biol, 2014. **24**(9): p. 546-53.
122. Qi, H.H., et al., *Prolyl 4-hydroxylation regulates Argonaute 2 stability.* Nature, 2008. **455**(7211): p. 421-4.
123. Wu, C., et al., *Hypoxia potentiates microRNA-mediated gene silencing through posttranslational modification of Argonaute2.* Mol Cell Biol, 2011. **31**(23): p. 4760-74.
124. Rudel, S., et al., *Phosphorylation of human Argonaute proteins affects small RNA binding.* Nucleic Acids Res, 2011. **39**(6): p. 2330-43.
125. Golden, R.J., et al., *An Argonaute phosphorylation cycle promotes microRNA-mediated silencing.* Nature, 2017. **542**(7640): p. 197-202.
126. Zeng, Y., et al., *Phosphorylation of Argonaute 2 at serine-387 facilitates its localization to processing bodies.* Biochem J, 2008. **413**(3): p. 429-36.
127. Horman, S.R., et al., *Akt-mediated phosphorylation of argonaute 2 downregulates cleavage and upregulates translational repression of MicroRNA targets.* Mol Cell, 2013. **50**(3): p. 356-67.
128. Yang, M., et al., *Dephosphorylation of tyrosine 393 in argonaute 2 by protein tyrosine phosphatase 1B regulates gene silencing in oncogenic RAS-induced senescence.* Mol Cell, 2014. **55**(5): p. 782-90.
129. Leung, A.K., et al., *Poly(ADP-ribose) regulates stress responses and microRNA activity in the cytoplasm.* Mol Cell, 2011. **42**(4): p. 489-99.
130. Smibert, P., et al., *Homeostatic control of Argonaute stability by microRNA availability.* Nat Struct Mol Biol, 2013. **20**(7): p. 789-95.
131. Elbashir, S.M., et al., *Functional anatomy of siRNAs for mediating efficient RNAi in Drosophila melanogaster embryo lysate.* EMBO J, 2001. **20**(23): p. 6877-88.
132. Jackson, A.L., et al., *Expression profiling reveals off-target gene regulation by RNAi.* Nat Biotechnol, 2003. **21**(6): p. 635-7.
133. Jackson, A.L., et al., *Widespread siRNA "off-target" transcript silencing mediated by seed region sequence complementarity.* RNA, 2006. **12**(7): p. 1179-87.
134. Birmingham, A., et al., *3′ UTR seed matches, but not overall identity, are associated with RNAi off-targets.* Nat Methods, 2006. **3**(3): p. 199-204.

135. Bashkirov, V.I., et al., *A mouse cytoplasmic exoribonuclease (mXRN1p) with preference for G4 tetraplex substrates.* J Cell Biol, 1997. **136**(4): p. 761-73.
136. Ingelfinger, D., et al., *The human LSm1-7 proteins colocalize with the mRNA-degrading enzymes Dcp1/2 and Xrnl in distinct cytoplasmic foci.* RNA, 2002. **8**(12): p. 1489-501.
137. Teixeira, D., et al., *Processing bodies require RNA for assembly and contain nontranslating mRNAs.* RNA, 2005. **11**(4): p. 371-82.
138. Chowdhury, A., J. Mukhopadhyay, and S. Tharun, *The decapping activator Lsm1p-7p-Pat1p complex has the intrinsic ability to distinguish between oligoadenylated and polyadenylated RNAs.* RNA, 2007. **13**(7): p. 998-1016.
139. Chowdhury, A. and S. Tharun, *Activation of decapping involves binding of the mRNA and facilitation of the post-binding steps by the Lsm1-7-Pat1 complex.* RNA, 2009. **15**(10): p. 1837-48.
140. Decker, C.J. and R. Parker, *P-bodies and stress granules: possible roles in the control of translation and mRNA degradation.* Cold Spring Harb Perspect Biol, 2012. **4**(9): p. a012286.
141. Yao, B., S. Li, and E.K. Chan, *Function of GW182 and GW bodies in siRNA and miRNA pathways.* Adv Exp Med Biol, 2013. **768**: p. 71-96.
142. Sen, G.L. and H.M. Blau, *Argonaute 2/RISC resides in sites of mammalian mRNA decay known as cytoplasmic bodies.* Nat Cell Biol, 2005. **7**(6): p. 633-6.
143. Andrei, M.A., et al., *A role for eIF4E and eIF4E-transporter in targeting mRNPs to mammalian processing bodies.* RNA, 2005. **11**(5): p. 717-27.
144. Chu, C.Y. and T.M. Rana, *Translation repression in human cells by microRNA-induced gene silencing requires RCK/p54.* PLoS Biol, 2006. **4**(7): p. e210.
145. Eulalio, A., et al., *P-body formation is a consequence, not the cause, of RNA-mediated gene silencing.* Mol Cell Biol, 2007. **27**(11): p. 3970-81.
146. Sheth, U. and R. Parker, *Decapping and decay of messenger RNA occur in cytoplasmic processing bodies.* Science, 2003. **300**(5620): p. 805-8.
147. Cougot, N., S. Babajko, and B. Seraphin, *Cytoplasmic foci are sites of mRNA decay in human cells.* J Cell Biol, 2004. **165**(1): p. 31-40.
148. Souquere, S., et al., *Unravelling the ultrastructure of stress granules and associated P-bodies in human cells.* J Cell Sci, 2009. **122**(Pt 20): p. 3619-26.
149. Luo, Y., Z. Na, and S.A. Slavoff, *P-Bodies: Composition, Properties, and Functions.* Biochemistry, 2018.
150. Morris, A.R., N. Mukherjee, and J.D. Keene, *Ribonomic analysis of human Pum1 reveals cis-trans conservation across species despite evolution of diverse mRNA target sets.* Mol Cell Biol, 2008. **28**(12): p. 4093-103.
151. Hubstenberger, A., et al., *P-Body Purification Reveals the Condensation of Repressed mRNA Regulons.* Mol Cell, 2017. **68**(1): p. 144-157 e5.
152. Vessey, J.P., et al., *Dendritic localization of the translational repressor Pumilio 2 and its contribution to dendritic stress granules.* J Neurosci, 2006. **26**(24): p. 6496-508.
153. Thomas, M.G., et al., *Staufen recruitment into stress granules does not affect early mRNA transport in oligodendrocytes.* Mol Biol Cell, 2005. **16**(1): p. 405-20.

154. Wang, X., et al., *N6-methyladenosine-dependent regulation of messenger RNA stability.* Nature, 2014. **505**(7481): p. 117-20.
155. Wang, X., et al., *N(6)-methyladenosine Modulates Messenger RNA Translation Efficiency.* Cell, 2015. **161**(6): p. 1388-99.
156. Aizer, A., et al., *Quantifying mRNA targeting to P-bodies in living human cells reveals their dual role in mRNA decay and storage.* J Cell Sci, 2014. **127**(Pt 20): p. 4443-56.
157. Bhattacharyya, S.N., et al., *Relief of microRNA-mediated translational repression in human cells subjected to stress.* Cell, 2006. **125**(6): p. 1111-24.
158. Arribere, J.A., J.A. Doudna, and W.V. Gilbert, *Reconsidering movement of eukaryotic mRNAs between polysomes and P bodies.* Mol Cell, 2011. **44**(5): p. 745-58.
159. Bartoli, K.M., D.L. Bishop, and W.S. Saunders, *The role of molecular microtubule motors and the microtubule cytoskeleton in stress granule dynamics.* Int J Cell Biol, 2011. **2011**: p. 939848.
160. Rajgor, D., et al., *Mammalian microtubule P-body dynamics are mediated by nesprin-1.* J Cell Biol, 2014. **205**(4): p. 457-75.
161. Leung, A.K., J.M. Calabrese, and P.A. Sharp, *Quantitative analysis of Argonaute protein reveals microRNA-dependent localization to stress granules.* Proc Natl Acad Sci U S A, 2006. **103**(48): p. 18125-30.
162. Stoecklin, G. and N. Kedersha, *Relationship of GW/P-bodies with stress granules.* Adv Exp Med Biol, 2013. **768**: p. 197-211.
163. Ding, X.C. and H. Grosshans, *Repression of C. elegans microRNA targets at the initiation level of translation requires GW182 proteins.* EMBO J, 2009. **28**(3): p. 213-22.
164. Petersen, C.P., et al., *Short RNAs repress translation after initiation in mammalian cells.* Mol Cell, 2006. **21**(4): p. 533-42.
165. Cowling, V.H., *Regulation of mRNA cap methylation.* Biochem J, 2009. **425**(2): p. 295-302.
166. Hocine, S., R.H. Singer, and D. Grunwald, *RNA processing and export.* Cold Spring Harb Perspect Biol, 2010. **2**(12): p. a000752.
167. Wickramasinghe, V.O. and R.A. Laskey, *Control of mammalian gene expression by selective mRNA export.* Nat Rev Mol Cell Biol, 2015. **16**(7): p. 431-42.
168. Jackson, R.J., C.U. Hellen, and T.V. Pestova, *The mechanism of eukaryotic translation initiation and principles of its regulation.* Nat Rev Mol Cell Biol, 2010. **11**(2): p. 113-27.
169. Passmore, L.A., et al., *The eukaryotic translation initiation factors eIF1 and eIF1A induce an open conformation of the 40S ribosome.* Mol Cell, 2007. **26**(1): p. 41-50.
170. Kimball, S.R., *Eukaryotic initiation factor eIF2.* Int J Biochem Cell Biol, 1999. **31**(1): p. 25-9.
171. Yang, W. and A.G. Hinnebusch, *Identification of a regulatory subcomplex in the guanine nucleotide exchange factor eIF2B that mediates inhibition by phosphorylated eIF2.* Mol Cell Biol, 1996. **16**(11): p. 6603-16.
172. Hinnebusch, A.G., *eIF3: a versatile scaffold for translation initiation complexes.* Trends Biochem Sci, 2006. **31**(10): p. 553-62.

173. Marintchev, A., et al., *Topology and regulation of the human eIF4A/4G/4H helicase complex in translation initiation.* Cell, 2009. **136**(3): p. 447-60.
174. Rogers, G.W., Jr., et al., *Modulation of the helicase activity of eIF4A by eIF4B, eIF4H, and eIF4F.* J Biol Chem, 2001. **276**(33): p. 30914-22.
175. Lejbkowicz, F., et al., *A fraction of the mRNA 5' cap-binding protein, eukaryotic initiation factor 4E, localizes to the nucleus.* Proc Natl Acad Sci U S A, 1992. **89**(20): p. 9612-6.
176. von der Haar, T., et al., *The mRNA cap-binding protein eIF4E in post-transcriptional gene expression.* Nat Struct Mol Biol, 2004. **11**(6): p. 503-11.
177. von Der Haar, T., P.D. Ball, and J.E. McCarthy, *Stabilization of eukaryotic initiation factor 4E binding to the mRNA 5'-Cap by domains of eIF4G.* J Biol Chem, 2000. **275**(39): p. 30551-5.
178. Marcotrigiano, J. and S.K. Burley, *Structural biology of eIF4F: mRNA recognition and preparation in eukaryotic translation initiation.* Adv Protein Chem, 2002. **61**: p. 269-97.
179. Das, S. and U. Maitra, *Functional significance and mechanism of eIF5-promoted GTP hydrolysis in eukaryotic translation initiation.* Prog Nucleic Acid Res Mol Biol, 2001. **70**: p. 207-31.
180. Pestova, T.V., et al., *The joining of ribosomal subunits in eukaryotes requires eIF5B.* Nature, 2000. **403**(6767): p. 332-5.
181. Chendrimada, T.P., et al., *MicroRNA silencing through RISC recruitment of eIF6.* Nature, 2007. **447**(7146): p. 823-8.
182. Ceci, M., et al., *Release of eIF6 (p27BBP) from the 60S subunit allows 80S ribosome assembly.* Nature, 2003. **426**(6966): p. 579-84.
183. Pisarev, A.V., C.U. Hellen, and T.V. Pestova, *Recycling of eukaryotic posttermination ribosomal complexes.* Cell, 2007. **131**(2): p. 286-99.
184. Alkalaeva, E.Z., et al., *In vitro reconstitution of eukaryotic translation reveals cooperativity between release factors eRF1 and eRF3.* Cell, 2006. **125**(6): p. 1125-36.
185. Jia, Y., et al., *Cap-Dependent Translation Initiation Factor eIF4E: An Emerging Anticancer Drug Target.* Med Res Rev, 2012.
186. Pestova, T.V. and V.G. Kolupaeva, *The roles of individual eukaryotic translation initiation factors in ribosomal scanning and initiation codon selection.* Genes Dev, 2002. **16**(22): p. 2906-22.
187. Komar, A.A. and M. Hatzoglou, *Cellular IRES-mediated translation: the war of ITAFs in pathophysiological states.* Cell Cycle, 2011. **10**(2): p. 229-40.
188. Park, E.H., et al., *Internal translation initiation mediated by the angiogenic factor Tie2.* J Biol Chem, 2005. **280**(22): p. 20945-53.
189. Leppek, K., R. Das, and M. Barna, *Functional 5′ UTR mRNA structures in eukaryotic translation regulation and how to find them.* Nat Rev Mol Cell Biol, 2018. **19**(3): p. 158-174.
190. Faye, M.D. and M. Holcik, *The role of IRES trans-acting factors in carcinogenesis.* Biochim Biophys Acta, 2015. **1849**(7): p. 887-97.

191. Spriggs, K.A., et al., *Canonical initiation factor requirements of the Myc family of internal ribosome entry segments.* Mol Cell Biol, 2009. **29**(6): p. 1565-74.
192. Cobbold, L.C., et al., *Upregulated c-myc expression in multiple myeloma by internal ribosome entry results from increased interactions with and expression of PTB-1 and YB-1.* Oncogene, 2010. **29**(19): p. 2884-91.
193. Somers, J., T. Poyry, and A.E. Willis, *A perspective on mammalian upstream open reading frame function.* Int J Biochem Cell Biol, 2013. **45**(8): p. 1690-700.
194. Fernandez, J., et al., *Ribosome stalling regulates IRES-mediated translation in eukaryotes, a parallel to prokaryotic attenuation.* Mol Cell, 2005. **17**(3): p. 405-16.
195. Chen, T.M., et al., *Overexpression of FGF9 in colon cancer cells is mediated by hypoxia-induced translational activation.* Nucleic Acids Res, 2014. **42**(5): p. 2932-44.
196. Ji, X., et al., *Research progress of RNA quadruplex.* Nucleic Acid Ther, 2011. **21**(3): p. 185-200.
197. Cammas, A., et al., *Stabilization of the G-quadruplex at the VEGF IRES represses cap-independent translation.* RNA Biol, 2015. **12**(3): p. 320-9.
198. Nottrott, S., M.J. Simard, and J.D. Richter, *Human let-7a miRNA blocks protein production on actively translating polyribosomes.* Nat Struct Mol Biol, 2006. **13**(12): p. 1108-14.
199. Wang, B., A. Yanez, and C.D. Novina, *MicroRNA-repressed mRNAs contain 40S but not 60S components.* Proc Natl Acad Sci U S A, 2008. **105**(14): p. 5343-8.
200. Zekri, L., et al., *The silencing domain of GW182 interacts with PABPC1 to promote translational repression and degradation of microRNA targets and is required for target release.* Mol Cell Biol, 2009. **29**(23): p. 6220-31.
201. Wakiyama, M., et al., *Let-7 microRNA-mediated mRNA deadenylation and translational repression in a mammalian cell-free system.* Genes Dev, 2007. **21**(15): p. 1857-62.
202. Way, J.C. and M. Chalfie, *mec-3, a homeobox-containing gene that specifies differentiation of the touch receptor neurons in C. elegans.* Cell, 1988. **54**(1): p. 5-16.
203. Freyd, G., S.K. Kim, and H.R. Horvitz, *Novel cysteine-rich motif and homeodomain in the product of the Caenorhabditis elegans cell lineage gene lin-11.* Nature, 1990. **344**(6269): p. 876-9.
204. Karlsson, O., et al., *Insulin gene enhancer binding protein Isl-1 is a member of a novel class of proteins containing both a homeo- and a Cys-His domain.* Nature, 1990. **344**(6269): p. 879-82.
205. Li, P.M., et al., *The LIM region of a presumptive Caenorhabditis elegans transcription factor is an iron-sulfur- and zinc-containing metallodomain.* Proc Natl Acad Sci U S A, 1991. **88**(20): p. 9210-3.
206. Michelsen, J.W., et al., *The LIM motif defines a specific zinc-binding protein domain.* Proc Natl Acad Sci U S A, 1993. **90**(10): p. 4404-8.
207. Kadrmas, J.L. and M.C. Beckerle, *The LIM domain: from the cytoskeleton to the nucleus.* Nat Rev Mol Cell Biol, 2004. **5**(11): p. 920-31.
208. Michelsen, J.W., et al., *Mutational analysis of the metal sites in an LIM domain.* J Biol Chem, 1994. **269**(15): p. 11108-13.

209. Coleman, J.E., *Zinc proteins: enzymes, storage proteins, transcription factors, and replication proteins.* Annu Rev Biochem, 1992. **61**: p. 897-946.
210. Perez-Alvarado, G.C., et al., *Structure of the carboxy-terminal LIM domain from the cysteine rich protein CRP.* Nat Struct Biol, 1994. **1**(6): p. 388-98.
211. Xue, D., Y. Tu, and M. Chalfie, *Cooperative interactions between the Caenorhabditis elegans homeoproteins UNC-86 and MEC-3.* Science, 1993. **261**(5126): p. 1324-8.
212. Zheng, Q. and Y. Zhao, *The diverse biofunctions of LIM domain proteins: determined by subcellular localization and protein-protein interaction.* Biol Cell, 2007. **99**(9): p. 489-502.
213. Macalma, T., et al., *Molecular characterization of human zyxin.* J Biol Chem, 1996. **271**(49): p. 31470-8.
214. Crawford, A.W. and M.C. Beckerle, *Purification and characterization of zyxin, an 82,000-dalton component of adherens junctions.* J Biol Chem, 1991. **266**(9): p. 5847-53.
215. Drees, B.E., K.M. Andrews, and M.C. Beckerle, *Molecular dissection of zyxin function reveals its involvement in cell motility.* J Cell Biol, 1999. **147**(7): p. 1549-60.
216. Foxler, D.E., et al., *The LIMD1 protein bridges an association between the prolyl hydroxylases and VHL to repress HIF-1 activity.* Nat Cell Biol, 2012. **14**(2): p. 201-8.
217. Sharp, T.V., et al., *LIM domains-containing protein 1 (LIMD1), a tumor suppressor encoded at chromosome 3p21.3, binds pRB and represses E2F-driven transcription.* Proc Natl Acad Sci U S A, 2004. **101**(47): p. 16531-6.
218. Feng, Y., et al., *The LIM protein, Limd1, regulates AP-1 activation through an interaction with Traf6 to influence osteoclast development.* J Biol Chem, 2007. **282**(1): p. 39-48.
219. Kiss, H., et al., *A novel gene containing LIM domains (LIMD1) is located within the common eliminated region 1 (C3CER1) in 3p21.3.* Hum Genet, 1999. **105**(6): p. 552-9.
220. Zabarovsky, E.R., M.I. Lerman, and J.D. Minna, *Tumor suppressor genes on chromosome 3p involved in the pathogenesis of lung and other cancers.* Oncogene, 2002. **21**(45): p. 6915-35.
221. Kost-Alimova, M. and S. Imreh, *Modeling non-random deletions in cancer.* Semin Cancer Biol, 2007. **17**(1): p. 19-30.
222. Wistuba, II, et al., *High resolution chromosome 3p allelotyping of human lung cancer and preneoplastic/preinvasive bronchial epithelium reveals multiple, discontinuous sites of 3p allele loss and three regions of frequent breakpoints.* Cancer Res, 2000. **60**(7): p. 1949-60.
223. Kondo, M., et al., *Overexpression of candidate tumor suppressor gene FUS1 isolated from the 3p21.3 homozygous deletion region leads to G1 arrest and growth inhibition of lung cancer cells.* Oncogene, 2001. **20**(43): p. 6258-62.
224. Lai, H.C., et al., *Hypermethylation of two consecutive tumor suppressor genes, BLU and RASSF1A, located at 3p21.3 in cervical neoplasias.* Gynecol Oncol, 2007. **104**(3): p. 629-35.
225. Hesson, L.B., W.N. Cooper, and F. Latif, *Evaluation of the 3p21.3 tumour-suppressor gene cluster.* Oncogene, 2007. **26**(52): p. 7283-301.

226. Knudsen, E.S. and K.E. Knudsen, *Tailoring to RB: tumour suppressor status and therapeutic response.* Nat Rev Cancer, 2008. **8**(9): p. 714-24.
227. Nevins, J.R., *The Rb/E2F pathway and cancer.* Hum Mol Genet, 2001. **10**(7): p. 699-703.
228. Wistuba, II, et al., *Molecular changes in the bronchial epithelium of patients with small cell lung cancer.* Clin Cancer Res, 2000. **6**(7): p. 2604-10.
229. Sharp, T.V., et al., *The chromosome 3p21.3-encoded gene, LIMD1, is a critical tumor suppressor involved in human lung cancer development.* Proc Natl Acad Sci U S A, 2008. **105**(50): p. 19932-7.
230. Spendlove, I., et al., *Differential subcellular localisation of the tumour suppressor protein LIMD1 in breast cancer correlates with patient survival.* Int J Cancer, 2008. **123**(10): p. 2247-53.
231. Huggins, C.J. and I.L. Andrulis, *Cell cycle regulated phosphorylation of LIMD1 in cell lines and expression in human breast cancers.* Cancer Lett, 2008. **267**(1): p. 55-66.
232. Ghosh, S., et al., *LIMD1 is more frequently altered than RB1 in head and neck squamous cell carcinoma: clinical and prognostic implications.* Mol Cancer, 2010. **9**: p. 58.
233. Sarkar, S., et al., *Differential molecular signature alterations of RBSP3, LIMD1 and CDC25A in normal oral epithelium during oral tumorigenesis.* Biosci Rep, 2016.
234. Hou, X., et al., *Novel BRCA2-Interacting Protein, LIMD1, Is Essential for the Centrosome Localization of BRCA2 in Esophageal Cancer Cell.* Oncol Res, 2016. **24**(4): p. 247-53.
235. Epstein, A.C., et al., *C. elegans EGL-9 and mammalian homologs define a family of dioxygenases that regulate HIF by prolyl hydroxylation.* Cell, 2001. **107**(1): p. 43-54.
236. Semenza, G.L., *HIF-1: mediator of physiological and pathophysiological responses to hypoxia.* J Appl Physiol (1985), 2000. **88**(4): p. 1474-80.
237. Bruick, R.K. and S.L. McKnight, *A conserved family of prolyl-4-hydroxylases that modify HIF.* Science, 2001. **294**(5545): p. 1337-40.
238. Jaakkola, P., et al., *Targeting of HIF-alpha to the von Hippel-Lindau ubiquitylation complex by O2-regulated prolyl hydroxylation.* Science, 2001. **292**(5516): p. 468-72.
239. Yan, Y., et al., *Ste20-related proline/alanine-rich kinase (SPAK) regulated transcriptionally by hyperosmolarity is involved in intestinal barrier function.* PLoS One, 2009. **4**(4): p. e5049.
240. Winship, P.R., *An improved method for directly sequencing PCR amplified material using dimethyl sulphoxide.* Nucleic Acids Res, 1989. **17**(3): p. 1266.
241. Eschenfeldt, W.H., et al., *A family of LIC vectors for high-throughput cloning and purification of proteins.* Methods Mol Biol, 2009. **498**: p. 105-15.
242. Edgar, R.C., *MUSCLE: a multiple sequence alignment method with reduced time and space complexity.* BMC Bioinformatics, 2004. **5**: p. 113.
243. Sanjana, N.E., O. Shalem, and F. Zhang, *Improved vectors and genome-wide libraries for CRISPR screening.* Nature methods, 2014. **11**(8): p. 783-4.
244. Paddock, S.W., *An introduction to confocal imaging.* Methods Mol Biol, 1999. **122**: p. 1-34.

245. Curtis, A.E., et al., *The Mystery of the Z-Score.* Aorta (Stamford), 2016. **4**(4): p. 124-130.
246. Sezonov, G., D. Joseleau-Petit, and R. D'Ari, *Escherichia coli physiology in Luria-Bertani broth.* J Bacteriol, 2007. **189**(23): p. 8746-9.
247. Kapust, R.B. and D.S. Waugh, *Escherichia coli maltose-binding protein is uncommonly effective at promoting the solubility of polypeptides to which it is fused.* Protein Sci, 1999. **8**(8): p. 1668-74.
248. Bornhorst, J.A. and J.J. Falke, *Purification of proteins using polyhistidine affinity tags.* Methods Enzymol, 2000. **326**: p. 245-54.
249. Schmitt, M., et al., *CD44 functions in Wnt signaling by regulating LRP6 localization and activation.* Cell Death Differ, 2015. **22**(4): p. 677-89.
250. De, N. and I.J. Macrae, *Purification and assembly of human Argonaute, Dicer, and TRBP complexes.* Methods Mol Biol, 2011. **725**: p. 107-19.
251. Iwasaki, S., et al., *Hsc70/Hsp90 chaperone machinery mediates ATP-dependent RISC loading of small RNA duplexes.* Mol Cell, 2010. **39**(2): p. 292-9.
252. Gomes, R.S., et al., *Efficient pro-survival/angiogenic miRNA delivery by an MRI-detectable nanomaterial.* ACS Nano, 2013. **7**(4): p. 3362-72.
253. Bridge, K.S., et al., *Argonaute Utilization for miRNA Silencing Is Determined by Phosphorylation-Dependent Recruitment of LIM-Domain-Containing Proteins.* Cell Rep, 2017. **20**(1): p. 173-187.
254. Nishi, H., K. Hashimoto, and A.R. Panchenko, *Phosphorylation in protein-protein binding: effect on stability and function.* Structure, 2011. **19**(12): p. 1807-15.
255. La Rocca, G., et al., *In vivo, Argonaute-bound microRNAs exist predominantly in a reservoir of low molecular weight complexes not associated with mRNA.* Proc Natl Acad Sci U S A, 2015. **112**(3): p. 767-72.
256. Pfaff, J., et al., *Structural features of Argonaute-GW182 protein interactions.* Proc Natl Acad Sci U S A, 2013. **110**(40): p. E3770-9.
257. Wang, D., et al., *Quantitative functions of Argonaute proteins in mammalian development.* Genes Dev, 2012. **26**(7): p. 693-704.
258. Elkayam, E., et al., *Multivalent Recruitment of Human Argonaute by GW182.* Mol Cell, 2017. **67**(4): p. 646-658 e3.
259. Saetrom, P., et al., *Distance constraints between microRNA target sites dictate efficacy and cooperativity.* Nucleic Acids Res, 2007. **35**(7): p. 2333-42.
260. Broderick, J.A., et al., *Argonaute protein identity and pairing geometry determine cooperativity in mammalian RNA silencing.* RNA, 2011. **17**(10): p. 1858-69.
261. Flamand, M.N., et al., *A non-canonical site reveals the cooperative mechanisms of microRNA-mediated silencing.* Nucleic Acids Res, 2017. **45**(12): p. 7212-7225.
262. Azuma-Mukai, A., et al., *Characterization of endogenous human Argonautes and their miRNA partners in RNA silencing.* Proc Natl Acad Sci U S A, 2008. **105**(23): p. 7964-9.
263. Soderberg, O., et al., *Direct observation of individual endogenous protein complexes in situ by proximity ligation.* Nat Methods, 2006. **3**(12): p. 995-1000.
264. Valdmanis, P.N., et al., *Expression determinants of mammalian argonaute proteins in mediating gene silencing.* Nucleic Acids Res, 2012. **40**(8): p. 3704-13.

265. Maunoury, N. and H. Vaucheret, *AGO1 and AGO2 act redundantly in miR408-mediated Plantacyanin regulation.* PLoS One, 2011. **6**(12): p. e28729.
266. Boyce, K.J. and A. Andrianopoulos, *Ste20-related kinases: effectors of signaling and morphogenesis in fungi.* Trends Microbiol, 2011. **19**(8): p. 400-10.
267. Dan, I., N.M. Watanabe, and A. Kusumi, *The Ste20 group kinases as regulators of MAP kinase cascades.* Trends Cell Biol, 2001. **11**(5): p. 220-30.
268. Gagnon, K.B. and E. Delpire, *Molecular physiology of SPAK and OSR1: two Ste20-related protein kinases regulating ion transport.* Physiol Rev, 2012. **92**(4): p. 1577-617.
269. Kilili, G.K. and J.M. Kyriakis, *Mammalian Ste20-like kinase (Mst2) indirectly supports Raf-1/ERK pathway activity via maintenance of protein phosphatase-2A catalytic subunit levels and consequent suppression of inhibitory Raf-1 phosphorylation.* J Biol Chem, 2010. **285**(20): p. 15076-87.
270. Lin, J.L., et al., *MST4, a new Ste20-related kinase that mediates cell growth and transformation via modulating ERK pathway.* Oncogene, 2001. **20**(45): p. 6559-69.
271. Nakano, K., et al., *NESK, a member of the germinal center kinase family that activates the c-Jun N-terminal kinase pathway and is expressed during the late stages of embryogenesis.* J Biol Chem, 2000. **275**(27): p. 20533-9.
272. Johnston, A.M., et al., *SPAK, a STE20/SPS1-related kinase that activates the p38 pathway.* Oncogene, 2000. **19**(37): p. 4290-7.
273. Tassi, E., et al., *Human JIK, a novel member of the STE20 kinase family that inhibits JNK and is negatively regulated by epidermal growth factor.* J Biol Chem, 1999. **274**(47): p. 33287-95.
274. Ushiro, H., et al., *Molecular cloning and characterization of a novel Ste20-related protein kinase enriched in neurons and transporting epithelia.* Arch Biochem Biophys, 1998. **355**(2): p. 233-40.
275. DeAizpurua, H.J., et al., *Expression of mixed lineage kinase-1 in pancreatic beta-cell lines at different stages of maturation and during embryonic pancreas development.* J Biol Chem, 1997. **272**(26): p. 16364-73.
276. Yan, Y., et al., *Cloning and characterization of a new intestinal inflammation-associated colonic epithelial Ste20-related protein kinase isoform.* Biochim Biophys Acta, 2007. **1769**(2): p. 106-16.
277. Gagnon, K.B., R. England, and E. Delpire, *Characterization of SPAK and OSR1, regulatory kinases of the Na-K-2Cl cotransporter.* Mol Cell Biol, 2006. **26**(2): p. 689-98.
278. Vitari, A.C., et al., *The WNK1 and WNK4 protein kinases that are mutated in Gordon's hypertension syndrome phosphorylate and activate SPAK and OSR1 protein kinases.* Biochem J, 2005. **391**(Pt 1): p. 17-24.
279. Delpire, E. and T.M. Austin, *Kinase regulation of Na+-K+-2Cl- cotransport in primary afferent neurons.* J Physiol, 2010. **588**(Pt 18): p. 3365-73.
280. Gagnon, K.B., K. Rios, and E. Delpire, *Functional insights into the activation mechanism of Ste20-related kinases.* Cell Physiol Biochem, 2011. **28**(6): p. 1219-30.

281. Polek, T.C., M. Talpaz, and T. Spivak-Kroizman, *The TNF receptor, RELT, binds SPAK and uses it to mediate p38 and JNK activation.* Biochem Biophys Res Commun, 2006. **343**(1): p. 125-34.
282. Vitari, A.C., et al., *Functional interactions of the SPAK/OSR1 kinases with their upstream activator WNK1 and downstream substrate NKCC1.* Biochem J, 2006. **397**(1): p. 223-31.
283. Piechotta, K., et al., *Characterization of the interaction of the stress kinase SPAK with the Na+-K+-2Cl- cotransporter in the nervous system: evidence for a scaffolding role of the kinase.* J Biol Chem, 2003. **278**(52): p. 52848-56.
284. Xu, B.E., et al., *Regulation of WNK1 by an autoinhibitory domain and autophosphorylation.* J Biol Chem, 2002. **277**(50): p. 48456-62.
285. Anselmo, A.N., et al., *WNK1 and OSR1 regulate the Na+, K+, 2Cl- cotransporter in HeLa cells.* Proc Natl Acad Sci U S A, 2006. **103**(29): p. 10883-8.
286. Flatman, P.W., *Cotransporters, WNKs and hypertension: important leads from the study of monogenetic disorders of blood pressure regulation.* Clin Sci (Lond), 2007. **112**(4): p. 203-16.
287. Piechotta, K., J. Lu, and E. Delpire, *Cation chloride cotransporters interact with the stress-related kinases Ste20-related proline-alanine-rich kinase (SPAK) and oxidative stress response 1 (OSR1).* J Biol Chem, 2002. **277**(52): p. 50812-9.
288. Gagnon, K.B., R. England, and E. Delpire, *A single binding motif is required for SPAK activation of the Na-K-2Cl cotransporter.* Cell Physiol Biochem, 2007. **20**(1-4): p. 131-42.
289. Richardson, C., et al., *Activation of the thiazide-sensitive Na+-Cl- cotransporter by the WNK-regulated kinases SPAK and OSR1.* J Cell Sci, 2008. **121**(Pt 5): p. 675-84.
290. Gamba, G., *Molecular physiology and pathophysiology of electroneutral cation-chloride cotransporters.* Physiol Rev, 2005. **85**(2): p. 423-93.
291. Richardson, C. and D.R. Alessi, *The regulation of salt transport and blood pressure by the WNK-SPAK/OSR1 signalling pathway.* J Cell Sci, 2008. **121**(Pt 20): p. 3293-304.
292. Verissimo, F. and P. Jordan, *WNK kinases, a novel protein kinase subfamily in multi-cellular organisms.* Oncogene, 2001. **20**(39): p. 5562-9.
293. Wilson, F.H., et al., *Human hypertension caused by mutations in WNK kinases.* Science, 2001. **293**(5532): p. 1107-12.
294. Gagnon, K.B., R. England, and E. Delpire, *Volume sensitivity of cation-Cl- cotransporters is modulated by the interaction of two kinases: Ste20-related proline-alanine-rich kinase and WNK4.* Am J Physiol Cell Physiol, 2006. **290**(1): p. C134-42.
295. Rinehart, J., et al., *WNK2 kinase is a novel regulator of essential neuronal cation-chloride cotransporters.* J Biol Chem, 2011. **286**(34): p. 30171-80.
296. Glover, M., A.M. Zuber, and K.M. O'Shaughnessy, *Renal and brain isoforms of WNK3 have opposite effects on NCCT expression.* J Am Soc Nephrol, 2009. **20**(6): p. 1314-22.
297. Lenertz, L.Y., et al., *Properties of WNK1 and implications for other family members.* J Biol Chem, 2005. **280**(29): p. 26653-8.

298. Moriguchi, T., et al., *WNK1 regulates phosphorylation of cation-chloride-coupled cotransporters via the STE20-related kinases, SPAK and OSR1.* J Biol Chem, 2005. **280**(52): p. 42685-93.
299. Zagorska, A., et al., *Regulation of activity and localization of the WNK1 protein kinase by hyperosmotic stress.* J Cell Biol, 2007. **176**(1): p. 89-100.
300. Seyberth, H.W. and K.P. Schlingmann, *Bartter- and Gitelman-like syndromes: salt-losing tubulopathies with loop or DCT defects.* Pediatr Nephrol, 2011. **26**(10): p. 1789-802.
301. Carmosino, M., et al., *NKCC2 is activated in Milan hypertensive rats contributing to the maintenance of salt-sensitive hypertension.* Pflugers Arch, 2011. **462**(2): p. 281-91.
302. Ohta, A., et al., *Targeted disruption of the Wnk4 gene decreases phosphorylation of Na-Cl cotransporter, increases Na excretion and lowers blood pressure.* Hum Mol Genet, 2009. **18**(20): p. 3978-86.
303. Meyer, J.W., et al., *Decreased blood pressure and vascular smooth muscle tone in mice lacking basolateral Na(+)-K(+)-2Cl(-) cotransporter.* Am J Physiol Heart Circ Physiol, 2002. **283**(5): p. H1846-55.
304. Bergaya, S., et al., *WNK1 regulates vasoconstriction and blood pressure response to alpha 1-adrenergic stimulation in mice.* Hypertension, 2011. **58**(3): p. 439-45.
305. San-Cristobal, P., et al., *Angiotensin II signaling increases activity of the renal Na-Cl cotransporter through a WNK4-SPAK-dependent pathway.* Proc Natl Acad Sci U S A, 2009. **106**(11): p. 4384-9.
306. Yang, S.S., et al., *SPAK-knockout mice manifest Gitelman syndrome and impaired vasoconstriction.* J Am Soc Nephrol, 2010. **21**(11): p. 1868-77.
307. Wang, Y., et al., *From the Cover: Whole-genome association study identifies STK39 as a hypertension susceptibility gene.* Proc Natl Acad Sci U S A, 2009. **106**(1): p. 226-31.
308. Fava, C., et al., *Serine/threonine kinase 39 is a candidate gene for primary hypertension especially in women: results from two cohort studies in Swedes.* J Hypertens, 2011. **29**(3): p. 484-91.
309. Chen, L.Y., et al., *STK39 is an independent risk factor for male hypertension in Han Chinese.* Int J Cardiol, 2012. **154**(2): p. 122-7.
310. Xu, J., et al., *Lack of association between STK39 and hypertension in the Chinese population.* J Hum Hypertens, 2013. **27**(5): p. 294-7.
311. Kidambi, S., et al., *Non-replication study of a genome-wide association study for hypertension and blood pressure in African Americans.* BMC Med Genet, 2012. **13**: p. 27.
312. Shen, M.R., C.Y. Chou, and J.C. Ellory, *Volume-sensitive KCI cotransport associated with human cervical carcinogenesis.* Pflugers Arch, 2000. **440**(5): p. 751-60.
313. Shen, M.R., et al., *The KCl cotransporter isoform KCC3 can play an important role in cell growth regulation.* Proc Natl Acad Sci U S A, 2001. **98**(25): p. 14714-9.
314. Chen, Y.F., et al., *The emerging role of KCl cotransport in tumor biology.* Am J Transl Res, 2010. **2**(4): p. 345-55.

315. Giese, A. and M. Westphal, *Glioma invasion in the central nervous system.* Neurosurgery, 1996. **39**(2): p. 235-50; discussion 250-2.
316. Sontheimer, H., *An unexpected role for ion channels in brain tumor metastasis.* Exp Biol Med (Maywood), 2008. **233**(7): p. 779-91.
317. Garzon-Muvdi, T., et al., *Regulation of brain tumor dispersal by NKCC1 through a novel role in focal adhesion regulation.* PLoS Biol, 2012. **10**(5): p. e1001320.
318. Haas, B.R., et al., *With-No-Lysine Kinase 3 (WNK3) stimulates glioma invasion by regulating cell volume.* Am J Physiol Cell Physiol, 2011. **301**(5): p. C1150-60.
319. Chiu, M.H., et al., *SPAK mediates KCC3-enhanced cervical cancer tumorigenesis.* FEBS J, 2014. **281**(10): p. 2353-65.
320. Li, Z., et al., *Role of high expression levels of STK39 in the growth, migration and invasion of non-small cell type lung cancer cells.* Oncotarget, 2016. **7**(38): p. 61366-61377.
321. Qi, H., et al., *Androgens induce expression of SPAK, a STE20/SPS1-related kinase, in LNCaP human prostate cancer cells.* Mol Cell Endocrinol, 2001. **182**(2): p. 181-92.
322. Shaulian, E. and M. Karin, *AP-1 in cell proliferation and survival.* Oncogene, 2001. **20**(19): p. 2390-400.
323. Belguise, K., et al., *The PKCtheta pathway participates in the aberrant accumulation of Fra-1 protein in invasive ER-negative breast cancer cells.* Oncogene, 2012. **31**(47): p. 4889-97.
324. Hendriksen, P.J., et al., *Evolution of the androgen receptor pathway during progression of prostate cancer.* Cancer Res, 2006. **66**(10): p. 5012-20.
325. Cleator, S., et al., *Gene expression patterns for doxorubicin (Adriamycin) and cyclophosphamide (cytoxan) (AC) response and resistance.* Breast Cancer Res Treat, 2006. **95**(3): p. 229-33.
326. Ko, B., L.L. Cooke, and R.S. Hoover, *Parathyroid hormone (PTH) regulates the sodium chloride cotransporter via Ras guanyl releasing protein 1 (Ras-GRP1) and extracellular signal-regulated kinase (ERK)1/2 mitogen-activated protein kinase (MAPK) pathway.* Transl Res, 2011. **158**(5): p. 282-9.
327. Zhou, B., et al., *WNK4 inhibits NCC protein expression through MAPK ERK1/2 signaling pathway.* Am J Physiol Renal Physiol, 2012. **302**(5): p. F533-9.
328. Rincon, M. and R.J. Davis, *Regulation of the immune response by stress-activated protein kinases.* Immunol Rev, 2009. **228**(1): p. 212-24.
329. Chang, L. and M. Karin, *Mammalian MAP kinase signalling cascades.* Nature, 2001. **410**(6824): p. 37-40.
330. Kyriakis, J.M. and J. Avruch, *Mammalian MAPK signal transduction pathways activated by stress and inflammation: a 10-year update.* Physiol Rev, 2012. **92**(2): p. 689-737.
331. Pimienta, G. and J. Pascual, *Canonical and alternative MAPK signaling.* Cell Cycle, 2007. **6**(21): p. 2628-32.
332. Morrison, D.K. and R.J. Davis, *Regulation of MAP kinase signaling modules by scaffold proteins in mammals.* Annu Rev Cell Dev Biol, 2003. **19**: p. 91-118.
333. Raman, M., W. Chen, and M.H. Cobb, *Differential regulation and properties of MAPKs.* Oncogene, 2007. **26**(22): p. 3100-12.

334. Buchsbaum, R.J., B.A. Connolly, and L.A. Feig, *Interaction of Rac exchange factors Tiam1 and Ras-GRF1 with a scaffold for the p38 mitogen-activated protein kinase cascade.* Mol Cell Biol, 2002. **22**(12): p. 4073-85.
335. Kelkar, N., C.L. Standen, and R.J. Davis, *Role of the JIP4 scaffold protein in the regulation of mitogen-activated protein kinase signaling pathways.* Mol Cell Biol, 2005. **25**(7): p. 2733-43.
336. Enslen, H., J. Raingeaud, and R.J. Davis, *Selective activation of p38 mitogen-activated protein (MAP) kinase isoforms by the MAP kinase kinases MKK3 and MKK6.* J Biol Chem, 1998. **273**(3): p. 1741-8.
337. Kondoh, K. and E. Nishida, *Regulation of MAP kinases by MAP kinase phosphatases.* Biochim Biophys Acta, 2007. **1773**(8): p. 1227-37.
338. Soares-Silva, M., et al., *The Mitogen-Activated Protein Kinase (MAPK) Pathway: Role in Immune Evasion by Trypanosomatids.* Front Microbiol, 2016. **7**: p. 183.
339. Wada, T. and J.M. Penninger, *Mitogen-activated protein kinases in apoptosis regulation.* Oncogene, 2004. **23**(16): p. 2838-49.
340. Arthur, J.S. and S.C. Ley, *Mitogen-activated protein kinases in innate immunity.* Nat Rev Immunol, 2013. **13**(9): p. 679-92.
341. Yoon, S. and R. Seger, *The extracellular signal-regulated kinase: multiple substrates regulate diverse cellular functions.* Growth Factors, 2006. **24**(1): p. 21-44.
342. Hanahan, D. and R.A. Weinberg, *Hallmarks of cancer: the next generation.* Cell, 2011. **144**(5): p. 646-74.
343. Dhillon, A.S., et al., *MAP kinase signalling pathways in cancer.* Oncogene, 2007. **26**(22): p. 3279-90.
344. Garnett, M.J. and R. Marais, *Guilty as charged: B-RAF is a human oncogene.* Cancer Cell, 2004. **6**(4): p. 313-9.
345. Sebolt-Leopold, J.S. and R. Herrera, *Targeting the mitogen-activated protein kinase cascade to treat cancer.* Nat Rev Cancer, 2004. **4**(12): p. 937-47.
346. Davies, H., et al., *Mutations of the BRAF gene in human cancer.* Nature, 2002. **417**(6892): p. 949-54.
347. Roberts, P.J. and C.J. Der, *Targeting the Raf-MEK-ERK mitogen-activated protein kinase cascade for the treatment of cancer.* Oncogene, 2007. **26**(22): p. 3291-310.
348. Hui, L., et al., *Proliferation of human HCC cells and chemically induced mouse liver cancers requires JNK1-dependent p21 downregulation.* J Clin Invest, 2008. **118**(12): p. 3943-53.
349. Ouyang, X., et al., *Activator protein-1 transcription factors are associated with progression and recurrence of prostate cancer.* Cancer Res, 2008. **68**(7): p. 2132-44.
350. Yoshida, S., et al., *Head-to-head juxtaposition of Fas-associated phosphatase-1 (FAP-1) and c-Jun NH2-terminal kinase 3 (JNK3) genes: genomic structure and seven polymorphisms of the FAP-1 gene.* J Hum Genet, 2002. **47**(11): p. 614-9.
351. Wagner, E.F. and A.R. Nebreda, *Signal integration by JNK and p38 MAPK pathways in cancer development.* Nat Rev Cancer, 2009. **9**(8): p. 537-49.
352. Iyoda, K., et al., *Involvement of the p38 mitogen-activated protein kinase cascade in hepatocellular carcinoma.* Cancer, 2003. **97**(12): p. 3017-26.

353. Junttila, M.R., et al., *p38alpha and p38delta mitogen-activated protein kinase isoforms regulate invasion and growth of head and neck squamous carcinoma cells.* Oncogene, 2007. **26**(36): p. 5267-79.
354. Greenberg, A.K., et al., *Selective p38 activation in human non-small cell lung cancer.* Am J Respir Cell Mol Biol, 2002. **26**(5): p. 558-64.
355. Mantovani, A., et al., *Cancer-related inflammation.* Nature, 2008. **454**(7203): p. 436-44.
356. Kaelin, W.G., Jr., *The concept of synthetic lethality in the context of anticancer therapy.* Nat Rev Cancer, 2005. **5**(9): p. 689-98.
357. Nijman, S.M., *Synthetic lethality: general principles, utility and detection using genetic screens in human cells.* FEBS Lett, 2011. **585**(1): p. 1-6.
358. Shen, D.W., et al., *Cisplatin resistance: a cellular self-defense mechanism resulting from multiple epigenetic and genetic changes.* Pharmacol Rev, 2012. **64**(3): p. 706-21.
359. Manning, G., et al., *The protein kinase complement of the human genome.* Science, 2002. **298**(5600): p. 1912-34.
360. Lahiry, P., et al., *Kinase mutations in human disease: interpreting genotype-phenotype relationships.* Nat Rev Genet, 2010. **11**(1): p. 60-74.
361. Futreal, P.A., et al., *A census of human cancer genes.* Nat Rev Cancer, 2004. **4**(3): p. 177-83.
362. Greenman, C., et al., *Patterns of somatic mutation in human cancer genomes.* Nature, 2007. **446**(7132): p. 153-8.
363. Kan, Z., et al., *Diverse somatic mutation patterns and pathway alterations in human cancers.* Nature, 2010. **466**(7308): p. 869-73.
364. Moore, C.B., et al., *Short hairpin RNA (shRNA): design, delivery, and assessment of gene knockdown.* Methods Mol Biol, 2010. **629**: p. 141-58.
365. Golsteyn, R.M., et al., *Cell cycle regulation of the activity and subcellular localization of Plk1, a human protein kinase implicated in mitotic spindle function.* J Cell Biol, 1995. **129**(6): p. 1617-28.
366. Zitouni, S., et al., *Polo-like kinases: structural variations lead to multiple functions.* Nat Rev Mol Cell Biol, 2014. **15**(7): p. 433-52.
367. Strebhardt, K., *Multifaceted polo-like kinases: drug targets and antitargets for cancer therapy.* Nat Rev Drug Discov, 2010. **9**(8): p. 643-60.
368. Yang, H.Y., et al., *Cell type and transfection reagent-dependent effects on viability, cell content, cell cycle and inflammation of RNAi in human primary mesenchymal cells.* Eur J Pharm Sci, 2014. **53**: p. 35-44.
369. Zhang, J.D., et al., *Time-resolved human kinome RNAi screen identifies a network regulating mitotic-events as early regulators of cell proliferation.* PLoS One, 2011. **6**(7): p. e22176.
370. Huang da, W., B.T. Sherman, and R.A. Lempicki, *Systematic and integrative analysis of large gene lists using DAVID bioinformatics resources.* Nat Protoc, 2009. **4**(1): p. 44-57.

371. Huang da, W., B.T. Sherman, and R.A. Lempicki, *Bioinformatics enrichment tools: paths toward the comprehensive functional analysis of large gene lists.* Nucleic Acids Res, 2009. **37**(1): p. 1-13.
372. Kanehisa, M., et al., *KEGG: new perspectives on genomes, pathways, diseases and drugs.* Nucleic Acids Res, 2017. **45**(D1): p. D353-D361.
373. Zarubin, T. and J. Han, *Activation and signaling of the p38 MAP kinase pathway.* Cell Res, 2005. **15**(1): p. 11-8.
374. Schmierer, B. and C.S. Hill, *TGFbeta-SMAD signal transduction: molecular specificity and functional flexibility.* Nat Rev Mol Cell Biol, 2007. **8**(12): p. 970-82.
375. Zhao, F., et al., *MicroRNA-26b inhibits hepatitis B virus transcription and replication by targeting the host factor CHORDC1 protein.* J Biol Chem, 2014. **289**(50): p. 35029-41.
376. Feng, X.H. and R. Derynck, *Specificity and versatility in tgf-beta signaling through Smads.* Annu Rev Cell Dev Biol, 2005. **21**: p. 659-93.
377. Yoo, J., et al., *Transforming growth factor-beta-induced apoptosis is mediated by Smad-dependent expression of GADD45b through p38 activation.* J Biol Chem, 2003. **278**(44): p. 43001-7.
378. Clements, M., et al., *Crosstalk between Nodal/activin and MAPK p38 signaling is essential for anterior-posterior axis specification.* Curr Biol, 2011. **21**(15): p. 1289-95.
379. Yamashita, M., et al., *TRAF6 mediates Smad-independent activation of JNK and p38 by TGF-beta.* Mol Cell, 2008. **31**(6): p. 918-24.
380. Suwaki, N., et al., *A HIF-regulated VHL-PTP1B-Src signaling axis identifies a therapeutic target in renal cell carcinoma.* Sci Transl Med, 2011. **3**(85): p. 85ra47.
381. Bandarra, D., et al., *HIF-1alpha restricts NF-kappaB-dependent gene expression to control innate immunity signals.* Dis Model Mech, 2015. **8**(2): p. 169-81.
382. Xi, B., et al., *STK39 polymorphism is associated with essential hypertension: a systematic review and meta-analysis.* PLoS One, 2013. **8**(3): p. e59584.
383. Huang, Y.T., et al., *Genome-wide analysis of survival in early-stage non-small-cell lung cancer.* J Clin Oncol, 2009. **27**(16): p. 2660-7.
384. Hornbeck, P.V., et al., *PhosphoSite: A bioinformatics resource dedicated to physiological protein phosphorylation.* Proteomics, 2004. **4**(6): p. 1551-61.
385. Kulshreshtha, R., et al., *A microRNA signature of hypoxia.* Mol Cell Biol, 2007. **27**(5): p. 1859-67.
386. McMahon, S., et al., *Transforming growth factor beta1 induces hypoxia-inducible factor-1 stabilization through selective inhibition of PHD2 expression.* J Biol Chem, 2006. **281**(34): p. 24171-81.